



Universiteit Gent
Faculteit Wetenschappen

A combined EMR and DFT study of radiation-induced defects in sucrose and glucose 1-phosphate

door

Hendrik De Cooman

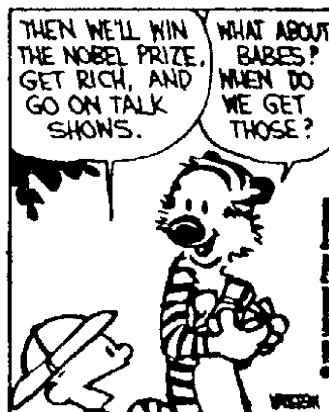
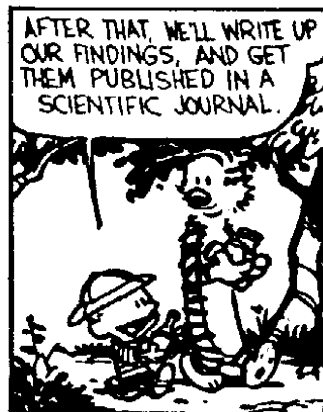
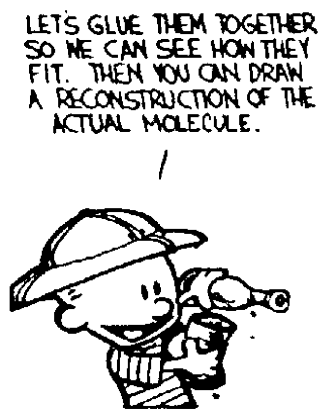
Promotoren:

prof. dr. Freddy Callens (Vakgroep Vastestofwetenschappen)
prof. dr. Michel Waroquier (Centrum voor Moleculaire Modelling)

Proefschrift voorgelegd tot het behalen van de graad van
Doctor in de wetenschappen: fysica

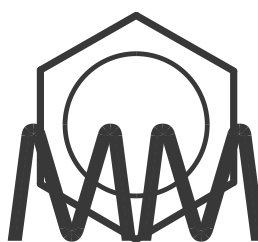
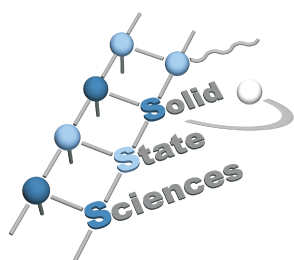
Academiejaar 2008-2009

CALVIN AND HOBBS



Physics is like sex. Sure, it may give some practical results, but that's not why we do it.

R. P. Feynman



This research was conducted at the Ghent University in the EPR/ENDOR research group at the Department of Solid State Sciences and in the Center for Molecular Modeling, and was supervised by prof. dr. Freddy Callens and prof. dr. Michel Waroquier.

Leden van de examencommissie

Voorzitter

prof. dr. Jan Ryckebusch (Universiteit Gent, WE05)

Leescommissie

prof. dr. Freddy Callens (Universiteit Gent, WE04)

prof. dr. Frank De Proft (Vrije Universiteit Brussel)

prof. dr. Einar Sagstuen (University of Oslo)

prof. dr. Sabine Van Doorslaer (Universiteit Antwerpen)

prof. dr. Michel Waroquier (Universiteit Gent, WE05)

Overige leden

prof. dr. Paul Clauws (Universiteit Gent, WE04)

dr. Ewald Pauwels (Universiteit Gent, WE05)

prof. dr. ir. Veronique Van Speybroeck (Universiteit Gent, IR17)

dr. ir. Henk Vrielinck (Universiteit Gent, WE04)

A word of thanks

This thesis represents almost four years of hard work. I count myself lucky to have had so many people who helped and supported me in this period, both professionally and on a personal level. I wish to thank some of them here.

First of all, I am grateful to my promoters Freddy Callens and Michel Waroquier for having given me the opportunity to start my doctoral research and for their guidance throughout, and to all my colleagues – the members of the CMM and the EPR group in particular – for all their help and the pleasant work climate. Particular thanks are due to Ewald Pauwels and Henk Vrielinck for their supervision of my research on a daily basis, and to Reinout Declerck and Frank Loncke for all the silliness.

A special word of thanks goes to Einar Sagstuen for his help with all aspects of scientific research. His willingness to answer a seemingly endless list of questions as well as his e-mail writing stamina and literature knowledge have never ceased to amaze me. I am also very grateful to both him and Eli Olaus Hole for their generous hospitality during my stays in Oslo.

Furthermore, I wish to thank Freddy, Michel, Ewald, Henk and Einar, but also Anna Dimitrova, Yordanka Karakirova, Adela Tarpan, Sabine Van Doorslaer, Gauthier Vanhaelewyn and Nicola Yordanov for their invaluable scientific contributions to this work.

Last but not least, I would like to thank my family and friends simply for being there. In particular, I am greatly indebted to my mother and father for their unconditional support and for giving me all opportunities in life, and to my girlfriend Sarah, for letting me share joy and sorrow with her and for letting me be who I am.

Hendrik De Cooman
May 22th 2009

Contents

Nederlandstalige samenvatting	xv
-------------------------------	----

English summary	xxi
-----------------	-----

List of abbreviations	xxvii
-----------------------	-------

Introduction	xxix
Context and motivation of the study	xxix
Structure of this thesis	xxx

1 Interaction of ionising radiation with matter	1
1.1 General concepts	1
1.1.1 Ionising radiation	1
1.1.2 Initial deposition of radiation energy in matter	2
1.2 Radiation damage to DNA	6
1.2.1 The DNA structure	6
1.2.2 Direct and indirect effect	9
1.2.3 Strand breaks	9
1.2.4 The direct effect: initial ionisations and charge migration	9
1.2.5 Sugar radicals	11

2 Electron magnetic resonance	17
2.1 The Zeeman effect	17
2.1.1 Spins and magnetic moments	17
2.1.2 The Zeeman effect for a free electron	18
2.1.3 The spin Hamiltonian	19
2.2 Magnetic-resonance experiments	21
2.2.1 Saturation and relaxation	22

2.2.2	EPR transition in an $S = 1/2$ system	22
2.2.3	EPR and NMR transitions in an $S = 1/2, I = 1/2$ system .	24
2.2.4	ENDOR	26
2.2.5	ENDOR-induced EPR	28
2.2.6	Field-frequency ENDOR	29
2.3	EPR and ENDOR spectra for an $S = I = 1/2$ system	29
2.3.1	The g tensor	29
2.3.2	The HFC tensor	31
2.3.3	Site splitting	40
2.4	Determining g tensors and HFC tensors from EMR experiments	43
2.4.1	The principle	43
2.4.2	Ambiguities	44
2.5	Experimental procedures	46
2.5.1	Sample preparation	46
2.5.2	Sample orientation	47
2.5.3	Sample irradiation	47
2.5.4	EPR spectrometer and equipment	48
2.5.5	Data analysis	51

3 Density functional theory **53**

3.1	Introduction	53
3.2	Basic principles of DFT	54
3.2.1	The Schrödinger equation	54
3.2.2	The many-body problem and the Born-Oppenheimer approximation	54
3.2.3	Electron and spin density	56
3.2.4	The Hohenberg-Kohn theorems	57
3.2.5	The Kohn-Sham approach of DFT	58
3.3	The g -tensor and HFC-tensor in DFT	61
3.3.1	The g tensor	63
3.3.2	The HFC tensor	64
3.4	DFT in practice	64
3.4.1	Density functionals	64
3.4.2	Basis sets	66
3.4.3	The pseudopotential approximation	68
3.4.4	The hybrid Gaussian and (augmented-)plane-wave method	68
3.5	DFT calculations on organic radicals	69
3.5.1	General procedure	69
3.5.2	Geometry optimisation	70
3.5.3	Calculation of g tensors and HFC tensors	71

3.5.4	Comparing DFT-calculated and experimental tensors . . .	73
-------	---	----

4	Solid-state organic radicals	75
----------	-------------------------------------	-----------

4.1	Introduction	75
4.2	Basic concepts	76
4.2.1	Nomenclature of radicals	76
4.2.2	Electronic configuration of carbon and oxygen	77
4.3	The HFC interaction in organic radicals	80
4.3.1	Isotropic and dipolar HFC interactions	80
4.3.2	α protons	86
4.3.3	β protons	91
4.3.4	Protons at γ positions and further away	96
4.4	The g tensor in organic radicals	97
4.4.1	Spin-orbit coupling	97
4.4.2	Interpretation of the g tensor	98

5	Radiation-induced radicals in sucrose single crystals	105
----------	--	------------

5.1	Chemical structure and crystal structure	105
5.2	EMR results in the literature	106
5.2.1	Dosimetric studies	106
5.2.2	Fundamental studies	110
5.3	Own research results	114
5.3.1	Stable radicals	115
5.3.2	EPR-spectrum evolution during first hours after RT irradiation	120
5.3.3	Radicals present after <i>in-situ</i> X-ray irradiation at 10 K	125
5.3.4	Overview and possible reaction mechanism	149

6	Radiation-induced radicals in K2G1P single crystals	153
----------	--	------------

6.1	Chemical structure and crystal structure	153
6.2	EMR results in the literature	155
6.3	Own research results: radicals present in K2G1P single crystals after <i>in-situ</i> X irradiation at 77 K	156

7	Papers	167
----------	---------------	------------

7.1	Paper I : Radiation-induced defects in sucrose single crystals, revisited: a combined electron magnetic resonance and density functional theory study	167
-----	---	-----

7.2	Paper II : Identification and conformational study of stable radiation-induced defects in sucrose single crystals using density functional theory calculations of electron magnetic resonance parameters	181
7.3	Paper III : ENDOR and HYSCORE analysis and DFT-assisted identification of the third major stable radical in sucrose single crystals X-irradiated at room temperature	193
7.4	Paper IV : Radiation-induced radicals in glucose-1-phosphate. I. Electron paramagnetic resonance and electron nuclear double resonance analysis of in situ X-irradiated single crystals at 77 K	205
7.5	Paper V : Radiation-induced radicals in glucose-1-phosphate. II. DFT analysis of structures and possible formation mechanisms	217
7.6	Paper VI : Schonland ambiguity in the electron nuclear double resonance analysis of hyperfine interactions: principles and practice	229
<hr/>		
8	Conclusions	241
<hr/>		
A	Atomic coordinates of the sucrose lattice	245
<hr/>		
B	Atomic coordinates of the K2G1P lattice	247
<hr/>		
	Bibliography	249
<hr/>		

Nederlandstalige samenvatting

Wanneer organische materialen blootgesteld worden aan ioniserende straling, dan resulteert de depositie van de stralingsenergie in *radicalen*, i.e. moleculen met één of meerdere ongepaarde elektronen. Radicalen zijn doorgaans onstabiel en zeer reactief, en ondergaan vaak chemische reacties die tot structurele veranderingen van de molecule leiden: de molecule wordt beschadigd.

Stralingsschade kan de functionaliteit van biologische macromoleculen zoals DNA veranderen en op die manier een zeer schadelijk effect hebben op levende organismen. Dit schadelijk effect kan evenwel ook gebruikt worden om bijvoorbeeld farmaceutische producten en voedingswaren te steriliseren. Bovendien kan men stralingsgeïnduceerde radicalen, wanneer deze stabiel zijn in een materiaal, aanwenden voor dosimetrische doeleinden: uit hun concentratie en eigenschappen kunnen het type en de hoeveelheid straling die dat materiaal ontvangen heeft, afgeleid worden.

De stralingschemie – dit omvat alle chemische processen geïnitieerd door straling – van organische materialen is een zeer actief onderzoeksdomein. Desondanks is de fundamentele kennis met betrekking tot de processen die plaatgrijpen onmiddellijk na de initiële stralingsabsorptie en, *a fortiori*, met betrekking tot de onderliggende fysische en chemische principes, zeer beperkt. Deze kennis is belangrijk vanuit een algemeen, fundamenteel standpunt, maar kan ook concreet nuttig zijn, bijvoorbeeld om inzicht te verwerven in de specifieke stralingsgeïnduceerde processen in DNA of om de haalbaarheid en de betrouwbaarheid van een dosimetrisch protocol te helpen bepalen.

De initiële stralingsgeïnduceerde processen (energieabsorptie, ionisaties, ladingsmigraties en de daarop volgende radicaalreacties) grijpen meestal plaats in een fractie van een seconde bij kamertemperatuur (KT), wat de studie van de radicalen aanzienlijk compliceert. Radicalen kunnen echter (gemakkelijker) gestabiliseerd worden *in eenkristallen* en de verschillende stappen in het radicaalvormingsproces kunnen onderzocht worden via *in-situ*-bestraling bij lage temperatuur (zodat er onvoldoende thermische energie aanwezig is om de radicaalreactie door te laten gaan). Omdat grote systemen zoals DNA-moleculen bovendien te complex zijn, moeten kleinere modelsystemen, die een aantal essentiële eigenschappen gemeenschappelijk hebben met (één

of meerdere componenten van) het 'echt' systeem, onderzocht worden om inzicht te verwerven in hun stralingschemie. Eenkristallen van suikers (en suikerderivaten) kunnen gebruikt worden als modelsystemen voor de studie van directe stralingsschade aan de suikerfosfaatgroep in DNA (*direct*: zonder de tussenkomst van een radicaal dat door de straling geïnduceerd werd in de watermoleculen die het DNA omringen). De kristalstructuur bootst tot op zekere hoogte de compacte en rigide DNA-structuur na en wordt bovendien samengehouden door waterstofbindingen die ook een cruciale rol spelen in de stralingsschade aan DNA. Een bijkomend voordeel is dat radicalen in eenkristallen experimenteel in detail gekarakteriseerd kunnen worden.

Deze doctoraatsthesis omvat een gedetailleerde studie van stralingsgeïnduceerde radicalen in eenkristallen en poeders van sucrose (het vertrouwde tafelsuiker) en in dikaliumzoutkristallen van glucose 1-fosfaat (dipotassium salt of glucose 1-phosphate, K₂G1P). De stralingschemie van beide materialen is relevant in de context van stralingsschade aan DNA, zoals hoger besproken. K₂G1P is daarbij een bijzonder geschikt model voor de studie van de directe stralingsschade aan de suikerfosfaatgroep in DNA. Deze laatste is van cruciaal belang omdat het breken van een suikerfosfaatbinding (een zogenaamde *strand break*) de belangrijkste soort DNA-schade is met betrekking tot schadelijke biologische effecten. De stralingsgeïnduceerde radicalen in sucrose zijn ook relevant omwille van andere redenen: sucrose heeft potentieel als stralingsdosimeter (voor nucleaire noodgevallen) en vele voedingswaren bevatten sucrose en gelijkaardige suikers.

Vooraleer de eigenlijke onderzoeksresultaten samen te vatten, bespreken we de algemene strategie die in deze studie gebruikt werd om de moleculaire structuur van radicalen te bepalen. Deze omvat twee hoofdingrediënten: elektronen-magnetische-resonantiemetingen (EMR-metingen) en kwantumchemische berekeningen op basis van dichtheidsfunctionaaltheorie (DFT). EMR is een krachtige spectroscopische techniek voor het onderzoeken van paramagnetische centra (moleculen of atomen met één of meerdere ongepaarde elektronen, zoals radicalen). In EMR-experimenten (elektronen paramagnetische resonantie (EPR), elektronen-nucleaire dubbele resonantie (ENDOR), ...), wordt een kwantummechanische eigenschap van het ongepaard elektron, gekend als de *spin*, gebruikt om de geometrie en elektronische structuur van het paramagnetisch centrum te onderzoeken. Via een sterk magnetisch veld worden elektronspin- (en kernspin) energieniveaus opgesplitst, en tussen die niveaus worden dan transitieën geïnduceerd door micro- (en radio)golven op het sample in te sturen. De verschillende spininteracties van het ongepaard elektron (de ongepaarde elektronen) worden weerspiegeld in het aantal en

de grootte van de energieopsplitsingen, en kunnen geparametriseerd worden via een zogenaamde spinhamiltoniaan. De parameters in deze spinhamiltoniaan worden *EMR-parameters* genoemd. De radicalen die in het doctoraal onderzoek bestudeerd werden, hebben één ongepaard elektron en kunnen gekarakteriseerd worden via twee soorten EMR-parameters: een *g-tensor*, die de interactie tussen de spin van het ongepaard elektron en het magnetisch veld parametriseert, en *hyperfijntensoren* (HF-tensoren), die de interacties tussen de spin van het ongepaard elektron en de kernspins van waterstofatomen in de directe omgeving van het radicaalcentrum parametriseren.

De *g-tensor* en de HF-tensoren van een radicaal bevatten gedetailleerde (maar abstracte) informatie over de radicaalstructuur. Deze informatie kan gebruikt worden om plausibele radicaalmodellen op te stellen, maar volstaat voor vele organische radicalen (inclusief deze bestudeerd in dit werk) niet om het radicaal met zekerheid te kunnen identificeren. Kwantumchemische berekeningen op basis van DFT zijn bijzonder nuttig in deze context.

DFT is een *ab-initio*-theorie (i.e. een theorie die enkel gebaseerd is op de fundamentele wetten van de kwantumfysica) die toelaat om de eigenschappen van de materie op de nanoschaal te bepalen door de Schrödingervergelijking voor een kwantummechanisch veeldeeltjessysteem (zoals een molecule of een vastestofrooster) op te lossen. In DFT wordt het elektronisch systeem beschreven via zijn elektronendichtheid, en niet – zoals het geval is in de meeste andere *ab-initio*-theorieën – via zijn veeldeeltjesgolffunctie. De laatste is een functie van $4n$ variabelen ($3n$ ruimtelijke variabelen en n spinvariabelen, met n het aantal elektronen), terwijl de elektronische dichtheid een functie is van slechts 3 (ruimtelijke) variabelen, wat zowel conceptueel als praktisch (in termen van benodigde computerkracht) een enorm voordeel betekent. DFT werd reeds tientallen jaren geleden ontwikkeld, maar het is pas recent mogelijk geworden, dankzij de ontwikkeling van nieuwe theoretische methoden en meer efficiënte algoritmes, alsook dankzij de steeds toenemende computerkracht, om berekeningen uit te voeren op voldoende grote systemen op een accurate manier en binnen een redelijke tijdspanne.

Met behulp van DFT-berekeningen kan de geometrie van een bepaald radicaal (bijvoorbeeld voorgesteld op basis van de experimentele data) geoptimaliseerd worden en kunnen de EMR-parameters van deze geoptimaliseerde structuur berekend worden. Op basis van de (mate van) overeenkomst tussen de experimentele en DFT-berekende EMR-parameters kan een radicaalmodel dan aanvaard, verworpen of verbeterd worden. DFT-berekeningen kunnen ook aangewend worden om informatie te bekomen die experimenteel niet beschikbaar is (relatieve energieën van radicalen, mogelijke vormingsmechanismen, ...) en laten zo toe om een radicaal grondiger en uitgebreider te analyseren.

Het doctoraal onderzoek spitst zich voornamelijk toe op stralingsgeïnduceerde radicalen in *sucrose*, een disaccharide bestaande uit een fructose- en een glucose-eenheid die verbonden zijn via een glycosidische binding. Het EPR-spectrum dat verkregen wordt na bestraling van sucrose-eenkristallen met X-stralen bij KT, ondergaat continu veranderingen en wordt pas stabiel na ongeveer vier uren. Het stabiele EPR-spectrum kan grotendeels toegeschreven worden aan drie radicalen (T1, T2 en T3), waarvan er twee (T2 en T3) zeer gelijkaardige EMR-parameters hebben en hoogstwaarschijnlijk verschillende conformaties zijn van eenzelfde chemische structuur. Accurate en eenduidige HF-tensoren werden bepaald voor deze drie dominante radicalen en de invloed van de meettemperatuur op de EPR- en ENDOR-spectra werd onderzocht, wat toeliet klaarheid te scheppen in de discrepanties in de literatuur. De chemische structuren van T1 en T2/T3 werden geïdentificeerd. Ze vereisen het breken van de glycosidische binding en de vorming van een carbonylgroep op een koolstofatoom naast het radicaalcentrum. De radicaalcentra van T1 en T2/T3 zijn respectievelijk C2' (in de fructose-eenheid) en C1 (in de glucose-eenheid), en de carbonylgroepen bevinden zich op respectievelijk C1' en C2. In deze structuren is ongeveer de helft van de spindensiteit gelokaliseerd op de carbonylgroep en het naburige ringzuurstofatoom, wat een plausibele verklaring biedt voor hun relatieve stabiliteit. Een afdoende verklaring kon niet gevonden worden voor de aanwezigheid van de twee zeer gelijkaardige – maar onderscheidbare – radicalen T2 en T3.

De transformatie van het EPR-spectrum gedurende de eerste vier uren na bestraling bij KT kan toegeschreven worden aan het verval van verschillende semistabiele radicalen in diamagnetische producten. Eén van deze semistabiele radicalen (U1) domineert initieel het EPR-spectrum. U1 werd nog niet geïdentificeerd, hoewel een aantal structurele eigenschappen ervan reeds bepaald werden. U1 treedt niet op als precursor voor de dominante stabiele radicalen want de concentraties van deze laatsten veranderen niet (beduidend) gedurende die eerste vier uren.

In-situ-bestraling met X-stralen bij 10 K induceert minstens negen verschillende radicalen in eenkristallen van sucrose. Vier daarvan (R1, R2, R3 en R6) zijn dominant. R1, R2 en R6 werden geïdentificeerd als radicalen met het spincentrum op C5, C1 en O3' respectievelijk, verkregen door netto H-abstractie van deze atomen. Het radicaalmodel voor R6 was reeds voorgesteld in de literatuur, maar onze DFT-berekeningen verklaarden een aantal bijzondere eigenschappen van dit radicaal. Het geabstraheerde proton in R6 is gemigreerd naar het zuurstofatoom waarmee het een waterstofbinding aangaat in de intacte kristalstructuur. Voor R3 lijkt het meest plausibele model een H-geabstraheerd, C6-gecentreerd radicaal te zijn, maar de overeenkomst

tussen de DFT-berekende en de experimentele HF-tensoren is nog verre van overtuigend. Een mogelijke verklaring is dat een (diamagnetisch) bijproduct van de radicaalvorming, zoals H_2 , in de directe omgeving van het radicaalcentrum blijft en zo de geometrie van het radicaal (en bijgevolg de HF-tensoren) beïnvloedt.

Wanneer een sucrose-eenkristal na *in-situ*-bestraling bij 10 K opgewarmd wordt tot KT, ondergaat het EPR-spectrum continue veranderingen en transformeert het uiteindelijk in het EPR-spectrum dat verkregen wordt onmiddellijk na bestraling bij KT (en vervolgens in het stabiele EPR-spectrum). De precursoren voor de stabiele radicalen moeten dus aanwezig zijn bij 10 K. Een plausibel vormingsmechanisme kon voorgesteld worden voor het T2/T3-radicaal, waarbij T2/T3 uit R2 gevormd wordt via een 1,2-H-shift gevolgd door een β -eliminatiereactie.

In **K2G1P** werden de radicalen aanwezig bij 77 K na *in-situ*-bestraling bij 77 K onderzocht. Minstens zeven verschillende koolstofgecentreerde radicalen werden geobserveerd. Vier daarvan (R1, R2, R3 en R4), inclusief het dominante radicaal (R2), werden geïdentificeerd. R1 is een H-geabstraheerd radicaal met C3 als radicaalcentrum. DFT-berekeningen geven aan dat het geabstraheerde proton migreert naar de fosfaatgroep van een naburige molecule en op een indirecte manier de radicaalgeometrie aanzienlijk beïnvloedt. De chemische structuur van R2 is identiek aan die van T2/T3 in sucrose: C1 is het radicaalcentrum en er is een carbonylgroep aanwezig op C2. In plaats van de glycosidische binding is hier de glucose-fosfaatbinding gebroken. Een plausibel vormingsmechanisme, analoog aan dat voor T2/T3, werd voorgesteld. R3 en R4 zijn verschillende conformaties van eenzelfde H-geabstraheerde radicaal met C6 als radicaalcentrum, en corresponderen met verschillende lokale minima op het potentiële-energieoppervlak. Bij opwarming van een K2G1P-eenkristal tot KT na *in-situ*-bestraling bij 77 K wordt een fosfaatradaal gevormd maar het kon niet bepaald worden welke van de koolstofgecentreerde radicalen er de precursor van is.

Energieberekeningen van alle K2G1P-radicalen die bekomen worden door een enkelvoudige H-abstractie tonen aan dat de radicaalvorming in K2G1P kinetisch gecontroleerd is, en niet thermodynamisch. Het lijkt waarschijnlijk dat dit ook geldt voor andere vastestofsuikers en -suikerderivaten.

Tot slot hebben we via eerste-orde-perturbatietheorie aangetoond dat er onder bepaalde voorwaarden (die vaak van toepassing zijn in de praktijk) een ambiguïteit optreedt bij de bepaling van de HF-tensoren voor laag-symmetrische paramagnetische centra met $S=1/2$ en $I=1/2$: er bestaan dan twee HF-tensoren die een even goede fit aan de experimentele data geven

maar slechts één van de twee is fysisch relevant. Omdat deze zogenaamde *Schonland-geconjugeerde* tensoren aanzienlijk van elkaar kunnen verschillen met betrekking tot zowel hoofdwaarden als hoofdrichtingen, moet deze ambiguïteit geëlimineerd worden wanneer men HF-tensoren wil gebruiken om een radicaal te identificeren.

Ondanks het feit dat het optreden van deze ambiguïteit in de praktijk reeds lang gekend is, wordt zij niet altijd onderkend in de literatuur en was er nog geen stevige theoretische basis voor. Onze studie geeft deze basis: er werd uitgewerkt wat de precieze voorwaarden zijn opdat een dergelijke ambiguïteit kan optreden en een overzicht werd opgesteld van mogelijke methodes om de ambiguïteit te elimineren – waaronder enkele die in de literatuur nog niet gebruikt of voorgesteld waren. We hebben ook een analytische procedure uitgewerkt die toelaat de *Schonland-geconjugeerde* van een bepaalde tensor te berekenen.

Vanuit een meer algemeen standpunt bekeken, tonen onze resultaten aan dat carbonylgroepvorming en breking van een zuurstof-koolstofbinding (in het geval van sucrose: de glycosidische binding; in het geval van K2G1P: de suikerfosfaatbinding) mogelijks algemeen voorkomende processen zijn in vastestofsuikers en -suikerderivaten, en dat de aanwezigheid van een fosfaatgroep daarbij niet essentieel is. Een uitbreiding van dit soort EMR- en DFT-studies naar andere, verwante materialen is vereist opdat dergelijke besluiten met enige zekerheid getrokken mogen worden.

Een aanzienlijke hoeveelheid informatie werd reeds verzameld, maar (meer) volledige schema's van de stralingschemie van sucrose en K2G1P, en van andere, gelijkaardige materialen moeten opgesteld worden. Alleen dan zal het mogelijk zijn om op een betrouwbare manier algemene principes af te leiden voor de stralingsgeïnduceerde processen in vastestofsuikers en -suikerderivaten.

Een andere en laatste algemene conclusie is dat de combinatie van gedetailleerde EMR-metingen en geavanceerde DFT-berekeningen een zeer succesvolle en betrouwbare strategie is voor de studie van organische radicalen in een vastestofomgeving.

English summary

When organic matter is exposed to ionising radiation, the energy deposited by the radiation gives rise to *radicals*, i.e. molecules with one or more *unpaired* electrons. These typically are unstable, highly reactive species and often participate in chemical reactions which result in structural alterations of the molecule: the molecule is damaged.

Radiation damage can alter the functionality of biological macromolecules such as DNA and thus have a highly detrimental effect on living organisms. This detrimental effect can, however, also be exploited for the sterilisation of e.g. pharmaceutical products and foodstuffs. Moreover, radiation-induced radicals, when stabilised in a substance, can be used for dosimetric purposes: the type and amount of radiation that substance has received can be determined from their concentration and characteristics.

Although the radiation chemistry – this comprises all chemical processes initiated by radiation – of organic materials is a very active research field, fundamental knowledge is still lacking with respect to the processes taking place after the initial absorption of the radiation energy and, *a fortiori*, with respect to the underlying physical and chemical principles governing these processes. Such knowledge is important from a general, fundamental point of view, but can also be useful for e.g. obtaining insight in the specific pathways of radiation damage to DNA or assessing the feasibility and limitations of a dosimetric protocol.

The study of radiation-induced radicals is complicated by the fact that the initial radiation-induced processes (energy absorption, ionisations, charge migrations and subsequent radical reactions) typically take place in a fraction of a second at ambient temperatures. Radicals can be stabilised (more easily), however, *in single-crystal systems* and the consecutive steps in a radical formation process can be studied by *in-situ* irradiation at low temperature (so that insufficient thermal energy is present for a radical reaction to proceed). Also, because large systems such as DNA molecules are too complex, smaller model systems bearing key features similar to one or more of their components have to be studied in order to gain insight in their radiation chemistry. Carbohydrate(-derivative) single crystals can be used as a model to study the

direct radiation effect on the sugar(-phosphate) group in DNA (*direct*: not via a mediating radical species induced by the radiation in the hydration layer surrounding the DNA). The crystal structure mimics to some extent the tight, rigid packing of DNA in the chromosomes and is held together by hydrogen bonds which also play a crucial role in DNA radiation damage. An additional important advantage is that radicals trapped in single crystals can be characterised in great detail experimentally.

This doctoral thesis deals with a detailed study of radiation-induced radicals in solid sucrose (a carbohydrate, also known as common household sugar) and in the dipotassium salt of glucose 1-phosphate (K₂G1P). The radiation chemistry of both materials is relevant in the context of radiation damage to DNA, as discussed above. K₂G1P is a particularly suitable model for studying the direct radiation effect to the DNA sugar-phosphate group. The latter plays a crucial role because scission of the sugar-phosphate bond (so-called strand breaks) is the most important type of damage to DNA with respect to harmful biological effects. The radiation-induced radicals in sucrose are also of interest for other reasons: sucrose has potential as an (emergency) radiation dosimeter and many foodstuffs contain sucrose and similar carbohydrates.

Before summarising the actual research results, we discuss the general strategy employed for this study. This comprises two main ingredients: electron magnetic resonance (EMR) experiments and quantum-chemical calculations based on density functional theory (DFT).

EMR is a powerful spectroscopic technique for the investigation of paramagnetic centres (molecules or atoms with one or more unpaired electrons, such as radicals). In EMR experiments (electron paramagnetic resonance (EPR), electron-nuclear double resonance (ENDOR), ...), a quantum-mechanical property of the unpaired electron(s), known as the *spin*, is used to probe the geometry and electronic structure of the paramagnetic centre. A strong magnetic field is used to split up electron-spin (and nuclear-spin) energy levels, and transitions are induced between these levels by applying microwave (and radiofrequency) radiation. The various spin interactions of the unpaired electron(s) are reflected in the number and size of the energy splittings and can be parametrised via a so-called spin Hamiltonian. The parameters in this spin Hamiltonian are called *EMR parameters*. The radicals studied in the doctoral research have one unpaired electron and can be characterised by two types of EMR parameters: a *g tensor*, which parametrises the interaction of the unpaired-electron spin with the magnetic field, and *hyperfine coupling (HFC) tensors*, which parametrise the interactions between the electron spin and the various nuclear spins of the hydrogen atoms near the radical centre.

The g tensor and HFC tensors of a radical provide detailed (but abstract) information about the radical structure. Using this information, plausible radical models can be devised but for many organic radicals (including those studied in this work), this information is not sufficient for an unambiguous identification of the radical. One particularly successful approach to help overcome this problem are quantum-chemical calculations based on DFT.

DFT is an *ab-initio* theory (i.e. a theory based solely on the fundamental laws of quantum physics) that allows determining the properties of matter at the nanoscale by solving the Schrödinger equation for a quantum-mechanical multi-particle system (such as a molecule or a solid-state lattice). In DFT, the electronic system is described in terms of its electron density, and not – as in most other *ab-initio* theories – in terms of the multi-particle wave function. While the latter is a function of $4n$ variables ($3n$ spatial variables and n spin variables, with n the number of electrons), the electron density is a function of only three (spatial) variables, which is a tremendous advantage, both conceptually and practically (in terms of required computer power). DFT was developed decades ago, but it has only recently become possible, due to the development of new theoretical methods and more efficient algorithms, as well as to ever-increasing computer power, to deal with sufficiently large systems at a reasonable computational cost in an accurate way.

Using DFT calculations, the geometry of a certain radical model (proposed on the basis of the experimental data, e.g.) can be optimised and the EMR parameters of this optimised structure can be calculated. By comparing the experimental and DFT-calculated EMR parameters, the validity of the model can be assessed. DFT calculations can also be employed to obtain information that is experimentally not available (relative energies of radicals, possible formation mechanisms, ...) and thus allow a more thorough and more extensive analysis of a radical.

The doctoral research has for the greater part focused on radiation-induced radicals in *sucrose*. After X-ray irradiation of sucrose single crystals at room temperature (RT), the EPR spectrum undergoes continuous changes and reaches a stable state only after approximately four hours. The stable EPR spectrum is mainly due to three radical species (T1, T2 and T3), two of which (T2 and T3) have very similar EMR parameters and most likely are different conformations of the same chemical structure. An accurate, unambiguous set of HFC tensors was determined for these dominant radicals and the dependence of the EPR and ENDOR spectrum on the measurement temperature was studied, which brought clarity to several discrepancies in the literature. The chemical structures of the T1 and the T2/T3 species were identified. They require scission of the glycosidic bond and formation of a

carbonyl group at a carbon atom adjacent to the radical centre. The radical centres of T1 and T2/T3 are C2' (in the fructose unit) and C1 (in the glucose unit) respectively, and the carbonyl groups are at C1' and C2 respectively. About half of the spin density is delocalised onto the carbonyl group and the neighbouring ring oxygen in these structures, which offers a plausible explanation for their relative stability. No conclusive explanation was found for the presence of the two very similar – but distinguishable – radical species T2 and T3.

The transformation of the EPR spectrum during the first four hours after RT irradiation can be attributed to the decay of several semistable species into diamagnetic products. One of these semistable species (U1) initially dominates the EPR spectrum. Some structural features of U1 were determined, but this species has not been identified yet. It does not act as a precursor for any of the dominant stable radicals as the concentrations of the latter do not change (significantly) during those first four hours.

In-situ X-ray irradiation at 10 K of sucrose single crystals yields at least nine different radical species, four of which (R1, R2, R3 and R6) are dominant. R1, R2 and R6 have been identified as C5-, C1- and O3'-centred species respectively, obtained by net hydrogen abstraction at these sites. The model for R6 had already been suggested in the literature, but our DFT calculations provided an explanation for some particular features of this radical. In this species, the abstracted proton has migrated to its hydrogen-bound oxygen partner on a neighbouring molecule. The R3 species has been tentatively identified as a H-abstracted C6-centred radical, but the agreement between DFT-calculated and experimental HFC tensors is far from convincing. One plausible explanation is that a (diamagnetic) side product of the radical formation, such as H₂, remains in the direct vicinity of the radical centre and thus influences the radical geometry (and, consequently, the HFC tensors).

Upon annealing after *in-situ* irradiation at 10 K, the EPR spectrum continuously changes and finally transforms into the EPR spectrum observed immediately after RT irradiation (and subsequently into the stable EPR spectrum). The precursors for the stable radicals must therefore be among the radicals present at 10 K. For the T2/T3 radical species, a plausible reaction mechanism could be proposed, starting from the R2 species and involving a 1,2-H-shift and a β -elimination reaction.

In **K2G1P**, the radicals present at 77 K after *in-situ* X-ray irradiation at 77 K were studied. At least seven carbon-centred radical species were observed. Four of these (R1, R2, R3 and R4), including the dominant one (R2), were identified. R1 is an H-abstracted species with the radical centre at C3. DFT calculations indicate the abstracted proton migrates to the phosphate

group of a neighbouring molecule and, indirectly, influences the radical geometry substantially. The chemical structure of the R2 radical species is identical to that of the T2/T3 species in sucrose: the radical centre is C1 and a carbonyl group is present at the C2 carbon. Instead of the glycosidic bond, the glucose-phosphate junction is broken here. A plausible formation mechanism, analogous to that for T2/T3, was proposed. R3 and R4 are different conformations of the same H-abstracted species with the radical centre at C6, which correspond to different local minima on the potential-energy surface. Upon annealing after *in-situ* irradiation at 77 K of K2G1P powder, a phosphate radical is formed but it could not be established which of the carbon-centred radicals acts as its precursor.

Energy calculations of all radicals obtained by a single H abstraction indicate that the radical formation in K2G1P is kinetically controlled, and not thermodynamically. This observation is likely to apply for other solid-state carbohydrates as well.

Finally, we showed via first-order perturbation theory that under certain conditions (which often apply in practice), an ambiguity can arise in the determination of HFC tensors for low-symmetry paramagnetic centres with $S=1/2$ and $I=1/2$: two HFC tensors can be found that fit the experimental data equally well, and of which only one is physically relevant. Since these so-called *Schonland-conjugate tensors* can differ substantially in both principal values and principal directions, this ambiguity must be eliminated when the HFC tensors are to be used for radical identification.

Although this ambiguity was since long known to exist in practice, it was not always recognised in the literature and had not been given a firm theoretical basis. The latter is provided by our study, which clearly formulates the conditions under which such an ambiguity arises and gives an overview of different possible methods to eliminate it – including some that had not been used or suggested in the literature yet. We also derived an analytical procedure to obtain the Schonland-conjugate of a particular HFC tensor.

Our results indicate that carbonyl-group formation and scission of an oxygen-carbon linkage (in the case of sucrose: the glycosidic bond; in the case of K2G1P: the sugar-phosphate bond) possibly are common processes in solid-state carbohydrates and that the presence of a phosphate group is not essential for these processes to occur. Extended EMR and DFT studies on similar compounds are required before conclusions of this kind can be drawn with any certainty.

Similarly, although a considerable amount of information was already gathered, (more) complete radiation chemistry schemes of sucrose and K2G1P,

as well as of other, similar materials have to be obtained. Only then will it be possible to establish in a reliable way (some of) the general principles governing the radiation-induced processes in solid-state carbohydrates.

Another and final general conclusion is that the combination of detailed EMR measurements and advanced DFT calculations provides a very successful and reliable strategy for the study of organic radicals in a solid-state environment.

List of abbreviations

A	adenine
AE	all-electron
AO	atomic orbital
B	DNA base
BO	Born-Oppenheimer
CGF	contracted Gaussian function
CPGF	contracted periodic Gaussian function
CW	continuous wave
C	cytosine
DEA	dissociative electron capture
DFPT	density functional perturbation theory
DFT	density functional theory
DNA	deoxyribonucleic acid
DPPH	2,2-diphenyl-1-picrylhydrazyl
DSB	double strand break
EA	electron affinity
EIE	ENDOR-induced EPR
EMR	electron magnetic resonance
ENDOR	electron-nuclear double resonance
EPR	electron paramagnetic resonance
FF-ENDOR	field-frequency electron-nuclear double resonance
FFT	fast Fourier transform
G1P	glucose 1-phosphate
GAPW	Gaussian and augmented plane wave
GGA	generalized gradient approximation
GIPAW	gauge-including projector-augmented wave
GPW	Gaussian and plane wave
G	guanine
GTO	Gaussian-type orbital

HF	hyperfine
HFC	hyperfine coupling
HYSCORE	hyperfine sublevel correlation spectroscopy
IP	ionisation potential
IR	infrared
K2G1P	dipotassium glucose 1-phosphate dihydrate
KS	Kohn-Sham
LCAO	linear combination of atomic orbitals
LEE	low-energy electron
LEO	lone-electron orbital axis
LET	linear energy transfer
LDA	local density approximation
LOT	level of theory
LSDA	local spin density approximation
MLCFA	maximum likelihood common factor analysis
MO	molecular orbital
MW	microwave
NMR	nuclear magnetic resonance
PAW	projector-augmented wave
PBC	periodic boundary conditions
PES	potential-energy surface
PSP	pseudopotential
PW	plane wave
RT	room temperature
RF	radio frequency
RNA	ribonucleic acid
S	DNA deoxyribose unit
SM	single molecule
SP	DNA sugar-phosphate backbone
SOMO	singly occupied molecular orbital
SSB	single strand break
SS/EPR	solid-state EPR
T	thymine
TRIPLE	electron-nuclear-nuclear triple resonance
TZV2P	triple-zeta double-polarised valence
UV	ultraviolet

Introduction

Context and motivation of the study

In most matter electrons occur in *pairs*. When organic matter is exposed to high-energy radiation, the energy deposited by the radiation gives rise to molecules with an *unpaired* electron, commonly called *free radicals* or simply *radicals*. These are typically unstable, highly reactive species and often participate in chemical reactions which result in structural alterations of the molecule: the molecule is damaged.

Radiation damage can alter the functionality of biological macromolecules and thus poses a serious health risk. One of the most prominent examples is radiation damage to DNA (deoxyribonucleic acid), which gives rise to point mutations in the genetic code and can ultimately lead to, among others, cancer. These radiation-induced radical structures and processes are studied in a branch of science called *radiation chemistry*. On the other hand, if somehow radiation-induced radicals are stabilised in a substance, their concentration and characteristics can be used to determine the type and amount of radiation that this substance has received (*radiation dosimetry*). The detrimental effect of radiation on biological organisms can also be exploited: many pharmaceutical products and foodstuffs, e.g., are sterilised by radiation to increase the shelf life and reduce health risks from bacteria and viruses (*radiation sterilisation*).

This doctoral thesis deals with the *identification of radiation-induced radicals in solid sucrose* (also known as common household sugar) *and in the dipotassium salt of glucose 1-phosphate* (K₂G1P). The radiation chemistry of K₂G1P is relevant mainly in the context of DNA radiation damage, while the radiation-induced radicals in sucrose are of a more general interest as they are at the crossroads of the three branches of radiation science mentioned above: (i) DNA contains a carbohydrate unit (deoxyribose) which plays a crucial role in the radiation chemistry of DNA, (ii) sucrose is a potential (emergency) radiation dosimeter and (iii) many foodstuffs contain sucrose and similar carbohydrates. Although this doctoral research is, in itself, *applied*, the general scientific goal to which it contributes is of a (more) *fundamental* nature:

acquiring insight in the principles governing the radiation chemistry of solid-state carbohydrate-containing materials.

The main research tools employed in the doctoral research are electron-magnetic-resonance (EMR) measurements and density functional theory (DFT) calculations. The basic strategy is to identify radical structures by comparing DFT-calculated EMR parameters on (selected) radical structures with experimentally obtained EMR parameters. The radicals we are dealing with are characterised by two types of parameters: the g tensor and the hyperfine coupling (HFC) tensors. Although not trivial from a practical point of view, the experimental determination of these tensors is in principle straightforward and has been possible for several decades now. On the theoretical side, on the other hand, it has only recently become feasible to perform geometry optimisations and EMR-parameter calculations on sufficiently large systems at a reasonable computational cost and in an accurate way. Here emerges another more general goal of this doctoral research: *to explore the use and reliability of modern DFT calculations for the study of solid-state organic radicals.*

Structure of this thesis

At the time this doctoral thesis is written, two quite different thesis *format types* exist and are accepted. The *old format* typically comprises a thorough account of the general background of the study (including literature results) and of the own research results, as well as of the scientific and technical methods used during the research. The *new format*, which is rapidly growing more popular the last few years, is far more compact: the core of the thesis are the integral reproductions of the scientific papers published during the doctoral research. Personally I agree with the new format in that there is no sense in recasting scientific publications into a form fit for a doctoral thesis. On the other hand, writing a doctoral thesis in the old-format style forces the writer to contemplate more deeply on his research and look at it from a different perspective, which I believe to be crucial in an academic institution.

Therefore, I have opted for a mixture of both formats in this doctoral thesis: the scientific papers published during and directly relevant for the doctoral research are integrally reproduced and the main results and conclusions of these papers are only summarised. However, the basic theory and information one needs as a background for the papers are discussed – often in considerable detail – and not yet published research results are presented in full length.

In Chapter 1, some general information is provided with respect to the interaction of radiation with matter and a brief overview is given of the current

(and vast) knowledge on the radiation chemistry of DNA, with emphasis on the role of sugar radicals. The relevance of the systems studied in the doctoral research in this context is also discussed.

Chapters 2 and 3 deal with the theory and practical aspects of the main research tools: EMR measurements and DFT calculations. A section of Chapter 2 is concerned with the so-called Schonland ambiguity, on which we also published a paper during the doctoral research.

Chapter 4 focuses on the interpretation of HFC tensors and g tensors in solid-state organic radicals, and on the identification of radicals on the basis of those tensors.

The results in the literature and those obtained during the doctoral research on radiation-induced radicals in sucrose and K2G1P are discussed in Chapters 5 and 6 respectively. Already published results are summarised and not yet published material is presented and discussed in detail.

Chapter 7 contains the integral reproductions of the papers published in the context of the doctoral research.

Chapter 8, finally, provides some general conclusions on the research results as well as an outlook for future research.

Chapter 1

Interaction of ionising radiation with matter

1.1 General concepts

1.1.1 Ionising radiation

Radiation can be described as any process in which energy emitted by one body is ultimately absorbed by another body. Radiation with sufficient energy to ionise the absorbing substance (that is, to expel electrons from their atomic or molecular orbitals) is called *ionising radiation*. In this doctoral thesis, we will only be concerned with ionising radiation, but the term *ionising* is often dropped, as is customary in the literature. Ionising radiation is produced by natural as well as man-made sources, and all living organisms are exposed to it to some extent.

Forms of ionising radiation include high-energy electromagnetic radiation (X and γ rays), electrons (β radiation) and heavy particles (protons, α particles, heavy ions, ...). The emphasis in the next section will be on X and γ rays, since these are the most common types of radiation and X-ray irradiation was used in the doctoral research. Originally, the distinction between X and γ rays was made on the basis of their wavelengths – X rays having larger wavelengths than γ rays. Now, however, the label usually refers to the origin of the radiation: X rays are produced by accelerating electrons in a high-voltage electric field, while γ rays result from subatomic-particle interactions (usually radioactive decay of a nucleus). X and γ rays have wavelengths smaller than 10 nm, corresponding to frequencies larger than $3 \cdot 10^{16}$ Hz and photon energies larger than 120 eV.

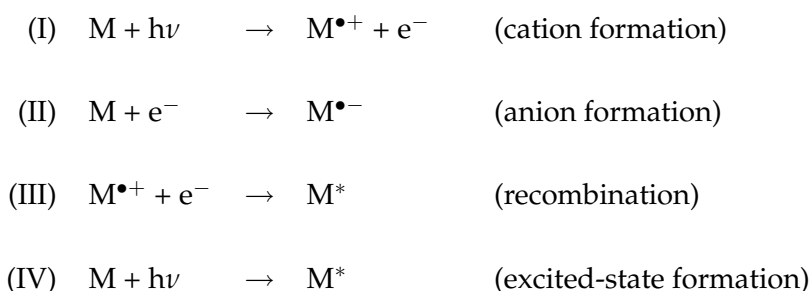
1.1.2 Initial deposition of radiation energy in matter

1.1.2.1 Primary radiation-matter interactions

X and γ rays interact with matter mainly by *ionisation*: knocking electrons out of their molecular orbitals (usually valence orbitals) [1–3]. This proceeds primarily via Compton scattering and photoelectric absorption [1].¹ Most of the primary radiation energy is converted to kinetic energy of these secondary electrons, which induce ionisations further down their tracks. The cations resulting from this cascade of ionisations constitute the major part of the initial *oxidative* radiation damage to the matter. The expelled electrons, when slowed down sufficiently by subsequent scattering processes, eventually either recombine with a cation (forming a neutral, diamagnetic molecule) or attach to an undamaged molecule. The anions thus formed constitute the major part of the initial *reductive* radiation damage.

Radiation will also give rise to molecular *excitations* and the primary cations and anions commonly are in an excited state initially. Excited states can lead to, e.g., homolytic bond cleavage, but they are generally considered to be of minor importance in the condensed phase because many efficient relaxation pathways are available via the surrounding lattice (or liquid) [3, 4]. More recent discoveries, however, suggest that excited states may play a role of considerable importance in radiation damage to DNA (see Sections 1.2.5.2 and 1.2.5.3).

In summary, when an organic molecule is exposed to X or γ rays with frequency ν , the main primary reactions are



where the * superscript indicates excited states and the \bullet superscript indicates a radical. As stated above, the cations and anions in (I) and (II) are usually also excited initially.

Electrons and other charged particles also interact with matter primarily via scattering events, thereby ejecting molecular valence electrons out of their

¹There is a third possible process for energies larger than 1.02 MeV: electron-positron-pair production.

orbitals, but the spatial distribution of the ionisations differs from that for X and γ rays. This is discussed in the next section.

1.1.2.2 Spatial distribution of initial ionisations

An important characteristic of radiation is its *linear energy transfer* (LET), the energy deposited by the radiation per unit length of the track. Irradiating a solid material with X or γ rays (low LET) gives rise to sparse, almost homogeneously distributed ionisations throughout the matter. Multiply-charged and/or heavy particles such as α particles and heavy ions (high LET) result in an inhomogeneous spatial distribution of the ionisations, with a much higher density along the track core. Fast electrons (like in typical β irradiation) behave as low-LET particles but when their kinetic energy decreases they also become more densely ionising. This gives rise to a so-called *spur*: a small cluster of ionisations [2]. Consequently, both low- and high-LET radiation give rise to spurs but in the case of low-LET radiation (X, γ and β radiation), the spurs are isolated and distributed approximately homogeneously in the matter, whereas for high-LET radiation the spurs are concentrated along the track core.

Clustered ionisations often result in clustered radicals at a later stage, even if recombination reactions are more effective in such regions. This is a crucial fact since the detrimental effect of radiation damage to biologically relevant systems depends to a large extent on the spatial distribution of the induced radicals: isolated regions of dense damage are more harmful than sparse, homogeneously distributed damage. Double strand breaks in DNA (often considered as two closely located single strand breaks) provide an excellent example of this principle (see Section 1.2.3) [5].

Another crucial point is that the probability of oxidative ionisation at a certain site by low-LET radiation is roughly proportional to the electron density at that site.

1.1.2.3 Evolution of the initial radiation damage

The primary cations and anions can be stable, but usually are (highly) unstable species and the excess charges will migrate through the matter. This charge migration may proceed by *charge transfer* (transfer of positive holes or negative electrons) and/or by *(de)protonation reactions* (transfer of protons between neighbouring molecules).

In charge-transfer processes, the holes and electrons will either recombine or form energetically more favourable cations and anions. When the transfer

processes are thermodynamically controlled, holes will end up at the molecule with the lowest ionisation potential (IP²) and electrons at the molecule with the highest electron affinity (EA³). In certain cases, however, the energetically most favourable location for an electron is in between molecules: in a series of single crystal compounds the electron has been observed to be trapped in a void in between two or more neighbouring hydroxy groups, assumedly stabilised by the (partially induced) dipolar fields of the hydroxy groups (see Section 5.2.2.2.1, page 111).

Proton-transfer reactions, on the other hand, induce a *spin-charge separation* and yield neutral radicals. These are much less prone to possible recombination reactions than cations and anions, and therefore often are more stable.⁴ Proton-transfer reactions can be reversible (shallow radical traps) or irreversible (deep radical traps). The relative rates of proton-transfer and charge-migration processes determine the number and type of initially stabilised radicals. Hydrogen bonds, often encountered in organic substances (including DNA), usually provide excellent pathways for proton-transfer reactions and can therefore play a crucial role in the evolution of radiation damage. Note that cations and anions resulting from charge-transfer processes may also participate in proton-transfer reactions and form a neutral radical.

The initially stabilised neutral and charged radicals can subsequently participate in one or more chemical reactions, often called *secondary radical processes*, eventually resulting in either stable (usually neutral) radicals or diamagnetic end products. An immense amount of reactions in *aqueous* free-radical carbohydrate chemistry has been documented [6, 7], some of the most common processes being 1,2-hydrogen shifts (1,2-H-shifts) and β elimination reactions (Figure 1.1), but much less data are available on free-radical carbohydrate chemistry in the *solid state*. Results obtained in aqueous environments cannot automatically be extrapolated to solid-state systems but they do provide a rich source of information. Indisputable evidence for the occurrence of 1,2-H-shifts in carbohydrate single crystals has been obtained [8] and many results in the literature indicate that β elimination processes very likely also take place in the solid state.

The stable radicals and altered diamagnetic structures in biomolecules (e.g. DNA) can influence genetic or metabolic functions, which can ultimately lead to tumors, cancer or the death of an organism.

²The IP of a neutral atom or molecule is a measure of the energy change when an electron is removed from it, a positive IP indicating an increase in energy.

³The EA of a neutral atom or molecule is a measure of the energy change when an electron is attached to it, a positive EA indicating a decrease in energy.

⁴Note that the neutral radical is not necessarily thermodynamically more stable than that anion/cation.

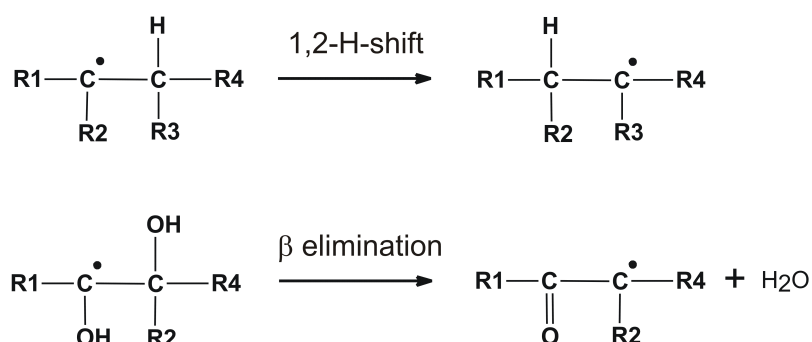


Figure 1.1: Examples of two common reaction processes in aqueous free-radical carbohydrate chemistry: 1,2-H-shift and β elimination. Here, H_2O is eliminated but elimination of H_2 or larger fragments is also possible.

1.1.2.4 The role of temperature

In DNA, the initial energy absorption, ionisations, charge migrations, and secondary radical processes all typically take place in less than 10^{-4} s at ambient temperatures [2, 5]. The time range in which the different stages proceed depends on the system but this number likely applies to most organic systems.⁵ Continuous-wave electron magnetic resonance (CW-EMR, the main experimental technique employed in the doctoral research, see Chapter 2) is not a time-resolved technique and can therefore, in first instance, only be employed to study (the most) stable radicals. However, intermediate radicals are often semistable and can be trapped if the thermal energy in the system is sufficiently reduced (cf. Figure 1.2). This requires irradiation of the sample at low temperature and subsequent EMR measurements without letting the sample warm up. The experimental setup at the EPR (electron paramagnetic resonance) lab in Oslo, which was used in the doctoral research, allows for such *in-situ* X irradiation and is discussed in Section 2.5. By controlled annealing, the subsequent semistable radicals in the formation process of a stable radical can be trapped. Thus, detailed mechanistic information about the radical formation can be obtained.

The central assumption in this type of studies is that the reaction pathway is not influenced by the irradiation temperature: the reactions observed upon annealing of the sample are assumed to be the same as those occurring (in very short time spans) at room temperature (RT). In other words, lowering of the temperature is assumed to merely freeze time. This is not necessarily true. For instance, if there are two competitive reaction paths, one might be favoured

⁵In solid-state organic systems the lifetime of (semi)stable radicals can be dramatically increased due to their limited possibility to react or recombine. In sucrose, e.g., a semistable radical observed after RT irradiation takes several hours to decay (Section 5.3.2.2, page 121).

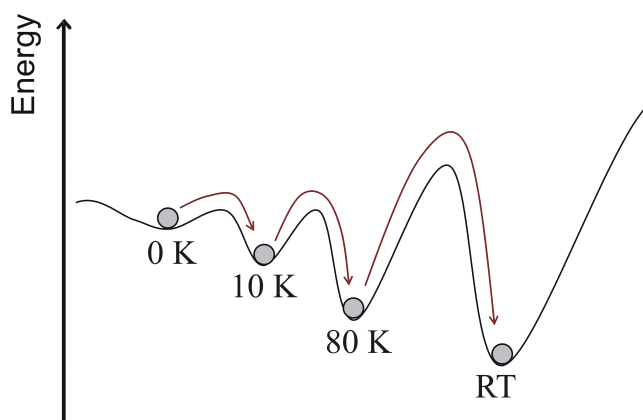


Figure 1.2: Illustration of the role of temperature in radiation-induced radical processes by analogy with a 1D potential-energy surface. When the radiation is performed at 0 K, the primary anion or cation radical may be stable. At 10 K, sufficient thermal energy may be available to allow for e.g. proton-transfer reactions which lead to more stable radicals, etc.

at RT because of the higher stability of the end product (thermodynamic control), while the other might be favoured at low temperatures because of a lower activation energy (kinetic control) (Figure 1.3). Another consideration is that the fraction of radicals recombining might be substantially larger when annealing to RT after low-temperature irradiation because all secondary radical processes are initiated at the same time.

Most often, however, the same stable radicals are observed after irradiation at RT and after low-temperature *in-situ* radiation and subsequent annealing to RT. This indicates that the aforementioned assumption likely is valid in many cases. It does not prove it, however, since in principle two different pathways may eventually result in the same final product.

1.2 Radiation damage to DNA

1.2.1 The DNA structure

DNA consists of two long polymers (*strands*) of nucleotides entwined like vines in the famous double-helix structure (Figure 1.4). A nucleotide contains a sugar (deoxyribose) group (S), a phosphate group (P) and a nitrogen-containing base. Four bases occur in DNA: adenine (A), guanine (G), cytosine (C) and thymine (T).⁶ Consequently, there are four nucleotides. The backbone of a vine consists of alternating sugar and phosphate groups linked together

⁶The former two are purines, while the latter two are pyrimidines.

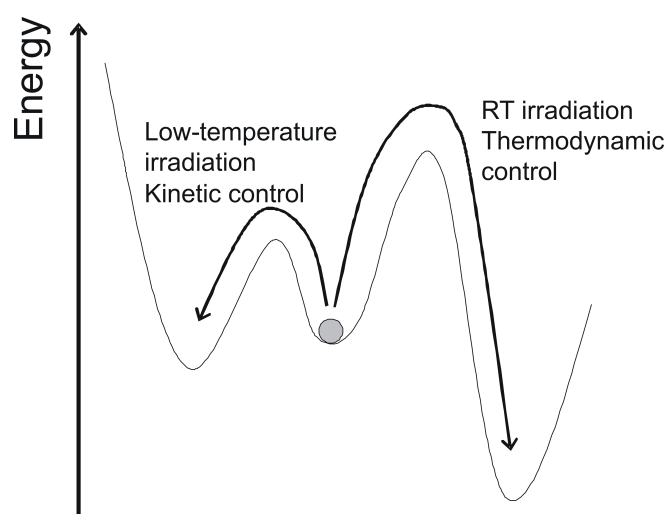


Figure 1.3: Possible influence of radiation temperature on radical processes, illustrated by an analogy with a 1D potential energy surface. When the radiation is performed at low enough temperature, the reaction with the lower activation energy proceeds (*kinetic control*), while at sufficiently high temperatures, the reaction yielding the most stable product is favoured (*thermodynamic control*).

by phosphodiester bonds. In between the vines and connected to a sugar unit are the bases, which engage in specific hydrogen bonds with each other: only the *base pairs* A-T and G-C are formed (this is called the *complementarity* of the bases). The genetic information of a living organism is basically stored in the specific sequence of bases and the complementarity of the strands allows DNA to be copied easily: if the hydrogen bonds linking the two strands are broken, each strand can function as a template for its complementary strand and the result is a net duplication of the original DNA molecule. Also by virtue of the complementarity, the major part of DNA damage can readily be repaired.

DNA is present in nearly all cells of a living organism and most of the time it is in an extremely compact form: the DNA is tightly wrapped around proteins (called histones) into *nucleosomes*. The nucleosomes are in turn coiled together in tightly packed loops and form *chromosomes*. In spite of its dense packing, the DNA in the chromosomes is extensively hydrated (typically 25 - 100 water molecules per nucleotide [5]), with water molecules located in between the strands as well as in between the loops and coils of the chromosomes. However, the major part of the water behaves like crystalline (and not bulk) water due to the compact, rigid packing in combination with strong hydrogen bonds (and other electrostatic forces).

1.2. Radiation damage to DNA

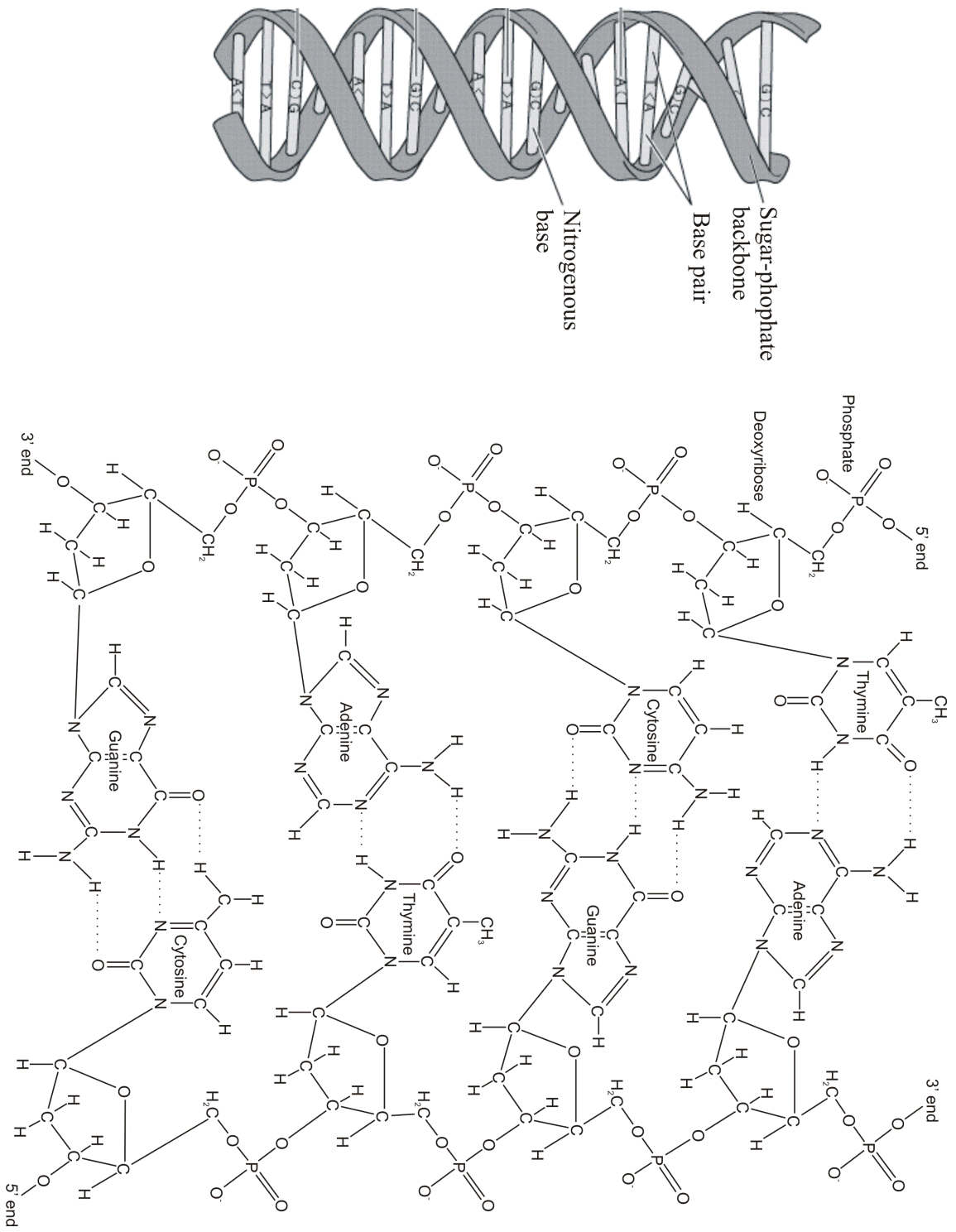


Figure 1.4: The chemical structure of DNA.

1.2.2 Direct and indirect effect

Radiation can inflict damage to a DNA molecule either by direct interaction (*direct effect*) or indirectly, through a mediating radical species induced by the radiation in another molecule (*indirect effect*). An example of the indirect effect are OH• radicals, created in the surrounding hydration layer, that abstract H-atoms from deoxyribose units. The relative importance of direct and indirect effects in DNA radiation damage has been the subject of much scientific debate. At present there is a more or less general consensus that indirect effects account for ~60 % and direct effects for ~40 % [3, 5, 6]. Indirect DNA radiation damage is rather well characterised and understood, both quantitatively and mechanistically [6, 9]. The direct effects have proven more elusive, although a vast amount of data has been collected and much progress has been made the last decades in mapping and rationalising them.

1.2.3 Strand breaks

There are different types of radiation damage to a DNA molecule. Two of the more conspicuous examples are *free-base releases* (scission of a sugar-base junction) and *single strand breaks* (SSB, scission of a sugar-phosphate junction). Two single strand breaks in close proximity to each other on opposite strands are called a *double strand break* (DSB). DSBs are considered to be the single most important type of damage to DNA with respect to harmful (and even lethal) biological effects. They are, in comparison to other types of damage, much more likely not to be repaired or to be repaired incorrectly since the complementarity of the strands cannot be employed. The spur pattern of the initial ionisations (Section 1.1.2.2) greatly increases the chance of a DSB occurring. This is why ionising radiation is far more harmful than normal metabolic processes, which also continuously cause damage to DNA but with a much more uniform spatial distribution.

1.2.4 The direct effect: initial ionisations and charge migration

In this section a short overview is presented of the current knowledge on the initial, direct-effect-type events in DNA irradiated with low-LET radiation. This is a very active research field and not all 'facts' presented below are equally well established. Sometimes discrepancies are encountered in the literature, in which case I have adopted what seemed to be the majority's point of view. For a more detailed and balanced discussion on the subject and for more specific references, the reader should consult Refs. [2, 3, 9–12].

The number of initial ionisations in a certain part of a DNA molecule is approximately proportional to the fraction of the electrons in that part (Section 1.1.2.2). Since roughly half of the electrons in a nucleotide are located in the sugar-phosphate (SP) moiety, $\sim 50\%$ of the holes are initially formed at the SP backbone ($\sim 15\%$ at S, $\sim 35\%$ at P) and the other 50% at the bases.

In the gas phase, the IPs of the different DNA moieties increase as

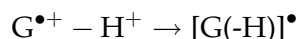
$$G < A < T < C < SP$$

The DNA environment - base pairing in particular - affects the IPs but the relative order is found not to change [12]. Not considering recombination processes, charge-transfer processes should therefore direct all the holes to guanine bases (forming $G^{\bullet+}$). Analogously, the EAs of the moieties have the following order:

$$SP < G < A < T \lesssim C$$

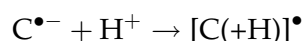
so that all electrons should migrate to cytosine and thymine bases (forming $C^{\bullet-}$ and $T^{\bullet-}$).

Experimentally, it is found that recombination is the dominant radical process: even at 4 K, only 30 - 50 % of the initial ionisations evolve into stabilised radicals. That recombination is not even more extensive is due to the limited electron and hole mobility in DNA.⁷ Of the holes that escape recombination, about 75 % stabilise as deprotonated (neutral) guanine radicals ($[G(-H)]^{\bullet}$). The latter are formed by a proton-transfer reaction from the guanine cation to its cytosine base-pair partner along a hydrogen bond:⁸



The other 25 % yield neutral sugar radicals ($[S(-H)]^{\bullet}$) through rapid deprotonation of sugar-cation radicals. This implies that $\sim 50\%$ of the holes that are initially generated at the SP backbone (and do not recombine) are trapped there, which indicates that the rate of deprotonation of the sugar cations is comparable to the charge-transfer rate in DNA.

The majority ($\sim 85\%$) of the electrons that do not recombine are trapped as protonated (neutral) cytosine radicals ($[C(+H)]^{\bullet}$), formed by proton transfer to the cytosine anion from its guanine base-pair partner along a hydrogen bond:



⁷It has been estimated that electrons and holes on average travel less than 10 base pairs along the DNA axis [5].

⁸It is in general very hard to unambiguously determine the protonation state of a base radical and the protonation states are often unknown. In the literature, 'cation' and 'anion' are used even if (de)protonation is suspected (or even known) to occur.

A smaller fraction ($\sim 10\%$) forms thymine anion radicals ($T^{\bullet-}$). The dominance of the cytosine radicals is due to the stabilising effect of the deprotonation reaction. A small portion of the electrons ($\sim 5\%$) has been suggested to engage in dissociative electron attachment (DEA), giving rise to a variety of radicals. This point is addressed in the next section.

The deprotonation of the sugar cations is irreversible, but the (de)protonation processes at the guanine and cytosine bases are thought to be reversible. Consequently, the base radicals are thermally less stable: annealing of a DNA sample induces back transfers of the protons, after which charge migration can again take place and a variety of different processes, including recombination, may occur.

1.2.5 Sugar radicals

1.2.5.1 Relative abundance

From the discussion above we conclude that $\sim 12.5\%$ of all the radicals initially stabilised in DNA are sugar radicals. The numbers reported in the literature vary, but are usually in the range 10 to 20% in the more recent studies and reviews. Since sugar radicals are thermally more stable, their relative yield should increase upon annealing. Bernhard and Close indeed suggest that annealing to 120 K after irradiation at 4 K results in the sugar radical yield being about half of the total radical yield [3]. Sevilla *et al.*, on the other hand, do not report any noticeable change in the sugar radical yield upon annealing to 140 K after irradiation at 77 K [2]. Also, an increase in the sugar radical yield has been observed when high-LET radiation is used – a possible explanation is given in Section 1.2.5.3.

1.2.5.2 Primary precursors to strand breaks

Sugar radicals are the *primary* precursors for DSBs. Base radicals are relatively ineffective in inducing strand breaks. Low-energy electrons (LEEs) can give rise to strand breaks via dissociative electron capture (DEA) at the SP backbone,⁹ but, even if LEEs are produced in large amounts in DNA by

⁹Sanche and co-workers have shown that low-energy electrons are capable of inducing, among others, strand breaks and free-base release in DNA, even when their energy is below the ionisation threshold (~ 7 eV in DNA) [11, 13]. This supposedly proceeds via DEA and a transient anion which can be considered as an excited state of the electron adduct of the parent molecule. Different hypotheses about the exact mechanism exist in the literature, but we refrain from a detailed discussion here.

radiation (typically $5 \cdot 10^4$ LEEs with energies < 15 eV per MeV of deposited energy [14]), the number of radicals associated with this process is small [2] (cf. Section 1.2.4).

1.2.5.3 Direct formation of sugar radicals

As discussed in Section 1.2.4, neutral sugar radicals are generated through rapid deprotonation of sugar cations formed by the initial oxidative ionisation events. There appears to be a second pathway for the direct formation of sugar radicals: recently, Sevilla and co-workers have shown that photoexcitation can induce transformations of guanine cation radicals into neutral sugar radicals in frozen aqueous solutions of DNA model systems, double-stranded DNA and RNA (ribonucleic acid) [2, 12, 15–17]. The proposed mechanism comprises hole transfer via an excited state onto the sugar unit, after which the sugar cation rapidly deprotonates. Time-dependent DFT calculations indeed indicate that certain excited states of the $G^{\bullet+}$ (and also $[A(-H)]^{\bullet}$ radicals) are substantially delocalised onto the SP moiety in mononucleotides. This mechanism offers a plausible explanation for the increased yield of sugar radicals for high-LET (as opposed to low-LET) radiation: the more dense clustering of ionisations and excitations yields a higher probability of hole transfer from sugar to base.

Even if the pathway suggested would not be correct, the experimental results show that transfer of radicals from the bases to the SP moiety is possible and that excited states are involved in the transfer mechanism. This is an important finding because it leads to a higher total yield of sugar radicals, and hence more SSBs and DSBs (Section 1.2.5.2).

1.2.5.4 Chemical identity and secondary radical processes

So far we have not specified the chemical nature of the sugar radicals that are trapped at the SP backbone. Mainly H-abstracted carbon-centred radicals are detected in both DNA and DNA model systems (see Figure 1.5 for the labelling scheme of the carbons). The relative concentrations and precise identities of the sugar radicals strongly depend on the system under study and it is essentially not yet understood which factors (electronic, geometrical, environmental) direct the radical to a specific site. Results in the literature do suggest, however, that [12, 17]

- the radical formation is not thermodynamically controlled (i.e. the C-H bond energies are not the determining factor).

- phosphate substitution at a specific site in a nucleoside tends to deactivate sugar-radical formation at that site.

The precise reaction mechanisms that lead from neutral sugar radicals to strand breaks in the direct effect¹⁰ are also not known. Although sugar radicals correspond to deeper traps than base radicals (Section 1.2.4), they are expected to participate in secondary processes at RT. Not much, if anything, is known at present about these thermally driven transformations of the sugar radicals or the final stable radicals and/or diamagnetic structures. The main reason for this deficiency in the literature is that studying the detailed structure of the sugar radicals involved in direct radiation damage to DNA is difficult, as is discussed in the next section.

1.2.5.5 Studying DNA sugar radicals with EMR

If detailed information on the structure of a radical is required, EMR measurements are usually the best option. Originally, sugar radicals were detected in X-irradiated nucleosides and nucleotides after low-temperature irradiation,¹¹ but not in actual DNA samples. This led many researchers to believe that sugar radicals were simply not present in DNA, or only in very low concentrations. This conclusion was rationalised in terms of a complete hole transfer to the guanine bases. In 1997, however, Close [21] pointed out that H-abstracted sugar radicals may easily escape detection, because

- the radicals can be located on all five carbon atoms of the deoxyribose unit.
- each radical is expected to occur in a wide variety of conformations in the DNA helix, thus broadening the resonance lines.
- the unpaired spin typically interacts with several protons, giving rise to multiply split EPR lines.

This gives rise to featureless EPR spectra with small amplitudes, largely obscured by the EPR spectra of the base radicals. As is apparent from the discussion in the previous sections, it is now generally accepted that sugar radicals are produced in significant yields by the direct effect, but clear, direct observation of sugar radicals in X-irradiated DNA by EPR remains

¹⁰For strand scission resulting from any of the five possible H-abstracted radical centres through specific product mediation, see Ref. [18].

¹¹For instance, sugar radicals located on all 5 carbon atoms were detected in 5'dCMP (deoxycytidine 5'-monophosphate). [19, 20]

scarce [22, 23]. There is perhaps only one study where a specific sugar radical was convincingly identified in X-irradiated DNA: a C3'-centred radical in a crystalline polynucleotide [22].

Electron-nuclear double resonance (ENDOR) measurements can (in principle) yield a large amount of detailed and unequivocal information on the radical structure. ENDOR would consequently greatly facilitate the study of radicals in DNA in general, and of sugar radicals in particular. One specific problem to which ENDOR measurements could provide a definite answer is the protonation state of the initial base radicals (cf. Section 1.2.4). Up to now, however, there are no published results showing ENDOR signals in DNA, even if several research groups have made considerable efforts [10].

1.2.5.6 Relevance of sucrose and glucose 1-phosphate single crystals as model systems

EMR studies can be carried out on radicals in gaseous, aqueous, frozen, polycrystalline (powder) or single-crystal samples. Because of the specific orientation of the radicals in single crystals, the latter provide by far the most detailed information. For unambiguous structural characterisation and identification of the radicals, single crystals are therefore in general the best choice. In the context of the direct effect of DNA radiation damage, additional benefits of single crystals emerge: the crystal structure mimics to some extent the tight, rigid packing of DNA in the chromosomes (Section 1.2.1) and is held together by hydrogen bonds which also play a crucial role in DNA radiation damage (Section 1.2.4).

The complexity of a DNA molecule and experimental difficulties necessitate the study of smaller model systems with similar key features if detailed information about the radicals and their formation mechanisms is sought. The central goal behind this type of studies is not the identification of the radicals itself – although this is a necessary first step –, but rather obtaining insight in the fundamental principles governing the radical formation, which *should* be transferable. The objective essentially is to construct mechanistic models with the capability of predicting reaction outcomes.

In the doctoral research, radicals induced by X irradiation in single crystals of sucrose and glucose 1-phosphate (G1P) have been studied (Chapters 5 and 6 respectively). Their chemical structures and that of the SP backbone in DNA are depicted in Figure 1.5. G1P has a sugar-phosphate junction so that a first and most important reason to study it is obtaining information on strand-break formation in DNA. Sucrose has a glycosidic bond that bears some resemblance to the sugar-phosphate junction but is of course far from

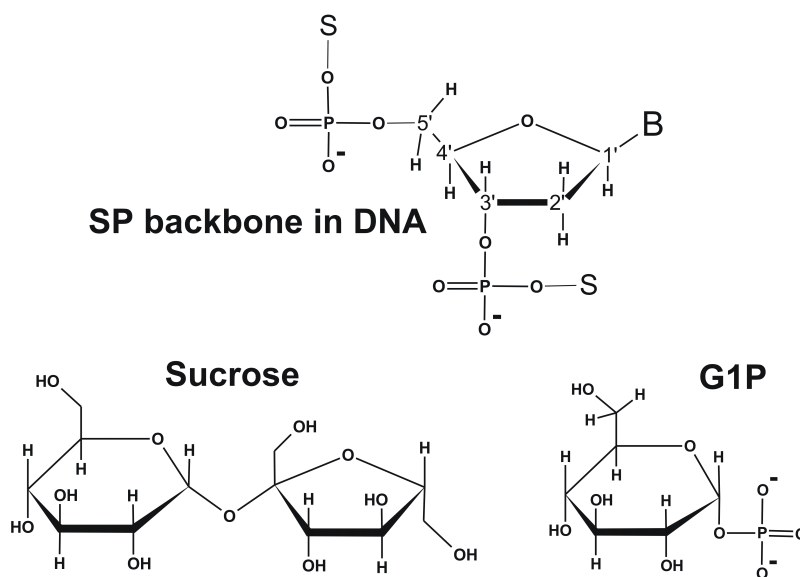


Figure 1.5: The chemical structure of the SP backbone in DNA (B = base, S = sugar) and of the molecules of the two systems studied in the doctoral research: sucrose and G1P.

the best model in this respect. However, as stated in Section 1.2.5.3, it is not known which factors determine the specific trapping site in the sugar ring, or which secondary radical processes the initially stabilised radicals participate in (and why). The prerequisite for answering these questions is knowledge of the radical identities (primary as well as intermediate and stable). The results obtained in the doctoral research, both on sucrose and G1P, are relevant in this context. Since identifying radicals in DNA is so complex, the reduction to 'simple' sugar single crystals is justified.

Chapter 2

Electron magnetic resonance

2.1 The Zeeman effect

2.1.1 Spins and magnetic moments

A ring current of electrons induces a magnetic moment perpendicular to the plane of the current. Classically, the relation between the electronic orbital angular momentum \vec{L} of the electron and the associated electronic magnetic moment $\vec{\mu}_L$ is given by

$$\vec{\mu}_L = -\mu_B \vec{L} \quad (2.1)$$

Here, \vec{L} is expressed in units \hbar (the reduced Planck constant) and μ_B is the Bohr magneton, given by

$$\mu_B = \frac{e\hbar}{2m_e} \quad (2.2)$$

where e and m_e are the absolute charge and the mass of the electron respectively.

In order to explain the experimental results of the famous Stern-Gerlach experiment [24] in 1922,¹ Goudsmit en Uhlenbeck postulated (in 1925) the existence of an additional electronic spin momentum (or: *spin*) \vec{S} , with size $S = \hbar/2$. This spin is a purely quantum-mechanical phenomenon – it has no valid classical analogon. The associated spin magnetic moment $\vec{\mu}_S$ is

$$\vec{\mu}_S = -g_e \mu_B \vec{S} \quad (2.3)$$

¹Basically, a beam of silver atoms sent through an inhomogeneous magnetic field, with the field gradient perpendicular to the incoming beam, was observed to split up in two discrete components, instead of the classically expected continuous spectrum.

2.1. The Zeeman effect

where $g_e \approx 2.0023$ is the free-electron g factor. Equation 2.3 above is rigorously valid only for the free electron. In general, one can write

$$\vec{\mu}_S = -g\mu_B\vec{S} \quad (2.4)$$

where a general g factor is introduced and \vec{S} is an *effective* spin (see Section 2.1.3).

Nuclei can also possess an intrinsic spin, the nuclear spin \vec{I} , and the associated spin magnetic moment $\vec{\mu}_I$ is

$$\vec{\mu}_I = g_N\mu_N\vec{I} \quad (2.5)$$

where g_N is the nuclear g factor (its value depending on the specific nucleus) and the nuclear magneton μ_N is defined as

$$\mu_N = \frac{e\hbar}{2m_p} \quad (2.6)$$

with m_p is the mass of the proton. Nuclear-spin interactions are far weaker than electron-spin interactions because μ_N is approximately three orders of magnitude smaller than μ_L ($m_p \approx 1836m_e$ and g factors are of the order of 1).

We will adopt the usual convention of expressing spin values in units of \hbar . E.g., the electron spin has size $S = 1/2$.

2.1.2 The Zeeman effect for a free electron

The classical interaction energy between a magnetic moment $\vec{\mu}$ and a magnetic field \vec{B} is

$$E = -\vec{B} \cdot \vec{\mu} \quad (2.7)$$

The corresponding Hamiltonian for this interaction in quantum mechanics is

$$\hat{H} = -\vec{B} \cdot \hat{\vec{\mu}} \quad (2.8)$$

In the case of a free electron, we can apply Eq. (2.3) and obtain

$$\hat{H} = g_e\mu_B\vec{B} \cdot \hat{\vec{S}} \quad (2.9)$$

If we assume the magnetic field to lie along the positive $\langle z \rangle$ axis ($\vec{B} = B\vec{e}_z$), this yields

$$\hat{H} = g_e\mu_B B \hat{S}_z \quad (2.10)$$

The operator \hat{S}_z has eigenvalues $M_S = \pm 1/2$ and we find two energy levels:

$$E_+ = \frac{1}{2}g_e\mu_B B \quad E_- = -\frac{1}{2}g_e\mu_B B \quad (2.11)$$

Thus, in the presence of magnetic field, *spin-up electrons* (spin parallel to \vec{B} , and consequently a spin magnetic moment antiparallel to \vec{B}) have a higher energy than *spin-down electrons*, and the energy difference is proportional to the strength of the magnetic field (Figure 2.1):

$$\Delta E = E_+ - E_- = g_e \mu_B B \quad (2.12)$$

Analogous equations of course apply for the *nuclear* Zeeman effect for nuclei with $I = 1/2$: g_e should be replaced by g_N and μ_B by μ_N .

This splitting of degenerate energy levels by the interaction of a magnetic field with the electron and nuclear spins is the basis for magnetic-resonance experiments (Section 2.2). First, the concept of the spin Hamiltonian needs to be introduced.

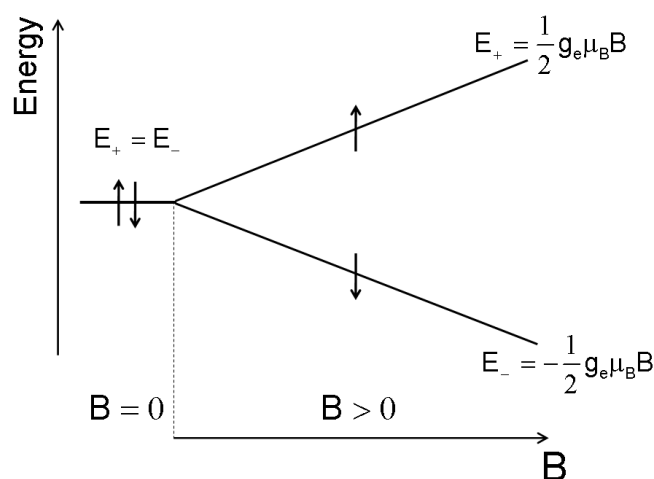


Figure 2.1: The Zeeman effect for a free electron.

2.1.3 The spin Hamiltonian

Within the Born-Oppenheimer approximation, the electronic wave function of a molecule obeys a time-independent Schrödinger equation, in which the Hamiltonian is dominated by the kinetic and (Coulombic) potential energy of the electrons. Electron- and nuclear-spin interactions represent only a small perturbation on these terms (see Section 3.2.2, page 54). In general, the total Hamiltonian is very complex and the system has many different eigenstates and energy eigenvalues. However, in thermal equilibrium, only a limited number of energy levels close to the ground state is occupied significantly

(Boltzmann distribution, cf. Section 2.2.1). Also, in EMR experiments transitions are only induced between a small number of the lowest-lying energy levels, split up by electron and nuclear-spin interactions. Therefore, it is common practice to use a so-called *spin Hamiltonian* for the analysis of EMR spectra: an *effective* Hamiltonian which only contains (electron and nuclear) spin interactions, characterised by one or more coupling coefficients, called *spin-Hamiltonian parameters*. We will only discuss the general concept here. For a detailed discussion, the reader should consult e.g. Ref. [25] or [26].

Essentially, a certain number of energy levels is regarded as an isolated set, effective electron-spin operators are introduced such that the right number of energy levels is obtained² and the coupling coefficients are determined by demanding that the energy levels of the real, complete Hamiltonian are reproduced. Mixing of the "isolated" set of energy levels with higher-lying states (by interactions that are not explicitly considered in the spin Hamiltonian) make the coupling coefficients differ from the values they would have if the system really would be isolated.

Sometimes a coupling coefficient can be understood as an expectation value of the full Hamiltonian operating on the orbital part of the electronic wave function, in which case the spin operator corresponds to a true (physical) spin operator. This applies e.g. to the dipolar HFC interaction (see Section 4.3.1, page 80). In general, however, the spin-Hamiltonian parameters do not have a direct physical interpretation. Their values can then only indirectly yield information about physically relevant parameters (e.g. via perturbation theory) and the operators are *effective* operators. One example is the g tensor, whose principal values and directions are to a large extent determined by spin-orbit coupling interactions (see Sections 3.3.1 and 4.4, pages 63 and 97 respectively). For the sake of simplicity, we will simply adopt the notation \vec{S} for the effective spin, and \hat{H} for the spin Hamiltonian.

The systems studied in this doctoral thesis are molecular defects with one unpaired electron. All other electrons are part of a closed shell ($\sum_i \vec{S}_i = \sum_i \vec{L}_i = \vec{0}$), so that $S = 1/2$ and a quasi single-electron picture can be used. Nearly all³ the $S = 1/2$ systems studied have N nuclear spins \vec{I}_k with $I_k = 1/2$ and the following spin Hamiltonian is adequate:

$$\hat{H} = \mu_B \vec{B} \cdot \vec{g} \cdot \hat{S} + \sum_{k=1}^N \hat{S} \cdot \vec{A}_k \cdot \hat{I}_k - \sum_{k=1}^N g_{N,k} \mu_N \vec{B} \cdot \hat{I}_k \quad (2.13)$$

²If only electron-spin interactions need to be considered, an effective spin \vec{S}' is introduced such that $2S' + 1$ equals the number of levels experimentally observed.

³Measurements were also performed on deuterated crystals, in which deuterium with $I = 1$ is present.

The first term is the *electronic Zeeman interaction* and accounts for the interaction of \vec{S} with the external magnetic field \vec{B} , with \bar{g} the g tensor. The second term represents the *hyperfine coupling* (HFC) *interactions*⁴ between \vec{S} and the various nuclear spins, \bar{A}_k being the HFC tensor for the k^{th} nuclear spin. The third and last term accounts for the *nuclear Zeeman interactions* between the nuclear spins and the external magnetic field. Note that the latter interaction is taken to be isotropic (i.e. scalar), which indeed is a very good approximation, while the first two interactions in general are anisotropic:

$$\bar{g} = \begin{bmatrix} g_{xx} & g_{xy} & g_{xz} \\ g_{yx} & g_{yy} & g_{yz} \\ g_{zx} & g_{zy} & g_{zz} \end{bmatrix} \quad \bar{A} = \begin{bmatrix} A_{xx} & A_{xy} & A_{xz} \\ A_{yx} & A_{yy} & A_{yz} \\ A_{zx} & A_{zy} & A_{zz} \end{bmatrix} \quad (2.14)$$

These matrices are commonly called *tensors* while they in fact do not have the transformation properties of tensors [25]. The origin and interpretation of the g tensor and HFC tensors in organic radicals is discussed extensively in Chapters 3 and 4. In the remainder of this chapter, we take spin Hamiltonian (2.13) as a given.

2.2 Magnetic-resonance experiments

In magnetic-resonance experiments (EPR⁵ (electron paramagnetic resonance), NMR (nuclear magnetic resonance), ENDOR (electron-nuclear double resonance)), magnetic dipole transitions are induced between energy levels associated with electron (EPR) and/or nuclear (NMR, ENDOR) spins by applying one (EPR, NMR) or two (ENDOR) radiation fields in the presence of a static magnetic field.⁶ In Sections 2.2.2 2.2.3 and 2.2.4, the basic principles of these experiments are explained. Only continuous-wave (and not pulsed) magnetic-resonance experiments will be discussed. First, the concepts saturation and lattice relaxation need to be introduced.

⁴In principle, *hyperfine* is used when the electron spin interacts with the nuclear spin of the atom where it is mainly located, while *superhyperfine* is used to refer to interactions of the electron spin with nuclear spins of other atoms. In a molecule the electron spin is in general delocalised over several atoms and this distinction cannot be retained.

⁵Note that, in this work, *EMR* is a general term and refers to *any* electron-magnetic-resonance technique, while *EPR* refers to a specific, well-defined technique (cf. Section 2.2.2). In the literature, EPR is often used as a general term.

⁶It can be shown via time-dependent perturbation theory that such transitions are only induced when the oscillating magnetic field associated with the radiation field is perpendicular to the static magnetic field [25].

2.2.1 Saturation and relaxation

Consider an ensemble of identical systems with energy levels E_1, E_2, \dots . Provided this ensemble is in thermal equilibrium, it has a Boltzmann distribution: the number of systems N_i that occupy a certain energy level E_i is

$$N_i = A e^{-\frac{E_i}{kT}} \quad (2.15)$$

where A is a normalisation constant, k is the Boltzmann constant and T is the temperature (in K). Consequently, the population difference $\Delta N = N_1 - N_2$ for two energy levels E_1 and E_2 with $E_1 < E_2$ is

$$\Delta N = N_1 \left(1 - e^{-\frac{\Delta E}{kT}} \right) \quad (2.16)$$

where $\Delta E = E_2 - E_1$. Note that the population of an energy level decreases exponentially with increasing energy. When a radiation field supplies energy quanta ΔE , the transition probabilities $W_{1 \rightarrow 2}$ and $W_{2 \rightarrow 1}$ are equal, but since $N_1 > N_2$, there are more transitions from E_1 to E_2 and the net effect is that the system absorbs energy. However, these transitions equalise the population levels and there no longer is net absorption. This is called *saturation* of a transition.

In real systems, various *relaxation* mechanisms allow deexcitation of E_2 to E_1 and saturation of an energy level only occurs when the rate of transitions induced by the radiation field is larger than the relaxation rate.

2.2.2 EPR transition in an $S = 1/2$ system

To illustrate the basic principle of an EPR experiment, consider a free electron in a static magnetic field $\vec{B}_0 = B_0 \vec{e}_z$ and assume that an oscillating magnetic field $\vec{B}_1 = B_1 \cos \omega t \vec{e}_x$ (with $B_1 \ll B_0$) is applied [27]. The electron is thus submitted to a total magnetic field

$$\vec{B} = (B_1 \cos \omega t) \vec{e}_x + B_0 \vec{e}_z \quad (2.17)$$

The spin Hamiltonian of this system is

$$\hat{H} = g_e \mu_B B_0 \hat{S}_z + g_e \mu_B B_1 \hat{S}_x \cos \omega t = \hat{H}_0 + \hat{H}_1 \quad (2.18)$$

Since $B_0 \gg B_1$, the energy eigenvalues are in a very good approximation those of \hat{H}_0 :

$$E_+ = \frac{1}{2} g_e \mu_B B_0 \quad E_- = -\frac{1}{2} g_e \mu_B B_0 \quad (2.19)$$

The point now is that the oscillating magnetic field can induce a transition between E_+ and E_- when the energy quanta $h\nu = \hbar\omega$ of this field match $\Delta E = E_+ - E_-$:

$$h\nu = g_e\mu_B B_0 \quad (2.20)$$

This is the *resonance condition*. In an EPR experiment, the radiation frequency ν is kept constant and the static magnetic field B_0 is varied. At a certain value of B_0 (B_{res}) the resonance condition (2.20) is met and the radiation is absorbed.

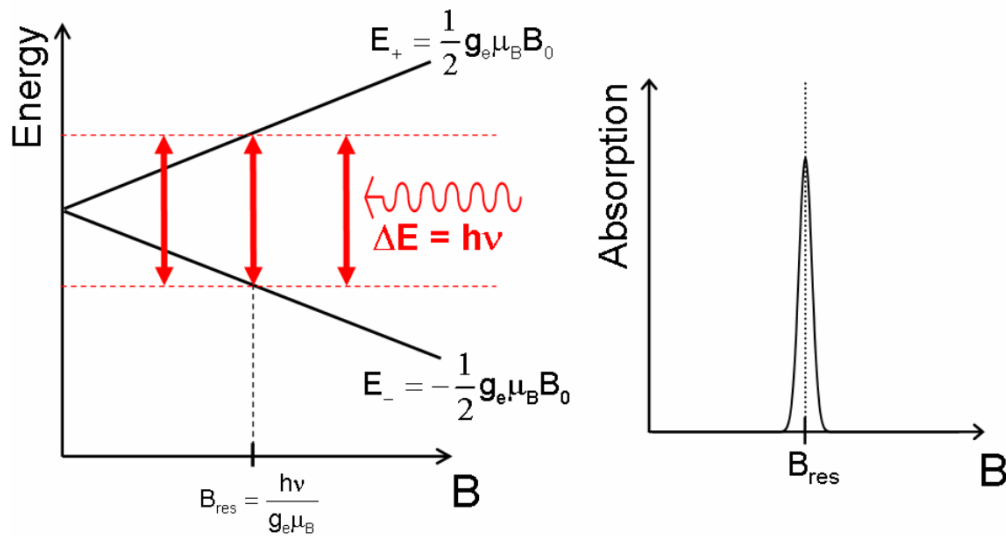


Figure 2.2: The basic principle of an EPR experiment.

This absorption basically constitutes the EPR signal (Figure 2.2).

When the electron interacts with e.g. its lattice environment, the free electron value g_e should be replaced by an orientation-dependent g factor (see Section 2.3.1):

$$h\nu = g\mu_B B_0 \quad (2.21)$$

We see that g factors can be determined from the magnetic field at which an EPR transition is observed.

Analogously, transitions can be induced between the two nuclear-spin levels of a nucleus with spin $I = 1/2$, which is the basic principle of an NMR experiment. An example is provided in the next section.

2.2.3 EPR and NMR transitions in an $S = 1/2$, $I = 1/2$ system

Assume an $S = 1/2$, $I = 1/2$ system is described by the following spin Hamiltonian:⁷

$$\hat{H} = g\mu_B \vec{B} \cdot \hat{S} + A \hat{S} \cdot \hat{I} - g_N \mu_N \vec{B} \cdot \hat{I} \quad (2.22)$$

which follows from spin Hamiltonian (2.13) if there is only one nuclear spin and if both the g tensor and the HFC tensor are isotropic. If we additionally assume that $|A| \ll |g_e \mu_B B|$, this reduces to

$$\hat{H} = g\mu_B B \hat{S}_z + A \hat{S}_z \hat{I}_z - g_N \mu_N B \hat{I}_z \quad (2.23)$$

in a first-order approximation. The energy eigenvalues of this spin Hamiltonian are

$$E(M_S, M_I) = E_e M_S + A M_S M_I - E_N M_I \quad (2.24)$$

where the quantities E_e and E_N are defined as

$$E_e = g\mu_B B \quad (2.25)$$

$$E_N = g_N \mu_N B$$

An energy-level scheme is given in Figure 2.3 for the case $A > 2g_N \mu_N B > 0$. The following selection rules apply for the EPR transitions [26]:

$$|\Delta M_S| = 1 \quad \Delta M_I = 0 \quad (2.26)$$

Consequently, an EPR signal is observed when

$$h\nu = g\mu_B B \pm \frac{1}{2} A \quad (2.27)$$

or, since the field is swept:

$$B = \frac{h\nu}{g\mu_B} \mp \frac{A}{g\mu_B} \quad (2.28)$$

Thus, the EPR spectrum is a doublet of lines centred at $\frac{h\nu}{g\mu_B}$ and with a splitting

$$\left| \frac{A}{g\mu_B} \right|.$$

For NMR transitions, the selection rules are

$$\Delta M_S = 0 \quad |\Delta M_I| = 1 \quad (2.29)$$

⁷We employ the notations \vec{B} (and B) – without the subscript 0– for the static magnetic field (and its size) again from now on.

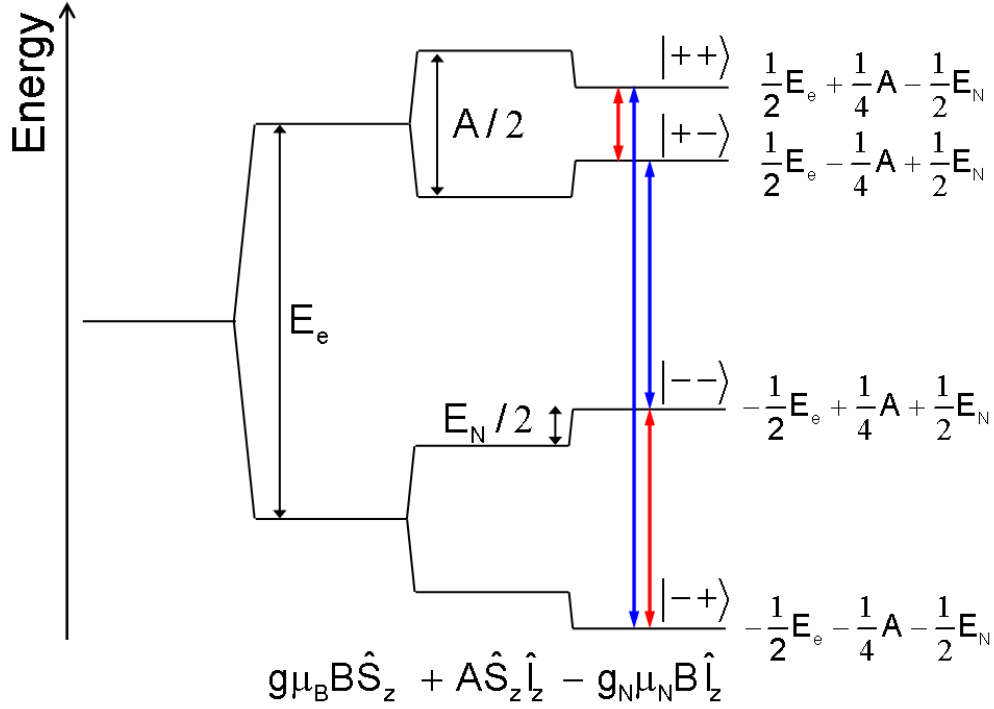


Figure 2.3: Energy level scheme for a system with $S = 1/2$ and $I = 1/2$, described by spin Hamiltonian (2.23), for the case $A > 2g_N\mu_N B > 0$. E_e and E_N are defined by Eqs. (2.25). The eigenstates are labelled $|M_S M_I\rangle$ (+ corresponding to $+1/2$ and $-$ to $-1/2$). The two EPR transitions allowed by selection rules (2.26) are marked in blue, the two NMR transitions allowed by selection rules (2.29) are marked in red.

and an NMR transition occurs when

$$\nu = \frac{1}{h} \left| \pm \frac{1}{2} A - g_N \mu_N B \right| \quad (2.30)$$

In the case $|A| > |2g_N\mu_N B|$ (*strong coupling*), this yields a doublet centred at $|\frac{A}{2h}|$, with a splitting of $|\frac{2g_N\mu_N B}{h}|$, while in the case $|A| < |2g_N\mu_N B|$ (*weak coupling*) the doublet is centred at $|\frac{g_N\mu_N B}{h}|$ and has a splitting $|\frac{A}{h}|$. Thus, both the g factor and $|A|$ can be determined from the EPR spectrum, while the NMR spectrum also yields $|A|$, as well as $|g_N|$. The latter immediately allows identification of the interacting nucleus.

In the derivation of Eqs. (2.28) and (2.30) three major assumptions were made:

1. Both the HFC and the nuclear Zeeman terms are very small compared to the electronic Zeeman term.
2. The electronic Zeeman interaction is isotropic.

3. The HFC interaction is isotropic.

The first two are (very) good approximations for all the organic radicals encountered in this doctoral thesis, but the latter is not. The repercussions of the HFC anisotropy on the EPR and NMR line positions is discussed in Section 2.4.

2.2.4 ENDOR**2.2.4.1 Combining the advantages of EPR and NMR**

Although both EPR and NMR spectra allow determination of the HFC interaction, there is a fundamental difference in their inherent resolution, which becomes bigger with an increasing number of HFC interactions. This is essentially due to a difference in the coupling strength between electron and nuclear spins on the one hand, and between nuclear spins mutually on the other hand.

In an EPR experiment, the electron spin is the measuring probe and this spin is coupled to, say, N nuclear spins I_1, \dots, I_N . According to the EPR selection rules

$$|\Delta M_S| = 1 \quad \Delta M_{I_i} = 0 \quad (i = 1, \dots, N) \quad (2.31)$$

the number of allowed EPR transitions is

$$n_{EPR} = 2S \prod_{k=1}^N (2I_k + 1) \quad (2.32)$$

In an NMR experiment, the nuclear spins are the measuring probe. These are in general coupled much more strongly to the electron spin than to each other, and only the coupling to the electron spin should be considered for practical purposes. The NMR selection rules

$$\Delta M_S = 0 \quad |\Delta M_{I_j}| = 1 \quad \Delta M_{I_i} = 0 \quad (i \neq j) \quad (2.33)$$

yield

$$n_{NMR} = (2S + 1) \sum_{k=1}^N 2I_k \quad (2.34)$$

allowed NMR transitions. Comparing Eqs. (2.32) and (2.34), it is obvious that NMR is more advantageous for studying HFC interactions. Other advantages of NMR over EPR include the – in principle – easy identification of the interacting nucleus (see Section 2.2.3).

However, there also is a major downside to NMR experiments: the signals

are typically much less intense than EPR signals, because (i) the probability for a transition between nuclear-spin levels is smaller and (ii) the population difference between two nuclear-spin levels is smaller (Boltzmann distribution, see Section 2.2.1). ENDOR combines the advantages of both techniques by inducing an EPR and an NMR transition at the same time. This makes it a very powerful tool to study paramagnetic defects in great detail. Most of the results obtained in the doctoral research required the use of ENDOR. The basic principle of an ENDOR measurement is explained in the next section.

2.2.4.2 ENDOR: an example

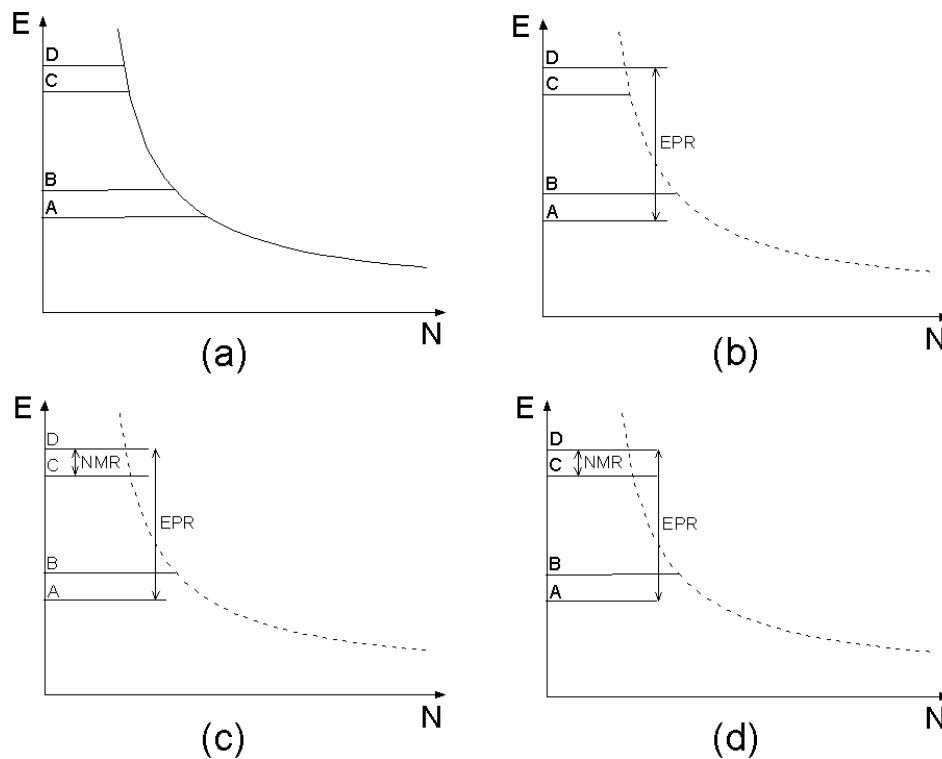


Figure 2.4: Evolution of the energy-level populations during an ENDOR experiment for an $S = I = 1/2$ system (cf. Figure 2.3). The curved line represents the Boltzmann distribution of the energy-level populations.

Consider again an $S = I = 1/2$ system described (in a first-order approximation) by spin Hamiltonian (2.23) and with energy levels as given in Figure 2.3. The evolution of the energy-level populations of this system during an ENDOR experiment is shown in Figure 2.4 [27]. Before the experiment, the system is in thermal equilibrium (a). In an ENDOR experiment, the static magnetic field is fixed such that the microwave radiation saturates an EPR transition ($A \leftrightarrow D$), thus equalising the populations of those levels (b).

Radiation with a varying radio frequency is now supplied to the system. At a certain frequency, the NMR transition $C \leftrightarrow D$ is induced, which equalises the population of those levels (c). The EPR transition $A \leftrightarrow D$ temporarily desaturates, after which a new equilibrium (with equal populations for levels A, C and D) is found (d). The change in the EPR-signal intensity is present as long as the NMR transition is induced. Thus, the NMR transition frequency can be detected by monitoring the intensity of the EPR spectrum while sweeping the radio frequency field. This essentially constitutes an ENDOR spectrum. Note that ENDOR is *species selective*: only NMR transitions for which one of the nuclear-spin levels is addressed by the EPR transition are observed.

Spin-relaxation processes should be included in the discussion for a more detailed description of the ENDOR mechanism [27]. We merely note here that the (relative) intensities of ENDOR signals are very dependent on the spin-relaxation times in the system, and are in general not reliable indicators for the (relative) concentrations of species.

2.2.5 ENDOR-induced EPR

EPR spectra often are multicomposite: they consist of overlapping EPR signals of several paramagnetic species. This is particularly true for radiation-induced radicals in organic systems, where usually a multitude of radical species with very similar g tensors are present. One way to separate the different contributions are high-frequency/high-field measurements (which ‘magnify’ small differences in g tensors), but these bring about technical problems, among others in sample preparation, and the signal intensity can drastically diminish due to strain effects.⁸ Another – and for the systems studied in this doctoral thesis the most powerful – method is ENDOR-induced EPR (EIE).⁹ In an EIE experiment, the radio frequency is kept fixed at a certain NMR transition, say $A \leftrightarrow B$. The ENDOR intensity is then monitored while sweeping the static magnetic field. With the basic mechanism of ENDOR in mind (Section 2.2.4), it can easily be understood that when an EPR transition involving level A or B is induced, the NMR transition (temporarily) desaturates, which can be detected. An EIE spectrum is the graph of the ENDOR intensity as a function of the static magnetic field. An EIE spectrum only contains EPR signals originating from the same species that gives rise to the ENDOR transition. Moreover, for a system with $S = 1/2$ and all nuclear spins $I \leq 1/2$, the EIE spectrum is the *complete* EPR spectrum of that species [27]. By

⁸Small variations in the local geometry can cause a slight spread of the g tensors, which causes broadening of the signal at high magnetic fields.

⁹EIE is sometimes also referred to as field-swept ENDOR.

performing EIE measurements on all ENDOR lines, a decomposition of the EPR spectrum in its individual components can be obtained and the HFC interactions belonging to one radical species can be grouped. Since EIE measurements essentially are ENDOR measurements, one should be cautious in interpreting the (relative) intensities of EIE spectra. In papers I and IV, as well as in Section 5.3.3 (page 125) the use of EIE measurements is extensively demonstrated.

Note that, since the magnetic field is swept, the ENDOR line shifts during an EIE scan. In a first-order approximation (see Section 2.2.3), the ENDOR frequency depends linearly on the magnetic field strength:

$$\frac{d\nu}{dB} = \pm g_N \mu_N \quad (2.35)$$

where the sign depends on the relative size of $|A|$ and $|2g_N \mu_N B|$ and on which of the two ENDOR signals (high or low frequency) is probed. In (modern) standard EPR/ENDOR spectrometers, the radiofrequency during an EIE scan can be adjusted automatically according to this linear relation. When it is not clear which sign should be chosen in (2.35), both options should be checked. In general, the linear dependence does not hold and too large deviations from linearity lead to distorted EIE spectra.

2.2.6 Field-frequency ENDOR

A field-frequency ENDOR (FF-ENDOR) spectrum is a 2D plot of the ENDOR spectrum intensity as a function of the static magnetic field. It is obtained simply by performing ENDOR scans for a series of different magnetic field values (at regular intervals). If the magnetic field interval is small enough, EIE spectra can be reconstructed from the FF-ENDOR spectrum. FF-ENDOR measurements are quite time-consuming but can offer a very condensed and clear overview of the different species and their main characteristics in systems with multicomposite EPR spectra. Their use is demonstrated in Section 5.3.2 (page 120).

2.3 EPR and ENDOR spectra for an $S = I = 1/2$ system

2.3.1 The g tensor

Consider an $S = 1/2$ system described by the spin Hamiltonian

$$\hat{H} = \mu_B \vec{B} \cdot \vec{g} \cdot \hat{S} \quad (2.36)$$

where the g tensor in general is anisotropic (cf. Eq. (2.14)). We will now determine the energy eigenvalues of this system by calculating the matrix elements of the spin Hamiltonian in the $|M_S\rangle$ basisset ($M_S = \pm\frac{1}{2}$).

When $\vec{B} = B\vec{l}$ with $\vec{l} = [l_x \ l_y \ l_z]$, (2.36) expands to

$$\hat{H} = \mu_B B [(l_\alpha g_{\alpha x}) \hat{S}_x + (l_\alpha g_{\alpha y}) \hat{S}_y + (l_\alpha g_{\alpha z}) \hat{S}_z] \quad (2.37)$$

where we have used the *Einstein summation convention* for α .¹⁰ The matrix elements are easily calculated:

$$\begin{aligned} \langle \frac{1}{2} | \hat{H} | \frac{1}{2} \rangle &= \frac{1}{2} \mu_B B l_\alpha g_{\alpha z} \\ \langle \frac{1}{2} | \hat{H} | -\frac{1}{2} \rangle &= \frac{1}{2} \mu_B B (l_\alpha g_{\alpha x} - i l_\alpha g_{\alpha y}) \\ \langle -\frac{1}{2} | \hat{H} | \frac{1}{2} \rangle &= \frac{1}{2} \mu_B B (l_\alpha g_{\alpha x} + i l_\alpha g_{\alpha y}) \\ \langle -\frac{1}{2} | \hat{H} | -\frac{1}{2} \rangle &= -\frac{1}{2} \mu_B B l_\alpha g_{\alpha z} \end{aligned} \quad (2.38)$$

The eigenvalues of the Hamiltonian matrix are readily found to be

$$E = \pm \frac{1}{2} \mu_B B [(l_\alpha g_{\alpha x})^2 + (l_\alpha g_{\alpha y})^2 + (l_\alpha g_{\alpha z})^2]^{\frac{1}{2}} \quad (2.39)$$

which can be written as

$$E(M_S) = (\vec{l} \cdot \vec{g} \cdot \vec{g}^T \cdot \vec{l}^T)^{\frac{1}{2}} \mu_B B M_S \quad (2.40)$$

Comparing this with Eq. (2.21), it is clear that

$$g = \sqrt{\vec{l} \cdot \vec{g} \cdot \vec{g}^T \cdot \vec{l}^T} \quad (2.41)$$

Note that in the eigenframe of the g tensor, this reduces to¹¹

$$g = \sqrt{l_x^2 g_x^2 + l_y^2 g_y^2 + l_z^2 g_z^2} \quad (2.42)$$

Eqs. (2.40) and (2.41) were derived for an $S = 1/2$ system here, but it can be shown that they hold for any value of S [26]. Eq. (2.41) gives the relation between the experimentally observable g factor and the g tensor. Note that the

¹⁰If an index appears twice in a term, a summation has to be performed over all possible values of the index.

¹¹We distinguish tensor diagonal elements in the tensor's eigenframe – the eigenvalues – from those in other reference frames by using only one index, e.g. g_x instead of g_{xx} .

g factor is actually determined by $\overline{\overline{g}} \cdot \overline{\overline{g}}^T$, which *does* have the transformation properties of a tensor. Eq. (2.41) also demonstrates that the overall sign of the g tensor cannot be determined from (regular) EPR experiments. This will be discussed in Section 2.4.2.1 .

2.3.2 The HFC tensor

Assume an $S = I = \frac{1}{2}$ system with spin Hamiltonian

$$\hat{H} = \mu_B \vec{B} \cdot \overline{\overline{g}} \cdot \hat{S} + \hat{S} \cdot \overline{\overline{A}} \cdot \hat{I} - g_N \mu_N \vec{B} \cdot \hat{I} \quad (2.43)$$

which is spin Hamiltonian (2.13) in the case of one nuclear spin \vec{I} . It is straightforward to calculate the matrix elements of this spin Hamiltonian in an $|M_S M_I\rangle$ basis. However, the resulting secular equation for the energy eigenvalues does not have an analytical solution when the magnetic field is assumed to lie in an arbitrary direction and when no constraints are put on the relative orientations of the g and HFC tensor principal axes. Therefore, the energy eigenvalues have to be computed by numerical diagonalisation of the spin Hamiltonian matrix.

For the type of systems this doctoral thesis deals with, however, we can (i) employ the *high-field approximation*¹² and (ii) assume an isotropic g tensor. Using $\vec{B} = B\vec{l}$ and $\vec{S} = S_z\vec{l}$, Hamiltonian (2.43) then reduces to [26]

$$\hat{H} = g\mu_B B \hat{S}_z + \hat{S}_z \vec{l} \cdot \overline{\overline{A}} \cdot \hat{I} - g_N \mu_N B \vec{l} \cdot \hat{I} \quad (2.44)$$

This Hamiltonian is diagonal in the electron-spin operator so that the 4×4 $\langle M_S M_I | \hat{H} | M_S M_I \rangle$ matrix is reduced to two 2×2 matrices. The matrix elements within one block are

$$\begin{aligned} \langle M_S \frac{1}{2} | \hat{H} | M_S \frac{1}{2} \rangle &= M_S \nu_e + \frac{1}{2} M_S R_z - \frac{1}{2} \nu_N l_z \\ \langle M_S \frac{1}{2} | \hat{H} | M_S - \frac{1}{2} \rangle &= \frac{1}{2} (M_S R_x - \nu_N l_x) + \frac{i}{2} (-M_S R_y + \nu_N l_y) \\ \langle M_S - \frac{1}{2} | \hat{H} | M_S \frac{1}{2} \rangle &= \frac{1}{2} (M_S R_x - \nu_N l_x) - \frac{i}{2} (-M_S R_y + \nu_N l_y) \\ \langle M_S - \frac{1}{2} | \hat{H} | M_S - \frac{1}{2} \rangle &= M_S \nu_e - \frac{1}{2} M_S R_z + \frac{1}{2} \nu_N l_z \end{aligned} \quad (2.45)$$

¹²When the HFC term is much smaller than the electronic Zeeman term, the influence of the HFC interaction on the electron spin can be neglected. This means that the electron spin is assumed to align with \vec{B} .

2.3. EPR and ENDOR spectra for an $S = I = 1/2$ system

where we have switched (for convenience) to frequency units and have defined

$$\nu_e = \frac{1}{h} g \mu_B B \quad (2.46)$$

$$\nu_N = \frac{1}{h} g_N \mu_N B \quad (2.47)$$

$$R_i = l_\alpha A_{\alpha i} \quad (2.48)$$

with the understanding that the matrix elements of $\bar{\bar{A}}$ are also expressed in frequency units. The secular equations for the eigenvalues ν are

$$(M_S \nu_e - \nu)^2 - \frac{1}{4} \sum_i (M_S R_i - \nu_N l_i)^2 = 0 \quad (2.49)$$

where i runs over x, y and z . This can be written as

$$(M_S \nu_e - \nu)^2 - \frac{1}{4} \left[\vec{l} \cdot (M_S \bar{\bar{A}} - \nu_N \bar{\bar{1}}) \right] \cdot \left[\vec{l} \cdot (M_S \bar{\bar{A}} - \nu_N \bar{\bar{1}}) \right]^T = 0 \quad (2.50)$$

with $\bar{\bar{1}}$ the 3x3 unit matrix. The expression for ν can be cast in the following convenient form:

$$\nu(M_S, M_I) = \nu_e M_S + K(M_S) M_I \quad (2.51)$$

where $K(M_S)$ is defined by

$$K^2(M_S) = \vec{l} \cdot \bar{\bar{K}}(M_S) \cdot \left[\bar{\bar{K}}(M_S) \right]^T \cdot \vec{l}^T \quad (2.52)$$

$$\bar{\bar{K}}(M_S) = M_S \bar{\bar{A}} - \nu_N \bar{\bar{1}} \quad (2.53)$$

Denoting the *positive* roots of $K^2(M_S)$ by K_+ for $M_S = \frac{1}{2}$ and by K_- for $M_S = -\frac{1}{2}$, the four eigenvalues are

$$\begin{aligned} \nu_{++} &= \frac{1}{2} \nu_e + \frac{1}{2} K_+ \\ \nu_{+-} &= \frac{1}{2} \nu_e - \frac{1}{2} K_+ \\ \nu_{-+} &= -\frac{1}{2} \nu_e + \frac{1}{2} K_- \\ \nu_{--} &= -\frac{1}{2} \nu_e - \frac{1}{2} K_- \end{aligned} \quad (2.54)$$

Note that, since we have chosen $K(M_S) \geq 0$, we always have $\nu_{++} \geq \nu_{+-} \geq \nu_{-+} \geq \nu_{--}$. The first sign in the subscript can be identified with M_S ($+ = +1/2$, $- = -1/2$), but the second sign cannot be identified with M_I : the eigenstate corresponding to ν_{++} , e.g., in general is a linear combination of $|\frac{1}{2} \frac{1}{2}\rangle$ and $|\frac{1}{2} -\frac{1}{2}\rangle$. As a consequence, the EPR selection rules (2.26) are in general not valid for a system with spin Hamiltonian (2.43) and all four different transitions for which $|\Delta M_S| = 1$ have a finite transition probability (see Section 2.3.2.1).

Before investigating the shape of the EPR and ENDOR spectrum for this system, we consider two limiting cases. First, when the HFC term is much smaller than the nuclear Zeeman term for all orientations, neglecting terms quadratic in the HFC term leads to (using Eqs. (2.52) and (2.53))

$$K^2(M_S) \approx \nu_N^2 - 2M_S \nu_N \left(\vec{l} \cdot \overline{\overline{A}} \cdot \vec{l}^T \right) \quad (2.55)$$

Taking out the factor ν_N^2 and expanding the square root to first order yields

$$|K(M_S)| \approx \left| \nu_N - M_S \left(\vec{l} \cdot \overline{\overline{A}} \cdot \vec{l}^T \right) \right| \quad (2.56)$$

Second, in the opposite limiting case of a HFC term much larger than the nuclear Zeeman term for all orientations,

$$|K(M_S)| \approx \left| \left(\vec{l} \cdot \overline{\overline{A}} \cdot \overline{\overline{A}}^T \cdot \vec{l}^T \right)^{\frac{1}{2}} M_S - \nu_N \frac{\left(\vec{l} \cdot \overline{\overline{A}} \cdot \vec{l}^T \right)}{\left(\vec{l} \cdot \overline{\overline{A}} \cdot \overline{\overline{A}}^T \cdot \vec{l}^T \right)^{\frac{1}{2}}} \right| \quad (2.57)$$

is obtained by neglecting terms quadratic in the nuclear Zeeman term. If, additionally, the HFC tensor anisotropy is small, it can be shown that $\vec{l} \cdot \overline{\overline{A}} \cdot \overline{\overline{A}}^T \cdot \vec{l}^T \approx \left(\vec{l} \cdot \overline{\overline{A}} \cdot \vec{l}^T \right)^2$, and (2.57) can be further reduced to

$$|K(M_S)| \approx \left| \left(\vec{l} \cdot \overline{\overline{A}} \cdot \overline{\overline{A}}^T \cdot \vec{l}^T \right)^{\frac{1}{2}} M_S - \nu_N \right| \quad (2.58)$$

2.3.2.1 The EPR spectrum

As noted above, the selection rules (2.26) in general do not apply. Using Eqs. (2.54), the transition frequencies for the four $|\Delta M_S| = 1$ transitions are

$$\nu_1 = \nu_{++} - \nu_{--} = \nu_e + \frac{1}{2} (K_+ + K_-)$$

$$\nu_2 = \nu_{+-} - \nu_{-+} = \nu_e - \frac{1}{2}(K_+ + K_-) \quad (2.59)$$

$$\nu_3 = \nu_{++} - \nu_{-+} = \nu_e + \frac{1}{2}(K_+ - K_-)$$

$$\nu_4 = \nu_{+-} - \nu_{--} = \nu_e - \frac{1}{2}(K_+ - K_-)$$

It can be shown that the corresponding transition probabilities are [26]

$$P_1 = P_2 = \frac{1-x}{2} \quad (2.60)$$

$$P_3 = P_4 = \frac{1+x}{2}$$

with

$$x = \frac{\nu_N^2 - \frac{1}{4} \left(\vec{l} \cdot \overline{\overline{A}} \cdot \overline{\overline{A}}^T \cdot \vec{l}^T \right)}{\left[\left[\frac{1}{4} \left(\vec{l} \cdot \overline{\overline{A}} \cdot \overline{\overline{A}}^T \cdot \vec{l}^T \right) + \nu_N^2 \right]^2 - \nu_N^2 \left(\vec{l} \cdot \overline{\overline{A}} \cdot \vec{l}^T \right)^2 \right]^{\frac{1}{2}}} \quad (2.61)$$

Therefore, the EPR spectrum in general consists of two doublets (ν_1, ν_2) and (ν_3, ν_4) – the lines in a doublet having the same intensity –, both centred around ν_e and with splittings

$$d_{12} = |K_+ + K_-| \quad d_{34} = |K_+ - K_-| \quad (2.62)$$

respectively.

It is instructive to first consider some special cases:

1. *isotropic HFC tensor or \vec{l} parallel to an eigenvector of the HFC tensor*

Denoting the isotropic HFC value or the HFC principal value with A , we obtain

$$\vec{l} \cdot \overline{\overline{A}} \cdot \overline{\overline{A}}^T \cdot \vec{l}^T = \left(\vec{l} \cdot \overline{\overline{A}} \cdot \vec{l}^T \right)^2 = A^2$$

$$K_+ = \left| \frac{1}{2}A - \nu_N \right|$$

$$K_- = \left| -\frac{1}{2}A - \nu_N \right|$$

$$x = \text{sign} \left(\nu_N^2 - \frac{1}{4}A^2 \right) = \text{sign} \left(|\nu_N| - \frac{1}{2}|A| \right)$$

Thus, there is always one doublet with zero intensity (which one

depends on whether $\frac{1}{2}|A|$ is smaller or larger than $|\nu_N|$, and it can readily be checked (using Eq. (2.62)) that the splitting of the allowed transition is always $|A|$.

2. *the HFC term is much smaller than the nuclear Zeeman term*

In this case $x \approx 1$ and doublet (ν_3, ν_4) is the most intense. Using Eqs. (2.56) and (2.62), the splitting of the prominent doublet is

$$d_{34} \approx \left| \vec{l} \cdot \overline{\overline{A}} \cdot \vec{l}^T \right| \quad (2.63)$$

and that of the low-intensity doublet

$$d_{12} \approx 2|\nu_N| \quad (2.64)$$

These weak lines are called spin-flip transitions¹³ and are frequently observed in systems where several protons are weakly coupled to the unpaired electron.

3. *the HFC term is much larger than the nuclear Zeeman term*

Now we find $x \approx -1$ and doublet (ν_1, ν_2) is the most intense one. Using Eqs. (2.57) and (2.62), we find that the prominent doublet has a splitting

$$d_{12} \approx \left| \left(\vec{l} \cdot \overline{\overline{A}} \cdot \overline{\overline{A}}^T \cdot \vec{l}^T \right)^{\frac{1}{2}} \right| \quad (2.65)$$

and the low-intensity doublet

$$d_{34} \approx \left| 2\nu_N \frac{\vec{l} \cdot \overline{\overline{A}} \cdot \vec{l}^T}{\left(\vec{l} \cdot \overline{\overline{A}} \cdot \overline{\overline{A}}^T \cdot \vec{l}^T \right)^{\frac{1}{2}}} \right| \quad (2.66)$$

which in the case of a small HFC tensor anisotropy can be further simplified to (cf. Eq. (2.58))

$$d_{34} \approx 2|\nu_N| \quad (2.67)$$

Note that the nuclear Zeeman interaction does not have any influence on the EPR spectrum in the first case, and only a marginal influence in the last two. It is therefore a good approximation to neglect the nuclear Zeeman term in a first analysis in such cases. However, this is not so when the HFC term and

¹³These EPR transitions have $|\Delta M_S| = |\Delta M_I| = 1$, that is: the electron-spin flip is accompanied by a nuclear-spin flip.

the nuclear Zeeman term are comparable in size.¹⁴ This is best demonstrated by an example: assume a proton HFC tensor¹⁵

$$\bar{\bar{A}} = \begin{bmatrix} -70 & 0 & 0 \\ 0 & -40 & 0 \\ 0 & 0 & -10 \end{bmatrix} \text{ MHz} \quad (2.68)$$

and assume that EPR measurements are performed in X band (microwave frequency of 9.5 GHz) on a single crystal while rotating from $\vec{B} \parallel \langle x \rangle$ to $\vec{B} \parallel \langle z \rangle$ in the tensor's eigenframe. Assuming $g = g_e = 2.0023$, $\nu_N = 14.43$ MHz, both regimes (dominant HFC term and dominant nuclear Zeeman term) are encountered during the rotation. Figures 2.5 and 2.6 give the variation of the

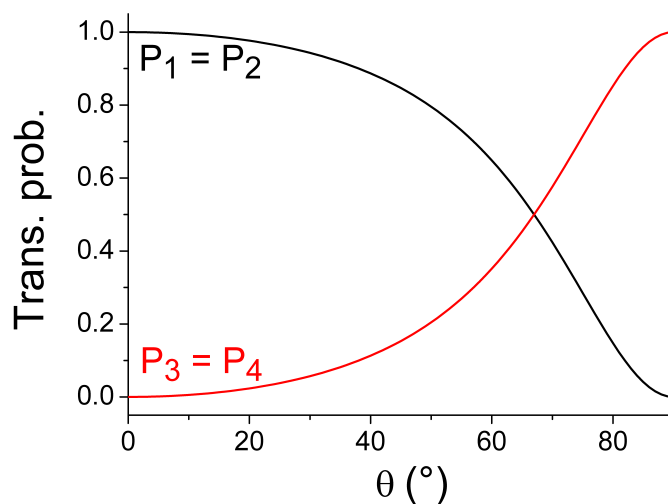


Figure 2.5: Transition probabilities $P_1 = P_2$ and $P_3 = P_4$ (for transitions ν_1, ν_2, ν_3 and ν_4 respectively, cf. Eq. (2.59)), as a function of the rotation angle θ in the $\{xz\}$ plane, calculated via Eqs. (2.60) and (2.61), for a system with spin Hamiltonian (2.44), assuming $g = g_e = 2.0023$ and a proton HFC tensor $\bar{\bar{A}}$ given by Eq. (2.68). $\theta = 0^\circ$ corresponds to $\vec{B} \parallel \langle x \rangle$, $\theta = 90^\circ$ to $\vec{B} \parallel \langle z \rangle$.

transition probabilities $P_1 = P_2$ and $P_3 = P_4$ (Eqs. (2.60) and (2.61)) and the doublet splittings d_{12} and d_{34} (Eqs. (2.62) and (2.52)) with the rotation angle. The latter figure clearly demonstrates that $\left(\vec{l} \cdot \bar{\bar{A}} \cdot \bar{\bar{A}}^T \cdot \vec{l}^T\right)^{\frac{1}{2}}$ and $\vec{l} \cdot \bar{\bar{A}} \cdot \vec{l}^T$ are good approximations for the dominant doublet splitting for large and small HFC values respectively, but deviate significantly from the effective splittings

¹⁴More accurately: when the HFC term and *twice* the nuclear Zeeman term are comparable in size.

¹⁵This tensor could arise from an α proton in a radical with a bent centre, see Section 4.3.2, page 86.

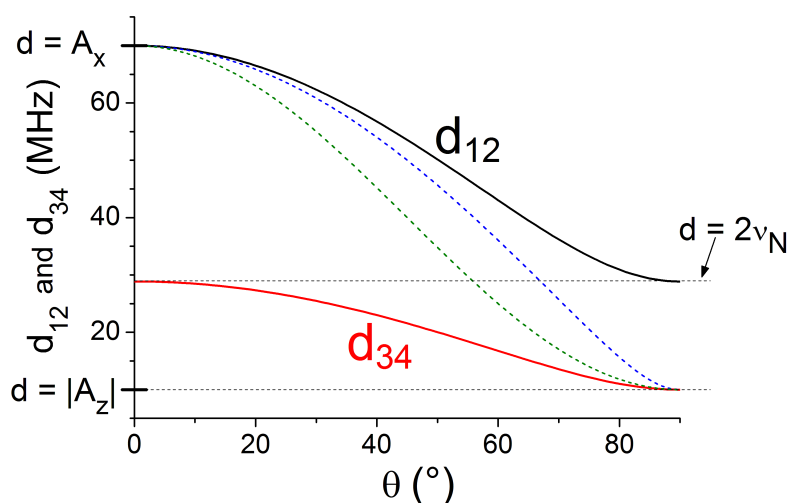


Figure 2.6: Doublet splittings d_{12} and d_{34} (Eqs. (2.62) and (2.52)) as a function of the rotation angle θ (cf. Figure 2.5). The dashed lines are $\left(\vec{I} \cdot \vec{A} \cdot \vec{A}^T \cdot \vec{I}^T\right)^{\frac{1}{2}}$ (blue) and $\left|\vec{I} \cdot \vec{A} \cdot \vec{I}^T\right|$ (green). $\theta = 0^\circ \sim \vec{B} \parallel \langle x \rangle$, $\theta = 90^\circ \sim \vec{B} \parallel \langle z \rangle$.

when the HFC term is approximately $2\nu_N$.

In Figure 2.7 the simulated EPR spectra are shown at 10° intervals throughout the plane. Note that

- at $\theta = 0^\circ$ and $\theta = 90^\circ$, one doublet has exactly zero intensity because these directions coincide with HFC tensor eigenvectors.
- at 60° and 70° – where $P_1 = P_2 \approx P_3 = P_4$ (Figure 2.5) – the two doublets are comparable in intensity. Such a pattern could easily be interpreted as arising from two (proton) HFC interactions. This demonstrates that care should be taken when interpreting EPR spectra, even when they appear simple.
- the EPR spectrum at $\theta = 80^\circ$ provides an example of the aforementioned spin-flip spectra.

Figure 2.8, finally, demonstrates how larger line widths can further complicate the interpretation of the EPR spectrum.

2.3.2.2 The ENDOR spectrum

Because Hamiltonian (2.44) is diagonal in the electron-spin operator, NMR selection rules (2.29) can be employed and the ENDOR frequencies are found

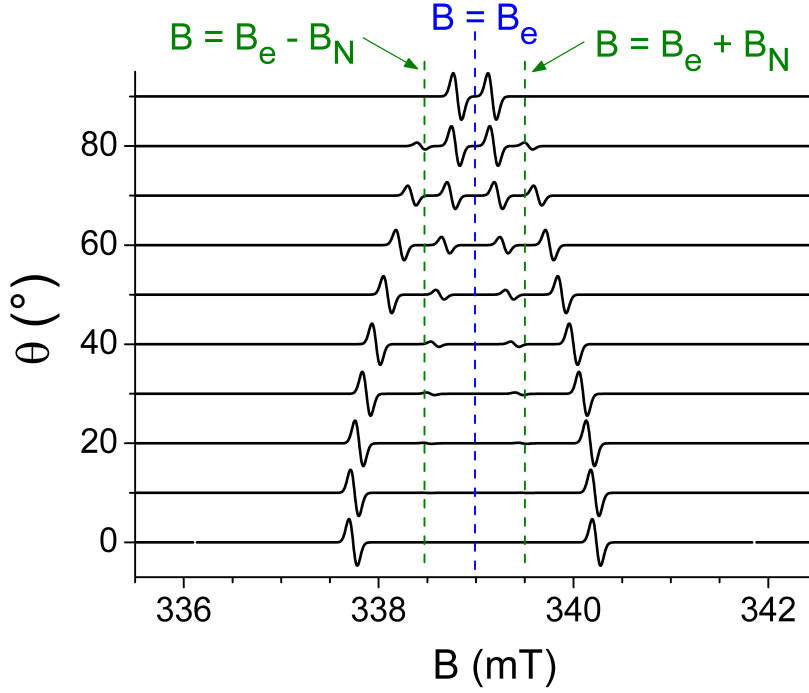


Figure 2.7: Simulated X-band (9.5 GHz) EPR angular variation for a system with spin Hamiltonian (2.44), assuming $g = 2.0023$ and \bar{A} a proton HFC tensor given by Eq. (2.68). $\theta = 0^\circ$ corresponds to $\vec{B} \parallel \langle x \rangle$ and $\theta = 90^\circ$ to $\vec{B} \parallel \langle z \rangle$. B_e and B_N are defined as $B_e = \frac{h\nu_e}{g_e\mu_B}$ and $B_N = \frac{h\nu_N}{g_e\mu_B}$. The resonance lines are first derivatives of Gaussian functions with a linewidth of 0.1 mT. Their positions and intensities are determined via Eqs. (2.59) and Eqs. (2.60) respectively.

at (using Eq. (2.54))

$$|\nu_{++} - \nu_{+-}| = |K_+| \quad (2.69)$$

$$|\nu_{-+} - \nu_{--}| = |K_-|$$

When the HFC term is much smaller than the nuclear Zeeman term, we can employ Eq. (2.56) and find that the ENDOR lines form a doublet centred around ν_N , with a splitting

$$D_1 \approx \left| \vec{l} \cdot \bar{A} \cdot \vec{l}^T \right| \quad (2.70)$$

In the opposite case where the HFC term is much larger than the nuclear Zeeman term, Eq. (2.57) shows that the ENDOR lines form a doublet centred

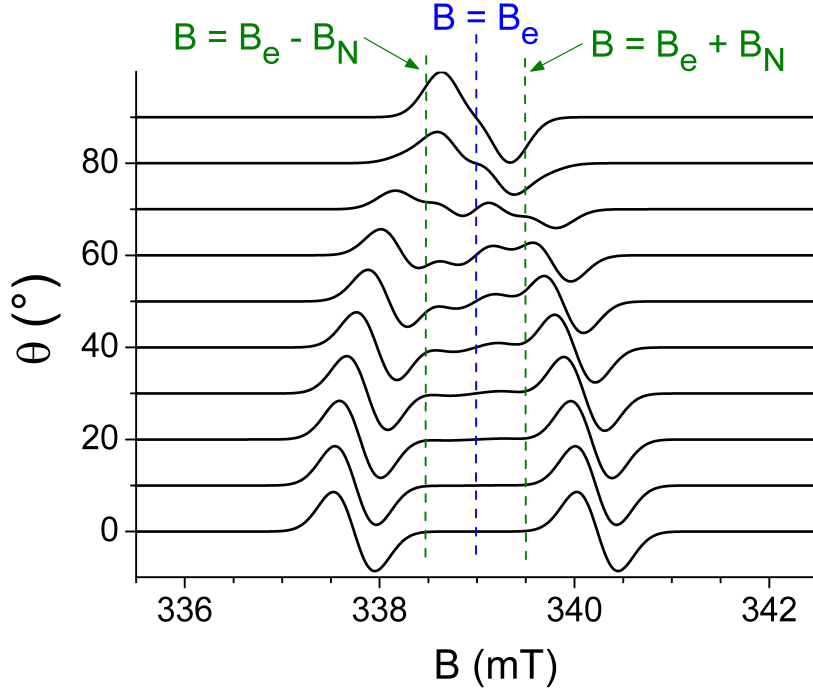


Figure 2.8: The same as Figure 2.7, but with Gaussian linewidths of 0.5 mT.

around

$$\left(\vec{l} \cdot \overline{\overline{A}} \cdot \overline{\overline{A}}^T \cdot \vec{l}^T \right)^{\frac{1}{2}} \quad (2.71)$$

with a splitting

$$D_2 \approx \left| 2\nu_N \frac{(\vec{l} \cdot \overline{\overline{A}} \cdot \vec{l}^T)}{(\vec{l} \cdot \overline{\overline{A}} \cdot \overline{\overline{A}}^T \cdot \vec{l}^T)^{\frac{1}{2}}} \right| \quad (2.72)$$

which in the case of small HFC tensor anisotropy reduces to

$$D_2 \approx 2|\nu_N| \quad (2.73)$$

This equation is exact when the HFC tensor is isotropic or when \vec{l} is along a HFC eigenvector. Figure 2.9 shows the simulated ENDOR positions for the EPR angular variation considered in Section 2.3.2.1 and illustrates both limiting cases. Note that high-frequency branch corresponds to $|K_+|$, and the low-frequency branch to $|K_-|$. If the sign of HFC tensor (2.68) is inverted, the $|K_+|$ and $|K_-|$ labels would be interchanged.

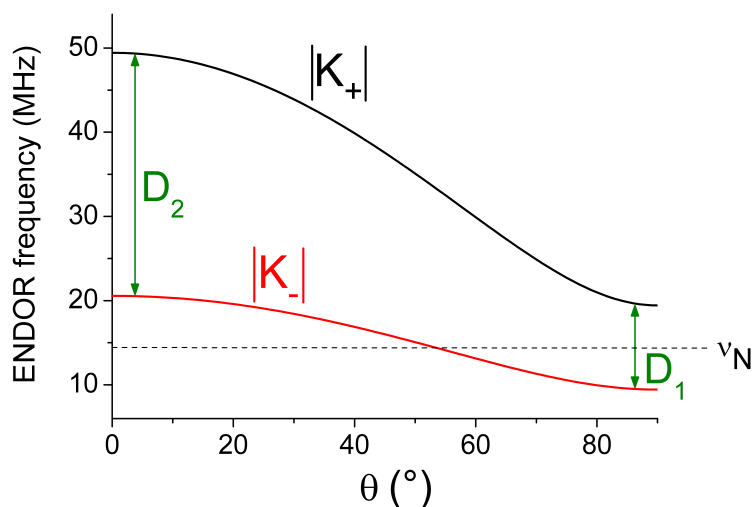


Figure 2.9: Simulated X-band (9.5 GHz) ENDOR angular variation for a system with spin Hamiltonian (2.44), assuming $g = 2.0023$ and \bar{A} a proton HFC tensor given by Eq. (2.68). $\theta = 0^\circ$ corresponds to $\vec{B} \parallel \langle x \rangle$ and $\theta = 90^\circ$ to $\vec{B} \parallel \langle z \rangle$. D_1 and D_2 are given by Eqs. (2.70) and (2.72) respectively.

2.3.3 Site splitting

We have so far ignored a very important aspect of EMR experiments on single crystals: a unit cell usually contains several symmetry-related, chemically equivalent subunits (e.g. molecules) over which the paramagnetic centres are distributed. The (g and HFC) tensors of these centres are transformed into each other by the symmetry operations of the crystal's point group and in general have different relative orientations with respect to the applied magnetic field. It is clear from Sections 2.3.2.1 and 2.3.2.2 that this leads to different EPR and ENDOR positions. The result is that for a general orientation of the applied magnetic field, several sets of resonance lines, due to chemically identical but magnetically distinguishable paramagnetic species, are observed. This phenomenon is called *site splitting*.

Due to the typically low symmetry of molecules, most defects in organic crystals are *triclinic*, i.e. they have no overall symmetry. In this case, the site splitting is entirely determined by the point group of the crystal. We will take as an example triclinic defects in monoclinic crystals (of which the systems studied in this doctoral thesis are examples). The unit cell of a monoclinic crystal can in principle contain four molecules, related by the monoclinic and inversion symmetry operations $((a, b, c) \rightarrow (-a, b, -c)$ and $(a, b, c) \rightarrow (-a, -b, -c)$ respectively). Because tensors of centres related by

inversion symmetry always make the same angle with an applied magnetic field, they do not give rise to site splitting and we will not consider them here. The two centres (sites I and II) related by the monoclinic symmetry operation have the same relative orientation with respect to the magnetic field only when $\vec{B} \parallel \langle b \rangle$ or $\vec{B} \perp \langle b \rangle$ (Figure 2.10). Thus, EMR resonance positions of the two centres coincide *with certainty* only for these orientations (*fundamental*

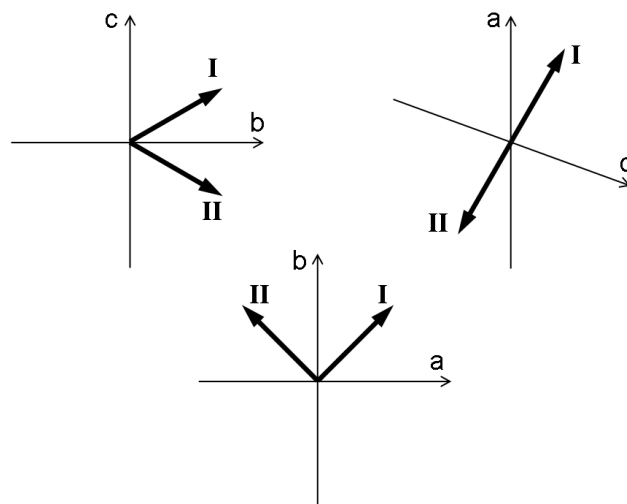


Figure 2.10: Schematic illustration of site splitting for a monoclinic crystal. The vectors I and II represent triclinic entities related by the monoclinic symmetry operation. When the magnetic field \vec{B} is rotated through the $\{bc\}$ and $\{ab\}$ planes, it makes different angles with the two vectors, except when $\vec{B} \parallel \langle a \rangle$, $\vec{B} \parallel \langle b \rangle$ or $\vec{B} \parallel \langle c \rangle$. In the $\{ac\}$ plane, however, the angles with the vectors are always equal.

degeneracy) – they can of course still coincide *accidentally* for other orientations (*accidental degeneracy*).

Figure 2.11 (where \vec{a}^* is defined as the projection of \vec{a} in the plane perpendicular to $\langle c \rangle$) gives the X-band ENDOR angular variation in the plane perpendicular to $\langle c \rangle$ for a typical α proton HFC (see Section 4.3.2, page 86) in a monoclinic crystal. Notice that the two sites are mirrored around the $\langle a^* \rangle$ and $\langle b \rangle$ axes so that a well-chosen 90° rotation in fact contains all the information. An analogous pattern is present in the plane perpendicular to $\langle a \rangle$. Therefore it is customary in the literature to present angular variation graphs as in Figure 2.12. Such mirror symmetry is only encountered in planes containing $\langle b \rangle$. In other planes, it is in general necessary to rotate over 180° .

Clearly, site splitting complicates EMR spectra. This is particularly true for the EPR spectra of organic radicals because of the often small g tensor anisotropy and – typically – multiple proton HFC splittings. For this reason, EIE measurements (aimed at decomposing the EPR spectrum in its individual

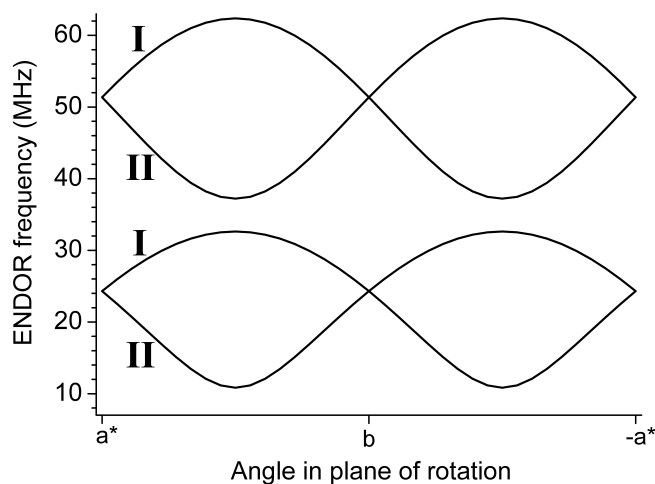


Figure 2.11: X-band ENDOR angular variation of a typical α -proton HFC tensor for a monoclinic crystal in the plane perpendicular to $\langle c \rangle$. The angular variation patterns of the two monoclinic sites exhibit a mirror symmetry around the $\langle a^* \rangle$ and $\langle b \rangle$ axes.

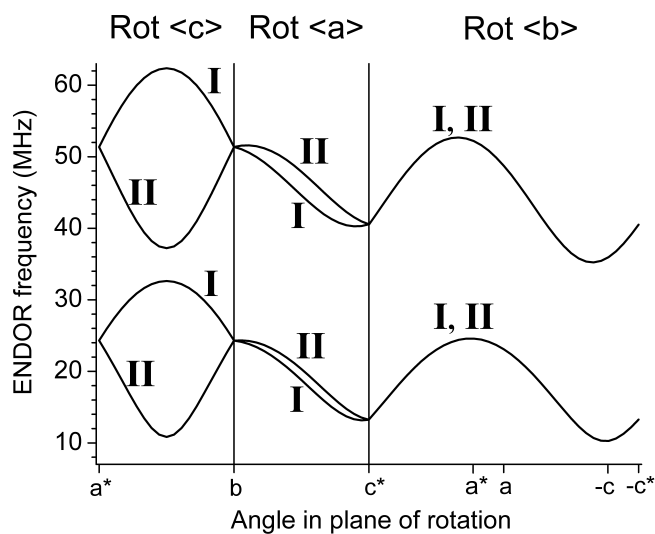


Figure 2.12: X-band (9.5 GHz) ENDOR angular variation of a typical α proton HFC tensor for a monoclinic crystal in the planes perpendicular to the $\langle a \rangle$, $\langle b \rangle$ and $\langle c \rangle$ axes, as usually presented in the literature: in the planes perpendicular to $\langle a \rangle$ and $\langle c \rangle$, the angular variation is only displayed in a 90° interval.

components and at grouping the different HFC interactions) are usually carried out at the crystal axes or, in the case of monoclinic crystals, in the plane perpendicular to $\langle b \rangle$. Site splitting can however also be a very useful feature,

e.g. when one wants to orient a sample accurately.

2.4 Determining g tensors and HFC tensors from EMR experiments

2.4.1 The principle

Both the g factor¹⁶ for an $S = 1/2$ system with spin Hamiltonian (2.36) and the ENDOR-line positions $|K_+|$ and $|K_-|$ for an $S = I = 1/2$ system with spin Hamiltonian (2.44) are dependent on the magnetic field orientation \vec{l} as

$$X = \left(\vec{l} \cdot \overline{\overline{M}} \cdot \vec{l}^T \right)^{\frac{1}{2}} \quad (2.74)$$

where

$$\begin{aligned} \overline{\overline{M}} &= \overline{\overline{g}} \cdot \overline{\overline{g}}^T \\ \overline{\overline{M}} &= \overline{\overline{K}} \begin{pmatrix} 1 \\ 2 \end{pmatrix} \cdot \left[\overline{\overline{K}} \begin{pmatrix} 1 \\ 2 \end{pmatrix} \right]^T \\ \overline{\overline{M}} &= \overline{\overline{K}} \begin{pmatrix} -1 \\ 2 \end{pmatrix} \cdot \left[\overline{\overline{K}} \begin{pmatrix} -1 \\ 2 \end{pmatrix} \right]^T \end{aligned} \quad (2.75)$$

respectively (see Eqs. (2.41) and (2.52)). Note that $\overline{\overline{M}}$ is symmetric and therefore has six independent elements. For a general orientation of \vec{B} we have

$$X^2 = l_x^2 M_{xx} + l_y^2 M_{yy} + l_z^2 M_{zz} + 2l_x l_y M_{xy} + 2l_x l_z M_{xz} + 2l_y l_z M_{yz} \quad (2.76)$$

For a rotation from the $\langle x \rangle$ axis ($\theta = 0^\circ$) to the $\langle y \rangle$ axis ($\theta = 90^\circ$), e.g., we have $\vec{l} = [\cos \theta \ \sin \theta \ 0]$ and Eq. (2.76) simplifies to

$$X^2 = \cos^2 \theta M_{xx} + 2 \sin \theta \cos \theta M_{xy} + \sin^2 \theta M_{yy} \quad (2.77)$$

The tensor elements M_{ij} are typically determined by fitting X^2 to angular variations in one or more planes (depending on the symmetry of the system) simultaneously via Eq. (2.76). Diagonalisation of $\overline{\overline{M}}$ and taking the square root then yields the eigenvectors and principal values of $\overline{\overline{g}}$ or $\overline{\overline{K}}$ (M_S) (from which the HFC tensor can easily be derived).

¹⁶which is related to the experimentally accessible EPR resonance field via Eq. (2.21)

2.4.2 Ambiguities

2.4.2.1 Sign ambiguities

From Eq. (2.74) it is clear that the overall sign of the g or HFC tensor cannot be determined from regular EPR and ENDOR experiments because only the square of the tensor (and thus only the square of the principal eigenvalues) is experimentally available. In the case of organic radicals, there is in practice no problem for the g tensor, since the deviation from g_e is small and g values can safely be assumed to be positive. For the HFC tensor, however, it is in general not straightforward to know the correct sign *a priori*.

Most often the sign choice is based on precedents and/or theoretical considerations. When this is not possible, usually one will attempt to determine the *relative* sign of the HFC tensor compared to another HFC tensor of the same radical species. This is possible e.g. by means of electron-nuclear-nuclear triple resonance (commonly called TRIPLE) measurements, where one monitors the effect on an ENDOR absorption intensity when simultaneously exciting two NMR transitions. TRIPLE requires sufficient radio frequency power for both channels and its success is highly dependent on spin-relaxation times. Pulsed EPR measurements can also yield the relative signs of two HFC tensors in certain cases. This is demonstrated in Paper III, where we used HYSORE (hyperfine sublevel correlation spectroscopy) measurements to determine the sign of one of the HFC interactions of a stable radical (T1) in X-ray irradiated sucrose single crystals.

2.4.2.2 The Schonland ambiguity

There is another, more subtle ambiguity, commonly referred to as the *Schonland ambiguity*, after D. S. Schonland who was the first to recognize it [28] for the determination of the g tensor from EPR angular variations for low-symmetry paramagnetic $S = 1/2$ centres in crystals with orthorhombic and monoclinic symmetry (although the problem is not restricted to these classes of crystal symmetry). In Paper VI, we demonstrate that a similar ambiguity can arise when a HFC tensor is determined from ENDOR angular variations for an $S = I = 1/2$ system with spin Hamiltonian (2.44). The central idea and the key results are summarised below. For a detailed discussion we refer to Paper VI. Eq. (2.74) can always be written in the form

$$X^2 = \alpha + \beta \cos 2\theta + \gamma \sin 2\theta \quad (2.78)$$

where α , β and γ are functions of the matrix elements of $\overline{\overline{M}}$. It can easily be verified that for rotation in the {xy} plane, e.g.,

$$\begin{aligned}\alpha &= \frac{M_{xx} + M_{yy}}{2} \\ \beta &= \frac{M_{xx} - M_{yy}}{2} \\ \gamma &= M_{xy}\end{aligned}\tag{2.79}$$

Note that reversing the sense of rotation (i.e. the sign of θ) is equivalent to changing the sign of γ :

$$X^2(-\theta) = X^2(-\gamma) = \alpha + \beta \cos 2\theta - \gamma \sin 2\theta\tag{2.80}$$

When analysing data in three rotation planes, the positive sense of rotation can be chosen freely for two planes, but is fixed by that choice in the third plane. The point is that it is not *a priori* clear which sign choice should be made. Consequently, two best-fit solutions can be found (called *Schonland-conjugate* tensors in Paper VI), and only one of them has physical relevance. One possible way to circumvent this is using the same single crystal sample for all three rotation planes and physically labelling the axes in some way. This is, however, often not possible or inconvenient. Moreover, if there is site splitting, even this will not help, because it is not clear which branches belong to the same site and should be fit together (cf. Figure 2.12 for the case of the HFC tensor).

Whereas the Schonland ambiguity is "perfect" for the g tensor in $S = 1/2$ systems, in principle it does not occur for the HFC tensor in the $S = I = 1/2$ system: there is a "perfect" ambiguity for both $\overline{\overline{K}}(\frac{1}{2})$ and $\overline{\overline{K}}(-\frac{1}{2})$, but in general only one solution fits both M_S ENDOR branches. In practice, however, often the nuclear-spin resonances in only one of the M_S multiplets can be used for analysis¹⁷ and the ambiguity reappears.

There are several ways to solve the ambiguity:

1. Perform additional measurements in a fourth, tilted plane. The two solutions will in general only coincide in three planes, so that a tilted plane allows distinguishing between them.
2. Perform additional measurements at another frequency. E.g., an X-band angular variation in three planes can be complemented by Q band

¹⁷In X-band measurements, e.g., the lower frequency branch is often located in a very crowded frequency range.

measurements in one of the planes – the two solutions will in general only coincide at one experimental frequency. Sufficiently large and anisotropic HFC tensors are required, as well as an accurate knowledge of the single crystal orientation, because the differences typically are small (at conventional microwave frequencies).

3. Measure both M_S branches (in the case of the HFC tensor).
4. Measure the powder spectrum (in the case of the g tensor): Schonland-conjugate tensors have different principal values, so that a powder spectrum in principle allows discrimination between them. In the case of multicomposite and/or poorly resolved EPR spectra this method is less likely to work. High microwave frequencies are preferable.
5. Exclude one of the solutions on the basis of theoretical knowledge and/or precedents. One should always be aware that this is an *educated guess* rather than actually solving the ambiguity.

If the ambiguity is recognised in the literature, the first or the last method is usually employed to solve it. If it has not been recognised, it is possible to reconstruct the other best-fit solution for a given tensor, as illustrated in the appendix of Paper VI. The Schonland-conjugate tensor depends on various details of the experiment: which ENDOR frequency branches (high or low) were used, the microwave frequency, the measurement planes and even the choice of reference frame. Of course, if the (complete set of) experimental data are available, one can find the Schonland-conjugate tensor by (re)fitting the data.

2.5 Experimental procedures

2.5.1 Sample preparation

During the doctoral thesis, EMR measurements were performed on single crystals and powders of sucrose and on single crystals of K2G1P¹⁸. The crystal structures are discussed in Sections 5.1 (page 105) and 6.1 (page 153) respectively. The crystals were grown from H₂O or D₂O powder solutions by slow evaporation at RT. Sucrose single crystals have a very characteristic *habitus* (Figure 2.13), allowing for visual identification of the crystal axes, and samples of several millimeters are easily obtained. In Figure 2.13, \vec{c}^* is defined as the projection of \vec{c} in the plane perpendicular to \vec{a} . Deuterated

¹⁸The dipotassium salt of glucose 1-phosphate dihydrate.

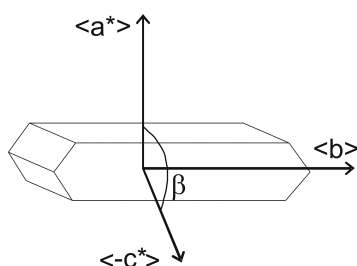


Figure 2.13: The *habitus* of a typical sucrose single crystal. The $\langle a^* \rangle$ axis is perpendicular to the top face, while the $\langle -c^* \rangle$ axis is perpendicular to the crystal face "closest to the reader", which makes an angle $\beta \approx 103^\circ$ with the top face.

sucrose single crystals were obtained by three consecutive (re)crystallisations from D_2O . Approximately 99 % of the exchangeable protons¹⁹ are replaced by deuterium in this case. Both growing K2G1P single crystals and identifying their crystal axes is considerably more difficult. Repeated recrystallization of deuterated crystals was not successful and measurements were performed on partially deuterated crystals.

2.5.2 Sample orientation

A single crystal is first glued to a goniometer head and, if possible, oriented roughly by visual inspection. Two different systems were used for orienting the samples more accurately. In the EPR lab in Oslo, the goniometer is mounted on a Weissenberg X-ray diffraction camera and oscillation diagrams are used to align the crystal along a crystal axis ($\langle a \rangle$, $\langle b \rangle$ or $\langle c \rangle$). In the EPR lab in Ghent, the goniometer is mounted on a Bruker D8 Discover X-ray diffraction machine and stereographic projections of Bragg-reflection peaks are used for aligning the crystal perpendicular to a crystal plane ($\{ab\}$, $\{ac\}$ or $\{bc\}$). With these methods, accuracies of 0.5° and 1° respectively are in principle attainable. The crystals are then transferred from the goniometer head to a quartz (Ghent, Oslo) or copper (Oslo, *in-situ* irradiation) sample holder for EPR/ENDOR measurements.

2.5.3 Sample irradiation

In Ghent a Philips tungsten anode X-ray tube (with a thin (< 0.2 mm) beryllium window) is used. For the doctoral research, it was always operated at 60 kV and 40 mA, at dose rates up to 1.3 kGy per minute. Only *ex-situ* X-ray

¹⁹I.e. oxygen-bound protons, as opposed to carbon-bound protons, which are non-exchangeable.

2.5. Experimental procedures

irradiation is possible in Ghent. Samples can, however, be irradiated at liquid N₂ temperature (77 K) using a special dewar. By precooling the EPR cavity with liquid N₂ or He, the rise in sample temperature upon transfer into the cavity can be limited. In Oslo, a Philips chromium-anode X-ray tube is used. It was also operated at 60 kV and 40 mA, and *in-situ* irradiation can be performed at temperatures between 10 K and RT at a typical dose rate of 0.5 kGy per minute.

2.5.4 EPR spectrometer and equipment

2.5.4.1 Principles of design

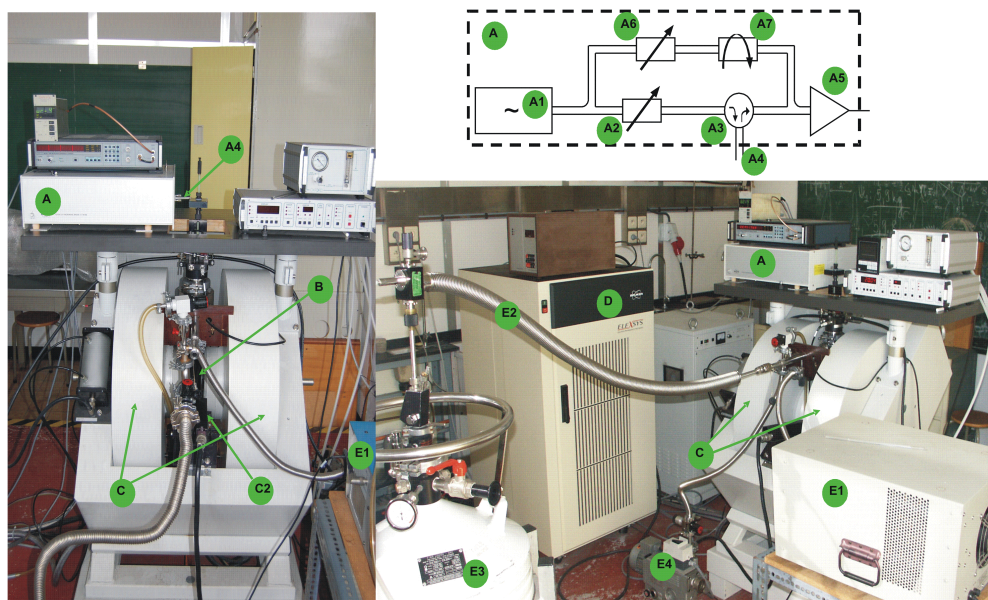


Figure 2.14: Two pictures of the Q-band spectrometer in the EPR lab, Ghent. The upper drawing is a block scheme of the MW bridge (A).

In this section, only a simplified description of the Q-band EPR spectrometer in Ghent is given. For more details and a more general treatment, the reader can consult various EPR-related books [29, 30] or the manuals of the spectrometers (e.g. [31]).

The EPR spectrometer consists of 4 major parts, indicated in Figure 2.14 : the microwave (MW) bridge (A), the cavity (B), the electromagnet (C) and the console (D).

The *microwave bridge* (A, see block scheme in Figure 2.14), contains the MW source (A1). A variable attenuator (A2) controls the power of the MWs which, via the circulator (A3) and through an external waveguide (A4), reach the

sample in the cavity (B). The reflected MWs are directed to the detector (A5) via the circulator. The detector is a diode, which converts the MW power to an electrical current. For quantitative signal-intensity measurements as well as optimal sensitivity, the diode should operate in the *linear region*, where the diode current is proportional to the MW power. To ensure this, a fraction of the source power is split off into a reference arm, where it passes through a second attenuator (A6) and a phase shifter (A7), and serves as reference (bias) signal for the detector.

The *cavity* (B) contains the sample and is placed between the poles of the electromagnet. A cavity is a rectangular or cylindrical metal box that can store MW energy at a certain frequency (the resonance frequency ν_{res}). At this frequency, MWs exhibit a standing wave pattern and are not reflected but stored in the cavity. The quality factor Q of a cavity,

$$Q = 2\pi \frac{\text{energy stored}}{\text{energy dissipated per cycle}}$$

is a measure for the efficiency with which MW energy can be stored. EPR cavities typically have a Q factor of the order 10^3 - 10^4 . The electric and magnetic field components of standing electromagnetic waves are exactly out of phase and by putting the sample in the magnetic field maximum (and hence in the electric field minimum), the signal intensity is maximised and the dielectric losses are minimised. When the resonance condition (see Eq. (2.21)) is fulfilled, the sample absorbs MW energy quanta. The result is a change in the reflected MW power, which constitutes the EPR signal. For practical reasons, it is easier to keep the MW frequency constant and vary the magnetic field. Consequently, EPR spectrometers operate at a certain MW frequency and are labelled accordingly. X band ($\nu \approx 9.5$ GHz) and Q band ($\nu \approx 34$ GHz) are the most common.

The *electromagnet* (C) generates the static magnetic field, whose strength can be varied linearly. Via a built-in Hall probe, the console (D) adjusts the current through the magnetic coils to obtain the desired field. The Hall probe is, however, not exactly located at the sample position, so that the measured field and the actual field at the sample can differ up to 1 mT. For accurate measurements, extra calibrations are carried out with an external Gauss probe (C2) which is placed in the vicinity of the sample, and a calibration sample with a well-documented g value.²⁰ To improve the signal-to-noise ratio, the magnetic field is modulated at high frequency (1-100 kHz) by a small (~ 0.1 mT) modulation field, which is generated by a current running through the EPR modulation coils (inside the cavity (B)). As a side effect, the first derivative

²⁰For lower MW frequencies, DPPH (2,2-diphenyl-1-picrylhydrazyl, $g = 2.0036$) is often used.

of the EPR signal – rather than the EPR absorption itself – is detected.

The *console* (D) contains the necessary electronics for spectrometer control and data acquisition.

2.5.4.2 ENDOR extensions to the EPR spectrometer

An RF synthesiser (inside the console (D)) generates a low-power signal with variable radio frequency (RF). This signal passes through an RF amplifier (E1) and is fed to the ENDOR coils inside the cavity, thus generating an NMR excitation field (perpendicular to the static magnetic field and the EPR excitation field). Similar to the static magnetic field modulation, the RF signal is *frequency* modulated in ENDOR measurements to enhance the signal-to-noise ratio, and again the first derivative of the ENDOR spectrum is recorded in practice.

2.5.4.3 Cryogenics

For measurements at low temperatures liquid N₂ or liquid He are used. With an external pump, the liquid is transferred via the transferline (E2) from the vessel (E3) to the cryostat which cools the sample in the cavity (B). An extra pump (E4) has to be used to achieve temperatures below 4 K.

2.5.4.4 Used spectrometers

During the doctoral research, EMR measurements were carried out with the X- and Q-band spectrometers in Ghent (Bruker ESP300E and Bruker Elexsys E500 respectively – see Figure 2.14 for the latter), and with both X-band spectrometers (Bruker Elexsys 560 and Bruker ESP300E) in Oslo, all of which have ENDOR extensions. The Bruker Elexsys 560 spectrometer in Oslo was equipped with a home-built thermal shield system (Figure 2.15) and telescoping cryostat holder for *in-situ* X-ray irradiation at low temperature (cf. Section 5.3.3, page 125). The sample, glued with silver-epoxy glue to a copper sample holder and cooled via a cold-finger method, is first positioned above the cavity entrance next to a thin (0.2 mm) aluminum window, through which it can be irradiated. After irradiation, the sample is lowered using the telescoping cryostat holder into the cavity, and the whole system can be moved in between the magnet poles for EMR measurements. For further details, we refer to [32].

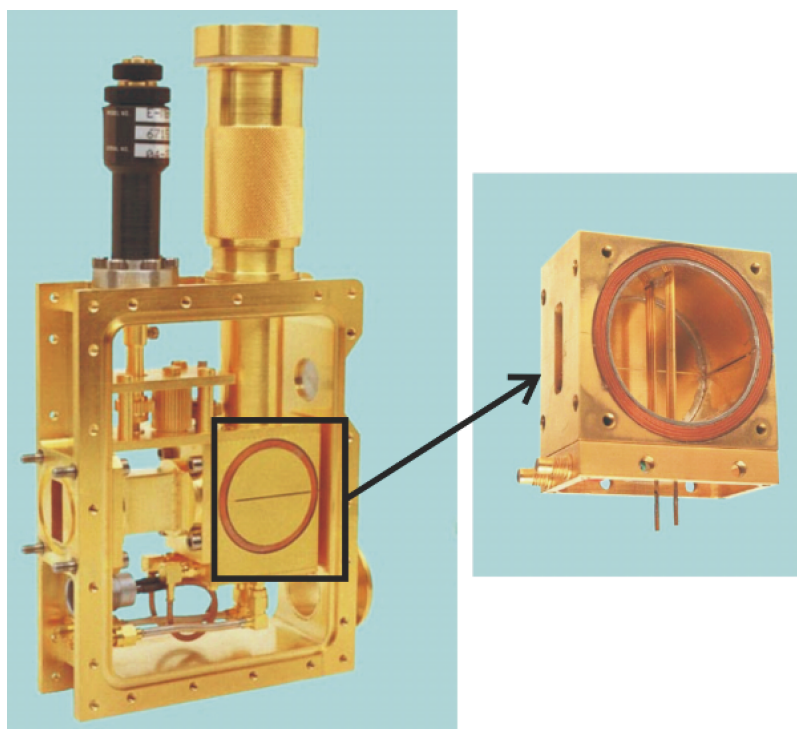


Figure 2.15: The home-built vacuum-shield system (opened up) at the EPR lab in Oslo. On the right-hand side, the inside of cylindrical EPR/ENDOR cavity is shown. The pictures were taken from [32].

2.5.5 Data analysis

HFC tensors were fitted from ENDOR data with the program MAGRES [33, 34]. It assumes an $S = I = 1/2$ system with spin Hamiltonian (2.44) and is based on the formulas developed from this spin Hamiltonian (see Section 2.3.2.2). The HFC tensor elements are determined through least-squares fitting routines as outlined in Section 2.4.1 but plane parameters can also be included in the fitting process.

For simulations of ENDOR angular variations and EPR spectra, on the other hand, *EasySpin* [35] subroutines in Matlab were used. These rely on exact diagonalisation of the spin Hamiltonian. The good agreement between simulated and experimental results throughout the doctoral research indicates that the approximations made in spin Hamiltonian (2.44) are valid for the systems studied here.

Chapter 3

Density functional theory

3.1 Introduction

As will be discussed in Chapter 4, the g tensors and HFC tensors of a radical contain a lot of information about the radical geometry and electronic structure. Although this information can be used to limit the number of plausible models for the radical, it rarely suffices to unambiguously identify the radical. Theoretical quantum-chemical calculations can then be employed to validate (or falsify) a particular radical model, or to obtain information that is not accessible experimentally. In the last four decades, ever more complex and more accurate theoretical calculations have become possible due to the development of new theoretical methods, more efficient algorithms and ever-increasing computer capacities. When the theoretical method is based solely on the fundamental laws of quantum physics, it is called *ab initio*. A particularly successful *ab-initio* theory is *density functional theory* (DFT), which was used throughout the doctoral research.

In Section 3.2 the basic theoretical framework of DFT is discussed and Section 3.3 comprises a brief discussion on the calculation of g tensors and HFC tensors in *ab-initio* codes. Some of the more practical aspects of DFT calculations are discussed in Section 3.4. Section 3.5, finally, deals with the 'computational protocol' for determining the g tensors and HFC tensors of organic radicals.

Elaborating on all (technical) details of DFT and the calculation of EMR parameters within DFT would be far beyond the scope of this doctoral thesis. The goal of this chapter is to give an *impression* of the theoretical framework and to summarise the practical experience gathered during the doctoral research. For a detailed discussion on DFT, one should consult Ref. [36] or – for a less formal approach – Ref. [37]. The calculation of EMR parameters in

ab-initio codes (including DFT) is reviewed in, e.g., Refs. [38, 39] and a rather detailed account of specific implementations of the g tensor and HFC tensors in DFT-based codes used in the doctoral research can be found in Ref. [40].

3.2 Basic principles of DFT

3.2.1 The Schrödinger equation

The stationary quantum states Ψ_i and the corresponding energy values E_i of a time-independent system described by a Hamiltonian \hat{H} , are the solutions of the time-independent Schrödinger equation, which constitutes an eigenvalue problem:

$$\hat{H}|\Psi_i\rangle = E_i|\Psi_i\rangle \quad (3.1)$$

The Ψ_i are called eigenstates or *eigenvectors* and the E_i (energy) *eigenvalues*. For a non-relativistic many-body system of n electrons (with positions $\vec{r}_1, \dots, \vec{r}_n$) and N atomic nuclei (with positions $\vec{R}_1, \dots, \vec{R}_N$), and neglecting electron and nuclear-spin interactions, Eq. (3.1) can be more explicitly written as

$$\hat{H}|\Psi_i(\vec{r}_1, \dots, \vec{r}_n, \vec{R}_1, \dots, \vec{R}_N)\rangle = E_i|\Psi_i(\vec{r}_1, \dots, \vec{r}_n, \vec{R}_1, \dots, \vec{R}_N)\rangle \quad (3.2)$$

where \hat{H} contains the operators corresponding to the electronic and nuclear kinetic energy, the Coulomb repulsion between the electrons mutually and between the nuclei mutually, and the Coulomb attraction between electrons and nuclei.

3.2.2 The many-body problem and the Born-Oppenheimer approximation

Eq. (3.2) is drastically simplified in the *Born-Oppenheimer (BO) approximation* [36, 41] by decoupling the electronic and nuclear degrees of freedom. Essentially, the electron movement¹ is assumed to instantaneously follow the motion of the nuclei. In other words, the nuclei are assumed to be fixed from the point of view of the electrons. This assumption is reasonable since nuclear masses are more than three orders of magnitude larger than the electron mass. In the BO approximation, the total wave function Ψ can be written as the product of an electronic wave function Ψ^{el} and a nuclear wave function Ψ^{nuc} :

$$\Psi(\vec{r}_1, \dots, \vec{r}_n, \vec{R}_1, \dots, \vec{R}_N) = \Psi^{el}(\vec{r}_1, \dots, \vec{r}_n) \Psi^{nuc}(\vec{R}_1, \dots, \vec{R}_N) \quad (3.3)$$

¹The term 'movement' can be somewhat misleading as the system does not evolve in time – we are assuming a time-independent Schrödinger equation –, but is often used in this context.

and Eq. (3.2) can be split up in two separate, time-independent Schrödinger equations: one for the electrons moving in a constant potential field of fixed atomic nuclei, and one for the nuclei, moving in a potential field derived from the electronic ground state. A geometry optimisation essentially comprises alternately solving these two equations in an iterative scheme. The wave equation for the electrons is

$$\hat{H}^{el} |\Psi_i^{el}(\vec{r}_1, \dots, \vec{r}_n)\rangle = E_i^{el} |\Psi_i^{el}(\vec{r}_1, \dots, \vec{r}_n)\rangle \quad (3.4)$$

with the electronic Hamiltonian \hat{H}^{el} given by

$$\hat{H}^{el} = \hat{T} + \hat{V}_{ee} + \hat{V}_{ext} \quad (3.5)$$

where the operators represent the electronic kinetic energy (\hat{T}), and the electronic potential energy due to the Coulombic interaction (i) between the electrons mutually (\hat{V}_{ee}) and (ii) between the electrons and the nuclei (\hat{V}_{ext}). The explicit forms of the operators in (3.5) are²

$$\begin{aligned} \hat{T} &= -\frac{1}{2} \sum_{i=1}^n \nabla_i^2 \\ \hat{V}_{ee} &= \sum_{i=1}^n \sum_{j < i}^n \frac{1}{|\vec{r}_i - \vec{r}_j|} \\ \hat{V}_{ext} &= -\sum_{i=1}^n \sum_{I=1}^N \frac{Z_I}{|\vec{r}_i - \vec{R}_I|} \end{aligned} \quad (3.6)$$

where we have switched to atomic units (which we will use throughout this chapter), defined by $\hbar = m_e = e = 4\pi\epsilon_0 = 1$. ∇^2 is the Laplacian operator and Z_I is the charge number of nucleus I . Note that \hat{V}_{ext} , and consequently (via Eq. (3.4)) Ψ_i^{el} and E_i^{el} , still *parametrically* depend on the (fixed) nuclear positions $\vec{R}_1, \dots, \vec{R}_N$. The corresponding energies for an electronic system with wave function Ψ^{el} are

$$\begin{aligned} T &= \langle \Psi^{el} | \hat{T} | \Psi^{el} \rangle \\ E_{ee} &= \langle \Psi^{el} | \hat{V}_{ee} | \Psi^{el} \rangle \\ E_{ext} &= \langle \Psi^{el} | \hat{V}_{ext} | \Psi^{el} \rangle \end{aligned} \quad (3.7)$$

²Lower-case indices i and j refer to electrons, upper-case indices I and J to nuclei.

Since we will only be concerned with the electronic wave function, the *el* superscript (and often also the term 'electronic') are dropped from now on.

Because the energies of electron-spin interactions are (very) small compared to the energy terms in Eq. (3.7), these interactions are neglected for the purpose of a geometry optimisation. If they are of interest, as is the case e.g. for the calculation of EMR parameters, they are usually treated perturbatively afterwards (cf. Section 3.3). We will, however, make explicit that the electron spin S_i represents an additional coordinate by writing \vec{x}_i instead of \vec{r}_i , with $\vec{x}_i = (\vec{r}_i, S_i)$. Furthermore, wave functions are always assumed to be normalised in this chapter, i.e.:

$$\int |\Psi(\vec{x}_1, \dots, \vec{x}_n)|^2 d\vec{x}_1 \dots d\vec{x}_n = 1 \quad (3.8)$$

For reasons of convenience, the summation over the possible (discrete) values of the spin is also written as an integration here.

Eq. (3.4) can in general not be solved analytically and a wide variety of techniques have been developed to obtain approximate solutions. DFT is one of these techniques and its theoretical framework will be discussed in Sections 3.2.4 and 3.2.5.

3.2.3 Electron and spin density

The electron density $\rho(\vec{r}_i)$ of a system of n electrons with wave function Ψ is defined as the following multiple integral over the spin coordinates of all electrons and over the spatial coordinates of all but one electron:

$$\rho(\vec{r}_i) = n \int |\Psi(\vec{x}_1, \dots, \vec{x}_n)|^2 d\vec{x}_1 \dots d\vec{x}_{i-1} dS_i d\vec{x}_{i+1} \dots d\vec{x}_n \quad (3.9)$$

It yields the probability of finding any of the n electrons with arbitrary spin within the volume element $d\vec{r}_i$ while the other $n-1$ electrons have arbitrary positions and spin. The factor n ensures that the electron density integrates to the total number of electrons:

$$\int \rho(\vec{r}_i) d\vec{r}_i = n \int |\Psi(\vec{x}_1, \dots, \vec{x}_n)|^2 d\vec{x}_1 \dots d\vec{x}_n = n \quad (3.10)$$

where we have used Eq. (3.8). Similarly, $\rho^\alpha(\vec{r}_i)$ and $\rho^\beta(\vec{r}_i)$, the density of α electrons ('spin up') and β electrons ('spin down') respectively, can be defined. We have

$$\rho(\vec{r}) = \rho^\alpha(\vec{r}) + \rho^\beta(\vec{r}) \quad (3.11)$$

and the *spin density* $\rho_S(\vec{r})$ is defined as

$$\rho_S(\vec{r}) = \rho^\alpha(\vec{r}) - \rho^\beta(\vec{r}) \quad (3.12)$$

3.2.4 The Hohenberg-Kohn theorems

DFT is founded on two theorems proven by Hohenberg and Kohn [42]. Essentially, they state that

1. *the external potential is a functional of the electron density $\rho(\vec{r})$:*

$$\hat{V}_{ext} \equiv \hat{V}_{ext}[\rho] \quad (3.13)$$

Since \hat{V}_{ext} determines \hat{H} (Eq. (3.5)),³ which in turn determines all properties of the system, the energy must also be a functional of the electron density:

$$E \equiv E[\rho] \quad (3.14)$$

Applied to the ground state with electron density ρ_0 and energy E_0 , we have

$$E_0 = E[\rho_0] \quad (3.15)$$

2. *the electron density that minimises the energy functional for a given external potential is the ground-state density:*

$$E[\rho] \geq E_0 \quad (3.16)$$

This constitutes a variational principle that allows determining the ground-state electron density and energy by calculating the energy for all possible (physically sound⁴) densities.

The first theorem provides the proof that – in principle – all information about the system can be extracted from its electron density. The second theorem provides a way to determine – again in principle – the ground-state density. The idea of describing an electronic system by its electron density (which is a function of three variables) instead of its multi-particle wave function (which is a function of $4n$ variables) is obviously attractive from both a computational and a conceptual point of view. It is this enormous reduction in the number of

³ \hat{T} and \hat{V}_{ee} in Eq. (3.5) are *universal operators*: their shape is independent of the system (although the number of electrons n must be known). From this point of view, the Hamiltonian is entirely determined by (n and) \hat{V}_{ext} .

⁴The concept ‘physically sound’ is an important issue in DFT, but going into detail on this would be beyond the scope of this work.

degrees of freedom that makes DFT calculations possible for realistic chemical systems with a relatively high accuracy at a relatively low computational cost.

Since E is a functional of ρ , all the separate contributions to E must also be:

$$E[\rho] = T[\rho] + E_{ee}[\rho] + E_{ext}[\rho] \quad (3.17)$$

The explicit expression for the latter functional is

$$E_{ext}[\rho] = \int \rho(\vec{r}) V_{ext}(\vec{r}) d\vec{r} \quad (3.18)$$

The E_{ee} term can be split up in a classical Coulombic part J and a non-classical part E_{ncl} :

$$E_{ee}[\rho] = J[\rho] + E_{ncl}[\rho] \quad (3.19)$$

The latter contains the exchange-interaction and Coulomb-correlation terms. The explicit functional form is only known for J :

$$J[\rho] = \frac{1}{2} \iint \frac{\rho(\vec{r}_1)\rho(\vec{r}_2)}{|\vec{r}_1 - \vec{r}_2|} d\vec{r}_1 d\vec{r}_2 \quad (3.20)$$

Eq. (3.17) can now be written as

$$E[\rho] = T[\rho] + E_{ncl}[\rho] + \frac{1}{2} \iint \frac{\rho(\vec{r}_1)\rho(\vec{r}_2)}{|\vec{r}_1 - \vec{r}_2|} d\vec{r}_1 d\vec{r}_2 + \int \rho(\vec{r}) V_{ext}(\vec{r}) d\vec{r} \quad (3.21)$$

The functional forms of $T[\rho]$ and $E_{ncl}[\rho]$ are unknown. Thus, even if the first Hohenberg-Kohn theorem proves that the energy is a functional of the electron density, we do not know the expression for that functional.

3.2.5 The Kohn-Sham approach of DFT

The idea of describing a system in terms of its electron density rather than its wave function had emerged several decades before Hohenberg and Kohn formulated their theorems, but none of the density-based approaches at the time came even remotely close to describing chemical systems accurately. Kohn and Sham realised (i) that the main reason for this was that a good determination of the kinetic energy was lacking, and (ii) that orbital-based approaches performed much better in this respect. Therefore, they introduced the concept of a non-interacting reference system built from a set of orbitals such that the major part of the kinetic energy can be computed with high accuracy [43]. We will now outline the main features of the KS procedure.

First, consider a system of n non-interacting particles, with Hamiltonian

$$\hat{H}_{ni} = -\frac{1}{2} \sum_{i=1}^n \nabla_i^2 + \sum_{i=1}^n \hat{V}_{eff}(\vec{r}_i) \quad (3.22)$$

where \hat{V}_{eff} accounts for the potential energy of the particles in an effective potential and consists of one-particle operators. The exact ground state of such a non-interacting system is given by a Slater determinant Φ_{SD} of n one-particle orbitals ϕ_i (the *KS orbitals*):

$$\Phi_{SD} = \begin{vmatrix} \phi_1(\vec{x}_1) & \dots & \phi_n(\vec{x}_1) \\ \vdots & \ddots & \vdots \\ \phi_1(\vec{x}_n) & \dots & \phi_n(\vec{x}_n) \end{vmatrix} \quad (3.23)$$

The ϕ_i are the solutions of the n single-particle equations (*KS equations*)

$$\hat{h}^{KS} \phi_i = \epsilon_i \phi_i \quad (3.24)$$

with the one-electron KS operator defined as

$$\hat{h}^{KS} = -\frac{1}{2} \nabla^2 + \hat{V}_{eff}(\vec{r}) \quad (3.25)$$

The kinetic energy of this non-interacting system is

$$T_{ni} = -\frac{1}{2} \sum_{i=1}^n \langle \phi_i | \nabla^2 | \phi_i \rangle \quad (3.26)$$

Second, assume (for now) that the electron density ρ_{ni} of the artificial, non-interacting system exactly equals the electron density of the real system, i.e. that

$$\rho_{ni}(\vec{r}) = \sum_i \sum_S |\phi_i(\vec{r}, S)|^2 = \rho(\vec{r}) \quad (3.27)$$

It can be shown that T_{ni} is a functional of the electron density of the real system in this case. This allows us to define the *exchange-correlation energy functional* E_{XC} as

$$E_{XC}[\rho] = \Delta T[\rho] + E_{ncl}[\rho] \quad (3.28)$$

where $E_{ncl}[\rho]$ is defined by Eq. (3.19) and

$$\Delta T[\rho] = T[\rho] - T_{ni}[\rho] \quad (3.29)$$

Eq. (3.21) can now be rewritten as

$$E[\rho] = T_{ni}[\rho] + J[\rho] + E_{ext}[\rho] + E_{XC}[\rho] \quad (3.30)$$

If the KS orbitals (from which the electron density ρ is obtained via Eq. (3.27)) are known, E_{XC} is the only unknown in the right-hand side of this equation. It contains the residual part of the true kinetic energy (not included in T_{ni}) and all non-classical Coulombic contributions.

Now, the point is that Eq. (3.27) is fulfilled when the following form is chosen for \hat{V}_{eff} :

$$\hat{V}_{eff}(\vec{r}) = \int \frac{\rho(\vec{r}')}{|\vec{r} - \vec{r}'|} d\vec{r}' + \hat{V}_{XC}(\vec{r}) - \sum_{I=1}^N \frac{Z_I}{|\vec{r} - \vec{R}_I|} \quad (3.31)$$

Here, the *exchange-correlation potential* V_{XC} is defined as the functional derivative of E_{XC} with respect to the electron density:

$$V_{XC}(\vec{r}) = \frac{\delta E_{XC}}{\delta \rho(\vec{r})} \quad (3.32)$$

In summary, the energy E of a system of n interacting electrons can be calculated via Eq. (3.30), which can be recast in the form

$$\begin{aligned} E[\rho] = & -\frac{1}{2} \sum_{i=1}^n \langle \phi_i | \nabla^2 | \phi_i \rangle + \frac{1}{2} \iint \frac{\rho(\vec{r}_1)\rho(\vec{r}_2)}{|\vec{r}_1 - \vec{r}_2|} d\vec{r}_1 d\vec{r}_2 \\ & + \int \rho(\vec{r}) V_{ext}(\vec{r}) d\vec{r} + E_{XC}[\rho] \end{aligned} \quad (3.33)$$

and the KS orbitals⁵ ϕ_i are the solutions of the following one-particle Schrödinger equations (combining Eqs. (3.24), (3.25) and (3.31)):

$$\left[-\frac{1}{2} \nabla^2 + \int \frac{\rho(\vec{r}')}{|\vec{r} - \vec{r}'|} d\vec{r}' + \hat{V}_{XC}(\vec{r}) - \sum_{I=1}^N \frac{Z_I}{|\vec{r} - \vec{R}_I|} \right] \phi_i = \epsilon_i \phi_i \quad (3.34)$$

The second and third term of the operators on the left-hand side depend on the electron density ρ , however, so that an iterative, self-consistent-field (SCF) procedure must be employed to determine the ground-state energy and electron density:

1. Generate a set of initial trial orbitals ϕ_i and calculate the electron density $\rho(\vec{r})$ via Eq. (3.27).

⁵We again remind the reader that these yield the electron density ρ via Eq. (3.27).

2. Solve the eigenvalue equations (3.34) to obtain 'new' orbitals and a 'new' electron density, and calculate E via Eq. (3.33).
3. Repeat step 2 until convergence is reached, i.e. until the change in E between two consecutive steps in the SCF procedure drops below a certain threshold.

If the exact functional form of $V_{XC}[\rho]$ were known, this procedure would yield the real ground-state electron density and energy. This is, however, not the case and $V_{XC}[\rho]$ is approximated (see Section 3.4.1), so that only an approximate solution of the Schrödinger equation is obtained.

The KS formulation of DFT can be generalised to spin-polarised systems, in which case the exchange-correlation potential, and consequently the KS orbitals, become spin dependent. The set of Eqs. (3.34) is then replaced by two sets (one for each spin).

Strictly speaking, the KS orbitals ϕ_i are only connected to the real system by Eq. (3.27). In the literature, however, the KS orbitals are regularly interpreted as the 'normal' molecular orbitals of the interacting many-particle system. In many cases this has proven to be a legitimate approach from a practical point of view. In this context, it is also interesting to note that, if $V_{XC}[\rho]$ would be exact, the energy of the highest-lying KS orbital would exactly equal (after sign inversion) the ionisation energy of the real system.

3.3 The g -tensor and HFC-tensor in DFT

In most of the implementations in DFT-based codes – and in all codes used during the doctoral thesis (Gaussian 03 [44, 45], CPMD [46, 47], CP2K [48–50]) –, the g and HFC tensor are calculated in a perturbational approach as second-order properties. In this approach, the g tensor components are formally defined as second-order partial derivatives of the energy of the electronic system with respect to the components of the net electron spin $\vec{S} = \sum_i \vec{S}_i$ and the components of a homogeneous external magnetic field \vec{B} , e.g.

$$g^{xy} = \frac{2}{\alpha} \left. \frac{\partial^2 E}{\partial B_x \partial S_y} \right|_{\vec{B}=\vec{S}=\vec{0}} \quad (3.35)$$

where $\alpha \approx \frac{1}{137}$ is the fine structure constant. As we put $\vec{B} = \vec{S} = \vec{0}$ after the partial derivation, only the energy components bilinear in \vec{S} and \vec{B} are considered.

Similarly, the HFC tensor components of a nucleus with nuclear spin \vec{I} are defined as, e.g.,

$$A_{xy} = \left. \frac{\partial^2 E}{\partial I_x \partial S_y} \right|_{\vec{I}=\vec{S}=\vec{0}} \quad (3.36)$$

In Eqs. (3.35) and (3.36), E is given by

$$E = \langle \Psi | \hat{H} | \Psi \rangle \quad (3.37)$$

where \hat{H} is the relevant Hamiltonian (see below) which depends on the perturbation operators (\vec{B} , \hat{S} , \hat{I}), and $|\Psi\rangle$ is the ground-state electronic wave function for that Hamiltonian.

By applying the Hellmann-Feynman theorem [51, 52] for double perturbation theory, Eqs. (3.35) and (3.36) can be written as

$$g_{xy} = \frac{2}{\alpha} \frac{\partial}{\partial B_x} \langle \Psi_{B_x} | \left. \frac{\partial \hat{H}}{\partial S_y} \right|_{\vec{S}=\vec{0}} | \Psi_{B_x} \rangle \Big|_{\vec{B}=\vec{0}} \quad (3.38)$$

$$A_{xy} = \frac{\partial}{\partial I_x} \langle \Psi_{I_x} | \left. \frac{\partial \hat{H}}{\partial S_y} \right|_{\vec{S}=\vec{0}} | \Psi_{I_x} \rangle \Big|_{\vec{I}=\vec{0}} \quad (3.39)$$

where $|\Psi_{B_x}\rangle$ ($|\Psi_{I_x}\rangle$) is the electronic wave function in the presence of a magnetic field (nuclear spin) along the x axis. From these equations it can be derived that for the calculation of the g tensor (HFC tensor)

- only the first-order corrections to the electronic wave function for each of the components of the magnetic field (nuclear spin) need to be calculated.
- only those perturbations in the Hamiltonian need to be considered that (i) depend linearly on the electron-spin components and (ii) are of the order 0 or 1 in the magnetic-field (nuclear-spin) components.

In order to derive a suitable Hamiltonian \hat{H} for the evaluation of the g tensor or the HFC tensor, one generally starts from the Dirac-Coulomb-Breit Hamiltonian⁶[53–55], of which the electronic component is projected out via e.g. a Foldy-Wouthuysen transformation [56]⁷ and then selects terms that meet criteria (i) and (ii).

⁶The Dirac equation is a special-relativistic, quantum-mechanical wave equation that describes spin-1/2 particles in the presence of an external electromagnetic field. The Dirac-Coulomb-Breit equation is an extension of the Dirac equation, which gives an approximative description of a system of n spin-1/2 particles in the presence of N atomic nuclei and in the presence of an external electromagnetic field.

⁷The Dirac-Coulomb-Breit Hamiltonian contains both electronic and positronic solutions. Foldy-Wouthuysen transformations allow a systematical reduction of the coupling terms between them.

3.3.1 The g tensor

Usually the following Hamiltonian is employed for the theoretical calculation of the g tensor (as a second-order property):

$$\begin{aligned} \hat{H}^g = & \hat{H}_Z + \hat{H}_{SO(N)} + \hat{H}_{SO(2e)} + \hat{H}_{SOO} \\ & + \hat{H}_{SO(N)}^{dia} + \hat{H}_{SO(2e)}^{dia} + \hat{H}_{SOO}^{dia} + \hat{H}_{ZKE} \end{aligned} \quad (3.40)$$

The different terms at the right-hand side are (from left to right)

- the electronic Zeeman term \hat{H}_Z , which represents the coupling between the electron spins and the external magnetic field. This term gives rise to the free-electron contribution (g_e) to the g tensor.
- the nuclear spin-orbit coupling term $\hat{H}_{SO(N)}$ (*nuclear*: the spin of an electron couples to the orbital angular momentum originating from the rotation of that electron around a nucleus).
- the two-electron spin-orbit coupling term $\hat{H}_{SO(2e)}$ (*two-electron*: the spin of electron 1 couples to the orbital angular momentum originating from the rotation of electron 1 around electron 2).
- the two-electron spin-other-orbit coupling term \hat{H}_{SOO} (*other-orbit*: the spin of electron 1 couples to the orbital angular momentum originating from the rotation of electron 2 around electron 1).
- the gauge-correction terms (also called diamagnetic terms) $\hat{H}_{SO(N)}^{dia}$, $\hat{H}_{SO(2e)}^{dia}$ and \hat{H}_{SOO}^{dia} , which are the result of imposing gauge-invariance (i.e. the result should not depend on the choice of origin for the calculation of the orbital angular momenta).
- the (isotropic) Zeeman kinetic-energy-correction term \hat{H}_{ZKE} , which is a purely kinematic-relativistic correction.

For many organic radicals, the first two terms are the dominant contributions. Their explicit expressions are

$$\hat{H}_Z = \frac{\alpha g_e}{2} \sum_i \hat{S}_i \cdot \vec{B} \quad (3.41)$$

$$\hat{H}_{SO(N)} = \frac{\alpha^2 (g_e - 1)}{2} \sum_i \sum_I Z_I \hat{S}_i \cdot \frac{(\vec{r}_i - \vec{R}_I) \times \hat{p}_i}{|\vec{r}_i - \vec{R}_I|^3} \quad (3.42)$$

where \vec{p}_i is the impulse momentum of electron i .

3.3.2 The HFC tensor

In many cases the Hamiltonian employed for the calculation of the HFC tensor (as a second order property) for a nucleus with spin \vec{I} and nuclear g factor $g_{N,I}$ is

$$\hat{H}^{HFC} = \hat{H}_{FC} + \hat{H}_{DC} \quad (3.43)$$

where the isotropic Fermi-contact interaction term \hat{H}_{FC} and the anisotropic dipole-dipole interaction term \hat{H}_{DC} are given by

$$\hat{H}_{FC} = \frac{2\mu_0}{3} g_e g_{N,I} \mu_B \mu_N \sum_i \delta(\vec{r}'_i) \hat{S}_i \cdot \hat{I} \quad (3.44)$$

$$\hat{H}_{DC} = \frac{\mu_0}{4\pi} g_e g_{N,I} \mu_B \mu_N \sum_i \hat{S}_i \cdot \left[\frac{3\vec{r}'_i \cdot \vec{r}'_i - \bar{1} |\vec{r}'_i|^2}{|\vec{r}'_i|^5} \right] \cdot \hat{I} \quad (3.45)$$

where $\vec{r}'_i = \vec{r}_i - \vec{R}_I$ is a row vector and $\bar{1}$ is the 3x3 unit matrix. Because both \hat{H}_{FC} and \hat{H}_{DC} are linear in the nuclear-spin components, Eq. (3.39) reduces to

$$A_{xy} = \langle \Psi | \left. \frac{\partial^2 H^{HFC}}{\partial I_x \partial S_y} \right|_{\vec{I}=\vec{S}=\vec{0}} | \Psi \rangle \quad (3.46)$$

so that corrections to the electronic wave function do not need to be considered. Consequently, HFC tensors can be calculated relatively easily at a low computational cost, provided Hamiltonian (3.43) is adequate. Assuming $S = \left| \sum_i \vec{S}_i \right| = 1/2$, Eq. (3.46) can be shown to reduce to [40]

$$\begin{aligned} A_{xy} = & \delta_{xy} \frac{2\mu_0}{3} g_e g_{N,I} \mu_B \mu_N \rho_S(\vec{R}_I) \\ & + \frac{\mu_0}{4\pi} g_e g_{N,I} \mu_B \mu_N \int \rho_S(\vec{r}') \frac{3x'y' - \delta_{x'y'} |\vec{r}'|^2}{|\vec{r}'|^5} d\vec{r}' \end{aligned} \quad (3.47)$$

where $\vec{r}' = \vec{r} - \vec{R}_I = (x', y', z')$. We see that only the spin density ρ_S is required, which is immediately available from a KS SCF run.

3.4 DFT in practice

3.4.1 Density functionals

The exchange-correlation-energy functional E_{XC} clearly is a key entity in DFT (see Section 3.2.5). Since its functional form is not known, approximations

have to be used. The most common approximations are briefly discussed here. In the *local density approximation* (LDA), E_{XC} is taken to be

$$E_{XC}^{LDA}[\rho] = \int \rho(\vec{r})\epsilon(\rho(\vec{r}))d\vec{r} \quad (3.48)$$

where $\epsilon(\rho(\vec{r}))$ is the exchange-correlation energy per particle of a uniform electron gas of density $\rho(\vec{r})$. The functional can be split up in an exchange and a correlation contribution: $E_{XC}^{LDA} = E_X^{LDA} + E_C^{LDA}$. An exact expression is known for the exchange-energy functional of a uniform electron gas [57]. This is not the case for the correlation-energy functional, but highly accurate, analytical expressions are available. The VWN correlation functional developed by Vosko, Wilk and Nusair [58] is one (popular) example. In the *local spin density approximation* (LSDA), the spin-polarised variant of LDA, an analogous expression is used, but the functional is now dependent on both the α - and β -electron densities:

$$E_{XC}^{LSDA}[\rho^\alpha, \rho^\beta] = \int \rho(\vec{r})\epsilon(\rho^\alpha(\vec{r}), \rho^\beta(\vec{r}))d\vec{r} \quad (3.49)$$

and again $E_{XC}^{LSDA} = E_X^{LSDA} + E_C^{LSDA}$.

Considering the utter simplicity of L(S)DA, these functionals perform surprisingly well. For many applications in chemistry, however, their accuracy is insufficient.

In the *generalised gradient approximation* (GGA), E_{XC} depends not only on the (spin-polarised) electron density, but also on its spatial derivatives:

$$\begin{aligned} E_{XC}^{GGA}[\rho] &= \int f(\rho(\vec{r}), \nabla\rho(\vec{r}))d\vec{r} \\ E_{XC}^{GGA}[\rho^\alpha, \rho^\beta] &= \int f(\rho^\alpha(\vec{r}), \rho^\beta(\vec{r}), \nabla\rho^\alpha(\vec{r}), \nabla\rho^\beta(\vec{r}))d\vec{r} \end{aligned} \quad (3.50)$$

The inclusion of gradients accounts (to some extent) for the non-homogeneity of the electron density. GGA functionals are usually also split up into an exchange and a correlation contribution (although, strictly speaking, this split-up has no physical interpretation):

$$E_{XC}^{GGA} = E_X^{GGA} + E_C^{GGA} \quad (3.51)$$

and approximations for the two parts are sought individually. The most widely used GGA exchange-correlation functionals are BP86 and BLYP. In both cases, the Becke exchange functional E_X^{B88} [59] is used, together with the correlation functional E_C^{P86} derived by Perdew [60], or the correlation functional E_C^{LYP} derived by Lee, Yang and Parr [61] respectively.

Another and – from a practical point of view – most important class comprises the *hybrid functionals*. These are constructed by mixing L(S)DA functionals and/or GGA functionals with the exchange-energy functional of the non-interacting KS reference system (denoted E_X^{KS} below), for which the exact expression is known from Hartree-Fock theory [62]:

$$E_X^{KS} = -\frac{1}{2} \sum_{i,j} \delta_{S_i S_j} \iint \frac{\phi_i^*(\vec{r}) \phi_j^*(\vec{r}') \phi_j(\vec{r}) \phi_i(\vec{r}')}{|\vec{r} - \vec{r}'|} d\vec{r} d\vec{r}' \quad (3.52)$$

where $\delta_{S_i S_j} = 1$ when $S_i = S_j$ and $\delta_{S_i S_j} = 0$ when $S_i \neq S_j$. The most widely used hybrid functional for chemical applications is B3LYP [63]:

$$E_{XC}^{B3LYP} = (1-a)E_X^{LSDA} + aE_X^{KS} + bE_X^{B88} + cE_C^{LYP} + (1-c)E_C^{LSDA} \quad (3.53)$$

where the three empirical parameters are $a = 0.20$, $b = 0.72$ and $c = 0.81$.⁸

3.4.2 Basis sets

The KS orbitals ϕ_i (Section 3.2.5) are expressed as linear combinations of a set of fixed functions ψ_j , called *basis functions*:

$$\phi_i(\vec{r}) = \sum_j c_{ij} \psi_j(\vec{r}) \quad (3.54)$$

Once the basis set (i.e. the set of basis functions) is chosen, the KS orbitals are entirely defined by the coefficients c_{ij} . The more basis functions employed, the more precise the KS orbitals can be described but also the higher the computational cost. The type of basis functions also has repercussions on the computational cost. In the calculations performed during the doctoral research, two types of basis functions were used: Gaussian functions and plane waves (PW).

3.4.2.1 Gaussian functions

A *primitive Gaussian function* χ^{GTO} (also called Gaussian-type orbital (GTO)) has the form

$$\chi^{GTO}(\vec{r}) = (x - x_0)^{n_x} (y - y_0)^{n_y} (z - z_0)^{n_z} e^{-\zeta(\vec{r} - \vec{r}_0)^2} \quad (3.55)$$

and is determined by the natural numbers n_x , n_y and n_z , a positive exponent ζ and the origin of the Gaussian function, $\vec{r}_0 = (x_0, y_0, z_0)$. In the present context,

⁸These values were determined by fitting calculated values to a large set of experimental reference data (the so-called G2 database).

the latter is the position of a nucleus. The use of Gaussian functions allows certain integrals in the Kohn-Sham procedure to be calculated analytically. Another advantage of Gaussian functions is their localised character, which allows an efficient description of the electron density. They are however rather inefficient with respect to the calculation of $J[\rho]$ and $E_{XC}[\rho]$ in the energy functional (3.30).

In practice, quantum-chemical programs use *contracted Gaussian functions* (CGF) as basis functions ψ_j . These are linear combinations of primitive Gaussian functions and (approximately) represent atomic orbitals:

$$\psi_j^{CGF}(\vec{r}) = \sum_k d_{jk} \chi_k^{GTO}(\vec{r}) \quad (3.56)$$

Primitive *periodic* Gaussian functions can be defined in a straightforward way. This gives rise to *contracted periodic Gaussian functions* (CPGF).

Among the most widely used basis sets are the *split-valence* CGF basis sets developed by the group of Pople, denoted as X-Y₁...Y_nG (e.g. 6-311G): the core atomic orbitals⁹ are each represented by one CGF of X primitive Gaussians, while every valence atomic orbital is represented by n CGFs of Y₁,...,Y_n primitive Gaussians respectively. For n=2, n=3 and n=4, these are called double-zeta, triple-zeta and quadruple-zeta basis sets respectively.

A * superscript (e.g. 6-311G*) indicates that, in addition, *polarisation functions* are used for all elements except H and He. The ** supercript (e.g. 6-311G**) indicates that polarisation functions are also added for the latter two. In the case of carbohydrate systems, this boils down to adding p-type orbitals for H and d-type orbitals for O and C.

3.4.2.2 Plane waves

In a PW basis set, the basis functions are of the form

$$\psi_j^{PW}(\vec{r}) \sim e^{i\vec{k}\cdot\vec{r}} \quad (3.57)$$

PWs form an infinite basis set and the number of PWs is controlled by specifying a maximum value for the kinetic energy of a PW.

Because of their periodicity and infinite extent, PWs are naturally suited for simulations of periodic systems, e.g. single crystals. Moreover, in a PW basis set, efficient fast Fourier-transform (FFT) techniques can be used for many algebraic manipulations which, among others, allows a rapid evaluation of $J[\rho]$ in Eq. (3.30). However, a huge number of PWs is needed to describe the electron density in the region close to a nucleus (where it rapidly fluctuates)

⁹I.e. all atomic orbitals except the valence orbitals.

satisfactorily, and all space is described equally well, which is a waste of computational resources. This can (in part) be remedied by the use of pseudopotentials.

3.4.3 The pseudopotential approximation

The chemical properties of a molecule can mainly be ascribed to the valence electrons of the constituting atoms. In this respect, core electrons do not need to be taken into account explicitly. Moreover, for many chemical properties (e.g. chemical bonding), the part of the valence electronic wave function situated in the core region is of minor importance. The pseudopotential approach takes advantage of both these facts: instead of explicitly taking into account the atomic nucleus and the core electrons, a so-called pseudo-potential (PSP) models their interactions with the surrounding particles. This approach also requires replacing the real valence-electron orbitals by pseudo orbitals, which can strongly differ from the real orbitals in the core regions. A PSP approach offers a considerable reduction in the computational cost because (i) less electrons are treated explicitly and (ii) the size of a PW basis set can be reduced substantially. The reason for the latter is that the rapid fluctuations of wave functions in the core region do not have to be represented.

3.4.4 The hybrid Gaussian and (augmented-)plane-wave method

As discussed in Sections 3.4.2.1 and 3.4.2.2, Gaussian functions and PWs each have their own merits as basis set functions. In the Gaussian and plane-wave (GPW) method [64], the advantages are combined. Gaussian functions – to be more precise: CPGFs – are used as a primary basis set, but an auxiliary PW basis set is employed additionally. The electron density is collocated onto this PW basis set. A PSP approximation has to be used to reduce the size of the PW basis set and make calculations practically feasible. Even with a PSP approach, however, a rather large PW basis set is typically necessary.

In the Gaussian and augmented-plane-wave (GAPW) method [65], the auxiliary basis set of PWs is extended with the primitive periodic Gaussian functions from which the CPGFs are constructed. The heavily oscillating part of the electron density close to the atomic nuclei is expressed in these 'extra' Gaussian functions, while the more slowly varying part in the regions in between the nuclei is expressed in PWs (as in the GPW method). This split-up allows a very efficient evaluation of $E_{XC}[\rho]$ and $J[\rho]$. The GAPW method offers two major advantages over the GPW method: (i) the size of the PW basis set can be strongly reduced and (ii) the use of PSPs is not obligatory –

all-electron (AE) calculations can even be performed with virtually the same *computational efficiency* [66].¹⁰

3.5 DFT calculations on organic radicals

3.5.1 General procedure

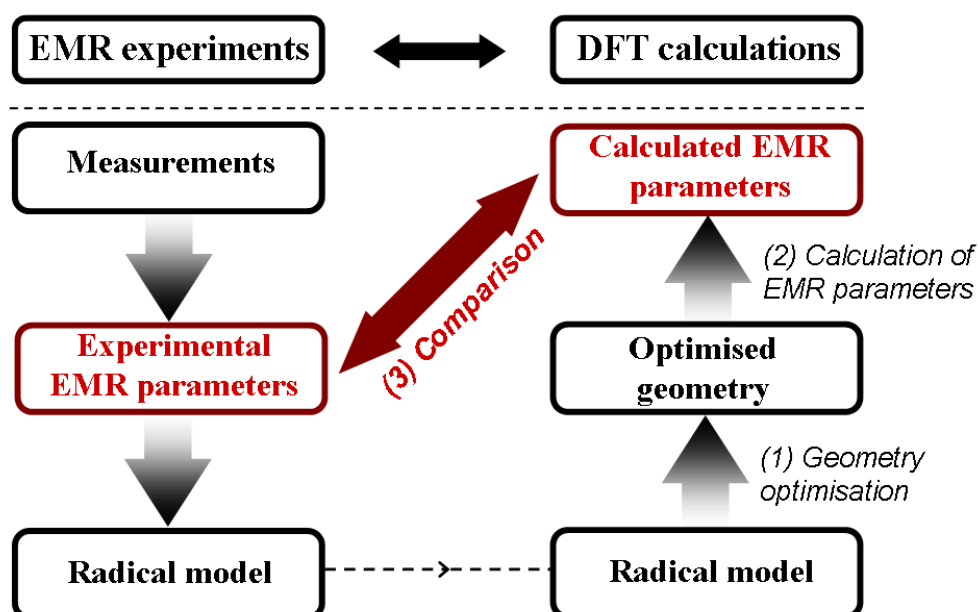


Figure 3.1: General procedure for identifying radicals by means of EMR experiments and DFT calculations.

Figure 3.1 gives a schematic overview of the ‘ideal’ procedure for the identification of radicals by combining EMR experiments and DFT calculations. The experiments yield EMR parameters, such as the g tensor and HFC tensors (cf. Chapter 2). These contain (indirect) information about the radical’s geometry and electronic structure, which can be used to devise plausible radical models (as will be discussed in Chapter 4). The latter then serve as input for the DFT calculations: a geometry optimisation of the radical is performed and EMR parameters are calculated on the optimised radical structure. By comparing the DFT-calculated and experimentally obtained

¹⁰I.e., the computational cost *per* (explicitly considered) *electron* is approximately the same.

EMR parameters, the validity of the radical model can be assessed.

In the next sections, the geometry optimisation, the calculation of EMR parameters (more specifically: g tensors and HFC tensors) and the comparison of theoretical and experimental results are discussed in the case of radicals in organic single crystals.

3.5.2 Geometry optimisation

The accuracy of a radical structure obtained by DFT calculations depends on the *level of theory* (LOT) as well as on the *model space*. The LOT is defined very broadly here and includes the type and size of basis set, the exchange-correlation functional, whether an AE or a PSP approach is employed (and in the case of the latter: which type of PSP is used), and the convergence criteria. With model space we refer to the degree to which the environment of the radical centre is taken into account in the geometry optimisation.

For the DFT calculations performed during the doctoral research, well-established functionals, basis sets, etc. were always used. We will focus here on the role of the model space, which is in general more crucial. Three approaches are commonly encountered in the literature for solid-state systems:

- *the single-molecule (SM) approach*: only the molecule containing the radical centre is considered. This corresponds to a gas-phase optimisation.
- *the cluster approach*: a certain group of surrounding molecules, with the geometry of the single crystal, is additionally taken into account.
- *the periodic approach*: the periodicity of the system is explicitly taken into account by applying periodic boundary conditions (PBC).

The computational cost is of course the lowest in the SM approach, but the total neglect of the surrounding lattice in general often is a too crude approximation. This is definitely the case for the organic crystals studied in this work: the molecules are held together by intermolecular hydrogen bonds and the conformation of a molecule in a lattice is to a large extent determined by these bonds. A *partial-optimisation scheme*, in which certain atoms (e.g. the OH groups) are kept fixed, can be used to mimic to some extent the presence of the surrounding lattice, but such calculations are biased. Since modern computer resources can cope with larger structures at a reasonable computational cost, the SM approach is somewhat outdated.

In a cluster approach, only a limited part of the crystalline environment is considered. The choice of the cluster (size) is more or less arbitrary. A larger cluster should in general yield more reliable results, but also implies

a higher computational cost. An important disadvantage of this approach is that, since the cluster is simulated in the gas-phase, it unavoidably suffers from boundary-effect problems: its outermost layer may easily adopt a conformation differing substantially from that in the single crystal, the spin density may be delocalised over the outer surface, etc. For sugars, it usually is a good approximation to construct the cluster such that it contains the radical and all molecules hydrogen-bound to it, and to use a partial-optimisation scheme in which only the radical (molecule) is allowed to relax.

In the periodic approach, the model space is an infinite structure of a periodically repeated *supercell*. This supercell contains a number of crystal unit cells (at least one) and should be such that no gaps appear in the periodic structure. The size of the supercell should also be large enough to ensure that the radical is sufficiently separated from its periodic images. PBC calculations offer the most natural description for single crystals and do not suffer from boundary-effect problems. On the other hand, a charged supercell results in an infinite charge of the periodic structure in PBC simulations, which is compensated by adding a uniformly distributed background countercharge. Some problems were encountered in the doctoral research that are possibly related to this background charge (see Paper V and Section 5.3.3.8).

PBC simulations with a PSP approach were used for most geometry optimisations in this work. For a number of radicals, however, we also performed geometry optimisations in a cluster approach and/or in an AE scheme (not reported in this work). The geometries obtained with PSP and AE approaches did not differ significantly but in a few cases the cluster and the periodic approach resulted in essentially different radical conformations. The cause of the discrepancy was a 'gap' in the adopted cluster, which was not present in the periodic structure.

From the discussion above the periodic approach clearly emerges as superior to SM and cluster approaches for geometry optimisations of radicals in organic single crystals. A systematic and more quantitative study by Declerck *et al.* [67], performed at the CMM in Ghent, arrives at the same conclusion. An important point here is that PSPs can be employed to reduce the computational cost substantially without a significant loss in accuracy.

3.5.3 Calculation of g tensors and HFC tensors

The accuracy of calculated g tensors and HFC tensors also depends on both the LOT and the model space, although the latter is far less crucial than in the

case of geometry optimisations (see below). We will only discuss one specific aspect of the LOT here: the use of PSPs. The influence of the temperature on HFC tensors has also been studied [40, 67, 68] but was found to be (very) small for proton HFC tensors and is therefore not discussed here.

3.5.3.1 Model space

All calculations performed during the doctoral research indicate that, with respect to HFC tensors, the SM and the cluster approach yield comparable results for both principal values and eigenvectors, and that the differences between the periodic and the cluster approach typically are (very) small. This is again substantiated by the study by Declerck *et al.* [67]. There are exceptions – HFC tensor $H_{\beta 3}(T1)$ of the stable T1 sucrose radical changes significantly when the crystalline environment is taken into account (Paper III), e.g. – but if the calculated HFC tensors are compared with the experimental ones ‘in the right way’ (see Section 3.5.4), SM calculations suffice to make a good (initial) assessment of the validity of the radical model. This does, however, not imply that the surrounding lattice is unimportant for the determination of HFC tensors: the accuracy of the calculated tensors chiefly depends on the accuracy of the radical geometry, and the latter in turn strongly depends on the incorporation of the crystalline environment, as discussed above.

g tensors appear to be more dependent on the model space (as indicated e.g. by the results in Paper II), but not enough g -tensor calculations were performed in the doctoral research to draw definite conclusion in this respect. Especially in the case of oxygen-centred radicals one should be cautious: as will be discussed in Section 4.4.2.2 (page 102), these are assumed to strongly depend on the intermolecular hydrogen bond(s).

3.5.3.2 Pseudopotential versus all-electron approach

Both a PSP and an AE approach can be employed for the calculation of g - and HFC-tensor calculations. The computational cost of the former is considerably lower but (i) the pseudo valence orbitals in general do not exhibit the correct behaviour in the core regions (see Section 3.4.3) and (ii) core-polarisation effects are not included in a PSP approach. This introduces only small errors for the g tensor of radicals consisting of light elements (up to Ne) [40, 47],¹¹ but poses an essential problem for the HFC tensor, as it is clear from Eq. (3.47) that

¹¹For radicals with heavier elements, good results can still be obtained if more core electrons (than typically used for geometry optimisation) are treated explicitly, which also implies an increase in size of the PW basis set.

the spin density in the region close to the nucleus has to be described well. This can (for both the g tensor and the HFC tensor) in part be remedied by applying (gauge-including) projector-augmented-wave ((GI)PAW) methods, in which the AE valence orbitals are reconstructed from the PSP valence orbitals [69, 70]. Most g - and HFC-tensor calculations in the doctoral research were performed in an AE approach, but in our DFT study on K2G1P we employed a PSP approach together with such an AE reconstruction scheme (Paper V). The reliability of this method has been established for the determination of HFC tensors in crystalline biomolecules [50].

The efficiency of a PSP approach can be combined with the accuracy of an AE approach by employing a hybrid scheme, in which an AE description is used for the radical centre and the nuclei in the direct vicinity, and a PSP description for the remaining atoms in the supercell. This is possible via the GAPW method (Section 3.4.4), which exists in both a PSP and an AE approach and readily allows for a combination of both approaches in a single calculation [50]. Although a periodic approach based on the GAPW method is the most accurate and natural choice – and when a hybrid scheme is adopted: also a very efficient one – for the systems studied in this doctoral thesis, it was employed only for the most recent calculations because of practical reasons: the GAPW method has only recently become available for non-orthogonal supercells in CP2K.

3.5.4 Comparing DFT-calculated and experimental tensors

When comparing theoretical and experimental HFC tensors, one should keep in mind that

- the anisotropic part is, in first instance, more important than the isotropic part. A DFT-calculated isotropic HFC value is more sensitive to both the LOT and the model space and is in general less accurately reproduced – especially when a PSP/PAW method is used.
- certain eigenvectors are more important than others. For α protons¹² there should be a good correspondence for all eigenvectors if the model is correct. For β protons and, especially, more remote protons, however, the eigenvectors associated with the two smallest principal values may differ more (several tens of degrees) from their experimental counterparts. These eigenvectors are also more dependent on the LOT and the model space.

¹²For the definition of α and β protons, see Chapter 4.

- the overall sign of the tensor has often not been determined experimentally (cf. Section 2.4.2.1, page 44), in which case inversion of the sign may be considered.
- an experimental tensor is always reported for a certain site. The eigenvectors obtained by performing symmetry operations of the crystal's symmetry group on the reported eigenvectors should always be considered.
- the Schonland ambiguity (see Section 2.4.2.2, page 44 and Paper VI) may not have been resolved for the experimental HFC tensors, in which case the Schonland-conjugate tensor should be considered. The difference between two Schonland-conjugate tensors can be quite substantial.

As already stated, not many g -tensor calculations were performed and we only note here that the last two 'warnings' of the list above also apply to g tensors. The sign of the g tensor is not an issue for organic radicals as the deviation of the principal g values from g_e is (very) small.

Chapter 4

Solid-state organic radicals

4.1 Introduction

Experimental hyperfine coupling (HFC) tensors and g tensors, formally introduced in Chapter 2, can provide a wealth of detailed information on the spin-density distribution and the geometry of radicals. The central 'theme' throughout the doctoral research has been the identification of radicals by comparing DFT-calculated proton HFC tensors and g tensors for model structures with experimentally determined tensors. In principle, DFT calculations can be employed to test every conceivable radical model but the number of possible models increases tremendously when more complex structural damage has to be considered. Also, DFT calculations sometimes need a 'push' in the right direction. E.g., a certain radical structure may have different stable conformations, in which case the geometry of the optimised structure depends to some extent on the original input structure. It is therefore still essential to deduce as much information as possible from the experimental g and HFC tensors. This requires a basic insight in the underlying physics as well as some familiarity with archived experimental data, which is what this chapter aims to provide.

Most of the theory that relates g tensors and HFC tensors of organic radicals to their electronic and geometrical structure was developed in the period 1950 - 1970.¹ Many analytical tools and rules of thumb have emerged from this research and over the decades a vast amount of experimental data have become available. An overview will be given of the analytical tools relevant in the context of radical identification in organic radicals, as well as of 'typical' experimental data. Simplified models and theoretical calculations are

¹Not by accident shortly after the discovery of EPR by Zavoisky in 1944: EPR was (and is) the leading experimental technique that thrusts (thrusts) this kind of research.

presented to provide the reader with enough insight to assess the limitations of the theoretical models from which the analytical tools emerge, without submerging him/her in mathematics. Though not always explicitly referred to, Refs. [26] and [71] often served as a guide in writing this chapter.

To put things in the right perspective, following remark should be made: DFT calculations are by all means superior to these older theoretical models when one wants to assess specific radical structures – as this doctoral thesis testifies. This is most pronounced when the radical geometry differs substantially from the pristine crystal structure. DFT calculations allow unambiguous identifications that otherwise would simply not be possible (or at least much more difficult) and often yield information that cannot be (directly) obtained experimentally. The principal use of the analytical tools lies in *a priori* reducing the number of plausible radical models and providing the necessary basic insight in the physics involved.

Some chemical vocabulary is important to avoid confusion and misinterpretations in this and the following chapters. Therefore, a few basic terms and concepts are first (re)defined.

4.2 Basic concepts

4.2.1 Nomenclature of radicals

Carbohydrates are compounds entirely consisting of hydrogen, carbon and oxygen. *Hydrocarbons* contain only hydrogen and carbon atoms, and are divided into two classes: *aromatic* compounds, which contain e.g. a benzene ring, and *aliphatic* compounds, which do not contain aromatic constituents. The term *alkyl radical* refers to a hydrocarbon radical with chemical formula C_nH_{2n+1} , e.g. $C^\bullet H_2-CH_3$. In the literature, however, the term alkyl radical is regularly used for any carbon-centred radical $C^\bullet(R1)(R2)(R3)$ with R1-R3 consisting of C, O and H, and we will adopt this convention. In a *hydroxyalkyl radical* at least one hydroxy group (i.e. an OH group) is bound to the radical centre, e.g. $C^\bullet HOH-CH_3$. The *allyl radical* has the structure $H_2C=C-C^\bullet H_2 \leftrightarrow H_2C^\bullet-C=CH_2$. With *alkoxy radical* we refer to any oxygen-centred radical $R1-C(R2)-O^\bullet$ in which R1 and R2 may consist of C, O and H.

Figure 4.1 depicts a typical alkyl radical. The unpaired electron is formally localised in a $2p_z$ orbital on a certain carbon. This carbon is denoted C_α and is referred to as the α carbon. A proton attached to an α carbon is an α proton (H_α , one bond away from C_α). An adjacent carbon is referred to as a β carbon (C_β) and a proton bound to it as a β proton (H_β , two bonds away from C_α). Similarly one can define γ protons (three bonds away from C_α), δ protons

(four bonds away from C_α), ... This nomenclature is also used

- for alkoxy radicals and for carbon-centred radicals containing one or more oxygen atoms. For instance, the hydrogen proton of a hydroxy group attached to a β carbon can be referred to as a γ proton (cf. Figure 4.1).
- in certain radicals where the spin density is delocalised over several atoms (e.g. on a ring oxygen or on a carbonyl group). The C_α carbon is then the one carrying the largest part of the spin density.

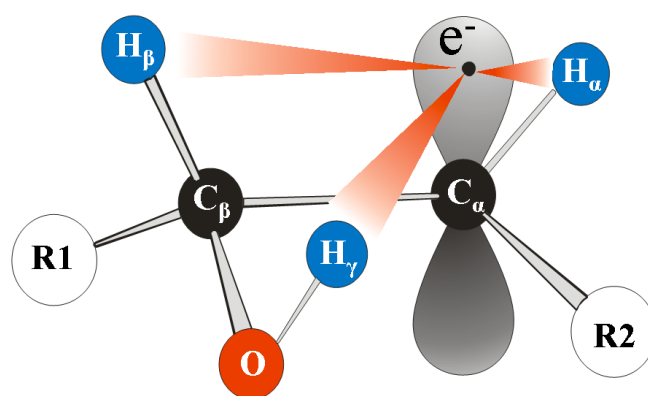


Figure 4.1: Nomenclature of carbons and protons in a typical alkyl radical.

4.2.2 Electronic configuration of carbon and oxygen

The ground state valence electron configurations of carbon and oxygen atoms are shown in Figure 4.2. Carbon has only two $2p$ electrons that can engage in chemical bonding. The typical and well-known tetrahedral configuration of saturated carbon compounds is explained by *hybridisation*: the $2s$ orbital mixes with the three $2p$ orbitals, which yields four equivalent sp^3 hybrid orbitals that make angles of 109.5° with each other (sp^3 hybridisation). Each sp^3 orbital contains one electron and can engage in chemical bonding.

In an alkyl radical one of the carbon valence electrons is unpaired and does not participate in a chemical bond. Usually the carbon centre becomes approximately planar: the three bonds are in a plane and make angles of approximately 120° . This can be explained in terms of sp^2 hybridisation (Figure 4.2): the $2s$ orbital mixes with two $2p$ orbitals, yielding three sp^2

hybrid orbitals containing one electron each, while the remaining electron occupies one of the 'original' $2p$ orbitals. Conventionally the unpaired electron is assigned to the $2p_z$ orbital. We will adopt this convention throughout this chapter. The hybridisation schemes for oxygen can be constructed in a completely analogous fashion (Figure 4.2).

The sp^3 and sp^2 orbitals can, in turn, mix with atomic orbitals of adjacent carbons to form a σ bond. (Figure 4.3). All single covalent bonds (e.g. C-H

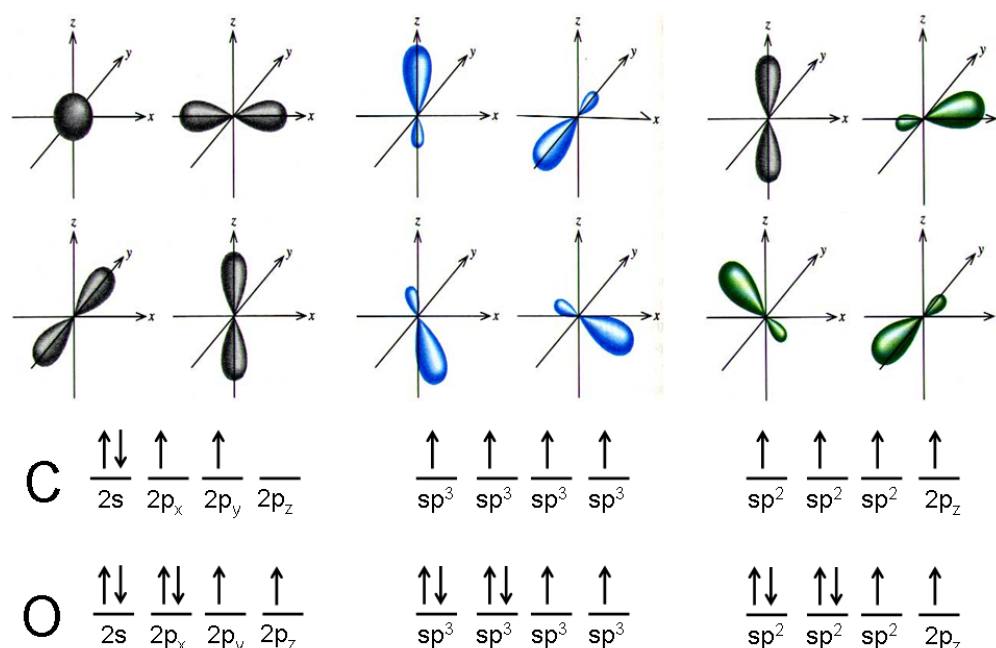


Figure 4.2: The valence electronic configuration and orbitals of carbon and oxygen atoms in their (atomic) ground state (*left*), in sp^3 hybridisation (*middle*) and in sp^2 hybridisation (*right*). The sp^3 orbitals are in a tetrahedral configuration, making angles of 109.5° with each other. In the sp^2 hybridisation, the hybridised orbitals are in a plane, making angles of 120° with each other, and the $2p_z$ orbital is perpendicular to this plane.

bonds) are σ bonds. The $2p_z$ orbital of an sp^2 hybridised carbon can overlap with the $2p_z$ orbital of an adjacent oxygen or carbon and thus give rise to a π bond (in addition to the σ bond). This is the case in, e.g., ethene ($\text{H}_2\text{C}=\text{CH}_2$, Figure 4.3) and in a carbonyl group ($\text{C}=\text{O}$).² We note that also sp hybridisation can occur, where the two remaining $2p$ orbitals can both participate in π bonds. This is the case in, e.g., ethyn ($\text{HC}\equiv\text{CH}$).

A σ bond orbital results from head-on overlap of atomic orbitals and it has

²Such bonds, consisting of a σ as well as a π bond, are often referred to as 'double bonds'.

cylindrical symmetry around the bond axis with maximum electron density on this axis. A π orbital results from sideways overlap and is shaped like two 'arches' with a nodal plane passing through the nuclei of both atoms. π bonds are weaker than σ bonds due to the lower degree of overlap of the constituting atomic orbitals in the former.

In the literature the symmetry of the lone-electron orbital (LEO) often determines the nomenclature, and not the distinction between atomic and molecular orbitals. For instance, atomic $2p$ orbitals can be referred to as π or $2p\pi$ orbitals, even if they do not participate in a π bond. Similarly, ' π radical'

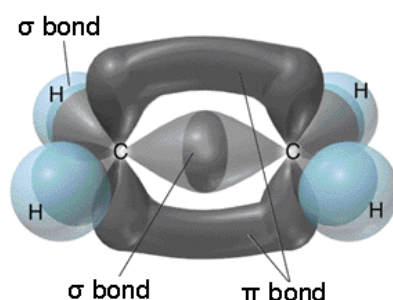


Figure 4.3: Electronic orbitals of the valence electrons in an ethene molecule. The carbons are sp^2 hybridised and have a σ as well as a π bond

or ' π -electron radical' is often used in the literature for alkyl radicals (where the unpaired electron is mainly localised at a single atom) because the $2p_z$ orbital is approximately perpendicular to the hydrocarbon skeleton. This can be confusing but sometimes this habit is so deeply rooted in the literature that we have adopted it.

In an isolated atom the angular parts of the orbital wavefunctions are the spherical harmonics $|L, M_L\rangle$.³ These are eigenfunctions of the operators \hat{L}^2 and \hat{L}_z with eigenvalues $L(L + 1)$ and M_L respectively.⁴ Now, organic molecules/crystals typically have a low local symmetry and the surrounding nuclei and electrons exert different (mainly electrostatic) forces in different directions. The result is that the $(2L + 1)$ orbital degeneracy present in the isolated atom is lifted. Since orbitally nondegenerate states have zero angular momentum ($L = 0$),⁵ this phenomenon is referred to as *orbital quenching*. Therefore it makes more sense, when dealing with the electronic configuration

³The spherical harmonics are often denoted Y_{LM_L} or $Y_L^{M_L}$.

⁴These operators are defined as $\hat{L} = \sum_i \hat{L}_i$ and $\hat{L}_z = \sum_i \hat{L}_{z,i}$.

⁵This property of orbitally nondegenerate states can be proven mathematically [30]: essentially, nondegenerate states must be real and the only possible eigenvalue of the purely imaginary operator \hat{L}_i operating on a real eigenfunction is zero.

of a carbon or oxygen atom in a molecule, to work with the real eigenfunctions

$$|2p_x\rangle = \frac{1}{\sqrt{2}}(|1, -1\rangle - |1, +1\rangle) \quad (4.1)$$

$$|2p_y\rangle = \frac{i}{\sqrt{2}}(|1, -1\rangle + |1, +1\rangle) \quad (4.2)$$

$$|2p_z\rangle = |1, 0\rangle \quad (4.3)$$

which have zero orbital angular momentum. Consider e.g. $|2p_x\rangle$:

$$\langle 2p_x | \hat{L}_z | 2p_x \rangle = \frac{1}{2} (\langle 1, -1 | - \langle 1, +1 |) (-|1, -1\rangle - |1, +1\rangle) = 0. \quad (4.4)$$

More intuitively: $|p_x\rangle$ is an equal admixture of components with opposite angular momentum (see Eq. (4.1)). It can readily be checked that $\langle 2p_j | \hat{L}_i | 2p_j \rangle = 0$ for all $i, j = x, y, z$.

4.3 The HFC interaction in organic radicals

4.3.1 Isotropic and dipolar HFC interactions

We can derive a spin Hamiltonian for the HFC interaction in organic radicals by treating it as a classical interaction between the point-dipole magnetic moments generated by the electron and the nucleus. In this approximation, the energy of the interaction between magnetic moments $\vec{\mu}_1$ at position \vec{r}_1 and $\vec{\mu}_2$ at position \vec{r}_2 is

$$E = -\frac{\mu_0}{4\pi r^3} \left[\frac{3(\vec{\mu}_1 \cdot \vec{r})(\vec{\mu}_2 \cdot \vec{r})}{r^2} - \vec{\mu}_1 \cdot \vec{\mu}_2 \right] \quad (4.5)$$

where μ_0 is the vacuum permeability, $\vec{r} = \vec{r}_2 - \vec{r}_1$ and $r = |\vec{r}|$. The magnetic moments are (cf. Eq. (2.4))

$$\vec{\mu}_S = -g\mu_B\vec{S} \quad (4.6)$$

$$\vec{\mu}_I = g_N\mu_N\vec{I} \quad (4.7)$$

where g is the electronic g factor, g_N the nuclear g factor, μ_B the Bohr magneton and μ_N the nuclear magneton. This yields

$$E = \frac{\mu_0 g g_N \mu_B \mu_N}{4\pi r^3} \left[\frac{3(\vec{S} \cdot \vec{r})(\vec{I} \cdot \vec{r})}{r^2} - \vec{S} \cdot \vec{I} \right] \quad (4.8)$$

Expansion in Cartesian coordinates yields

$$\begin{aligned}
 E = & \frac{\mu_0}{4\pi r^5} g g_N \mu_B \mu_N [(3x^2 - r^2) S_x I_x + (3y^2 - r^2) S_y I_y \\
 & + (3z^2 - r^2) S_z I_z + 3xy (S_x I_y + S_y I_x) \\
 & + 3yz (S_y I_z + S_z I_y) + 3xz (S_x I_z + S_z I_x)]
 \end{aligned} \quad (4.9)$$

The quantum-mechanical spin Hamiltonian is obtained by integrating the right-hand side of this equation over the orbital part of the electronic wavefunction and replacing the vectors \vec{S} and \vec{I} by their respective operators \hat{S} and \hat{I} . This yields⁶

$$\begin{aligned}
 \hat{H}_{HF,dip} = & A_{xx}^0 \hat{S}_x \hat{I}_x + A_{yy}^0 \hat{S}_y \hat{I}_y + A_{zz}^0 \hat{S}_z \hat{I}_z + A_{xy}^0 (\hat{S}_x \hat{I}_y + \hat{S}_y \hat{I}_x) \\
 & + A_{yz}^0 (\hat{S}_y \hat{I}_z + \hat{S}_z \hat{I}_y) + A_{xz}^0 (\hat{S}_x \hat{I}_z + \hat{S}_z \hat{I}_x)
 \end{aligned} \quad (4.10)$$

where

$$A_{ii}^0 = \frac{\mu_0}{4\pi} g g_N \mu_B \mu_N \int_V \psi^*(x, y, z) \frac{3i^2 - r^2}{r^5} \psi(x, y, z) dV \quad (4.11)$$

$$A_{ij}^0 = A_{ji}^0 = \frac{\mu_0}{4\pi} g g_N \mu_B \mu_N \int_V \psi^*(x, y, z) \frac{3ij}{r^5} \psi(x, y, z) dV$$

with $i, j = x, y, z$ and $i \neq j$. In matrix notation we can write

$$\hat{H}_{HF,dip} = \hat{S} \cdot \overline{\overline{A}}_{dip} \cdot \hat{I} \quad (4.12)$$

where $\overline{\overline{A}}_{dip}$ is called the *dipolar hyperfine coupling tensor* or *anisotropic hyperfine coupling tensor* and is given by

$$\overline{\overline{A}}_{dip} = \begin{bmatrix} A_{xx}^0 & A_{xy}^0 & A_{xz}^0 \\ A_{xy}^0 & A_{yy}^0 & A_{yz}^0 \\ A_{xz}^0 & A_{yz}^0 & A_{zz}^0 \end{bmatrix} \quad (4.13)$$

From Eqs. (4.11) it is clear that this tensor is anisotropic (in general), symmetric and traceless. Consequently, it can always be cast into a diagonal form.⁷ We

⁶The reason for adding the subscript *dip* and the superscript 0 will become clear below.

⁷As in Chapter 2, the diagonal elements in the tensor's eigenframe (which are the principal values of the tensor) are distinguished from those in other reference frames by denoting them as A_i^0 instead of A_{ii}^0 ($i = x, y, z$).

note that, as intuitively expected, this dipolar interaction averages to zero in solutions due to the rapid random movement of the molecules [72].

We have so far ignored the fact that the r^{-3} factor in the integrands of Eqs. (4.11) diverge to ∞ for $r \rightarrow 0$. The integration will still yield a finite value for any orbital wavefunction ψ with a non-vanishing angular momentum because such a wavefunction decays exponentially to 0 for $r \rightarrow 0$. Thus, only for s orbitals a problem arises. The cause of this problem is that the point-dipole approximation – which is at the basis of our derivation – breaks down for $r \rightarrow 0$ and Eqs. (4.11) are simply not valid for s orbitals.

The spherical symmetry of s orbitals implies that the hyperfine interaction between an s -orbital electron spin \vec{S} and a nuclear spin \vec{I} must be isotropic, so that the corresponding spin Hamiltonian should have the form

$$\hat{H}_{HF,iso} = a_{iso} \hat{S} \cdot \hat{I} \quad (4.14)$$

For a one-electron system, Fermi obtained (in a rigorous quantum-mechanical approach) [73]:

$$a_{iso} = \frac{2\mu_0}{3} g g_N \mu_B \mu_N |\Psi(\vec{0})|^2 \quad (4.15)$$

where $|\Psi(\vec{0})|$ is the amplitude of the electronic wavefunction at the nucleus. This *isotropic hyperfine interaction* is also referred to as the *Fermi-contact interaction* since in a one-electron system $|\Psi(\vec{0})|^2$ is the probability of finding the electron at the nucleus. Eq. (4.15) can also be retrieved in a semi-classical approach, treating the nucleus as a spinning charged shell of finite size and calculating the energy of interaction between the electron-spin magnetic moment and the magnetic field generated by the nucleus within the shell (see e.g. Ref. [74]). This approach gives an intuitive grasp of the physics involved. For multi-electron systems, Eq. (4.15) has to be generalised to

$$a_{iso} = \frac{2\mu_0}{3} g g_N \mu_B \mu_N \rho_S(\vec{0}) \quad (4.16)$$

where $\rho_S(\vec{0})$ is the spin density at the nucleus (cf. Eq. 3.12). Note that Eqs. (4.11) and (4.16) correspond to Eq. (3.47) for a system with one electron and if $\vec{R} = \vec{0}$.

In summary, the HFC interaction between an electron spin \vec{S} and a nuclear spin \vec{I} in organic radicals is adequately described by following spin Hamiltonian:

$$\hat{H}_{HF} = \hat{S} \cdot \bar{A} \cdot \hat{I} \quad (4.17)$$

with

$$\bar{A} = \bar{A}_{dip} + a_{iso} \bar{1} \quad (4.18)$$

where $\bar{1}$ is the 3x3 unit matrix, the matrix elements of \bar{A}_{dip} are given by Eqs. (4.11), and a_{iso} is given by Eq. (4.16). The matrix elements of \bar{A} are denoted A_{ij} .

The statement made above that the isotropic hyperfine interaction vanishes for all orbitals except s orbitals only holds for a one-electron system. In multi-electron atoms and in molecules, hyperfine interactions will in general have both an isotropic and dipolar component due to among others spin-exchange interactions. Several examples are discussed in Sections 4.3.2 and 4.3.3.

Before proceeding to the specific cases of α protons, β protons, ..., two different approximations for the dipolar hyperfine coupling are presented: the *pure point-dipole approximation* and the *two-centre approximation*.

4.3.1.1 The pure point-dipole approximation

In this approximation, the spatial distribution of the electron is completely neglected: the electron is assumed to be localised at the X_α nucleus ($X = \text{C}$ or O). If we put the origin of our reference frame at X_α , the point-dipole approximation boils down to replacing $\psi(x, y, z)$ by the Dirac-delta function $\delta(\vec{0})$ in Eqs. (4.11). If we chose the $\langle x \rangle$ axis along the line connecting X_α and the proton (so that the coordinates of H_β are $(x, 0, 0)$ and $r = x$), Eq. (4.11) yields

$$\bar{A}_{dip} = \begin{bmatrix} +2b & 0 & 0 \\ 0 & -b & 0 \\ 0 & 0 & -b \end{bmatrix} \quad (4.19)$$

with

$$b = \frac{\mu_0}{4\pi} \frac{g g_N \mu_B \mu_N}{r^3} \quad (4.20)$$

If the spin density at the X_α nucleus differs from unity ($\rho \neq 1$), an extra factor ρ should be introduced in Eq. (4.20):

$$b = \rho \frac{\mu_0}{4\pi} \frac{g g_N \mu_B \mu_N}{r^3} \quad (4.21)$$

Note the following properties:

1. the dipolar hyperfine interaction is diagonal in this reference frame.
2. the eigenvalues exhibit the axial symmetric $(+2b, -b, -b)$ pattern characteristic of the classical point-dipole interaction.
3. the eigenvector corresponding to the $2b$ eigenvalue (\vec{V}_{2b}) points from X_α to the proton. The other two eigenvectors cannot be related to the radical geometry (which is logical considering the approximation made), their

only limitation being that they have to be perpendicular to \vec{V}_{2b} and to each other.

The position of the proton with respect to X_α can be deduced from $\overline{\overline{A}}_{dip}$: Eq. (4.20) yields the distance and \vec{V}_{2b} yields the direction. This makes the dipolar part of the HFC tensor a very useful analytical tool.

In practice, the point-dipole approximation is only valid when the distance between the proton and the X_α nucleus is large compared to the spatial spread of the electron density. Also, Eqs. (4.19) and (4.21) strictly speaking only hold when the g tensor is isotropic [25]. For the (very) small g -tensor anisotropies encountered in this work, however, they can safely be employed.

4.3.1.2 The two-centre approximation

Assuming the electron is localised in a $2p_z$ orbital on X_α ($X = \text{C}$ or O), we can partially account for the spatial delocalisation of the electron by considering two 'effective spin centres', located at a distance R_p from X , along the symmetry axis of the $2p_z$ orbital (Figure 4.4). This 'two-centre approach', originally due to Gordy [75], is quite suited for gaining insight in α proton HFC interactions (see Section 4.3.2).

Assuming the proton is located in the nodal plane of the $2p_z$ orbital, we can calculate the dipolar HFC values when the field is directed along the $\langle x \rangle$, $\langle y \rangle$ and $\langle z \rangle$ axis (Figure 4.4), which are, because of the symmetry of the system, also the principal axes. It follows from Eq. (4.5) that the classical interaction energy between two magnetic moments $\vec{\mu}_1$ and $\vec{\mu}_2$ is

$$E = -\frac{\mu_0}{4\pi} \frac{\mu_1 \mu_2}{r^3} (3 \cos^2 \theta - 1) \quad (4.22)$$

when $\vec{\mu}_1 \parallel \vec{\mu}_2 \parallel \vec{B}$ is assumed. Here, θ is the angle between \vec{B} and \vec{r} (which connects the point-dipoles). In the present case, the magnetic moments arise from an electron spin \vec{S} and a proton spin \vec{I} (cf. Eqs. (4.6) and (4.7)). The magnitudes of the magnetic moments are

$$\mu_S = \frac{\rho^\pi}{2} g \mu_B M_S \quad (4.23)$$

$$\mu_I = g_N \mu_N M_I \quad (4.24)$$

where the factor $\frac{\rho^\pi}{2}$ appears because each of the effective spin centres carries half of the spin density.⁸ Because the dipolar interaction energy is also given

⁸Note that the superscript π is used, even if a $2p_z$ orbital is considered (cf. the discussion in Section 4.2.2).

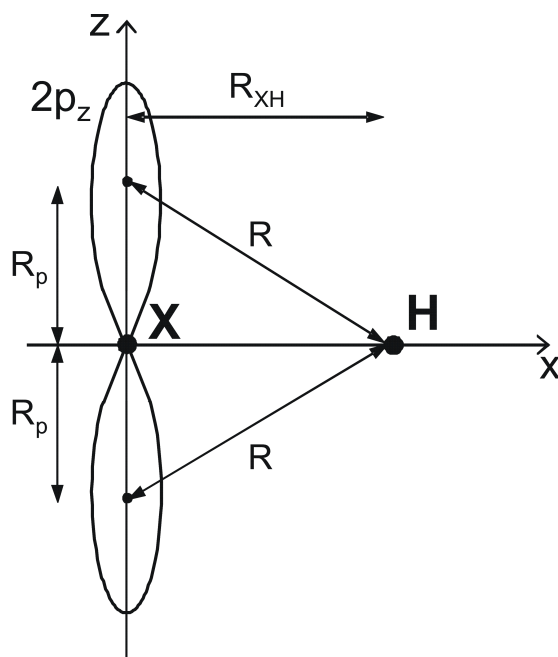


Figure 4.4: The two-centre approach for the dipolar HFC interaction between a proton (H) and a nucleus X (X = C or O). R_p is the distance between an effective spin centre and X. The proton is assumed to lie in the nodal plane of the $2p_z$ orbital. The $\langle y \rangle$ axis (not drawn) is perpendicular to the plane of the paper, pointing out of it.

by $E = A_{dip} M_S M_I$ (Chapter 2), the dipolar HFC value for one effective spin centre is

$$\frac{\rho^\pi}{2} \frac{\mu_0}{4\pi} \frac{g g_N \mu_B \mu_N}{R^3} (3 \cos^2 \theta - 1) \quad (4.25)$$

When \vec{B} is oriented along a principal direction, θ is the same for the two effective centres: $\theta = \frac{\pi}{2}$ for $\vec{B} \parallel \langle y \rangle$, $\cos \theta = \frac{R_{XH}}{R}$ for $\vec{B} \parallel \langle x \rangle$ and $\cos \theta = \frac{R_p}{R}$ for $\vec{B} \parallel \langle z \rangle$. Since $R = \sqrt{R_{XH}^2 + R_p^2}$ (Figure 4.4), we finally obtain

$$\begin{bmatrix} A_{dip,x} \\ A_{dip,y} \\ A_{dip,z} \end{bmatrix} = \rho^\pi \frac{\mu_0}{4\pi} \frac{g g_N \mu_B \mu_N}{(R_{XH}^2 + R_p^2)^{\frac{3}{2}}} \begin{bmatrix} \frac{2R_{XH}^2 - R_p^2}{R_{XH}^2 + R_p^2} \\ -1 \\ \frac{2R_p^2 - R_{XH}^2}{R_{XH}^2 + R_p^2} \end{bmatrix} \quad (4.26)$$

Note that for $R_p = 0$, Eq. (4.19) is retrieved.

In Figure 4.5 the variation is shown of the dipolar HFC values for an alkyl radical (X = C) as a function of the distance R_{CH} for both the pure point-dipole approximation and the two-centre approximation. The spatial extensiveness of the $2p_z$ orbital has two main consequences: (i) the degeneracy of the A_y and

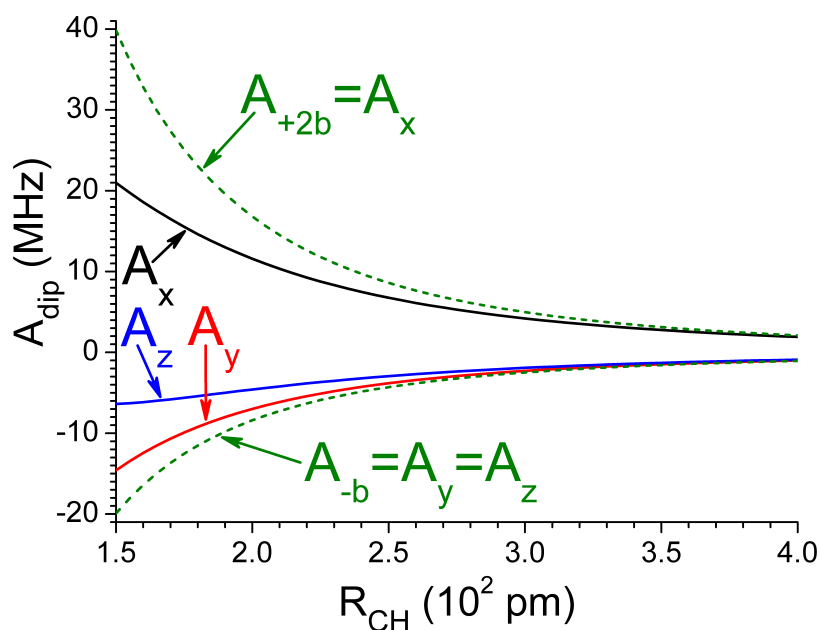


Figure 4.5: Dipolar HFC values for the hyperfine interaction between a proton and an unpaired electron in a $2p_z$ orbital centred on a carbon (i) in the pure point-dipole approximation, using Eqs. (4.19) and (4.21) (green dotted line) and (ii) in the two-centre approximation (Figure 4.4), using Eq. (4.26) (full lines), with $g = 2.0023$, $\rho = \rho^\pi = 0.85$ and $R_p = 72$ pm. The latter two values are typical for alkyl radicals.

A_z values is lifted and (ii) the magnitude of the values is decreased. Figure 4.5 also indicates that the point-dipole approximation is in general 'safe' to use for R_{XH} distances of more than 300 pm.

4.3.2 α protons

4.3.2.1 The isotropic hyperfine coupling

In a planar alkyl radical, values of typically -60 to -70 MHz are found experimentally for the isotropic HFC value of α protons - the seminal example being the radiation-induced malonic acid radical [76]. Because the proton is located in the nodal plane of the $2p_z$ orbital in which the unpaired electron resides, there is no direct contribution of the unpaired electron to the isotropic HFC interaction (cf. Eq. (4.15)). Partial sp^3 hybridisation would lead to a positive spin density and, hence, a *positive* isotropic HFC. Moreover, perfectly planar structures also yield such negative a_{iso}^α values. Weissman *et al.* have suggested zero-point hydrogen out-of-plane vibrations as a possible explanation [77],

but calculations show the resulting values for a_{iso}^α are at least an order of magnitude smaller than experimentally observed [78]. It was among others McConnell who finally showed that the isotropic α proton HFC value arises mainly from a *spin-polarisation* mechanism through σ - p -electron exchange interactions [79, 80]. An intuitive explanation is presented in Figure 4.6: by virtue of the Pauli-exclusion principle, the C-H σ bond electrons must have opposite spins. Due to the atomic exchange interaction with the (polarised) electron in the carbon $2p_z$ orbital, configurations I and II in Figure 4.6 have different energies.⁹ The result is a net positive spin density at the carbon side of the σ orbital and a net negative spin density at the hydrogen side. The latter accounts, via Eq. (4.16) for the observed negative isotropic HFC values of α protons. Note that, since the isotropic HFC value in a hydrogen atom is ~ 1420 MHz, the spin density in the hydrogen $1s$ orbital must be $\sim \frac{-65}{1420} \approx -0.05$. Based on several experimental studies (see, e.g. the references in Ref. [76]), a linear dependence of the α proton isotropic HFC value on the (unpaired) electron density ρ^π at the carbon $2p_z$ orbital was proposed:

$$a_{iso}^\alpha = Q\rho^\pi \quad (4.27)$$

where Q is a constant. This is the well-known *McConnell equation*. McConnell and Chesnut derived this equation theoretically under certain conditions. The derivation and the expression for Q are rather involved and we refer to Ref. [80] for details. The McConnell equation (4.27) has given rise to an impressive amount of fruitful research but caution is needed in applying it. There are essentially two things to keep in mind:

1. Q in Eq. (4.27) is not truly a constant.

Its value depends on the geometry and the charge state of the radical as well as on the chemical nature of the radical. Fessenden and Schuler reported a comprehensive set of measurements on alkyl radicals from which the values and concepts essentially became the standard for applying the McConnell relation in analytical problems [81]. For an aliphatic π radical they proposed $Q \approx 63$ MHz. However, in the literature often $Q \approx 72$ MHz is assumed, even if this value was originally proposed for aromatic rather than aliphatic π radicals [82]. A concise overview of Q values for a range of different radical types is presented in Ref. [4].

2. Equation (4.27) is not always valid.

The proportionality between a_{iso}^α and ρ^π does not always hold. The two

⁹This can be understood in the context of Hund's rules: in the atomic ground state the valence electron spins in a carbon atom are aligned.

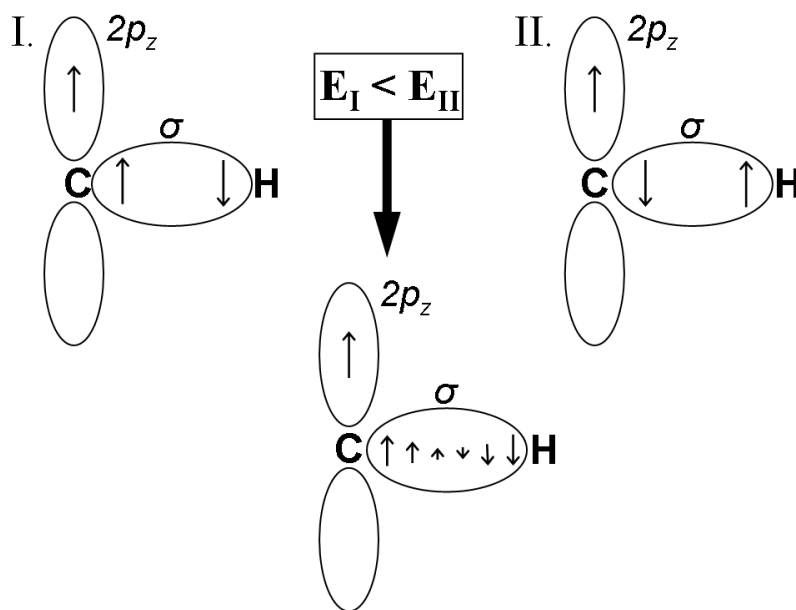


Figure 4.6: Spin polarisation in a $-\text{C}^\bullet\text{H}_\alpha-$ fragment: the (filled) σ orbital is spin polarised through σ - p electron-exchange interactions, resulting in a net negative spin density at the proton.

most drastic assumptions in its derivation are (i) perfect planarity of the spin centre and (ii) neglect of spin density in adjacent bonds and on adjacent atoms. The influence of radical centre bending is dramatic: the isotropic HFC value can vary by as much as 200 % (e.g. from -65 MHz to +65 MHz, assuming $\rho^\pi = 1$) when the centre is significantly bent. This was shown both experimentally (by Dobbs *et al.*, who used ^{13}C hyperfine couplings to determine the bending of a centre [83, 84]) and by means of DFT calculations [85, 86]. Spin density not located in the carbon $2p_z$ orbital can also be quite important: spin density at β sites will give a positive contribution to a_{iso}^α (see Section 4.3.3). The contribution to a_{iso}^α resulting from a β oxygen can easily be a significant portion of that arising from the spin-polarisation mechanism, as argued by Bernhard [87]. The latter also pointed out that this effect may account for a part of the variation in Q values discussed above. The effect is even more pronounced when the radical centre deviates from planarity [84, 88].

Finally, we note that the DFT calculations carried out during the doctoral research revealed that hydrogen-bonds with the surrounding lattice can easily cause shifts in the isotropic HFC values of 5-10 MHz.

The aim of this rather detailed discussion was to emphasise the limited validity

of Eq. (4.27). As will be discussed in the next section, the dipolar HFC values of an α proton offer a much more reliable indicator of ρ^π .

4.3.2.2 The dipolar hyperfine coupling

α -proton dipolar HFC tensors have been determined for a vast number of organic radicals. The first relatively accurate report was that of the α proton HFC in a malonic acid radical [76]:

$$(A_{dip,x}, A_{dip,y}, A_{dip,z}) = (32, -30, -2) \text{ MHz} \quad (4.28)$$

where the $\langle x \rangle$ axis was found to be along the $C_\alpha-H_\alpha$ bond and the $\langle z \rangle$ axis along the symmetry-axis of the $2p_z$ orbital in which the unpaired electron resides. These features indeed are the trademark of an α proton in a π -electron radical, and they follow immediately from the two-centre approximation (Section 4.3.1.2).¹⁰ Gordy proposed values of 72 pm for R_p and 108 pm for R_{CH} [75]. Assuming $\rho^\pi = 1$, Eq. (4.26) yields

$$(A_{dip,x}, A_{dip,y}, A_{dip,z}) = (38.7, -36.0, -2.8) \text{ MHz} \quad (4.29)$$

If a more realistic spin density $\rho^\pi = 0.85$ is assumed, we get

$$(A_{dip,x}, A_{dip,y}, A_{dip,z}) = (32.9, -30.6, -2.4) \text{ MHz} \quad (4.30)$$

which is in remarkably good agreement with the experimental values (4.28). The $(+a, 0, -a)$ pattern is reproduced, calculated and experimental values agree well in size, and for the eigenvector directions we find

$$\vec{V}_{+a} \parallel C_\alpha-H_\alpha \text{ bond} \quad (4.31)$$

$$\vec{V}_0 \parallel \text{LEO axis} \quad (4.32)$$

$$\vec{V}_{-a} \perp C_\alpha-H_\alpha \text{ bond and LEO axis} \quad (4.33)$$

When the carbon is sp^2 hybridised in the parent molecule, the radical centre is expected not to reorient much upon radical formation and the directions at the right-hand side can be calculated directly from the atomic coordinates. When the carbon is sp^3 hybridised in the parent molecule, usually the $X-C^\bullet H_\alpha-Y$ radical centre is approximately planar (sp^2 hybridised) and the H_α proton

¹⁰In the seminal paper by McConnell and Strathdee [89], the A_{dip} matrix elements of Eqs. (4.11) are calculated by integrating over the $2p_z$ electron orbital by employing a Slater $2p$ -orbital wavefunction. The derivation is rather lengthy but yields results comparable to the much simpler two-centre approach.

reorients. In this case, good approximate directions are

$$\vec{V}_{+a} \parallel \text{in-plane bisector of the X-C}^\bullet\text{-Y angle} \quad (4.34)$$

$$\vec{V}_0 \perp \text{X-C}^\bullet\text{-Y plane} \quad (4.35)$$

$$\vec{V}_{-a} \perp \text{both of the above} \quad (4.36)$$

Of course, when there is severe structural reorganisation - as can be the case in e.g. sugar ring opening events - it is in general impossible to predict how the radical is oriented without using (advanced) quantum-chemical calculations.

In principle, each of the $A_{dip,i}$ ($i = x, y, z$) values allows determination of ρ^π through Eqs. (4.26) provided accurate values for R_{CH} and R_p are known. Gordy and, later, Bernhard showed that $A_{dip,x}$ is in general least dependent on the precise conformation of the radical and proposed following relation between ρ^π and $A_{dip,x}$:

$$A_{dip,x} = Q_{dip}\rho^\pi \quad (4.37)$$

where $Q_{dip} = 38.7$ MHz (cf. Eq. (4.29)). The study by Bernhard indicates this relation holds well for rather large deviations from planarity ($\leq 20^\circ$) and in a broad range of R_{CH} values (100 - 115 pm) - although Q_{dip} strongly depends on R_p . Therefore, Eq. (4.37) is considerably more accurate than the McConnell relation (4.27) to determine ρ^π . A DFT-based study by Erling and Nelson on radical structures $C_\alpha^\bullet H_\alpha(R1)(R2)$ ($R1, R2 = H, Me, COOH, NH_2$ and OH) corroborates this: bending of the C_α centre from a planar to a tetrahedral configuration only leads to minor changes in the $A_{dip,x}$ component (less than 6 %) (whereas the isotropic component can vary by ~ 200 %, as mentioned in Section 4.3.2.1). Large discrepancies between ρ^π values obtained from Eq. (4.37) and Eq. (4.27) may indicate a significant deviation from planarity at the radical centre.

Eq. (4.26) holds for any value of ρ^π , but in practice large deviations from 1 typically imply significant spin densities in the σ bonds of the carbon or in orbitals centred on adjacent atoms, which will of course also contribute to the dipolar HFC values. However, because of the r^{-3} dependence the contribution of the carbon ρ^π spin density still is the dominant contribution for relatively small values of ρ^π . For instance, our own experimental data on the dominant stable sucrose radicals T2 and T3 (Table 5.3, page 117) shows that Eq. (4.26) still holds well for $\rho^\pi \approx 0.5$. For a more in-depth discussion and quantitative estimations of these contributions, the reader should consult Ref. [87].

Eqs. (4.31) and (4.32) cannot both be valid when the radical centre deviates

from planarity. In the literature it is commonly assumed that the \vec{V}_{+a} eigenvector is still parallel with the C-H bond (leaving the orientation of the LEO axis undetermined). The DFT-study by Erling and Nelson corroborates this assumption: the \vec{V}_{+a} direction does not deviate by more than 6° (and often less than 3°) from the $C_\alpha-H_\alpha$ bond direction upon bending from a planar to a tetrahedral configuration [86]. Therefore, the \vec{V}_{+a} eigenvector direction is a reliable indicator of the $C_\alpha-H_\alpha$ bond direction, even in the case of extreme bending. Consequently, the \vec{V}_0 eigenvector can easily deviate by 10° or more from the LEO axis upon bending. The \vec{V}_0 eigenvector direction is, however, still a valuable criterion in the search for a suitable model.

Using values for ρ^π obtained by Eq. (4.37), Bernhard calculated R_{CH} and R_P for the α protons in numerous alkyl radicals as well as electron-gain and electron-loss aromatic radicals from the experimental $A_{dip,x}$ and $A_{dip,y}$ values via

$$R_{CH} = \left(-\rho^\pi \frac{\mu_0 g g_N \mu_B \mu_N}{4\pi A_{dip,y}} \right)^{\frac{1}{3}} \left(\frac{A_{dip,y} - A_{dip,x}}{3A_{dip,y}} \right)^{\frac{1}{2}} \quad (4.38)$$

$$R_P = \left(-\rho^\pi \frac{\mu_0 g g_N \mu_B \mu_N}{4\pi A_{dip,y}} \right)^{\frac{1}{3}} \left(\frac{2A_{dip,y} + A_{dip,x}}{3A_{dip,y}} \right)^{\frac{1}{2}} \quad (4.39)$$

which can be obtained from Eq. (4.26) [87]. These R_{CH} and R_P values are remarkably constant within one class of radicals (alkyl, electron-gain, electron-loss) and the differences between classes are significant enough to distinguish between them.

4.3.3 β protons

4.3.3.1 Isotropic hyperfine coupling

Consider a $-C_\alpha^\bullet-C_\beta H_\beta-$ radical fragment with the spin density residing in the $2p_z$ orbital on the α carbon (Figure 4.7). Experimentally, the β protons in this type of radical fragments are found to have isotropic HFC values between 0 and ~ 126 MHz, depending on the dihedral angle θ (Figure 4.7). Unlike for α protons, (secondary) spin-polarisation effects usually only play a minor role for β protons. Their isotropic HFC arises mainly from a mechanism called *hyperconjugation*: the $2p_z$ orbital partially delocalises onto the β carbon (yielding a π -like molecular orbital) and directly overlaps with the $C_\beta-H_\beta$ σ bond. The effect is a net positive spin density at the H_β proton, which results in the observed positive isotropic HFC. It is clear that the amount of overlap between the (delocalised) $2p_z$ orbital and the σ orbital depends on their relative orientations.

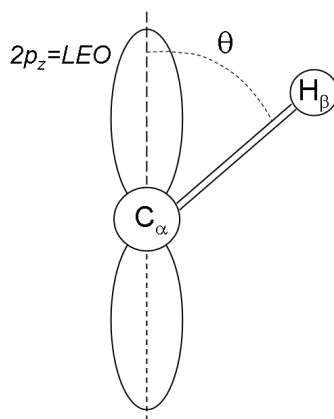


Figure 4.7: A $-C_{\alpha}^{\bullet}-C_{\beta}H_{\beta}-$ radical fragment with the spin density residing in the $2p_z$ orbital on the α carbon, viewed along the $C_{\alpha}-C_{\beta}$ bond. The angle between the plane containing the LEO and the $C_{\alpha}-C_{\beta}$ bond and the plane containing the $C_{\alpha}-C_{\beta}$ bond and the $C_{\beta}-H_{\beta}$ bond is called the dihedral angle θ .

On the basis of theoretical arguments and experimental data, Heller and McConnell proposed the following dependence of the β -proton isotropic HFC value a_{iso}^{β} on the spin density in the $2p_z$ orbital (ρ^{π}) and on the geometry of the radical structure [90, 91]:

$$a_{iso}^{\beta} = \rho^{\pi} (B_0 + B_2 \cos^2 \theta) \quad (4.40)$$

which is known as the **Heller-McConnell relation**. θ is the dihedral angle between the LEO and the $C_{\alpha}-H_{\alpha}$ bond, viewed along the $C_{\alpha}-C_{\beta}$ bond (Figure 4.7) and B_0 and B_2 are empirical constants. The second term on the right-hand side is due to hyperconjugation. It is maximal when $\theta = 0^{\circ}$ and vanishes when $\theta = 90^{\circ}$. The first term arises from spin polarisation through the intervening bonds.

The Heller-McConnell relation (4.40) can more generally be applied to radical fragments of the type $-X^{\bullet}-Y-H_{\beta}-$, where X and Y need not necessarily be carbon atoms. The values of B_0 and B_2 vary strongly with the nature of X and Y , the only general rule being that B_0 is substantially smaller than B_2 . Considerable experimental effort has been made to determine values for B_0 and B_2 for different $-X^{\bullet}-Y-H_{\beta}-$ radical types. A concise overview is presented in Ref. [4]. B_0 is in general assumed to be between -14 MHz and $+14$ MHz, and for alkyl ($X \equiv C, Y \equiv C$), hydroxyalkyl ($X \equiv C, Y \equiv O$) and alkoxy ($X \equiv O, Y \equiv C$) radicals, values for B_2 of ~ 126 MHz [92], ~ 73 MHz [93] and ~ 336

MHz respectively are commonly employed in the literature.¹¹ For all three types of radicals, it is acceptable to neglect the B_0 term altogether to obtain an indication of θ from Eq. (4.40), as is indeed often done in the literature.

The Heller-McConnell equation (4.40) can in principle be used to obtain an estimate of ρ^π when the local radical geometry is known. In practice it is mostly used the other way round: obtaining a value for θ by inserting a value for ρ^π obtained from, e.g., an α -proton HFC tensor. In this context two remarks should be made:

1. based on ab-initio molecular orbital calculations, Sevilla *et al.* found that in non-planar radical centres a term $B_1 \cos \theta$ should be added to the right-hand side of Eq. (4.40) with typically $5 \leq B_2/B_1 \leq 10$ [95, 96]. This extra term was chosen empirically (to give the best fit) and is not based on theoretical arguments.
2. hyperconjugation can be enhanced (or diminished) quite drastically by the so-called *Whiffen-effect* [97] when the spin density does not reside on one, but on both sides of the C_β - H_β fragment. In this case, ρ^π should be changed to $(\sqrt{\rho_1^\pi} + \sqrt{\rho_2^\pi})^2$ in Eq. (4.40), where ρ_1^π and ρ_2^π are the adjacent spin densities. Even when ρ_2^π is (very) small compared to ρ_1^π , the effect can be quite substantial.¹²

4.3.3.2 The dipolar hyperfine coupling

β protons typically are 190-230 pm separated from the α carbon in a $-C_\alpha^\bullet-C_\beta H_\beta$ -radical. Figure 4.5 indicates that this distance is too small to employ the pure point-dipole approximation. Experimentally, it is found that [4]

- the deviation from axial symmetry can be quite big, especially when $\theta \rightarrow 0^\circ$.¹³
- the anisotropy depends strongly on the value of the dihedral angle θ . For $\theta \rightarrow 0^\circ$ and $\theta \rightarrow 90^\circ$, the difference between maximum and minimum HFC values is typically ~ 11 MHz and ~ 17 MHz respectively in alkyl radicals [98] and typically ~ 15 MHz and ~ 23 MHz respectively in alkoxy radicals.

¹¹The latter value was taken from Ref. [94] and is significantly higher than the 263 MHz reported in [4].

¹²E.g., for $\rho_1^\pi = 0.85$ and $\rho_2^\pi = 0.05$, we find $(\sqrt{\rho_1^\pi} + \sqrt{\rho_2^\pi}) = 1.31$.

¹³E.g., eigenvalues of $\sim (+7, -6, -1)$ MHz are not seldom encountered.

- the eigenvector associated with the largest principal value (denoted \vec{V}_{2b} for brevity) still roughly corresponds to the $C_\alpha \cdots H_\beta$ direction [90]. For $\theta \approx 0^\circ$ the correspondence is very good, while for $\theta \rightarrow 90^\circ$, \vec{V}_{2b} moves somewhat towards the $C_\beta \cdots H_\beta$ direction [99].
- In the case of a hydroxyalkyl radical $C^\bullet OH$, the deviation from axial symmetry can be further enhanced and the anisotropy increases significantly (the difference between maximum and minimum principal values being ~ 30 MHz when $\rho^\pi \approx 1$ [98, 100]). \vec{V}_{2b} is approximately parallel to $C_\alpha \cdots H_\beta$ for all values of θ [101].

Some of these observations can be understood in the context of the two-centre approximation (Section 4.3.1.2), even if we can only employ it when the proton is in the nodal plane of the $2p_z$ orbital (which corresponds to $\theta = 90^\circ$):

- Eq. (4.26) yields $(A_{dip,x}, A_{dip,y}, A_{dip,z}) \approx (+10, -6, -4)$ MHz for a β proton at 215 pm from C_α , when $R_p = 72$ pm and $\rho^\pi = 0.85$ are used. This is in good accordance with typical experimental values for alkyl radicals.
- the increase in anisotropy for a β hydroxy proton in a hydroxyalkyl radical is in part due to the presence of spin density on the intervening oxygen atom, but can also be in part attributed to a difference in R_{CH} in Eq. (4.26). The former value typically is 215 pm in alkyl radicals, but 195 pm in a hydroxyalkyl radical.¹⁴ The variation of the anisotropic HFC values with R_{CH} according to Eq. (4.26) is given in Figure 4.8.
- likewise, the increase in anisotropy for a β proton in an alkoxy radical (as compared to an alkyl radical) can in part be attributed to a difference in R_{OH} (cf. previous item), but also to a difference in R_p in Eq. (4.26). R_p is typically 72 pm in an alkyl radical, but 52 pm in an alkoxy radical (the oxygen $2p_z$ orbital is more 'compact'). The variation of the anisotropic HFC values with R_p according to Eq. (4.26) is given in Figure 4.9.

The dipolar HFC values in a $-C_\alpha^\bullet-C_\beta H_\beta-$ radical fragment deviate from Eq. (4.26) mainly because of spin density in the $C_\beta-H_\beta$ σ bond and on C_β , resulting from hyperconjugation and secondary spin-polarisation effects. Because of the r^{-3} dependence of the dipolar HFC values, these spin densities can be quite important, even if they are small compared to ρ^π .¹⁵ The largest deviations from the two-centre approximation can be expected for $\theta = 0^\circ$, since hyperconjugation effects are strongest then. We note that Derbyshire [90]

¹⁴Assuming tetrahedral configuration of the C_β carbon and typical values for the C-C, C-H, C-O and O-H bonding distances of 152 pm, 110 pm, 142 pm and 95 pm respectively.

¹⁵This causes Eq. (4.26) to be less reliable for β than for α protons.

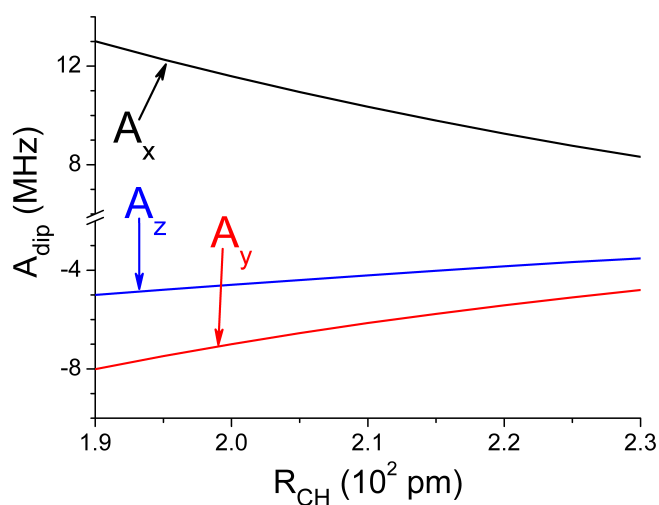


Figure 4.8: The dipolar HFC values for the HFC interaction between a β proton H and an unpaired electron in a $2p_z$ orbital centred on a carbon C, as a function of R_{CH} (the distance between C and H) in the two-centre approximation (Figure 4.4). Eq. (4.26) was used with $g = 2.0023$, $\rho^\pi = 0.85$ and $R_p = 72$ pm. This is in fact a 'zoomed in' graph of Figure 4.5.

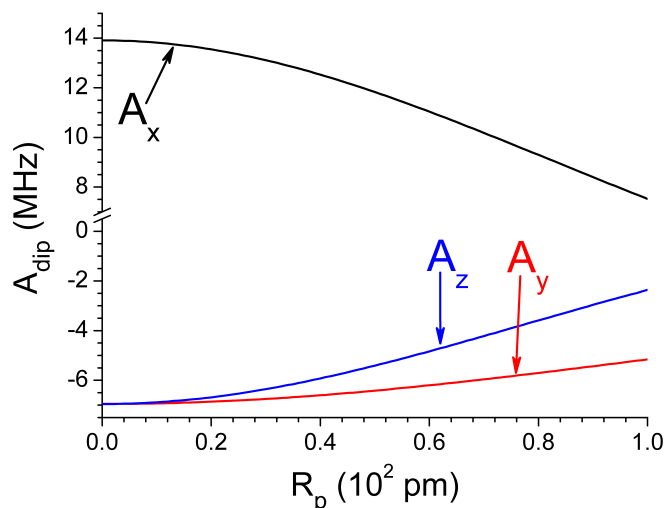


Figure 4.9: The dipolar HFC values for the HFC interaction between a β proton and an unpaired electron in a $2p_z$ orbital centred on a carbon, as a function of R_p (the distance between the effective spin centres and the carbon) in the two-centre approximation (Figure 4.4). Eq. (4.26) was used with $g = 2.0023$, $\rho^\pi = 0.85$ and $R_{CH} = 215$ pm. Note that for $R_p \rightarrow 0$ pm the point-dipole approximation is retrieved.

derived theoretical expressions for the dipolar components in which both the spatial distribution and the non-vanishing spin densities in the C_β - H_β bond and on C_β are taken into account. Some test calculations on typical radical fragments indicate that the results are very similar to those of the two-centre approach.

4.3.4 Protons at γ positions and further away

With increasing distance of the proton to the C_α nucleus, the dipolar HFC tensor will approach that of a pure point-dipole interaction (cf. Section 4.3.1.1). This approximation should apply rather well to γ protons (typically at 270 - 300 pm) and definitely to even more distant protons (at δ , ϵ , ... positions). The HFC tensors of these more distant protons can be very useful for radical identification because the distance and the $C_\alpha \cdots H$ direction can be determined relatively accurately from them.¹⁶ Distant-proton ENDOR lines are typically found in the (very crowded) free-proton frequency region, so that considerable experimental effort is usually necessary, and higher microwave frequencies are preferable.¹⁷ In practice, one should be aware that

- *because of the r^{-3} dependence, relatively small spin densities on atoms adjacent to the proton can disturb the $(2b, -b, -b)$ pattern quite strongly.* This is usually not the case in carbon-centred radicals, but is frequently encountered for alkoxy radicals:¹⁸ when the C_γ - H_γ bond is parallel to the LEO-orbital axis on the oxygen atom, the HFC principal values often exhibit a $\sim(-10, 0, +10)$ MHz pattern due to (secondary) hyperconjugation effects – while for other conformations an approximately axially symmetric pattern is found (in correspondence with the point-dipole approximation) [94].
- *distant protons need not necessarily have small isotropic HFC values.* Substantial spin delocalisation as well as (secondary) hyperconjugation effects often yield 10-20 MHz for γ protons and, again, conformations in which the $C_\gamma - H_\gamma$ bond is parallel to the LEO-orbital axis have larger isotropic HFC values, especially in the case of alkoxy radicals. Alkoxy radicals can also give unexpectedly high isotropic HFC values for δ and even ϵ

¹⁶E.g., Budzinski *et al.* demonstrated the use of HFC interactions to remote protons for radical identification [102].

¹⁷For organic radicals, the low-frequency lines of strong interactions are often situated in the proton-frequency region in X band, which complicates the analysis of the weakly coupled protons further. This is (much) less the case in Q band (35 GHz) and V band (70 GHz).

¹⁸This is in part because in an alkoxy radical only 50 - 75 % of the spin density resides on the oxygen atom [103, 104], while in an alkyl radical typically 80 - 90 % of the spin density resides on the carbon.

protons. In rhamnose, an isotropic δ proton HFC of almost 70 MHz was observed [103], while in sucrose values of 26 MHz and 15 MHz have been found for a δ and an ϵ proton respectively (Section 5.3.3.8, page 143).

4.4 The g tensor in organic radicals

4.4.1 Spin-orbit coupling

As discussed in Chapter 2, the interaction of an external magnetic field \vec{B} with the spin \vec{S} of an electron in a crystal can be described by the electronic Zeeman Hamiltonian

$$\mu_B \hat{B} \cdot \bar{g} \cdot \hat{S} \quad (4.41)$$

where \bar{g} is the g tensor:

$$\bar{g} = \begin{bmatrix} g_{xx} & g_{xy} & g_{xz} \\ g_{yx} & g_{yy} & g_{yz} \\ g_{zx} & g_{zy} & g_{zz} \end{bmatrix} \quad (4.42)$$

For a direction $\vec{l} = [l_x \ l_y \ l_z]$ of the magnetic field, the EPR resonance condition is

$$h\nu = g\mu_B B \quad (4.43)$$

where

$$g = \sqrt{\vec{l} \cdot \bar{g} \cdot \bar{g}^T \vec{l}^T} \quad (4.44)$$

In the principal axes frame of the g tensor, this reduces to

$$g = \sqrt{l_x^2 g_x^2 + l_y^2 g_y^2 + l_z^2 g_z^2} \quad (4.45)$$

where g_x , g_y and g_z are the principal values of the g tensor.

Based on the discussion in Section 4.2.2, we would expect orbital quenching to lead to an isotropic g value equal to g_e in organic radicals. Experimentally, however, anisotropic g factors are observed and the anisotropy can even be considerable (of the order of 0.1 in alkoxy radicals, e.g.). The main cause is the *spin-orbit interaction*: the coupling between the electron spin (\vec{S}) and its orbital angular momentum (\vec{L}) around the various nuclei in the molecule. This interaction mixes up the $|2p_x\rangle$, $|2p_y\rangle$ and $|2p_z\rangle$ orbitals with higher lying excited states, thereby restoring some orbital angular momentum and, hence, g anisotropy. This idea will be developed quantitatively in the next sections.

4.4.2 Interpretation of the g tensor

Consider a radical in which the unpaired electron is localised at a specific atom. Assume the Hamiltonian is given by

$$\hat{H} = \hat{H}_0 + \hat{H}_1 + \hat{H}_2 \quad (4.46)$$

where \hat{H}_0 contains the electronic kinetic and potential energy terms, \hat{H}_1 is the Zeeman Hamiltonian for the electron spin ($g_e \mu_B \vec{B} \cdot \hat{S}$), and

$$\hat{H}_2 = \mu_B \vec{B} \cdot \hat{L} + \lambda \hat{L} \cdot \hat{S} \quad (4.47)$$

contains both the Zeeman Hamiltonian for the electron orbital momentum and the spin-orbit coupling between the electron spin and its orbital momentum, with λ the spin-orbit coupling constant of the atom. It can be shown that the g -tensor elements are then given by [26, 71]

$$g_{ij} = g_e \delta_{ij} - 2\lambda \sum_n \frac{\langle \psi_0 | \hat{L}_i | \psi_n \rangle \langle \psi_n | \hat{L}_j | \psi_0 \rangle}{E_n - E_0} \quad (i, j = x, y, z) \quad (4.48)$$

where the summation over n runs over all excited states. $|\psi_0\rangle$ and $|\psi_n\rangle$ are the singly occupied molecular orbitals (SOMOs) in the ground state and the excited states respectively, E_0 and E_n are the corresponding orbital energies and \hat{L}_i is the i th component of the electron orbital angular momentum around the atom.¹⁹ Note that, although there is an infinite number of excited orbital states, their contribution to the g anisotropy will decrease with increasing $|E_n - E_0|$. We will now apply Eq. (4.48) to some typical organic radicals. It will be shown that the size of the g anisotropy as well as the g -tensor eigenvectors reflect key properties of the radical geometry and electronic structure of the radical.

Both carbon- and oxygen-centred radicals are often to a good approximation sp^2 hybridised (Section 4.2.2). Assume that the $|2p_z\rangle$ orbital is the ground state SOMO, with orbital energy E_0 . The hybrid orbitals h_i ($i = 1, 2, 3$) are the following linear combinations of the $2s$, $2p_x$ and $2p_y$ orbitals (see Eqs. (4.1)

¹⁹Based on the principle of gauge invariance, Stone also developed a theoretical expression for the g -tensor principal values in a *polyatomic* $S = 1/2$ system where the unpaired electron density is delocalised over several atoms [105].

- (4.3) [71]:

$$|h_1\rangle = \frac{1}{\sqrt{3}}|2s\rangle + \sqrt{\frac{2}{3}}|2p_x\rangle \quad (4.49)$$

$$|h_2\rangle = \frac{1}{\sqrt{3}}|2s\rangle - \frac{1}{\sqrt{6}}|2p_x\rangle + \frac{1}{\sqrt{2}}|2p_y\rangle \quad (4.50)$$

$$|h_3\rangle = \frac{1}{\sqrt{3}}|2s\rangle - \frac{1}{\sqrt{6}}|2p_x\rangle - \frac{1}{\sqrt{2}}|2p_y\rangle \quad (4.51)$$

Note that $|2p_z\rangle$, $|h_1\rangle$, $|h_2\rangle$ and $|h_3\rangle$ form an orthonormal basis. The hybrid orbitals either carry a lone electron pair or overlap with orbitals ϕ_i ($i = 1, 2, 3$) of adjacent atoms to form the molecular orbitals ψ_i ($i = 1, 2, 3$):

$$\psi_i = A_i|h_i\rangle + B_i|\phi_i\rangle \quad (i = 1, 2, 3) \quad (4.52)$$

where $|A_i|^2 + |B_i|^2 = 1$ ($i = 1, 2, 3$). The ψ_i orbital energies (E_i) are lower than E_0 . For every ψ_i orbital there is an antibonding orbital²⁰

$$\psi_i^* = A_i^*|h_i\rangle + B_i^*|\phi_i\rangle \quad (i = 1, 2, 3) \quad (4.53)$$

with an orbital energy E_i^* higher than E_0 . The * superscript indicates the antibonding character. The \hat{L}_i operate on the atomic orbitals according to following equations:

$$\hat{L}_i|2s\rangle = 0 \quad (i = x, y, z) \quad (4.54)$$

$$\hat{L}_i|2p_i\rangle = 0 \quad (i = x, y, z) \quad (4.55)$$

$$\hat{L}_x|2p_y\rangle = i|2p_z\rangle \quad \hat{L}_x|2p_z\rangle = -i|2p_y\rangle \quad (4.56)$$

$$\hat{L}_y|2p_x\rangle = -i|2p_z\rangle \quad \hat{L}_y|2p_z\rangle = i|2p_x\rangle \quad (4.57)$$

$$\hat{L}_z|2p_x\rangle = i|2p_y\rangle \quad \hat{L}_z|2p_y\rangle = -i|2p_x\rangle \quad (4.58)$$

If we ignore the overlap of orbitals centred on different atoms, we can apply Eq. (4.48) to calculate the contribution of various excited states (cf. Figure 4.10) to the g -tensor principal values. We assume the A_i to be real. For excited states **1-3** ($\psi_i \rightarrow 2p_z$ transitions), we find (Δ is the deviation from g_e)

$$\Delta^{(1)}g_{xx} = 0$$

$$\Delta^{(1)}g_{yy} = -\frac{4\lambda A_1^2}{3(E_1 - E_0)}$$

$$\Delta^{(2)}g_{xx} = -\frac{\lambda A_2^2}{E_2 - E_0}$$

²⁰The * superscript indicates the antibonding character.

where $\overline{\mathbf{1}}$ is the 3x3 unit matrix and

$$\overline{\Delta g} = \lambda \begin{bmatrix} \frac{A_2^2}{E_0-E_2} + \frac{A_3^2}{E_0-E_3} & \frac{1}{\sqrt{3}} \left(-\frac{A_2^2}{E_2-E_0} + \frac{A_3^2}{E_3-E_0} \right) & 0 \\ \frac{1}{\sqrt{3}} \left(-\frac{A_2^2}{E_2-E_0} + \frac{A_3^2}{E_3-E_0} \right) & \frac{1}{3} \left(\frac{4A_1^2}{E_0-E_1} + \frac{A_2^2}{E_0-E_2} + \frac{A_3^2}{E_0-E_3} \right) & 0 \\ 0 & 0 & 0 \end{bmatrix} \quad (4.60)$$

We find that $g_{zz} = g_z$ is a principal value and equals g_e . This can be understood intuitively by noting that the transitions we have considered involve electrons 'rotating' about the $\langle x \rangle$ and $\langle y \rangle$ axes but not about the $\langle z \rangle$ axis. The contributions from excited states **4-6** ($2p_z \rightarrow \psi_i^*$ transitions) are readily obtained by substituting E_i with E_i^* and A_i with A_i^* in Eq. (4.60).

We will now apply Eq. (4.60) (and the equivalent expressions for the $2p_z \rightarrow \psi_i^*$ transitions) to carbon- and oxygen-centred radicals.

4.4.2.1 Carbon-centred radicals

In the case of an sp^2 hybridised carbon, ψ_1 , ψ_2 and ψ_3 are all molecular orbitals that engage in σ bonds with adjacent atoms. To a first approximation we can assume that their orbital energies as well as those of the antibonding orbitals are equal: $E_1 = E_2 = E_3$ and $E_1^* = E_2^* = E_3^*$. In the case all bonding atoms are carbon or hydrogen atoms, it is reasonable to assume $A_i = B_i = 1/\sqrt{2}$ ($i = 1, 2, 3$) in Eq. (4.60).²¹ We obtain

$$\overline{\Delta g} = \lambda_C \begin{pmatrix} \frac{1}{E_0 - E_1} - \frac{1}{E_1^* - E_0} \end{pmatrix} \begin{bmatrix} 1 & 0 & 0 \\ 0 & 1 & 0 \\ 0 & 0 & 0 \end{bmatrix} \quad (4.61)$$

where $\lambda_C = 28 \text{ cm}^{-1}$ is the carbon spin-orbit coupling constant. The reference frame turns out to be the principal axes frame and the diagonal elements are therefore the principal values. We find that $g_z = g_e$, while g_x and g_y are shifted from g_e with the same amount. Since $E_i^* > E_0 > E_i$, the $\psi_i \rightarrow 2p_z$ transitions yield a positive shift, and the $2p_z \rightarrow \psi_i^*$ transitions yield a negative shift.²² Furthermore, we expect a positive shift for g_x and g_y since, usually, $E_i^* - E_0 \gg E_0 - E_i$.

These predictions are in good agreement with experimental findings. For example, the g tensor of the malonic acid radical $HC^\bullet(COOH)_2$ has principal

²¹C-C bonds are not polarised and C-H bonds not much.

²²This observation is of a general nature: mixing of the LEO orbital with lower lying states yields a positive shift of g principal values, mixing with higher lying states yields a negative shift.

values (2.0033, 2.0035, 2.0026) [76]. Using $g = 2.0035$ and neglecting the term due to $2p_z \rightarrow \psi_i^*$ transitions, Eq. (4.61) yields $E_0 - E_1 \approx 3$ eV, which is in the range experimentally observed. Also important in the context of radical identification is the conclusion that the eigenvector corresponding to the minimum principal value is parallel to the LEO axis. In a real radical system this is not strictly true, but the deviation in general is quite small.

4.4.2.2 Alkoxy radicals

In an alkoxy radical, two of the three sp^2 hybridised orbitals, say ψ_2 and ψ_3 , will each contain a lone electron pair. Consequently, $A_2 = A_3 = 1$ (and $B_2 = B_3 = 0$) in Eq. (4.52). The third hybrid orbital (ψ_1) overlaps with the orbital of an adjacent atom - in many cases: a carbon atom - to form a molecular orbital. Because a C-O bond is strongly polarised towards oxygen, $A_1 = 3/4$ is reasonable. We may assume $E_1 < E_2 = E_3 (< E_0)$, since lone electron pairs are energetically less favourable than electron pairs in a molecular bond. Finally, we also neglect the $2p_z \rightarrow \psi_i^*$ transitions (which is reasonable since these levels tend to lie relatively high in oxygen). Eq. (4.60) now yields

$$\overline{\Delta g} = \lambda_O \begin{bmatrix} \frac{2}{E_0 - E_2} & 0 & 0 \\ 0 & \frac{3}{4(E_0 - E_1)} + \frac{2}{3(E_0 - E_2)} & 0 \\ 0 & 0 & 0 \end{bmatrix} \quad (4.62)$$

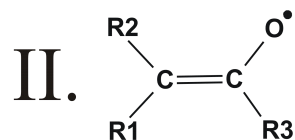
with $\lambda_O = 151 \text{ cm}^{-1}$ the oxygen spin-orbit coupling constant. Again, the tensor is diagonal and we directly obtain the g -tensor principal values. $g_z = g_e$ and g_x and g_y are shifted upwards. The shifts are, however, not equal anymore:

$$\Delta g_x - \Delta g_y = \lambda_O \left(\frac{4}{3(E_0 - E_2)} - \frac{3}{4(E_0 - E_1)} \right) \quad (4.63)$$

Because $E_0 - E_1 > E_0 - E_2$, we conclude that $g_x > g_y$. Thus, in an alkoxy radical fragment -C-O^\bullet the eigenvector corresponding to the smallest principal value of the g tensor is oriented along the LEO axis and the one corresponding to the largest principal value along the C-O bond. Especially the last property is extensively used in the literature to identify alkoxy radicals. Note that the overall anisotropy of the g tensor is markedly larger for alkoxy radicals than for carbon-centred radicals for three reasons:

1. *the electron density on the oxygen is larger* (due to its larger electronegativity and the presence of lone electron orbital pairs). This is reflected in the different values we inserted for the coefficients A_i and B_i .
2. *the spin-orbit coupling constant of oxygen is larger*: $\lambda_O \approx 5.4\lambda_C$.

In other words, there is a resonance structure **II** with a contribution of $\sim 25\%$. Based on the previous sections, we expect that the contributions of the



alkoxy radical to the g -tensor anisotropy will outweigh that of the carbon-centred radical. The eigenvector corresponding to the largest principal value will therefore be along the C=O bond (in structure I). Also, we would expect the g -tensor anisotropy to be considerably smaller than for alkoxy radicals, but significantly increased as compared to that for carbon-centred radicals. These predictions indeed agree with experimental findings. Experimentally, the maximum principal value for radicals of type **I** typically varies between 2.0060 and 2.0080. It should be noted, however, that small shifts in the electron-density distribution give rise to relatively large differences in g -tensor principal values.

Chapter 5

Radiation-induced radicals in sucrose single crystals

5.1 Chemical structure and crystal structure

Sucrose or saccharose, commonly known as table sugar,¹ is a disaccharide. It consists of the monosaccharides glucose and fructose that are linked together by a glycosidic bond (Figures 5.1 and 5.2A). The molecular formula of sucrose is $C_{12}O_{11}H_{22}$ and its systematic name is α -D-glucofuranosyl-(1 \leftrightarrow 2)- β -D-fructofuranoside.² The glucose unit is in its pyranosic form (six-membered ring) while the fructose unit is in its furanosic form (five-membered ring).³ The crystal structure of sucrose was most accurately determined from a neutron diffraction analysis by Brown and Levy [111]. The atomic coordinates determined in this study are listed in Table A.1 (Appendix A). In Figure 5.2, a unit cell of the crystal structure is depicted as viewed along the $\langle a \rangle$, $\langle b \rangle$ and $\langle c \rangle$ axes. The crystals are monoclinic: the cell vector \vec{b} (the *monoclinic axis*) is perpendicular to both cell vectors \vec{a} and \vec{c} but the latter two make an angle of $\beta \neq 90^\circ$. The cell parameters are $a = 1.0868$ nm, $b = 0.8710$ nm, $c = 0.7761$ nm and $\beta = 102.97^\circ$. A unit cell contains two molecules, corresponding to a total of 90 atoms. The crystal space group is $P2_1$: the lattice is primitive ('P') and there is a twofold screw axis along $\langle b \rangle$ (' 2_1 ').⁴ This means that one molecule is transformed into the other by a rotation of 180° about the $\langle b \rangle$

¹Scientifically, the term *sugar* refers to any monosaccharide or disaccharide, but in popular, non-scientific use it refers to sucrose.

²The anomeric symbols α and β and the configurational symbols L and D refer to the relative orientations of certain OH- and CH₂OH-groups and serve to distinguish between different stereoisomers.

³In fructose single crystals the fructose molecule occurs in its pyranosic form.

⁴This is the short hand Hermann-Mauguin notation. The full Hermann-Mauguin notation is $P12_11$.

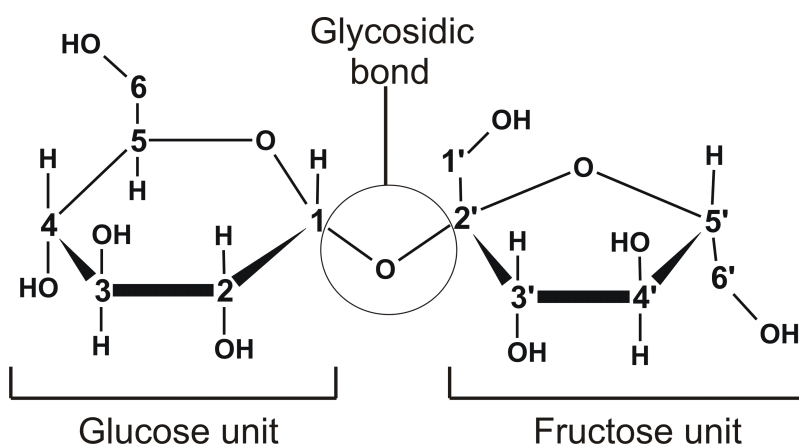


Figure 5.1: The chemical structure of a sucrose molecule with the IUPAC atomic numbering. Carbons are referred to in this chapter as CX, hydrogens and oxygens bound to CX as HX and OX, and hydroxy hydrogens at CX as HOX (X=1-6,1'-6')

axis and a subsequent translation over $\frac{b}{2}$ along the $\langle b \rangle$ axis. This can be seen in Figure 5.2C. If (x, y, z) are the coordinates in the $\langle abc \rangle$ reference frame of one molecule, the coordinates of the symmetry-related molecule are given by $(-x, y \pm \frac{1}{2}b, -z)$. In practice usually an orthogonal reference frame is used: $\langle a^*bc^* \rangle$ or $\langle abc^* \rangle$.⁵ The coordinates of the two molecules in a unit cell are related in the same way in these reference frames: $(x, y, z) \leftrightarrow (-x, y \pm \frac{1}{2}b, -z)$.

5.2 EMR results in the literature

5.2.1 Dosimetric studies

The last two decades, a substantial amount of research has been devoted to the radiation dosimetric properties of sucrose powder: time dependency of the EPR spectrum, dose response, radiation type sensitivity, variation of the EPR spectrum with experimental parameters such as microwave power and modulation amplitude, . . . [39].

The main motivation for these studies is the ongoing search for new and better SS/EPR (solid-state EPR) dosimetric systems, both for detection and characterisation of irradiated foodstuffs and for radiation dosimetry purposes. Because sucrose is so widely used, universally available, cheap and tissue-equivalent,⁶ especially its potential use as (nuclear) emergency dosimeter for

⁵ \vec{a}^* is defined as the projection of \vec{a} onto the plane perpendicular to \vec{c} , and \vec{c}^* as the projection of \vec{c} onto the plane perpendicular to \vec{a} .

⁶This means that its interaction with radiation is comparable to that of typical biological tissues.

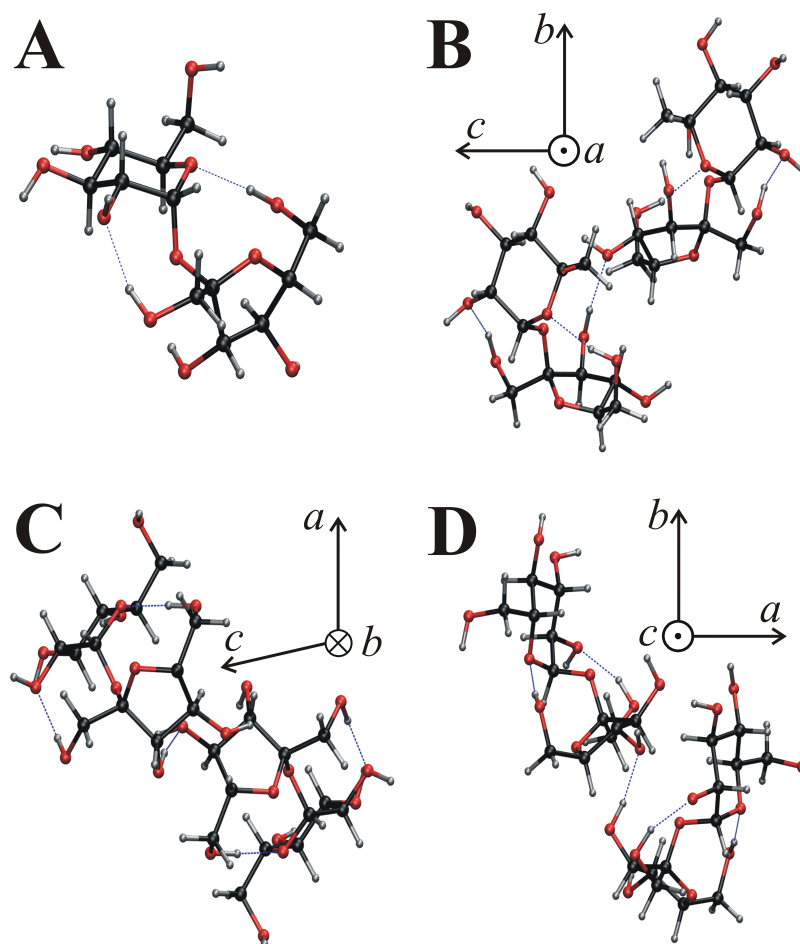


Figure 5.2: A single sucrose molecule in its lattice conformation (A) and a unit cell of the sucrose lattice viewed along the $\langle a \rangle$, $\langle b \rangle$ and $\langle c \rangle$ axes (B-D). Carbon atoms are in black, oxygen atoms in red and hydrogen atoms in grey.

the general populace has been investigated. Initial studies revealed

- a low background signal [112].
- a high radiation sensitivity, allowing for determination of doses down to 5 mGy [113] and even 0.5 mGy [114].
- a linear dose response up to 10 kGy [115] or even 21 kGy [116].
- a good time stability of the EPR signal up to 11 months after irradiation [114, 116, 117].

- a complete independence of the EPR signal on the precise origin of the sugar [113].

A NIST/ISS (National Institute of Standards and Technology/Istituto Superiore di Sanità) study by Fattibene *et al.* [118] assessed the sugar-EPR dosimeter system more thoroughly and critically in 1996, thereby resolving several conflicting results and uncertainties in the literature. *The minimum detectable dose* was estimated to be 50-100 mGy - at least an order of magnitude larger than the numbers put forward by Nakajima *et al.* [113, 114] - and the EPR spectrum of irradiated sucrose powder was found to undergo subtle but complex, *dose-dependent changes during the first 80 - 100 hours after irradiation*. A more accurate study by Desrosiers and Wadley in 2006 confirmed this time dependence but showed it to be less complex and more consistent than proposed by Fattibene *et al.*, and concluded that it does not pose a fundamental problem for the use of sucrose as a radiation dosimeter [119].

One of the major problems in SS/EPR dosimetry (regardless of the specific dosimeter used) is that the EPR calibration is only valid for a particular spectrometer and a particular dosimeter batch [120]. Two alternative approaches have emerged to overcome this problem in the case of sucrose. The first is based on the conventional idea of 'self-calibration': next to the sugar (the radiation-sensitive material) Mn^{2+} magnetically diluted in MgO (the internal standard) is included in the dosimeter, both substances being held together by a paraffin binder [121]. The second approach is based on the presence of several distinct bands in the IR and UV region of irradiated solid sucrose, whose intensities change with the irradiation dose, first observed by Flores *et al.* [122]. Particularly interesting in the context of this doctoral thesis is that specific UV absorption signals are found at wavelengths typically associated with carbonyl groups. As will be discussed in Section 5.3, all three major stable radicals in sucrose indeed have such a carbonyl group. From the radiation-dosimetry point of view, this observation opens up the possibility of independently calibrating SS/EPR dosimeters, since UV intensities can readily be calibrated. The following results emerged from UV-spectroscopic studies [116, 121, 123–125] on sucrose and other sugars:

- The UV-absorption-band intensities of irradiated solid samples are linearly dependent on the radiation dose (in the case of both γ and N-ion radiation) and correlate linearly with the EPR signal, in the range 0.44 - 10 kGy [116, 125].
- The UV spectra of water solutions of γ irradiated sucrose powder also show these absorption bands. Their intensities are time dependent but reach steady values (15 % higher than initial values) ca. 10 days after

dissolution (when kept in closed vessels in the dark at room temperature (RT)). This steady value is also reached when the solution is heated to 70°C for 1 hour [116, 123].

- The minimum detectable dose using the UV spectrum of these water solutions is estimated to be about 55 Gy, with possible improvement by at least an order of magnitude if more sophisticated UV spectrophotometers would be used [123].
- The UV absorption is linearly dependent on the concentration of the sucrose solution in the range 5-20 % [123].

The authors suggest that these properties allow (i) sucrose to be used for independent calibration of any SS/EPR dosimeter (alanine or 'self-calibrated'), thus providing a significant increase in the precision of dose estimation [124] and (ii) water solutions of irradiated solid sucrose to be used as simple, cheap and sensitive high-energy dosimeters when provided with a UV spectrophotometric readout [123].

Finally, several studies in the literature investigated the radical production in sucrose by radiation with electrons [122] and with heavy ions [125–129]. It was found that

- the spin concentration increases linearly with the absorbed dose for irradiation with electrons, He-, C-, Ne-, Ar-, Si- and Fe-ions and decreases logarithmically with the LET (Linear Energy Transfer) of the ions.
- the LET dependence is in general different for different ions.
- the EPR spectrum is (virtually) identical to that observed after γ irradiation.

These results suggest sucrose could also be used as a dosimeter for heavy-ion radiation, although it does not readily allow discrimination between different types of radiation. It was also suggested, based on the experimentally determined radical-production crosssections, that formation of the stable radicals involves multiple ionisations of the same molecule. Our own research results do not seem to corroborate this hypothesis (Section 5.3.3.4): radicals induced at 10 K by X irradiation transform spontaneously into the stable radicals (which give rise to the EPR signal observed in dosimetric studies). This means thermal energy is sufficient as driving force for the radical transformations to proceed, and multiple ionising radiation-matter interactions at a specific site need not be invoked.

5.2.2 Fundamental studies

Another type of EMR studies has focused on the interpretation of the EPR spectrum of solid sucrose X irradiated and measured at different temperatures [130–134] (Table 5.1). The EPR spectrum of irradiated sucrose powder

Table 5.1: Overview of some experimental parameters in the most important EMR literature studies on radiation-induced defects in solid sucrose.

Reference	[130, 131, 135]	[132]	[133]	[134]
Irrad. temp.	~4 K	285 K	RT	RT
Meas. temp.	≤4 K	RT	60 K	5 K - RT
Micr. freq. (GHz)	9.5, 70	9.5, 35	9.15	9.73, 94, 190, 285

is quite difficult to interpret mainly due to its multicomposite character and the presence of various anisotropic hyperfine coupling (HFC) interactions for each of the radicals. In general, this is an undesirable feature for a dosimeter because the different radical species may exhibit different dose response, time stability, saturation behaviour, ... Knowledge of the individual components allows interpreting observed spectral changes in terms of the individual components and can thus be helpful in developing dosimetric protocols. This was the primary aim in the studies by Vanhaelewyn *et al.* [133] and Georgieva *et al.* [134] Another motivation for studying the radiation-induced radicals in sucrose is to gain insight in the direct radiation effects in the deoxyribose moiety of DNA, as was the case in Refs. [130–132, 135]. Comparable EMR studies were performed on numerous other saccharides, e.g. rhamnose [103, 109, 130, 136–139], glucose [140, 141], methylglucose [8, 99, 142, 143], glucose 1-phosphate [108, 144, 145], fructose [146, 147], and trehalose [148, 149]. The primary aims of these studies were identification of the radiation-induced radicals and radical processes. In the current context, however, it makes more sense to group the studies on sucrose according to the temperature at which radiation was performed: approximately RT [132–134] or 4 K [130, 131, 135] (Table 5.1).

5.2.2.1 Irradiation at RT

After irradiation of sucrose single crystals at RT, composite EPR spectra are observed at conventional microwave frequencies (X and Q band) [132–134]. EPR and ENDOR measurements at *RT* on sucrose single crystals by Sagstuen *et al.* [132] allowed for the determination of *five* proton HFC tensors that were assigned to *two* different radicals. The *g* tensor of one of these species was

extracted from Q-band EPR angular variations and possible radical models were proposed for both species. In the study by Vanhaelewyn *et al.* [133] EPR, ENDOR and EIE measurements at **60 K** revealed *nine* proton HFC tensors that were assigned to *three* dominant species. Two of these were found to be very similar, but clearly distinguishable. The three radicals were shown to dominate the EPR spectrum, but an analysis using a multivariate statistical method called MLCFA⁷ (Maximum Likelihood Common Factor Analysis) revealed that there are at least three other minority radical species contributing to the EPR powder spectrum. The number and characteristics of the HFC tensors are clearly different from those reported by Sagstuen *et al.*, although several tensors are *similar*.

Finally, a multifrequency EPR study at different temperatures (Table 5.1) by Georgieva *et al.* confirmed the presence of at least *three* different stable radicals. By means of EPR spectrum simulations and using the proton HFC tensors reported by Vanhaelewyn *et al.* [133] the *g* tensors of these three radical species were derived.

As will be discussed in Section 5.3.1, we showed all three studies to be erroneous (to some extent) in a new, extensive EMR study (Paper I).

5.2.2.2 Irradiation at 4 K

EMR measurements at 4 K after X irradiation at 4 K or lower (see Table 5.1) reveal the presence of several radiation-induced radical species in sucrose single crystals [130, 131, 135]. Two species were characterised in detail and identified: an intermolecularly trapped electron [130, 131] and an O3'-centred alkoxy radical [135]. The results of these studies will be of interest in Section 5.3.3 and are discussed in more detail below. A significant part of the EPR absorption observed in these studies cannot be attributed to either of these species and are, based on the small *g* anisotropy around $g \approx 2.0030$, most likely due to carbon-centred radicals.

5.2.2.2.1 The trapped electron Sucrose is one of several organic single crystals in which electrons are trapped at intermolecular sites after low-temperature irradiation. Other examples include arabinose, rhamnose, glucose 1-phosphate, xylitol, sorbitol, dulcitol, hexanediol and octanediol [108, 130, 131, 151–157]. The electrons are trapped in between two or more neighbouring hydroxy groups and are assumedly stabilized by the (partially induced) dipolar fields of these hydroxy groups. Such trapped electrons are characterised by

⁷For more information, the reader should consult Ref. [150]

- strongly anisotropic HFC interactions with two or more exchangeable protons. The anisotropic part exhibits axial symmetry (in the case of sucrose: $\sim(-15, -15, +30)$ MHz) while the isotropic part is positive and can be quite large (in the case of sucrose: $\sim+50$ MHz).
- a nearly isotropic g tensor with all principal g values slightly smaller than the free-electron value (in the case of sucrose: $g\sim 2.0020$).

These features are quite specific and clearly different from those of carbon- or oxygen-centred radicals (cf. Sections 4.4.2.1 and 4.4.2.2).

Budzinski *et al.* used ENDOR angular variations to determine two HFC tensors due to exchangeable protons for the trapped electron in sucrose [130]. A more detailed study was undertaken by Box *et al.*, in which four extra HFC tensors were determined: one exchangeable and three non-exchangeable [131]. Interestingly, the non-exchangeable couplings all have negative isotropic components, which was qualitatively explained by the authors in terms of a simple valence bond model. By calculating the electric potentials arising from hydroxy dipoles and by using the HFC tensors of the three non-exchangeable protons,⁸ the trapping site was identified: along (but not on) the C5-C6 and C6-O6 bonds (site I in Figure 5.3). Finally, it should be noted that the trapped electron in sucrose was reported to be stable up to 61 K.⁹

5.2.2.2 The alkoxy radical The alkoxy radical present in sucrose at 4 K after X irradiation at 4 K was thoroughly characterized by Box and Budzinski [135]. Six proton HFC tensors as well as the g tensor were determined from EPR and ENDOR angular variations. Because these will be of interest in Section 5.3.3, they are listed in Table 5.2. We note that the choice of sign of the HFC tensors is arbitrary. It will be shown in Section 5.3.3 that the correct sign was chosen by the authors with exception of A3. Box and Budzinski proposed the radical structure depicted in Figure 5.4: an O3'-centred alkoxy radical where the HO3' proton has migrated (*hopped*) to the O4' oxygen of a neighbouring molecule (to which it is hydrogen bound in the pristine lattice). The maximum principal g value of alkoxy radicals in other organic compounds typically varies between 2.020 and 2.110 (but are most often larger than 2.040), and the minimum principal g value between 1.970

⁸Using the point-dipole approximation, approximate values can be calculated from the anisotropic HFC values for the distance between the electron and the interacting proton and for the orientation of the line connecting them, relative to the crystal lattice (cf. Section 4.3.1.1). The exchangeable protons may be expected to reorient when the electron is trapped, while the non-exchangeable protons are more distant and therefore more reliable for this purpose.

⁹Our own results, however, indicate it is not stable after *in-situ* X irradiation at 10 K. This is discussed in Section 5.3.3.3, page 126.

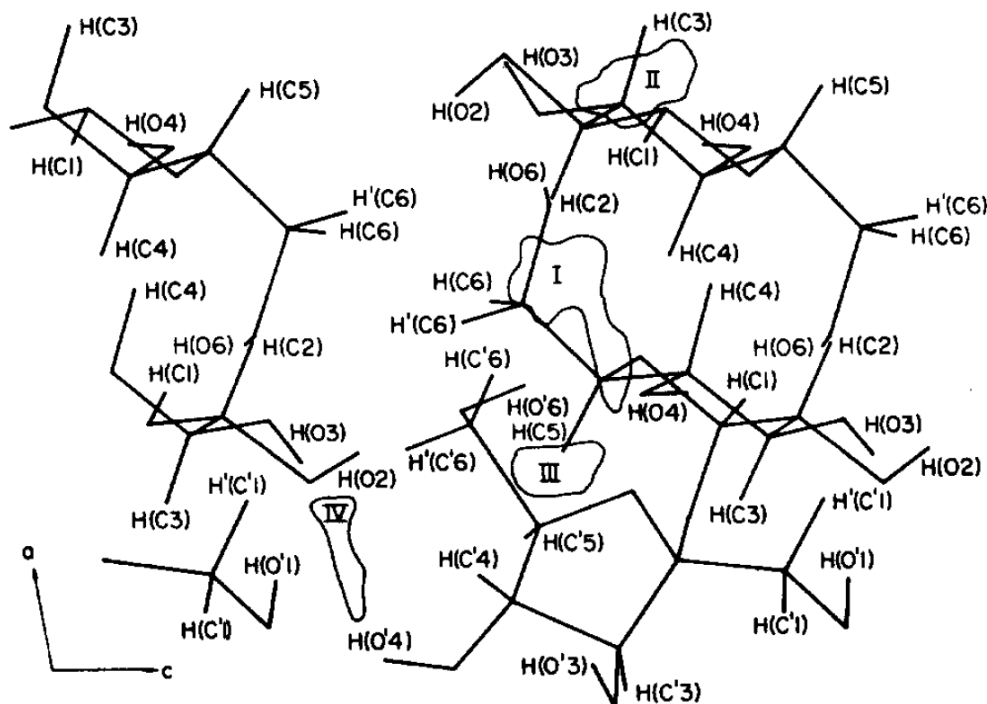


Figure 5.3: Possible sites for electron trapping (indicated with Roman numerals), based on calculations of the electric potentials arising from hydroxy dipoles in the sucrose lattice. Using the anisotropic part of the non-exchangeable proton HFC tensors, site I is found to be the most likely trapping site. The figure is taken from Ref. [131].

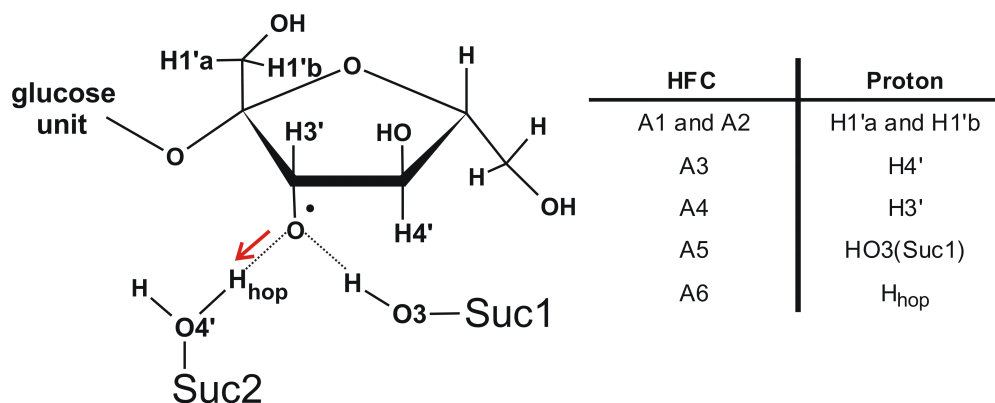


Figure 5.4: *Left*: the chemical structure of the alkoxy radical present in sucrose single crystals after *in-situ* X irradiation at 4 K, proposed by Box and Budzinski [135]. *Right*: attribution by Box and Budzinski of the HFC tensors A1-A6 (cf. Table 5.2) to the protons in this model.

and 2.002 [94, 103, 106–110]. For the present alkoxy radical the maximum value (2.027) is small but within the range, while the minimum value (2.0037) is markedly larger than any value observed so far. Furthermore, the HFC

Table 5.2: Proton HFC tensors ((an)isotropic values in MHz) and g tensor of an alkoxy radical present in sucrose single crystals at 4 K after *in-situ* X irradiation at 4 K, as reported by Box and Budzinski [135]. Our own DFT study on this species indicates the principal values of A3 have signs opposite to those listed here (see Section 5.3.3.8).

Proton	Iso	Aniso	Eigenvectors		
			a*	b	c
A1	26.00	-1.82	0.205	0.942	0.262
		-0.54	0.644	0.071	-0.761
		2.36	0.736	-0.325	0.593
A2	15.09	-1.58	0.445	0.772	0.452
		-0.29	-0.246	-0.380	0.891
		1.87	0.860	-0.508	0.021
A3	10.05	-11.31	0.552	0.611	-0.566
		0.69	-0.407	0.791	0.456
		10.62	0.727	-0.021	0.686
A4	15.13	-5.59	0.926	-0.375	0.002
		-3.24	0.051	0.132	0.989
		8.83	0.372	0.917	-0.142
A5	-0.59	-5.09	0.417	0.752	0.510
		-4.47	0.129	-0.604	0.785
		9.57	0.899	-0.261	-0.349
A6	-1.11	-8.01	0.928	-0.356	0.100
		-6.59	-0.011	0.246	0.969
		14.61	0.370	0.901	-0.224
		Princ	Eigenvectors		
			a*	b	c
g tensor		2.0037	-0.072	0.046	0.996
		2.0087	-0.889	-0.454	-0.043
		2.0270	0.450	-0.889	0.074

tensors indicate that there is substantial delocalisation of the spin density with unusually strong spin polarisation at certain distant protons. As will be discussed in Section 5.3.3, our own research indicates that the model suggested by Box and Budzinski is essentially correct, but the attribution of some of the HFC tensors is erroneous.

5.3 Own research results

The results of our own research on radicals induced by X rays in solid sucrose are discussed here. Section 5.3.1 deals with the stable radicals and is a summary of Papers I, II and III. In Section 5.3.2 we report on the evolution of the EPR spectrum during the first hours after irradiation at RT. This study was only recently performed in the EPR lab in Ghent, in collaboration with

the EPR group of Prof. Yordanov (Institute of Catalysis, 'Bulgarian Academy of Sciences', Sofia, Bulgaria), and a paper has been submitted to *Radiation Research*. Section 5.3.3 is concerned with the radicals present at 10 K after *in-situ* X irradiation at this temperature. This research was performed at the EPR lab in Oslo and at the CMM in Ghent, and a paper will soon be submitted.

5.3.1 Stable radicals

In order to clear up the discrepancies between the studies performed by Vanhaelewyn *et al.* [133] and Sagstuen *et al.* [132], we carried out an EMR study on RT X-irradiated sucrose single crystals. This included extensive EPR, ENDOR and EIE measurements in four different crystallographic planes at 110 K, both in X and Q band. The variation of EPR and ENDOR spectra with measuring temperature was also studied and advanced DFT calculations were performed to evaluate the radical model structures proposed by Sagstuen *et al.* [132]. The results of these studies are reported in Paper I. We summarise the main results/conclusions here.

- The proton HFC tensors reported in both studies [132, 133] are erroneous to some extent. Consequently, the g tensors reported by Georgieva *et al.* [134] (and determined based on the HFC tensors in Ref. [133]) are also incorrect, although the size of the g anisotropy probably is approximately correct.
- The study by Vanhaelewyn *et al.* [133] is qualitatively correct: there are three dominant radical species, two of them being very similar - but distinguishable - in all respects. These are labelled T1, T2 and T3, where T2 and T3 are the similar radicals. Each of the three radical species exhibits three HFC interactions with appreciable isotropic HFC values.
- The difference in measuring temperature accounts for the difference in number of radicals and HFC interactions between Refs. [132] (RT) and [133] (60 K): the ENDOR lines of some HFC interactions are not or hardly visible at RT.
- The difference in measuring temperature also has a small effect on the HFC tensors themselves. However, the maximum shift of the ENDOR lines observed between 60 K and RT are about 2 MHz, and the EPR spectrum is almost unaltered in the range 60 K - RT. This suggests that the HFC tensors most likely are essentially the same throughout this temperature range.

- The correct tensors were determined accurately for eight of the nine HFC interactions. For one of the T1 HFC tensors, however, the Schonland ambiguity could not be eliminated with the available experimental data. Moreover, both sign choices were equally (im)probable because this tensor has somewhat peculiar properties.
- The most plausible radical models proposed in the literature [132] cannot account for the experimental data.

We eliminated the remaining ambiguities for that T1 HFC tensor (see next-to-last item above) by means of ENDOR measurements on a sucrose single crystal at 110 K in yet another, carefully selected skewed plane and RT hyperfine sublevel correlation spectroscopy (HYSCORE) measurements on sucrose powder (Paper III). The final set of the nine proton HFC tensors belonging to radical species T1, T2 and T3 is given in Table 5.3. Experimental ENDOR angular variations and corresponding simulations using the tensors in Table 5.3 are given in Papers I and III. Using the point-dipole approximation and semi-empirical rules, a limited set of plausible radical models was inferred. Extensive DFT calculations (in a periodic approach for the geometry optimisation and in a cluster approach for the calculation of the EMR parameters) were employed to identify the chemical structure of all three radicals (T1 in Paper III, T2/T3 in Paper II). These are shown in Figure 5.5.¹⁰ The HFC tensors calculated for the radical models in Figure 5.5 are listed and compared to the experimental data in Table 5.4. From our DFT study on T2/T3 (Paper II) we concluded that in order for T2 and T3 to have such similar HFC tensors, they must have essentially the same chemical structure (T2_M in Figure 5.5) and that the differences most likely arise from a difference in the conformations of T2 and T3, which in turn probably is due to a difference in the conformation of their immediate surroundings. The DFT calculations also suggest that the T2 and T3 conformations must differ rather substantially to account for the observed discrepancies. Note that the calculated eigenvector directions of T2_M match the experimental eigenvector directions of T2 better than those of T3.

T1_M and T2_M share three common features:

- a broken glycosidic linkage.
- a carbonyl group adjacent to the radical centre.

¹⁰Although this assignation is quite certain, we wish to make a clear distinction between the real, physical radical species and the proposed radical models by labelling the models with a subscript M.

Table 5.3: Proton HFC tensors ((an)isotropic values in MHz) of the three dominant radical species T1, T2 and T3 in sucrose single crystals X irradiated at RT, determined from ENDOR measurements at 110 K approximately two days after irradiation. The HFC tensors are taken from Paper I, except $H_{\beta 3}(T1)$, which is taken from Paper III.

Radical	Proton	Iso	Aniso	Eigenvectors		
				a*	b	c
T1	$H_{\beta 1}$	46.80	-3.99	0.616	0.121	-0.778
			-2.38	0.072	0.975	0.209
			6.37	0.784	-0.185	0.592
	$H_{\beta 2}$	15.88	-2.69	0.106	0.825	0.555
			-2.31	0.989	-0.144	0.025
			5.00	0.101	0.546	-0.832
	$H_{\beta 3}$	-11.07	-6.41	0.711	-0.241	-0.660
			-3.73	0.380	0.922	0.073
			10.14	0.591	-0.302	0.748
T2	H_{α}	-38.69	-19.66	0.424	-0.163	-0.891
			-2.11	0.886	0.280	0.371
			21.77	0.189	-0.946	0.263
	$H_{\beta 1}$	16.37	-2.32	0.869	-0.355	-0.344
			-1.72	-0.209	0.368	-0.906
			4.04	0.448	0.860	0.246
	$H_{\beta 2}$	13.68	-3.09	0.718	-0.650	0.248
			-2.17	0.638	0.473	-0.608
			5.26	0.278	0.595	0.754
T3	H_{α}	-35.81	-18.98	0.584	-0.184	-0.790
			-2.11	0.755	0.481	0.446
			21.09	0.298	-0.857	0.420
	$H_{\beta 1}$	16.42	-2.10	0.840	-0.541	-0.034
			-1.77	0.178	0.334	-0.926
			3.87	0.512	0.772	0.377
	$H_{\beta 2}$	12.24	-3.62	0.528	-0.822	0.214
			-2.12	0.804	0.402	-0.439
			5.74	0.275	0.403	0.873

Table 5.4: DFT-calculated proton HFC tensors for the radical models $T1_M$ (taken from paper III) and $T2_M (= T3_M)$ (taken from paper II) depicted in Figure 5.5. The geometry optimisations were performed periodically in an $\langle ab2c \rangle$ supercell, while the HFC tensors were calculated in a cluster cut out of the periodic structure, consisting of the radical surrounded by the ten sucrose molecules to which it is hydrogen bound in the lattice. δ is the angle between the calculated and the corresponding experimental eigenvector directions (cf. 5.3).

Mo- del	Pro- ton	Iso	Aniso	Eigenvectors			Pro- ton	δ ($^\circ$)	
				a*	b	c		T1	T2
$T1_M$	H3'	43.47	-3.86	0.624	-0.220	-0.750	H $_{\beta 1}$	6	
			-2.27	-0.021	0.954	-0.298		6	
			6.13	0.781	0.202	0.590		1	
	H5'	15.42	-2.37	-0.286	0.788	-0.546	H $_{\beta 2}$	11	
			-2.24	0.950	0.307	-0.055		11	
			4.61	-0.124	0.535	0.836		2	
	H1'	-10.58	-6.81	0.709	-0.136	-0.692	H $_{\beta 3}$	7	
			-4.62	0.362	0.912	0.193		7	
			11.43	0.605	-0.387	0.696		6	
								T2	T3
$T2_M$	H1	-34.60	-20.23	-0.451	0.155	0.879	H $_{\alpha}$	2	9
			-4.66	0.875	0.267	0.403		2	14
			24.89	-0.173	0.951	-0.256		1	13
=	H3	16.18	-2.16	0.874	0.462	0.154	H $_{\beta 1}$	30	12
			-1.86	-0.249	0.152	0.957		30	11
			4.02	-0.418	0.874	-0.248		2	11
$T3_M$	H5	12.59	-2.88	0.675	0.673	0.303	H $_{\beta 2}$	4	13
			-2.06	0.698	-0.450	-0.557		5	10
			4.95	0.239	-0.588	0.773		3	12

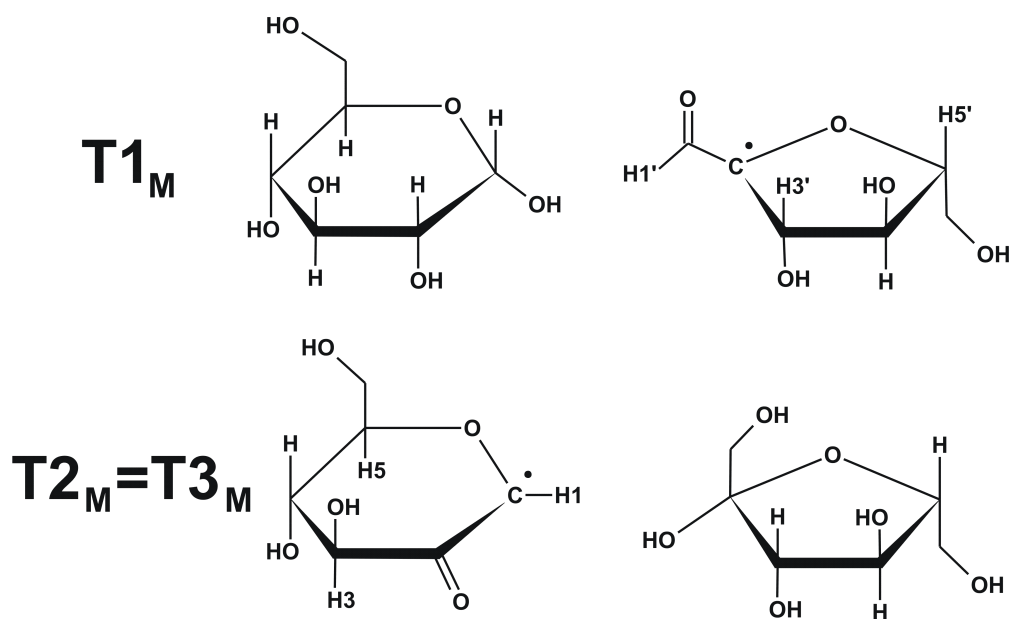


Figure 5.5: The chemical structures of the models for the three dominant radical species ($T1$, $T2$ and $T3$) in sucrose single crystals X irradiated at RT, determined from DFT calculations as reported in Paper II (for $T2_M/T3_M$) and Paper III (for $T1_M$).

- a ring oxygen adjacent to the radical centre.

Roughly half of the spin density is localised on the ring oxygen and the carbonyl group. This delocalisation likely contributes significantly to the stability of the radical, which may explain the dominant presence of these radicals in the stable state.

In the past, the smaller proton HFC interactions were always assumed to arise from β protons because the isotropic components were believed to be too large for γ protons. However, as discussed in papers II and III, the spin delocalisation onto the ring oxygen and the carbonyl group, and the specific orientation of the $C_\gamma-H_\gamma$ bonds can indeed induce the observed isotropic HFC's in γ protons.¹¹ This type of proton HFC tensors probably does not occur for other types of radical species and they may therefore be considered as fingerprints for radicals similar to $T1_M$ and $T2_M$. On the other hand, radical structures may easily be conceived with features similar to those of $T1_M$ and $T2_M$ (spin delocalisation onto a carbonyl group and/or a ring oxygen), but e.g. without γ protons or with γ protons oriented differently with respect to the molecular orbitals carrying the spin density.

Our DFT calculations also provided an explanation for the peculiar $H_{\beta 3}(T1)$

¹¹Because of the delocalisation, the discrimination between β and γ protons is in fact somewhat vague.

HFC tensor in terms of a change in the spin density on the carbonyl carbon. The latter originates mainly from the presence of the adjacent ring oxygen and from hydrogen bonding with a neighbouring molecule in the lattice. To the best of our knowledge, this type of proton HFC tensor was not reported before in the literature. Because of the unusual combination of a dipolar-type anisotropic coupling and a negative isotropic coupling, one could easily believe this tensor to be the wrong Schonland variant (when insufficient data are at hand to eliminate the ambiguity, cf. 2.4.2.2, page 44). Clearly, care has to be taken. A HFC tensor similar to $H_{\beta 3}(T1)$ may be considered as an indication of an allylic-type radical fragment like in $T1_M$ (Figure 5.5). But again, an allylic-type radical like $T1_M$ does not necessarily exhibit a proton HFC exactly like $H_{\beta 3}(T1)$.

5.3.2 EPR-spectrum evolution during first hours after RT irradiation

Already in 1996, Fattibene *et al.* [118] reported that the EPR spectrum of sucrose powder changes significantly during the first hours after X irradiation and that the stable state is only reached 80 - 100 hours after irradiation. Desrosiers *et al.* [119] repeated this study more accurately in 2006 and confirmed the general time-dependent trend. The most plausible explanation are slow radical processes: transformation of unstable radicals into stable radicals or decay of unstable radicals into diamagnetic products. An explanation for the EPR spectral changes in terms of the individual radical components and their time-dependent behaviour can be of value for establishing dosimetric protocols and yield important insights in the underlying radical processes. E.g., the spectra of the immediate precursors of the stable radicals could be isolated. Therefore, we studied the evolution of the EPR and ENDOR spectrum of X-irradiated solid sucrose during the first days after irradiation, with the primary aim of understanding the nature of the observed changes (radical transformation or decay, the number of species involved, ...).

5.3.2.1 Experimental procedures

The crystals were X irradiated at RT for 5 minutes (estimated total dose of 5 kGy). After the irradiation, the samples were put in a Q-band EPR/ENDOR sample tube for the EMR measurements. The time-dependence of the EPR spectra was recorded at RT. For these experiments a modulation amplitude of 0.1 mT and a total recording time for each spectrum of 41 s were used and the magnetic field was measured using a Bruker ER035 NMR Gauss meter and calibrated with a standard DPPH field marker ($g = 2.0036$). All spectra (of this

time series) were normalised to a microwave frequency of 33.9935 GHz. The field-frequency ENDOR (FF-ENDOR) measurements (see Section 2.2.6) were performed at 80 K and for the measurements 'immediately after irradiation' the cavity was precooled to 80 K to minimise further radical transformations after sample insertion. The total time between the start of the irradiation and the stabilisation of the sample temperature at 80 K is estimated to be about 10 minutes. The spectra were normalised to a microwave frequency of 33.9700 GHz.

The samples were always mounted in the tube with the long axis (the rotation axis) approximately parallel to $\langle b \rangle$. The orientation of the magnetic field in the plane perpendicular to $\langle b \rangle$ was determined visually, on the basis of the well defined geometrical features of the single crystals, and checked more accurately afterwards using the well known stable radical ENDOR signals. The actual orientation may still deviate by about 5° from the reported one.

5.3.2.2 Results and discussion

Immediately after irradiation at RT, following observations can be made

- when the sample is kept at RT, the EPR spectrum continuously changes. After approximately 4 hours the spectrum becomes essentially stable and during the subsequent days only minor changes were observed.
- when the sample is kept at 80 K, the spectrum is stable for at least 6 hours. This indicates that the radical processes observed at RT do not proceed at 80 K – the radicals are trapped.
- the measuring temperature (80 K or RT) has no significant influence on the shape of the EPR spectrum.

In Figure 5.6 FF-ENDOR scans are presented at different stages of the EPR-spectrum evolution for approximately $B \parallel \langle c \rangle$. This is achieved by cooling the sample to 80 K after different time intervals of RT annealing. Note that

- several ENDOR transitions have decreased in intensity after 3 hours and have virtually disappeared after 10 hours of RT annealing.
- no new ENDOR transitions emerge upon RT annealing.
- the ENDOR transitions due to the stable radicals T1, T2 and T3 do not gain noticeably in intensity during 10 hours of RT annealing.

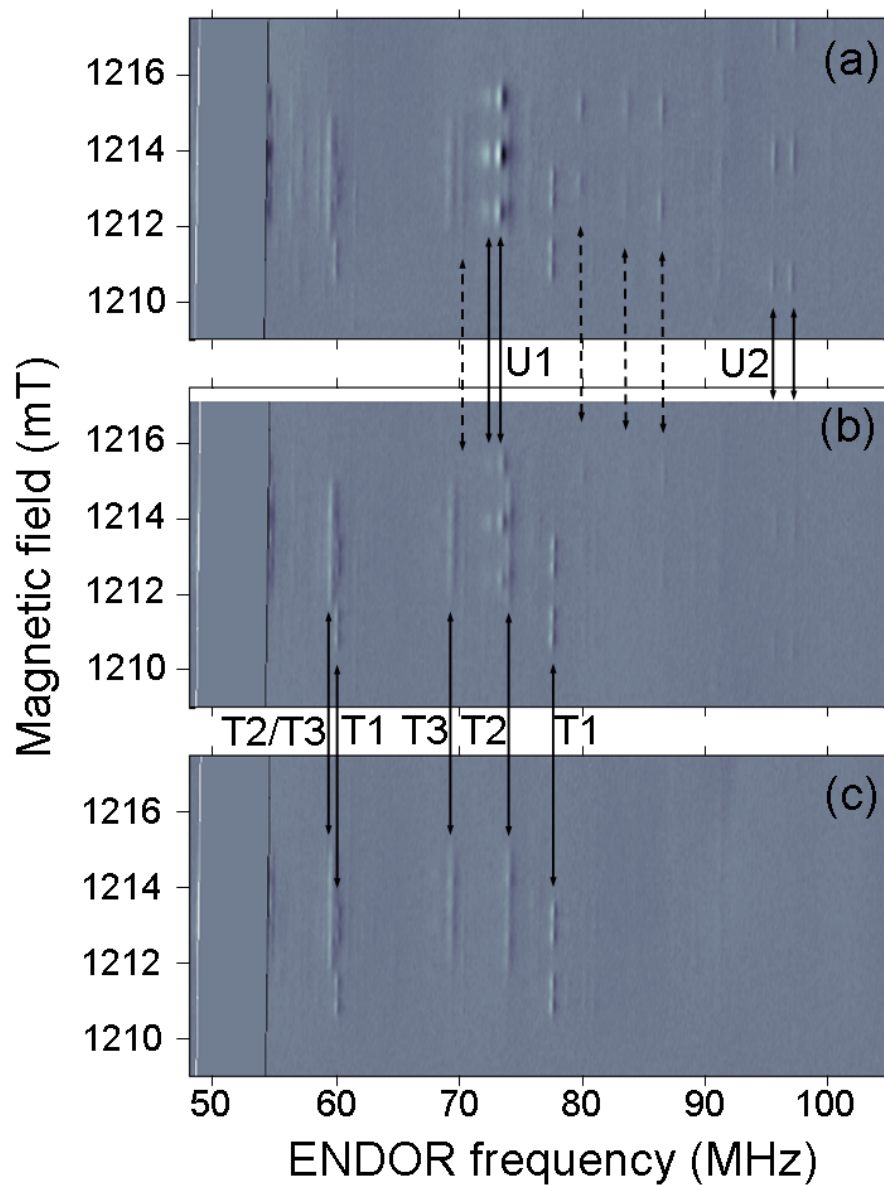


Figure 5.6: FF-ENDOR spectra of sucrose single crystals with B approximately parallel to $\langle c \rangle$ after (a) 10 minutes, (b) 3 hours and (c) 10 hours of RT annealing. T1, T2 and T3 are the stable radicals characterised and identified in Papers I-III. U1, U2 and the features indicated with dashed arrows belong to six different semistable species. The spectra were normalised to a microwave frequency of 33.9700 GHz.

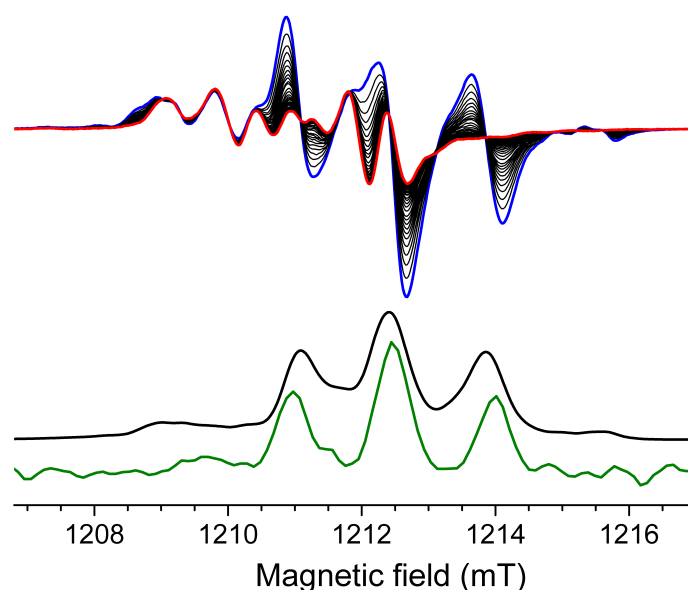


Figure 5.7: *Top:* first-derivative Q-band EPR spectra (B approximately parallel to $\langle c \rangle$) recorded on sucrose single crystals at RT, starting from 10 minutes after irradiation (blue) and ending 6 hours after irradiation (red). *Bottom:* field integration of the spectrum obtained by subtracting the red from the blue spectrum (black) and the EIE spectrum of U1, reconstructed from the FF-ENDOR spectrum of Figure 5.6 (green).

These observations suggest that the transformation of the EPR spectrum is the result of the decay of several semistable radicals into diamagnetic species. At least six different semistable radical species can be observed (Figure 5.6a). However, Figure 5.7 indicates that a single species (U1) dominates the EPR spectrum immediately after irradiation and, consequently, that the EPR spectrum changes can be attributed mainly to its decay. In this figure the first derivative EPR spectra are shown in a time series covering approximately the first 6 hours after the start of the irradiation. The transformation corresponds to a gradual fading of a component dominated by a broad-line triplet, which can be attributed to U1. This time series also indicates that the final (stable) components are already present immediately after irradiation, in accordance with the FF-ENDOR-spectrum evolution. The time dependence of the total signal intensity (Figure 5.8) then indicates that the stable radicals account for less than half of the total radical yield immediately after irradiation. For $B \parallel \langle c \rangle$, U1 exhibits a broad-triplet EIE spectrum arising from two HFC tensors whose ENDOR transitions practically coincide at ~ 73 MHz (Figures 5.6 and 5.7). One of the other (minor) semistable radical species (U2), whose

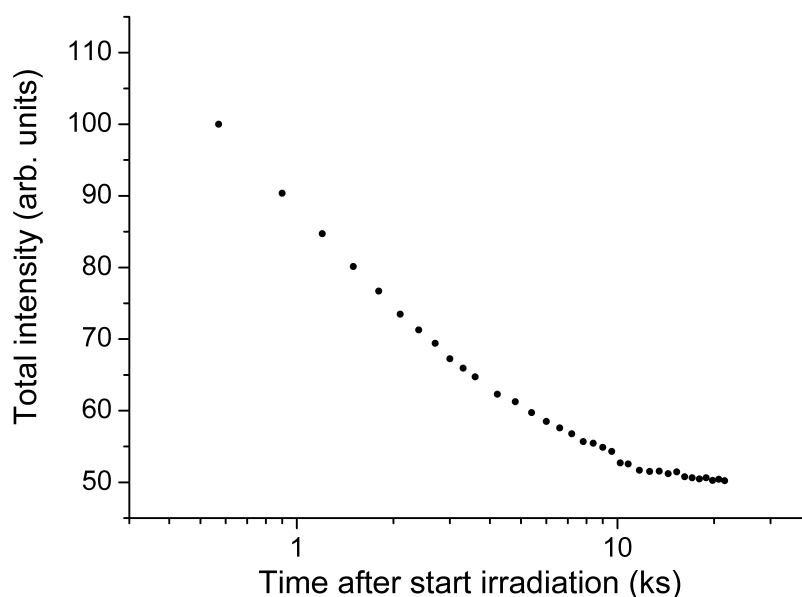


Figure 5.8: Time dependence of the total intensity (double integration) of the first-derivative Q-band EPR spectrum of sucrose single crystals recorded at RT and with B approximately parallel to $\langle c \rangle$, during roughly the first 3 hours after irradiation (cf. Figure 5.7).

EI-EPR spectrum is a wider-split triplet and whose ENDOR transitions appear in the 95 - 98 MHz range, may account for some of the weaker EPR signals at the left- and right-hand sides of the spectrum recorded 10 minutes after irradiation. FF-ENDOR spectra were recorded at a number of other magnetic field orientations (all in the plane perpendicular to $\langle b \rangle$). Although these did not allow structural identification of the metastable radicals, they indicate that radical U1 has an α and a β proton (the latter with an isotropic HFC value in the range 40 - 50 MHz), whereas U2 has two β protons with large isotropic HFC values (probably in the range 85 - 95 MHz).

5.3.2.3 Conclusion

The EPR spectrum of RT irradiated sucrose single crystals undergoes drastic changes during the first 3-4 hours after irradiation, which can to a large extent be attributed to the decay of a metastable radical species (U1) into a diamagnetic species. Structural characterisation of U1 would be interesting from a fundamental point of view. There is, however, no (significant) conversion of this metastable radical species into stable radicals so that

such knowledge would not yield information on the processes of glycosidic bond cleavage and carbonyl group formation, which characterize the stable radicals (T1, T2 and T3). If we are to obtain information on those formation mechanisms, we must therefore perform EMR measurements after *in-situ* irradiation at temperatures below RT to stabilise the precursors. We have carried out such measurements at 10 K after X irradiation at 10 K in the EPR lab in Oslo. The results of this study are discussed in the next section.

Furthermore, FF-ENDOR spectroscopy proves to be a very powerful tool for mapping spectral changes (and, consequently, radical processes) of multicomposite EPR spectra.

5.3.3 Radicals present after *in-situ* X-ray irradiation at 10 K

5.3.3.1 Experimental procedures

The crystal axes $\langle a \rangle$, $\langle b \rangle$ and $\langle c \rangle$ were aligned parallel to the rotation axis as described in Section 2.5. The orientation of the skewed plane was first estimated by means of the visible crystal features, and accurately determined afterwards during the tensor fitting process. The transfer of the single crystals, the home-built X band (microwave frequency of about 9.75 GHz) spectrometer in the EPR lab in Oslo used for the low-temperature EMR measurements and the X ray tube used for X irradiation of the samples are described in Section 2.5. The irradiation and measurement temperature was about 10 K, the lowest temperature attainable with the current experimental setup. The total delivered dose is estimated to be 45 - 60 kGy.

The polar coordinates θ and ϕ of a vector are defined as the angle between the vector and the positive $\langle c \rangle$ axis and the angle between the projection of the vector in the $\{a^*b\}$ plane and the positive $\langle a^* \rangle$ axis.

5.3.3.2 Computational procedures

Geometry optimisations were performed in a periodic approach on an $\langle ab2c \rangle$ supercell, employing the CP2K program package [48] with the Gaussian and plane-waves method [64] (plane-wave cutoff of 320 Ry), T2V2P GTH basis sets [158] and GTH pseudopotentials [159, 160]. HFC- and g -tensor calculations were also performed with the CP2K program package in a periodic approach, but using the Gaussian augmented-plane-wave method [65] (plane-wave cutoff of 250 Ry) and TZV2P basissets. A BLYP functional [59, 61] was employed for geometry optimisations and HFC-tensor calculations. The code for the calculation of HFC tensors and g tensors was only very recently implemented in CP2K [49, 50].

5.3.3.3 EPR, ENDOR and EIE spectra

X-band EPR spectra of sucrose single crystals at 10 K after *in-situ* X irradiation at this temperature are shown in Figure 5.9 for three different orientations of the crystal in the external magnetic field. EPR angular variations in the three planes perpendicular to the $\langle a \rangle$, $\langle b \rangle$ and $\langle c \rangle$ axes indicate that the bulk of the absorption signal exhibits only small g -tensor anisotropy and is therefore likely due to carbon-centred radicals. A broad absorption signal

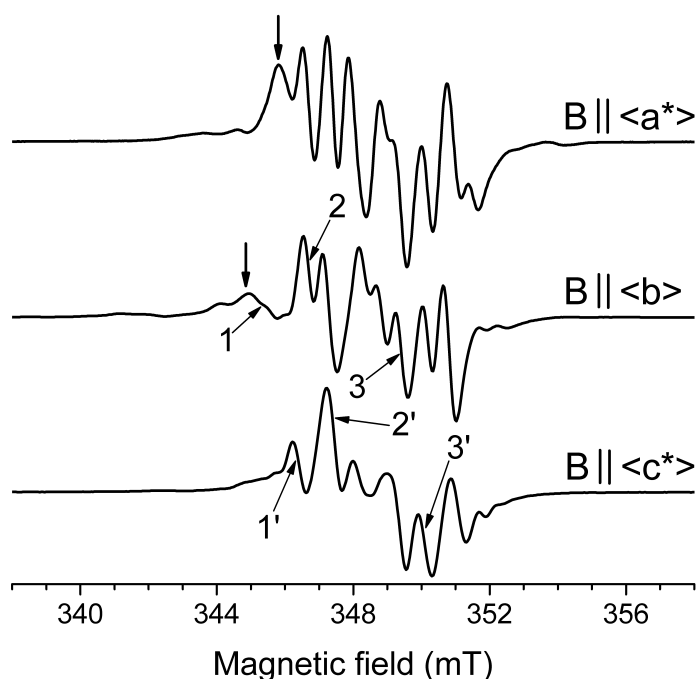


Figure 5.9: X-band EPR spectra of sucrose single crystals at 10 K after *in-situ* X irradiation at 10 K for three different orientations of the crystal with respect to the magnetic field. All spectra are normalised to a microwave frequency of 9.7600 GHz. The numbered arrows indicate the positions at which the ENDOR spectra of Figure 5.12 were recorded. The vertical arrows indicate signals arising from the alkoxy radical reported and identified in Ref. [135] (labelled R6 in the present study.)

emerges at somewhat lower field values for certain orientations (see e.g. $B \parallel \langle a^* \rangle$ and $B \parallel \langle b \rangle$ in Figure 5.9). As will be discussed below, this is due to the alkoxy radical reported by Box and Budzinski [135]. Other, more anisotropic EPR signals were observed, but these were very weak and were therefore not further investigated.

Extensive ENDOR measurements in the three planes perpendicular to the $\langle a \rangle$, $\langle b \rangle$ and $\langle c \rangle$ axes and in two different skewed planes revealed a large

Table 5.5: Proton HFC tensors ((an)isotropic values in MHz) of radical species R1-R6 present in sucrose single crystals after *in-situ* X irradiation at 10 K, determined from ENDOR measurements at 10 K. All couplings arise from non-exchangeable protons, except HF1(R3) which is due to a hydroxy proton.

Radical	Proton	Iso	Aniso	Eigenvectors		
				a*	b	c
R1	HF1	100.61	-5.46	0.480	-0.591	-0.649
			-1.46	0.828	0.550	0.111
			6.92	0.292	-0.590	0.753
	HF2	22.41	-6.40	0.388	0.921	-0.019
			-3.53	0.829	-0.340	0.443
			9.93	0.402	-0.188	-0.896
R2	HF1	29.88	-5.93	0.759	-0.001	-0.651
			-4.80	0.272	0.909	0.316
			10.73	0.591	-0.417	0.690
R3	HF1	51.64	-11.05	0.568	0.777	-0.272
			-6.49	0.386	0.041	0.921
			17.54	0.727	-0.628	-0.277
	HF2	-54.21	-35.16	0.988	-0.095	-0.119
			0.12	0.042	0.923	-0.383
			35.05	0.146	0.373	0.916
R4	HF1	48.08	-11.60	0.951	-0.241	-0.194
			-0.93	0.028	-0.558	0.829
			12.52	0.308	0.794	0.524
R5	HF1	-50.56	-30.75	0.098	-0.896	0.433
			4.71	0.973	-0.006	-0.232
			26.04	0.211	0.444	0.871
R6	HF1	26.02	-1.90	0.176	-0.949	0.263
			-0.49	0.661	-0.084	-0.746
			2.39	0.730	0.305	0.612
	HF2	-10.08	-10.70	0.708	-0.012	0.706
			-0.16	0.442	0.787	-0.430
			10.86	0.550	-0.617	-0.563

number of proton HFC lines. For nine interactions, assigned to five different radical species R1 - R5 using EIE (see below), enough data could be collected to determine the corresponding tensors. These are listed in Table 5.5.

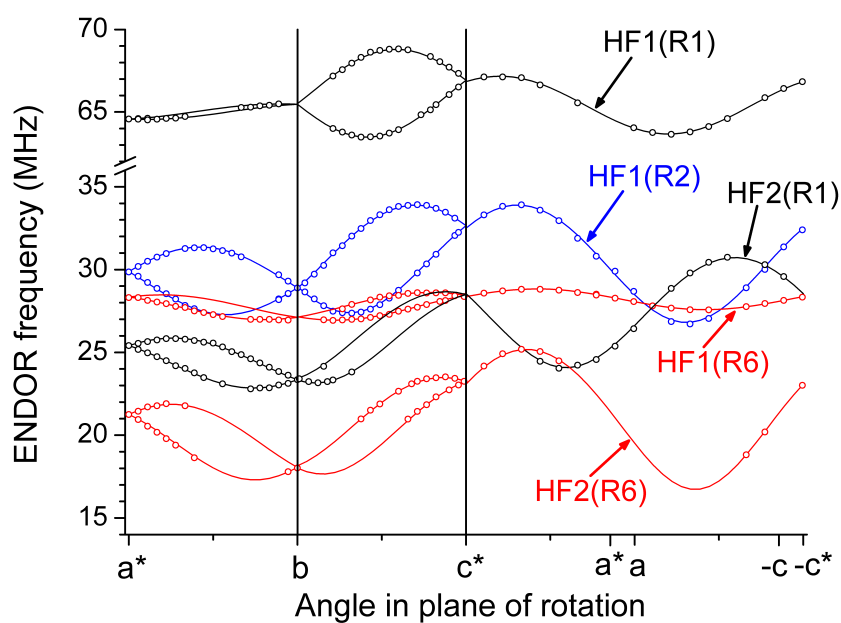
The Schonland ambiguity was eliminated for all HFC tensors by using at least one of the skewed planes for their determination. The experimental ENDOR frequencies and the simulations using the tensors of Table 5.5 are presented in Figure 5.10. From measurements on deuterated sucrose single crystals it could be concluded that all HFC interactions of Table 5.5 originate from non-exchangeable protons, except for HF1(R3) which therefore is due to a hydroxy proton. ENDOR and EIE spectra reveal that there are at least three other radical species present, for which no HFC tensors could be determined. This means that there are at least nine different radical species present. However, as will be demonstrated in Section 5.3.3.5, the major part (90 %) of the absorption can be assigned to the four radical species R1, R2, R3 and R6.

In Figure 5.11 two of the EPR spectra of Figure 5.9 are repeated, together with the corresponding EIE spectra of radicals R1-R6. Treating linewidths and g factors as variables, all EIE spectra could be accurately simulated using only the HFC tensors listed in Table 5.5. Comparison of Figures 5.11a and 5.11b reveals that the R6 g -tensor anisotropy is considerably larger than for the other radicals, indicating that it is the alkoxy radical reported by Box and Budzinski [135] (cf. Paragraph 5.2.2.2.2). The HF1 and HF2 HFC tensors of Table 5.5 indeed correspond well with tensors A1 and A3 respectively (Table 5.2, page 114), with regard to both principal values (maximum deviation of about 0.5 MHz) and principal directions (maximum deviation of about 3°). We were unable to determine tensors for the other HFC interactions (A2, A4, A5 and A6 in Table 5.2), but clear evidence for their presence was found in the ENDOR and EIE spectra.

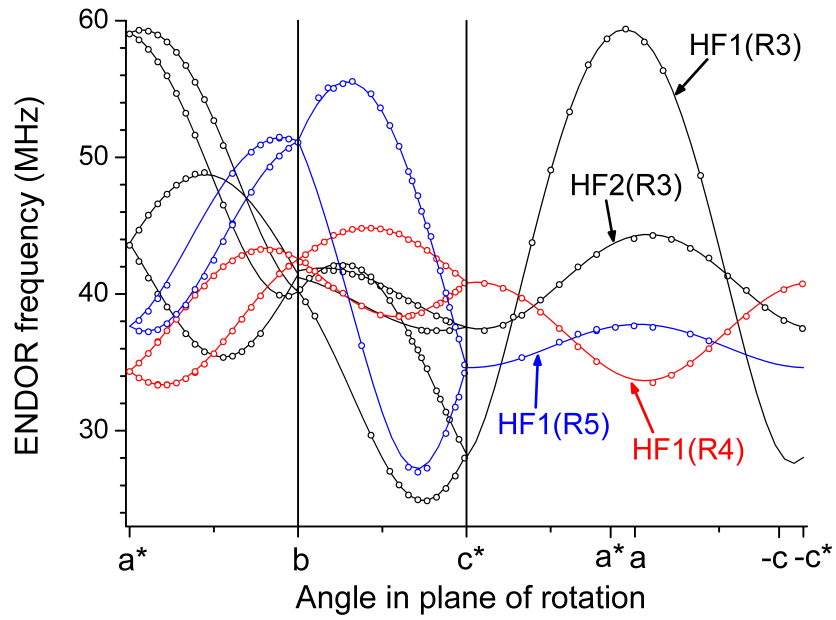
A trapped electron was observed at 4 K after *in-situ* irradiation at this temperature and was reported to be stable up to 61 K [130, 131] (cf. Paragraph 5.2.2.2.1). However, the EPR, ENDOR and EIE spectra obtained in the current study do not yield any clear evidence for the presence of the trapped electron. Either the trapped electron can somehow not be generated by X irradiation and subsequently trapped at 10 K (even though it is stable up to 61 K after X irradiation at 4 K) or the decay temperature reported in Ref. [130] is substantially overestimated.

Figure 5.12 shows ENDOR spectra recorded at different magnetic field values for the two orientations in Figures 5.12(a) and 5.12(b). Each of the ENDOR lines associated with radical R1 were accompanied by one or more other lines, usually of weaker intensity. These lines were typically 0.2 - 0.5 MHz separated from the R1 ENDOR lines, but exhibited the same ENDOR angular variation and yielded very similar EIE spectra. In Figure 5.12 these groups

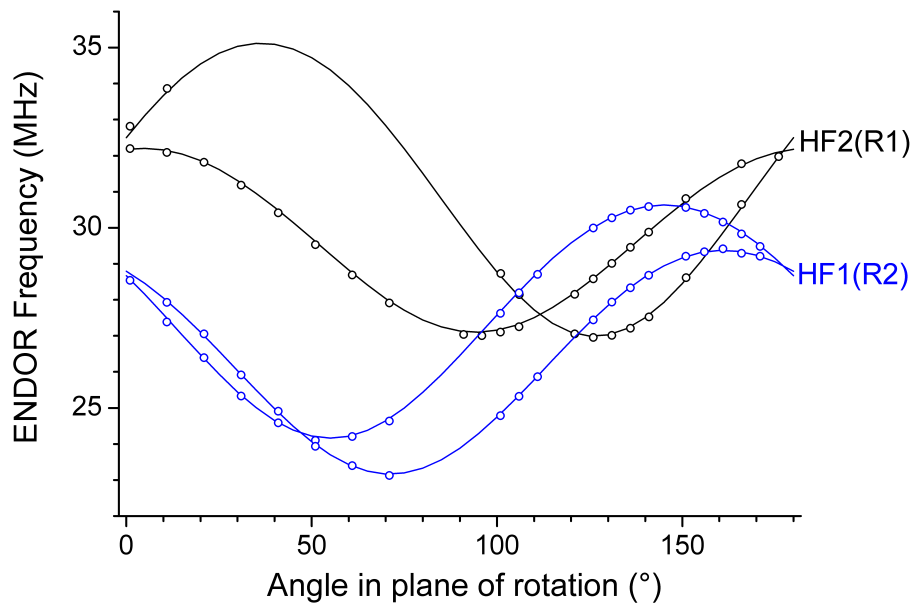
Figure 5.10: Angular variation of the ENDOR transitions in sucrose single crystals, measured at 10 K after *in-situ* X irradiation at this temperature, for the HFC interactions associated with radicals R1-R6 in the three planes perpendicular to the crystal axes (a,b), and in the skewed planes defined by $\theta = 96.2^\circ$ and $\phi = 48.4^\circ$ (c) and $\theta = 99.5^\circ$ and $\phi = -46.9^\circ$ (d). In each of the skewed planes, the angle of 0° corresponds to the projection of the $\langle c \rangle$ axis in the plane. The labelling scheme of Table 5.5 is used. All spectra were normalised to a proton frequency of 14.83 MHz. The circles represent experimentally determined ENDOR positions, the full lines are the simulations of the ENDOR angular variations using the tensors in Table 5.5.



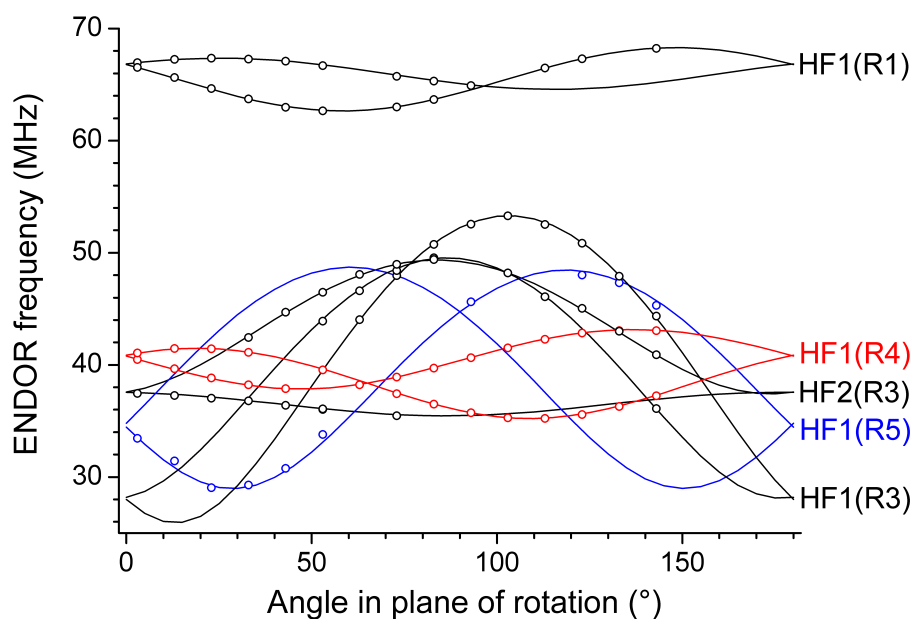
(a)



(b)



(c)



(d)

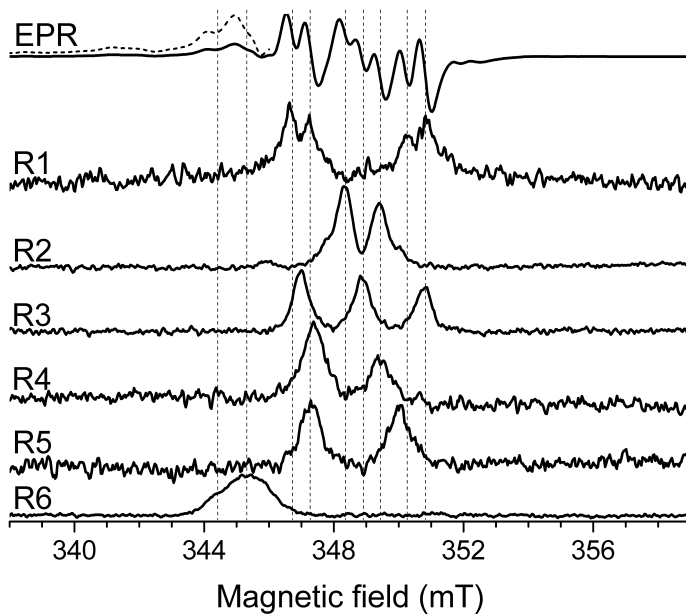
of HF1(R1) and "HF1(R1)-like" ENDOR lines are shown for both the high- and the low-frequency branch (labelled A and B respectively). Similar observations have been made for sorbose [161], fructose [146] and for the stable radicals in sucrose (Paper I). They are most easily interpreted in terms of slightly different conformations of one radical species. This (resolved) spread of resonance lines decreases the ENDOR signal intensity, which in turn explains why the EIE spectra of R1 suffer from a relatively low signal-to-noise ratio (Figure 5.11), while on the other hand R1 accounts for a significant portion of the EPR spectrum (see Section 5.3.3.5).

5.3.3.4 EPR annealing experiments after *in-situ* X irradiation at 10 K

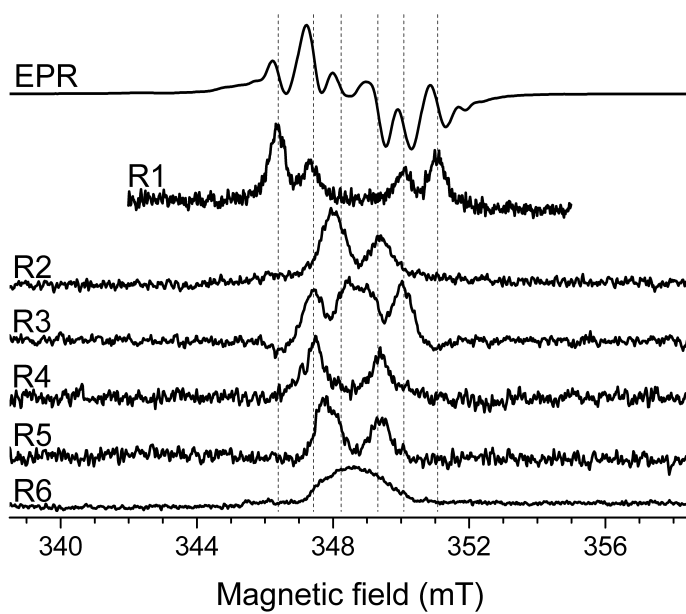
Upon annealing to RT after *in-situ* X irradiation at 10 K, the EPR spectrum of sucrose single crystals continuously undergoes changes (Figure 5.13). When RT is reached, the transformation continues for at least the next 2 days, but after 3 to 4 hours already the EPR spectrum shape remains essentially unaltered. Figure 5.13b demonstrates that

- the final spectrum resembles well that of the stable state after RT irradiation.

Figure 5.11: EPR spectrum and EIE spectra of radicals R1-R6 for $B \parallel \langle b \rangle$ (a) and $B \parallel \langle c^* \rangle$ (b). All spectra are normalised to 9.7600 GHz. The dashed line in (a) is the EPR spectrum multiplied with a factor of 3.

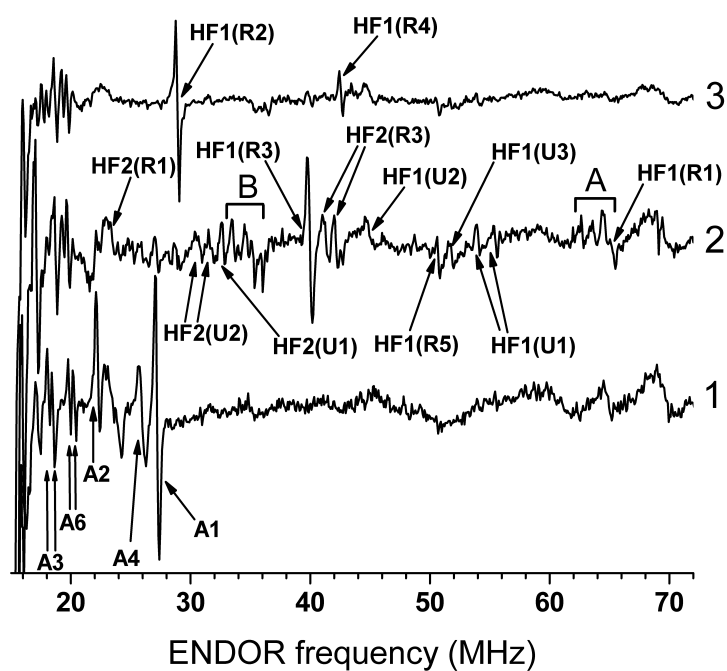


(a)

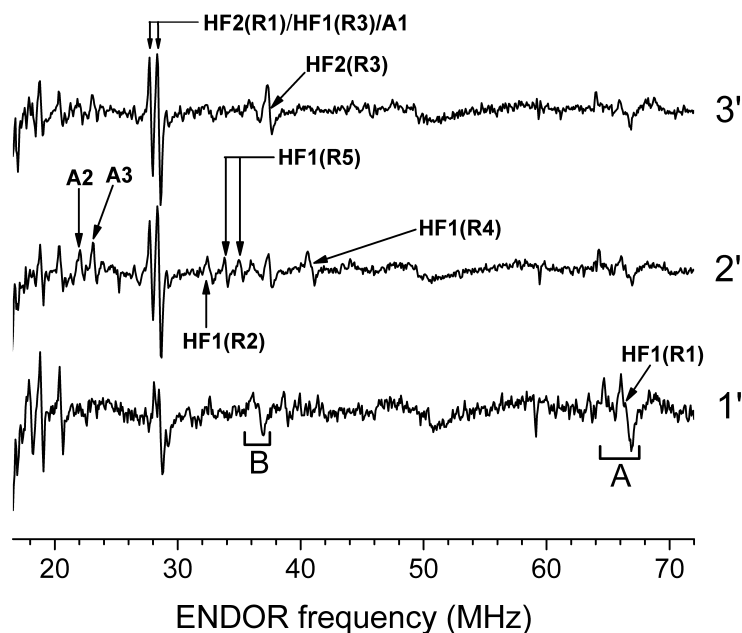


(b)

Figure 5.12: ENDOR spectra of sucrose single crystals at 10 K after *in-situ* X irradiation at 10 K for $B \parallel \langle b \rangle$ (a) and $B \parallel \langle c^* \rangle$ (b), normalised to a proton frequency of 14.83 MHz. The numbers on the right-hand side indicate at which positions in the EPR spectra of Figure 5.9 the ENDOR spectra were recorded. ENDOR lines are labelled according to the scheme of Table 5.5, except for R6, where the labelling of Ref. [135] is used: A1-A6 (HF1(R6) = A1 and HF2(R6) = A3). In (a) five other ENDOR lines, belonging to three different radical species, for which HFC tensors could not be obtained, are labelled: HF1(U1), HF2(U1), HF1(U2), HF2(U2) and HF1(U3). The letters 'A' and 'B' indicate high- and low-frequency ENDOR lines respectively, originating from radical species R1 and 'R1-like' (see text).



(a)



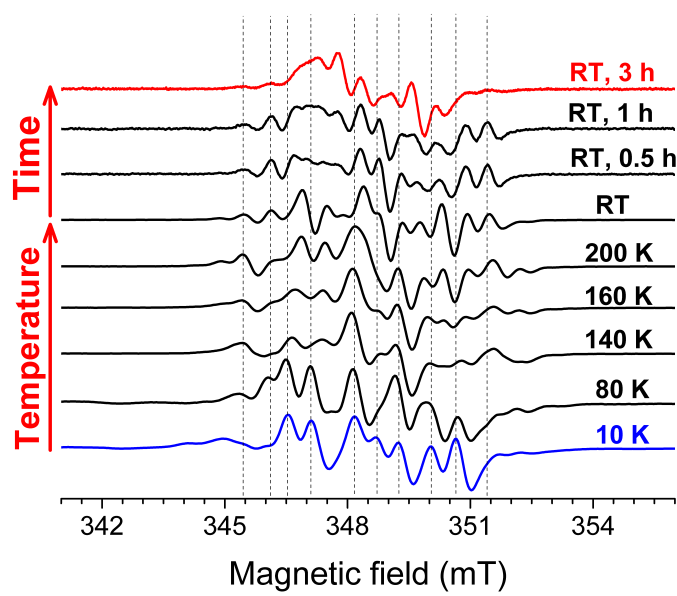
(b)

- the spectrum obtained immediately after annealing to RT most likely corresponds to the spectrum obtained immediately after RT irradiation (compare with the blue spectrum in Figure 5.7, page 123).¹² The broad triplet component dominating the spectrum for $B \parallel \langle c^* \rangle$ can then be assigned to radical species U1 (Section 5.3.2).

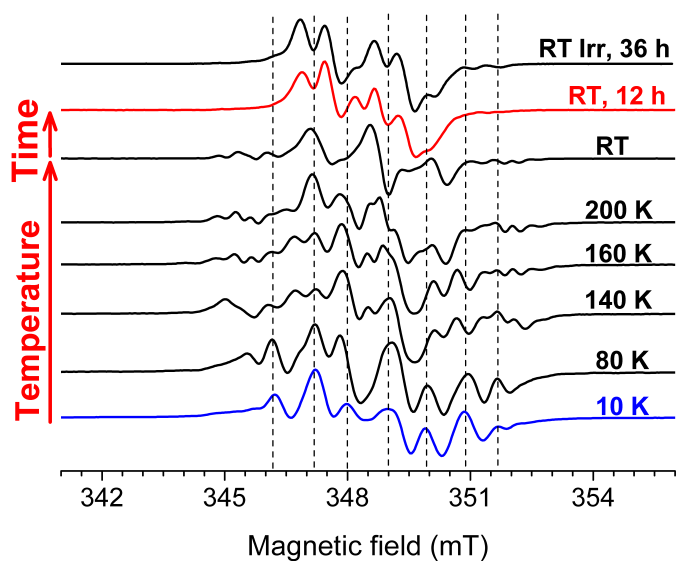
This strongly suggests that irradiating at low temperature only inhibits secondary radical processes and does not influence significantly the nature of the primary radicals formed (cf. Section 1.1.2.4, page 5). Since the stable radicals T1, T2 and T3 are formed upon annealing, relevant information about their formation mechanisms can certainly be extracted from low-temperature measurements after *in-situ* irradiation. Figure 5.13 indicates, however, that there could be several steps (intermediate radicals) between the radicals present at 10 K and the final stable radicals. Performing a full EPR/ENDOR/EIE analysis for all the other intermediate stages (80 K, 140 K, 200 K, ...) is quite challenging and time-consuming. Based on the results obtained in Section 5.3.2.2, it seems plausible that FF-ENDOR measurements could help guide these measurements and reduce the amount of work considerably.

¹²A direct comparison is not possible because of the difference in orientation and in microwave frequency (Figure 5.13b: $B \parallel \langle c^* \rangle$ and Q band; Figure 5.7: $B \parallel \langle c \rangle$ and X band).

Figure 5.13: EPR spectra recorded on sucrose single crystals for $B \parallel \langle b \rangle$ (a) and $B \parallel \langle c^* \rangle$ (b) during annealing to RT after *in-situ* X irradiation at 10 K – except for the top spectrum in (b), which was recorded at RT on a sample approximately 36 hours after RT irradiation. The measuring temperature is given on the right-hand side. For reasons of clarity, the spectrum intensities have been adjusted manually.



(a)



(b)

5.3.3.5 Relative abundances of the different radical species

As mentioned above, the EIE spectra of radicals R1-R6 recorded at the orientations $B \parallel \langle b \rangle$ and $B \parallel \langle c^* \rangle$ can be reproduced well using the HFC tensors in Table 5.5. Using the (isotropic) g values from the EIE simulations and treating the linewidths as variables, the experimental EPR spectra are reproduced satisfactorily when only contributions of R1, R2, R3 and R6 are considered. Small improvements can be made by mixing in minor amounts of radicals R4 and R5. By visual inspection, the relative contributions¹³ listed in Table 5.6 were obtained as a best fit for the two orientations simultaneously. The experimental and simulated spectra are shown in Figure 5.14. The

Table 5.6: Relative weights of radical species R1-R6 in the EPR spectrum, obtained from simulations of EPR spectra for two orientations (Figure 5.14). The first-order derivative spectra of R1-R6 were first normalised (double integral set to one) and the weight factors of these spectra in the best fit to the experimental EPR spectra are the relative concentrations listed here.

Radical	Conc. (%)
R1	15
R2	20
R3	30
R4	5
R5	5
R6	25

general agreement is good but there are still minor discrepancies between experimental and simulated spectra, mainly with regard to relative intensities. The simulations indicate that a relative concentration of 10 % is an upper limit for R4 as well as for R5, because larger concentrations give rise to features not observed in the experimental spectra.

5.3.3.6 DFT-assisted identification of R1 and R2

Radical R1 exhibits two typical β -proton HFCs (Table 5.5). Using the point-dipole approximation, carbon atom C5 emerges as the most plausible radical centre: the \vec{V}_{+2b} eigenvectors of HFC tensors HF1(R1) and HF2(R1) make angles of approximately 17° and 3° with the $C5 \cdots H4$ and $C5 \cdots H6b$ directions in the pristine lattice respectively. Radical R2 is characterised by only one β proton HFC of appreciable size and the point-dipole approximation here yields C1, C4 and C5 as most plausible sites for the unpaired electron: angles

¹³I.e. the weight factors of the first order derivative spectra with a normalised double integral (= total absorbance).

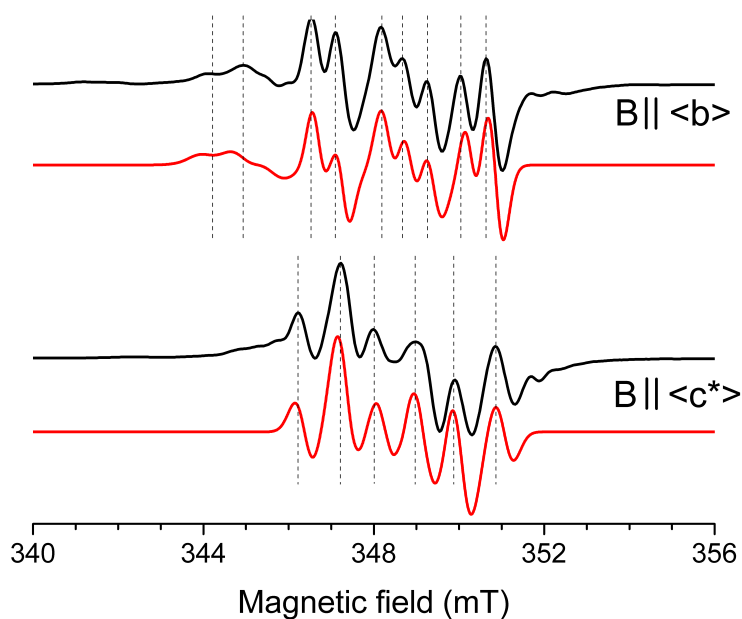


Figure 5.14: Experimental (black) and simulated (red) EPR spectra for two different orientations of the crystal in the magnetic field (cf. Figure 5.9). The simulations include contributions of radical species R1-R6, with the relative weights as listed in Table 5.6.

of $3 - 4^\circ$ are calculated between the \vec{V}_{+2b} eigenvector of HF1(R2) and C1...H2, C4...H5 and C5...H4. Assuming that the LEO is oriented along the original $C_\alpha - H_\alpha$ bond after H abstraction (that is, no or only minor rehybridization at C_α has taken place, the Heller-McConnell relation [91] can be used to calculate the expected isotropic HFC value for a β proton (see Section 4.3.3.1, page 91). These calculations support the C5-centred radical as model for R1 and favour the C1-centred radical over the others for R2. These radical models, labelled $R1_M$ and $R2_M$,¹⁴ are depicted in Figure 5.15. The DFT-calculated HFC tensors for $R1_M$ and $R2_M$ are listed and compared to the experimental data in Table 5.7. The agreement is very good in all respects, providing convincing evidence that $R1_M$ and $R2_M$ are the correct chemical structures of radical species R1 and R2. The DFT calculations do not predict any other proton HFC interaction that should have been detected experimentally, which further strengthens the radical model assignments.

¹⁴The subscript M again serves to distinguish between the real radical species and the proposed radical models.

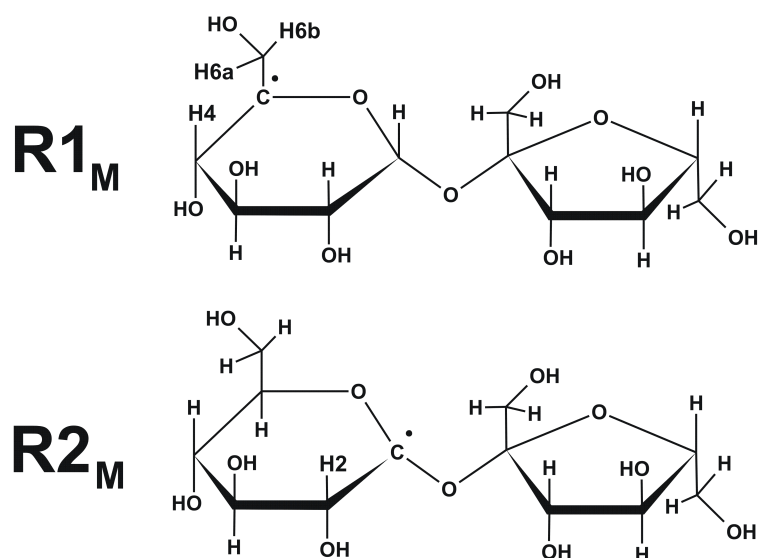


Figure 5.15: The chemical structure of radical models $R1_M$ and $R2_M$ for radical species R1 and R2 respectively. The DFT-calculated proton HFC tensors for these models are listed and compared to the experimental tensors in Table 5.7.

5.3.3.7 Tentative DFT-assisted identification of R3

Two proton HFC interactions were detected for radical R3 (Table 5.5). The HF1(R3) coupling is not observed in sucrose single crystals grown from a D_2O solution and must therefore arise from a hydroxy proton. The magnitude of the isotropic and anisotropic components indicates that it is in a β position. The HF2(R3) HFC tensor exhibits isotropic and anisotropic coupling elements typical of an α proton. Judging by the maximum positive dipolar coupling, the spin density at C_α is ~ 0.90 . The relative values of the isotropic coupling and the maximum positive dipolar coupling components indicates the radical centre is possibly slightly bent (cf. Section 4.3.2.1, page 86). When only net H-abstraction events are considered, three possible radical sites emerge: C6, C1' and C6'. The corresponding models ($R3_{Ma}$, $R3_{Mb}$ and $R3_{Mc}$ respectively) are depicted in Figure 5.16. The \vec{V}_{+a} eigenvector of an α proton is expected to be roughly parallel to the $C_\alpha^\bullet-H_\alpha$ bond direction and the α proton in a $CC_\alpha^\bullet H_\alpha OH$ radical is expected to reorient so that the $C_\alpha^\bullet - H_\alpha$ bond is approximately parallel to the bisector of the angle formed by C, C_α^\bullet and O. For models $R3_{Ma}$, $R3_{Mb}$ and $R3_{Mc}$, the angle between this bisector and the \vec{V}_{+a} eigenvector is 9° , 47° and 51° respectively. Also, the \vec{V}_0 eigenvector of an α proton is roughly parallel to the LEO axis. Assuming the latter is perpendicular to the plane formed by C, C_α^\bullet and O, angles of 24° , 62° and 70° are calculated for models $R3_{Ma}$, $R3_{Mb}$ and $R3_{Mc}$ respectively. These numbers suggest that $R3_{Ma}$ is the

Table 5.7: DFT-calculated proton HFC tensors ((an)isotropic values in MHz) for radical models $R1_M$ and $R2_M$ (Figure 5.15). δ is the angle between the calculated and the corresponding experimental eigenvector directions (cf. Table 5.5).

Mo- del	Pro- ton	Iso	Aniso	Eigenvectors			Pro- ton	δ (°)
				a*	b	c		
$R1_M$	H4	91.61	-5.68	0.375	-0.604	-0.703	HF1(R1)	7
			-1.08	0.846	0.533	-0.007		7
			6.75	0.379	-0.592	0.711		6
	H6b	15.84	-5.79	0.201	0.971	-0.128	HF2(R1)	13
			-3.49	0.894	-0.128	0.429		13
			9.28	0.400	-0.201	-0.894		1
$R2_M$	H2	28.88	-6.01	0.733	-0.082	-0.675	HF1(R2)	5
			-4.41	0.370	0.881	0.295		6
			10.42	0.571	-0.466	0.676		3

most plausible model.

However, a $CC_\alpha^\bullet H_\alpha OH$ group may have considerable conformational freedom and in order to exclude $R3_{Mb}$ and $R3_{Mc}$ with more certainty we performed DFT calculations on all three models. For each model, the final geometry was independent of which of the two carbon-bound hydrogen atoms was initially removed from the hydroxymethyl group. The calculated HFC tensors are given in Table 5.8. Neither of the models agree convincingly with the experimental data, but $R3_{Ma}$ gives the best fit between DFT-calculated and experimental HFC tensors.¹⁵ There are several possible explanations for the discrepancies:

1. *The actual radical geometry is trapped in a local minimum of the potential-energy surface (PES) different from the one that the DFT calculations end up in.*

Checking this requires scanning the PES for other minima. The most obvious degree of freedom is rotation of the O6-HO6 hydroxy group about the C5-C6 bond. We constructed an energy profile for this rotation using the same methodology as in Paper II: geometry optimisations were performed with the C5-C6-O6-HO6 dihedral angle constrained to values between 0° and 345° in 15° steps. We performed similar scans for the hydroxy groups of neighbouring molecules that are hydrogen bound to O6 or HO6. Although we found several alternative minima, some of them comparable in energy to the 'original' one, the DFT-calculated tensors were always in (much) worse agreement than for the conformation originally found. Other possible conformational alterations are currently

¹⁵It is noteworthy that the optimised geometry of $R3_{Ma}$ deviates significantly from planarity at C6: the C5-C6-H6-O6 dihedral angle is $\sim 152^\circ$.

Table 5.8: DFT-calculated proton HFC tensors ((an)isotropic values in MHz) for radical models $R3_{Ma}$, $R3_{Mb}$ and $R3_{Mc}$ (Figure 5.16). δ is the angle between the calculated and the corresponding experimental eigenvectors directions (cf. Table 5.5).

Model	Proton	Iso	Aniso	Eigenvectors			Proton	δ (°)
				a*	b	c		
$R3_{Ma}$	H6	-50.23	-34.69	0.980	0.067	-0.188	HF2(R3)	10
			-2.68	-0.180	0.697	-0.694		26
			37.36	0.085	0.714	0.695		24
	HO6	75.79	-12.96	0.259	-0.082	-0.962	HF1(R3)	70
			-8.76	0.794	0.585	0.164		61
			21.72	0.550	-0.807	0.217		32
	H5	15.18	-6.73	0.260	-0.497	0.828		
			-4.05	0.113	0.867	0.485		
			10.78	0.959	0.032	-0.281		
$R3_{Mb}$	H1'	-44.45	-33.58	0.352	0.237	-0.905	HF2(R3)	64
			-3.02	0.872	0.269	0.410		83
			36.61	-0.341	0.934	0.111		66
	HO1'	25.05	-12.44	0.578	0.257	0.774	HF1(R3)	71
			-9.63	-0.766	-0.154	0.624		74
			22.07	0.279	-0.954	0.108		39
$R3_{Mc}$	H6'	-53.68	-33.60	0.603	0.727	-0.327	HF2(R3)	55
			-1.86	-0.779	0.450	-0.437		57
			35.47	-0.171	0.518	0.838		21
	HO6'	17.62	-10.36	0.916	-0.282	0.284	HF1(R3)	77
			-9.32	-0.400	-0.651	0.645		66
			19.68	0.003	-0.705	-0.709		50
	H5'	1.68	-6.19	-0.081	0.577	0.813		
-4.32			0.765	-0.486	0.422			
			10.51	0.639	0.656	-0.402		

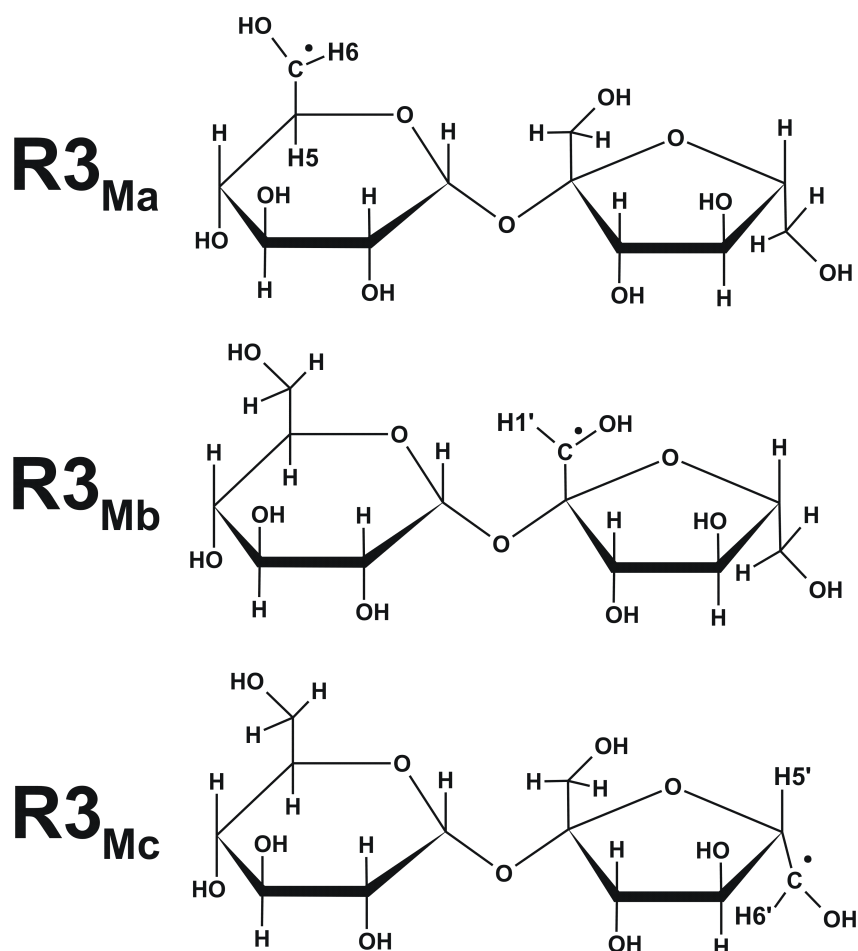


Figure 5.16: The chemical structure of radical models $R3_{Ma}$, $R3_{Mb}$ and $R3_{Mc}$ for radical species R3. The DFT-calculated proton HFC tensors are listed and compared to the experimental tensors in Table 5.8.

being explored, but our results (so far) suggest the explanation for the discrepancies must be sought elsewhere.

2. *The DFT calculations simply fail to predict the correct radical geometry.*

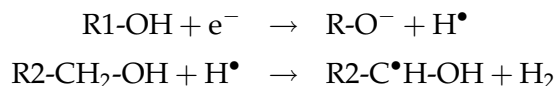
This explanation addresses the accuracy of the computational methodology used. A recent study at the CMM in Ghent clearly shows that the accuracy of the calculated EMR parameters mainly depends on the radical *geometry* [67].¹⁶ This study also shows that periodic calculations are superior to cluster calculations for geometry optimisations, which does however not mean that periodic calculations always yield correct results. The basis set and exchange-correlation functional might have

¹⁶The excellent agreement between experimental and DFT-calculated HFC tensors for radical species R1 and R2 (Table 5.7) is a further indication that the cause of the discrepancy is due to an erroneous radical geometry and not to an erroneous calculation of the HFC tensors.

a considerable influence on the optimised geometry in the case of a $CC_{\alpha}^{\bullet}H_{\alpha}OH$ radical fragment, which has more conformational freedom than radicals located on the ring carbons. In this context it is interesting to note that an overall good agreement between calculated and experimental HFC tensors can be obtained for both the H6 and the HO6 proton if (i) the H6 proton is repositioned so that the C6 radical centre is more planar and (ii) the O6-HO6 group is rotated by $\sim 30^{\circ}$ about the O6-C6 bond. In our current calculations, however, this does not correspond to a minimum of the PES.

3. *The proximity of a diamagnetic fragment resulting from radiation damage significantly influences the radical geometry.*

In our study on glucose 1-phosphate single crystals we showed that the fragments resulting from radiation damage can indeed have an important influence on the geometry of the radical and, consequently, EMR parameters (see Chapter 6 and Paper V). At 10 K, such fragments (H, H₂, ...) would have very limited mobility in the lattice. UV bleaching of sucrose crystals at 4 K after *in-situ* irradiation at 4 K seems to induce a conversion of the trapped electron to the R1 radical: the EPR absorption of R1 grows in, while the EPR absorption of the trapped electron fades.¹⁷ This could be explained in terms of the following reaction scheme [149]:



The H₂ molecule may stabilise in the direct vicinity of radical R1 and affect its geometry. Preliminary calculations have been performed, but so far without relevant results.

4. *Model R3_{Ma} is not correct.*

Based on the crystal structure and the limitations imposed by the experimental HFC tensors, and on a limited set of DFT calculations, radical models R3_{Mb} and R3_{Mc} do not appear to be plausible candidates. However, thorough and extensive DFT calculations are necessary to exclude these with more certainty. The possibility that R3 does not result from a net H-abstraction event should also be considered, even if more complex structural damage at 10 K does not seem very likely.

¹⁷These are unpublished results which we learned about through personal communication with Prof. E. Sagstuen (Oslo, Norway).

5.3.3.8 DFT-assisted validation of the literature model for R6

As noted in Section 5.3.3.3, this is the alkoxy radical thoroughly characterised by Box and Budzinski [135]. Because six proton HFC tensors were reported in that work (Table 5.2), as opposed to only two in the current work (HF1(R6) and HF2(R6) in Table 5.5), their data will be used here. Box and Budzinski assigned the HFC interactions to the structure depicted in Figure 5.4 on page 113. This structure is reproduced in Figure 5.17 and is labelled R6_{Ma}. It is an O3'-centred alkoxy radical where the HO3' proton (H_{Hop}) has migrated to the O4' oxygen of the neighbouring molecule (labelled Suc2 in Figure 5.17), to which it is hydrogen bound in the pristine lattice. The DFT geometry optimisation yields a stable conformation where the local hydrogen-bonding network is rearranged (Conf1, depicted in Figure 5.18b): the original HO4'(Suc2) hydrogen is located in between the O4'(Suc2) oxygen and the O1' oxygen of yet another molecule. The HFC and g tensors calculated for configuration Conf1 of model R6_{Ma} are given in Tables 5.9 and 5.10 respectively. The overall agreement between the experimental and calculated HFC tensors is striking and confirms the model assignment by Box and Budzinski. The correspondence in eigenvector directions between the experimental and DFT-calculated g tensors of Conf1 is also very good but the principal values agree only qualitatively. A strongly reduced g anisotropy is indeed predicted. The attribution by Box and Budzinski of the various HFC interactions to specific protons (summarised in Figure 5.4) is correct for A3-A6 (although the DFT calculations indicate the sign of the A3 tensor should be inversed). HFC interactions A1 and A2, however, originate from H1'b and H6'a, a δ and an ϵ proton respectively, and not from protons H1'a and H1'b. Substantial isotropic couplings to remote protons have been reported before for alkoxy radicals: in rhamnose, a δ proton with an isotropic HFC value of 76 MHz was even observed [103].

In spite of the generally good agreement, some (minor) discrepancies are encountered between DFT-calculated and experimental HFC tensors with respect to the isotropic HFC values, e.g. for H3' (-4 MHz in the DFT calculation versus 15 MHz experimentally). Also, DFT calculations predict an isotropic value of about 9 MHz for a HFC interaction (H5'(Suc1) in Table 5.9) with the H5' proton of a neighbouring molecule (Suc1 in Figure 5.17), but such a HFC was not reported experimentally. Possible explanations are:

- Isotropic HFC values are very sensitive to both small variations in the precise electronic configuration and the specific computational methodology (basis set, exchange-correlation functional, ...).

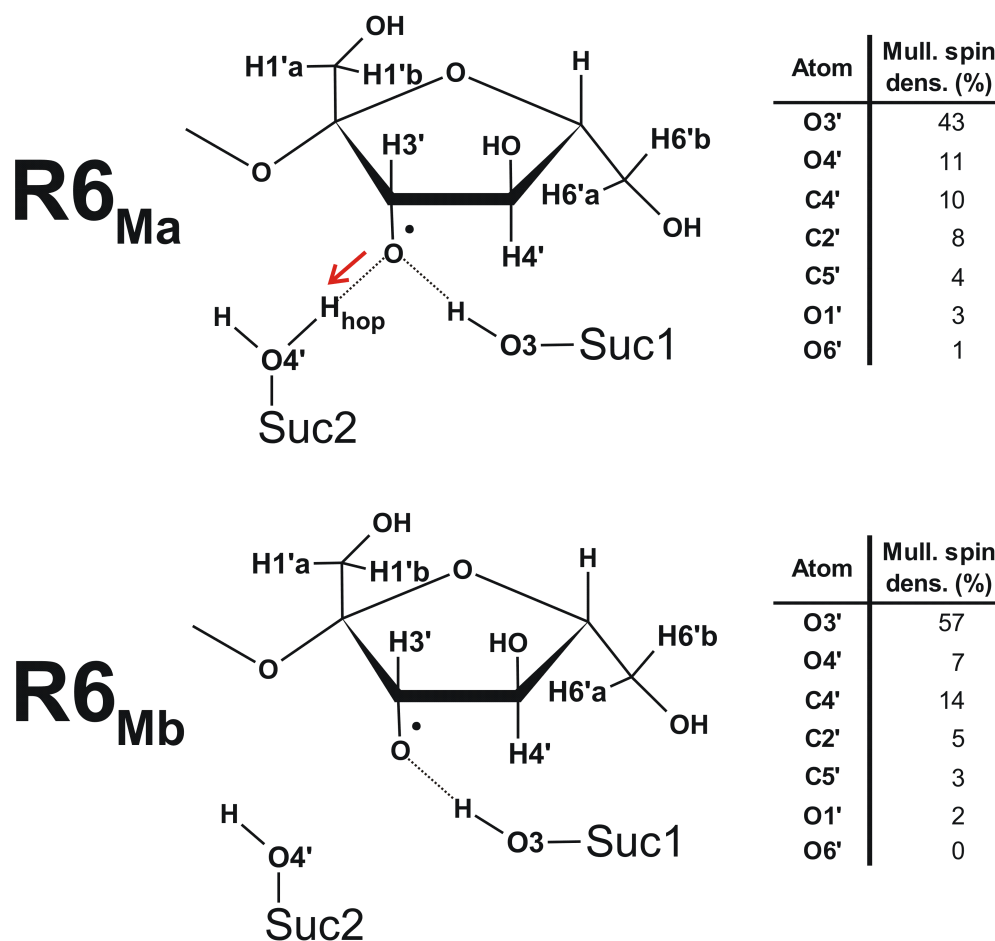


Figure 5.17: The chemical structure of models R6_{Ma} and R6_{Mb} for radical species R6. R6_{Ma} is a singly positively charged species where the abstracted HO3' proton has migrated to the hydrogen-bonded O4' oxygen of a neighbouring molecule (Suc2). R6_{Mb} is a neutral species where the HO3' hydrogen is removed altogether. On the right-hand side, Mulliken spin densities are given some radical atoms are given.

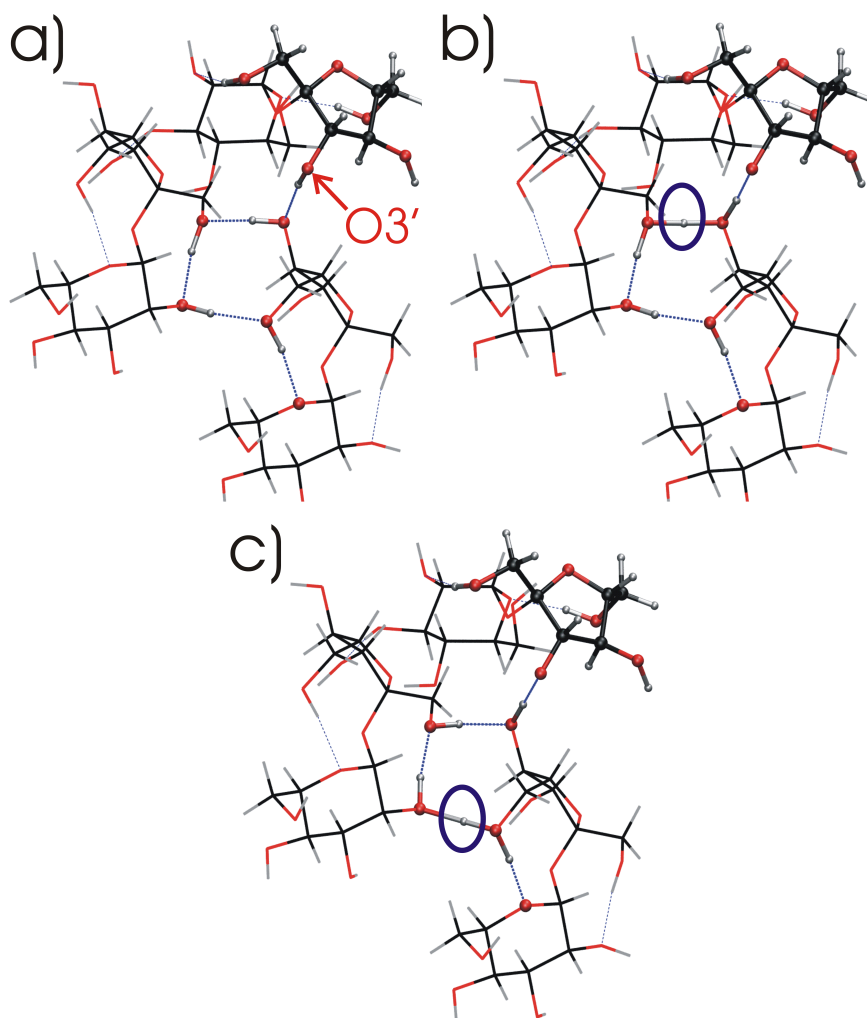


Figure 5.18: The periodically optimised geometry of the intact lattice (a) and conformations Conf1 (b) and Conf2 (c) of radical model R6_{Ma} (see Figure 5.17). The HO3' hydrogen is part of a hydrogen-bonding network (blue dotted lines) terminating in the ring oxygen of the glucose unit of a neighbouring molecule. Conf1 and Conf2 have a net positive charge. The circles in (b) and (c) indicate where the hopping proton is located. The DFT-calculated proton HFC tensors of Conf1 are given in Table 5.9.

Table 5.9: DFT-calculated proton HFC tensors ((an)isotropic values in MHz) for radical model $R6_{Ma}$ in conformation Conf1 (see Figures 5.17 and 5.18b). δ is the angle between the calculated and the experimentally determined eigenvector directions (see Table 5.2, page 114). The signs of the A3 principal values have to be inverted to obtain a good agreement with the H4' proton HFC tensor.

Proton	Iso	Aniso	Eigenvectors			Proton	δ (°)
			a*	b	c		
H1'b	41.70	-2.10	0.165	0.941	0.296	A1	4
		-0.60	0.497	0.180	-0.849		12
		2.70	0.852	-0.287	0.438		11
H6'a	19.35	-1.47	0.362	0.750	0.554	A2	8
		-0.30	-0.319	-0.459	0.830		7
		1.76	0.876	-0.477	0.073		4
H4'	-5.75	-6.80	0.711	0.025	0.703	A3	3
		-1.03	-0.422	0.815	0.397		4
		7.83	0.564	0.578	-0.590		3
H3'	-4.02	-4.47	0.902	-0.359	0.240	A4	14
		-3.12	-0.138	0.287	0.948		14
		7.59	0.409	0.888	-0.209		5
HO3(Suc1)	-0.59	-4.79	0.377	0.815	0.441	A5	6
		-4.33	0.230	-0.543	0.807		7
		9.12	0.897	-0.203	-0.392		5
H _{hop}	-1.48	-7.09	0.921	-0.385	-0.066	A6	10
		-6.14	0.154	0.204	0.967		10
		13.24	0.358	0.900	-0.247		2
HO4'	-1.63	-7.56	-0.860	-0.469	-0.201		
		-3.38	-0.502	0.711	0.493		
		10.94	0.088	-0.525	0.847		
H5'(Suc1)	9.26	-3.72	-0.905	-0.187	0.383		
		-1.98	0.123	0.745	0.656		
		5.70	0.408	-0.640	0.651		

Table 5.10: Experimental g tensor [135] (cf. Table 5.2) and DFT-calculated g tensor of conformations Conf1 and Conf2 of radical model $R6_{Ma}$ (Figures 5.18b and 5.18c respectively) and for radical model $R6_{Mb}$ (Figure 5.17). δ is the angle between the calculated and the experimental eigenvector directions.

	Princ	Eigenvectors			$\delta(^{\circ})$	
		a*	b	c		
Experiment [135]	2.0037	-0.072	0.046	0.996		
	2.0087	-0.889	-0.454	-0.043		
	2.0270	0.450	-0.889	0.074		
$R6_{Ma}$	Conf1	2.0057	-0.011	0.022	1.000	4
		2.0102	-0.928	-0.373	-0.002	6
		2.0210	0.373	-0.927	0.024	6
	Conf2	2.0055	-0.019	0.011	1.000	4
		2.0098	-0.886	-0.464	-0.012	3
		2.0211	0.464	-0.886	0.019	4
$R6_{Mb}$	2.0044	-0.288	-0.177	0.941	18	
	2.0091	-0.702	-0.630	-0.333	22	
	2.0324	0.652	-0.756	0.057	14	

- The positive charge of the structure may render periodic calculations less accurate, as we have experienced in our study on glucose 1-phosphate single crystals (Paper V).
- The H5'(Suc1) proton could really be present but could have escaped experimental detection: its ENDOR lines would only appear in a very crowded frequency range and R6 has a broad EPR (EIE) signal with unresolved hyperfine structure.

In our opinion, these discrepancies do not invalidate $R6_{Ma}$ we will proceed assuming it is correct.

The present alkoxy radical has two peculiar properties (see Section 5.2.2.2.2, page 112): a small g anisotropy and a high degree of spin polarisation at certain remote protons. We performed DFT calculations on model $R6_{Mb}$ (Figure 5.17, the O3'-centred alkoxy radical where the HO3' hydrogen is removed altogether) to assess the possible role of the hopped HO3' proton (H_{hop} in Figure 5.17) with respect to these properties. The calculated HFC tensors are comparable to those of Conf1 of $R6_{Ma}$ - although the agreement with the experimental HFC tensors is somewhat less good - and are therefore not reported here. The g -tensor anisotropy is considerably larger than for Conf1 of $R6_{Ma}$, but still small for an alkoxy radical (Table 5.10). Clearly, the presence of the hopped proton is not crucial for the aforementioned peculiar properties of the alkoxy radical.

As noted above, the A6 HFC tensor can readily be attributed to the migrated

proton. This raises the question whether further proton-hopping events may occur and, if so, where the hopping proton is finally trapped. In a previous study, possible extended proton-hopping mechanisms were investigated for an alkoxy radical in rhamnose [162]. On the basis of energetic considerations, that study suggests that successive proton transfers along hydrogen bonds might occur until the proton is trapped in a lattice defect or recombines with a (radical) anion. In the present case, the hydrogen-bonding network in the pristine lattice terminates at the ring oxygen of a glucose unit, five hydrogen bonds away from O3' (Figure 5.18a). Conformations resulting from subsequent proton-hopping events along this hydrogen bond chain were considered. Apart from Conf1 (Figure 5.18b), one other conformation was found that corresponds to a local minimum on the PES: Conf2 (4 proton hops), depicted in Figure 5.18c. Other initial conformations were found to be unstable and readily transformed to either Conf1 or Conf2. The energy of Conf2 is 14 kJ/mol higher than that of Conf1 and the DFT-calculated HFC tensors for Conf2 are in slightly worse agreement with their experimental counterparts than for Conf1 with respect to the eigenvector directions. Also, the g tensors of Conf1 and Conf2 differ from each other only marginally (Table 5.10). These results indicate that the HFC and g tensors do not allow discriminating between the different conformations. Thus, we can only rely on energetic considerations and these suggest that extended proton-hopping events do not occur at 10 K in the present alkoxy radical.

5.3.3.9 R4 and R5: some observations

Suitable H-abstracted radical models could not readily be found for R4 and R5. As discussed in Section 5.3.3.5, these are apparently minority species and therefore no further (thorough) attempts were made at identifying them. We will limit our discussion to a brief description of their characteristics.

The EIE spectra of radical species R4 (Figure 5.11) are broad-line doublets. Only for the major HFC interaction a HFC tensor could be extracted (HF1(R4) in Table 5.5). The magnitude of the principal values may indicate that the proton is in the proximity of the radical centre, but the coupling cannot readily be attributed to either an α or a β proton: the anisotropy is too small for the former and does not have the right symmetry for the latter. The anisotropic HFC values do resemble, however, those of certain γ protons in alkoxy radicals (e.g. A3 in Table 5.2). However, alkoxy radicals have maximum principal g values typically varying between 2.021 and 2.110 (see Section 4.4.2.2, page 102). The EIE spectra of Figure 5.11 do suggest that R4 has principal g values slightly higher than those of common carbon-centred radicals, but the data

currently available do not allow determination of the g tensor. Limited (< 20 %) delocalisation of the spin density onto an oxygen may explain both the somewhat odd HF1(R4) tensor shape and the slightly elevated g -tensor principal values. Also note that the principal values of the HF1(R4) tensor could have signs opposite to those in Table 5.5.

Radical species R5 is also characterised by a broad-line doublet and, again, only the tensor of the major HFC interaction could be determined (HF1(R5) in Table 5.5). It has the typical characteristics of an α proton. As discussed in Section 5.3.3.7, only three simple H-abstracted radical models can be envisaged: R3_{Ma}, R3_{Mb} and R3_{Mc} (Figure 5.16, page 141). The DFT-calculated α -proton HFC tensor of R3_{Mc} (Table 5.9) yields the best agreement with HF1(R5) with respect to the eigenvector directions, but the deviations are still too large: 22°, 49° and 43°. Also, the EIE spectrum cannot accommodate the DFT-calculated HO6' HFC tensor.

5.3.4 Overview and possible reaction mechanism

Figure 5.19 provides an overview of the radicals identified in X-irradiated sucrose single crystals so far. Next to the identification of radicals, one of the goals of the doctoral research was to identify formation mechanisms of the stable radicals. A considerable amount of the information necessary to achieve this goal has already been collected. However,

- the formation of the stable radicals may well involve several semistable precursors (cf. Section 5.3.3.4).
- one or more (very) short-lived intermediate radicals might be involved, that cannot be detected by CW-EPR experiments, even when using *in-situ* X irradiation at low temperatures.
- the stable radicals might be the end products of (primary) radicals that are not dominant at 10 K.
- there are many possible formation routes. A number of radical processes have been established in the literature, β -elimination reactions and 1,2-H-shifts probably being the most important ones.¹⁸ Starting from the radical species identified at 10 K, numerous reaction routes can be constructed with these 'building blocks' that finally end up in the stable radical structures.

¹⁸As commented in Section 1.1.2.3, these processes were studied and identified mainly in aqueous solution chemistry, but are generally assumed to take place in the solid state as well.

Taking these considerations into account, it is clear that at present we can only make an educated guess about the formation mechanisms. For T1 there is no obvious reaction path starting from the radicals present and identified at 10 K. For T2/T3, however, a particularly simple reaction route can be invoked, starting from $R2_M$ and involving only one intermediate step (Figure 5.20). Low-temperature measurements (at 80 K, 140 K and 200 K, cf. Section 5.3.3.4) after *in-situ* X irradiation at 10 K are likely to yield information on the radical formation mechanisms.

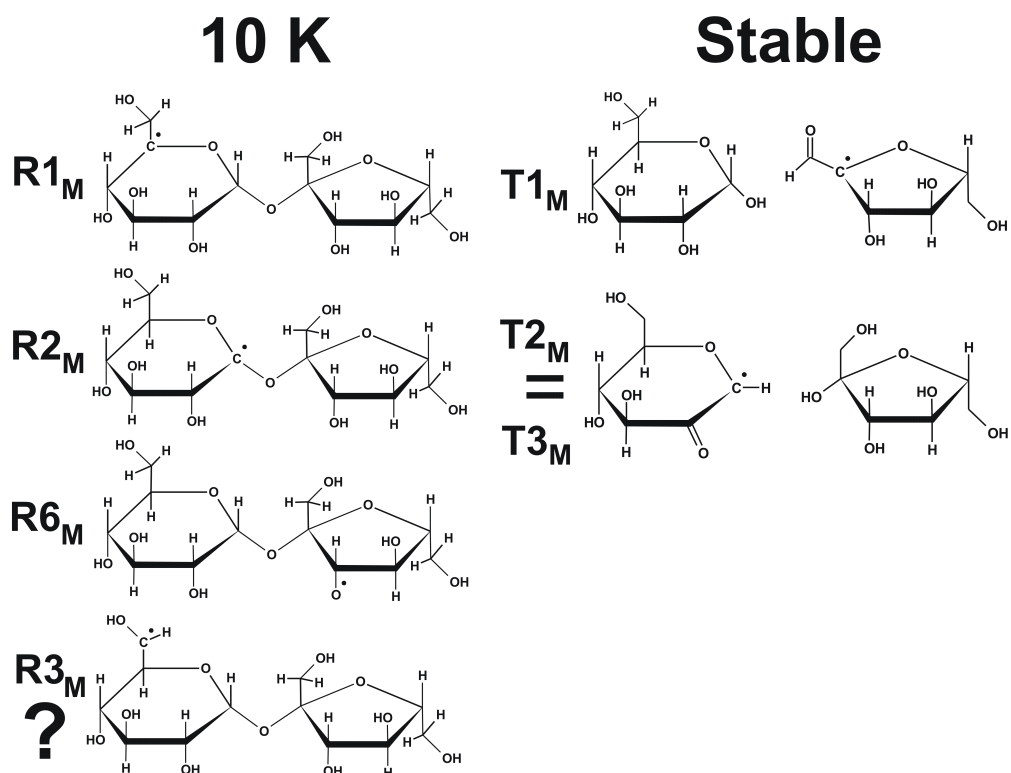


Figure 5.19: Overview of the radicals identified in X-irradiated sucrose single crystals after *in-situ* irradiation at 10 K (left) and in the stable state (right). Model $R3_M$ is still tentative.

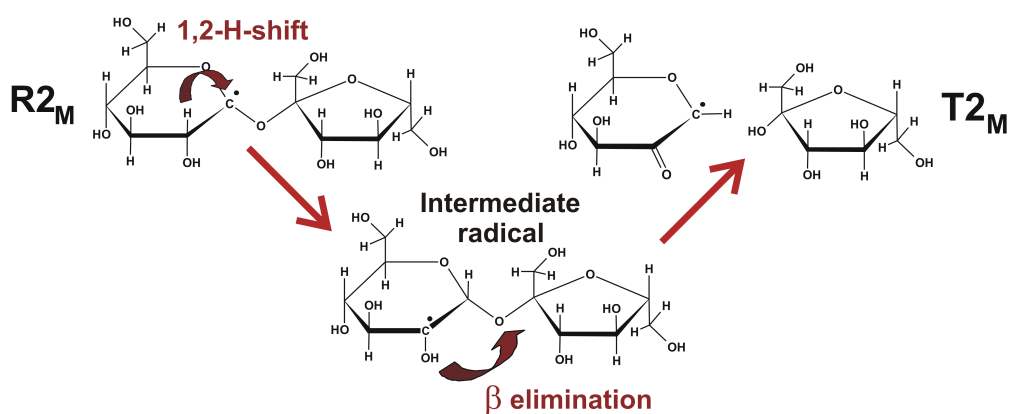


Figure 5.20: Possible formation mechanism of stable radical species $T2/T3$, starting from radical species $R2$ detected after *in-situ* X-ray irradiation at 10 K.

Chapter 6

Radiation-induced radicals in K₂G₁P single crystals

6.1 Chemical structure and crystal structure

Glucose 1-phosphate (systematic name: *α*-D-glucose 1-phosphate and abbreviated G1P henceforth) consists of a glucose molecule with a phosphate group attached to the C1 position (Figures 6.1 and 6.2A). Single crystals can be grown

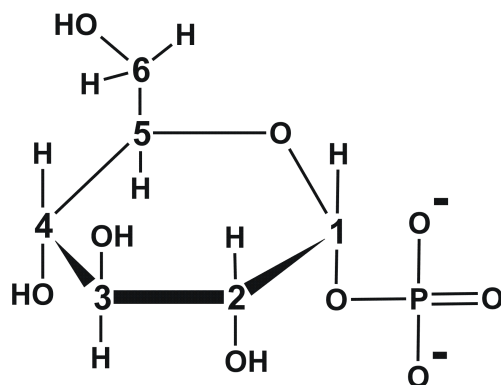


Figure 6.1: The chemical structure of a glucose 1-phosphate (G1P) molecule. In this chapter, carbon atoms are numbered as CX ($X=1-6$) according to the IUPAC convention, hydrogen atoms and oxygen atoms bound to CX are labelled HX and OX respectively, hydroxy hydrogen atoms at CX are labelled HOX.

of the dipotassium salt of glucose 1-phosphate dihydrate (K₂G₁P). Several studies have reported on its crystal structure [163–165]. We used the results of the study by Sugawara and Iwasaki [165], which provides the most accurate and complete set of atomic coordinates (listed in Table B.1 of Appendix B). The crystal is monoclinic with space group P2₁ (as was the case for sucrose

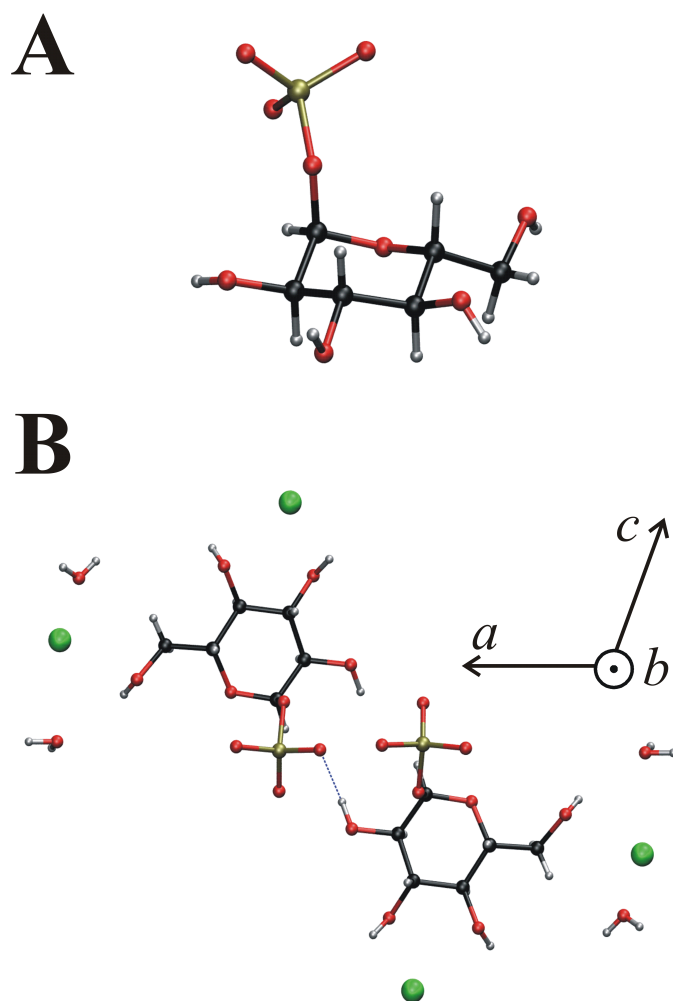


Figure 6.2: The G1P molecule in the K2G1P lattice conformation (**A**) and a unit cell of the K2G1P lattice viewed along the monoclinic $\langle b \rangle$ axis (**B**). C atoms are depicted in black, O atoms in red, H atoms in grey, K^+ ions in green and P atoms in gold.

single crystals, see Section 5.1) and the unit-cell parameters are $a = 1.0458$ nm, $b = 0.9027$ nm, $c = 0.7532$ nm and $\beta = 110.39^\circ$. A unit cell contains two G1P molecules (each of them with a double negative charge on the phosphate group, cf. Figure 6.1), four K^+ -ions and four water molecules (70 atoms in total). Figure 6.2 shows the unit cell of the lattice viewed along the monoclinic $\langle b \rangle$ axis.

Table 6.1: Proton HFC tensors ((an)isotropic values in MHz) for a hydroxyalkyl radical present in K2G1P single crystals after *in-situ* X irradiation at 4.2 K, as reported by Locher and Box [108].

Proton	Iso	Aniso	Eigenvectors		
			a*	b	c
A1	-53.12	-32.10	0.983	-0.089	0.159
		0.69	-0.131	0.263	0.957
		31.41	-0.127	-0.961	0.247
A2	22.28	-7.32	0.298	0.583	-0.756
		-2.73	0.688	0.400	0.539
		10.04	0.644	-0.708	-0.292
A3	44.64	-13.25	0.645	-0.383	-0.662
		-9.03	0.194	-0.755	0.627
		22.28	0.739	0.532	0.412

6.2 EMR results in the literature

From V-band (70 GHz) EPR and ENDOR measurements on K2G1P crystals at 4.2 K after *in-situ* X irradiation at this temperature, Locher and Box [108] characterized three alkoxy radicals, one of which was identified as the O6-centred species. In addition, these authors identified an intermolecularly trapped electron and a C6-centred hydroxyalkyl radical. The HFC tensors of the latter species will be of interest in Section 6.3 and are listed in Table 6.1. Because detailed crystal data were not available for these authors, no further analysis was made. The bulk of the absorption was reported to occur around $g \approx 2.0030$ where the EPR signal is strongly composite, indicating that the major part of the radicals present at 4 K are carbon centred. No evidence for phosphate radicals was observed. Bungum et al. studied K2G1P single crystals X irradiated at 280 K using X- and Q-band EPR techniques at RT [144]. Two varieties of the phosphoryl radical ($\text{P}^\bullet\text{O}_3^{2-}$) were observed. Furthermore, their reanalysis of the data of Locher and Box [108] and comparison with the crystal structure of Refs. [163, 164] confirmed the identity of both the O6-centred alkoxy radical and the C6-centred hydroxyalkyl radical and suggests that the other two alkoxy radicals are the O2- and the O4-centred species [145].

Nelson et al. performed measurements on irradiated frozen aqueous solutions of monosodium D-glucose 6-phosphate [166]¹ which revealed that after X irradiation at 77 K phosphoranyl radicals ($\text{P}^\bullet\text{O}_4^{3-}$) are formed. This species decays into two new, different centres upon annealing to RT. One of these centres most likely is a phosphoryl radical, but the identity of the second one is uncertain. The composite central part of the spectrum arising from

¹The authors of Ref. [166] erroneously reported these results to be obtained on the disodium salt instead of the monosodium salt. A correction was made in Ref. [167].

6.3. Own research results: radicals present in K2G1P single crystals after *in-situ* X irradiation at 77 K

carbon-centred glucose radicals also transforms upon annealing, but only very tentative attributions were made in terms of radical models.

A more elaborate and general study on phosphate radicals² was published in 1996 by Sanderud and Sagstuen [167]. From powder-EPR studies on several phosphate esters at both 77 K and 275 K after *in-situ* X irradiation at these temperatures, they tentatively concluded that phosphoryl radicals may be formed through several distinct pathways, depending on the net charge and the protonation state of the parent phosphate group with hydroxyalkyl sugar radicals acting as precursors in each pathway suggested. In the case of K2G1P, no phosphoryl or phosphoranyl radicals were detected after X irradiation at 77 K, but two varieties of phosphoryl radicals were observed after X irradiation at 275 K, in agreement with the results reported by Bungum et al. [144]. It was suggested that a sugar radical acts as a precursor for it.

An interesting question thus arises for K2G1P: which initially formed species (detectable after low-temperature irradiation) transforms into the phosphate radicals detected at RT, and how? The prerequisite for answering this question is knowledge of the chemical identity of the sugar radicals present after 77 K X irradiation. In Papers IV and V, the composite EPR signal at $g \approx 2.0030$ of K2G1P single crystals irradiated and measured at 77 K was analysed using EMR measurements and DFT calculations. In the next section, the main results and conclusions of these papers are summarised.

6.3 Own research results: radicals present in K2G1P single crystals after *in-situ* X irradiation at 77 K

We performed an extensive EMR analysis at 77 K on defects present in K2G1P single crystals after *in-situ* X irradiation at this temperature. This included ENDOR angular variations in the three planes perpendicular to the $\langle a \rangle$, $\langle b \rangle$ and $\langle c \rangle$ axes (for several magnetic field values at each orientation) as well as EIE measurements at a large number of orientations. From these data we were able to determine the thirteen proton HFC tensors listed in Table 6.2. The experimental ENDOR frequencies and the simulations using the tensors of Table 6.2 are given in Figure 6.3. Following remarks should be made:

- Eight of the tensors could be assigned to four different radical species (R1 to R4).
- Both R3 and R4 exhibit a substantial HFC interaction for which the tensor could not be determined (HF2(R3) and HF3(R4) respectively) and only

²I.e. any phosphorus-centred radical

the (observed) range of the principal values is given in Table 6.2 for these couplings.

- tensors HFU1, HFU2 and HFU3 cannot be attributed to any of the radical species R1-R4. No conclusions could be drawn in this respect for HFU4 and HFU5.
- next to R1-R4, at least three other minority carbon-centred radical species are present. These could not be analysed in detail due to technical limitations (distortions of the ENDOR spectra, especially at higher ENDOR frequencies (> 60 MHz)). It was established, however, that two of the three (labelled R6 and R7 in Paper IV) are each characterized by at least two strong HFC interactions (isotropic HFC value > 85 MHz).
- Measurements on (partially) deuterated K2G1P single crystals revealed that HF3(R4) is due to an exchangeable proton, while all other HFC interactions of R1 to R4, except HF2(R3), are due to non-exchangeable protons. No conclusions could be drawn for HF2(R3) or any of the HFUX (X=1-5) interactions.
- The Schonland ambiguity (cf. Section 2.4.2.2 page 44) could not be eliminated for the HFC tensors with the available data. In most cases at hand, however, either the two HFC tensors were (accidentally) virtually identical or one HFC tensor was highly favoured over the other on account of the symmetry properties of the principal values. Because neither option applied to HF1(R2) and HF1(R4), both Schonland variants are reported in Table 6.2. Comparison of the HFC eigenvector directions with crystal directions and with DFT-calculated eigenvector directions for the radical models (see below) favour HF1b(R2) over HF1a(R2) and HF1a(R4) over HF1b(R4).

Using spectrum simulations, we showed that radical R2 dominates the EPR spectrum whereas the relative concentrations of R1, R3 and R4 are (very) small. R6 and R7 possibly account for some of the more intense outer features of the EPR spectrum, which cannot be attributed to R2.

When the sample is annealed to RT after irradiation at 77 K, phosphoryl radical signals are (immediately) observed. The signals are very faint at RT, but well detectable when the sample is re-cooled to 100 K. Due to the very low signal-to-noise ratio upon annealing, we could not establish at which temperature the phosphoryl radicals are formed and which sugar radical(s) act(s) as precursor(s).

6.3. Own research results: radicals present in K2G1P single crystals after *in-situ* X irradiation at 77 K

Table 6.2: Proton HFC tensors ((an)isotropic values in MHz) of radical species present in K2G1P single crystals after *in-situ* X irradiation at 77 K, determined from ENDOR measurements at 77 K. For HF2(R3) and HF3(R4), only the observed range of the coupling size is given. For HF1(R2) and HF1(R4), the two Schonland-conjugate tensors are given (a and b, see text).

Radical	Proton	Iso	Aniso	Eigenvectors		
				a*	b	c
R1	HF1	79.24	-3.86	0.546	-0.365	-0.754
			-3.30	0.626	0.776	0.077
			7.16	0.557	-0.514	0.653
	HF2	71.71	-4.81	0.062	0.612	-0.788
			-2.87	0.394	0.711	0.583
			7.68	0.917	-0.346	-0.197
R2	HF1a	-41.55	-22.97	0.705	-0.298	-0.643
			0.63	0.238	0.954	-0.182
			22.34	0.668	-0.024	0.744
	HF1b	-41.53	-21.45	0.744	0.134	-0.654
			-2.41	0.046	0.967	0.251
			23.86	0.666	-0.216	0.714
	HF2	15.78	-2.54	0.651	-0.754	0.087
			-1.78	0.596	0.436	-0.674
			4.31	0.471	0.491	0.733
	HF3	10.16	-3.40	0.333	-0.700	0.632
			-2.35	0.430	-0.484	-0.762
			5.75	0.839	0.525	0.140
R3	HF1	-50.97	-31.07	0.928	0.078	-0.363
			2.33	0.285	0.479	0.830
			28.75	0.239	-0.874	0.423
	HF2	0-25				
R4	HF1a	-61.22	-29.35	0.750	0.104	-0.653
			0.17	0.526	0.504	0.685
			29.18	0.400	-0.857	0.323
	HF1b	-61.01	-32.89	0.697	0.285	-0.658
			6.32	0.704	-0.099	0.703
			26.57	0.135	-0.953	-0.270
	HF2	24.03	-6.36	0.375	0.540	-0.753
			-3.58	0.627	0.451	0.636
			9.94	0.683	-0.711	-0.169
	HF3	36-62				

Table continued on the next page

6.3. Own research results: radicals present in K2G1P single crystals after *in-situ* X irradiation at 77 K

Table continued from the previous page						
Radical	Proton	Iso	Aniso	Eigenvectors		
				a*	b	c
	HFU1	46.78	-5.61	0.423	-0.520	-0.742
			-1.52	0.741	0.670	-0.047
			7.12	0.521	-0.530	0.669
	HFU2	41.51	-4.94	0.375	-0.528	-0.762
			-3.06	0.699	0.701	-0.142
			8.00	0.609	-0.479	0.632
	HFU3	21.04	-6.77	0.066	-0.030	0.997
			-6.39	0.994	-0.082	-0.068
			13.15	0.084	0.996	0.024
	HFU4	5.82	-1.47	0.001	-1.000	0.002
			-0.64	0.284	-0.001	-0.959
			2.12	0.959	0.001	0.284
	HFU5	4.86	-1.52	0.159	-0.968	-0.194
			-0.63	0.228	0.227	-0.947
			2.15	0.961	0.107	0.257

By means of semi-empirical rules (cf. Chapter 4) a set of plausible radical models was constructed. Extensive DFT calculations on these models (in a periodic approach for both the geometry optimisation and the calculation of the EMR parameters) subsequently led to the identification of radical species R1-R4. It should be stressed that, here especially, the DFT calculations were crucial. The chemical structures of the radical models are depicted in Figure 6.4.³ The DFT-calculated HFC tensors for these models are listed and compared to the experimental data in Table 6.3.

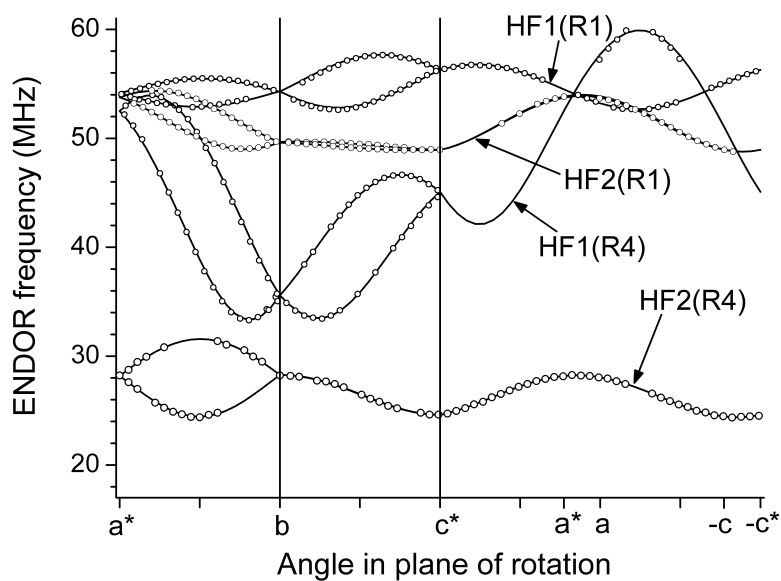
Some important comments need to be made here. For a more detailed explanation we refer to Paper V.

- The DFT calculations on radical model R1_M (Figure 6.4) reproduce the experimental HF1(R1) and HF2(R1) well, but also predict a HO3 isotropic HFC value of about 50 MHz, in strong disagreement with the experimental data. However, we showed that migration of the abstracted H3 proton to the (negatively charged) phosphate group of a neighbouring molecule causes a reorganisation of the hydrogen-bonding pattern and a reorientation of the O3-HO3 bond, resulting in a negligible isotropic HFC value for the HO3 proton (Figure 6.5). The HFC tensors reported in Table 6.3 were calculated on conformation 6.5C.

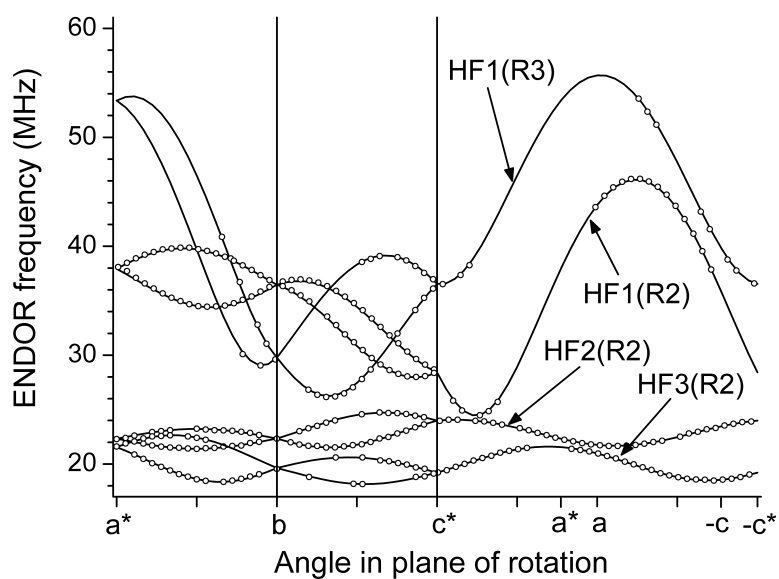
³The subscript M is again used to distinguish between the 'real' radical species and the proposed model.

6.3. Own research results: radicals present in K2G1P single crystals after *in-situ* X irradiation at 77 K

Figure 6.3: X-band angular variations of the ENDOR transitions in K2G1P single crystals, measured at 77 K after *in-situ* X irradiation at 77 K, in the three planes perpendicular to the crystal axes $\langle a \rangle$, $\langle b \rangle$ and $\langle c \rangle$. All spectra were normalised to a proton frequency of 14.77 MHz. The circles represent experimentally determined ENDOR positions, the full lines are the simulations of the ENDOR angular variations using the tensors in Table 6.2.

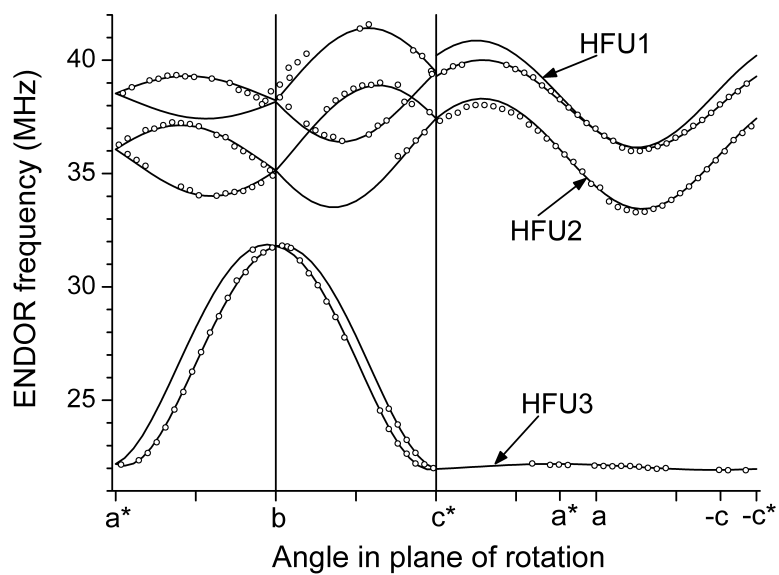


(a)

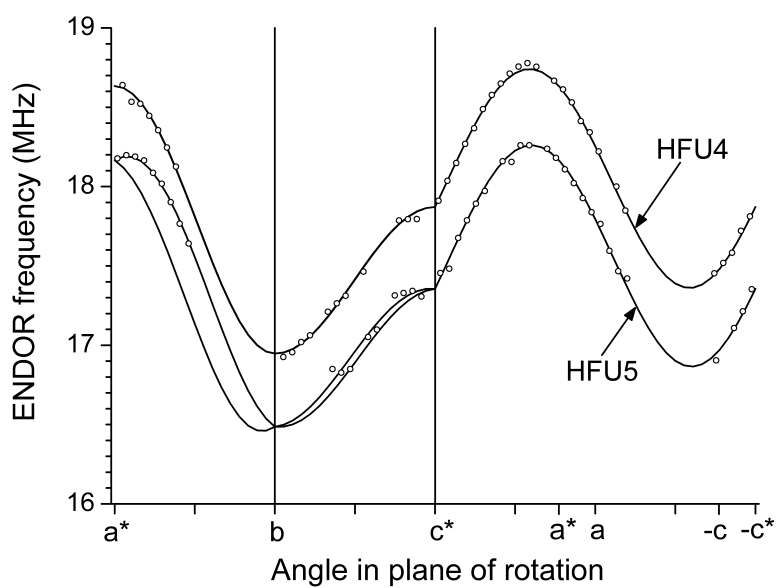


(b)

6.3. Own research results: radicals present in K2G1P single crystals after *in-situ* X irradiation at 77 K



(c)



(d)

6.3. Own research results: radicals present in K2G1P single crystals after *in-situ* X irradiation at 77 K

- In $R2_M$, an H atom has migrated from C2 to the phosphate group, yielding an HPO_3^{2-} fragment (Figure 6.4). DFT-calculated HFC tensors are almost identical when, instead, a PO_4^{3-} fragment is assumed to be present, so that it is in fact not possible to discriminate between the two possibilities based on the available experimental data. However, the former conformation (i.e. the one depicted in Figure 6.4) bears our preference because a rather simple and elegant formation mechanism can be conceived for it.
- Radical models $R3_M$ and $R4_M$ have the same chemical structure but differ in the conformation of the $C^{\bullet}H-OH$ group. The two conformations correspond to different local minima on the potential-energy surface (PES) and are depicted in Figure 6.6.
- $R4$ most likely is the same radical species detected and characterised by Locher and Box at 4 K after *in-situ* X irradiation at 4 K [108], although

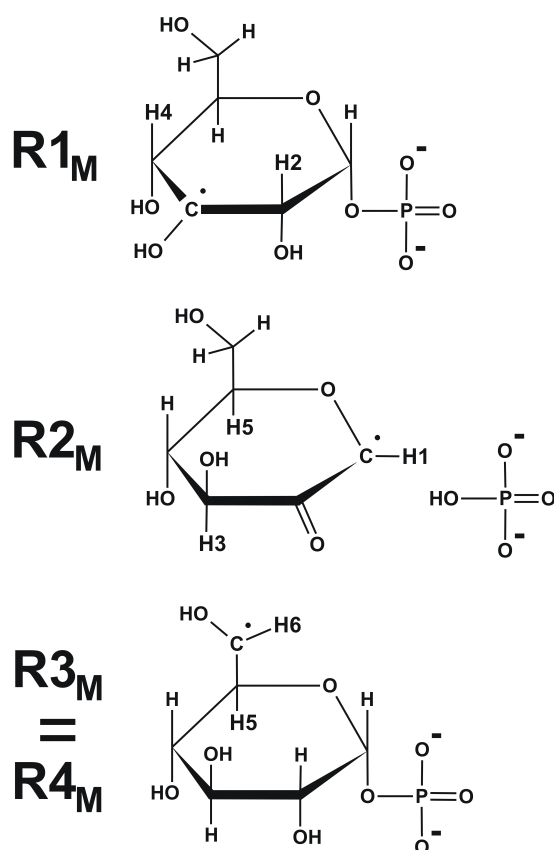


Figure 6.4: The chemical structure of the models proposed for radical species R1-R4 present in K2G1P single crystals at 77 K after *in-situ* X irradiation at 77 K (see Papers IV and V).

6.3. Own research results: radicals present in K2G1P single crystals after *in-situ* X irradiation at 77 K

there are considerable differences with respect to the HFC eigenvectors of the α -proton HFC tensors. The HO6 HFC tensor determined by Locher and Box (A3 in Table 6.1) should then correspond to HF3(R4) in Table 6.2. When an $\langle a \rangle \leftrightarrow -\langle a \rangle$ operation is applied to the eigenvectors (this is a valid possibility because Locher and Box did not eliminate the Schonland ambiguity), this tensor - denoted A3[-a] - is in good agreement with the available experimental data on HF3(R4) and with the DFT-calculated HFC tensors of R4_M (Table 6.3).

Table 6.3: DFT-calculated proton HFC tensors for radical models R1_M - R4_M (Figure 6.4). The geometry optimisations and the HFC-tensor calculations were performed periodically in an $\langle ab2c \rangle$ supercell. δ is the angle between the DFT-calculated and experimental eigenvector directions (Table 6.2). A3[-a] is the A3 tensor determined by Locher and Box in Ref. [108] (Table 6.1), after applying an $\langle a \rangle \leftrightarrow -\langle a \rangle$ operation. Model R1_M corresponds to 'H(C3) migrated proton' in Paper V, R2_M to 'H(C2)[C1-O1]', R3_M to 'H(C6)-2nd' and R4_M to 'H(C6)'.

Mo- del	Pro- ton	Iso	Aniso	Eigenvectors			Pro- ton	δ (°)
				a*	b	c		
R1 _M	H2	90.1	-4.7	0.483	-0.407	-0.775	HF1(R1)	5
			-1.7	0.780	0.602	0.170		14
			6.5	-0.397	0.687	-0.609		14
	H4	89.8	-5.4	-0.043	-0.174	-0.984	HF2(R1)	28
			-1.7	0.491	-0.861	0.131		28
			7.1	0.870	0.477	-0.122		9
	HO3	-5.5	-9.9	0.065	0.482	0.874		
			-6.3	-0.393	0.817	-0.421		
			16.2	-0.917	-0.317	0.243		
R2 _M	H1	-29.9	-20.5	0.774	-0.011	-0.633	HF1b(R2)	9
			-3.1	-0.242	-0.929	-0.280		12
			23.7	0.586	-0.369	0.722		10
	H3	12.6	-2.4	-0.565	0.733	-0.379	HF2(R2)	18
			-1.7	-0.725	-0.222	0.652		14
			4.1	-0.394	-0.643	-0.657		11
	H5	12.5	-3.2	-0.252	0.436	-0.864	HF3(R2)	21
			-1.9	-0.661	0.574	0.483		22
			5.1	-0.707	-0.693	-0.143		12

Table continued on the next page

6.3. Own research results: radicals present in K2G1P single crystals after *in-situ* X irradiation at 77 K

Table continued from the previous page									
Mo- del	Pro- ton	Iso	Aniso	Eigenvectors			Pro- ton	δ (°)	
				a*	b	c			
R3_M	H5	1.3	-5.4	0.704	-0.487	0.517			
			-4.9	-0.302	0.454	0.839			
			10.4	0.643	0.746	-0.172			
	H6	-40.9	-34.7	-0.948	-0.228	0.224	HF1(R3)	12	
			-0.6	0.179	0.203	0.963		19	
			35.2	0.265	-0.952	0.151		16	
	HO6	15.5	-13.0	-0.287	-0.423	0.860	HF2(R3) (?)		
			-8.7	0.218	0.845	0.488			
			21.7	0.933	-0.327	0.150			
R4_M	H5	32.3	-6.7	0.206	-0.470	-0.858	HF2(R4)	12	
			-3.2	0.739	-0.501	0.451		13	
			9.9	0.642	0.727	-0.244		5	
	H6	-51.2	-36.7	0.702	0.081	-0.708	HF1a(R4)	4	
			0.0	0.594	0.483	0.644		5	
			36.7	0.394	-0.872	0.291		2	
	HO6	52.4	-13.0	0.916	0.290	0.277	A3[-a]	12	
			-8.7	0.090	-0.821	0.564		~	11
			21.6	-0.391	0.491	0.778		HF3(R4)	6

The chemical structure of the dominant radical (R2) is identical to the stable T2/T3 species in sucrose, its main characteristics being a carbonyl group at C2 and a broken glucose-phosphate junction. Scission of this junction plays a crucial role in single and double strand breaks in DNA. The presence of this radical in X-irradiated sucrose suggests that the phosphate group is not essential for the formation process of radical R2 in K2G1P and indicates that the ester bond is in general vulnerable to radiation damage. However, as there is no hydroxy group at the C2 position in deoxyribose, a direct parallel cannot be made with possible radiation damage in DNA.

In many studies in the literature the lattice environment is not taken into account at all for geometry optimisation and EMR parameter calculations on single-crystal radicals. It should be stressed that our study proves not only that this 'single molecule approach' is in general not justified, but also that, at low temperatures, abstracted fragments resulting from radiation damage can remain in the vicinity of the generated radical and significantly influence its structural properties (cf. R1 and R3 in Figures 6.5 and 6.6 respectively).

Finally, energy calculations of all radicals obtained by a single H abstraction from the G1P molecule indicate that the radical formation in K2G1P is

6.3. Own research results: radicals present in K2G1P single crystals after *in-situ* X irradiation at 77 K

kinetically controlled, and not thermodynamically. This is in accordance with the results of some very recent studies in the literature on DNA model systems [12, 17].

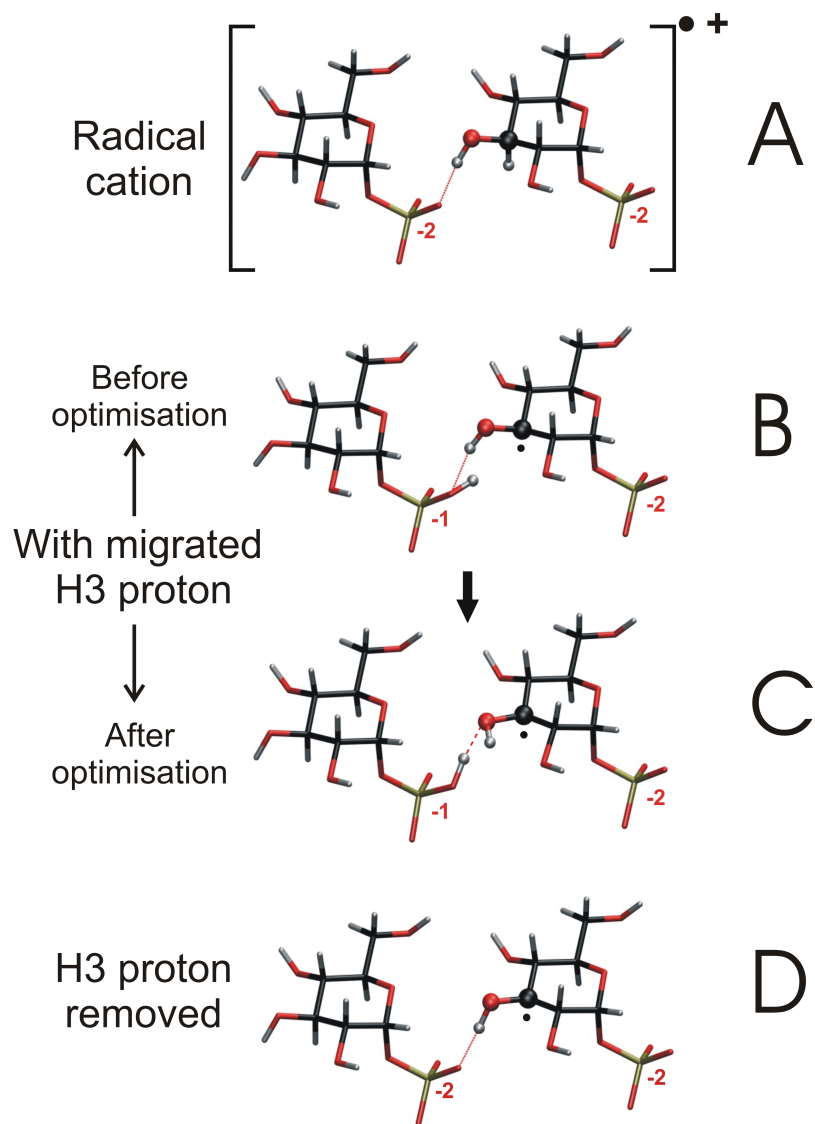


Figure 6.5: Tentative reaction scheme for generation of the R1 radical as a result of oxidative radiation damage. C3, O3, H3 and HO3 are represented as spheres. The DFT-calculated proton HFC tensors of the optimised structure including the migrated H3 proton (C) are given in Table 6.3.

6.3. Own research results: radicals present in K2G1P single crystals after *in-situ* X irradiation at 77 K

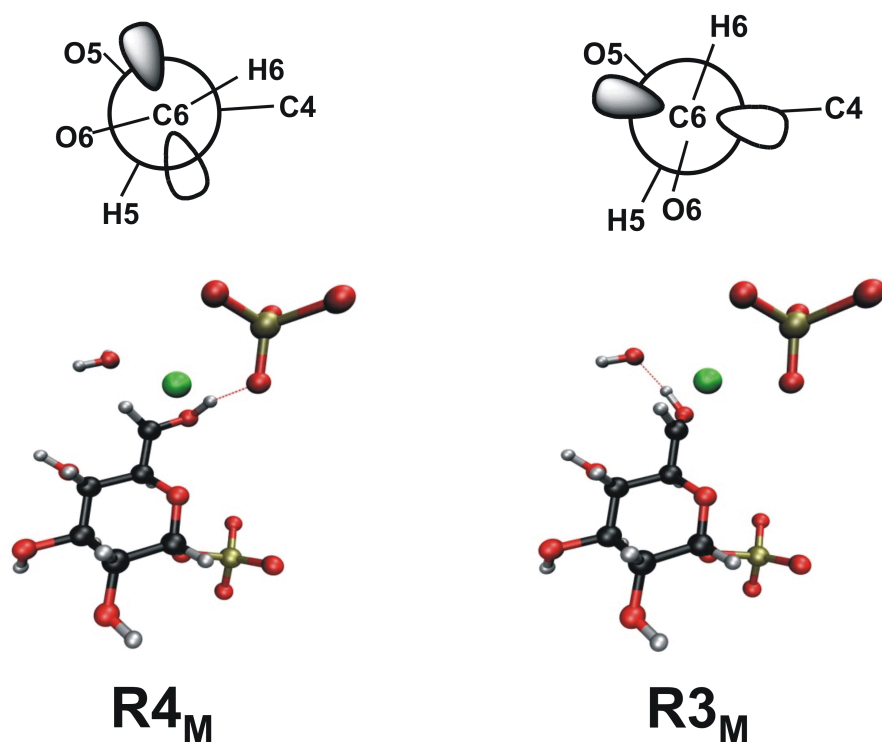


Figure 6.6: Newman projections along the C6-C5 axis and 3D representations of the DFT-optimised R3_M and R4_M structures and their immediate environment. The glucose moieties bound to the upper phosphate groups are not shown for reasons of clarity. The DFT-calculated proton HFC tensors of both structures are given in Table 6.3

Chapter 7

Papers

7.1 Paper I

**Radiation-induced defects in sucrose single
crystals, revisited: a combined electron
magnetic resonance and density functional
theory study**

H. De Cooman, E. Pauwels, H. Vrielinck, A. Dimitrova, N. Yordanov,
E. Sagstuen, M. Waroquier and F. Callens

Spectrochimica Acta Part A, 2008, 69, 1372 - 1383

Copyright 2008 by Elsevier.



Radiation-induced defects in sucrose single crystals, revisited: A combined electron magnetic resonance and density functional theory study

H. De Cooman^{a,b}, E. Pauwels^b, H. Vrielinck^a, A. Dimitrova^c, N. Yordanov^c,
E. Sagstuen^d, M. Waroquier^b, F. Callens^{a,*}

^a Department of Solid State Sciences, Ghent University, Krijgslaan 281-S1, B-9000 Gent, Belgium

^b Center for Molecular Modeling, Ghent University, Proefuinstraat 86, B-9000 Gent, Belgium

^c Bulgarian Academy of Sciences, Lab EPR, Inst Catalysis, BU-1113 Sofia, Bulgaria

^d Department of Physics, University of Oslo, P.O. Box 1048, Blindern, N-0316 Oslo, Norway

Received 6 June 2007; accepted 17 September 2007

Abstract

The results are presented of an electron magnetic resonance analysis at 110 K of radiation-induced defects in sucrose single crystals X-irradiated at room temperature, yielding a total of nine ¹H hyperfine coupling tensors assigned to three different radical species. Comparisons are made with results previously reported in the literature. By means of electron paramagnetic resonance and electron nuclear double resonance temperature variation scans, most of the discrepancies between the present 110 K study and a previous 295 K study by Sagstuen and co-workers are shown to originate from the temperature dependence of proton relaxation times and hyperfine coupling constants. Finally, radical models previously suggested in the literature are convincingly refuted by means of quantum chemical density functional theory calculations.

© 2007 Elsevier B.V. All rights reserved.

Keywords: EPR; ENDOR; DFT; Hyperfine coupling; Sucrose; Radiation; Temperature dependence

1. Introduction

The (in particular oxidative) radiation chemistry of saccharides has been the subject of intensive research the last decades for a number of reasons. Firstly, little is still known with certainty about the nature and reactions of radicals induced by direct radiation effects in the deoxyribose sugar of DNA and their roles with respect to important DNA damage processes [1,2]. Due to the complex nature of DNA, studying smaller model systems bearing key features similar to the DNA components has

proven useful for gaining insight in these radiation-induced processes. In this context, saccharide single crystals are suitable systems for modeling the direct effects of ionizing radiation on the deoxyribose sugar unit in DNA.

Secondly, understanding the nature of radiation-induced defects in sugar compounds is important for radiation dosimetry purposes and for the detection and characterisation of irradiated foodstuffs. Sucrose (or table sugar) is of particular interest for nuclear emergency dosimetry because of its widespread use, its radiation sensitivity, the stability of the induced radicals [3,4], and its linear dose response up to 10⁴ Gy [5]. More recent studies suggest sucrose to possibly be one of the best, universal materials for EPR (electron paramagnetic resonance)- and/or UV-dosimetry in the region 0.44–160 kGy [6,7].

Considerable efforts have been made to work out a comprehensive scheme of the radiation-induced radical chemistry of saccharides. Although a substantial number of sugars has been studied intensively and in great detail by means of EPR (electron paramagnetic resonance), ENDOR (electron nuclear

* Corresponding author. Tel.: +32 92644352; fax: +32 92644996.

E-mail addresses: hendrik.decooman@UGent.be (H. De Cooman),

ewald.pauwels@ugent.be (E. Pauwels),

henk.vrielinck@ugent.be (H. Vrielinck),

annadimitrovabg@yahoo.com (A. Dimitrova),

ndyepr@ic.bas.bg (N. Yordanov),

einar.sagstuen@fys.uio.no (E. Sagstuen),

michel.waroquier@ugent.be (M. Waroquier),

Freddy.callens@ugent.be (F. Callens).

double resonance) and EIE (endor-induced EPR) (e.g. sucrose [8–14], glucose-1-phosphate [15], methyl- α -D-glucopyranoside [16], α -D-glucopyranoside [17], β -D-fructose [18,19], rhamnose [20–25], trehalose [8,26,27]), the structures of the radiation-induced radicals could often not be unambiguously identified. Unravelling the detailed formation mechanism of the radicals is even more challenging, even if some more general mechanisms have emerged to be commonly operative from these studies.

In the past few years however, EMR (electron magnetic resonance) experimentalists have adopted a new tool to aid in solving these problems: density functional theory (DFT) quantum chemical calculations. Comparison of experimentally obtained EMR results with parameters calculated for a certain radical structure using DFT, may provide arguments for either rejection or validation of a proposed radical model. The energetics and feasibility of certain chemical reactions taking place can also, to some extent, be assessed by means of DFT. Due to the considerable increase in computer power and the availability of more accurate density functionals over the past few years, DFT calculations have evolved into a powerful tool for clarifying, interpreting and explaining experimental results. This synergy was nicely illustrated by e.g. the recent work of Vanhaelewyn and co-workers [19,28]. As a consequence, a renewed interest in the radiation-induced radical processes of saccharides has arisen and experimental results from the last few decades are re-investigated in search for new or more detailed radical models. An example is the computational study on rhamnose done by Pauwels and co-workers [29].

In the case of the disaccharide sucrose (see chemical structure in Fig. 1), the experimental results for RT (room temperature) radiation-induced defects in single crystals reported in literature, as obtained at different temperatures, are in disagreement at several points. This lack of reliable experimental data impedes the interpretation of the available data in terms of credible radical structures. In order to clear up this matter, a new EMR study at 110 K was undertaken in the present work and the role of the measuring temperature was carefully investigated by means of EPR and ENDOR temperature scans: for a number of specific orientations, spectra were recorded at temperatures between 20 K and RT. Careful and detailed comparisons are made with the most relevant literature results [11,13]. In addition, DFT calculations on the so far best radical models proposed in literature [11] are presented.

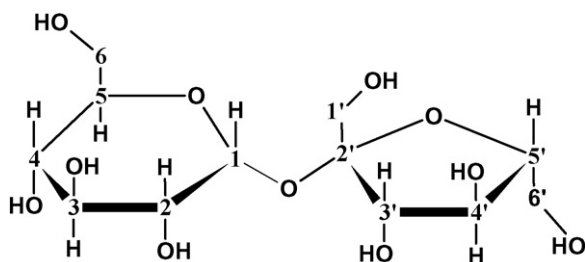


Fig. 1. The chemical structure of the sucrose molecule with the atomic numbering used in the present work.

2. Results reported in literature

Radiation-induced defects in sucrose have been investigated by means of EMR measurements at different temperatures (for both irradiation and measurements) in the past by a number of research groups [8–14]. After irradiation of sucrose single crystals at RT, composite EPR spectra are observed [8,11,13,14] at conventional microwave frequencies (X- and Q-band). This composite nature, in combination with the fairly small g-anisotropy of all involved radicals, impedes any analysis by means of EPR alone.

A first breakthrough was achieved by Sagstuen et al. [11]: RT EPR and ENDOR measurements were performed using sucrose single crystals X-irradiated at RT. Their analysis allowed for the determination of five proton hyperfine coupling tensors that were assigned to two different radicals. For one of these species these authors managed to extract a fairly precise g-tensor from Q-band measurements. They also used these data to propose radical structure models for the two species.

In 2000, a new EMR study on sucrose single crystals was published by Vanhaelewyn et al. [13]: their analysis of EPR, ENDOR and EIE measurements at 60 K using RT irradiated single crystals yielded altogether nine proton hyperfine coupling tensors, assigned to a total of three radicals. Two of these radicals were very similar, but clearly distinguishable. The number and characteristics of the coupling tensors were clearly different from those reported in [11], although some tensors did seem to show some similarity.

A third important study was recently carried out by Georgieva et al. [14]. Multifrequency EPR measurements on sucrose powders at different temperatures, including RT, confirmed the presence of at least three different radicals. The spectrum simulation analyses carried out in this work corroborated the results reported in [13] and allowed for estimations of the g-tensors of these three radical species.

3. Experimental

Analytical grade sucrose was obtained from Aldrich (98%) and was used to grow single crystals from H₂O or D₂O solutions. Recrystallisation from D₂O was performed three times, implying that approximately 99% of the exchangeable protons were replaced by deuterium. The crystal structure of sucrose is known from X-ray [30,31] as well as neutron [32] diffraction analysis. The crystals are monoclinic with space group $P2_1$ and a unit cell contains two molecules ($Z=2$). The crystal parameters were determined to be $a=1.0868$ nm, $b=0.8710$ nm, $c=0.7761$ nm and $\beta=102.97^\circ$, β being the angle between the $\langle a \rangle$ - and $\langle c \rangle$ -axes. The a^*bc system ($\langle a^* \rangle$ being orthogonal to both $\langle b \rangle$ and $\langle c \rangle$) was chosen as orthogonal reference frame in this work, in analogy with previous publications. Due to the monoclinic symmetry combined with $Z=2$, the only allowed symmetry operation to be applied on the eigenvector matrices in this reference frame is a twofold rotation around $\langle b \rangle$ (being equivalent to changing the signs of all the eigenvector $\langle a \rangle$ - and $\langle c \rangle$ -components simultaneously), next to, of course, the inversion symmetry operation that is always present in case of EMR measurements. For a cer-

tain direction vector, the polar coordinates θ and φ are defined in the current work as the angles measured from the positive z -axis ($=\langle c \rangle$ -axis) to the vector and the angle measured from the positive x -axis ($=\langle a^* \rangle$ -axis) to the projection of the vector in the xy -plane ($=\langle a^*b \rangle$ -plane), respectively.

The single crystal samples used for the temperature scans were X-irradiated at RT to doses of 60–90 kGy using a Philips chromium-anode X-ray tube operated at 60 kV and 40 mA. They were then mounted to a goniometer head. For alignment of the direct crystal axes $\langle a \rangle$, $\langle b \rangle$ and $\langle c \rangle$ parallel to the rotation axis, the goniometer was put in a Weissenberg X-ray diffraction camera and oscillation diagrams were used. For determining the orientation of the rotation axis of the skewed plane, the goniometer was placed in a Bruker D8 Discover X-ray diffraction machine and stereographic projections were recorded for several crystallographic planes. With these methods, an accuracy of 0.5° and 2° , respectively is obtained. The crystals were then transferred from the goniometer head to a quartz crystal holder for EPR/ENDOR measurements with a minimal loss of alignment. EPR, ENDOR and EIE spectra were recorded at X-band (9.5 GHz) on a Bruker ESP300E spectrometer with an ESP353 ENDOR-Triple extension (Ghent) or on a Bruker Elexsys 560 spectrometer (Oslo) and at Q-band (34 GHz) on a Bruker ElexSys E500 spectrometer (Ghent). The spectrometers are equipped with Oxford flow cryostats, ESR910 (2–300 K), ESR900 (4–300 K) and CF935 (4.2–300 K), respectively.

The program MAGRES [33,34] was used to derive the hyperfine coupling tensors from the ENDOR data. A six-parameter linear regression routine generates these tensors from the polar angles θ and φ of the rotation axes, the measurement angle α (in the plane of rotation), and the corresponding measured ENDOR frequencies. Further refinements consisting of additional small variations of a total of 12 angles (the two polar angles for each of the rotation axes and the in-plane rotation starting angle for each plane) were made, using a nonlinear refinement procedure converging to a minimal root mean square (rms) value for the complete data set.

As for the temperature scans, in each instance the sample was first cooled to 20 K and then both EPR and ENDOR spectra were recorded at a number of temperatures while gradually warming up the sample to RT. In order to guarantee thermal stabilisation of the sample at each temperature setting, the spectra were recorded several minutes after the temperature displayed by the temperature controller had stabilised. Using this method and in the probed temperature range, the recorded temperature is expected not to differ more than 5 K from the actual specimen temperature.

The details on the computational procedures are presented together with the results of the DFT calculations.

4. Results and discussion

4.1. EPR, ENDOR and EIE at 110 K

In Fig. 2, a typical X-band 110 K EPR spectrum of sucrose irradiated at RT is shown. At this orientation of the magnetic field the composite character of the resonance is apparent from

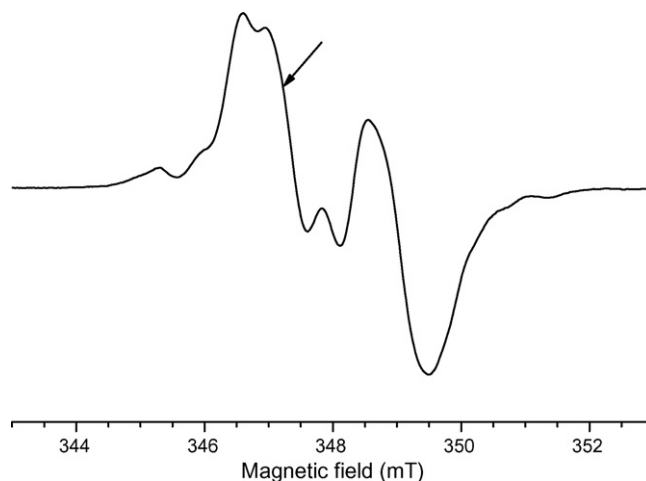


Fig. 2. X-band EPR spectrum at 110 K for RT X-irradiated sucrose crystals. The magnetic field was perpendicular to $\langle b \rangle$, 16° from $\langle a^* \rangle$ and 61° from $\langle c^* \rangle$; the microwave frequency was 9.748 GHz. The arrow marks the magnetic field at which the ENDOR spectrum of Fig. 3 was recorded.

the significant asymmetry of the spectrum. At other orientations, a spectrum resembling a doublet of triplets is observed, as seen in Fig. 7 and as also reported in previous publications [8,11,13].

Fig. 3 shows the corresponding ENDOR spectrum. This is one of the few orientations of the crystal in the external magnetic field for which the ENDOR lines in the generally crowded lower frequency range (18–25 MHz) are fairly well resolved. The ENDOR lines for which the analysis was successful and corresponding hyperfine coupling tensors were determined have been labelled in Fig. 3 in accordance with the labelling scheme in Table 1.

ENDOR measurements were performed at one or two magnetic field positions in the EPR spectrum in 5° steps over 130°

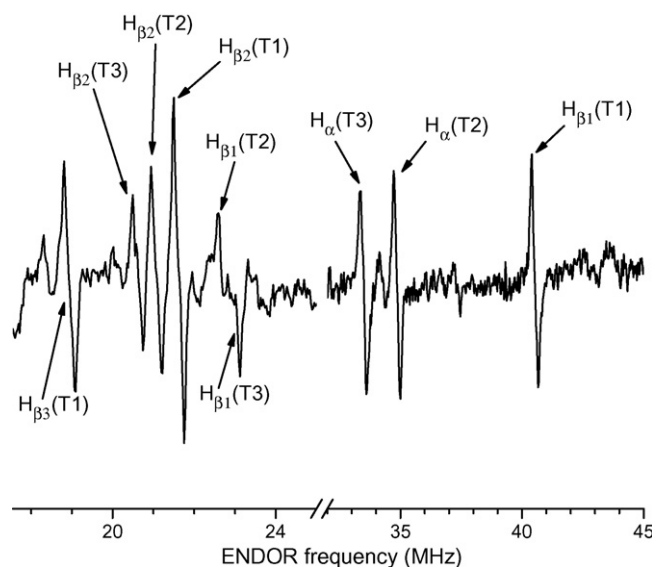


Fig. 3. X-band ENDOR spectrum at 110 K for RT X-irradiated sucrose. The magnetic field was perpendicular to $\langle b \rangle$, 16° from $\langle a^* \rangle$ and 61° from $\langle c^* \rangle$; the magnetic field was 347.2 mT. The ENDOR lines of the ^1H hyperfine interactions for which a tensor could be determined are marked using the labelling scheme of Table 1.

Table 1
Proton hyperfine coupling tensors (in MHz) of radicals T1, T2 and T3 in RT X-irradiated sucrose single crystals, measured at 110 K

Radical	Proton type	Isotropic values	Anisotropic values	Eigenvectors			
				<i>a</i> *	<i>b</i>	<i>c</i>	
T1	H _{β1}	46.80	−3.99	0.616	0.121	−0.778	
			−2.38	0.072	0.975	0.209	
			6.37	0.784	−0.185	0.592	
	H _{β2}	15.88	−2.69	0.106	0.825	0.555	
			−2.31	0.989	−0.144	0.025	
			5.00	0.101	0.546	−0.832	
	^A H _{β3}	−11.07	−6.50	0.707	−0.245	−0.664	
			−3.69	0.383	0.921	0.068	
			10.19	0.595	−0.302	0.745	
	^B H _{β3}	−11.20	−8.00	0.602	−0.558	−0.572	
			−0.59	0.580	0.797	−0.167	
			8.59	0.549	−0.231	0.803	
T2	H _α	−38.69	−19.66	0.424	−0.163	−0.891	
			−2.11	0.886	0.280	0.371	
			21.77	0.189	−0.946	0.263	
	H _{β1}	16.37	−2.32	0.869	−0.355	−0.344	
			−1.72	−0.209	0.368	−0.906	
			4.04	0.448	0.860	0.246	
	H _{β2}	13.68	−3.09	0.718	−0.650	0.248	
			−2.17	0.638	0.473	−0.608	
			5.26	0.278	0.595	0.754	
	T3	H _α	−35.81	−18.98	0.584	−0.184	−0.790
				−2.11	0.755	0.481	0.446
				21.09	0.298	−0.857	0.420
H _{β1}		16.42	−2.10	0.840	−0.541	−0.034	
			−1.77	0.178	0.334	−0.926	
			3.87	0.512	0.772	0.377	
H _{β2}		12.24	−3.62	0.528	−0.822	0.214	
			−2.12	0.804	0.402	−0.439	
			5.74	0.275	0.403	0.873	

The tensors were fitted using ENDOR angular variation plots in a total of four planes: three planes constituted by the direct crystal axes (Figs. 4 and 5) and a skewed plane (Fig. 6). For the H_{β3}(T1) coupling, two possible alternatives are presented, ^AH_{β3} being favoured by the fitting procedures over ^BH_{β3}. The assignment of the couplings to a total of three radical species was based on EIE measurements (Fig. 7).

(planes perpendicular to *a*) and *c*) or 180° (plane perpendicular to *b*), or in 10° steps over 180° (skewed plane). The ENDOR line angular variation plots in the four experimental rotation planes are shown as points in Figs. 4–6. These data allowed for the determination of a total of nine ¹H hyperfine coupling tensors. Using only data points in the three planes perpendicular to the direct crystal axes (Figs. 4 and 5), two essentially different tensors were found fitting the data equally well for each of the ¹H hyperfine couplings. For most of the couplings it was not possible to reject with certainty either one of the two possibilities based on empirical arguments alone. Therefore, measurements were performed in a fourth, skewed plane (Fig. 6). For most couplings, this fourth plane did allow for the determination of the correct tensor with certainty. However, as the strong overlap of ENDOR lines allowed for only a few data points to be attributed to the H_{β3}(T1) interaction, unambiguous differentiation of the obtained tensors for this coupling was not achieved, although one tensor seemed to be favoured (Fig. 6 and below).

The complete set of tensors finally arrived at are shown in Table 1. For the H_{β3}(T1) coupling, both possibilities are listed, ^AH_{β3}(T1) being favoured over ^BH_{β3}(T1). The expected angular variations of the ENDOR lines calculated from these tensors

are shown as solid lines in Figs. 4 and 5 (and for some also in Fig. 6). As discussed in Section 3, slight misorientations (<1.5°) of the crystals used for the recording of spectra were included in the final analysis. With exception of the H_{β3}(T1) coupling, a minimum of 10 data points per data set – corresponding to a single-line ENDOR angular variation in a certain plane and belonging to one certain crystal site – was included in the fitting. The spectra recorded using partially deuterated samples only differed from their non-deuterated counterparts in the distant proton region (13–17 MHz), implying that all nine interactions in Table 1 arise from non-exchangeable protons and are thus carbon-bound.

EIE measurements in X- as well as Q-band allowed for unambiguous attribution of the tensors to three different radical species, as indicated in Table 1. X-band EIE spectra of the three radicals are shown together with the EPR spectrum for a particular orientation in Fig. 7. For the EIE based assignment of the ¹H couplings to a certain radical, four different orientations were thoroughly probed at X-band, as well as two orientations at Q-band. In the Q-band spectra, radicals T2 and T3 were significantly better separated, but the signal to noise ratio was considerably lower.

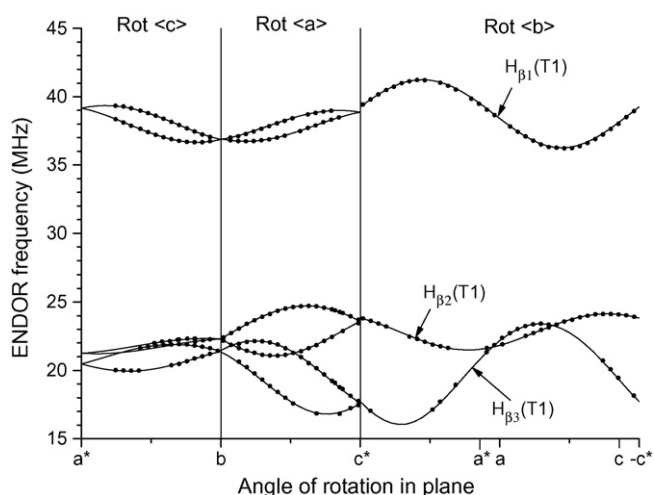


Fig. 4. X-band angular variation of the ENDOR transitions associated with radical T1 in RT X-irradiated sucrose, measured at 110 K. The labelling scheme of Table 1 is used. The spectra were normalised to a proton frequency of 14.480 MHz for the a^*b - and bc^* -planes, and 14.760 MHz for the ac -plane. The dots represent experimentally determined ENDOR resonance positions, the full lines are the simulations of the ENDOR angular variations using the tensors in Table 1. The lack of connectivity between the planes at some points is due to a combination of slight tilting of the planes and different magnetic fields at which the ENDOR was recorded.

For radical T1, the largest hyperfine coupling, $H_{\beta 1}(T1)$, exhibits the typical characteristics of an interaction with a carbon-bound β -proton [35] (Table 1). The $H_{\beta 2}(T1)$ tensor has anisotropic elements similar to those of $H_{\beta 1}(T1)$. However, the isotropic component is substantially smaller and the coupling may be due to a β - as well as a γ -proton interaction. As discussed above, there is still some uncertainty left with respect to the tensor of the $H_{\beta 3}(T1)$ coupling. The anisotropic part of ten-

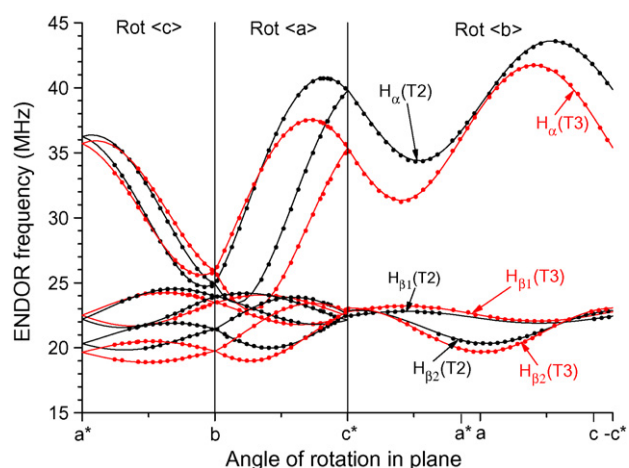


Fig. 5. X-band angular variation of the ENDOR transitions associated with radicals T2 and T3 in RT X-irradiated sucrose, measured at 110 K. The labelling scheme of Table 1 is used. The spectra were normalised to a proton frequency of 14.480 MHz for the a^*b - and bc^* -planes, and 14.760 MHz for the ac -plane. The dots represent experimentally determined ENDOR resonance positions, the full lines are the simulations of the ENDOR angular variations using the tensors in Table 1. The lack of connectivity between the planes at some points is due to a combination of slight tilting of the planes and different magnetic fields at which the ENDOR was recorded.

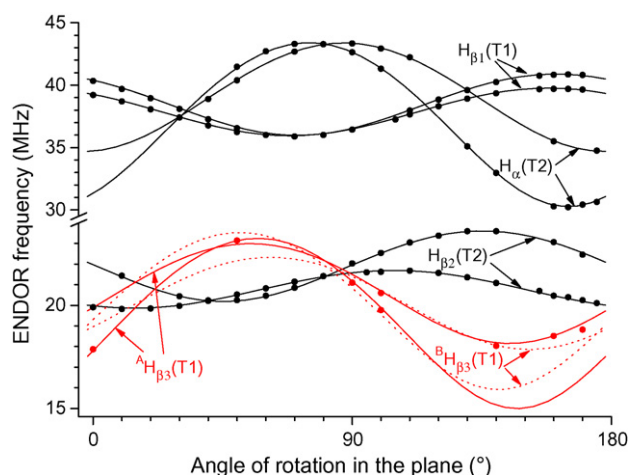


Fig. 6. X-band angular variation of the ENDOR transitions associated with some of the ^1H hyperfine couplings in RT X-irradiated sucrose, measured at 110 K. The polar angles of the plane are $\theta = 79.24^\circ$ and $\varphi = 68.95^\circ$ (reasonably close the ac -plane). The projections of $\langle a^* \rangle$, $\langle a \rangle$, $\langle -c \rangle$ and $\langle -c^* \rangle$ in this rotation plane are located at 20.4° , 33.8° , 105.7° and 118.2° , respectively. The dots represent experimentally determined ENDOR resonance positions, the full and dashed lines are the simulations of the ENDOR angular variations using the tensors in Table 1. The spectra were normalised to a proton frequency of 14.480 MHz. The labelling scheme of Table 1 is used.

sor ${}^A H_{\beta 3}(T1)$, favoured by the data points in the fourth plane, roughly exhibits the axial symmetry characteristic of an interaction with a β -proton. In order to obtain the typical $(-b, -b, +2b)$ anisotropy, with $b > 0$, the isotropic component has to be chosen negative, which is atypical for β -proton interactions. The other possible but slightly disfavoured tensor shape, ${}^B H_{\beta 3}(T1)$, is essentially different and exhibits the symmetry of an α -proton interaction. As sufficient data for further discriminating between

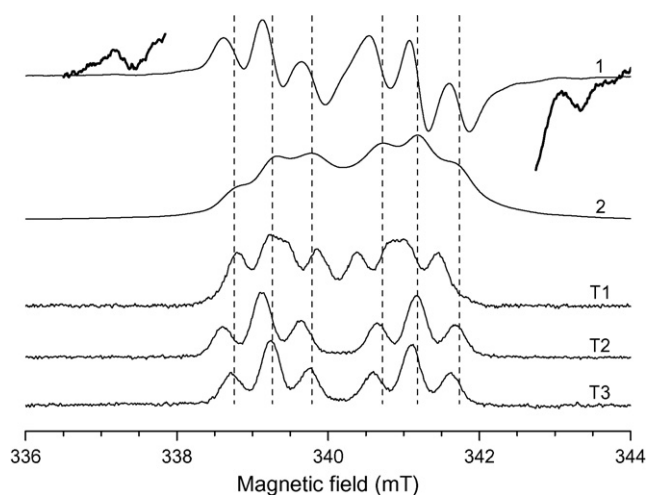


Fig. 7. Top: (1) first derivative X-band EPR spectrum of RT irradiated sucrose, measured at 110 K. The thick line was obtained by multiplying the intensity with a factor of 20. (2) Absorption EPR spectrum obtained by integrating spectrum 1. Under: absorption X-band EIE spectra of the three main radicals (Table 1), all in non-derivative absorption mode. All spectra are normalised to a microwave frequency of 9.550 GHz. The magnetic field is oriented perpendicular to $\langle b \rangle$, at 118° from $\langle a \rangle$ and 15° from $\langle c \rangle$. The weak features at either side of the EPR spectrum show that at least one other radical species, fundamentally different from T1, T2 and T3 is present in RT irradiated sucrose.

these two alternatives are presently not available, this matter will not be addressed further here. Both alternatives are included in Table 1.

The hyperfine coupling tensors due to radical species T2 and T3 are very similar, strongly suggesting that T2 and T3 are two slightly different geometrical configurations of the same radical entity. Similar observations have been made in other saccharides such as fructose [19] and sorbose [28]. A possible explanation for the observations made in sucrose would be that one or more minor structural differences in the immediate molecular environment of the radical are causing these relatively small differences. As will be discussed below, it is very likely that other slightly different conformations of this radical entity are present, albeit in considerably lower concentrations.

Both T2 and T3 are characterised by three ^1H hyperfine interactions. The largest coupling is clearly due to an α -proton interaction. The spin density on an α -proton can be estimated using either the isotropic (McConnell relation [36], Eq. (1)) or the anisotropic values (Gordy–Bernhard relation [37], Eq. (2)) of the hyperfine tensor:

$$a_{\alpha,\text{iso}} = Q_{\text{iso}}^{\alpha} \rho_{\pi} \quad (1)$$

$$b_{+,\text{dip}} = Q_{\alpha,\text{dip}}^{\text{H}} \rho_{\pi} \quad (2)$$

where $a_{\alpha,\text{iso}}$ is the isotropic component, $b_{+,\text{dip}}$ is the most positive dipolar component, ρ_{π} is the unpaired spin density localised on the carbon in the molecular π -orbital and Q_{iso}^{α} and $Q_{\alpha,\text{dip}}^{\text{H}}$ are empirical “constants”, dependent to some extent on the nature of the radical fragment. For Q_{iso}^{α} a value of -72 MHz will be assumed [38] and for $Q_{\alpha,\text{dip}}^{\text{H}}$, the value of 38.7 MHz, as proposed by Bernhard [39]. Eqs. (1) and (2) both yield unpaired electron densities of 0.50 – 0.55 for both radicals, indicating (i) that about 50% of the unpaired spin density is delocalised on a neighbouring oxygen or carbon and (ii) that the spin centres are essentially planar [39]. Sagstuen et al. [11] made similar observations and as a possible explanation the presence of a neighbouring carbonyl group was suggested. As the $\text{H}_{\beta 1}$ and $\text{H}_{\beta 2}$ tensors of radicals T2 and T3 have relatively small isotropic components, the possibility for these tensors to be due to couplings to β - as well as γ -protons should be considered.

A careful analysis of the ENDOR spectra revealed that the T2 and T3 signals in all rotation planes are closely accompanied by a number of considerably less intense resonance lines, some of which can be seen in Fig. 3. This was also reported by Vanhaelewyn et al. [13]. This indicates that other radicals, differing only slightly in geometry from the T2/T3 radicals, are present in RT irradiated sucrose. Yet other weak ENDOR lines clearly indicate the existence of at least one other radical species fundamentally different from the three characterised in Table 1. The presence of such a radical can also be deduced from comparison of the EIE spectra of radicals T1, T2 and T3 with the experimental EPR spectrum (Fig. 7).

4.2. EPR and ENDOR temperature scans

As indicated in Section 1, there are important qualitative and quantitative differences, between the 60 K results reported by

Vanhaelewyn et al. [13] and the RT results reported by Sagstuen et al. [11]. Moreover, the data presented in the current work were acquired at 110 K, a somewhat intermediate temperature. The study performed by Georgieva et al. [14] also covers a wide range of temperatures. In order to elucidate the effects of the measuring temperature on the ENDOR spectra and hence on the proton hyperfine coupling tensors extracted, a series of EPR and ENDOR temperature scans was performed on RT X-irradiated sucrose single crystals at different orientations in the magnetic field.

The high frequency EPR study by Georgieva et al. [14] provides convincing proof that three different radicals are present after X-irradiation at RT, and not two as suggested by Sagstuen et al. [11]. Since the samples in all studies were irradiated at RT, variations of the signal upon lowering the temperature followed by rewarming to RT, should be reversible. Therefore, one expects the same three radicals to be present at 60 K and at RT, possibly with some reversible geometrical alterations.

Figs. 8–11 show EPR (Fig. 8) and ENDOR (Figs. 9–11) temperature scans for both the weakly and the strongly coupled proton frequency ranges and at two different orientations of the crystal in the magnetic field. From Fig. 8 it is apparent that the Q-band EPR spectrum is only slightly temperature dependent in the region 60 – 300 K. In particular from 190 K onwards, a gradual shift of the resonance lines towards higher fields is apparent, without the overall pattern of the EPR signal being altered. Similar scans at other orientations all strongly suggest that there are in fact no fundamental differences between the radicals present at 60 K and at RT. As will be apparent from the discussion below, the magnetic field shifts cannot be explained solely by virtue of the variation of the hyperfine couplings with temperature. Therefore, a slight temperature dependence of the g -tensors accompanying the radical geometry changes seems to be the most plausible explanation. This matter was not further investigated.

Figs. 9 and 10 lead to the following conclusions with respect to the temperature dependence of the hyperfine interactions in

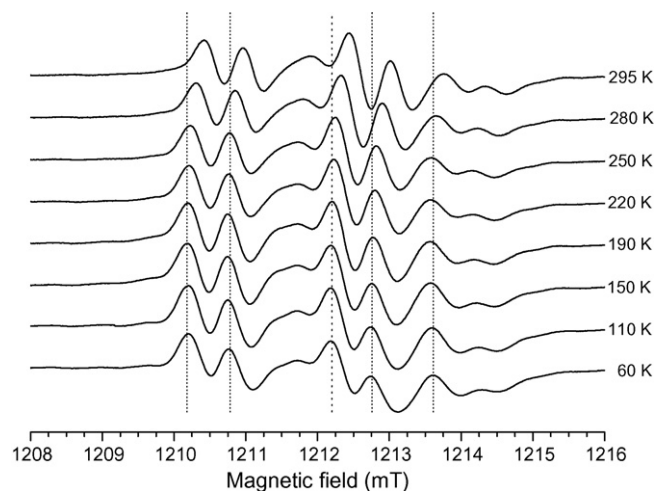


Fig. 8. Q-band EPR temperature scan for RT irradiated sucrose. The magnetic field was perpendicular to $\langle b \rangle$, 25° from $\langle a^* \rangle$ and 52° from $\langle c^* \rangle$. All spectra were normalised to a microwave frequency of 34.000 GHz.

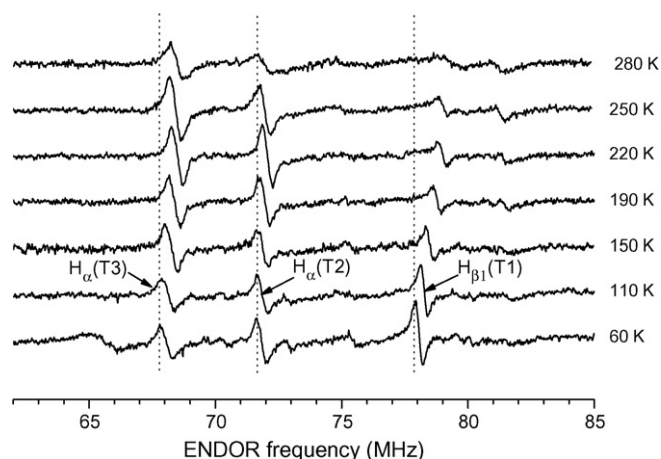


Fig. 9. Q-band ENDOR temperature scan for the strongly coupled frequency region. The magnetic field was perpendicular to the $\langle b \rangle$, 25° from $\langle a^* \rangle$ and 52° from $\langle c^* \rangle$. All spectra were 'normalised' to a magnetic field of 1214.29 mT using the proton frequencies as a reference. The labelling scheme of Table 1 is used.

the strongly coupled proton frequency range. These conclusions are supported by temperature scans at several other orientations not shown here:

- (i) At most orientations the signal of the $H_{\beta 1}(T1)$ resonance line gradually loses intensity with increasing temperature from 150 K and has almost completely disappeared at RT. This signal also shifts to somewhat higher frequencies with increasing temperature, with a difference between the signal positions at 60 K and at 280 K of typically 1–2 MHz. This effect is particularly well observable in Fig. 10.
- (ii) At most orientations the $H_{\alpha}(T2)$ resonance line is significantly reduced in intensity as compared to the $H_{\alpha}(T3)$ line when the temperature increases from 250 to 280 K. These two resonance line positions are only very slightly temperature dependent. It should be noted that the merging of the $H_{\alpha}(T2)$ and $H_{\alpha}(T3)$ signals at the orientation of Fig. 10 is

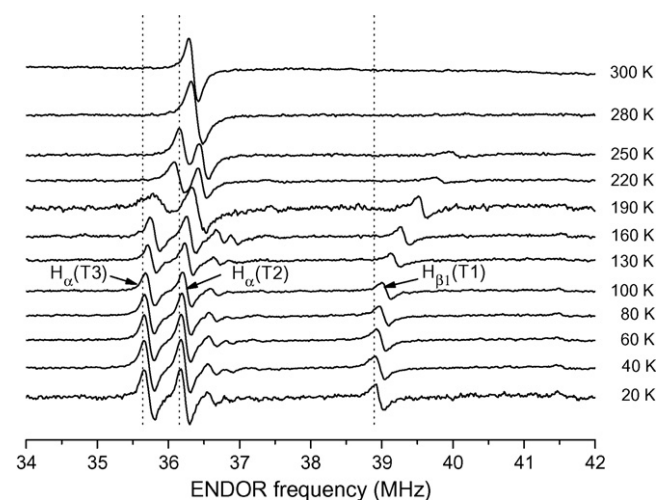


Fig. 10. X-band ENDOR temperature scan for the strongly coupled frequency region. The magnetic field was parallel to $\langle a^* \rangle$. All spectra were normalised to a magnetic field of 339.33 mT using the proton frequencies as a reference. The labelling scheme of Table 1 is used.

solely a coincidence. The practical fact remains that at RT, only one resonance line due to the $H_{\alpha}(T2)$ coupling is seen with reasonable intensity in this frequency range.

- (iii) In Fig. 10, the two weak resonance lines still accompanying the $H_{\alpha}(T2)$ and $H_{\alpha}(T3)$ signals at 160 K have disappeared, or possibly merged with their more intense neighbouring signals, at 190 K. These are examples of signals very likely arising from radical structures with geometrical configurations slightly different from those for the T2/T3 radicals (cf. Section 4.1).

As the frequency range for the weakly coupled protons is extremely crowded, attempts to derive detailed information for the ENDOR transitions in this frequency range were virtually unsuccessful. Fig. 11 shows one of the most illustrative scans obtained. Most resonance lines are subject to small frequency shifts as the temperature increases from 20 to 160 K. From 160 K upwards, some more clear changes are observed and most signals become reduced in intensity. At 280 K, only one resonance line with appreciable intensity is left. This line seems to be a superposition of the shifted and merged $H_{\beta 1}(T2)$ and $H_{\beta 1}(T3)$ resonance lines. The $H_{\beta 2}(T2)$, $H_{\beta 2}(T3)$ and $H_{\beta 2}(T1)$ lines are also present at 280 K, but with almost negligible intensity. However, it should be noted that the relative intensities of the resonance lines at RT are angular dependent and that, in general, the T2 and T3 radical resonance lines do not merge. Finally, from the available data it was not possible to draw any conclusions concerning the temperature dependence of the $H_{\beta 3}(T1)$ signal.

In summary, the differences between the EPR and ENDOR spectra at 60 K and at 110 K are practically negligible. Furthermore, a number of ENDOR lines show small frequency shifts and eventually disappear as the temperature is raised to RT. As the EPR spectrum is only slightly temperature dependent, the apparent disappearance of some of the ENDOR lines is proba-

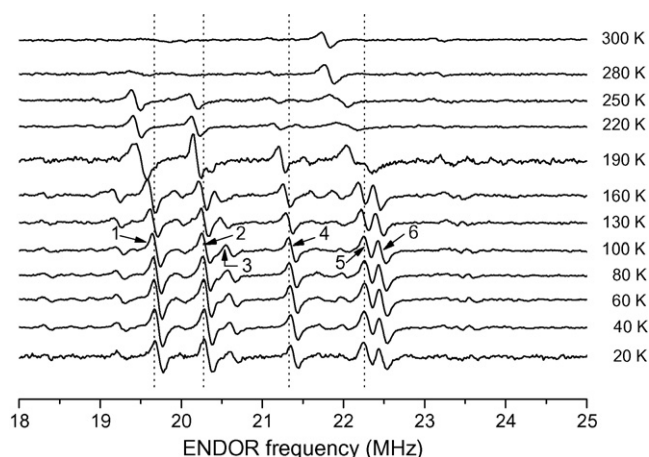


Fig. 11. X-band ENDOR temperature scan for the weakly coupled frequency region. The magnetic field was parallel to $\langle a^* \rangle$. All spectra were normalised to a magnetic field of 339.33 mT using the proton frequencies as a reference. Using the labelling scheme of Table 1, numbers 1–6 correspond to following interactions: 1 = $H_{\beta 2}(T3)$, 2 = $H_{\beta 2}(T2)$, 3 = $H_{\beta 3}(T1)$, 4 = $H_{\beta 2}(T1)$, 5 = $H_{\beta 1}(T2)$ and 6 = $H_{\beta 1}(T3)$.

bly due to temperature dependence of nuclear relaxation rates influencing the saturation behaviour of the ENDOR transitions. It is concluded that the same radicals are present and detected at RT and at 60/110 K with only some minor reversible changes in the radical geometry and/or spin density distributions. Thus, a fair agreement between the proton hyperfine coupling tensors acquired at different temperatures is to be expected.

4.3. Comparison with single crystal data obtained at other temperatures

In Tables 2 and 3 the tensors reported by Sagstuen et al. [11] (RT) and by Vanhaelewyn et al. [13] (60 K) are listed. Some sign changes have been applied in both tables, for principal values as well as for some eigenvector matrix elements. A number of these changes are actual corrections to the published tensors, and were made after consulting the authors concerned. Other changes are allowed symmetry operations applied with the aim of facilitating comparison with the tensors presented in the current work (Table 1). For the reader's convenience, the original radical and tensor labels are used.

Firstly the tensors obtained at 60 K ([13], Table 3) will be compared with those obtained at 110 K (current work, Table 1). It is instantly clear that radicals S1, S2 and S3 correspond to radicals T1, T2 and T3, respectively. Not only is the match for the isotropic components excellent for all interactions, the anisotropic couplings are also in the same range. However, the symmetry of the anisotropic parts shows some clear differences, especially for the six hyperfine couplings with smaller isotropic components. Moreover, although the eigenvector matrices do not seem to be entirely dissimilar, careful comparison reveals that the directional agreement is poor.

These quantitative discrepancies are far too large to be the result of a difference in measuring temperature, as is clear from the temperature scans discussed above. One possible explanation

could be the fact that Vanhaelewyn et al. [13] only used two planes of data points to extract the proton hyperfine coupling tensors from, whereas in the current study four planes were used. When the symmetry is lower than axial, three independent planes of data are in principle required for an accurate and unambiguous fitting. In practice, even a fourth, skewed plane is often a necessity, as was the case in the study presented in the current work. Based on the above arguments and supported by the discussion below, it is concluded that the tensors obtained in the present study at 110 K (Table 1) are the most accurate set of EPR parameters for the three main radical species in RT irradiated sucrose. With this new and more accurate data available, a re-evaluation of the g-tensor analysis reported in [14] may appear necessary.

When comparing the 110 K data set (current work, Table 1) and the RT one ([11], Table 2), a number of qualitative differences is immediately obvious. First of all, the $H_{\beta 1}(T1)$ coupling, very prominent in the ENDOR spectra recorded at 110 K (Fig. 3), is not reported in [11]. This is readily explained by means of the ENDOR temperature scans (Figs. 9 and 10), where the corresponding ENDOR line was clearly shown to have lost its intensity almost completely at RT. Secondly, only two radicals are reported in [11], whereas three radicals are observed at 110 K. The temperature scans again provide an explanation as Figs. 9 and 10 clearly show that the $H_{\alpha}(T2)$ resonance line is substantially reduced in intensity at RT, as compared to the $H_{\alpha}(T3)$ signal. Moreover, at a number of orientations this already (very) weak signal accidentally merges with the $H_{\alpha}(T3)$ resonance line, leaving it undetectable. Although no final conclusions could be arrived at with regard to the temperature dependency of the smaller couplings (Fig. 11), it is certainly possible that also the $H_{\beta 1}(T2)$ and $H_{\beta 2}(T2)$ signals lose intensity and/or accidentally merge with the $H_{\beta 1}(T3)$ and $H_{\beta 2}(T3)$ signals. Sagstuen et al. [11] did report on the presence of yet another ENDOR line, which they believed to be an α -proton hyperfine interaction.

Table 2

Proton hyperfine coupling tensors (in MHz) reported by Sagstuen et al. [11] of radicals R1 and R2 in RT X-irradiated sucrose single crystals, measured at RT

Radical	Proton type	Isotropic values	Anisotropic values	Eigenvectors			Comparison with tensors of Table 1					
				a^*	b	c	Tensor	ψ (°)	Tensor	ψ (°)		
R1	H_{α}	−37.67	−20.09	0.548	−0.175	−0.818	$H_{\alpha}(T2)$	8.2	$H_{\alpha}(T3)$	2.6		
			−1.49	0.793	0.421	0.441					10.4	3.8
			21.57	0.267	−0.890	0.369					8.3	4.1
	$H_{\beta 1}$	15.14	−2.15	0.856	−0.517	−0.023	$H_{\beta 1}(T2)$	20.7	$H_{\beta 1}(T3)$	1.1		
			−1.72	0.183	0.261	−0.950					23.3	2.5
			3.88	0.484	0.816	0.317					5.0	4.3
$H_{\beta 2}$	12.43	−3.39	0.625	−0.746	0.231	$H_{\beta 2}(T2)$	7.6	$H_{\beta 2}(T3)$	7.0			
		−2.15	0.726	0.447	−0.523					7.1	7.0	
		5.54	0.287	0.495	0.820					6.9	6.2	
R2	$H_{\beta 3}$	15.57	−2.89	0.227	0.802	0.552	$H_{\beta 2}(T1)$	7.2				
			−2.30	0.971	−0.233	−0.061					7.0	
			5.18	0.080	0.550	−0.832					1.5	
	$H_{\beta 4}$	18.57	−2.60	−0.127	−0.931	−0.343						
			−1.48	0.975	−0.054	−0.214						
			4.07	0.181	−0.362	0.915						

Some sign corrections and symmetry operations have been applied. At the right hand side, the angular deviations (ψ) with the corresponding eigenvectors of the tensors of Table 1 obtained at 110 K, are given.

Table 3
Proton hyperfine coupling tensors (in MHz) reported by Vanhaelewyn et al. [13] of radicals S1, S2 and S3 in RT X-irradiated sucrose single crystals, measured at 60 K

Radical	Proton type	Isotropic values	Anisotropic values	Eigenvectors		
				a^*	b	c
S1	H_{α}	46.4	-4.2	0.748	-0.348	0.565
			-2.5	0.427	0.904	-0.007
			6.7	-0.509	0.247	0.825
	$H_{\beta 1}$	16.0	-2.5	-0.853	-0.255	0.455
			-0.2	0.253	-0.965	-0.066
			2.8	0.456	0.059	0.888
$H_{\beta 2}$	11.4	-9.0	-0.327	0.145	0.934	
		2.5	0.165	-0.964	0.207	
		6.4	0.930	0.222	0.292	
S2	H_{α}	-38.9	-18.7	0.742	-0.034	0.669
			-0.6	-0.661	-0.200	0.723
			19.4	0.109	-0.979	-0.172
	$H_{\beta 1}$	16.5	-2.7	-0.895	0.378	-0.238
			-0.9	-0.142	0.265	0.954
			3.6	0.424	0.887	-0.183
$H_{\beta 2}$	13.8	-3.7	-0.880	-0.465	0.028	
		1.0	0.454	-0.874	-0.175	
		2.8	0.106	-0.142	0.984	
S3	H_{α}	-36.4	-17.5	0.869	0.005	0.494
			2.1	-0.467	-0.321	0.824
			15.4	0.163	-0.947	-0.276
	$H_{\beta 1}$	16.5	-3.1	-0.846	0.459	-0.272
			0.0	-0.148	0.289	0.946
			3.0	0.513	0.840	-0.176
$H_{\beta 2}$	12.4	-4.1	-0.883	-0.467	0.045	
		-0.4	0.454	-0.874	-0.174	
		4.5	0.121	-0.133	0.984	

Some sign corrections and symmetry operations have been applied.

The signal intensity was too weak, however, to allow for a full analysis.

Based on these observations one would thus expect radical R1 to correspond to radical T3 and radical R2 to radical T1. When comparing radicals R1 and T2/T3, a close correspondence in isotropy and anisotropy is observed for all three tensors, in particular when considering the different measuring temperatures. Based on these criteria, it is however not possible to distinguish with certainty between T2 and T3. In Table 2 an explicit comparison of the eigenvector directions is presented. In both cases the match is obvious, but a substantially better agreement emerges between the R1 and T3 radicals, especially in case of the $H_{\beta 1}(T2)/H_{\beta 1}(T3)$ tensors. The temperature clearly does not have much influence on the tensors. These observations already confirm a part of the prediction made above.

The comparison of radicals R2 and T1 is less straightforward. The agreement between the $H_{\beta 3}(R2)$ and $H_{\beta 2}(T1)$ tensors is excellent on all accounts (Table 2), strongly suggesting that radical R2 does indeed correspond to radical T1. However, the $H_{\beta 4}(R2)$ and the $H_{\beta 3}(T1)$ tensors are completely different (for both possible tensor shapes of the $H_{\beta 3}(T1)$ coupling). For this interaction, no clear-cut information was obtained from the temperature scans. One possible explanation is that with increasing temperature, a substantial shift in unpaired electron density occurs, prompted by geometric alterations of the radical, in turn

giving rise to either a β -coupling with significantly different characteristics, or even a coupling with another proton. Extended investigations would be necessary to resolve this matter.

4.4. DFT study on radical models proposed in literature

As described in Section 2, numerous studies have been performed in the past on RT radiation-induced defects in sucrose. However, only Sagstuen et al. [11] made some effort in searching for suitable radical models by taking into account the specific characteristics of all tensors. The radical structures they proposed as candidate models for the R1/T2/T3 radical are shown in Fig. 12 (structures III and IV in Sagstuen et al. [11]). In both cases a carbonyl group is positioned in a β -position to the carbon at which the main spin density is localised. The presence of this functional group was proposed to cause substantial delocalisation of the unpaired electron spin density onto the oxygen atom, which would result in isotropic and anisotropic components of the α -coupling to become considerably reduced, as is experimentally observed (Table 1). This would also account for the g-factor anisotropy being larger than for a typical carbon centred radical [11]. The assignment of these radical models was only tentative, however.

A first attempt at checking the validity of these models by means of DFT was made by Georgieva et al. [14]. That study

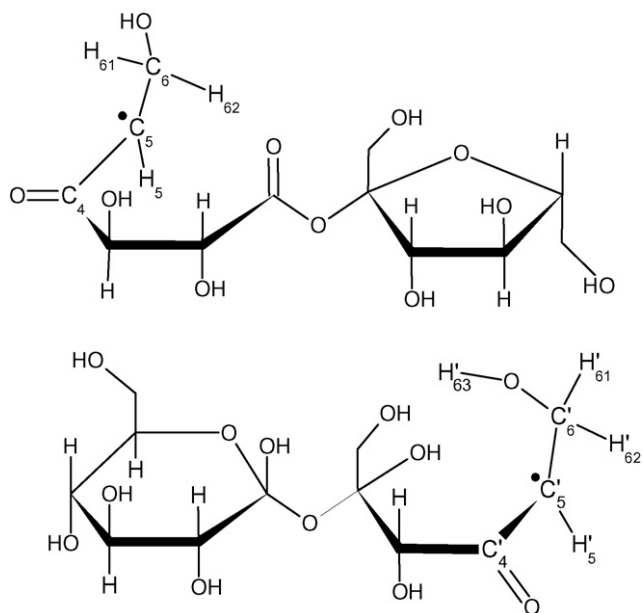


Fig. 12. Chemical structures of radical structures III (top) and IV (bottom) proposed by Sagstuen et al. [11] as possible models for the R1/T2/T3 radical in RT irradiated sucrose.

points out some general tendencies for coupling sizes and, in this context, gives some indications as to which kind of radical models should be pursued for the T2/T3 radical. It did however not present any final conclusions on this issue.

For this reason, a more advanced DFT study was undertaken in the present work. As the crystalline environment can evidently be crucial for the geometry of the radical, especially in the case of broken ring structures, geometry optimisations should be performed in a theoretical methodology that appropriately accounts for this environment. In the literature, both cluster [19,29] and periodic [40] approaches have been successfully adopted to simulate free radical structures in the solid state. In a cluster approach, only part of the molecular environment is explicitly taken up in the calculations, whereas a periodic scheme exploits the translational symmetry of the crystal and hence, automatically and fully incorporates the lattice environment. The latter approach is in principle best suited as it offers the most complete description of a crystalline system and does not require the constraints that are usually imposed on the boundary molecules/atoms of a cluster. Therefore, a periodic approach was adopted in this work for all geometry optimisations. To ensure that the radical was well separated from its periodic images, an $\langle ab2c \rangle$ supercell was used, obtained by doubling the original crystal unit cell in the $\langle c \rangle$ direction. All calculations were performed with the CPMD software package [41], using a BP86 gradient-corrected density functional [42,43], together with a plane wave basis set (with a maximum kinetic energy of 25 Ry for the plane waves) and ultra-soft pseudopotentials of the Vanderbilt type [44]. No geometric restrictions were imposed on the atoms of the supercell.

The EPR properties of the free radical were subsequently calculated adopting a cluster scheme. A cluster was cut out of each periodically optimised structure such that it contained the radi-

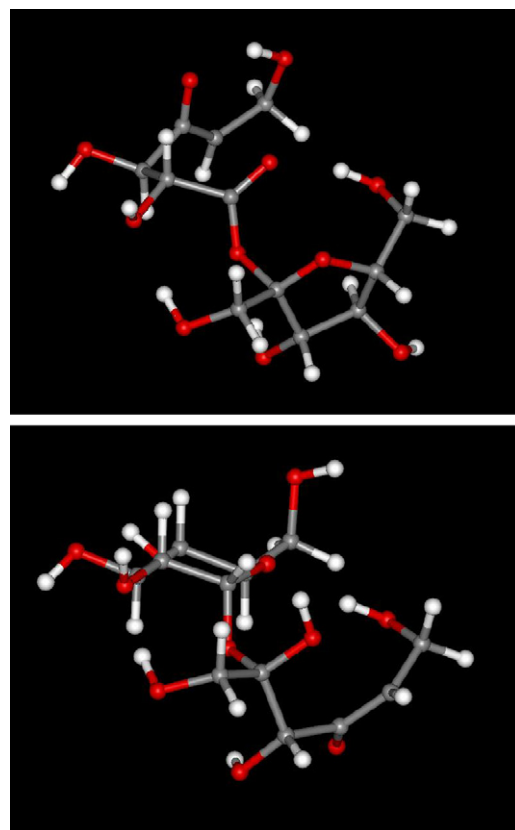


Fig. 13. 3D figures of radical structures III (top) and IV (bottom) (Fig. 12) after DFT geometry optimisation on a $\langle ab2c \rangle$ supercell in a periodical scheme.

cal and all (intact) molecules hydrogen bound to it (10 sucrose molecules in total). Hyperfine coupling tensors were calculated with the aid of the Gaussian 03 software suite [45], employing the B3LYP functional [46] and a 6-311G(d,p) basis set [47,48] for all atoms within the cluster. It has been shown [49] that incorporating the molecular environment in an EPR calculation can sometimes considerably improve its accuracy. In this respect, the proposed hybrid periodic/cluster scheme meets this demand at a sufficient level of theory [50].

The optimised radical structures are depicted in Fig. 13. The results of the EPR calculations on the optimised structures are presented in Table 4. As the α -tensors are often giving the most crucial information, these will be discussed first. The isotropic components of the α -proton couplings are indeed considerably reduced (as compared to 'normal' α -couplings [35]) but neither of the values obtained match the experimentally determined values for the T2 and T3 radicals (Table 1). Also, the calculated anisotropic coupling constants exceed the experimental values by about 50% in both cases. Although DFT calculations are known not to reproduce experimental values for isotropic couplings very accurately in some cases, the differences in anisotropy seem too big to be attributed to the inherent inaccuracy of DFT methods.

Using Eq. (2) (which is most reliable as the value of $Q_{\alpha, \text{dip}}^{\text{H}}$ is only slightly dependent on the radical geometry [39]), unpaired spin densities on the α -carbon of $\rho_{\pi} \approx 0.88$ and $\rho_{\pi} \approx 0.92$ are obtained for radical structures III and IV, respectively, which is

Table 4
Proton hyperfine coupling tensors for radical structures III and IV, obtained by means of cluster DFT calculations on radical structures acquired from periodic optimisations (Figs. 12 and 13)

Radical model	Proton	Isotropic values (MHz)	Anisotropic values (MHz)	Eigenvectors		
				a^*	b	c
III	H ₅	−49.45	−31.48	−0.365	0.166	0.916
			−2.54	−0.330	0.897	−0.293
			34.02	0.871	0.409	0.273
	H ₆₁	68.33	−4.41	0.599	0.248	0.761
			−2.53	−0.431	0.901	0.045
			6.94	0.675	0.355	−0.647
H ₆₂	4.82	−4.68	0.845	0.428	0.319	
		−3.51	−0.302	0.877	−0.374	
		8.19	−0.440	0.220	0.871	
IV	H' ₅	−30.50	−29.69	0.873	−0.294	−0.390
			−5.99	0.434	0.102	0.895
			35.68	0.223	0.950	−0.217
	H' ₆₁	43.74	−4.46	0.172	0.814	−0.555
			−3.88	0.198	0.523	0.829
			8.33	0.965	−0.253	−0.071
	H' ₆₂	98.80	−4.87	−0.388	0.776	−0.497
			−1.91	0.582	0.624	0.521
			6.78	0.714	−0.088	−0.694
	H' ₆₃	10.70	−3.35	0.422	0.902	−0.088
			−1.91	0.769	−0.408	−0.491
			5.26	0.479	−0.139	0.867

surprisingly high. The Mulliken atomic spin densities reported by the Gaussian program on the α -carbon atoms are 0.84 and 0.78 for models III and IV, respectively, confirming these results on a qualitative level. Eq. (1), on the other hand, yields $\rho_\pi \approx 0.69$ and $\rho_\pi \approx 0.42$ for structures III and IV. Such differences normally indicate that the radical centres are significantly bent [37,39], thus prohibiting significant delocalisation of the unpaired spin onto the carbonyl group. The Mulliken atomic spin densities on the carbonyl group are 0.26 and 0.21 for models III and IV, respectively corroborating this reasoning. However, as the calculated radical geometries are known, the planarity can be readily assessed. For structure III, the dihedral angle C₄–C₅–C₆–H₅ (i.e. the angle between the C₄–C₅–C₆ plane and the C₅–C₆–H₅ plane) is 179.9°, for structure IV, a dihedral angle C'₄–C'₅–C'₆–H'₅ of 170.8° is found (Fig. 12). The almost perfect planarity for radical structure III (and, correspondingly, the surprisingly high actual spin density on the α -carbon) possibly suggests that the differences in calculated spin densities mentioned above are due to some other factor than bending of the radical centre. As this is of no importance for the goal of the present study, this was not further investigated.

It can be concluded that the general shapes of the α -tensors obtained by DFT calculations on radical structures III and IV do not bear much resemblance with the experimentally observed α -tensor shapes of radicals T2 and T3.

Some more results, suggesting that radical structures III and IV are not valid models, emerge from the DFT calculations (Table 4). Firstly, the isotropic components of the H_{β1} proton in model III and of both H_β protons in model IV are far too large as compared to the experimental values. Secondly, careful examinations show no match whatsoever between the calculated

and experimentally determined eigenvectors for either of the couplings. Finally, the calculations on radical structure IV indicate that an appreciable coupling with the hydroxylproton H'₆₃ (Fig. 12) should be observable. No such coupling was observed in the ENDOR spectra. Moreover, spectra recorded using partially deuterated samples clearly indicated that none of the major couplings are due to exchangeable protons.

5. Conclusion

The present study was undertaken to provide an understanding of the various differences in the experimental EMR as well as computational DFT data previously reported in the literature on RT radiation-induced radicals in single crystals of sucrose [11,13]. A new set of nine ¹H hyperfine coupling tensors was obtained from EMR measurements at 110 K. These were attributed to a total of three radical species as also was indicated in previous studies [13,14]. Good quantitative agreement was found with the data published by Sagstuen et al. [11] on most accounts and a qualitative agreement was found with the data by Vanhaelewyn et al. [13]. For radicals T2/T3, differences in measuring temperature cause only minor and reversible changes in the 20–295 K range. The T1 radical seems to be somewhat more temperature dependent, especially in the 250–295 K range. The data set presented in this work (Table 1) should be considered as the most accurate for the main RT radiation-induced radical species in sucrose in the 20–295 K temperature range with regard to radicals T2 and T3, and in the 20–250 K range – and possibly up to RT – with regard to radical T1. Some ambiguity concerning one of the smaller T1 hyperfine interactions still exists, however.

The results from DFT calculations performed on the radical structures proposed by Sagstuen et al. [11] strongly suggest that these structures are not suitable models for the T2/T3 radicals. Consequently, the molecular structures of all RT radiation-induced radicals in crystalline sucrose remain unknown.

References

- [1] W.K. Pogożelski, T.D. Tullius, *Chem. Rev.* 98 (1998) 1089–1107.
- [2] W.A. Bernhard, D.M. Close, in: A. Mozumdar, Y. Hatano (Eds.), *Charged Particle and Photon Interactions with Matter Chemical, Physicochemical and Biological Consequences with Applications*, Marcel Dekker, Inc., New York, 2004, pp. 431–470.
- [3] T. Nakajima, *Health Phys.* 55 (1988) 951–955.
- [4] T. Nakajima, *Appl. Radiat. Isot.* 46 (1995) 819–825.
- [5] F. Americo, M. Silveira, O. Baffa, *Appl. Radiat. Isot.* 46 (1995) 827–830.
- [6] N.D. Yordanov, V. Gancheva, E. Georgieva, *Radiat. Chem. Phys.* 65 (2002) 269–276.
- [7] N.D. Yordanov, E. Georgieva, *Spectrochim. Acta Part A* 60 (2004) 1307–1314.
- [8] A. Gräslund, G. Löfroth, *Acta Chem. Scand. B* 29 (1975) 475–482.
- [9] E.E. Budzinski, W.R. Potter, G. Potienko, H.C. Box, *J. Chem. Phys.* 70 (1979) 5040–5044.
- [10] H.C. Box, E.E. Budzinski, *J. Chem. Phys.* 79 (1983) 4142–4145.
- [11] E. Sagstuen, A. Lund, O. Awaldelkartim, M. Lindgren, J. Westerling, *J. Chem. Phys.* 90 (1986) 5584–5588.
- [12] H.C. Box, E.E. Budzinski, H.G. Freund, *J. Chem. Phys.* 93 (1) (1990) 55–57.
- [13] G. Vanhaelewyn, J. Sadlo, F. Callens, W. Mondelaers, D. De Frenne, P. Matthys, *Appl. Radiat. Isot.* 52 (2000) 1221–1227.
- [14] E.R. Georgieva, L. Pardi, G. Jeschke, D. Gatteschi, L. Sorace, N.D. Yordanov, *Free Radic. Res.* 40 (2006) 553–563.
- [15] B. Bungum, E.O. Hole, E. Sagstuen, M. Lindgren, *Radiat. Res.* 139 (1994) 194–202.
- [16] K.P. Madden, W.A. Bernhard, *J. Phys. Chem.* 84 (1980) 1712–1717.
- [17] K.P. Madden, W.A. Bernhard, *J. Phys. Chem.* 86 (1982) 4033–4036.
- [18] G. Vanhaelewyn, P. Lahorte, F. De Proft, W. Mondelaers, P. Geerlings, F. Callens, *Phys. Chem. Chem. Phys.* 3 (2001) 1709–1716.
- [19] G. Vanhaelewyn, E. Pauwels, F. Callens, M. Waroquier, E. Sagstuen, P. Matthys, *J. Phys. Chem. A* 110 (2006) 2147–2156.
- [20] P.O. Samskog, A. Lund, G. Nilsson, M.C.R. Symons, *J. Chem. Phys.* 73 (1980) 4862–4866.
- [21] P.O. Samskog, A. Lund, *Chem. Phys. Lett.* 75 (1980) 525–527.
- [22] P.O. Samskog, L.D. Kispert, A. Lund, *J. Chem. Phys.* 79 (1983) 635–638.
- [23] E.E. Budzinski, H.C. Box, *J. Chem. Phys.* 82 (1985) 3487–3490.
- [24] H.C. Box, E.E. Budzinski, H.G. Freund, *Radiat. Res.* 121 (1990) 262–266.
- [25] E. Sagstuen, M. Lindgren, A. Lund, *Radiat. Res.* 128 (1991) 235–242.
- [26] P.O. Samskog, L.D. Kispert, A. Lund, *J. Chem. Phys.* 77 (1982) 2330–2335.
- [27] P.O. Samskog, L.D. Kispert, A. Lund, *J. Chem. Phys.* 78 (1983) 5790–5794.
- [28] G. Vanhaelewyn, B. Jansen, E. Pauwels, E. Sagstuen, M. Waroquier, F. Callens, *J. Phys. Chem. A* 108 (2004) 3308–3314.
- [29] E. Pauwels, V. Van Speybroeck, M. Waroquier, *J. Phys. Chem. A* 110 (2006) 6504–6513.
- [30] C.A. Beevers, T.R.R. McDonald, J.H. Robertson, F. Stern, *Acta Crystallogr., Sect. B: Struct. Crystallogr. Cryst. Chem.* 5 (1952) 689.
- [31] G.M. Brown, H.A. Levy, *Science* 141 (1963) 921–923.
- [32] G.M. Brown, H.A. Levy, *Acta Crystallogr., Sect. B: Struct. Crystallogr. Cryst. Chem.* 29 (1973) 790–797.
- [33] W.H. Nelson, *J. Magn. Reson.* 38 (1980) 71–78.
- [34] A.R. Sørnes, E. Sagstuen, A. Lund, *J. Phys. Chem.* 99 (1995) 16867–16876.
- [35] W. Gordy, *Theory and Applications of Electron Spin Resonance*, Wiley, New York, 1980.
- [36] H.M. McConnell, D.B. Chesnut, *J. Chem. Phys.* 28 (1958) 107–117.
- [37] P.A. Erling, W.H. Nelson, *J. Phys. Chem. A* 108 (2004) 7591–7595.
- [38] W.A. Bernhard, *Adv. Radiat. Biol.* 9 (1981) 199.
- [39] W.A. Bernhard, *J. Chem. Phys.* 81 (1984) 5928–5935.
- [40] R. Declerck, E. Pauwels, V. Van Speybroeck, M. Waroquier, *J. Phys. Chem. B*, submitted for publication.
- [41] CPMD V3.11 Copyright IBM Corp. 1990–2006, Copyright MPI fuer Festkoerperforschung Stuttgart 1997–2001.
- [42] J.P. Perdew, *Phys. Rev. B* 33 (1986) 8822–8824.
- [43] A.D. Becke, *J. Chem. Phys.* 96 (1992) 2155–2160.
- [44] D. Vanderbilt, *Phys. Rev. B* 41 (1990) 7892–7895.
- [45] M.J. Frisch, G.W. Trucks, H.B. Schlegel, G.E. Scuseria, M.A. Robb, J.R. Cheeseman, J.J.A. Montgomery, T. Vreven, K.N. Kudin, J.C. Burant, J.M. Millam, S.S. Lyengar, J. Tomasi, V. Barone, B. Mennucci, M. Cossi, G. Scalmani, N. Rega, G.A. Petersson, H. Nakatsuji, M. Hada, M. Ehara, K. Toyota, R. Fukuda, J. Hasegawa, M. Ishida, T. Nakajima, Y. Honda, O. Kitao, H. Nakai, M. Klene, X. Li, J.E. Knox, H.P. Hratchian, J.B. Cross, C. Adamo, J. Jaramillo, R. Gomperts, R.E. Stratmann, O. Yazyev, A.J. Austin, R. Cammi, C. Pomelli, J.W. Ochterski, P.Y. Ayala, K. Morokuma, G.A. Voth, P. Salvador, J.J. Dannenberg, V.G. Zakrzewski, S. Dapprich, A.D. Daniels, M.C. Strain, O. Farkas, D.K. Malick, A.D. Rabuck, K. Raghavachari, J.B. Foresman, J.V. Ortiz, Q. Cui, A.G. Baboul, S. Clifford, J. Cioslowski, B.B. Stefanov, G. Liu, A. Liashenko, P. Piskorz, I. Komaromi, R.L. Martin, D.J. Fox, T. Keith, M.A. Al-Laham, C.Y. Peng, A. Nanayakkara, M. Challacombe, P.M.W. Gill, B. Johnson, W. Chen, M.W. Wong, C. Gonzalez, J.A. Pople, *Gaussian 03, Revision B.03*, Gaussian, Inc., Pittsburgh, PA, 2003.
- [46] A.D. Becke, *J. Chem. Phys.* 104 (1996) 1040–1046.
- [47] R. Krishnan, J.S. Binkley, R. Seeger, J.A. Pople, *J. Chem. Phys.* 72 (1980) 650–654.
- [48] A.D. McLean, G.S. Chandler, *J. Chem. Phys.* 72 (1980) 5639–5648.
- [49] E. Pauwels, V. Van Speybroeck, M. Waroquier, *J. Phys. Chem. A* 108 (2004) 11321–11332.
- [50] E. Pauwels, R. Declerck, V. Van Speybroeck, M. Waroquier, *Radiat. Res.*, accepted for publication.

7.2 Paper II

Identification and conformational study of stable radiation-induced defects in sucrose single crystals using density functional theory calculations of electron magnetic resonance parameters

H. De Cooman, E. Pauwels, H. Vrielinck, E. Sagstuen, F. Callens and
M. Waroquier

Journal of Physical Chemistry B, 2008, 112, 7298-7307

Copyright 2008 by the American Chemical Society.

Identification and Conformational Study of Stable Radiation-Induced Defects in Sucrose Single Crystals using Density Functional Theory Calculations of Electron Magnetic Resonance Parameters

H. De Cooman,^{†,‡} E. Pauwels,[‡] H. Vrielinck,[†] E. Sagstuen,[§] F. Callens,[†] and M. Waroquier^{*,‡}

Department of Solid State Sciences, Ghent University, Krijgslaan 281-S1, B-9000 Gent, Belgium, Center for Molecular Modeling, Ghent University, Proeftuinstraat 86, B-9000 Gent, Belgium, and Department of Physics, University of Oslo, P.O. Box 1048 Blindern, N-0316 Oslo, Norway

Received: December 21, 2007

One of the major stable radiation-induced radicals in sucrose single crystals (radical T2) has been identified by means of density functional theory (DFT) calculations of electron magnetic resonance parameters. The radical is formed by a net glycosidic bond cleavage, giving rise to a glucose-centered radical with the major part of the spin density residing at the C₁ carbon atom. A concerted formation of a carbonyl group at the C₂ carbon accounts for the relatively small spin density at C₁ and the enhanced g factor anisotropy of the radical, both well-known properties of this radical from several previous experimental investigations. The experimentally determined and DFT calculated proton hyperfine coupling tensors agree very well on all accounts. The influence of the exact geometrical configuration of the radical and its environment on the tensors is explored in an attempt to explain the occurrence and characteristics of radical T3, another major species that is most likely another conformation of T2. No definitive conclusions with regard to the actual structure of T3 could be arrived at from this study. However, the results indicate that, most likely, T3 is identical in chemical structure to T2 and that changes in the orientation of neighboring hydroxy groups or changes in the configuration of the neighboring fructose ring can probably not account for the type and size of the discrepancies between T2 and T3.

1. Introduction

Considerable efforts were made during the last few decades to gain insight into the radiation chemistry of saccharides. These experimental studies typically rely on electron magnetic resonance (EMR) techniques, such as electron paramagnetic resonance (EPR), electron–nuclear double resonance (ENDOR), and ENDOR-induced EPR (EIE). They have been quite successful in identifying radiation-induced radicals and suggest that some common mechanisms are operative with respect to their formation (rhamnose,^{1–6} glucose-1-phosphate,⁷ methyl- α -D-glucopyranoside,⁸ α -D-glucopyranoside,⁹ β -D-fructose,¹⁰ trehalose,^{11–13} sucrose^{13–19}). However, both identifying radical structures and unraveling their formation mechanisms are still far from trivial tasks, and particularly with regard to radicals stable at room temperature (RT), these studies often have been less conclusive.

In sucrose, trapped electrons¹⁷ and alkoxy radical formation¹⁵ have been reported after irradiation at 4 K. Until recently, however, the experimental studies on stable RT radicals in sucrose single crystals^{13,16,18,19} were in disagreement on several points, impeding any attempt at identifying the radical structures and their formation mechanisms. In a recent study,²⁰ this matter was cleared up, and unambiguous data are now available. In summary, three different radicals, labeled T1, T2, and T3, were spectroscopically characterized, with T2 and T3 being very similar. Furthermore, density functional theory (DFT) calculations presented in that study²⁰ convincingly showed that the so

far most attractive radical model for the T2/T3 radicals proposed in literature¹⁶ was incapable of properly reproducing the experimental data.

A number of semiempirical rules and relations, for example, the McConnell relation²¹ and the Heller–McConnell relation,²² can be used to interpret experimental data in terms of possible radical models. However, if complex molecular changes occur, more general and more powerful tools are necessary. As illustrated in, for example, refs 23–27, DFT based quantum chemical calculations have proven to be particularly useful for assisting in structure assignments: comparison of experimentally obtained EMR results with parameters calculated for a certain radical structure using DFT may provide arguments for either rejection or validation of a proposed radical model. However, DFT calculations are not capable of predicting which radicals will be formed, and often a large number of radical models can be devised that potentially could account for a certain set of experimental results. For carbohydrates, this problem is pronounced, as there are no characteristic functional groups distinguishing between possible radical sites and there are no characteristic magnetic nuclei distinguishing between possible radical models. In this context, the semiempirical rules provide valuable information to discriminate between different radical models. For the limited list of plausible radical candidates thus obtained, DFT calculations can be employed in order to identify the actual radical structure. The current work provides an excellent illustration of this synergy: a set of possible radical models is inferred from the experimental data, and DFT calculations are subsequently employed to positively identify one of these as the proper structure of the T2 radical. Furthermore, the sensitivity of the calculated hyperfine (HF)

* To whom all correspondence should be addressed. Phone: 003292646559. Fax: 003292646697. E-mail: michel.waroquier@ugent.be.

[†] Department of Solid State Sciences, Ghent University.

[‡] Center for Molecular Modeling, Ghent University.

[§] Department of Physics, University of Oslo.

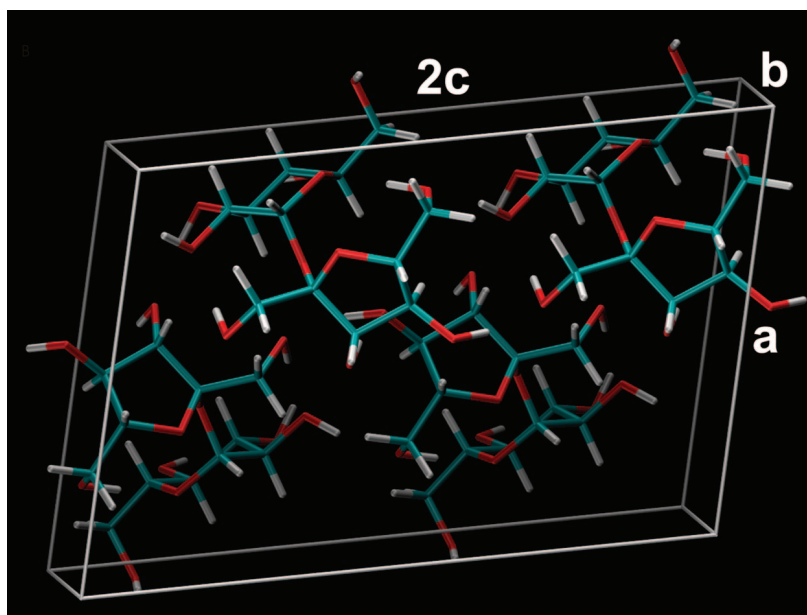


Figure 1. Three-dimensional structure of the $\langle ab2c \rangle$ supercell used for periodic geometry optimizations in the current work, obtained by doubling the crystal unit cell in the $\langle c \rangle$ direction. The atomic coordinates were taken from ref 50.

coupling tensors to the precise conformation of the radical and its environment is explored in an attempt to understand the coexistence and the characteristics of the T3 radical.

2. Computational Procedures

2.1. Geometry Optimizations. The stable geometry of a given molecular radical species obviously depends on the actual environment. In sugar single crystals, this environment consists of a periodic lattice, primarily governed by inter- and intramolecular hydrogen bonds. When the radical model is expected to involve considerable nuclear and electronic reorganization, geometry optimizations should be performed using a theoretical methodology that appropriately accounts for this environment. In the literature, both cluster^{24,25} and periodic²⁸ approaches have proven successful in modeling free radical structures in the solid state. As a periodic model exploits the translational symmetry of the crystal, it automatically and fully incorporates the full lattice environment and therefore offers the most complete description of a crystalline system. This approach does not require the artificial constraints that have to be imposed on the boundary molecules/atoms within a cluster methodology. Because the number of atoms can be substantially decreased as compared with a typical, physically sound cluster, the computational cost can also be considerably reduced. Moreover, a very recent study by Declerck and co-workers on sugar radicals²⁹ has shown that (i) the accuracy of the calculated EMR parameters depends chiefly on the accuracy of the geometry and (ii) that this geometry is most accurately predicted within a periodic model. Therefore, a periodic approach was adopted in the present work for all geometry optimizations. To ensure that the radical was well-separated from its periodic images, an $\langle ab2c \rangle$ supercell (180 atoms) was used, obtained by doubling the original crystal unit cell in the $\langle c \rangle$ direction. This supercell is depicted in Figure 1. To corroborate the validity of this model, a reference calculation was performed with the considerably larger and therefore computationally much more demanding $\langle 2a2b2c \rangle$ supercell (720 atoms). All calculations were performed with the CPMD software package,³⁰ using a BP86 gradient-corrected density functional,^{31,32} together with a plane wave basis set (with a maximum kinetic energy of 25 Ry for

the plane waves) and ultrasoft pseudopotentials of the Vanderbilt type.³³ Unless explicitly mentioned, no constraints were imposed on the atoms of the supercell.

2.2. Calculation of EMR Parameters. Within the CPMD software package, pseudopotentials are employed in the calculation of EMR parameters. This method is known to reproduce less accurately the HF coupling tensors, in particular, the isotropic values, as compared with an all electron approach.³⁴ On the other hand, several studies, for example, refs 29 and 35, have clearly shown that incorporation of the molecular environment can have an appreciable effect on the calculated EMR parameters. Therefore, the same hybrid periodic/cluster model used in our previous work²⁰ was adopted: HF coupling tensors were calculated using the Gaussian03 software suite³⁶ on a cluster that was cut out of each periodically optimized structure such that it contained the radical and all (intact) molecules hydrogen bound to it (10 surrounding sucrose molecules in total). The B3LYP functional³⁷ and a 6-311G(d,p) basis set^{38,39} were used for all atoms within the cluster. This hybrid model provides highly accurate EMR parameters at a reasonable computational cost.

The cluster approach applied for the calculation of the HF parameters would be computationally too demanding in the case of the g tensor. Therefore, g tensor calculations were performed, also using the Gaussian03 software suite, but only on the optimized radical molecule cut out of the periodically optimized $\langle ab2c \rangle$ supercell (referred to as Approach #1). Because the environment is completely neglected in this approach, calculations were also performed using the optimized $\langle ab2c \rangle$ supercell with the CPMD software package (referred to as Approach #2), even if the pseudopotential model is inherently less accurate, also for the g tensor. The code for these calculations has recently been developed by Declerck and co-workers.⁴⁰ A BLYP functional form^{41,42} was used, together with a 100 Ry cutoff plane wave basis set and Goedecker type norm-conserving pseudopotentials.⁴³

Whenever a comparison is made between experimental eigenvectors on the one hand and crystal directions or calculated eigenvectors on the other hand, allowed symmetry operations

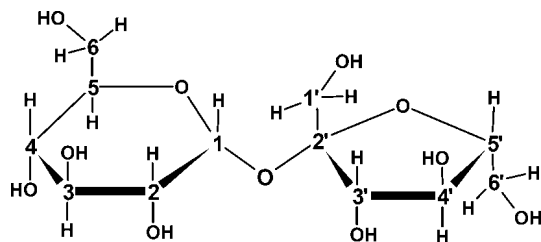


Figure 2. Chemical structure of the sucrose molecule with the atomic numbering used in the present work. Carbon bound hydrogen atoms and oxygen atoms are labeled according to the carbon to which they are bound, and hydroxy protons are labeled according to the oxygen to which they are bound. For example, H₃ is the hydrogen at C₃ and H(O₃) is the hydroxy proton at C₃.

TABLE 1: Proton Hyperfine Coupling Tensors (in MHz) of Stable Radicals T2 and T3 in Room Temperature X-Irradiated Sucrose Single Crystals, Measured at 110 K, Approximately Two Days after Irradiation^{a,20}

radical	proton	iso	aniso	eigenvectors			δ (°)
				a*	b	c	
T2	H _{α}	-38.69	-19.66	0.424	-0.163	-0.891	10.9
			-2.11	0.886	0.280	0.371	14.4
			21.77	0.189	-0.946	0.263	12.1
	H _{β1}	16.37	-2.32	0.869	-0.355	-0.344	20.9
			-1.72	-0.209	0.368	-0.906	22.4
			4.04	0.448	0.860	0.246	9.8
H _{β2}	13.68	-3.09	0.718	-0.650	0.248	14.9	
		-2.17	0.638	0.473	-0.608	14.2	
		5.26	0.278	0.595	0.754	13.0	
T3	H _{α}	-35.81	-18.98	0.584	-0.184	-0.790	
			-2.11	0.755	0.481	0.446	
			21.09	0.298	-0.857	0.420	
	H _{β1}	16.42	-2.10	0.840	-0.541	-0.034	
			-1.77	0.178	0.334	-0.926	
			3.87	0.512	0.772	0.377	
H _{β2}	12.24	-3.62	0.528	-0.822	0.214		
		-2.12	0.804	0.402	-0.439		
		5.74	0.275	0.403	0.873		

^a In the right hand column, the deviation δ between the eigenvectors of T2 and T3 are given.

were performed on the experimental eigenvectors in such a way that the best possible agreement is obtained.

3. Results and Discussion

3.1. Interpretation of Experimental Results. Figure 2 shows the chemical structure of the sucrose molecule, with the numbering model used in this work. The experimentally

determined tensors for the T2 and T3 radicals present in RT irradiated sucrose single crystals are listed in Table 1, as reported in ref 20. From comparison with ENDOR spectra of deuterated crystals, it was established that all of these interactions arise from nonexchangeable protons.^{16,20}

The T2 and T3 radicals are essentially characterized by three proton HF couplings: one larger coupling due to an α -proton interaction and two smaller couplings due to either β - or γ -proton interactions. The spin density on an α proton can be estimated using either the isotropic (McConnell relation,²¹ eq 1) or the anisotropic values (Gordy–Bernhard relation,⁴⁴ eq 2) of the HF coupling tensor:

$$a_{\text{iso}}^{\alpha} = Q_{\text{iso}}^{\alpha} \rho^{\pi} \quad (1)$$

$$b_{+, \text{aniso}}^{\alpha} = Q_{\text{aniso}}^{\alpha} \rho^{\pi} \quad (2)$$

where a_{iso}^{α} is the isotropic component, $b_{+, \text{aniso}}^{\alpha}$ is the most positive dipolar component, ρ^{π} is the unpaired spin density localized on the carbon in the $2p_z$ lone electron orbital (LEO), and Q_{iso}^{α} and $Q_{\text{aniso}}^{\alpha}$ are empirical “constants”, dependent to some extent on the nature of the radical fragment. For Q_{iso}^{α} , a value of -72 MHz is generally assumed,⁴⁵ and for $Q_{\text{aniso}}^{\alpha}$, a value of 38.7 MHz was proposed.⁴⁶ As stated previously,²⁰ eqs 1 and 2 both yield unpaired spin densities of 0.50 – 0.55 for both radicals (T2 and T3), indicating that about 50% of the unpaired spin density is delocalized on other nuclei and, furthermore, that the spin centers are essentially planar.⁴⁶ Sagstuen et al. made similar observations¹⁶ and suggested the presence of a neighboring carbonyl group as an explanation. This would account for the delocalization and also for the g factor anisotropy being larger than that for a typical carbon-centered radical. This proposal was further corroborated by the results obtained by Flores and co-workers⁴⁷ and Yordanov and Karakirova.⁴⁸ For X-irradiated sucrose powder and single crystals, these authors found an increase in the intensity of certain bands in the optical absorption spectrum in the UV region, linearly dependent on the applied radiation dose. Some of these absorption bands ($\lambda = 250$ and 320 nm) are typically associated with carbonyl groups in organic compounds.

Sagstuen et al. proposed two specific radical models containing a carbonyl group,¹⁶ but it was shown in ref 20 that these could not account for the experimentally observed proton HF couplings. Nevertheless, the compelling evidence for the presence of a neighboring carbonyl group urged us to explore this path further in the present work. A large variety of tentative radical models containing a carbonyl group next to the carbon site of the unpaired spin density can be envisioned, however.

TABLE 2: Comparison of C \cdots H Directions in the Pristine Crystal Molecule (Calculated Using the Atomic Coordinates Reported in Ref 50) with the Directions of the Eigenvectors Corresponding to the Most Positive Anisotropic Hyperfine Coupling Values of H _{β 1}(T2), H _{β 2}(T2), H _{β 1}(T3), and H _{β 2}(T3) (Table 1)^a

hydrogen position	distance (Å)	direction cosines			δ (°)		δ (°)		
		a*	b	c	H _{β1} (T2)	H _{β2} (T2)	H _{β1} (T3)	H _{β2} (T3)	
C ₁ \cdots H ₃	γ	2.78	0.428	-0.897	-0.112	20.7		29.6	
C ₁ \cdots H ₅	γ	2.74	0.138	-0.647	0.750		8.5		17.6
C ₃ \cdots H ₁	γ	3.46	-0.150	0.984	0.092	27.0		36.7	
C ₃ \cdots H ₅	γ	2.79	-0.082	0.235	-0.968		26.7		15.7
C ₄ \cdots H ₂	γ	2.69	-0.148	0.652	-0.744	36.0		30.8	
C ₄ \cdots H ₅	β	2.15	0.542	0.443	0.714		17.7		18.0
C ₃ \cdots H _{1'a}	γ	2.74	-0.173	0.534	-0.828		8.1		9.9
C ₃ \cdots H _{1'b}	γ	3.50	-0.568	0.203	-0.797		28.3		20.9
C ₃ \cdots H _{5'}	γ	2.87	-0.515	0.762	0.394	37.9		45.3	

^a δ denotes the angle between the directions.

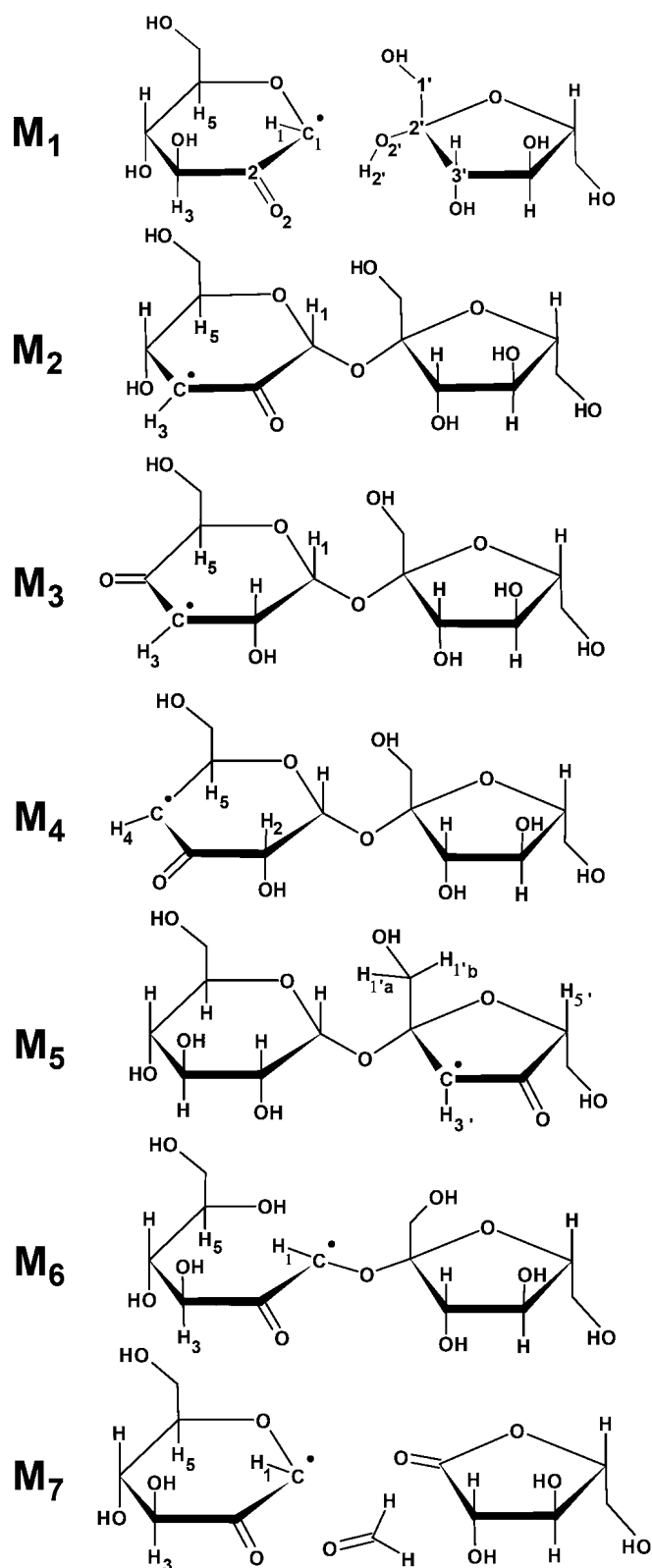


Figure 3. Chemical structure of the different radical models for which DFT geometry optimizations and EMR calculations were performed (see Table 3).

Important additional information can be obtained from the anisotropy of the two smaller HF couplings which is smaller than usual for regular β -type proton HF interactions. Because the experimental $H_{\beta 1}$ and $H_{\beta 2}$ tensors display a typical dipolar anisotropic shape (Table 1), a classical point dipole–dipole approximation is expected to be valid. In this approximation,

the most positive dipolar component $b_{+,dip}$ is dependent on the electron–nucleus distance r as

$$b_{+,dip} = \frac{\rho^\pi \mu_0 g \mu_B g_N \mu_N}{2\pi r^3}$$

where ρ^π is the unpaired spin density localized in the LEO, and μ_0 , g , μ_B , g_N , and μ_N are the vacuum permeability, the radical g value, the Bohr magneton, the proton nuclear g factor, and the nuclear magneton respectively. Approximating g by the free electron g value of 2.0023 and assuming $\rho^\pi = 0.5$ (see above), the values for $b_{+,dip}$ in Table 1 yield values for r of 2.7 Å and 2.4–2.5 Å for the $H_{\beta 1}$ and $H_{\beta 2}$ protons, respectively. These values are considerably higher than the typical $C_\alpha \cdots H_\beta$ distance of 2.1 Å in the sucrose molecule. The former value, in particular, more closely resembles the typical $C_\alpha \cdots H_\gamma$ distance of 2.7–2.8 Å. This suggests that $H_{\beta 1}$ and probably also $H_{\beta 2}$ are actually γ protons. The fact that the isotropic coupling values of about 15 MHz are rather large does not invalidate this hypothesis. Box and co-workers have convincingly argued⁴⁹ that the magnitude of the γ -proton isotropic HF couplings is strongly dependent on the exact conformation of the radical. Therefore, tentative models should be considered where $H_{\beta 1}$ and possibly also $H_{\beta 2}$ are in fact γ -protons, rather than β -protons as presumed by Sagstuen et al.

Unless a ring opening event occurs, $C_\alpha \cdots H_\gamma$ directions and distances are not expected to change much as compared to the values for the pristine crystal molecule because of the relatively large spatial separations. It is well-known that the eigenvector associated with $b_{+,dip}$ is oriented roughly along the line connecting the (main) site of the unpaired spin with the interacting nucleus. Therefore, a comparison was made between the eigenvectors associated with $b_{+,dip}$ and the directions of the different $C_\alpha \cdots H_\beta$ and $C_\alpha \cdots H_\gamma$ of the pristine crystal. For $H_{\beta 1}$, only hydrogen atoms at a γ -position were considered; for $H_{\beta 2}$, hydrogen atoms at both β - and γ -positions were considered. Also, only carbon bound hydrogen atoms should be considered, since all HF interactions arise from nonexchangeable protons. The directions were calculated from the atomic coordinates reported in ref 50.

For only a few cases, an acceptable agreement was found between the $C_\alpha \cdots H_\beta$ or $C_\alpha \cdots H_\gamma$ direction and the two smaller HF interactions. The results are shown in Table 2. The corresponding radical models are depicted in Figure 3 and labeled M_1 – M_5 . For the C_1 centered radical M_1 , a scission of the glycosidic bond is necessary whereas the other models require the net abstraction of a hydroxy group. Ring opening events are not considered: if a hydroxy group would be present at an α position, the hydroxy hydrogen hyperfine coupling should have been detected experimentally. Thus, a limited number of radical models is arrived at and these can now be investigated further by DFT methods.

3.2. Radical Model Assignment. Geometry optimizations and calculations of EMR parameters were performed for radical models M_1 to M_5 (Figure 3) as described in Computational Procedures. In Table 3, the results are reported and compared with the experimental data. For most models, the agreement between calculated and experimental HF tensors is very poor for at least one of the couplings. Apart from other discrepancies, models M_2 , M_3 , and M_4 may readily be discarded as they would give rise to a β -proton interaction with an isotropic component of more than 100 MHz. Model M_5 can also be dismissed, among others because the directions of the α -proton eigenvectors are off by 50° and more. For model M_1 , however, the agreement between the

TABLE 3: Proton Hyperfine Coupling Tensors (in MHz) for Radical Models M₁–M₇, Shown in Figure 3, Obtained by Means of DFT Calculations As Described in Computational Procedures^a

radical model	proton	iso	aniso	eigenvectors			proton	δ (°)	
				a*	b	c		T2	T3
M ₁	H ₁	-34.60	-20.23	-0.451	0.155	0.879	H _{α}	1.8	9.3
			-4.66	0.875	0.267	0.403		2.1	14.3
			24.89	-0.173	0.951	-0.256		1.2	13.0
	H ₃	16.18	-2.16	0.874	0.462	0.154	H _{β1}	29.5	11.9
			-1.86	-0.249	0.152	0.957		29.5	11.4
			4.02	-0.418	0.874	-0.248		1.9	10.9
H ₅	12.59	-2.88	0.675	0.673	0.303	H _{β2}	4.2	13.1	
		-2.06	0.698	-0.450	-0.557		4.7	9.5	
		4.95	0.239	-0.588	0.773		2.5	12.2	
M ₂	H ₃	-42.75	-24.29	0.513	0.635	-0.577	H _{α}	33.4	29.2
			-3.72	0.836	-0.218	0.503		8.9	16.2
			28.01	-0.194	0.741	0.643		33.6	32.1
	H ₁	0.53	-2.38	0.804	-0.071	0.590	H _{β1}	61.9	46.0
			-0.92	0.567	0.390	-0.726		66.7	25.5
			3.30	-0.178	0.918	0.353		38.5	41.4
H ₅	-1.29	-2.96	0.066	0.986	-0.151	H _{β2}	49.4	35.6	
		-1.71	0.974	-0.096	-0.204		37.7	24.3	
		4.67	0.215	0.134	0.967		44.8	31.8	
M ₃	H ₃	-45.44	-5.74	0.167	0.836	0.523	H _{α}	41.6	43.5
			-0.91	0.334	-0.547	0.767		20.9	35.0
			6.65	0.928	0.046	-0.371		42.1	40.0
	H ₁	-1.05	-2.23	0.796	0.155	-0.585	H _{β1}	18.5	39.4
			-1.47	0.600	-0.070	0.797		34.7	52.6
			3.69	-0.083	0.985	0.148		32.0	41.7
H ₅	-6.20	-2.87	0.880	-0.474	-0.018	H _{β2}	20.6	31.7	
		-1.25	0.432	0.817	-0.383		26.6	32.5	
		4.11	0.196	0.329	0.924		18.8	6.9	
M ₄	H ₄	-45.75	-5.60	0.036	0.357	0.933	H _{α}	9.6	18.7
			-1.41	0.881	0.429	-0.199		20.3	34.3
			7.01	-0.472	0.829	-0.299		19.4	28.5
	H ₂	2.25	-2.49	0.864	0.334	0.378	H _{β1}	42.3	26.6
			-1.29	-0.498	0.451	0.741		42.9	22.4
			3.78	-0.077	0.828	-0.556		28.0	27.4
H ₅	106.43	-5.56	0.639	0.626	-0.447	H _{β2}	86.6	74.1	
		-1.42	0.729	-0.679	0.090		84.9	74.1	
		6.98	0.247	0.383	0.890		14.5	2.2	
M ₅	H _{3'}	-47.77	-27.86	0.378	0.307	0.873	H _{α}	48.2	58.3
			-3.75	0.435	0.774	-0.461		64.5	60.3
			31.61	0.817	-0.554	-0.159		50.5	49.4
	H _{5'}	-0.71	-2.30	0.577	0.627	-0.523	H _{β1}	25.3	32.6
			-1.11	0.486	0.251	0.837		17.7	39.4
			3.40	-0.656	0.737	0.160		27.3	32.4
H _{1'a}	1.89	-4.20	0.725	-0.562	-0.399	H _{β2}	86.8	80.5	
		-1.69	0.689	0.575	0.441		84.2	82.6	
		5.89	-0.018	-0.595	0.804		17.3	20.5	
H _{1'b}	16.51	-2.12	0.278	0.952	0.127	H _{β2}	31.7	16.9	
		-1.09	0.667	-0.097	-0.739		23.0	26.0	
		3.21	0.691	-0.290	0.662		30.2	27.8	
M ₆	H ₁	-41.28	-22.43	0.649	0.521	0.554	H _{α}	72.3	81.1
			-3.48	0.677	-0.062	-0.734		71.9	81.1
			25.90	-0.348	0.851	-0.393		13.0	3.3
	H ₃	0.24	-2.70	0.703	-0.099	-0.704	H _{β1}	35.1	55.9
			-2.10	0.659	0.461	0.594		32.3	54.1
			4.80	-0.266	0.882	-0.390		13.4	15.5
H ₅	0.49	-1.36	-0.100	0.853	0.512	H _{β2}	52.4	40.7	
		-1.12	0.994	0.063	0.091		56.7	42.8	
		2.48	-0.045	-0.518	0.854		20.0	19.6	
M ₇	H ₁	-41.14	-22.64	-0.269	0.172	0.948	H _{α}	9.5	20.3
			-4.27	0.952	0.199	0.234		9.9	23.3
			26.90	-0.149	0.965	-0.217		3.7	15.8
	H ₃	6.48	-2.51	0.854	0.520	-0.020	H _{β1}	21.0	1.6
			-1.52	-0.085	0.178	0.980		20.6	10.9
			4.04	-0.513	0.835	-0.196		4.9	11.0
H ₅	13.05	-2.62	0.858	0.507	0.079	H _{β2}	15.1	27.6	
		-2.16	-0.410	0.586	0.698		15.5	29.3	
		4.79	0.307	-0.632	0.711		3.7	16.2	

^a The deviation δ between the calculated eigenvectors and the eigenvectors of T2 and T3 (Table 1) are given in the right-hand columns.

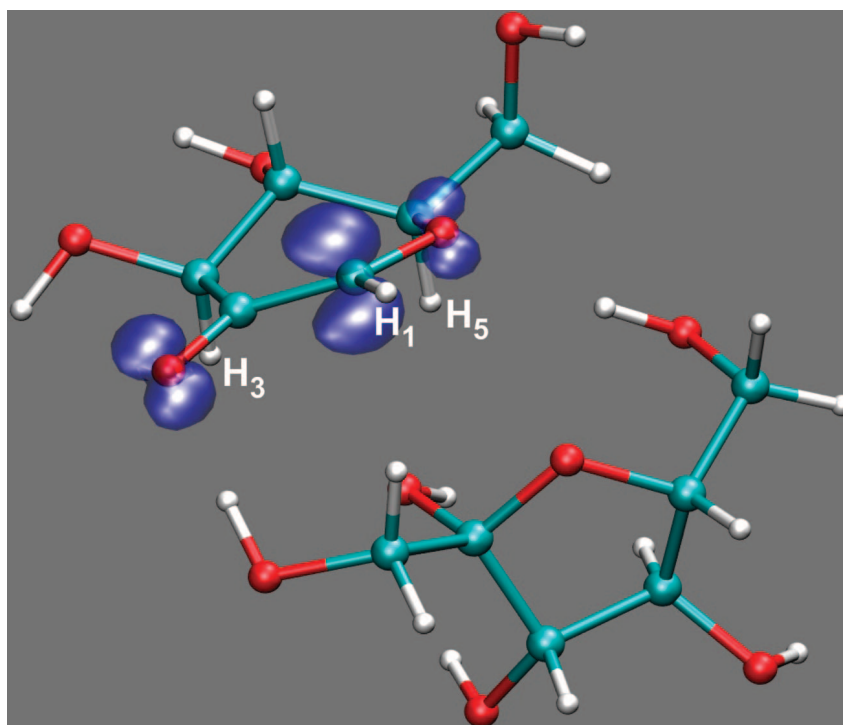


Figure 4. Optimized structure of radical model M_1 . The spin density distribution is visualized by means of a spin density isosurface with $\rho = 0.04$ (blue).

TABLE 4: Proton Hyperfine Coupling Tensors (in MHz) for Radical Model M_1 , Obtained by Means of DFT Calculations in a $\langle 2a2b2c \rangle$ Supercell^a

radical model	proton	iso	aniso	eigenvectors			proton	δ ($^\circ$)	
				a*	b	c		T2	T3
M_1	H_1	-35.22	-20.46	-0.441	0.164	0.882	H_α	1.2	9.8
			-4.64	0.889	0.215	4.2		17.3	
			25.10	-0.123	0.963	-0.241		4.1	15.6
	H_3	16.17	-2.17	0.905	0.416	0.091	$H_{\beta 1}$	25.5	10.8
			-1.84	-0.182	0.184	0.966		25.2	8.9
			4.02	-0.385	0.891	-0.242		4.0	12.6
	H_5	12.60	-2.85	0.733	0.610	0.302	$H_{\beta 2}$	4.0	17.7
			-2.06	0.650	-0.497	-0.576		2.4	13.0
			4.91	0.201	-0.618	0.760		4.6	14.6

^a The deviation δ between the calculated eigenvectors and the eigenvectors of T2 and T3 (Table 1) are given in the right-hand columns.

calculated parameters and the experimental data for T2 is striking. The eigenvectors are in remarkably good accordance, especially for the H_α HF coupling. The eigenvectors associated with $b_{+,dip}$ differ in direction by no more than 2.5° for all three tensors. The match in anisotropic values is excellent. Some minor discrepancies are encountered for the isotropic coupling values, in particular, for the H_α HF coupling, but these values are known to be much more sensitive to basis set effects and the level of theory.⁵¹ In conclusion, the overall agreement found between calculated and experimentally determined data strongly suggests that M_1 essentially is the correct model for the T2 radical in RT X-irradiated sucrose single crystals.

The optimized geometry of model M_1 is shown in Figure 4. The C_1 and C_2 centers attain a close-to-planar configuration and the glucose and fructose units have slightly shifted away from each other, obtaining stable configurations by way of the hydrogen bonds with the neighboring molecules. Figure 4 clearly shows that the unpaired spin density is localized not only on C_1 and the carbonyl oxygen but also on the ring oxygen. Furthermore, protons H_3 and H_5 are oriented roughly parallel with the LEO axes. These two observations explain

why both of the γ -proton couplings exhibit substantial isotropic components.

As the agreement between M_1 and T3 is also quite good (Table 3), one could also associate M_1 to T3. The differences in isotropic and anisotropic values between radicals T2 and T3 are indeed very small, but the eigenvector directions appear to provide a sufficient criterion for discriminating between them. Most strikingly, the eigenvectors associated with $b_{+,dip}$ all deviate more than 10° from the experimental ones for the T3 radical (Table 3). To assess the credibility of the calculated parameters in this context, the dependency of the calculated EMR parameters on the supercell size was investigated. A geometry optimization was performed in a $\langle 2a2b2c \rangle$ supercell, and EMR parameters were calculated in the same cluster approach employed above. The results are shown in Table 4. The agreement with the experimental data of T2 is still striking, but more importantly, the differences between the results of the two different supercell calculations are considerably smaller than the differences in experimental parameters for T2 and T3. Therefore, it appears to be meaningful to state that radical model M_1 corresponds to T2 and not to T3.

TABLE 5: Experimentally Determined g Tensor for Radical R1 at Room Temperature¹⁶ and Calculated g Tensors for Conformations A and B of Radical Model M₁, Obtained As Described in the Computational Procedures Section^a

			eigenvectors			δ (°)	
			principal values	a*	b		c
experiment	R1 ^b		2.0027	-0.882	0.187	-0.435	
			2.0049	0.022	-0.902	-0.432	
			2.0067	-0.472	-0.391	0.790	
calculations	conformation A	Approach #1	2.0021	-0.642	-0.208	-0.738	32.0
			2.0060	0.253	-0.966	0.052	31.3
			2.0076	-0.724	-0.153	0.673	21.1
		Approach #2	2.0022	-0.807	-0.192	-0.558	23.2
			2.0063	0.429	-0.841	-0.331	24.4
			2.0079	-0.406	-0.506	0.761	7.9
	conformation B	Approach #1	2.0022	-0.644	-0.194	-0.740	31.4
			2.0061	0.244	-0.969	0.042	30.5
			2.0073	-0.725	-0.154	0.672	21.1
		Approach #2	2.0020	-0.768	-0.164	-0.619	23.7
			2.0071	0.329	-0.931	-0.161	23.6
			2.0098	-0.549	-0.327	0.769	6.0

^a The deviation δ between the calculated eigenvectors and the eigenvectors of R1 are given in the right-hand columns. ^b Reference 16.

Next to HF parameters, g tensors were also calculated for Approach #1, using the two models discussed in Computational Procedures. Sagstuen and co-workers determined the g tensor for one of the stable radicals (labeled R1) in sucrose single crystals from Q-band EPR angular variations at RT.¹⁶ It was shown in our previous paper²⁰ that the R1 radical corresponds to the T3 radical in the current work (Table 1). In Table 5, the results of the g tensor calculations are given and compared to the experimental data. Concerning the latter, some corrections have been applied, after consulting the authors concerned. The calculated principal values are similar between the two models and in reasonable qualitative agreement with the experimental data. The eigenvectors obtained in Approach #2 are substantially better in accordance with the experimental eigenvectors than those obtained in Approach #1. This can be ascribed to the fact that in Approach #2, the radical environment is taken into account. It was concluded above that model M₁ corresponds to radical T2, whereas the g tensor determined experimentally is associated with radical T3. This probably accounts for part of the discrepancy between the calculations and the experimental data. No further conclusions can be drawn until more experimental data, the g tensor of the T2 radical in particular, are available.

Finally, another model closely related to M₁ was investigated. Labeled M₆ and depicted in Figure 3, it is a simple alternative to M₁ where all key features are maintained: the presence of the α proton, a neighboring carbonyl group, and two γ protons. This structure presumes a glucose ring rupture and not a glycosidic bond cleavage. However, the optimized geometry differs drastically from that of M₁, and consequently, the calculated HF parameters differ substantially from the experimental values (see Table 3). This supports the suggestion that the chemical structure of radical T2 is properly described by model M₁. Furthermore, it indicates that the T3 radical most likely differs from T2 by more subtle changes in conformation, for example, because of differences in the conformation of the environment. This point is further addressed in the next section.

3.3. In Search for T3: A Conformational Study of Radical Model M₁. The simultaneous presence of several quite similar radiation-induced radicals has previously been reported for a number of sugar derivatives, for example, sucrose,^{18,20} fructose,¹⁰ and sorbose.⁵² Possible reasons have been explored in literature:

for fructose in terms of temperature effects²⁹ and for sorbose in terms of the naturally present disorder in the pristine lattice.⁵³ Neither of the studies was able to provide an explanation, however. Therefore, it must be assumed that radiation, starting from the same pristine molecule, somehow gives rise to several distinguishable but structurally very similar radical species. As the calculations above indicate that the radicals most likely do not differ from each other in chemical structure, one might explore the two possible scenarios below. Evidently, an exhaustive exploration of these possibilities would be very time-consuming and is beyond the scope of the present paper. Therefore, a small set of alternative conformations was selected, in order to obtain a rough idea of the sensitivity of the hyperfine tensors on the radical conformation.

Scenario 1: The Similar Radicals Are Chemically Identical but Correspond to Different Local Minima on the Potential Energy Surface (PES). Comparison of the radical structure with the pristine crystal structure reveals that for two hydroxy groups, in particular, other orientations (than those in M₁) could give rise to alternative minima in the PES: the O₂-H(O₂) hydroxy group at the C₂-carbon of the fructose unit and the O₆-H(O₆) hydroxy group at the fructose C₆-carbon of a neighboring molecule. In the pristine lattice structure, the latter hydroxy group is connected through an intermolecular hydrogen bond to the H(O₂) hydroxy hydrogen. (Figure 5A,B).

In order to investigate this, rotational scans of both hydroxy groups were performed where the proper dihedral angles H(O₂)-O₂-C₂-C₃ (D₁) and H(O₆)-O₆-C₆-C₅ (D₂) (cf. Figure 5C,D, respectively) were varied over 360° in 15° steps. For each value of the dihedral angle, an optimization was performed for which the dihedral angle was constrained. The energy profile for the rotational scan of the O₂-H(O₂) group is shown in Figure 6A and reveals two local minima (D₁ \approx 90° and D₁ \approx 330°). Starting from the radical structures associated with each of these minima, a nonconstrained optimization was performed, and the corresponding points are marked in Figure 6A as points B and A, respectively. Conformer A (D₁ = 329.7°, Figure 5B) is the most stable and corresponds to model M₁ as discussed above. Conformer B (D₁ = 98.6°, Figure 5C) is about 9.2 kJ/mol (\approx 95 meV) higher in energy. The configuration of the glucose ring containing the radical site is virtually identical in the two conformers. The energy profile indicates that conformer B is unlikely to account for the T3 radical. Also, Tables 5 and 6 show that the differences between the calculated

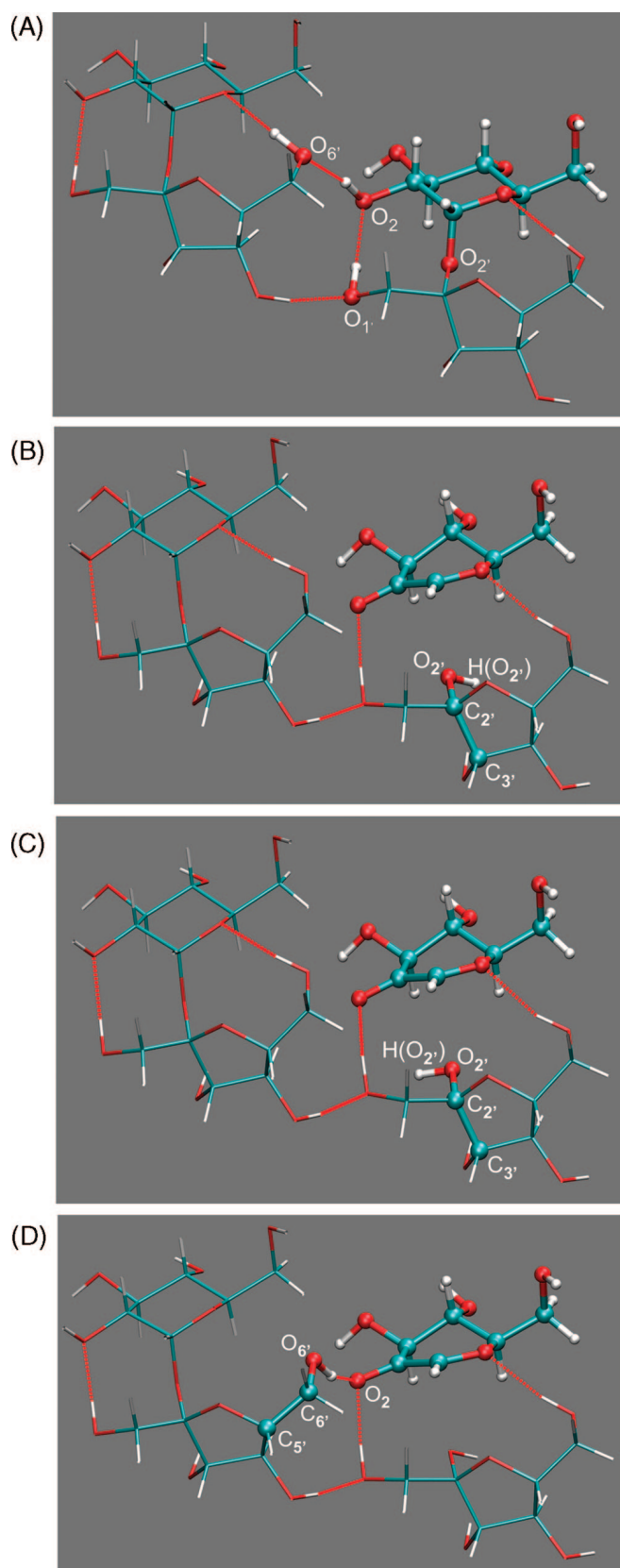


Figure 5. Conformation of the radical molecule and a neighboring molecule in the pristine lattice (A) and in the alternative local minima A, B, and C of model M₁ (B, C, and D, respectively; cf. Figure 6).

EMR parameters for the two conformers are very small and negligible as compared with the differences between T2 and T3.

The energy profile for the rotational scan of the O₆'–H(O₆') hydroxy group is shown in Figure 6B. Again, two local minima

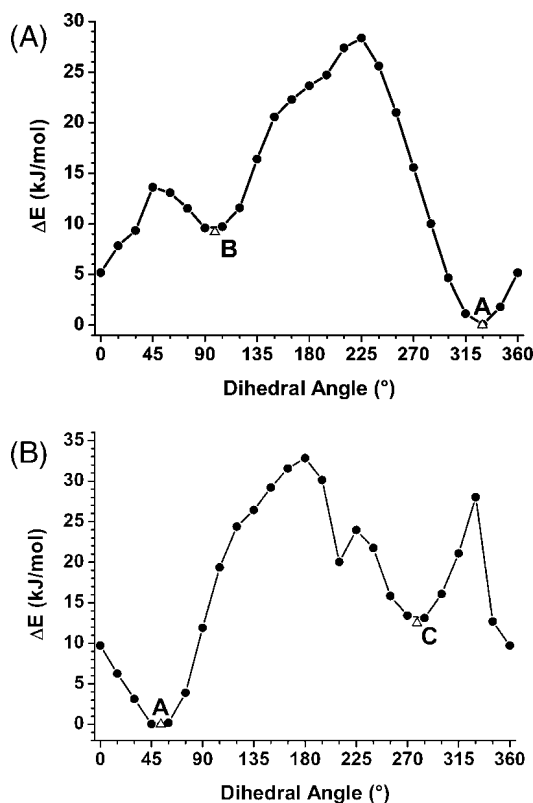


Figure 6. (A) Energy profile for the rotation of the O₂–H₂' hydroxy group about the O₂–C₂' bond in model M₁. (B) Energy profile for the rotation of the O₆'–H(O₆') hydroxy group about the O₆'–C₆' bond of the neighboring molecule (Figure 5) in model M₁. The round points indicate the results of constrained optimizations, the triangles those of nonconstrained optimizations. Conformer A has the lowest energy ($E = -2.708866 \times 10^6$ kJ/mol) and was taken as a reference.

are present with the deepest minimum corresponding to conformer A ($D_2 = 53.3^\circ$). Conformer C ($D_2 = 278.5^\circ$) is depicted in Figure 5D. Reorganization of the hydrogen bonds results in a slightly different configuration of the glucose ring where the unpaired spin is residing. Both the energy profile of Figure 6B and the EMR parameters calculated for conformer C (Table 6) again dismiss it as a candidate for T3.

Scenario 2: Immediate Environments of the Similar Radicals Differ in Chemical Structure. In model M₇ (Figure 3), a formaldehyde molecule is split off from the C₂' carbon of the fructose unit, implying that two additional hydrogens are removed as compared with model M₁. Thus, the intramolecular O₂–H(O₁') hydrogen bond (Figure 5A), which constitutes the most direct link from the fructose unit to the glucose unit for model M₁, is broken. This model may serve as a tool to probe the sensitivity of the calculated HF tensors to changes in the fructose ring. With regard to the radical center, the optimized geometry differs from M₁ mainly in that the C₂ center becomes substantially more planar. The results given in Table 3 show that this gives rise to relatively small but noticeable differences in the calculated tensors. The overall agreement with the experimental results is, however, worse. But more important from a general point of view, the calculated eigenvectors corresponding to $b_{+,dip}$ of all three couplings are only rotated by a few degrees as compared with those of M₁.

These results show that relatively subtle differences in conformation can easily lead to substantial changes in the isotropic coupling values, especially those of the γ -proton couplings, as well as in the direction of the eigenvectors associated with the intermediate and smallest anisotropic

TABLE 6: Calculated Proton Hyperfine Coupling Tensors (in MHz) for Conformations A, B, and C of Model M₁, Corresponding to Local Minima in the Energy Profiles of Figure 6, and Depicted in Figure 5B,C,D, respectively^a

conformation	proton	iso	aniso	Eigenvectors			proton	δ (°)	
				a*	b	c		T2	T3
A	H ₁	−34.60	−20.23	−0.451	0.155	0.879	H _α	1.8	9.3
			−4.66	0.875	0.267	0.403		2.1	14.3
			24.89	−0.173	0.951	−0.256		1.2	13.0
	H ₃	16.18	−2.16	0.874	0.462	0.154	H _{β1}	29.5	11.9
			−1.86	−0.249	0.152	0.957		29.5	11.4
			4.02	−0.418	0.874	−0.248		1.9	10.9
H ₅	12.59	−2.88	0.675	0.673	0.303	H _{β2}	4.2	13.1	
		−2.06	0.698	−0.450	−0.557		4.7	9.5	
		4.95	0.239	−0.588	0.773		2.5	12.2	
B	H ₁	−32.30	−18.82	−0.446	0.146	0.883	H _α	1.6	9.8
			−4.77	0.875	0.281	0.395		1.5	13.7
			23.59	−0.191	0.948	−0.253		0.3	12.5
	H ₃	18.86	−2.13	0.907	0.403	−0.125	H _{β1}	13.0	10.3
			−1.94	0.004	0.289	0.957		13.0	10.9
			4.07	−0.422	0.868	−0.261		1.8	10.1
H ₅	12.75	−2.85	0.643	0.699	0.314	H _{β2}	6.4	11.3	
		−2.03	0.725	−0.423	−0.544		6.9	7.6	
		4.88	0.247	−0.577	0.778		2.5	11.5	
C	H ₁	−34.25	−19.44	−0.412	0.125	0.903	H _α	2.3	12.3
			−4.80	0.893	0.254	0.372		1.6	15.8
			24.23	−0.183	0.959	−0.216		2.8	14.7
	H ₃	18.42	−2.28	0.889	0.440	−0.127	H _{β1}	13.5	8.4
			−1.91	0.009	0.261	0.965		13.4	11.7
			4.20	−0.458	0.859	−0.228		1.2	10.4
H ₅	13.61	−2.77	0.664	0.681	0.310	H _{β2}	5.0	12.6	
		−2.06	0.700	−0.420	−0.578		5.0	10.0	
		4.83	0.263	−0.601	0.755		0.8	13.2	

^aThe tensors were obtained as described in the Computational Procedures section. The deviation δ between the calculated eigenvectors and the eigenvectors of T2 and T3 (Table 1) are given in the right-hand columns.

coupling values. The anisotropic coupling constants and the direction of the eigenvector associated with $b_{+,dip}$ are less dependent on the exact conformation of the radical environment. The differences between T2 and T3, however, are rather opposite: very similar in isotropic and anisotropic coupling values but differing in eigenvector directions. It is tentatively concluded that T2 and T3 do not differ in chemical structure but that the differences in conformation, either of the radical or of its surrounding between T2 and T3, must be rather substantial to account for the differences in eigenvector directions.

EPR, ENDOR, and EIE measurements after in situ 10 K X-irradiation of sucrose single crystals together with corresponding DFT calculations are currently being made in our laboratories in order to determine the precursors and the formation mechanisms of the sucrose radicals stable at RT. This hopefully will give insight into the exact structure of the T3 radical and explain its presence. The results of these investigations will be the subject of a forthcoming publication.

4. Conclusions

Radical T2, one of the major stable radiation-induced radicals in sucrose single crystals, has been identified by means of DFT calculations as a C₁ centered radical. The radical structure involves scission of the glycosidic bond linkage at the glucose side and the presence of a carbonyl group at the C₂ position. The agreement between calculated and experimentally observed EMR parameters is excellent on all accounts. A limited conformational study of this radical model indicates that radical T3 is very likely chemically identical to T2 and that alternative orientations of neighboring hydroxy groups or alternative configurations of the neighboring fructose ring do not offer an explanation for the presence or characteristics of T3.

Acknowledgment. The authors H.D.C., E.P., and H.V. wish to thank the Fund for Scientific Research—Flanders for financial support.

References and Notes

- (1) Samskog, P. O.; Lund, A.; Nilsson, G.; Symons, M. C. R. *J. Chem. Phys.* **1980**, *73*, 4862–4866.
- (2) Samskog, P. O.; Lund, A. *Chem. Phys. Lett.* **1980**, *75*, 525–527.
- (3) Samskog, P. O.; Kispert, L. D.; Lund, A. *J. Chem. Phys.* **1983**, *79*, 635–638.
- (4) Budzinski, E. E.; Box, H. C. *J. Chem. Phys.* **1985**, *82*, 3487–3490.
- (5) Box, H. C.; Budzinski, E. E.; Freund, H. G. *Radiat. Res.* **1990**, *121*, 262–266.
- (6) Sagstuen, E.; Lindgren, M.; Lund, A. *Radiat. Res.* **1991**, *128*, 235–242.
- (7) Bungum, B.; Hole, E. O.; Sagstuen, E.; Lindgren, M. *Radiat. Res.* **1994**, *139*, 194–202.
- (8) Madden, K. P.; Bernhard, W. A. *J. Phys. Chem.* **1980**, *84*, 1712–1717.
- (9) Madden, K. P.; Bernhard, W. A. *J. Phys. Chem.* **1982**, *86*, 4033–4036.
- (10) Vanhaelewyn, G.; Lahorte, P.; De Proft, F.; Mondelaers, W.; Geerlings, P.; Callens, F. *Phys. Chem. Chem. Phys.* **2001**, *3*, 1709–1716.
- (11) Samskog, P.-O.; Kispert, L. D.; Lund, A. *J. Chem. Phys.* **1983**, *78*, 5790–5794.
- (12) Samskog, P.-O.; Kispert, L. D.; Lund, A. *J. Chem. Phys.* **1982**, *77*, 2330–2335.
- (13) Gräslund, A.; Löfroth, G. *Acta Chem. Scand. B* **1975**, *29*, 475–482.
- (14) Budzinski, E. E.; Potter, W. R.; Potienko, G.; Box, H. C. *J. Chem. Phys.* **1979**, *70*, 5040–5044.
- (15) Box, H. C.; Budzinski, E. E. *J. Chem. Phys.* **1983**, *79*, 4142–4145.
- (16) Sagstuen, E.; Lund, A.; Awaldelkartim, O.; Lindgren, M.; West-erling, J. *J. Chem. Phys.* **1986**, *90*, 5584–5588.
- (17) Box, H. C.; Budzinski, E. E.; Freund, H. G. *J. Chem. Phys.* **1990**, *93*, 55–57.
- (18) Vanhaelewyn, G.; Sadlo, J.; Callens, F.; Mondelaers, W.; De Frenne, D.; Matthys, P. *Appl. Radiat. Isot.* **2000**, *52*, 1221–1227.

- (19) Georgieva, E. R.; Pardi, L.; Jeschke, G.; Gatteschi, D.; Sorace, L.; Yordanov, N. D. *Free Radical Research* **2006**, *40*, 553–563.
- (20) De Cooman, H.; Pauwels, E.; Vrielinck, H.; Dimitrova, A.; Yordanov, N.; Sagstuen, E.; Waroquier, M.; Callens, F. *Spectrochim. Acta A* **2008**, *69*, 1372–1383.
- (21) McConnell, H. M.; Chesnut, D. B. *J. Chem. Phys.* **1958**, *28*, 107–117.
- (22) Heller, C.; McConnell, H. M. *J. Chem. Phys.* **1960**, *32*, 1535.
- (23) Øhman, K. T.; Sanderud, A.; Hole, E. O.; Sagstuen, E. *J. Phys. Chem. A* **2006**, *110*, 9585–9596.
- (24) Vanhaelewyn, G.; Pauwels, E.; Callens, F.; Waroquier, M.; Sagstuen, E.; Matthys, P. *J. Phys. Chem. A* **2006**, *110*, 2147–2156.
- (25) Pauwels, E.; Van Speybroeck, V.; Waroquier, M. *J. Phys. Chem. A* **2006**, *110*, 6504–6513.
- (26) Jayatilaka, N.; Nelson, W. H. *J. Phys. Chem. B* **2007**, *111*, 800–810.
- (27) Jayatilaka, N.; Nelson, W. H. *J. Phys. Chem. B* **2007**, *111*, 7887–7896.
- (28) Pauwels, E.; Declerck, R.; Van Speybroeck, V.; Waroquier, M. *Radiation Research* **2008**, *169*, 8–18.
- (29) Declerck, R.; Pauwels, E.; Van Speybroeck, V.; Waroquier, M. *J. Phys. Chem. B*, **2008**, *112*, 1508–1514.
- (30) CPMD V3.11, Copyright IBM Corp., 1990–2006, Copyright MPI fuer Festkoerperforschung, Stuttgart, 1997–2001.
- (31) Perdew, J. P. *Phys. Rev. B* **1986**, *33*, 8822–8824.
- (32) Becke, A. D. *J. Chem. Phys.* **1992**, *96*, 2155–2160.
- (33) Vanderbilt, D. *Phys. Rev. B* **1990**, *41*, 7892–7895.
- (34) Declerck, R.; Pauwels, E.; Van Speybroeck, V.; Waroquier, M. *Phys. Rev. B* **2006**, *74*, 245103.
- (35) Pauwels, E.; Van Speybroeck, V.; Waroquier, M. *Spectrochimica Acta Part A* **2006**, *63*, 795–801.
- (36) Frisch, M. J.; Trucks, G. W.; Schlegel, H. B.; Scuseria, G. E.; Robb, M. A.; Cheeseman, J. R.; Montgomery, J. J. A.; Vreven, T. N.; Kudin, K.; Burant, J. C.; Millam, J. M.; Lyengar, S. S.; Tomasi, J.; Barone, V.; Mennucci, B.; Cossi, M.; Scalmani, G.; Rega, N.; Petersson, G. A.; Nakatsuji, H.; Hada, M.; Ehara, M.; Toyota, K.; Fukuda, R.; Hasegawa, J.; Ishida, M.; Nakajima, T.; Honda, Y.; Kitao, O.; Nakai, H.; Klene, M.; Li, X.; Knox, J. E.; Hratchian, H. P.; Cross, J. B.; Adamo, C.; Jaramillo, J.; Gomperts, R.; Stratmann, R. E.; Yazyev, O.; Austin, A. J.; Cammi, R.; Pomelli, C.; Ochterski, J. W.; Ayala, P. Y.; Morokuma, K.; Voth, G. A.; Salvador, P.; Dannenberg, J. J.; Zakrzewski, V. G.; Dapprich, S.; Daniels, A. D.; Strain, M. C.; Farkas, O.; Malick, D. K.; Rabuck, A. D.; Raghavachari, K.; Foresman, J. B.; Ortiz, J. V.; Cui, Q.; Baboul, A. G.; Clifford, S.; Cioslowski, J.; Stefanov, B. B.; Liu, G.; Liashenko, A.; Piskorz, P.; Komaromi, I.; Martin, R. L.; Fox, D. J.; Keith, T.; Al-Laham, M. A.; Peng, C. Y.; Nanayakkara, A.; Challacombe, M.; Gill, P. M. W.; Johnson, B.; Chen, W.; Wong, M. W.; Gonzalez, C.; Pople, J. A. *Gaussian 03*, Revision B.03, Gaussian, Inc.: Pittsburgh, PA, 2003.
- (37) Becke, A. D. *J. Chem. Phys.* **1996**, *104*, 1040–1046.
- (38) Krishnan, R.; Binkley, J. S.; Seeger, R.; Pople, J. A. *J. Chem. Phys.* **1980**, *72*, 650–654.
- (39) McLean, A. D.; Chandler, G. S. *J. Chem. Phys.* **1980**, *72*, 5639–5648.
- (40) Declerck, R.; Van Speybroeck, V.; Waroquier, M. *Phys. Rev. B* **2006**, *73*, 115113.
- (41) Becke, A. D. *Phys. Rev. A* **1988**, *38*, 3098.
- (42) Lee, C.; Yang, W.; Parr, R. G. *Phys. Rev. B* **1988**, *37*, 785.
- (43) Goedecker, S.; Teter, M.; Hutter, J. *J. Phys. Rev. B* **1996**, *54*, 1703.
- (44) Erling, P. A.; Nelson, W. H. *J. Phys. Chem. A* **2004**, *108*, 7591–7595.
- (45) Bernhard, W. A. *Adv. Radiat. Biol.* **1981**, *9*, 199.
- (46) Bernhard, W. A. *J. Chem. Phys.* **1984**, *81*, 5928–5935.
- (47) Flores, J.; Cabrera, B. E.; Calderon, T.; Muñoz, P. E.; Adem, E.; Hernandez, J.; Boldu, B. L.; Murrieta, H. *Appl. Radiat. Isot.* **2000**, *52*, 1229–1234.
- (48) Yordanov, N. D.; Karakirova, Y. *Radiation Measurements*, in press, doi:10.1016/j.radmeas.2006.10.004.
- (49) Box, H. C.; Budzinski, E. E.; Potienko, G. *J. Chem. Phys.* **1980**, *73*, 2052–2056.
- (50) Brown, G. M.; Levy, H. A. *Acta Crystallogr., Sect. B: Struct. Crystallogr. Cryst. Chem.* **1973**, *29*, 790–797.
- (51) Improta, R.; Barone, V. *Chem. Rev.* **2004**, *104*, 1231–1253.
- (52) Jansen, B. *Radiation Induced Radicals in Single Crystals of α -L-sorbose. ESR-, ENDOR- and pulse radiolysis studies at room temperature*, Master Thesis, University of Oslo, 1992; in Norwegian.
- (53) Vanhaelewyn, G. C. A. M.; Jansen, B.; Pauwels, E.; Sagstuen, E.; Waroquier, M.; Callens, F. *J. Phys. Chem. A* **2004**, *108*, 3308–3314.

7.3 Paper III

ENDOR and HYSCORE analysis and DFT-assisted identification of the third major stable radical in sucrose single crystals X-irradiated at room temperature

H. De Cooman, E. Pauwels, H. Vrielinck, E. Sagstuen, S. Van Doorslaer,
F. Callens and M. Waroquier

Physical Chemistry Chemical Physics, 2009, 11, 1105-1114

Copyright 2009 by the Royal Society of Chemistry.

ENDOR and HYSCORE analysis and DFT-assisted identification of the third major stable radical in sucrose single crystals X-irradiated at room temperature†

Hendrik De Cooman,^{ab} Ewald Pauwels,^b Henk Vrielinck,^a Einar Sagstuen,^c Sabine Van Doorslaer,^d Freddy Callens^a and Michel Waroquier^{*b}

Received 23rd September 2008, Accepted 25th November 2008

First published as an Advance Article on the web 13th January 2009

DOI: 10.1039/b816641b

Recently, the chemical structure of two of the three major stable radicals (T2 and T3) produced in sucrose single crystals by X-irradiation at room temperature was identified by comparing Density Functional Theory (DFT) calculations of Electron Magnetic Resonance parameters with experimental results [H. De Cooman, E. Pauwels, H. Vrielinck, E. Sagstuen, F. Callens and M. Waroquier, *J. Phys. Chem. B*, 2008, **112**, 7298–7307]. Ambiguities concerning an unusual proton hyperfine coupling (HFC) tensor prevented the identification of the third major stable radical (T1). In the present work, experimental results of continuous wave Electron Nuclear Double Resonance experiments on sucrose single crystals and Hyperfine Sublevel Correlation Spectroscopy experiments on sucrose powder are presented that lift these remaining ambiguities. Using the final set of experimental HFC tensors and employing advanced DFT calculations, the chemical structure of the T1 radical is established: an allylic-type radical with approximately half of the spin density localised on the C2' carbon of the fructose unit, involving glycosidic bond cleavage at the fructose side and a concerted formation of a carbonyl group at the C1' carbon. The electronic structure of the T1 radical is discussed in more detail by means of additional DFT calculations, yielding a better understanding of the peculiar properties of the unusual proton HFC tensor mentioned above.

1. Introduction

Carbohydrates are important constituents of several biological systems including DNA and membrane systems. Elucidating their radiation physics and chemistry is therefore of general importance. Insight into the direct radiation effects occurring in the deoxy-ribose moiety of DNA is particularly relevant as these may lead to cleavage of sugar–phosphate ester bonds in the DNA backbone (single and double strand breaks) which may in turn result in cell death, cancer and mutagenesis.^{1–3} Most of the DNA in a nucleus is rigidly and tightly packed in chromosomes² and in this respect, carbohydrate single crystals are appropriate model systems. Consequently, attempts have been made since the early 1970s to identify radiation-induced processes taking place in solid-state carbohydrates. Electron Magnetic Resonance (EMR) experiments have played a major role in this field, as they can provide a wealth of detailed structural and dynamic information. Nonetheless, establishing reliable radical models and reaction pathways is a laborious and not always successful task, not in the least because these compounds do not contain any specific functional group and have considerable conformational freedom. Recently, highly

accurate quantum chemical Density Functional Theory (DFT) calculations on extended organic solid-state systems have become feasible due to advances in computing power and density functionals, as well as to the development of new codes for the calculation of EMR parameters. This has given a new and powerful impulse to the study of the radiation chemistry of solid-state carbohydrates.

The disaccharide sucrose (see Fig. 1 (top) for chemical structure) offers an extra advantage as a model system: the ester bond between the two carbohydrate units bears a similarity to the sugar–phosphate ester bond in the DNA backbone. Sucrose is also of particular interest for emergency dosimetry (see *e.g.* ref. 4 and references therein) and has been suggested to be the best, universal material for EPR- (Electron Paramagnetic Resonance) and UV-dosimetry in the region 0.44–160 kGy.^{5,6} Ultimately, an advanced understanding of the radiation-induced processes in sucrose may aid in establishing dosimetry protocols.

In single crystals of sucrose three major stable carbon-centred radical species (T1–T3) have been reported to form upon room temperature (RT) X-irradiation.⁷ Two of these (T2 and T3) are characterised by very similar HFC tensors, indicating that these species have the same chemical structure but differ only in conformation. Recently, the chemical structure of T2 and T3 has been identified by comparison between the experimental data and the results from advanced Density Functional Theory (DFT) calculations of proton hyperfine coupling (HFC) tensors, although the precise origin of the discrepancy between T2 and T3 was not established.⁸ This structure is shown in Fig. 1 (bottom).

For T1, however, a Schonland ambiguity⁹ was still present for the HFC tensor $H_{\beta 3}(T1)$. Two possible tensors were reported, fitting the available data equally well. These two tensors are

^a Department of Solid State Sciences, Ghent University, Krijgslaan 281-S1, B-9000 Gent, Belgium

^b Center for Molecular Modeling, Ghent University, Proeftuinstraat 86, B-9000 Gent, Belgium. E-mail: michel.waroquier@ugent.be; Fax: 003292646697; Tel: 003292646559

^c Department of Physics, University of Oslo, P.O. Box 1048 Blindern, N-0316 Oslo, Norway

^d Department of Physics, University of Antwerp, Universiteitsplein 1, B-2610 Wilrijk-Antwerp, Belgium

† Electronic supplementary information (ESI) available: Fig. S1–S3. See DOI: 10.1039/b816641b

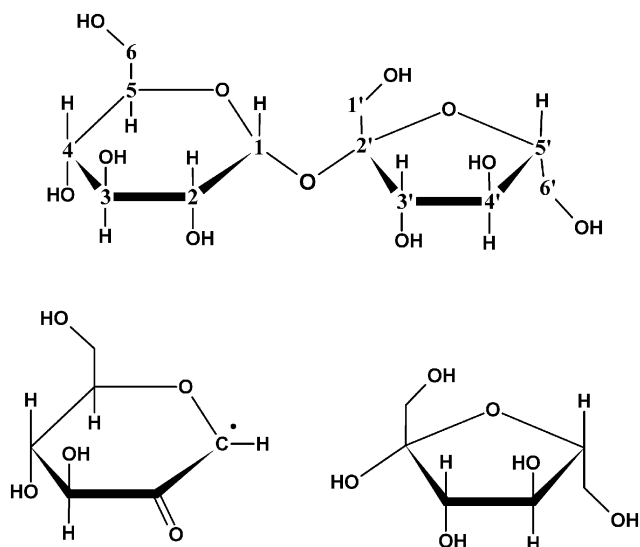


Fig. 1 Top: The chemical structure of the sucrose molecule with the atomic numbering used in the present work. Throughout this work, carbon-bound hydrogen atoms and oxygen atoms are labelled according to the carbon to which they are bound, hydroxy protons according to the oxygen to which they are bound. For example, H3 is the hydrogen at C3, HO3 is the hydroxy proton at C3. Bottom: the chemical structure of the T2/T3 radical species, identified in a previous work.⁸

reproduced in Table 1. Both exhibit unusual features: $^A\text{H}_{\beta 3}(\text{T1})$ has a β -type anisotropy (dipolar components $(-b, -b, +2b)$ with $b > 0$), but a significant negative isotropic component, atypical of β -protons. $^B\text{H}_{\beta 3}(\text{T1})$ has an α -type anisotropy $(-a, 0, +a)$, but the values of a and of the isotropic coupling are unusually small for an α -proton and would imply only about 20% spin density on the “ α -carbon”.^{10,11} The overall signs of the principal values are also uncertain since these cannot be determined from the standard cw-EPR and -ENDOR experiments that were performed. Such sign ambiguities are in most cases resolved on the basis of theoretical considerations and/or precedents. As noted above, however, both options are equally unusual in the case at hand.

In the present work, these ambiguities are resolved using both continuous wave Electron Nuclear Double Resonance (cw-ENDOR) and Hyperfine Sublevel Correlation (HYSCORE) spectroscopy. Starting from an initial set of radical models inferred from the final set of T1 proton HFC tensors, DFT calculations based on unconstrained optimisations within a periodic scheme and subsequent cluster single-point calculations of HFC tensors lead to the identification of T1: an allylic-type radical requiring glycosidic bond scission and the concerted

Table 1 Two possible HFC tensors ((an)isotropic values in MHz) for the $\text{H}_{\beta 3}$ proton HFC of radical T1 in sucrose single crystals X-irradiated at RT, determined from ENDOR measurements at 110 K. The tensors are taken from ref. 7

	Iso	Aniso	Eigenvectors		
			a*	b	c
$^A\text{H}_{\beta 3}$	-11.07	-6.50	0.707	-0.245	-0.664
		-3.69	0.383	0.921	0.068
		10.19	0.595	-0.302	0.745
$^B\text{H}_{\beta 3}$	11.20	-8.59	0.549	0.231	0.803
		0.59	0.580	-0.797	-0.167
		8.00	0.602	0.558	-0.572

formation of a carbonyl group. Finally, the T1 radical structure is studied in more detail with respect to its electronic structure.

2. Experimental and computational section

2.1 Experimental procedures

Analytical grade (98%) sucrose was obtained from Aldrich and was used to grow single crystals from H_2O or D_2O solutions, as previously described.⁷ The crystal structure of sucrose was most accurately determined from a neutron diffraction analysis.¹² The crystals are monoclinic with space group $P2_1$ and a unit cell contains two molecules. The a^*bc system ($\langle a^* \rangle$ being orthogonal to both $\langle b \rangle$ and $\langle c \rangle$) was chosen as the orthogonal reference frame, in analogy with previous publications.^{7,8} For a certain direction vector, the polar coordinates θ and φ are defined in the current work as the angles measured from the $\langle c \rangle$ -axis to the vector and the angle measured from the $\langle a^* \rangle$ -axis to the projection of the vector in the $\langle a^*b \rangle$ -plane, respectively. The single crystal was X-irradiated at RT (295 K approximately) to a dose of about 90 kGy using a Philips chromium-anode X-ray tube operated at 60 kV and 40 mA. The sample orientation was determined by stereographic projections and the sample was mounted as described previously.⁷ In accordance with previous investigations,⁷ the ENDOR spectra were recorded at 110 K approximately 2 days after irradiation, using a Bruker ESP300E spectrometer with an ESP353 ENDOR-TRIPLE extension. The program MAGRES^{13,14} was used to derive the HFC tensor from the complete set of previously and currently obtained ENDOR data, as described in *e.g.* ref. 7. The program Easyspin¹⁵ was used for the simulation of the ENDOR angular variations.

X-band pulsed Electron Paramagnetic Resonance (EPR) experiments were performed using a Bruker ESP380E spectrometer (with a microwave frequency of about 9.76 GHz). All experiments were done at RT using a repetition rate of 1 kHz. Instead of the standard HYSORE scheme,¹⁶ the SMART HYSORE sequence¹⁷ was used. This not only circumvents the well-known τ -dependent blind-spot effect of standard HYSORE experiments, but allows, by the appropriate choice of the high-turning-angle (HTA) pulse strength, enhancement of the intensity of specific hyperfine coupling signals. For the SMART-HYSORE experiments performed on the sucrose powder, X-irradiated at RT, the pulse sequence: HTA- t_1 - π - t_2 -HTA- τ - π - τ -echo was applied with $t_\pi = 16$ ns and HTA pulses with lengths of 40 ns. The proton HFCs of interest are weak (*i.e.* the HFC value is smaller than twice the proton Larmor frequency of $\nu_H \approx 14.8$ MHz), and the matching pulse frequency (ν_1) for this type of coupling is ν_H ,¹⁷ but $\nu_1 = 15.625$ MHz was used as this is the value closest to ν_H that can easily be obtained with the present experimental setup. A value of 96 ns was used for τ . The times t_1 and t_2 were changed from 96 ns to 2488 ns in steps of 8 ns. The time-domain HYSORE spectra were baseline corrected with a third-order polynomial, apodized with a Hamming window and zero filled. The absolute-value spectra were obtained by a two-dimensional Fourier transformation. Because of the large spectral asymmetry *versus* the diagonal, typical for SMART-HYSORE spectra, the spectra presented in the current work were symmetrised. Time-domain

HYSCORE spectra were simulated using a program developed at ETH Zurich,¹⁸ whereas the frequency-domain simulations were performed using EasySpin.¹⁵

2.2 Computational procedures

Unless explicitly mentioned otherwise, the computational scheme employed and discussed in ref. 8 was used for the geometry optimisations: periodic calculations were performed with the CPMD software package¹⁹ using an $\langle ab2c \rangle$ supercell (180 atoms), obtained by doubling the original crystal unit cell in the $\langle c \rangle$ direction. This supercell is depicted in Fig. 2. A BP86 gradient-corrected density functional^{20,21} was used, together with a plane wave basis set (with a maximum kinetic energy of 25 Ry for the plane waves) and ultra-soft pseudopotentials of the Vanderbilt type.²² No constraints were imposed on the atoms of the supercell during optimisation. For radical fragments I and II (section 3.3), the geometry optimisations were performed in the Gaussian03 program package²³ with a B3LYP functional²⁴ and a 6-311G(d,p) basis set^{25,26} for all atoms.

The single-point calculations of the HFC tensors were always performed within the Gaussian03 program package, also employing the B3LYP functional and a 6-311G(d,p) basis set. In previous publications,^{7,8} this type of calculation was performed on a cluster consisting of the radical and ten surrounding sucrose molecules, cut out of the periodically optimised $\langle ab2c \rangle$ supercell ('full cluster approach'). However, the accuracy of the calculated HFC tensors mainly depends on the accuracy of the radical geometry, as demonstrated in a recent paper by Declerck and co-workers on radicals in fructose single crystals.²⁷ We made similar observations in a previous work.⁸ Therefore, a simpler computational scheme was adopted in the present work for the calculations of HFC tensors in the initial search for a suitable radical model: only the optimised radical molecule (defined in the current work as the molecule on which the unpaired electron is located), cut out of the periodically optimised $\langle ab2c \rangle$ supercell, was considered ('single molecule approach'). For the radical model yielding the best agreement with the experimental data,

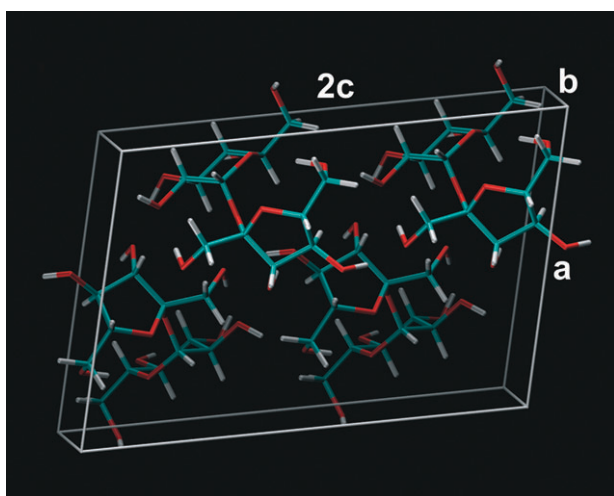


Fig. 2 3D structure of the $\langle ab2c \rangle$ supercell used for most of the periodic geometry optimisations in the current work, obtained by doubling the crystal unit cell in the $\langle c \rangle$ direction. The atomic coordinates were taken from ref. 9.

however, additional calculations were made using the full cluster approach described above.

Whenever a comparison is made between calculated eigenvector directions and experimentally determined eigenvector directions or crystal directions, allowed symmetry operations ($b \rightarrow -b$ and inversion of eigenvectors) are performed to obtain the best possible agreement.

3. Theory

For an $S = 1/2$, $I = 1/2$ system, the nuclear transition frequencies in the two m_S manifolds for a given orientation of the molecule *versus* the external magnetic field are²⁸

$$\nu_{\alpha(\beta)} = \sqrt{\left(\frac{A}{2} \pm \nu_I\right)^2 + \left(\frac{B}{2}\right)^2}$$

with ν_I the Larmor frequency, $A = A_{zz}$ and $B = \sqrt{A_{zx}^2 + A_{zy}^2}$ the secular and pseudo-secular hyperfine contributions, respectively. It is clear that, for a given nucleus, the sign of A will determine which of the two nuclear frequencies is the largest. For an $S = 1/2$, $I = 1/2$ system, the HYSCORE spectrum will show cross peaks between the two nuclear frequencies. For the system at hand, namely a system where the unpaired electron is interacting with many protons ($S = 1/2$, $I_n = 1/2$ with n the number of protons), additional HYSCORE cross peaks involving sum frequencies can be observed. Each observable sum frequency $\nu_{\alpha(\beta)}^\pm$ corresponds to the sum of basic frequencies within one electron-spin manifold for a particular radical:

$$\nu_{\alpha(\beta)}^\pm = \sum_i \nu_{\alpha(\beta)}^i$$

where i runs over the protons with which the unpaired electron interacts. This implies that changing the sign of one of the couplings will alter the corresponding sum frequency and, hence, the position of the HYSCORE cross peak. In most cases, only the cross peaks stemming from sum frequencies between two nuclei are clearly observable in the HYSCORE spectra, the higher multi-nuclei sum peaks having too low intensity. The sum frequencies can thus reveal the relative signs of two HFCs. In the HYSCORE spectra of disordered systems, like the sucrose powder in the case at hand, cross ridges instead of cross peaks are observed, resulting from the simultaneous observation of different molecular orientations. These ridges reflect the anisotropy of the proton HFC tensors and the sum frequency combination ridges again allow for the determination of the relative signs of two proton HFCs belonging to the same radical species.

4. Results and discussion

4.1 Determination of $H_{\beta 3}(T1)$

To determine the correct tensor symmetry of the $H_{\beta 3}(T1)$ HFC tensor (tensor A or B in Table 1), ENDOR measurements were carried out in a carefully selected skewed plane (Fig. 3). This method was attempted previously⁷ and proved successful for all HFC tensors except $H_{\beta 3}(T1)$ because the $H_{\beta 3}(T1)$ ENDOR lines could not be resolved at a sufficient number of orientations of the magnetic field in the rotation plane chosen at that time. For the new experiment, a suitable orientation of the rotation plane was first chosen by means of simulations. This orientation

of the skewed plane was then approximately obtained by means of XRD stereographic projections. Afterwards, the plane orientation was more accurately determined using the well known HFC tensors of radical species T1, T2 and T3. As shown in Fig. 3, $^A\text{H}_{\beta_3}(\text{T1})$ reproduces the experimental angular variation of the ENDOR signal accurately, whereas $^B\text{H}_{\beta_3}(\text{T1})$ clearly does not, allowing for the definitive conclusion that $^A\text{H}_{\beta_3}(\text{T1})$ exhibits the correct tensor symmetry. In Table 2, the final $\text{H}_{\beta_3}(\text{T1})$ tensor is presented, for which the data points in the skewed plane were now included in the fitting, resulting in some minor adjustments to the $^A\text{H}_{\beta_3}(\text{T1})$ tensor of Table 1.

We are, however, left with the problem of determining the overall sign of $\text{H}_{\beta_3}(\text{T1})$. A common method to determine relative signs of distinct HFCs of a single radical is TRIPLE (also known as double ENDOR) measurements.^{29,30} $\text{H}_{\beta_1}(\text{T1})$ is a typical β -proton coupling and its ENDOR signals are well isolated for most orientations, so that it may well serve as ‘reference coupling’ for the TRIPLE measurements. However,

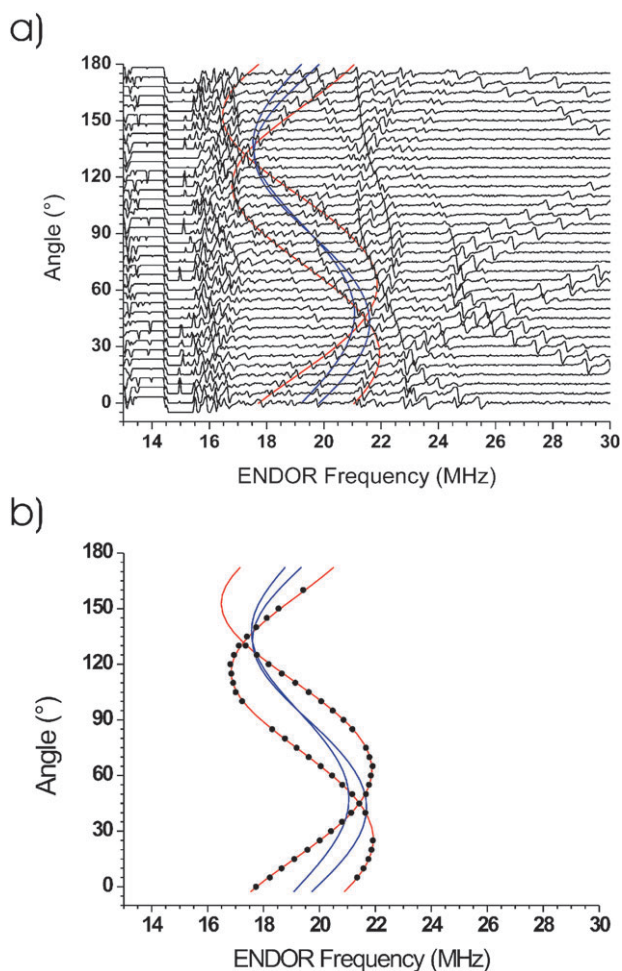


Fig. 3 (a) X-band ENDOR angular variation of sucrose single crystals X-irradiated at RT, recorded approximately 2 days after irradiation. The measurements were performed at 110 K. The spectra are normalised (shifted) to a proton frequency of 14.440 MHz. The direction of the rotation axis is given by $\theta = 26.1^\circ$ and $\phi = 190.3^\circ$ (definition: see section 2.1). (b) The ENDOR resonance positions of the $\text{H}_{\beta_3}(\text{T1})$ (dots), determined from the angular variation shown in (a). The lines in (a) and (b) are the simulations of the ENDOR angular variations using the $^A\text{H}_{\beta_3}(\text{T1})$ (red) and $^B\text{H}_{\beta_3}(\text{T1})$ (blue) HFC tensors (Table 1).

Table 2 Final set of proton HFC tensors ((an)isotropic values in MHz) associated with radical T1 in sucrose single crystals X-irradiated at RT, as determined from ENDOR measurements at 110 K. The $\text{H}_{\beta_1}(\text{T1})$ and $\text{H}_{\beta_2}(\text{T1})$ HFC tensors are reproduced from ref. 7. For $\text{H}_{\beta_3}(\text{T1})$, ENDOR resonance positions in an extra, skewed plane (Fig. 3) were included in the fitting, which results in additional small adjustments with respect to HFC tensor $^A\text{H}_{\beta_3}(\text{T1})$ reported in ref. 7 (also see Table 1)

Radical	Proton	Iso	Aniso	Eigenvectors		
				a*	b	c
T1	H_{β_1}	46.80	-3.99	0.616	0.121	-0.778
			-2.38	0.072	0.975	0.209
			6.37	0.784	-0.185	0.592
	H_{β_2}	15.88	-2.69	0.106	0.825	0.555
			-2.31	0.989	-0.144	0.025
			5.00	0.101	0.546	-0.832
H_{β_3}	-11.07	-6.41	0.711	-0.241	-0.660	
		-3.73	0.380	0.922	0.073	
		10.14	0.591	-0.302	0.748	

no significant intensity changes of the $\text{H}_{\beta_3}(\text{T1})$ ENDOR resonances could be observed within the limits of our instrumentation when saturating the $\text{H}_{\beta_1}(\text{T1})$ resonance.

Pulsed EPR experiments proved more successful. SMART HYSCORE spectra, recorded at RT on sucrose powder X-irradiated at RT, are shown in Fig. 4a. As noted in the Experimental Procedure Section, the proton HFCs of interest here (all HFCs of the major stable radicals in sucrose except for $\text{H}_{\beta_1}(\text{T1})$, $\text{H}_{\alpha}(\text{T2})$ and $\text{H}_{\alpha}(\text{T3})$) are all weak couplings. In addition to the strong ridge around ν_{H} corresponding to the correlations between the basic frequencies of the two M_S manifolds, a clear ridge is also present around $2\nu_{\text{H}}$, which corresponds to correlations between sum frequencies. The ridges around ν_{H} are not dependent on the sign of the HFC, but they could in principle be used to discern $^A\text{H}_{\beta_3}(\text{T1})$ from $^B\text{H}_{\beta_3}(\text{T1})$. Simulations indeed predict a slightly different shape for the corresponding ridges. In practice, however, this difference is not detectable because of the overlap with the $\text{H}_{\beta_2}(\text{T1})$, $\text{H}_{\beta_2}(\text{T2})$, $\text{H}_{\beta_3}(\text{T2})$, $\text{H}_{\beta_2}(\text{T3})$ and $\text{H}_{\beta_3}(\text{T3})$ HFC resonance lines and with the multitude of distant proton HFC resonance lines near the proton frequency (see Fig. S1 in the ESI).[†]

The sum frequency ridges, on the other hand, allow for clear discrimination between $^A\text{H}_{\beta_3}(\text{T1})$ and $^B\text{H}_{\beta_3}(\text{T1})$ as well as determination of the relative signs of $\text{H}_{\beta_2}(\text{T1})$ and $\text{H}_{\beta_3}(\text{T1})$ (which then yields the absolute sign of $\text{H}_{\beta_3}(\text{T1})$ when making the safe assumption that $\text{H}_{\beta_2}(\text{T1})$ has an overall positive sign). In Fig. 4b–e the shape of the combination ridges is simulated for $\text{H}_{\beta_2}(\text{T1})$ with $^A\text{H}_{\beta_3}(\text{T1})$ (Fig. 4b and c) and with $^B\text{H}_{\beta_3}(\text{T1})$ (Fig. 4d and e) for an overall negative (Fig. 4b and d) or an overall positive (Fig. 4c and e) sign of the $\text{H}_{\beta_3}(\text{T1})$ HFC. Fig. 4 clearly demonstrates that only $^A\text{H}_{\beta_3}(\text{T1})$ with the sign as given in Table 1 leads to the appropriate length and shape of the experimentally observed combination ridge. Discerning $^A\text{H}_{\beta_3}(\text{T1})$ from $^B\text{H}_{\beta_3}(\text{T1})$ is possible here because, in contrast with the ν_{H} ridge, there is no overlap with ridges originating from other interactions. In Fig. S2 in the ESI,[†] it is also explicitly shown that the experimentally observed combination ridge does not originate from the T2 or T3 proton HFCs and is not affected by them.

It should be noted that for the simulation above of HYSCORE spectra obtained at RT, HFC tensors determined from ENDOR measurements at 110 K were used. This is certainly reasonable because it was shown in a recent publication

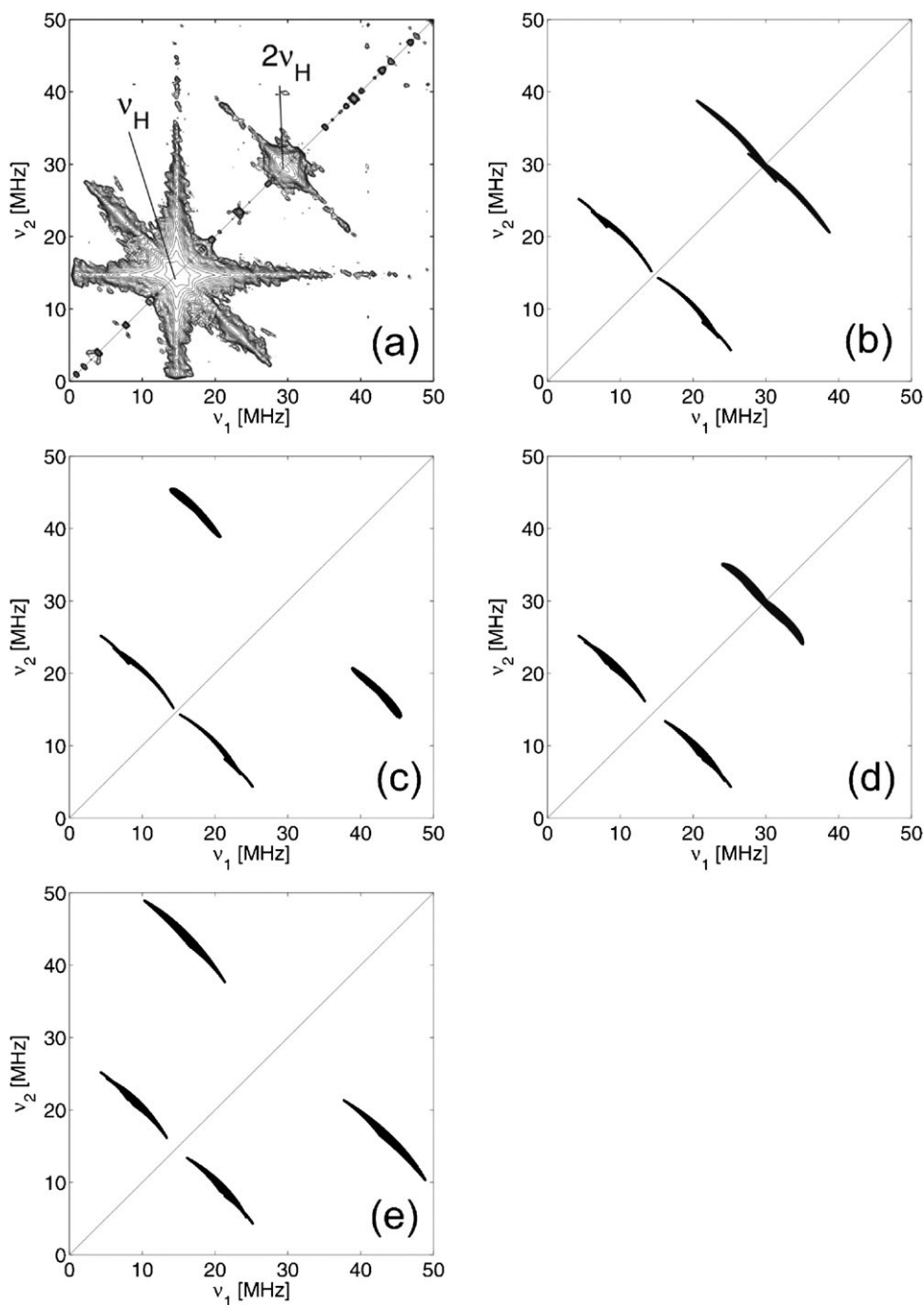


Fig. 4 (a) Experimental X-band SMART HYSORE spectrum of X-irradiated sucrose powder taken at $B_0 = 346.1$ mT. The measurement was performed at RT. (b–e) Simulation of the correlation ridges expected for a three-spin system $S = 1/2$, $I_{\beta_2} = 1/2$ and $I_{\beta_3} = 1/2$ assuming the HFC tensors of (b) $H_{\beta_2}(T1)$ and $^A H_{\beta_3}(T1)$ (assuming a negative sign of the latter HFC, *cf.* Table 1), (c) $H_{\beta_2}(T1)$ and $^A H_{\beta_3}(T1)$ (assuming a positive sign of the latter HFC) (d) $H_{\beta_2}(T1)$ and $^B H_{\beta_3}(T1)$ (assuming a negative sign of the latter HFC, *cf.* Table 1) (e) $H_{\beta_2}(T1)$ and $^B H_{\beta_3}(T1)$ (assuming a positive sign of the latter HFC). $H_{\beta_2}(T1)$ is taken as positive each time.

that the EPR spectrum stays essentially unaltered upon annealing from 110 K to RT.⁷ The excellent match between simulated and experimentally obtained sum correlation ridges of Fig. 4 justifies this approach further *a posteriori*.

4.2 Identification of T1

We will now first turn our attention to the other HFC interactions associated with T1 (Table 2). $H_{\beta_1}(T1)$ is a typical β -proton HFC.

$H_{\beta_2}(T1)$ could be due to a β - as well as to a γ -proton HFC interaction because the isotropic component is rather small and the magnitude of the anisotropy is in between those typical of β - and γ -protons. The $H_{\beta_2}(T1)$ HFC tensor is in fact quite comparable to the H_{β_1} and H_{β_2} HFC tensors of radicals T2 and T3.⁷ These were shown to arise from γ -protons neighbouring either a ring oxygen or a carbonyl group on which a substantial part of the spin density is localised.⁸ It is therefore reasonable to

consider that $H_{\beta 2}(T1)$ is also such a proton. As both $H_{\beta 1}(T1)$ and $H_{\beta 2}(T1)$ exhibit couplings with nearly axial anisotropy, the point dipole approximation should be valid. This implies that the eigenvector associated with the most positive anisotropic coupling is oriented roughly along the line connecting the (main) site of the unpaired spin density with the interacting nucleus. Considering furthermore that experiments on deuterated samples revealed that all T1 HFCs arise from non-exchangeable protons (*i.e.* protons bound to carbons),⁷ and assuming that the geometry of the radical does not deviate too much from that of the molecule in the pristine lattice, only three possible radical sites emerge: C1, C4 and C2' (see Fig. 1 for labelling). In Table 3, an overview is presented of relevant eigenvector directions compared with directions calculated from the pristine crystal structure. The resulting radical model structures are depicted in Fig. 5 as models M1 to M4. For the C1-centred model (M1), only an abstraction of the H1 hydrogen is needed. The C4-centred model (M2) requires hydrogen abstraction of H4 and a concerted formation of a carbonyl group at C3. For the C2'-centred model, there are two possibilities: splitting off a formaldehyde molecule (M3) or cleaving the glycosidic bond at the fructose side (M4).

For each of these four radical structures, periodic geometry optimisations and calculation of EMR parameters in the 'single molecule approach' were performed as described in section 2.2. The calculations did not yield a stable conformation in the case of M3. Additional constraints had to be applied on the formaldehyde molecule in order to prevent spontaneous reattachment and formation of the O1'-centred alkoxy radical. For the calculation of the HFC tensors of M3 the formaldehyde molecule was left out. The HFC tensors calculated for these four models are presented in Table 4. The agreement in HFC tensors is not satisfactory for any of the models. Most notably, (i) none of the models give rise to a HFC interaction that could account for $H_{\beta 3}(T1)$ (the HO4 HFC in model M2 has comparable principal values, but $H_{\beta 3}(T1)$ is known to arise from a non-exchangeable proton⁷), (ii) the isotropic parts of the γ -proton HFC interactions of models M1 and M3 are very small and even negative, in sharp contrast with the experimentally observed value of approximately 16 MHz for $H_{\beta 2}(T1)$, and (iii) for models M2 and M4, the DFT calculations predict HFC interactions (HO4 and H1'a respectively) that are definitely not detected experimentally.

Therefore, variations on the M1–M4 structures need to be considered where these discrepancies could be eliminated. Model M4 gives the best agreement in eigenvector directions for $H_{\beta 1}(T1)$ and $H_{\beta 2}(T1)$ (Table 4) and it is the only model that can relatively easily be adapted to eliminate its main deficiency, the H1'a HFC. The result is the allylic-type radical model M5 in Fig. 5. Moreover, the carbonyl group present in M5 would enhance the

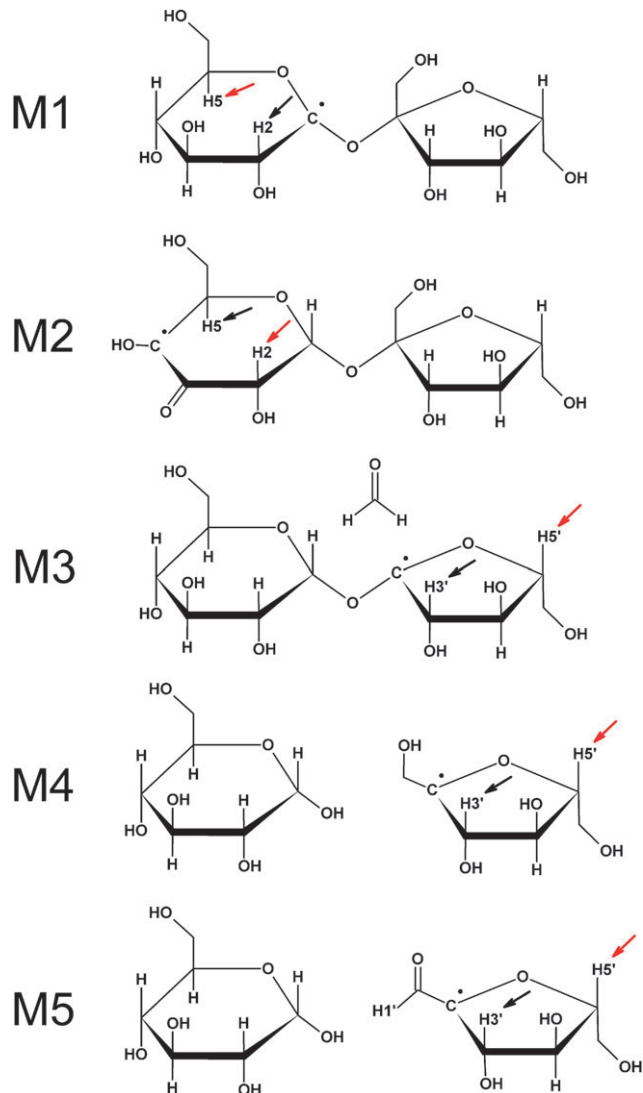


Fig. 5 The chemical structure of radical models M1 to M5, proposed on the basis of agreement between eigenvectors of the $H_{\beta 1}(T1)$ and $H_{\beta 2}(T1)$ HFC tensors and crystalline directions. The protons relevant for this comparison in directions (see Table 3) are labelled and indicated with arrows (black for $H_{\beta 1}(T1)$, red for $H_{\beta 2}(T1)$). DFT calculations indicate that M5 is the actual structure of radical species T1 (Table 5).

g -tensor anisotropy of T1, a feature that has been observed experimentally.³¹ The DFT calculations in the single molecule approach on radical species M5 indeed yield HFC tensors that are in excellent agreement on all accounts with the $H_{\beta 1}(T1)$ and $H_{\beta 2}(T1)$ HFC tensors (Table 5, Approach 1). For $H_{\beta 3}(T1)$ some

Table 3 Angle (δ) between crystalline interatomic directions (left hand column) and the eigenvectors associated with the most positive anisotropic coupling values of the HFC tensors specified at the top right hand side (*cf.* Table 2)

	Hydrogen position	Distance (\AA)	Direction cosines			δ ($^\circ$)	
			a*	b	c	$H_{\beta 1}(T1)$	$H_{\beta 2}(T1)$
C1...H2	β	2.14	-0.556	-0.454	-0.696	21.3	
C1...H5	γ	2.74	0.139	-0.647	0.750		15.7
C4...H5	β	2.15	0.542	0.443	0.714	21.6	
C4...H2	γ	2.69	-0.148	0.652	-0.744		16.4
C2'...H3'	β	2.16	0.854	0.420	0.307	21.7	
C2'...H5'	γ	3.01	-0.077	0.731	0.678		13.9

discrepancies remain, in particular with respect to the eigenvectors associated with the smaller anisotropic HFC values. These eigenvector directions are, however, known to be more sensitive to the basis set and level of theory³² as well as to the precise electronic structure.^{33,34} In section 3.3 it will be shown that the latter is substantially modified by the lattice environment. The results presented there are in excellent agreement with the experimental data and leave no doubt that M5 is essentially the correct radical model for T1.

The T1 radical structure (M5, Fig. 5) has key features very similar to the T2/T3 radical (Fig. 1, bottom): a cleaved glycosidic bond and a carbonyl group on which a substantial part of the spin density is localised. This clearly indicates the importance of the glycosidic bond in the radiation chemistry of sucrose. It is a plausible and interesting hypothesis that glycosidic bond cleavage and formation of a carbonyl group are commonly operative mechanisms in X-irradiated polysaccharides, but further work is necessary to test this hypothesis. Also, a very recent study by some of the authors of the current work has revealed that the major stable radical induced by X-ray irradiation at 77 K in single crystals of glucose 1-phosphate has the same chemical structure as

the T2/T3 radical. There, a glucose–phosphate bond is broken instead of a glycosidic bond.^{35,36} This suggests that those radiation-induced mechanisms may also be operative in glucose-1-phosphate and, by extension, in the sugar–phosphate moiety of DNA. Thus, these results strengthen the validity of sucrose single crystals as a model compound to study the fundamental radiation-induced processes occurring in that moiety. Currently, EMR experiments at low temperatures after *in situ* X-ray irradiation at those temperatures and accompanying DFT calculations are being performed to identify the precursors and unravel the formation mechanisms of the stable sucrose radicals. This will be the subject of a forthcoming publication.

Finally, it might be tempting, based on the chemical structures, to propose that the formation of radical T1 on the one hand and radicals T2 and/or T3 on the other hand are connected, or even that the discrepancies between T2 and T3 can be explained *e.g.* by the presence/absence of a neighbouring T1 radical. However, such radical pairs would yield singlet and triplet states and thus give rise to EPR and ENDOR spectra different from those observed. Moreover, they are not expected to be stable at RT.³⁷

Table 4 Proton HFC tensors ((an)isotropic values in MHz) calculated for models M1 to M4 depicted in Fig. 5 as described in section 2.2. δ is the angle between the computed eigenvector directions and the experimentally determined eigenvector directions of the T1 HFC tensors (Table 2)

Radical model	Proton	Iso	Aniso	Eigenvectors			Proton	δ (°)
				a*	b	c		
M1	H2	32.85	−6.08	0.808	−0.086	−0.583	H _{β1}	15.9
			−4.78	−0.180	0.906	−0.383		12.4
			10.86	0.561	0.414	0.717		19.8
	H5	−2.60 −1.33	−4.44 0.936 5.77	−0.221	0.656	0.721	H _{β2}	23.3
				0.351	−0.032	29.0		24.2
				0.274	−0.668	0.692		
M2	H5	56.60	−3.65	0.576	0.586	−0.570	H _{β1}	43.4
			−2.62	0.750	−0.656	0.083		44.7
			6.27	0.325	0.475	0.818		34.2
	H2	10.86	−2.65 −1.40 4.05	0.885	0.374	0.277	H _{β2}	56.3
				−0.412	0.356	0.839		64.0
				−0.215	0.857	−0.469		33.3
	HO4	−10.12	−8.38 −7.37 15.74	0.868	−0.365	0.336		
				0.492	0.553	−0.672		
				0.060	0.749	0.660		
M3	H3'	32.15	−5.82	−0.503	0.863	0.047	H _{β1}	63.2
			−5.23	−0.270	−0.208	0.940		67.7
			11.05	0.821	0.460	0.338		21.7
	H5'	−3.01	−3.31 −2.29 5.60	0.957	−0.184	0.223	H _{β2}	67.8
				−0.288	−0.545	0.788		69.9
				0.024	0.818	0.575		22.8
M4	H3'	66.83	−5.22	0.548	0.150	−0.823	H _{β1}	16.3
			−2.70	−0.148	0.986	0.081		17.3
			7.91	0.823	0.077	0.563		6.8
	H5'	6.95	−4.24 −2.90 7.14	−0.211	0.821	−0.531	H _{β2}	6.1
				0.940	0.319	0.118		11.7
				−0.266	0.475	0.839		10.3
	H1'a	56.66	−5.96 −2.77 8.73	0.936	−0.207	0.284		
				0.111	0.941	0.319		
				−0.334	−0.267	0.904		

Table 5 Proton HFC tensors ((an)isotropic values in MHz) calculated for model M5 (Fig. 5) using different computational approaches. The geometry optimisation is performed in an <ab2c> supercell (Approaches 1–3) or in a <2a2b2c> supercell (Approach 4). The calculation of EMR parameters is performed on the (isolated) radical molecule (Approach 1), on the radical molecule and the neighbouring molecule hydrogen-bound to the T1 carbonyl oxygen (Approach 2), or on a cluster consisting of the radical molecule and 10 hydrogen-bound molecules (Approaches 3 and 4). δ is the angle between the computed eigenvector directions and the experimentally determined eigenvector directions of the T1 HFC tensors (Table 2)

	Proton	Iso	Aniso	Eigenvectors			Proton	δ (°)
				a*	b	c		
Approach 1	H3'	44.4	-3.79	0.609	-0.056	-0.791	Hβ₁	3.9
			-2.52	-0.092	0.986	-0.140		4.1
			6.31	0.788	0.159	0.595		1.5
	H5'	12.9	-2.60	0.028	0.851	-0.525	Hβ₂	8.0
			-2.20	0.990	0.047	0.130		8.2
			4.80	-0.135	0.524	0.841		2.5
	H1'	-6.5	-5.08	0.617	0.777	-0.123	Hβ₃	70.6
			-3.30	0.575	-0.553	-0.604		70.4
			8.37	0.537	-0.302	0.788		3.9
Approach 2	H3'	41.1	-3.69	0.617	-0.094	-0.781	Hβ₁	1.4
			-2.52	-0.076	0.981	-0.178		1.8
			6.22	0.783	0.170	0.598		1.0
	H5'	14.4	-2.49	-0.021	0.847	-0.531	Hβ₂	5.2
			-2.21	0.992	0.083	0.094		5.3
			4.70	-0.124	0.525	0.842		1.9
	H1'	-9.4	-5.69	0.783	0.057	-0.619	Hβ₃	17.8
			-4.58	0.183	0.931	0.316		18.0
			10.27	0.594	-0.361	0.719		3.8
Approach 3	H3'	43.5	-3.86	0.624	-0.220	-0.750	Hβ₁	5.9
			-2.27	-0.021	0.954	-0.298		6.0
			6.13	0.781	0.202	0.590		1.0
	H5'	15.4	-2.37	-0.286	0.788	-0.546	Hβ₂	10.6
			-2.24	0.950	0.307	-0.055		10.7
			4.61	-0.124	0.535	0.836		1.5
	H1'	-10.6	-6.81	0.709	-0.136	-0.692	Hβ₃	6.5
			-4.62	0.362	0.912	0.193		7.3
			11.43	0.605	-0.387	0.696		5.7
Approach 4	H3'	41.9	-3.74	0.628	-0.198	-0.753	Hβ₁	4.7
			-2.33	-0.032	0.960	-0.280		4.7
			6.07	0.778	0.200	0.596		1.1
	H5'	16.3	-2.40	-0.261	0.797	-0.545	Hβ₂	9.0
			-2.26	0.957	0.286	-0.040		9.2
			4.67	-0.124	0.533	0.837		1.6
	H1'	-11.47	-6.92	0.702	-0.147	-0.697	Hβ₃	5.9
			-4.64	0.356	0.920	0.165		5.8
			11.56	0.617	-0.364	0.698		4.6

4.3 Electronic structure of T1

The electronic structure of the T1 radical, that gives rise to the unusual H β ₃(T1) HFC tensor, will now be discussed in more detail. It is well known that in an allylic radical fragment (Fig. 6a) the central carbon has a substantial negative π -spin density of about -20%, whereas the terminal carbons carry about +60% each.^{38,39} The isotropic HFC value of the proton bound to the central carbon is about 12 MHz. The positive sign is expected here because a positive (negative) spin density on a carbon is known to give rise to a negative (positive) isotropic HFC value for an α -proton through standard spin polarisation mechanisms. In the case of the allylic-type radical fragment depicted in Fig. 6b, the

spin density on the central (carbonyl) carbon is reduced.³⁹ For reference purposes, a calculation was carried out on such a radical fragment, yielding a Mulliken spin density of -12% at the carbonyl carbon (Fig. 7a). A negligible isotropic coupling of -0.4 MHz is calculated for the proton bound to the carbonyl carbon, indicating that spin polarisations arising from the various atoms with substantial spin densities cancel each other at that H-atom. However, in the T1 radical a substantial negative isotropic HFC value was found for the H β ₃(T1) HFC (Table 2).

The reason for this qualitative discrepancy was explored by means of additional DFT calculations on radical fragments (Fig. 7a–b) and on the T1 model in various computational approaches

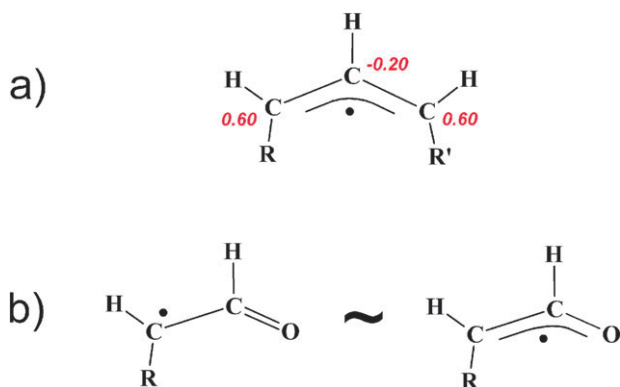


Fig. 6 An allylic (a) and an allylic-type (b) radical fragment. The red italic numbers indicate typical spin densities for the allylic radical fragment.

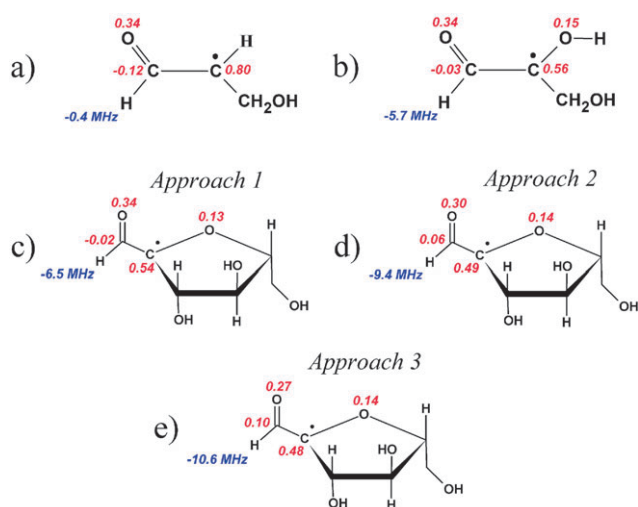


Fig. 7 DFT calculated Mulliken spin densities (red) and isotropic HFC value for the proton bound to the central carbon (blue) for two optimised allylic-type radical fragments (a and b), and for the T1 radical molecule optimised in an $\langle ab2c \rangle$ supercell (c–e). The single-point calculation was performed not taking the surrounding lattice into account (c), or only taking the molecule into account that is hydrogen-bonded to the carbonyl oxygen of the T1 radical (d), or taking the cluster of ten hydrogen-bonded molecules into account (e). This corresponds to Approaches 1, 2 and 3 in Table 5 respectively.

(Fig. 7c–e, corresponding to Approaches 1, 2 and 3 in Table 5 respectively). There appear to be essentially two main causes:

1. The presence of the ring oxygen neighbouring C2' in T1. Comparison of the results of DFT calculations for the radical fragments in Fig. 7a and b shows that the presence of an additional oxygen atom gives rise to a substantial shift in spin densities and an accompanying change in isotropic HFC value for the proton bound to the carbonyl carbon (from -0.4 MHz to -5.7 MHz). The spin densities and the isotropic HFC value of that proton obtained for the radical fragment in Fig. 7b are essentially the same as those obtained from DFT calculations on the isolated T1 radical molecule cut out of the periodically optimised structure (Fig. 7c, Approach 1 in Table 5).

2. The presence of a hydrogen bond between O1' and the neighbouring lattice. In the lattice, there is a hydrogen bond between the O1' carbonyl oxygen of the T1 radical, and the HO4'

hydrogen of a neighbouring molecule. In Fig. 7d, the Mulliken spin densities are given for a single-point DFT calculation on the radical molecule and that hydrogen-bonded neighbouring molecule, both cut out of the periodically optimised structure (Approach 2 in Table 5). Compared to the calculation on the isolated radical molecule (Fig. 7c and Table 5, Approach 1), there is an increase of positive spin density at C1' by 8% (from -2% to $+6\%$) and the calculated H1' HFC tensor is in substantially better agreement with the experimental $H_{\beta 3}(T1)$ tensor in all respects. Calculations indicate that subsequently adding hydrogen-bonded molecules to the structure on which the single-point DFT calculation is performed systematically improves the agreement with experimental values. Because the effects are minor, only the results for the cluster consisting of the radical molecule and 10 surrounding hydrogen-bonded molecules are given (Fig. 7e and Approach 3 in Table 5). In Fig. 8 the spin density distribution as obtained in Approach 3 is visualised.

For reference purposes, calculations were also performed using an even bigger $\langle 2a2b2c \rangle$ supercell for the geometry optimisation and the same cluster as in Approach 3 for the HFC tensor calculation. This is Approach 4 in Table 5. These calculations yield only negligible adjustments to the HFC tensors calculated in Approach 3. Finally, the conformational freedom of the 'dangling' O1-HO1 hydroxy group of the glucose unit was investigated: an energy profile was calculated for the rotation of this hydroxy group about the O1–C1 bond (see Fig. 8 for labelling). This profile indicates that the conformation on which DFT calculations were performed throughout the current work (*cf.* Fig. 8) corresponds to the global minimum. Since it provides no other information relevant for the current discussion, it is reported in the ESI (Fig. S3).[†]

5. Conclusion

A specifically designed ENDOR experiment at 110 K on a RT X-irradiated sucrose single crystal allowed for the determination

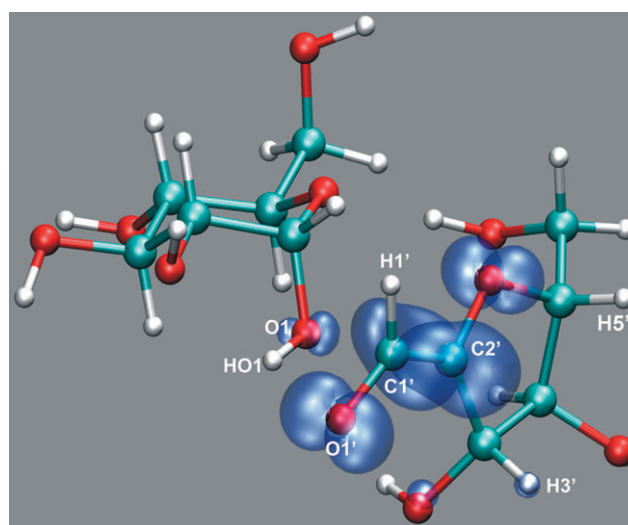


Fig. 8 Optimised structure of radical model M5 (Fig. 5). The spin density distribution, as obtained from the cluster single-point calculation (Approach 3 in Table 5) is visualised by means of a spin density isosurface with $\rho = +0.005$ (blue).

of the proper Schonland variant of the $H_{\beta_3}(T1)$ HFC tensor. HYSORE experiments at RT on X-irradiated sucrose powder not only confirmed this choice but also readily allowed determination of the sign of this tensor. The obtained HFC tensor has an anisotropy typical of a β -proton, but an uncommon substantial negative isotropic part. Employing advanced DFT calculations, the T1 radical was identified as an allylic-type radical, involving scission of the glycosidic bond and a concerted formation of a carbonyl group. Model DFT calculations provided an explanation for the peculiar $H_{\beta_3}(T1)$ HFC tensor in terms of a change in the spin density on the central (carbonyl) carbon of the allylic fragment. The latter is mainly caused by the presence of an adjacent ring oxygen and by hydrogen bonding with a neighbouring molecule in the lattice.

With the identification of the third of three major stable radicals, the EPR spectrum of solid-state sucrose X-irradiated at RT is now largely understood in terms of radical structures. The chemical structures of the three stable radicals are very similar and suggest that glycosidic bond scission and carbonyl group formation may be commonly operative mechanisms in the radiation chemistry of disaccharides, and possibly even in that of the DNA sugar-phosphate moiety.

Acknowledgements

This work was financially supported by the Flemish Research Foundation (FWO-Vlaanderen). The authors acknowledge a Postdoctoral Fellowship (E. Pauwels and H. Vrielinck) and a Research Assistant Fellowship (H. De Cooman) with the same institution.

References

- W. K. Pogozelski and T. D. Tullius, *Chem. Rev.*, 1998, **98**, 1089–1107.
- W. A. Bernhard and D. M. Close, in *DNA Damage Dictates the Biological Consequences of Ionizing Irradiation: The Chemical Pathways In Charged Particle and Photon Interactions with Matter: Chemical, Physicochemical, and Biological Consequences with Applications*, ed. A. Mozumder and Y. Hatano, Marcel Dekker, New York, 2003, pp. 431–470.
- D. Becker, A. Adhikary and M. D. Sevilla, in *The Role of Charge and Spin Migration in DNA Radiation Damage In Charge Migration in DNA Physics, Chemistry and Biology Perspectives*, ed. T. Chakraborty, Springer-Verlag, Berlin Heidelberg, 2007, pp. 139–175.
- M. Desrosiers and S. Wadley, *Radiat. Prot. Dosim.*, 2006, **118**, 479–481.
- N. D. Yordanov, V. Gancheva and E. Georgieva, *Radiat. Chem. Phys.*, 2002, **65**, 269–276.
- N. D. Yordanov and E. Georgieva, *Spectrochim. Acta, Part A*, 2004, **60**, 1307–1314.
- H. De Cooman, E. Pauwels, H. Vrielinck, A. Dimitrova, N. Yordanov, E. Sagstuen, M. Waroquier and F. Callens, *Spectrochim. Acta, Part A*, 2008, **69**, 1372–1383.
- H. De Cooman, E. Pauwels, H. Vrielinck, E. Sagstuen, F. Callens and M. Waroquier, *J. Phys. Chem. B*, 2008, **112**, 7298–7307.
- H. Vrielinck, H. De Cooman, M. A. Tarpan, E. Sagstuen, M. Waroquier and F. Callens, *J. Magn. Reson.*, DOI: 10.1016/j.jmr.2008.09.017.
- W. A. Bernhard, *J. Chem. Phys.*, 1984, **81**, 5928–5935.
- H. M. McConnell and D. B. Chesnut, *J. Chem. Phys.*, 1958, **28**, 1535.
- G. M. Brown and H. A. Levy, *Acta Crystallogr., Sect. B: Struct. Crystallogr. Cryst. Chem.*, 1973, **29**, 790–797.
- W. H. Nelson, *J. Magn. Reson.*, 1980, **38**, 71–78.
- A. R. Sørnes, E. Sagstuen and A. Lund, *J. Phys. Chem.*, 1995, **99**, 16867–16876.
- S. Stoll and A. Schweiger, *J. Magn. Reson.*, 2006, **178**, 42.
- P. Höfer, A. Grupp, H. Nebenführ and M. Mehring, *Chem. Phys. Lett.*, 1986, **132**, 279.
- L. Liesum and A. Schweiger, *J. Chem. Phys.*, 2001, **114**, 9478.
- Z. L. Madi, S. Van Doorslaer and A. Schweiger, *J. Magn. Reson.*, 2002, **154**, 181.
- CPMD V3.11 Copyright IBM Corp 1990–006, Copyright MPI fuer Festkoerperforschung, Stuttgart 1997–001.
- J. P. Perdew, *Phys. Rev. B*, 1986, **33**, 8822–8824.
- A. D. Becke, *J. Chem. Phys.*, 1992, **96**, 2155–2160.
- D. Vanderbilt, *Phys. Rev. B*, 1990, **41**, 7892–7895.
- M. J. Frisch, G. W. Trucks, H. B. Schlegel, G. E. Scuseria, M. A. Robb, J. R. Cheeseman, J. A. Montgomery, Jr., T. Vreven, K. N. Kudin, J. C. Burant, J. M. Millam, S. S. Iyengar, J. Tomasi, V. Barone, B. Mennucci, M. Cossi, G. Scalmani, N. Rega, G. A. Petersson, H. Nakatsuji, M. Hada, M. Ehara, K. Toyota, R. Fukuda, J. Hasegawa, M. Ishida, T. Nakajima, Y. Honda, O. Kitao, H. Nakai, M. Klene, X. Li, J. E. Knox, H. P. Hratchian, J. B. Cross, V. Bakken, C. Adamo, J. Jaramillo, R. Gomperts, R. E. Stratmann, O. Yazyev, A. J. Austin, R. Cammi, C. Pomelli, J. Ochterski, P. Y. Ayala, K. Morokuma, G. A. Voth, P. Salvador, J. J. Dannenberg, V. G. Zakrzewski, S. Dapprich, A. D. Daniels, M. C. Strain, O. Farkas, D. K. Malick, A. D. Rabuck, K. Raghavachari, J. B. Foresman, J. V. Ortiz, Q. Cui, A. G. Baboul, S. Clifford, J. Cioslowski, B. B. Stefanov, G. Liu, A. Liashenko, P. Piskorz, I. Komaromi, R. L. Martin, D. J. Fox, T. Keith, M. A. Al-Laham, C. Y. Peng, A. Nanayakkara, M. Challacombe, P. M. W. Gill, B. G. Johnson, W. Chen, M. W. Wong, C. Gonzalez and J. A. Pople, *GAUSSIAN 03 (Revision B.03)*, Gaussian, Inc., Wallingford, CT, 2004.
- A. D. Becke, *J. Chem. Phys.*, 1996, **104**, 1040–1046.
- R. Krishnan, J. S. Binkley, R. Seeger and J. A. Pople, *J. Chem. Phys.*, 1980, **72**, 650–654.
- A. D. McLean and G. S. Chandler, *J. Chem. Phys.*, 1980, **72**, 5639–5648.
- R. Declerck, E. Pauwels, V. Van Speybroeck and M. Waroquier, *J. Phys. Chem. B*, 2008, **112**, 1508–1514.
- A. Schweiger and G. Jeschke, in *Principles of Pulse Electron Paramagnetic Resonance*, Oxford University Press, Oxford, 2001.
- R. J. Cook and D. H. Whiffen, *Proc. Phys. Soc.*, 1964, **84**, 845.
- N. M. Atherton, in *Principles of electron spin resonance*, Ellis Horwood, PTR Prentice Hall, 1993, 429–438.
- R. Georgieva, L. Pardi, G. Jeschke, D. Gatteschi, L. Sorace and N. D. Yordanov, *Free Radical Res.*, 2006, **40**, 553–563.
- R. Improta and V. Barone, *Chem. Rev.*, 2004, **104**, 1231–1253.
- N. Jayatilaka and W. H. Nelson, *J. Phys. Chem. B*, 2007, **111**, 7887.
- E. Pauwels, V. Van Speybroeck and M. Waroquier, *J. Phys. Chem. A*, 2004, **108**, 11321–11332.
- H. De Cooman, G. Vanhaelewyn, E. Pauwels, E. Sagstuen, M. Waroquier and F. Callens, *J. Phys. Chem. B*, 2008, **112**, 15045–15053.
- E. Pauwels, H. De Cooman, E. Sagstuen, F. Callens and M. Waroquier, *J. Phys. Chem. B*, 2008, **112**, 15054–15063.
- H. C. Box, in *Radiation Effects: ESR and ENDOR analysis*, Academic Press, Inc., New York, 1977.
- C. Heller and T. Cole, *J. Chem. Phys.*, 1962, **37**, 243–250.
- L. Salem, in *Molecular orbital theory of conjugated systems*, W.A. Benjamin, New York-Amsterdam, 1966.

7.4 Paper IV

Radiation-induced radicals in glucose-1-phosphate. I. Electron paramagnetic resonance and electron nuclear double resonance analysis of in situ X-irradiated single crystals at 77 K

H. De Cooman, G. Vanhaelewyn, E. Pauwels, E. Sagstuen, M.
Waroquier and F. Callens

Journal of Physical Chemistry B, 2008, 112, 15045-15053

Copyright 2008 by the American Chemical Society.

Radiation-Induced Radicals in Glucose-1-phosphate. I. Electron Paramagnetic Resonance and Electron Nuclear Double Resonance Analysis of *in situ* X-Irradiated Single Crystals at 77 K

Hendrik De Cooman,^{†,‡} Gauthier Vanhalewyn,[†] Ewald Pauwels,[‡] Einar Sagstuen,[§] Michel Waroquier,[‡] and Freddy Callens^{*,†}

Department of Solid State Sciences, Ghent University, Krijgslaan 281-S1, B-9000 Gent, Belgium, Center for Molecular Modeling, Ghent University, Proeftuinstraat 86, B-9000 Gent, Belgium, and Department of Physics, University of Oslo, P.O. Box 1048 Blindern, N-0316 Oslo, Norway

Received: May 14, 2008; Revised Manuscript Received: June 26, 2008

Electron magnetic resonance analysis of radiation-induced defects in dipotassium glucose-1-phosphate dihydrate single crystals *in situ* X-irradiated and measured at 77 K shows that at least seven different carbon-centered radical species are trapped. Four of these (R1–R4) can be fully or partly characterized in terms of proton hyperfine coupling tensors. The dominant radical (R2) is identified as a C1-centered species, assumedly formed by a scission of the sugar–phosphate junction and the concerted formation of a carbonyl group at the neighboring C2 carbon. This structure is chemically identical to a radical recently identified in irradiated sucrose single crystals. Radical species R1 and R4 most likely are C3- and C6-centered species, respectively, both formed by a net hydrogen abstraction. R3 is suggested to be chemically similar to but geometrically different from R4. Knowledge of the identity of the sugar radicals present at 77 K provides a first step in elucidating the formation mechanism of the phosphoryl radicals previously detected after X-irradiation at 280 K. In paper II, the chemical identity, precise conformation, and possible formation mechanisms of these radical species are investigated by means of DFT calculations and elementary insight into the radiation chemistry of sugar and sugar derivatives is obtained.

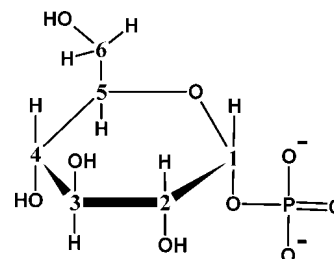
1. Introduction

Exposure of DNA to ionizing radiation initiates sequences of processes that eventually lead to various end points, among other single and double strand breaks. The primary precursors are free radicals formed in the base and the sugar–phosphate residues. Strand breaks appear to be induced primarily by damage to the sugar–phosphate groups, as indicated by a correlation between the yield of radiation-induced free radicals localized at the sugar and the yield of single strand breaks (ssb's) in irradiated DNA.^{1,2} Sugar radicals may act as immediate precursors for the release of a phosphate group by an elimination process, as is well-known from aqueous radiation chemistry.³ Both carbon-centered and phosphoryl radicals may be envisioned by such processes.

Recently, it has been suggested that low-energy electrons (LEE's) with energies below the ionization threshold may provoke direct damage to DNA through dissociative electron attachment (DEA), causing prompt cleavage of the sugar–phosphate ester bond.^{4–6} Even if the number of LEE's is large, the number of radicals associated with this process is small.² It has also been suggested that excited base cation-radical states can lead to free radical damage to the sugar–phosphate backbone.^{2,7}

Experimentally investigating radical processes leading to strand breaks, being initiated by direct radiation effects, necessitates the study of model systems containing the sugar–phosphate

SCHEME 1: Chemical Structure of a Glucose-1-phosphate Molecule



ester bond. A number of hydroxyalkyl phosphate derivatives have been studied by electron paramagnetic resonance (EPR) techniques in the solid state.^{8–14} Hydroxyalkyl radicals are the major products formed subsequent to low-temperature irradiation. These may be formed by reductive processes initiated either by trapped electrons¹⁵ or by DEA, by oxidative processes¹⁶ or by elimination processes (direct H-atom abstraction). Phosphate radicals have been detected only in a few cases after 77 K irradiation^{8,13} and not at all at very low temperatures (<77 K), so that, although prompt phosphate–ester bond breaks have been proposed to occur in irradiated DNA systems,¹⁷ there is no direct evidence for these processes taking place in hydroxyalkyl phosphate derivatives. However, carbon-centered radicals are commonly formed. Several of these may have been formed by inorganic phosphate elimination possibly immediately following DEA, as the inorganic phosphate species is EPR silent.

Glucose-1-phosphate (Scheme 1) is one such system where previous studies have demonstrated the formation of phosphate radicals at room temperature, implying processes involving the

* To whom all correspondence should be addressed. Phone: +3292644352. Fax: +32926464996. E-mail: freddy.callens@ugent.be.

[†] Department of Solid State Sciences, Ghent University.

[‡] Center for Molecular Modeling, Ghent University.

[§] Department of Physics, University of Oslo.

phosphate–ester bond. From V-band (70 GHz) EPR and electron nuclear double resonance (ENDOR) measurements on crystals of the dipotassium salt of glucose-1-phosphate dihydrate (abbreviated K2G1P in this work) at 4.2 K after *in situ* X-irradiation at this temperature, Locher and Box¹² characterized three alkoxy radicals, one of which was identified as the O6-centered species. In addition, these authors identified an intermolecularly trapped electron and a C6-centered hydroxyalkyl radical. As detailed crystal data were not available for these authors, no further analysis could be made. However, the bulk of the absorption was reported to occur in the free spin region ($g \approx 2$) where the EPR signal is strongly composite, indicating that a major part of the radicals present at this temperature are carbon-centered. No evidence for phosphate radicals was observed.

Bungum and co-workers studied K2G1P single crystals X-irradiated at 280 K using X- and Q-band (9.5 and 34 GHz, respectively) EPR techniques at RT.¹⁴ These authors observed two varieties of the phosphoryl radical (PO_3^{2-}). Furthermore, reanalysis of the data of Locher and Box¹² and comparison with the crystal structure^{18,19} by Bungum and co-workers confirm the identity of both the O6-centered alkoxy radical and the C6-centered hydroxyalkyl radical (H6b abstraction) and suggest that the other two alkoxy radicals are the O2- and O4-centered species.²⁰

Nelson and co-workers performed measurements on irradiated frozen aqueous solutions of monosodium D-glucose-6-phosphate^{21,22} which revealed that after X-irradiation at 77 K phosphoranyl radicals are formed. These species decay into two new different centers upon annealing to RT. One of these centers most likely is a phosphoryl radical, whereas no definite conclusion was arrived at with regard to the identity of the second one. For the composite central part of the spectrum arising from carbon-centered sugar radicals that also transform upon annealing, only very tentative attributions were made in terms of radical models.

A more elaborate and general study on phosphate radicals was published in 1996 by Sanderud and Sagstuen.¹³ From powder EPR studies on several phosphate esters at both 77 and 275 K after *in situ* irradiation at these temperatures, these authors tentatively concluded that phosphoryl radicals may be formed through several distinct pathways, depending on the net charge and the protonation state of the parent phosphate group with hydroxyalkyl sugar radicals acting as precursors in each pathway suggested. In the case of K2G1P, no phosphoryl or phosphoranyl radicals were detected after irradiation at 77 K, but two varieties of phosphoryl radicals were observed at 275 K, in agreement with the results reported by Bungum and co-workers.¹⁴ It was suggested that a sugar radical acts as a precursor for these phosphate radicals.

Thus, an interesting question arises for K2G1P: which initially formed species at low temperature transforms into the phosphate radicals detected at RT, and how? The prerequisite to answer this question is knowledge of the chemical identity of the sugar radicals present after 77 K X-irradiation. In the current work (this paper and the accompanying paper (paper II, ref 23)), the composite EPR signal at $g \approx 2$ of K2G1P single crystals irradiated and measured at 77 K was analyzed using experimental EPR techniques as well as computational density functional theory (DFT) calculations.

2. Experimental Procedures and Methods

Beevers and Maconochie¹⁸ and later Narendra and Viswamitra¹⁹ determined the crystal structure of K2G1P from X-ray

diffraction studies. The latter study was considerably more accurate but included neither the hydroxy hydrogen atoms nor the water hydrogen atoms. Sugawara and Iwasaki²⁴ refined the data from Beevers and Maconochie,¹⁸ thus providing the most accurate and complete set of atomic coordinates. The data of that study were used in the present work. The crystal is monoclinic with space group $P2_1$ and unit cell parameters $a = 10.458 \text{ \AA}$, $b = 9.027 \text{ \AA}$, $c = 7.532 \text{ \AA}$, and $\beta = 110.39^\circ$. The atomic coordinates in the $\langle a^*bc \rangle$ frame of ref 24 are given in Supporting Information Table S1. A unit cell contains two glucose-1-phosphate molecules (each of them with a double negative charge on the phosphate group), four K^+ ions, and four water molecules. The chemical structure of a glucose-1-phosphate molecule is depicted in Scheme 1, together with the IUPAC-based numbering used for the carbon atoms. Hydrogens and oxygens are numbered in this work according to the carbon to which they are bound. Hydroxy hydrogens are indicated as HOX, with X being the number of the carbon to which the hydroxy group is bound. The ring oxygen is labeled as O5.

K2G1P single crystals were grown from saturated H_2O or D_2O solutions at RT. Crystallization of deuterated crystals from D_2O was successful, but recrystallization of these deuterated crystals from D_2O was not. This implies that, making a conservative estimate, a deuteration rate of 90% may be expected. The samples were oriented using Weissenberg X-ray diffraction techniques with the rotation axes parallel to a given axis and subsequently transferred to copper sample holders with minimal loss of alignment. Although an accuracy of 1° in principle is attainable with this method, samples could often be oriented to only a few degrees of accuracy due to the rather strong absorption of the X-rays. The samples were irradiated *in situ* at 77 K for up to 12 h using a Philips chromium target X-ray tube operated at 60 kV and 40 mA, resulting in a total dose up to 110 kGy. The spectrometer and measurement procedures were as described elsewhere.²⁵

EPR and ENDOR angular variation measurements were performed in the three planes perpendicular to the $\langle a \rangle$, $\langle b \rangle$, and $\langle c \rangle$ axes in 5° intervals. At each orientation, ENDOR measurements were performed for at least two, and usually three or more, different magnetic field positions. An extensive number of ENDOR-induced EPR (EIE) measurements were carried out at several orientations in the three planes. The program MAGRES^{26,27} was used to derive the proton hyperfine coupling tensors from the ENDOR data as previously described in, e.g., ref 28.

The simulations of the EPR and EIE spectra were carried out using Easyspin²⁹ subroutines in Matlab. Linewidths and g values were treated as variables for the fitting process. For the EIE angular variation simulations, an isotropic g value is assumed.

Whenever a comparison is made between calculated eigenvector directions and experimentally determined eigenvector directions or crystal directions, allowed symmetry operations ($b \rightarrow -b$ and inversion of eigenvectors) are performed to obtain the best possible agreement.

Throughout this work, the different radical species that are experimentally detected are labeled as R_x , with x being a number from 1 to 7. For radical species R_1 to R_4 , plausible model structures are put forward. These are labeled M_x ($x = 1-4$) to emphasize the fact that these structures are “proposals”, and not necessarily the actual structures. When there are two model structures for radical R_x , they are labeled $\text{M}_{x\text{a}}$ and $\text{M}_{x\text{b}}$.

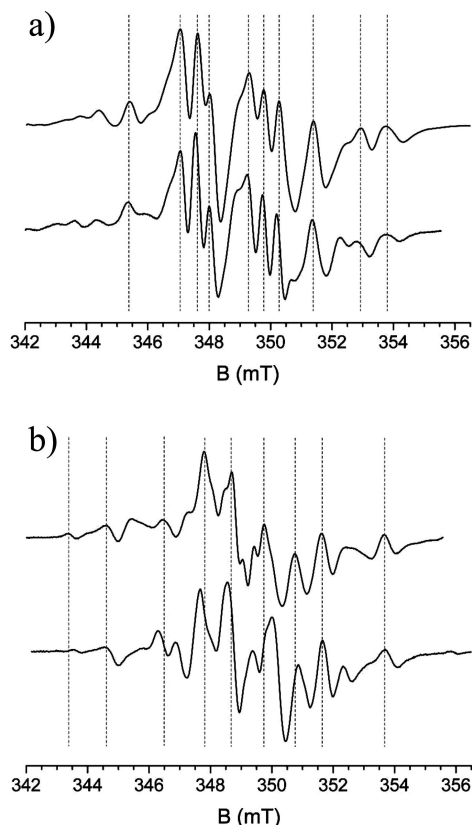


Figure 1. (a) EPR spectra obtained from measurements at 77 K after *in situ* X-irradiation at 77 K on K2G1P single crystals grown from an H₂O solution (top) and a D₂O solution (bottom). The magnetic field was perpendicular to $\langle b \rangle$, approximately 30° from $\langle a \rangle$, and 40° from $\langle c \rangle$. All spectra were normalized to a microwave frequency of 9.7750 GHz. (b) Same as part a but with the magnetic field approximately parallel to $\langle c^* \rangle$.

3. Results

Figure 1 shows EPR spectra for two different orientations of the crystal in the magnetic field, obtained from measurements on crystals grown from H₂O or D₂O solutions. Taking into account that orientations may differ up to 3° for the “H₂O spectrum” and the “D₂O spectrum”, the similarity of the spectra suggests that the major radical species present in nondeuterated and deuterated samples are essentially the same and that none of the major hyperfine interactions is due to exchangeable protons. Angular variations of the EPR spectrum reveal only small anisotropies of the g tensors, indicating that all radicals with appreciable signal intensity are carbon-centered. Some more anisotropic, but very faint features, possibly due to an alkoxy radical, were observed, but these were not studied further.

The ENDOR spectra revealed a large number of lines. Careful analysis of the angular variations of the ENDOR spectra in the three planes perpendicular to the reference axes and recorded for several magnetic field values at each orientation yielded 13 hyperfine coupling tensors in total, all originating from proton hyperfine interactions. The tensors are listed in Table 1. The angular variations of the ENDOR lines calculated from these tensors are shown as solid lines in Supporting Information Figure S1, together with the experimental data points.

Because of the so-called Schonland ambiguity,³⁰ in general, two different hyperfine coupling tensors are found for each hyperfine coupling, fitting the data points of high-frequency ENDOR branches in three orthogonal planes equally well. One of them is a mathematically valid solution without physical meaning. Traditionally, this problem is solved by measuring in

TABLE 1: Proton Hyperfine Coupling Tensors (in MHz) in K2G1P Single Crystals, Measured at 77 K after *in situ* X-Irradiation at This Temperature^a

radical	coupling	iso	aniso	eigenvectors		
				a^*	b	c
R1	HF1	79.24	-3.86	0.546	-0.365	-0.754
			-3.30	0.626	0.776	0.077
			7.16	0.557	-0.514	0.653
	HF2	71.71	-4.81	0.062	0.612	-0.788
			-2.87	0.394	0.711	0.583
			7.68	0.917	-0.346	-0.197
R2	HF1a	-41.55	-22.97	0.705	-0.298	-0.643
			0.63	0.238	0.954	-0.182
			22.34	0.668	-0.024	0.744
	HF1b	-41.53	-21.45	0.744	0.134	-0.654
			-2.41	0.046	0.967	0.251
			23.86	0.666	-0.216	0.714
	HF2	15.78	-2.54	0.651	-0.754	0.087
			-1.78	0.596	0.436	-0.674
			4.31	0.471	0.491	0.733
	HF3	10.16	-3.40	0.333	-0.700	0.632
			-2.35	0.430	-0.484	-0.762
			5.75	0.839	0.525	0.140
R3	HF1	-50.97	-31.07	0.928	0.078	-0.363
			2.33	0.285	0.479	0.830
			28.75	0.239	-0.874	0.423
R4	HF1a	-61.22	-29.35	0.750	0.104	-0.653
			0.17	0.526	0.504	0.685
			29.18	0.400	-0.857	0.323
	HF1b	-61.01	-32.89	0.697	0.285	-0.658
			6.32	0.704	-0.099	0.703
			26.57	0.135	-0.953	-0.270
	HF2	24.03	-6.36	0.375	0.540	-0.753
			-3.58	0.627	0.451	0.636
			9.94	0.683	-0.711	-0.169
	HFU1	46.78	-5.61	0.423	-0.520	-0.742
			-1.52	0.741	0.670	-0.047
			7.12	0.521	-0.530	0.669
	HFU2	41.51	-4.94	0.375	-0.528	-0.762
			-3.06	0.699	0.701	-0.142
			8.00	0.609	-0.479	0.632
HFU3	21.04	-6.77	0.066	-0.030	0.997	
		-6.39	0.994	-0.082	-0.068	
		13.15	0.084	0.996	0.024	
HFU4	5.82	-1.47	0.001	-1.000	0.002	
		-0.64	0.284	-0.001	-0.959	
		2.12	0.959	0.001	0.284	
HFU5	4.86	-1.52	0.159	-0.968	-0.194	
		-0.63	0.228	0.227	-0.947	
		2.15	0.961	0.107	0.257	

^a The tensors were determined by fitting the ENDOR data from angular variations in the three planes constituted by the direct crystal axes. The assignment of eight of these couplings to a total of four radical species was based on EIE measurements.

a fourth, skewed plane. As will be shown in a forthcoming paper from our laboratories, this ambiguity may also be solved by using both low- and high-frequency branches of a hyperfine coupling in a single crystal ENDOR experiment.³¹ Neither of these techniques were applied in the current work because, in most cases, either the two tensors were (accidentally) virtually identical or one of the two tensors could be readily dismissed on account of the symmetry properties of the principal values. However, neither of these options applied to HF1(R2) and HF1(R4), and therefore, both shapes are reported in Table 1. Especially for HF1(R4), the two possible tensors are distinctly different.

A large number of EIE measurements at several orientations showed that eight of the tensors could be assigned to four radical

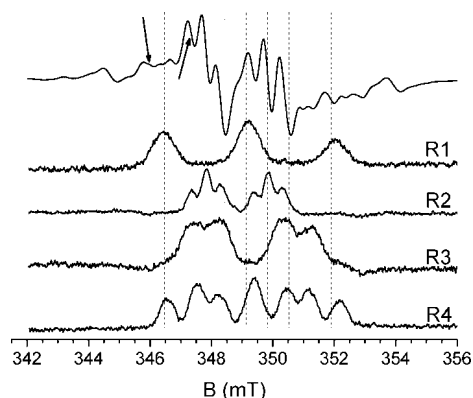


Figure 2. Top to bottom: EPR spectrum and EIE spectra of radical species R1–R4. All spectra are normalized to a microwave frequency of 9.7750 GHz. The magnetic field is oriented in the plane perpendicular to $\langle b \rangle$, approximately 10° from $\langle a \rangle$, and 10° from $\langle a^* \rangle$. The arrows indicate at which positions the ENDOR spectra of Figure 3 were recorded.

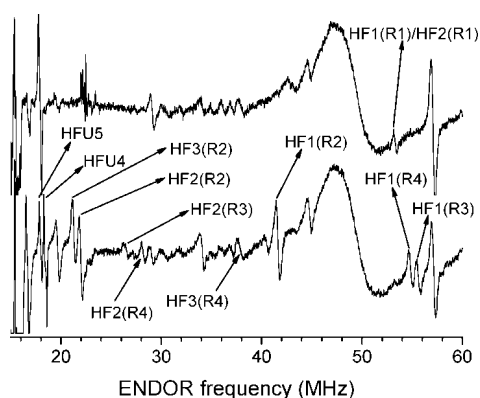


Figure 3. ENDOR spectra recorded on the EPR spectrum of Figure 2 at magnetic field values of 347.33 mT (bottom) and 345.94 mT (top). ENDOR lines are labeled according to the labeling scheme in Table 1.

species, labeled R1–R4, as indicated in Table 1. Detailed analysis of the EIE spectra at different orientations revealed that tensors HFU1–HFU3 cannot be attributed to any of those four radical species: the EIE spectra of radical species R1–R4 do not accommodate additional hyperfine couplings of the size of HFU1–HFU3, and on the few occasions where EIE spectra of some intensity were obtained on the HFU1–HFU3 ENDOR signals, they did not match those of R1–R4. The EIE spectra allowed for no conclusions concerning HFU4 and HFU5. These small hyperfine couplings would not be resolved in EIE, and the corresponding ENDOR signals are located in the very crowded region near the free proton frequency. A number of ENDOR lines could not be analyzed at all because of a very low signal-to-noise ratio at most orientations and/or because of large distortions of the ENDOR spectrum in the 45–50 MHz range as well as in the range above 60 MHz (due to technical reasons).

In the top of Figure 2, the EPR spectrum for an orientation in the plane perpendicular to $\langle b \rangle$ is shown. The ENDOR spectra obtained by probing this EPR spectrum at two different magnetic field values are shown in Figure 3. The ENDOR lines for which the corresponding hyperfine coupling tensors were determined have been labeled in Figure 3 according to the labeling scheme in Table 1. Some other lines were labeled additionally, as they will be referred to in section 4. The EIE spectra of radicals R1–R4, recorded by probing the ENDOR spectra of Figure 3, are also shown in Figure 2. Visual inspection indicates that

radical species R2, which also gives rise to the most intense ENDOR lines, is by far the most abundant one. This conclusion is confirmed by similar comparisons at a number of other orientations and by simulations (section 4.5).

In addition to radicals R1–R4, the ENDOR as well as EIE spectra reveal evidence for at least three other minority radicals that unfortunately could not be analyzed in detail. ENDOR lines were obtained at some orientations, yielding EIE spectra different from those of R1–R4. Supporting Information Figures S2 and S3 show these spectra with short descriptions of their origin in the corresponding figure captions. In particular, two different radicals (designated R6 and R7 in Supporting Information Figure S3) each appear to exhibit at least two hyperfine couplings giving rise to ENDOR lines at frequencies larger than 60 MHz at most orientations and hence out of reach for the present experiments. These radicals seem to account for the more intense outer features of the EPR spectrum (see Figure 1) that cannot be attributed to radicals R1–R4. The low-frequency ENDOR lines of these couplings were observed at several orientations, but they suffered from a low signal-to-noise ratio and were generally located in a crowded frequency range, so that insufficient data could be collected to allow for hyperfine tensor determinations.

Preliminary experiments were performed with the aim of determining if the phosphoryl radicals observed in refs 13 and 14 are formed upon annealing after 77 K irradiation. Phosphoryl radical signals were indeed observed after annealing to RT. The signals are very faint at RT but become well detectable when the sample is recooled to 100 K. Due to the very low signal-to-noise ratio upon annealing, it has not been established yet at which precise temperature the formation of the phosphoryl radicals takes place and which sugar radical(s) act(s) as precursor(s). This matter will be the subject of future work in our laboratories. In the next section, a detailed discussion of radical species R1–R4 will be given.

4. Discussion

4.1. Radical Species R1. Radical species R1 exhibits two typical β -proton hyperfine couplings with comparable isotropic hyperfine coupling values of approximately 72 and 79 MHz (Table 1), in agreement with the triplet structure of the EIE spectrum observed at most orientations. It is well-known that for β -proton hyperfine couplings the eigenvector associated with the most positive principal value ($b_{+,dip}$) is roughly parallel with the line connecting the site of the (main) spin density with the interacting nucleus. Therefore, a comparison was made between the $b_{+,dip}$ eigenvectors and the directions of the different crystallographic $C_\alpha \cdots H_\beta$ directions. Only for the C3 carbon a good agreement was found for both hyperfine couplings: the $b_{+,dip}$ eigenvector directions of HF1(R1) and HF2(R1) deviate less than 20° from the crystalline $C3 \cdots H2$ and $C3 \cdots H4$ directions, respectively (Table 2). This single experimental observation leads us to propose the radical model depicted in Figure 4 (M1) where the H3 hydrogen is removed from the C3 carbon.

Assuming that the β -proton hyperfine coupling is due to hyperconjugation, the Heller–McConnell relation³² can be applied:

$$a_{iso}^\beta = \rho^\pi (B_0 + B_2 \cos^2 \theta)$$

Here, a_{iso}^β is the isotropic β -proton hyperfine coupling, ρ^π is the spin density in the lone electron orbital (LEO), and θ is the dihedral angle between the LEO and the C_β – H_β bond, viewed along the C_α – C_β bond. B_0 and B_2 are empirical constants arising

TABLE 2: Comparison of Pristine Crystal Directions (Left-Hand Column) with the Eigenvectors Associated with the Most Positive Anisotropic Coupling Values of Certain Hyperfine Tensors (Top Right-Hand Side)^a

hydrogen position	distance (Å)	direction cosines			δ (deg)							
		a^*	b	c	HF1(R1)	HF2(R1)	HF2(R2)	HF3(R2)	HF1a(R4)	HF1b(R4)	HF2(R4)	
C3•••H2	β	2.08	0.355	0.758	0.548	19.2						
C3•••H4	β	2.04	-0.781	0.611	0.128		17.5					
C1•••H3	γ	2.73	-0.131	-0.329	-0.935			24.6				
C1•••H5	γ	2.68	-0.838	-0.481	-0.260				7.3			
C3•••H3	α	0.96	0.149	-0.984	-0.102					29.5	9.9	
C3•••H4	β	2.04	-0.781	0.611	0.128							8.3
C4•••H3	β	2.04	0.781	-0.586	-0.215							9.4
C4•••H4	α	1.00	-0.138	0.987	-0.081					21.9	19.3	
C6•••H5	β	2.19	0.654	-0.734	-0.182							1.8
C6•••H6b	α	1.00	0.148	0.988	0.041					23.1	18.0	

^a The labeling scheme of Table 1 is used.

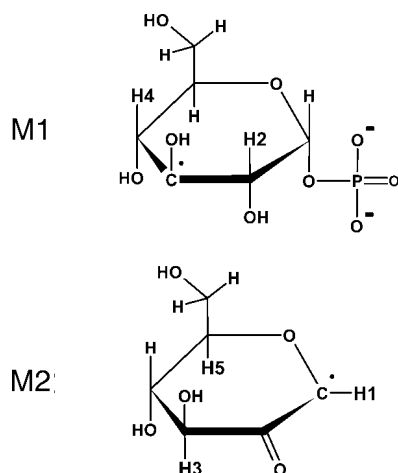


Figure 4. The chemical structures of model M1 for radical R1 and model M2 for radical R2.

from spin polarization and hyperconjugation, respectively. For a regular, planar alkyl radical, $B_0 \approx 0$ MHz and $B_2 \approx 126$ MHz can be assumed.³³ Assuming that the LEO is oriented along the original C3–H3 bond after H3 abstraction, dihedral angles of 2.8 and 10.5° are obtained for the H2 and H4 protons, respectively. Even when assuming a rather low spin density of 0.8, these dihedral angles would give rise to isotropic couplings of about 100 MHz according to the Heller–McCConnell relation above, substantially larger than the experimental values of approximately 80 and 70 MHz. Moreover, the O3–HO3 bond is nearly parallel with the C3–H3 bond, and therefore, a substantial isotropic coupling of the unpaired electron with the HO3 hydroxy proton is expected for the proposed radical model. However, no ENDOR transitions that could be assigned to this interaction were observed and the recorded EIE spectra can only accommodate an additional coupling of maximum 0.5 mT (≈ 14 MHz).

These observations do not necessarily invalidate the proposed model (M1). A possible explanation is that the molecule undergoes some structural reorganization upon hydrogen abstraction at C3. Apart from the rather convincing match in directions (Table 2) for both β -protons, another argument favoring the proposed radical model is the positive identification of radicals at similar loci in glucose,^{34–36} rhamnose,^{15,37} sorbose,³⁸ and fructose.^{39,40} These are all six-membered glucose ring carbohydrates, albeit with different molecular environments in the crystalline state.

4.2. Radical Species R2. As noted above (and as will be illustrated in section 4.5), R2 accounts for the major part of the

EPR spectrum, implying that it is by far the most abundant radical species present in X-irradiated K2G1P at 77 K. This radical exhibits three appreciable hyperfine interactions. The largest coupling is due to an α -proton hyperfine interaction, as indicated by the characteristic symmetry of its anisotropic components. Both isotropic and anisotropic coupling values are substantially reduced as compared to those for “typical” α -proton hyperfine couplings, however, indicating strong delocalization of the unpaired electron. The two smaller hyperfine couplings could originate from β - as well as γ -protons.

There is a striking similarity between the tensors of R2 and those of the stable T2/T3 radical species in room temperature irradiated sucrose single crystals,²⁸ both for the isotropic and anisotropic components. Also, the R2 resonance exhibits a marked shift toward higher g values (see, e.g., the EIE spectra in Figure 2), as is the case for the T2/T3 resonance. In ref 41, T2/T3 was identified as a glucose-centered radical with the major part of the unpaired spin residing at C1, resulting from glycosidic bond cleavage at the glucose side with a concerted formation of a carbonyl group at the C2 carbon. DFT calculations showed that a substantial part of the unpaired spin is localized on both this carbonyl group and the ring oxygen, giving rise to the reduced magnitude of the α -proton hyperfine coupling, the enhanced g -tensor anisotropy, and the two unusually strong γ -proton hyperfine interactions.

The similarity of the experimental data of T2/T3 and R2 suggests an analogous model for R2 in K2G1P, as depicted in Figure 4 (M2). It involves scission of the sugar–phosphate linkage and thus formation of a (not paramagnetic and thus) EPR silent inorganic phosphate group. In Table 2, a comparison is made between the $b_{+,dip}$ eigenvector directions of the HF2(R2) and HF3(R2) β -type tensors with the relevant directions calculated from the atomic coordinates of the K2G1P crystal structure analysis. Considering the expected delocalization of the unpaired spin density of this structure, the relatively small angular deviations (25 and 7°) support the proposed radical structure.

Additional arguments in favor of the proposed model can be obtained from the α -proton hyperfine coupling. For α -couplings, the eigenvector associated with the intermediate anisotropic coupling value ($a_{0,dip}$) is oriented roughly along the LEO axis and the eigenvector associated with the most positive anisotropic coupling value ($a_{+,dip}$) roughly along the C_α – H_α bond. Upon scission of the C1–O ester bond, the C1 radical center is expected to become nearly planar, with the LEO oriented perpendicular to the plane of the glucose ring. Defining this plane as the plane formed by the C1, C3, and C5 carbons,

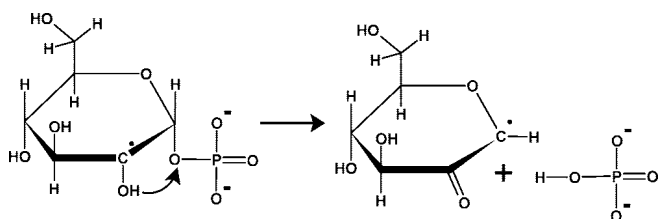


Figure 5. Possible formation mechanism of radical model R2.

angular deviations of 22 and 16° are found between the normal to the plane and the $a_{0,\text{dip}}$ eigenvectors of tensors HF1a(R2) and HF1b(R2), respectively. The H1 hydrogen atom should be oriented approximately along the bisector of the angle formed by the ring oxygen, the C1 carbon, and the C2 carbon. This direction deviates by about 34 and 25° from the $a_{+,\text{dip}}$ eigenvectors of HF1a(R2) and HF1b(R2), respectively. In conclusion, the evidence favoring model M2 proposed in Figure 4 is quite convincing and the comparison with crystal directions favors tensor HF1b(R2) over HF1a(R2).

A homolytic bond dissociation of the C1–OP ester bond automatically gives rise to a phosphoranyl-type radical in addition to a C1-centered radical. Although phosphate-centered radicals are present at RT, they have not been detected at 77 K.¹³ It is therefore more probable that radical R2 is a secondary radical species originating from a hydroxyalkyl radical precursor. Starting from a C2-centered hydroxyalkyl radical, a β -phosphate elimination process³ would directly lead to the radical structure proposed for radical R2 (M2 in Figure 4). Therefore, we suggest the formation mechanism presented in Figure 5.

4.3. Radical Species R3. At most orientations, the EIE spectrum of radical R3 is a broad doublet, arising from the α -proton hyperfine interaction reported in Table 1. At certain orientations, however, a smaller splitting, reaching up to 0.9 mT, is resolved in the EIE spectra, as demonstrated in Figure 2. Although the ENDOR signal of at least one smaller interaction was observed at some orientations, it is poorly or not resolved for most orientations and sufficient data to perform a reliable tensor analysis could not be collected. This ENDOR signal is labeled HF2(R3) and indicated in Figure 3. It could not be established whether or not this interaction is due to an exchangeable proton.

A large number of possible radical models can be envisioned if drastic geometric reorganizations such as ring opening events are considered. However, the two simplest radical models that may account for the experimental data are depicted in Figure 6: in model M3a, the sugar–phosphate linkage is broken at the glucose side, and in model M3b, a hydrogen atom at C6 is abstracted. If M3a is the correct model for R3, and assuming that the model proposed above for R2 is correct, one would expect the eigenvectors of HF1(R3) to be similar to those of HF1(R2). The data in Table 1 show that this is clearly not the case. Calculations analogous to those made above for HF1(R2) give an angle of about 60° between the $a_{0,\text{dip}}$ eigenvector of HF1(R3) and the direction perpendicular to the ring plane and an angle of about 30° between the $a_{+,\text{dip}}$ eigenvector and the bisector of the angle formed by the ring oxygen, the C1 carbon, and the C2 carbon. These values are large and suggest M3a is not a valid model.

For model M3b, the angle between the $a_{+,\text{dip}}$ eigenvector and the C₆–H_{6B} bond direction is about 26°. This indicates that the radical obtained by H_{6A} removal may be a plausible model. However, it is hard to assess how the remaining H_{6B} α -proton will reorient upon hydrogen abstraction and hence the small angular deviation could be fortuitous. M3b was suggested as a

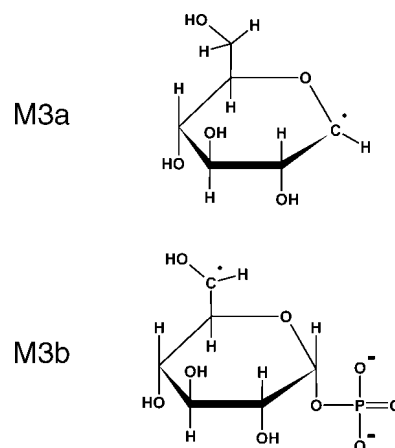


Figure 6. The chemical structure of models M3a and M3b for radical R3.

model for a radical formed and stabilized after 4 K irradiation by Locher and Box.¹² In Table 3, the three proton hyperfine coupling tensors determined by these authors are listed and compared with the R3 hyperfine coupling tensors from Table 1. The A1 tensor is quite similar to the HF1(R3) tensor in both isotropic and anisotropic hyperfine coupling values. The agreement in eigenvector directions is less good but not unreasonable considering the difference in irradiation and measurement temperatures. The A2 tensor could be accounted for by the smaller splitting observed in the EIE spectra, but the A3 hyperfine interaction originating from the HO6 hydroxy proton is not at all accommodated by the EIE spectra. Therefore, a reorientation of the hydroxy group, giving rise to a negligible isotropic component and a small anisotropic component throughout the plane perpendicular to $\langle b \rangle$ (where a number of EIE spectra were recorded), would be required for this model to be valid. Further discussions on this point are given in paper II (ref 23).

4.4. Radical Species R4. Radical R4 is characterized by three hyperfine coupling interactions, as demonstrated by the EIE spectrum shown in Figure 2, as well as by a number of EIE spectra obtained at other orientations. However, for one of the interactions (henceforth labeled HF3(R4) and indicated in Figure 3), it was not possible to obtain sufficient ENDOR data to allow for a hyperfine coupling tensor analysis, and therefore, only two hyperfine coupling tensors are presented in Table 1. HF1(R4) clearly is an α -proton hyperfine coupling. Both the isotropic (via the McConnell relation^{42,33}) and the anisotropic (via the Gordy–Bernhard relation^{43,44}) coupling values indicate that about 85% of the spin density is residing at the C _{α} carbon. HF2(R4) exhibits a typical β -proton hyperfine coupling character. The angular variation of the R4 EIE spectra in the plane perpendicular to $\langle b \rangle$, shown in Figure 7, indicates that the HF3(R4) coupling varies roughly between 1.3 and 2.2 mT in this plane, suggesting that the anisotropic part of the coupling varies at least about 25 MHz. This indicates that HF3(R4) is either an α -proton or a β -type hydroxy proton hyperfine coupling.

In Figure 8, a comparison is made between the EIE spectra obtained at nearly coincidental orientations for a nondeuterated (bottom, “H₂O spectrum”) and a deuterated sample (top, “D₂O spectrum”) by probing an ENDOR line of the HF1(R4) hyperfine interaction. The clear difference in spectrum shape indicates that the HF3(R4) interaction is indeed due to a hydroxy proton. The shape of the EIE spectrum for the deuterated sample can be explained only if incomplete deuteration is assumed. This point will be discussed further below.

TABLE 3: Hydrogen Hyperfine Tensors for a Hydroxyalkyl Radical Present after 4 K Irradiation of K2G1P Single Crystals, As Reported by Locher and Box^{12,a}

coupling	iso	aniso	eigenvectors				δ (deg)					
			a^*	b	c							
A1	-53.12	-32.10	0.983	-0.089	0.159	HF1(R3)	32.0	HF1a(R4)	51.3	HF1b(R4)	44.7	
			-0.131	0.263	0.957			28.1	44.1	86.2		
			0.69	-0.961	0.247			23.9	31.5	21.1		
A2	22.28	-7.32	0.298	0.583	-0.756			HF2(R4)	5.1			
			0.688	0.400	0.539							6.9
			10.04	-0.708	-0.292							7.4
A3	44.64	-13.25	0.645	-0.383	-0.662							
			0.194	-0.755	0.627							
			22.28	0.739	0.532							0.412

^a On the right-hand side, eigenvector directions are compared with those of tensors determined from 77 K measurements (this study, Table 1).

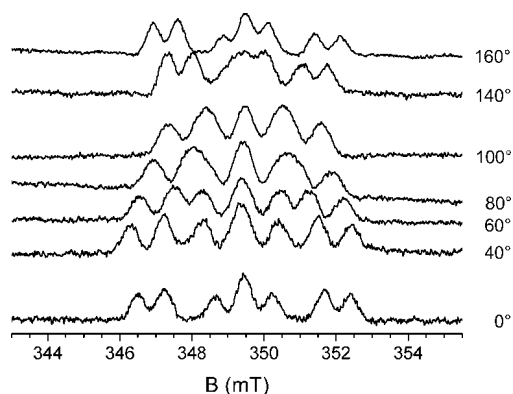


Figure 7. Angular variation of the EIE spectrum of radical R4 in the plane perpendicular to $\langle b \rangle$. The angle scale is such that $\langle a \rangle$, $\langle a^* \rangle$, $\langle c \rangle$, and $\langle c^* \rangle$ approximately correspond to 50, 70, 140, and 160°, respectively. All spectra are normalized to 9.7750 GHz.

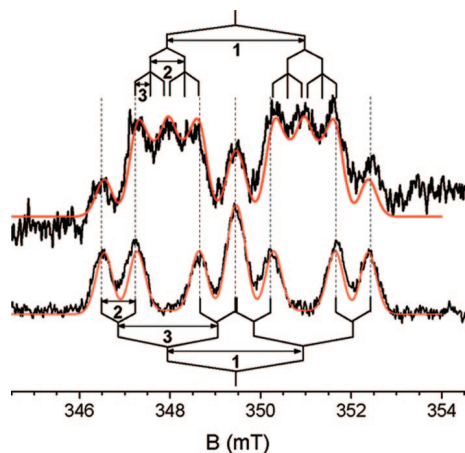


Figure 8. Experimental EIE spectrum of radical R4 in K2G1P single crystals grown from an H₂O solution (bottom, black) and from a D₂O solution (top, black). The magnetic field is oriented in the plane perpendicular to $\langle b \rangle$, approximately 20° from $\langle c \rangle$, and 40° from $\langle c^* \rangle$. The spectra are normalized to a microwave frequency of 9.7771 GHz. The numbers 1, 2, and 3 refer to hyperfine interactions HF1, HF2, and HF3, respectively. The red lines are simulations, using a line width of 0.40 mT. For other details concerning the simulation (parameters), we refer to the text.

The presence of an α -proton hyperfine coupling again severely limits the number of reasonably simple radical models, as it did for radical species R3. For R4, however, the information offered by the β -proton, which in general is expected to undergo less geometric reorganization as compared to an α -proton, can be used. As shown in Table 2, there are three $C_{\alpha} \cdots H_{\beta}$ directions that deviate less than 10° from the $b_{+,dip}$ eigenvector direction

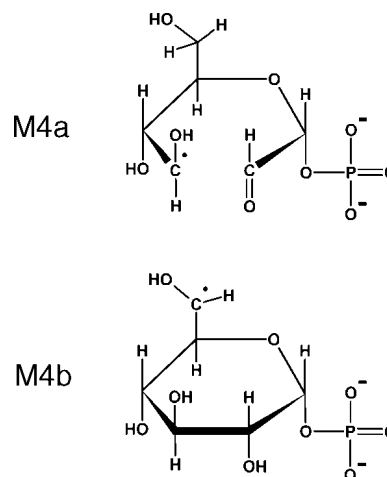


Figure 9. The chemical structure of models M4a and M4b for radical R4. Model M4b is the same as model M3b (Figure 6).

of HF2(R4), yielding C3, C4, and C5 as possible radical centers. For all three possibilities, an α -proton is present such that the $C_{\alpha}-H_{\alpha}$ is directed roughly along the $a_{+,dip}$ eigenvector of HF1(R4) (Table 2). The additional requirement of the presence of a β -type hydroxy proton then yields the two possible models depicted in Figure 9. Model M4a could be formed through spontaneous electronic reorganization from the O2-centered alkoxy radical, present at 4 K (see the Introduction). As model M4a has a broken ring structure, substantial geometric changes may occur and further analysis through comparison with pristine crystal directions is not warranted. Model M4b is the hydroxyalkyl radical suggested to be present at 4 K by Locher and Box¹² (Table 3), which was also found to be a possible model for radical R3 (model M3b). The A2 hyperfine coupling tensor is in good agreement with HF2(R4), both in principal values and eigenvector directions. This already strongly suggests that the R4 radical is very similar to the species detected at 4 K. Hyperfine tensors A1 and HF1(R4) are similar but show larger discrepancies. Again, such differences may be due to the differences in irradiation and measuring temperatures, which may lead to slight geometric differences in the radical structure. The anisotropy in the rot $\langle b \rangle$ plane predicted by the A3 tensor amounts to about 26 MHz, in very good agreement with the findings from the EIE angular variations and the isotropic component of A3 is also reconcilable with the findings from the EIE spectra. Nevertheless, the EIE angular variation of Figure 7 is reproduced poorly when the A3 tensor as reported by Locher and Box¹² (Table 3) is employed (Supporting Information Figure S4). However, there is a Schonland ambiguity (see above and refs 30 and 31) for the A3 tensor, and

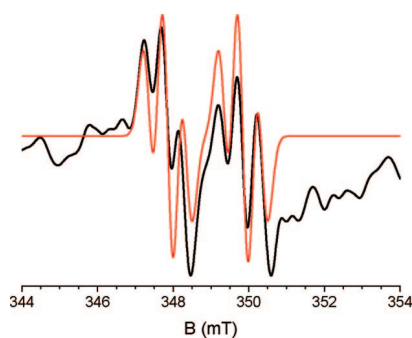


Figure 10. Experimental EPR spectrum of Figure 2 (black) and simulated EPR spectrum of radical R2 (red), using the hyperfine tensors listed in Table 1 and a line width of 0.40 mT. The spectra are normalized to a microwave frequency of 9.7750 GHz.

therefore, the seven other tensors, obtained by varying the sign of the off-diagonal elements of A3 in the reference frame, should also be considered. The EIE angular variation is in fact reproduced quite well when employing the tensor obtained by changing the signs of A_{312} ($=A_{321}$) and A_{313} ($=A_{331}$) tensor elements in the reference frame, as illustrated in Supporting Information Figure S4. As these changes of sign correspond to performing an $a \rightarrow -a$ operation on the principal directions, while leaving the principal values of A3 unaltered, this tensor is denoted A3[$-a$]. In paper II (ref 23), DFT calculations provide additional convincing arguments that A3[$-a$] is the correct tensor shape.

To interpret the spectrum shape of the “D₂O spectrum” in Figure 8, the “H₂O spectrum” was first reproduced as accurately as possible. Since HF1(R4) and HF2(R4) were determined in the present experiments, only adjustments of the A3[$-a$] coupling are justifiable. The best agreement (Figure 8, bottom red line) is found when an effective coupling size of 60 MHz is assumed for A3, which is about 9 MHz larger than the value the A3[$-a$] tensor yields for this orientation (and 25 MHz larger than the “original” A3 tensor yields). Using these parameters, the “D₂O spectrum” can be reproduced quite satisfactorily if a deuteration rate of about 60% is assumed (Figure 8, top red line). This is about 30% lower than may be expected (cf. section 2), which could be due to either differences in relaxation rates between the radical species in the deuterated and the nondeuterated crystal or an isotope effect on the radical formation of species R4.

4.5. Relative Abundance of the Different Radical Species.

The EIE spectra of radicals R1–R3 in Figure 2 can be accurately reproduced using the tensors in Table 1, treating the g values and linewidths as variables. As illustrated above, also for R4, the EIE spectrum can be reproduced satisfactorily at this orientation when increasing the isotropic component of A3 by 9 MHz. Using these parameters to simulate the (composite) EPR spectrum, an indication of the relative abundances of the different radical species can be obtained. Figure 10 shows the experimental EPR spectrum of Figure 2, together with a simulation of the R2 EPR spectrum, using a line width of 0.40 mT. The agreement is good, but apart from the complete absence of the outer features of the EPR spectrum in the simulation, there are also some minor discrepancies in the central part. Manually mixing in various small concentrations of R1, R3, and R4 did not noticeably improve the fitting. In fact, simulations indicate that even a relative abundance of 5% for any of these species would give rise to features not observed in the EPR spectrum. As no reliable lower limit can be given, we merely conclude that these species are far less abundant than

R2. The major part of the remaining discrepancies should therefore be attributed to one or more other radical species, most probably those also giving rise to the outer EPR signals (R6 and R7, see above and the Supporting Information).

5. Conclusions

At least seven different carbon-centered radical species are formed in K2G1P single crystals upon irradiation at 77 K. The dominant radical is identified as a C1-centered species, formed by a net scission of the glucose–phosphate bond and concerted formation of a carbonyl group at C2. Two of the minority radicals are most likely C3- and C6-centered, formed by net hydrogen abstractions at these positions, but some uncertainty about these interpretations from the experimental data alone remains. It could not be determined in the current work which radical species acts as a precursor for the phosphoryl radicals observed at 280 K. In paper II (ref 23), DFT calculations confirm the validity of the proposed radical structures and provide insight in their precise conformation and possible formation mechanisms in addition to providing elementary insight into the radiation chemistry of sugars.

Acknowledgment. The authors H.D.C. (Research Assistant) and E.P. (Postdoctoral Fellow) wish to thank the Fund for Scientific Research - Flanders (FWO) for financial support. The European Cooperation in the field of Scientific and Technical Research (COST action p15) is also acknowledged for financial support.

Supporting Information Available: Coordinates of 35 atoms in K2G1P single crystals, as reported by Sugawara and Iwasaki.²⁴ X-band angular variation of the ENDOR transitions in K2G1P single crystals measured at 77 K after *in situ* X-irradiation at this temperature for all hyperfine interactions listed in Table 1. EIE spectra of three other radicals (R5, R6, and R7) at the orientation of Figure 2. ENDOR spectra of Figure 3, where some ENDOR lines have been labeled additionally and are assigned to radicals R5–R7. Angular variation of the EIE spectrum of radical R4 in the plane perpendicular to $\langle b \rangle$ (same as Figure 7) and simulation of these spectra using tensors HF1(R4) and HF2(R4) (Table 1) and tensor A3 (Table 3) or tensor A3[$-a$] (see section 4.4 for details). This material is available free of charge via the Internet at <http://pubs.acs.org>.

References and Notes

- Bernhard, W. A.; Close, D. M. In *DNA Damage Dictates the Biological Consequences of Ionizing Irradiation: The Chemical Pathways In Charged Particle and Photon Interactions with Matter: Chemical, Physicochemical, and Biological Consequences with Applications*; Mozumber, A., Hatano, Y., Eds.; Marcel Dekker: New York, 2003; pp 431–470.
- Becker, D.; Adhikary, A.; Sevilla, M. D. In *The Role of Charge and Spin Migration in DNA Radiation Damage In Charge Migration in DNA Physics, Chemistry and Biology Perspectives*; Chakraborty, T.; Springer-Verlag: Berlin, Heidelberg, 2007; pp 139–175.
- von Sonntag, C. *The Chemical Basis of Radiation Biology*; Taylor and Francis: London, 1987.
- Boudaïffa, B.; Cloutier, P.; Hunting, D.; Huels, M. A.; Sanche, L. *Science* **2000**, *287*, 1658–1660.
- Simons, J. *Adv. Chem. Res.* **2006**, *39*, 772–779.
- Kumar, A.; Sevilla, M. D. In *Radiation Induced Molecular Phenomena in Nucleic Acids: A Comprehensive Theoretical and Experimental Analysis*; Shukla, M. K., Leszczynski, J.; Springer-Verlag: Berlin, Heidelberg, New York, 2008.
- Becker, D.; Bryant-Friedrich, A.; Trzasko, C.; Sevilla, M. D. *Radiat. Res.* **2003**, *160*, 174–185.
- Ezra, F. S.; Bernhard, W. A. *J. Chem. Phys.* **1973**, *59*, 3543–3549.
- Fouse, G. W.; Bernhard, W. A. *J. Chem. Phys.* **1979**, *70*, 1667–1670.

- (10) Baine, T. J.; Sagstuen, E. *Radiat. Res.* **1998**, *150*, 148–158.
- (11) Nelson, D.; Symons, M. C. R. *J. Chem. Soc., Perkin Trans. 2* **1977**, 286–293.
- (12) Locher, S. E.; Box, H. C. *J. Chem. Phys.* **1980**, *72*, 828–832.
- (13) Sanderud, A.; Sagstuen, E. *J. Chem. Soc., Faraday Trans.* **1996**, *92*, 995–999.
- (14) Bungum, B.; Hole, E. O.; Sagstuen, E.; Lindgren, M. *Radiat. Res.* **1994**, *193*, 194–202.
- (15) Sagstuen, E.; Lindgren, M.; Lund, A. *Radiat. Res.* **1991**, *128*, 235–242.
- (16) Madden, K. P.; Bernhard, W. A. *J. Phys. Chem.* **1980**, *84*, 1712–1717.
- (17) Becker, D.; Bryant-Friedrich, A.; Trzasko, C.; Sevilla, M. D. *Radiat. Res.* **2003**, *160*, 174–185.
- (18) Beevers, C. A.; Maconochie, G. H. *Acta Crystallogr.* **1965**, *18*, 232–236.
- (19) Narendra, N.; Viswamitra, M. A. *Curr. Sci.* **1984**, *53*, 1018–1020.
- (20) Bungum, B. MSc Thesis, Dept. Physics, University of Oslo, 1993.
- (21) Nelson, D. J.; Symons, M. C. R.; Wyatt, J. L. *J. Chem. Soc., Faraday Trans.* **1993**, *89*, 1955–1958.
- (22) The authors of ref 21 mistakenly reported these results to be obtained on the disodium salt. A correction was made in ref 13.
- (23) Pauwels, E.; De Cooman, H.; Vanhaelewyn, G.; Sagstuen, E.; Callens, F.; Waroquier, M. *J. Phys. Chem B* **2008**, *112*, 15054–15063.
- (24) Sugawara, Y.; Iwasaki, H. *Acta Crystallogr.* **1984**, *C40*, 389–393.
- (25) Ohman, K. T.; Sanderud, A.; Hole, E. I.; Sagstuen, E. *J. Phys. Chem. A* **2006**, *110*, 9585–9596.
- (26) Nelson, W. H. *J. Magn. Reson.* **1980**, *38*, 71–78.
- (27) Sørnes, A. R.; Sagstuen, E.; Lund, A. *J. Phys. Chem.* **1995**, *99*, 16867–16876.
- (28) De Cooman, H.; Pauwels, E.; Vrielinck, H.; Dimitrova, A.; Yordanov, N.; Sagstuen, E.; Waroquier, M.; Callens, F. *Spectrochim. Acta, Part A* **2008**, *69*, 1372–1383.
- (29) Stoll, S.; Schweiger, A. *J. Magn. Reson.* **2006**, *178* (1), 42–55.
- (30) Schonland, D. S. *Proc. Phys. Soc. London* **1959**, *73* (473), 788–792.
- (31) Vrielinck, H.; De Cooman, H.; Tarpan, M. A.; Sagstuen, E.; Waroquier, M.; Callens, F. *J. Magn. Reson.*, doi: 10.1016/j.jmr.2008.09.017.
- (32) Heller, C.; McConnell, H. M. *J. Chem. Phys.* **1960**, *32*, 1535.
- (33) Bernhard, W. A. *Adv. Radiat. Biol.* **1981**, *9*, 199.
- (34) Madden, K. P.; Bernhard, W. A. *J. Phys. Chem.* **1979**, *83* (20), 2643.
- (35) Pauwels, E.; Van Speybroeck, V.; Callens, F.; Waroquier, M. *Int. J. Quantum Chem.* **2004**, *99* (2), 102–108.
- (36) Pauwels, E.; Van Speybroeck, V.; Waroquier, M. *Spectrochim. Acta, Part A* **2006**, *63* (4), 795–801.
- (37) Pauwels, E.; Van Speybroeck, V.; Waroquier, M. *J. Phys. Chem. A* **2006**, *110* (20), 6504–6513.
- (38) Vanhaelewyn, G.; Jansen, B.; Pauwels, E.; Sagstuen, E.; Waroquier, M.; Callens, F. *J. Phys. Chem. A* **2004**, *108* (16), 3308–3314.
- (39) Vanhaelewyn, G.C.A.M.; Pauwels, E.; Callens, F. J.; Waroquier, M.; Sagstuen, E.; Matthys, P. F. A. E. *J. Phys. Chem.* **2006**, *110* (6), 2147.
- (40) Tarpan, M.; Sagstuen, E.; Pauwels, E.; Vrielinck, H.; Waroquier, M.; Callens, F. *J. Phys. Chem. A* **2008**, *112*, 3898.
- (41) De Cooman, H.; Pauwels, E.; Vrielinck, H.; Sagstuen, E.; Callens, F.; Waroquier, M. *J. Phys. Chem. B* **2008**, *112*, 7298–7307.
- (42) McConnell, H. M.; Chesnut, D. B. *J. Chem. Phys.* **1958**, *28*, 107–117.
- (43) Erling, P. A.; Nelson, W. H. *J. Phys. Chem. A* **2004**, *108*, 7591–7595.
- (44) Bernhard, W. A. *J. Chem. Phys.* **1984**, *81*, 5928–5935.

JP804290E

7.5 Paper V

Radiation-induced radicals in glucose-1-phosphate. II. DFT analysis of structures and possible formation mechanisms

E. Pauwels, H. De Cooman, G. Vanhaelewyn, E. Sagstuen, F. Callens
and M. Waroquier

Journal of Physical Chemistry B, 2008, 112, 15054-15063

Copyright 2008 by the American Chemical Society.

Radiation-Induced Radicals in Glucose-1-phosphate. II. DFT Analysis of Structures and Possible Formation Mechanisms

Ewald Pauwels,^{*,†} Hendrik De Cooman,^{†,‡} Gauthier Vanhaelewyn,[‡] Einar Sagstuen,[§] Freddy Callens,[‡] and Michel Waroquier[†]

Center for Molecular Modeling, Ghent University, Proeftuinstraat 86, B-9000 Gent, Belgium, Department of Solid State Sciences, Ghent University, Krijgslaan 281-S1, B-9000 Gent, Belgium, and Department of Physics, University of Oslo, P.O. Box 1048 Blindern, N-0316 Oslo, Norway

Received: May 14, 2008; Revised Manuscript Received: September 11, 2008

Four radiation-induced carbon-centered radicals in dipotassium glucose-1-phosphate dihydrate single crystals are examined with DFT methods, consistently relying on a periodic computational scheme. Starting from a set of plausible radical models, EPR hyperfine coupling tensors are calculated for optimized structures and compared with data obtained from EPR/ENDOR measurements, which are described in part I of this work. In this way, an independent structural identification is made of all the radicals that were observed in the experiments (R1–R4) and tentative reaction schemes are proposed. Also, the first strong evidence for conformational freedom in sugar radicals is established: two species are found to have the same chemical composition but different conformations and consequently different hyperfine coupling tensors. Analysis of the calculated energies for all model compounds suggests that the radiation chemistry of sugars, in general, is kinetically and not necessarily thermodynamically controlled.

1. Introduction

Strand breaks are important consequences of exposing DNA to ionizing radiation. They find their origin in damage to the sugar–phosphate backbone, resulting in a fissure of this linkage.¹ Radicals located on the 2-deoxyribose subunit are key intermediates in this process. Due to the size and complexity of the DNA structure, investigations of the radiation chemistry associated with strand breaks have often relied on model systems containing the sugar–phosphate ester bond. One such system is glucose-1-phosphate.

Several studies have been performed on irradiated crystals of the dipotassium salt of D-glucose-1-phosphate dihydrate (abbreviated K2G1P), whose structure is shown in Figure 1. Using electron paramagnetic resonance (EPR) and related techniques,² attempts were made to identify the nature of the radiation-induced radicals and to expose the associated processes. Locher and Box³ found three alkoxy radicals and a C6-centered hydroxy alkyl radical at 4.2 K. At room temperature, Bungum and co-workers⁴ observed phosphoryl radicals ($\bullet\text{PO}_3^{2-}$), clearly indicating scission of the glucose-1-phosphate bond. In a more elaborate study on K2G1P powders,⁵ it was proposed that these species are only formed at temperatures higher than 77 K, with sugar-centered radicals as precursors.

In paper I of this series of two papers,⁶ an EPR and ENDOR (electron nuclear double resonance) study was made of these sugar radicals, in order to further clarify their role in the formation of phosphoryl radicals and in the process of glucose-1-phosphate cleavage in general. Measurements of *in situ* X-irradiated K2G1P at 77 K indicated that at least seven different carbon-centered radical species are present, four of which (R1–R4) could be well characterized in terms of proton

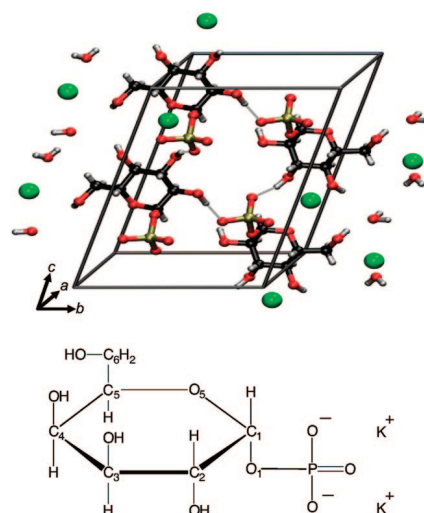


Figure 1. Illustration of the $(ab2c)$ supercell that is used in all periodic calculations. Grey dashed lines illustrate some of the hydrogen bonds. The atomic numbering scheme is indicated in the chemical structure of K2G1P. All hydrogen and oxygen atoms are labeled according to the carbon to which they are bound. Hydroxy hydrogens are labeled as HOx.

hyperfine coupling tensors. An overview of the hyperfine data for these species is presented in Table 1. On the basis of an analysis of these tensors, likely radical structures were proposed:

- R1: a C3-centered structure, obtained by net hydrogen abstraction at this site
- R2: a C1-centered radical, obtained by cleavage of the sugar–phosphate bond, with a carbonyl group on C2
- R3: a C6-centered structure, obtained by net hydrogen abstraction at this site
- R4: also a C6-centered structure but with a conformation different from R3

* To whom all correspondence should be addressed. Fax: 32 9 264 66 97. E-mail: ewald.pauwels@UGent.be.

[†] Center for Molecular Modeling, Ghent University.

[‡] Department of Solid State Sciences, Ghent University.

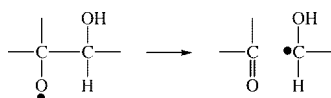
[§] University of Oslo.

TABLE 1: Summary of Experimental Hyperfine Coupling Tensors (See ref 6 for Details)^a

radical	tensor	A_{iso}	T_{aniso}	Principal directions			
R1	HF1	79.24	-3.86	0.546	-0.365	-0.754	
			-3.30	0.626	0.776	0.077	
			7.16	0.557	-0.514	0.653	
	HF2	71.71	-4.81	0.062	0.612	-0.788	
			-2.87	0.394	0.711	0.583	
			7.68	0.917	-0.346	-0.197	
R2	HF1a	-41.55	-22.97	0.705	-0.298	-0.643	
			0.63	0.238	0.954	-0.182	
			22.34	0.668	-0.024	0.744	
	HF1b	-41.53	-21.45	0.744	0.134	-0.654	
			-2.41	0.046	0.967	0.251	
			23.86	0.666	-0.216	0.714	
	HF2	15.78	-2.54	0.651	-0.754	0.087	
			-1.78	0.596	0.436	-0.674	
			4.31	0.471	0.491	0.733	
	HF3	10.16	-3.40	0.333	-0.700	0.632	
			-2.35	0.430	-0.484	-0.762	
			5.75	0.839	0.525	0.140	
R3	HF1	-50.97	-31.07	0.928	0.078	-0.363	
			2.33	0.285	0.479	0.830	
			28.75	0.239	-0.874	0.423	
R4	HF1a	-61.22	0-25	0.750	0.104	-0.653	
			0.17	0.526	0.504	0.685	
			29.18	0.400	-0.857	0.323	
	HF1b	-61.01	-32.89	0.697	0.285	-0.658	
			6.32	0.704	-0.099	0.703	
			26.57	0.135	-0.953	-0.270	
	HF2	24.03	-6.36	0.375	0.540	-0.753	
			-3.58	0.627	0.451	0.636	
			9.94	0.683	-0.711	-0.169	
	HF3		36-62				

^a A_{iso} indicates the isotropic coupling, T_{aniso} the anisotropic hyperfine components (both in MHz). The principal directions are given with respect to the $\langle a^*bc \rangle$ axes reference frame. For hyperfine interactions HF2(R3) and HF3(R4), an approximate range is given in which this coupling is observed in the plane perpendicular to $\langle b \rangle$.

SCHEME 1



In the current paper, a theoretical study is made of these four carbon-centered radicals, relying on density functional theory (DFT) calculations.⁷ In recent years, such calculations often complement EPR experiments,⁸⁻¹⁰ as they allow the explicit optimization of a radical structure and the calculation of its EPR properties,¹¹ which can then serve to verify the experimental models and assumptions. In paper I, convincing evidence was often found for particular model structures of the measured radicals. Although this information is obviously used in this part, the corroboration or verification of model structures for the detected radical is performed in an as much as possible unbiased way. Furthermore, the calculations provide valuable information on the precise conformation, the formation mechanism, and the stabilities of the radical defects.

2. Computational Details

All calculations on K2G1P radicals have been conducted in a periodic approach. This method exploits the translational symmetry of the crystal by imposing periodic boundary conditions and, as such, offers a natural and efficient description of the solid-state environment of a radical. However, the mono-

clinic unit cell of K2G1P (as determined by X-ray diffraction in ref 12) contains only two glucose-1-phosphate molecules, along with four potassium ions and four water molecules. To avoid direct interaction of a radical with its periodic image, this unit cell was doubled along $\langle c \rangle$, yielding a supercell with dimensions $\langle a \rangle = 10.458 \text{ \AA}$, $\langle b \rangle = 9.027 \text{ \AA}$, $\langle 2c \rangle = 15.064 \text{ \AA}$, and $\beta = 110.39^\circ$. The supercell is illustrated in Figure 1. As a starting point for the calculations, one of the four glucose-1-phosphate molecules was transformed into a tentative radical model, e.g., by removing a hydrogen atom.

The resulting structures were optimized within the periodic framework using the CPMD software package,¹³ with constant cell dimensions but without constraints on the individual atoms. The gradient-corrected BLYP density functional¹⁴ was used with a plane wave basis set (cutoff 120.0 Ry) and norm-conserving pseudopotentials of Goedecker and co-workers.¹⁵

Subsequently, hyperfine coupling tensors were determined for the optimized periodic structures using the method of Van de Walle and Blochl¹⁶ as implemented in CPMD. For these calculations, Troullier–Martins norm-conserving pseudopotentials¹⁷ were used with a cutoff value of 100.0 Ry in combination with the BLYP functional.¹⁴ Because this scheme relies on pseudopotentials, the electron density near the atomic core regions has to be reconstructed with the aid of atomic all-electron functions. The reliability of this method has been established for the determination of hyperfine tensors in crystalline biomolecules.¹⁸

Although similar supercell sizes were successfully applied in other studies of radiation-induced radicals in sugar crystals,^{19,20} the validity of the $\langle ab2c \rangle$ approach for K2G1P was further ascertained. For one radical model, the procedure outlined above was applied within a $\langle 2ab2c \rangle$ supercell approach and the results were compared with those of $\langle ab2c \rangle$ calculations. Optimized radical geometries and calculated EPR properties (see the Supporting Information) proved virtually identical, validating the use of the smaller supercell.

3. Results and Discussion

3.1. Initial Selection of Radical Models. From the analysis of the EPR/ENDOR experiments (paper I), a number of radical models were proposed. However, to ensure an (as much as possible) unbiased structural identification in this work, several other models were also examined. For the sake of clarity, they are divided into two classes of tentative structures. Class I comprises all models that give rise to at least one α -type hyperfine coupling. Class II contains all of the models without such an interaction.

The most straightforward modifications to the K2G1P structure are simple hydrogen atom or hydroxy group abstractions. These models are labeled H(X) or HO(X), where X indicates the atom at which abstraction has occurred (see Figure 1 for atomic numbering). Altogether, 10 H- or HO-abstraction models were taken into consideration. Models H(C6), HO(C2), HO(C3), HO(C4), and HO(C6) are included in class I. The other five models—H(C1), H(C2), H(C3), H(C4), and H(C5)—are included in class II and are in fact the only models without an α -type hyperfine interaction in the entire study.

These relatively simple H- or HO-abstraction models do not include the possibility that the pyranose ring of glucose-1-phosphate ruptures. Yet, in a recent paper on the radiation-induced radicals in β -D-fructose,⁹ it was found that such processes do occur at low temperatures. The suggested mechanism for this species is an electronic rearrangement of an alkoxy radical precursor, generating a carbonyl functional group

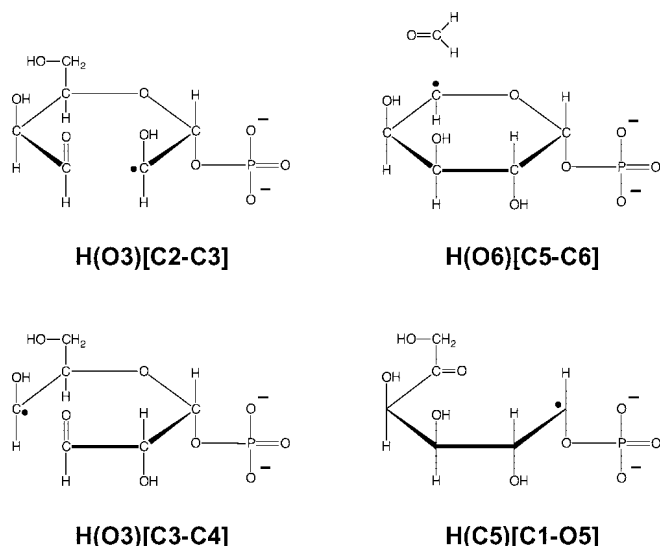


Figure 2. Chemical structure of radical models that involve more severe changes to the K2G1P structure.

and a hydroxy alkyl radical (Scheme 1). Applying a similar reaction scheme to the K2G1P structure, the four alkoxy radicals—H(O2), H(O3), H(O4), and H(O6)—can in principle lead to seven radical structures. However, geometry optimization of initial structures for these models established that four of them do not even constitute (local) minima and spontaneously revert to the corresponding alkoxy radical via the reverse of Scheme 1. The structures of the remaining three models—H(O3)-[C2–C3], H(O3)[C3–C4], and H(O6)[C5–C6]—are shown in Figure 2 and labeled according to the broken bond. In the H(O6)[C5–C6] model, the pyranose ring is not actually broken, but a formaldehyde molecule is split off. Furthermore, the opening structure of H(O3)[C2–C3] is only maintained when the HO and H substituents of C2 are rotated by $\sim 180^\circ$. These structures are included in class I, as is model H(C5)[C1–O5] (see Figure 2). This structure was suggested by Bungum and co-workers⁴ as an intermediate step in the formation of a phosphoryl radical from the H(C5) radical.

Using the computational procedures as described in section 2, optimum structures were determined for all models in both classes, after which EPR properties were calculated. For each calculated tensor, allowed symmetry operations (i.e., inversion of eigenvectors and 180° rotation of the tensor about the symmetry axis $\langle b \rangle$) were performed to get the best possible agreement with experiment. It should be noted that the removed fragment was initially not taken into consideration during any of these calculations. For the sake of brevity, tables contain only the calculated EPR properties of models that are relevant for the discussed radicals. Results for all other models are given in the Supporting Information.

3.2. Models for Radical R1. It was determined in paper I that this particular radical displays two β -type hyperfine interactions and no α -type couplings. Only the models of class II fit this criterion. Comparison between the calculated and measured hyperfine tensors shows that model H(C3) is in satisfactory agreement whereas all other models can be excluded as viable candidates (see the Supporting Information). This structure was already proposed in paper I and labeled M1. In Table 2, a comparison is made with the experimental data of R1. The calculated principal directions of H2 in model H(C3) are in very good correspondence with those of HF1(R1), with angular deviations no larger than 12° . Similar agreement for H4 and interaction HF2(R1) is only obtained for the eigenvector

TABLE 2: Comparison of Calculated EPR Properties for Model H(C3) with Experimental Data for Radical R1^a

		R1	
		HF1	HF2
A_{iso}		79.2	71.7
	T_{aniso}	-3.9	-4.8
		-3.3	-2.9
	Principal directions	7.2	7.7

H(C3)							
H2	89.7	-5.1	0.530	-0.344	-0.775	2	12
		-1.8	0.731	0.648	0.213		
		6.8	-0.429	0.680	-0.595		
H4	86.4	-5.4	-0.085	-0.177	-0.981	29	29
		-1.9	0.496	-0.861	0.112		
		7.4	0.864	0.477	-0.161		
HO3	54.7	-13.0	-0.844	-0.431	-0.320	8	8
		-8.9	0.204	-0.809	0.552		
		21.8	0.496	-0.401	-0.770		

H(C3) migrated proton							
H2	90.1	-4.7	0.483	-0.407	-0.775	5	14
		-1.7	0.780	0.602	0.170		
		6.5	-0.397	0.687	-0.609		
H4	89.8	-5.4	-0.043	-0.174	-0.984	28	28
		-1.7	0.491	-0.861	0.131		
		7.1	0.870	0.477	-0.122		
HO3	-5.5	-9.9	0.065	0.482	0.874	9	9
		-6.3	-0.393	0.817	-0.421		
		16.2	-0.917	-0.317	0.243		
H3abs	1.4	-6.0	0.945	-0.015	0.328		
		-3.6	-0.191	-0.836	0.514		
		9.6	-0.267	0.548	0.793		

^a Isotropic (A_{iso}) and anisotropic couplings (T_{aniso}) are in MHz, and principal directions are given with respect to the $\langle a^*bc \rangle$ axes reference frame. Isotropic and anisotropic couplings for the HF1 and HF2 tensors of R1 are recalled at the top of the table. The last two columns (in italics) specify the angle between the corresponding measured and calculated eigenvectors in degrees. The lower the angle, the better the concurrence of the directions.

associated with the maximum anisotropic component (8°). The other predicted eigenvectors deviate by about 30° from their experimental counterparts. This effect has been noticed earlier^{21–23} and can be attributed to the fact that these directions are extremely sensitive to even slight shifts in the unpaired electron density. The isotropic couplings for both H2 and H4 are somewhat overestimated but the agreement between calculation and experiment up to this point is of sufficient quality to conclude that model H(C3) is an attractive model for radical R1. The calculations independently corroborate the structural identification that was made in paper I.

However, the calculations also predict a substantial isotropic coupling of 55 MHz for the hydroxy proton HO3. A coupling of that magnitude would have been observed in both ENDOR and EIE (ENDOR-induced EPR), but this was not the case. The magnitude of the HO3 coupling is determined by the orientation of the hydroxy group with respect to the lone electron orbital (LEO) on C3. In the optimized structure of model H(C3), the HO3–O3–C3–C4 torsion angle is about 120° , as shown in the leftmost Newman projection of Figure 3. The O3–HO3 bond is virtually parallel to the LEO, resulting in a close to maximal coupling. The occurrence of other (local) minima on the potential energy surface for rotation about the O3–C3 bond is explored in Figure 3. The HO3–O3–C3–C4 torsion angle is varied over 360° in 10° steps, and at each point, the structure of the entire periodic supercell is optimized while only constraining the torsion angle. Two minima can be discerned in the plot: the global minimum of model H(C3) at about 120° and a shallow, local minimum at 280° that is 60 kJ/mol less

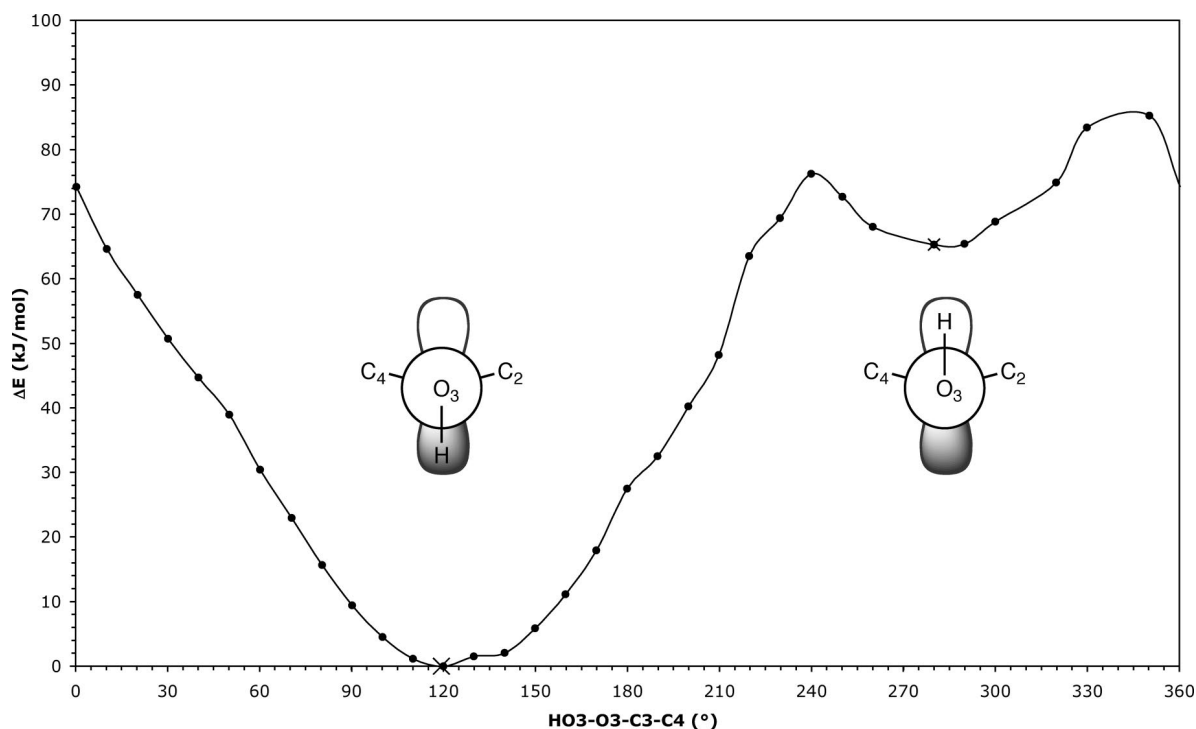


Figure 3. Cross section of the potential energy surface for hydroxy group rotation about the O3–C3 bond. Energy differences (in kJ/mol) are reported with respect to the minimum at about 120° (absolute energy = $-1127.212\ 567$ au). Circles indicate results from constrained geometry optimizations, whereas crosses refer to the results of unconstrained geometry optimizations. Newman projections illustrate the local conformation of the HO3–O3 hydroxy group at the two minima.

stable. Aside from energetic considerations, the hydroxy hyperfine coupling will not disappear in this second conformation, since the HO3–O3 axis is again oriented parallel to the LEO (Figure 3). This is confirmed by calculations at this point (included in the Supporting Information).

Usually, hydroxy alkyl type radicals such as H(C3) are considered to be oxidative radiation damage products. If so, their formation involves at least two steps: (1) ionization, giving rise to a transient cationic radical species, followed by (2) deprotonation. For model H(C3), it can be assumed that proton H3 is released from a radical cation state to obtain the radical. Given that each K2G1P molecule contains a 2-fold negatively charged phosphate group, it is likely that the proton will migrate to such a site where it will partly compensate the charge. Inspection of the immediate crystalline environment of H3 shows that the nearest phosphate group belongs to a neighboring molecule and is actually hydrogen bonded to the HO3–O3 hydroxy fragment of the radical, as illustrated in Figure 4. To examine the effect of proton migration on the radical structure, H3 was transferred to this phosphate group (instead of removed altogether) and the entire supercell was reoptimized with a total charge of +1. This resulted in a reorganization of the original hydrogen-bonding scheme. After optimization, the torsion angle HO3–O3–C3–C4 assumes a value of 192° and the hyperfine coupling of the hydroxy proton reduces significantly to -5.5 MHz (Table 2). The hydroxy coupling is thus sufficiently reduced to be consistent with the observations from EIE measurements: a strong broadening of the triplet lines, accommodating an extra coupling up to 0.5 mT (≈ 14 MHz). Moreover, the maximum broadening of the spectral lines in the experimental EIE angular variation (in the plane perpendicular to $\langle b \rangle$) occurs at an orientation along which the calculated HO3 coupling is also maximal. The migrated proton gives rise to an appreciable anisotropic component in the calculations, marked H3abs in Table 2. The additional line broadening that this

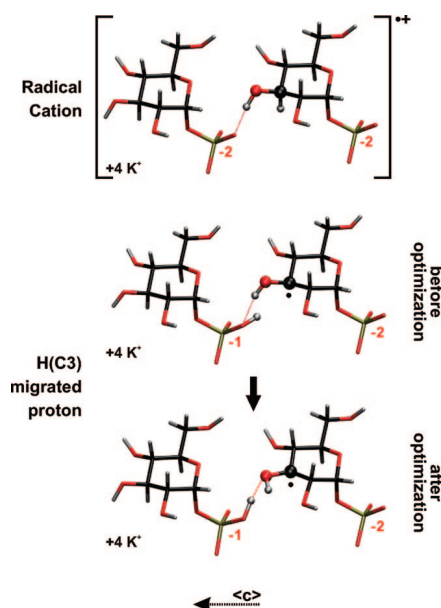


Figure 4. Tentative reaction scheme for generation of the H(C3) radical as a result of oxidative radiation damage. C3, O3, H3, and HO3 are represented as spheres.

predicted coupling would cause is, however, too small to be apparent in the EIE spectra, and is in that respect also consistent with the experimental data.

Summarizing, model H(C3) fully accounts for the EPR properties of radical R1, provided that the abstracted H3 proton migrates to the nearby phosphate group. Geometry optimization attests that this structure corresponds to a minimum, even though it is 23 kJ/mol less stable than the radical cation (which has an absolute energy of $-1127.924\ 680$ au). However, the reliability of this cation energy calculation may be questioned. Optimization of this species results in a structure that is still comparable

TABLE 3: Comparison of Measured Hyperfine Coupling Tensors of Radicals R3 and R4 and Calculated Tensors of Models H(C6) and H(C6)-2nd^a

		A_{iso}		T_{aniso}		Principal directions		R3		R4			LB	
								HF1	HF1a	HF1b	HF2	A3	A3[-a]	
								-51.0	-61.2	-61.0	24.0	44.6	44.6	
								-31.1	-29.4	-32.9	-6.4	-13.3	-13.3	
								2.3	0.2	6.3	-3.6	-9.0	-9.0	
								28.8	29.2	26.6	9.9	22.3	22.3	
H(C6)														
H1	6.8	-1.9	0.015	0.858	-0.513									
		-0.2	-0.243	0.501	0.831									
		2.1	0.970	0.113	0.216									
H5	32.3	-6.7	0.206	-0.470	-0.858						12			
		-3.2	0.739	-0.501	0.451							13		
		9.9	0.642	0.727	-0.244							5		
H6	-51.2	-36.7	0.702	0.081	-0.708			24	4	21				
		0.0	0.594	0.483	0.644			21	5	23				
		36.7	0.394	-0.872	0.291			12	2	31				
HO6	52.4	-13.0	0.916	0.290	0.277							73	12	
		-8.7	0.090	-0.821	0.564							8	11	
		21.6	-0.391	0.491	0.778							73	6	
H(C6)-2nd														
H1	1.7	-1.5	-0.003	0.904	-0.427									
		-0.4	-0.163	0.421	0.892									
		1.9	0.987	0.072	0.146									
H5	1.3	-5.4	0.704	-0.487	0.517							82		
		-4.9	-0.302	0.454	0.839							82		
		10.4	0.643	0.746	-0.172							3		
H6	-40.9	-34.7	-0.948	-0.228	0.224			12	28	42				
		-0.6	0.179	0.203	0.963			19	31	35				
		35.2	0.265	-0.952	0.151			16	14	24				
HO6	15.5	-13.0	-0.287	-0.423	0.860							24	24	
		-8.7	0.218	0.845	0.488							10	10	
		21.7	0.933	-0.327	0.150							22	22	

^a Comparison is also made with the experimental hyperfine coupling tensor for the hydroxy proton (marked LB), as determined by Locher and Box.³ A_{iso} indicates the isotropic coupling, and T_{aniso} indicates the anisotropic hyperfine components (both in MHz). Principal directions are given with respect to the $\langle a^*bc \rangle$ axes reference frame. The numbers in italics are the angular deviations (in degrees) between calculated and measured eigenvectors.

to the undamaged crystal, in which the unpaired spin density is delocalized over large parts of the periodic structure. This is an unphysical, though stable representation and probably results from the use of a negative background charge in the periodic scheme to counter the net positive charge of the supercell in these calculations.²⁴ Migration of the H3 proton destroys the symmetric character and resolutely localizes the unpaired electron on C3. Similar observations have been made in another study.³³

3.3. Models for Radical R4. Since radical R4 contains an α -type hyperfine interaction, only the models of class I need to be considered. Two significantly different forms of this α -tensor (HF1a and HF1b, both included in Table 1) fit the data points of the measurements equally well (see paper I for further details). Therefore, comparison is made with both forms. Of all structures in class I, the predicted EPR properties for model H(C6) best fit the measured data of R4. The comparison is shown in Table 3. The calculations independently confirm the model (labeled M4b) that was put forward in paper I.

In model H(C6), the calculated eigenvector directions for H6 deviate only 5° from those of HF1a(R4), making it highly probable that this is the correct tensor form. The HF2(R4) hyperfine interaction is closely reproduced by the H5 tensor. However, two calculated proton hyperfine couplings remain unassigned. ENDOR resonance lines of H1 would have been mainly “hidden” in the overcrowded region near the free proton frequency and in EIE spectra this proton would cause an additional splitting of 0.32 mT at most, which is within the experimentally observed line widths (see paper I). The hydroxy proton HO6 can be matched with the HF3(R4) coupling that

was detected at 77 K but for which no tensor could be determined. The complete hyperfine coupling tensor for this hydroxy proton was determined in the low-temperature study of K2GIP by Locher and Box³ (marked A3 in Table 3). However, agreement with the calculated hyperfine tensor of HO6 is only found when an $a \rightarrow -a$ symmetry operation is performed in the original $\langle abc^* \rangle$ axes reference frame, yielding the A3[-a] tensor form. This suggestion was also made in paper I, based on a comparison between the experimental angular variation of the EIE spectrum of radical R4 and simulations using the A3 and A3[-a] tensor forms. The DFT calculations clearly corroborate that the latter tensor form is indeed the correct one. In addition, simulations using the calculated HO6 tensor closely fit the experimental angular variation of the EIE spectrum of radical R4 upon rotation along the monoclinic $\langle b \rangle$ axis (Supporting Information). The striking agreement provides another strong argument for the validity of the H(C6) model.

3.4. Models for Radical R3. Although it was already assigned to radical R4, model H(C6) is the only structure in class I for which the calculated α -type hyperfine coupling tensor is in reasonable accordance with HF1(R3). This is apparent in Table 3. However, the substantial isotropic couplings of hyperfine tensor H5 and HO6 (30 and 50 MHz, respectively) are inconsistent with the experimental observation of only one additional signal HF2(R3) reaching up to 25 MHz (see paper I). It was already noted in paper I that the similarity between the measured α -type hyperfine coupling tensors of radicals R3 and R4 indicates that R3 is in fact a different stable conformation of the H(C6) structure.

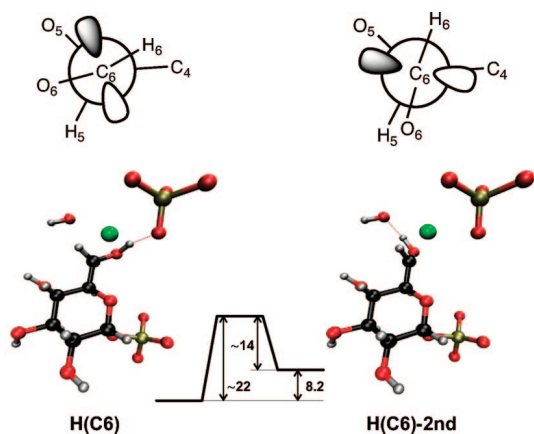


Figure 5. Newman projections along the C6–C5 axis and three-dimensional representations of the H(C6) and H(C6)-2nd structures and their immediate environment. The glucose moieties bound to the upper phosphate groups are not shown for the sake of clarity. The absolute energy of the H(C6) structure is used as reference (–1127.214 65 au).

This possibility was examined by considering conformational variations close to the main site of the unpaired electron. The –CH–OH group is the most flexible group of the radical and its local conformation is controlled by two torsion angles: O6–C6–C5–C4 and HO6–O6–C6–C5. In the H(C6) structure, these torsion angles are 192.4 and 243.1°, respectively. A Newman projection along the C6–C5 axis is presented in Figure 5, along with a three-dimensional representation of the H(C6) structure and its closest environment. To examine the presence of alternative minima, several scans of the potential energy surface were performed along these degrees of freedom. The adopted procedure and analyses are described in detail in the Supporting Information. Another minimum was identified in the scans, labeled H(C6)-2nd, with an energy that is only 8.2 kJ/mol higher than H(C6). The O6–C6–C5–C4 torsion angle in this structure is 249.8° and HO6–O6–C6–C5 137.8°. Approximate barrier heights were also determined: 22 kJ/mol for H(C6) → H(C6)-2nd and 14 kJ/mol for the reverse process.

The structural difference between these two minima is further clarified in Figure 5. In both structures, the HO6–O6 hydroxy group is involved in a hydrogen bond with its molecular environment. In H(C6), this H-bond connects to a phosphate group of a nearby glucose-1-phosphate and in H(C6)-2nd to the oxygen of a crystal water. The barriers for interconversion are therefore due to the temporary loss of the hydrogen bond. In both structures, the radical center at C6 is nonplanar. Taking the O6–H6–C5–C6 improper dihedral angle as a measure for (non)planarity, H(C6) (–6.1°) is more planar than H(C6)-2nd (13.8°) and the deviation occurs in opposite directions. This has some consequences with respect to the orientation of the LEO, as illustrated in the Newman projections of Figure 5. More specifically, the LEO makes an estimated angle of 50° with the C5–H5 bond in H(C6), whereas it is almost 90° in H(C6)-2nd. Obviously, this reorientation considerably influences the EPR properties, as demonstrated in Table 3, where the calculated hyperfine tensors for H(C6)-2nd are given. The isotropic couplings of H1 and H5 are virtually zero, making it very plausible that these interactions were not detected in the experiments. Furthermore, the HO6 coupling is considerably reduced, varying roughly between 3.2 MHz (≈0.1 mT) and 34 MHz (≈1.2 mT) in the plane perpendicular to $\langle b \rangle$. This is in good agreement with EIE spectra of R3 (see paper I). For a magnetic field orientation perpendicular to $\langle b \rangle$ and roughly 10°

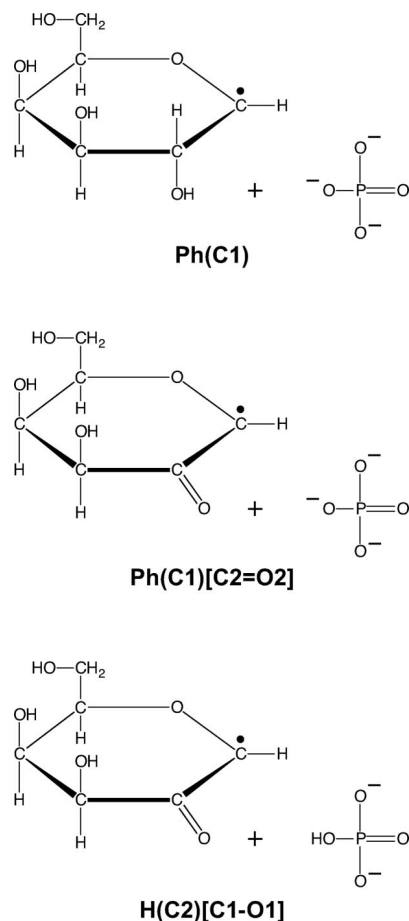


Figure 6. Chemical structure of the radical models that involve cleavage of the sugar–phosphate bond in K2G1P.

from $\langle a \rangle$ and $\langle a^* \rangle$ (shown in Figure 2 of paper I), a hyperfine splitting of about 0.75 mT (≈21 MHz) is observed, which is almost precisely the coupling size predicted by the calculation. The H6 tensor is slightly changed with respect to model H(C6), but the agreement with the HF1(R3) tensor is still satisfactory.

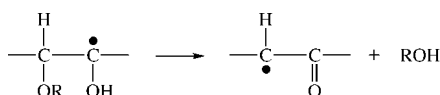
Thus, structure H(C6)-2nd is a good model for radical R3, as it is consistent with all experimental information available. Radicals R3 and R4 have an identical chemical composition but differ only in the specific conformation of their –CH–OH substituent of the sugar ring. Considering that the estimated barrier heights between these structures is of the order of 14–22 kJ/mol, it is conceivable that, as a result of irradiation at 77 K, the same radical may become “trapped” in two alternative conformations with comparable energies. Chemically similar radicals with slightly different conformations have often been suggested in other studies of irradiated sugars, such as fructose,^{9,19} sorbose,²⁵ and sucrose,²² to explain the occurrence of similar hyperfine tensors. The level of agreement in this work between measurements on radicals R3 and R4 and calculations on models H(C6) and H(C6)-2nd is strong evidence for such conformational freedom in sugar radicals.

An alternative model was suggested in the experimental part that was not yet included in class I: a C1-centered radical structure (labeled M3a in paper I) with a broken C1–O1 bond between the sugar ring and the phosphate group. Even though model H(C6)-2nd is able to explain all experimental EPR data of radical R3, this alternative was still examined for the sake of completeness. Calculations were performed on model Ph(C1), which is shown in Figure 6. This structure is the result of dissociative electron attachment (the supercell has a total charge

TABLE 4: Comparison of Measured Hyperfine Coupling Tensors of Radicals R2, R3, and R4 and Calculated Tensors of Models That Involve Cleavage of the Glucose-1-phosphate Bond^a

		A_{iso}		T_{aniso}		R2		R3	R4				
						HF1a	HF1b	HF2	HF3	HF1	HF1a	HF1b	HF2
						-41.5	-41.5	15.8	10.2	-51.0	-61.2	-61.0	24.0
						-23.0	-21.4	-2.5	-3.4	-31.1	-29.4	-32.9	-6.4
						0.6	-2.4	-1.8	-2.3	2.3	0.2	6.3	-3.6
				Principal directions		22.3	23.9	4.3	5.7	28.8	29.2	26.6	9.9
Ph(C1)													
H1	-44.8	-38.4	0.778	0.199	-0.596	<i>29</i>	<i>5</i>			<i>17</i>	<i>7</i>	<i>29</i>	
		-1.8	0.062	-0.968	-0.243	<i>30</i>	<i>6</i>			<i>50</i>	<i>52</i>	<i>77</i>	
		40.2	0.625	-0.152	0.765	<i>8</i>	<i>5</i>			<i>53</i>	<i>51</i>	<i>75</i>	
H2	85.9	-5.3	-0.669	0.557	-0.492			26					65
		-4.3	-0.728	-0.624	0.284			26					56
		9.6	0.149	-0.548	-0.823			37					51
H5	2.5	-4.3	0.223	0.139	-0.965				51				
		-2.2	-0.715	0.696	-0.065				54				
		6.5	-0.662	-0.705	-0.255				16				
Ph(C1)[C2=O2]													
H1	-28.6	-20.1	0.786	0.008	-0.618	<i>18</i>	<i>8</i>			<i>17</i>	<i>6</i>	<i>18</i>	
		-3.4	-0.158	-0.964	-0.213	<i>23</i>	<i>7</i>			<i>47</i>	<i>44</i>	<i>69</i>	
		23.5	0.598	-0.266	0.756	<i>14</i>	<i>5</i>			<i>46</i>	<i>45</i>	<i>68</i>	
H3	12.9	-2.4	-0.761	0.642	-0.094			9					
		-1.8	-0.513	-0.505	0.694			6					
		4.2	-0.398	-0.576	-0.713			7					
H5	10.4	-3.1	-0.062	0.302	-0.951				34				
		-1.7	-0.633	0.725	0.271				34				
		4.8	-0.772	-0.619	-0.146				7				
H(C2)[C1-O1]													
H1	-29.9	-20.5	0.774	-0.011	-0.633	<i>17</i>	<i>9</i>			<i>18</i>	<i>7</i>	<i>16</i>	
		-3.1	-0.242	-0.929	-0.280	<i>27</i>	<i>12</i>			<i>41</i>	<i>38</i>	<i>63</i>	
		23.7	0.586	-0.369	0.722	<i>20</i>	<i>10</i>			<i>39</i>	<i>38</i>	<i>62</i>	
H3	12.6	-2.4	-0.565	0.733	-0.379			18					
		-1.7	-0.725	-0.222	0.652			14					
		4.1	-0.394	-0.643	-0.657			11					
H5	12.5	-3.2	-0.252	0.436	-0.864				21				
		-1.9	-0.661	0.574	0.483				22				
		5.1	-0.707	-0.693	-0.143				12				

^a A_{iso} indicates the isotropic coupling, and T_{aniso} indicates the anisotropic hyperfine components (both in MHz). Principal directions are given with respect to the $\langle a^*bc \rangle$ axes reference frame. The numbers in italics are the angular deviations (in degrees) between calculated and measured eigenvectors.

SCHEME 2

of -1), disconnecting a phosphate trianion. A similar cationic process was not stable. Calculated EPR properties for model Ph(C1) deviate considerably from those of radical R3 (Table 4). Hence, the model was effectively ruled out.

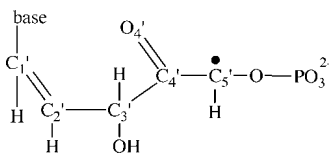
3.5. Models for Radical R2. None of the models in class I accurately reproduce the α -type hyperfine coupling tensor of R2 (Supporting Information). For model Ph(C1), the angles between the calculated eigenvectors of H1 and those of HF1b(R2) are quite small, but the predicted principal values are far too large (see Table 4). As was discussed in paper I, the relatively small magnitude of the α -tensor in R2 indicates excessive delocalization of the unpaired electron, which can occur when a carbonyl group is located next to the α -carbon, e.g., as a result of beta elimination (Scheme 2). Moreover, based on the similarity between the measured hyperfine tensors for R2 and those of a radical in irradiated sucrose,^{22,26} a convincing candidate structure was eventually found: a C1-centered species in which the sugar-phosphate bond is broken and with a carbonyl group on C2 (labeled M2 in paper I).

Model Ph(C1) can be transformed into such a structure by removing the HO2 and H2 hydrogens. The immediate benefit is that the inconveniently large H2 β -coupling is eliminated.

Reoptimization results in model Ph(C1)[C2=O2], shown in Figure 6, for which calculated EPR properties are reported in Table 4. Note that the supercell containing this structure still has an effective charge of -1 . The agreement with the experimental values is very good. The anisotropic hyperfine components are reproduced within 1 MHz, and the eigenvector directions differ 10° at the most, except for H5 where a similar effect is observed as in model H(C3) for radical R1. The magnitude of the isotropic component of H1 is too small, but this can be traced back to the use of pseudopotentials. Of the two alternative forms for the HF1 hyperfine interaction that were determined in the experiments, the HF1b form agrees best with the calculations.

The spectroscopic properties of model Ph(C1)[C2=O2] closely fit those of radical R2, but it is unclear how this species is formed. In paper I, an elegant formation mechanism was proposed that gives rise to the same glucose-1-phosphate radical structure without the involvement of a phosphate trianion. Starting from structure H(C2), a beta phosphate elimination produces H(C2)[C1-O1], in which HO2 is transferred to the phosphate group and the C1-O1 bond is broken (Figure 6). Calculated EPR properties for the optimized structure of this model are also presented in Table 4. There are only slight changes with respect to the EPR properties of model Ph(C1)-[C2=O2]. Given the level of agreement of both models with the experimental data, it is difficult to favor one over the other.

SCHEME 3



Scission of the sugar–phosphate bond is an important lesion in irradiated DNA, giving rise to strand breaks. Radicals located on the 2-deoxyribose unit act as precursors for backbone cleavage.¹ Such species can arise immediately through irradiation events (direct damage) or through mediation by a chemical agent or radiation-induced H• atom or HO• radical (indirect damage).^{1,28,29} The nature of these sugar radicals differs from that of R2: “simple” hydrogen abstraction products are usually observed which do not have a carbonyl group in the β position with respect to the radical site. Their structure is more similar to, e.g., model H(C2), which is actually proposed in this work to be a precursor for sugar–phosphate cleavage in K2G1P. The parallel with the DNA system is however not complete. The H(C2)[C1–O1] model is tentatively obtained from H(C2) by beta elimination. Such a reaction requires a hydroxy group vicinal to the phosphodiester substituent, which is not present in 2-deoxyribose. On the other hand, some support for the ionic route to sugar–phosphate scission in K2G1P (*vide infra*) is found in heavy-ion irradiation studies of DNA.²⁹ In these works, dissociative electron attachment to the backbone for the most part leads to C3'-centered 2-deoxyribose radicals and phosphate dianions and, to a far lesser degree, phosphoryl radicals.³⁰ The C3'-centered structure bears resemblance to the C1-centered K2G1P species and the phosphate trianion in model Ph(C1).

An allylic radical having much in common with the R2 species has been identified in irradiated monomers of DNA. Hole and Sagstuen³¹ examined irradiated crystals of 2'-deoxyguanosine 5'-monophosphate with EPR and characterized among several other base- and sugar-centered species a particular radical at room temperature with hyperfine tensors similar to those of R2 in K2G1P. Drawing on the work of Rakvin and Herak,³² the structure of Scheme 3 was proposed. This radical has in common the strong delocalization of the unpaired electron density (as in R2), but instead of the sugar–phosphate linkage, the C1'–O4' bond of 2-deoxyribose is broken. More intriguing in the present context is that an allylic radical identical to R2 was recently identified in irradiated sucrose crystals.^{22,26} Stable at room temperature, this radical is located on the glucose subunit of the dimer and is characterized by a ruptured glycosidic bond with fructose. Thus, instead of the phosphate substituent, the entire fructose molecule is eliminated as a result of radiation damage. This suggests that the ester bond is a vulnerable entity regardless of the chemical nature of the sugar (i.e., glucose instead of 2-deoxyribose) and indicates that the phosphate is not necessarily essential to the formation process of radical R2 in K2G1P.

3.6. Energetic Considerations. Since the majority of all considered radical models is obtained by hydrogen abstraction from K2G1P and possibly additional reorganizations, it is interesting to compare the relative energies of these species. In Figure 7, a graphical representation is made of the energy levels. Absolute energies for the entire supercell were obtained from the individual optimizations and considered relative to each other. This is valid, since the supercells have the same atomic composition and charge (zero in this case). The species with the lowest energies are carbon-centered radicals in which only minor atomic rearrangements have occurred. Alkoxy radicals

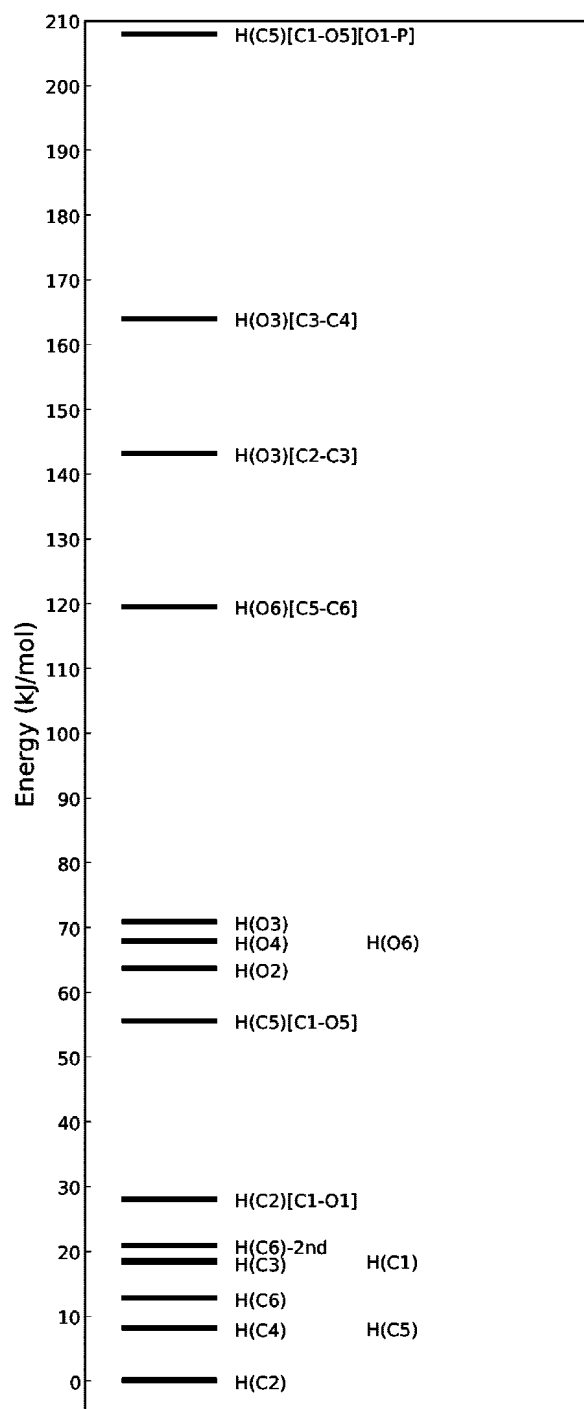
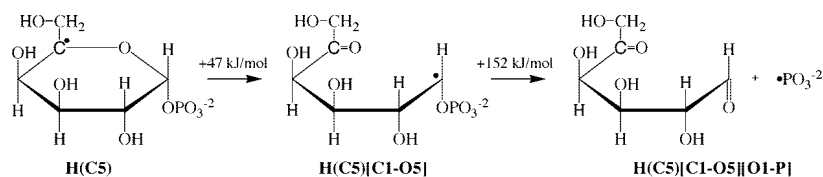


Figure 7. Comparison of energy levels for all (uncharged) structures that are obtained by hydrogen abstraction from K2G1P. The H(Ox) models refer to alkoxy radicals. The absolute energy for model H(C2) is $-1127.219\ 468$ au and is used as a reference.

(indicated by H(Ox) labels) are on average 50–60 kJ/mol less stable, corroborating their transient character.

Most carbon-centered radicals that involve significant atomic rearrangements of the K2G1P structure (e.g., with a broken glucose ring) have very high energies, apart from models H(C5)[C1–O5] and H(C2)[C1–O1] which are even more stable than alkoxy species. The energy for the latter is almost of the same magnitude as that of typical hydroxy alkyl type radicals and may provide a rationale for the occurrence and abundance of R2. The former model has been suggested as an intermediate step in the formation of a phosphoryl radical from H(C5).⁴ The tentative mechanism is reproduced in Scheme 4. The energy

SCHEME 4



change associated with the first step amounts to +47 kJ/mol. Furthermore, the final H(C5)[C1–O5][O1–P] structure is more than 150 kJ/mol less stable than the intermediate. It must be noted that the conformational freedom of this species was not investigated exhaustively and an alternative conformation with a lower energy was possibly overlooked. Still, on the basis of the current calculations, this particular mechanism for generation of phosphoryl radicals seems very unlikely from a thermodynamic point of view.

The energies for the models that are attributed to measured radicals—H(C3) for R1, H(C2)[C1–O1] for R2, H(C6)-2nd for R3, and H(C6) for R4—are of the same magnitude and only 15 kJ/mol apart. However, several other structures exist that have even lower energies. This implies that the formation of the observed radicals in K2G1P is not necessarily thermodynamically controlled. It is the kinetics of the individual reactions that will determine the better part of the radiation chemistry. Of course, the calculated energies rely to some extent on the accuracy of the adopted computational protocol. Furthermore, the approximation must be valid that the abstracted hydrogen can be removed from the model system. These fragments can influence the (electronic) structure and energy of a radical species; consider, e.g., the discussion on the migrated proton in model H(C3). To account for this factor in an energetic analysis, the exact nature of such secondary damage in a crystalline phase must be better understood. And the impact of even small fragments can be severe. In several crystals,^{33,34} “multiproton shuffles” resembling the Grotthuss mechanism have been identified following irradiation.

Still other experimental works seem to endorse the kinetic control, at least for the initial stages of radiation damage. Locher and Box found that X-irradiation of K2G1P at 4.2 K gave rise to three alkoxy radicals in the nondeuterated crystal but to only one in the deuterated crystal.³ Since formation of an alkoxy species involves the transfer of a hydroxy proton/deuteron to a neighboring molecule, it can be expected that the associated barrier differs between the two isotopes. In this respect, the more selective radiation chemistry of deuterated K2G1P should be approached in terms of kinetic control.

4. Conclusions

The radiation-induced radicals in dipotassium glucose-1-phosphate dihydrate crystals were examined with DFT methods, consistently relying on a periodic computational scheme. Geometries and spectroscopic properties were calculated for a selection of radical models and compared to data from EPR/ENDOR/EIE experiments, which are described in paper I. On the basis of the agreement between calculated and measured hyperfine tensors, structural models were selected and assigned. Although some of these models were suggested from the experimental part of this work (paper I), the identification procedure followed here proceeds independently, starting from a fairly large initial set of plausible radical models. In this way, the calculations provide an unbiased but firm verification of the four main radicals in glucose-1-phosphate:

- **Radical R1** corresponds to model H(C3). This structure is obtained by proton abstraction at C3 of K2G1P but requires that the proton is transferred to a nearby phosphate group of another glucose-1-phosphate molecule. Only then is good agreement found between calculated and measured hyperfine tensors.

- **Radical R2** is the major radiation-induced species and corresponds equally well to Ph(C1)[C2=O2] and H(C2)[C1–O1]. Both models describe a C1-centered radical, in which the glucose-1-phosphate bond is broken and a carbonyl group is present at C2, requiring the abstraction of two hydrogens. Only for model H(C2)[C1–O1] is a tentative formation mechanism available, involving beta elimination of the H(C2) hydroxy alkyl precursor.

- **Radicals R3 and R4** are assigned to models H(C6)-2nd and H(C6), respectively. These structures are identical in chemical composition (a hydrogen is abstracted from C6) but differ in the precise conformation of the –CH–OH substituent of the sugar ring. The level of agreement between measured and calculated hyperfine tensors as well as between EIE spectra and simulations provides the first strong evidence for conformational freedom in sugar radicals.

In addition, the energies are determined and compared for all considered radical models and some tentative reaction schemes. Initial analysis suggests that the radiation chemistry of K2G1P and sugars, in general, is kinetically and not necessarily thermodynamically controlled. Also, it is found that an abstracted fragment resulting from radiation damage can significantly influence the structural and spectroscopic properties of a radical when this fragment remains in the vicinity of the generated radical.

Acknowledgment. This work is supported by the Fund for Scientific Research - Flanders (FWO) and the Research Board of the Ghent University. The European Cooperation in the field of Scientific and Technical Research (COST action P15) is also acknowledged for financial support.

Supporting Information Available: Comparison between the $\langle ab2c \rangle$ and $\langle 2ab2c \rangle$ supercell approaches: optimized geometry and calculated EPR properties. Calculated EPR properties for all models in classes I and II. Calculated EPR properties for the second, less stable minimum of model H(C3) in which the HO3–O3–C3–C4 torsion angle is about 280°. Comparison between the experimental angular variation of the EIE spectrum of radical R4 (obtained in paper I) and simulations based on the calculated HO6 hyperfine tensor of model H(C6). Detailed procedures and results of an examination of the potential energy surface for model H(C6) along two degrees of freedom. This material is available free of charge via the Internet at <http://pubs.acs.org>.

References and Notes

- (1) Bernhard, W. A.; Close, D. M. In *Charged Particle and Photon Interactions with Matter: Chemical, Physicochemical, and Biological Consequences with Applications*; Mozumber, A., Hatano, Y., Eds.; Marcel Dekker: New York, 2003; Chapter 15.

- (2) Atherton, N. M. *Principles of Electron Spin Resonance*; Ellis Horwood, Prentice Hall: New York, 1993. Weil, J. A.; Bolton, J. R.; Wertz, J. E. *Electron Paramagnetic Resonance: Elementary Theory and Practical Applications*; Wiley-Interscience: New York, 1994.
- (3) Locher, S. E.; Box, H. C. *J. Chem. Phys.* **1980**, *72*, 828.
- (4) Bungum, B.; Hole, E. O.; Sagstuen, E.; Lindgren, M. *Radiat. Res.* **1994**, *139*, 194.
- (5) Sanderud, A.; Sagstuen, E. *J. Chem. Soc., Faraday Trans.* **1996**, *92*, 995.
- (6) De Cooman, H.; Vanhaelewyn, G.; Pauwels, E.; Sagstuen, E.; Waroquier, M.; Callens, F. *J. Phys. Chem. B* **2008**, *112*, 15045.
- (7) For an example of a reference work, see: Parr, R. G.; Yang, W. *Density-Functional Theory of Atoms and Molecules*; Oxford University Press: New York, 1989.
- (8) Pauwels, E.; Van Speybroeck, V.; Callens, F.; Waroquier, M. *Int. J. Quantum Chem.* **2004**, *99*, 102.
- (9) Vanhaelewyn, G.; Pauwels, E.; Callens, F.; Waroquier, M.; Sagstuen, E.; Matthys, P. *J. Phys. Chem. A* **2006**, *110*, 2147.
- (10) Tokdemir, S.; Nelson, W. H. *J. Phys. Chem. A* **2006**, *110*, 6552.
- (11) Kaupp, M.; Bühl, M.; Malkin, V. G. *Calculation of NMR and EPR Parameters: Theory and Applications*; Wiley-VCH: Weinheim, Germany, 2004.
- (12) Sugawara, Y.; Iwasaki, H. *Acta Crystallogr., Sect. C* **1984**, *40*, 389.
- (13) CPMD V3.11 Copyright IBM Corp 1990–2006, Copyright MPI fuer Festkoerperforschung Stuttgart 1997–2001.
- (14) Becke, A. D. *Phys. Rev. A* **1988**, *38*, 3098. Lee, C.; Yang, W.; Parr, R. G. *Phys. Rev. B* **1988**, *37*, 785.
- (15) Goedecker, S.; Teter, M.; Hutter, J. *Phys. Rev. B* **1996**, *54*, 1703. Hartwigsen, C.; Goedecker, S.; Hutter, J. *Phys. Rev. B* **1998**, *58*, 3641. Krack, M. *Theor. Chem. Acc.* **2005**, *114*, 145.
- (16) Van de Walle, C. G.; Blochl, P. E. *Phys. Rev. B* **1993**, *47*, 4244.
- (17) Troullier, N.; Martins, J. L. *Phys. Rev. B* **1991**, *43*, 1993. Boero, M.; Andreoni, W. *Chem. Phys. Lett.* **1997**, *265*, 24. Boero, M.; Parrinello, M.; Terakura, K. *J. Am. Chem. Soc.* **1998**, *120*, 2746. Ramaniah, L. M.; Bernasconi, M.; Parrinello, M. *J. Chem. Phys.* **1999**, *111*, 1587.
- (18) Declerck, R.; Pauwels, E.; Van Speybroeck, V.; Waroquier, M. *Phys. Rev. B* **2006**, *74*, 245103.
- (19) Tarpan, M.; Sagstuen, E.; Pauwels, E.; Vrielinck, H.; Waroquier, M.; Callens, F. *J. Phys. Chem. A* **2008**, *112*, 3898.
- (20) Pauwels, E.; Verstraelen, T.; Waroquier, M. *Spectrochim. Acta, Part A* **2008**, *69*, 1388.
- (21) Pauwels, E.; Van Speybroeck, V.; Waroquier, M. *J. Phys. Chem. A* **2004**, *108*, 11321.
- (22) De Cooman, H.; Pauwels, E.; Vrielinck, H.; Dimitrova, A.; Yordanov, N.; Sagstuen, E.; Waroquier, M.; Callens, F. *Spectrochim. Acta, Part A* **2008**, *69*, 1372.
- (23) Jayatilaka, N.; Nelson, W. H. *J. Phys. Chem. B* **2007**, *111*, 7887.
- (24) Marx, D.; Hutter, J. In *Modern Methods and Algorithms of Quantum Chemistry*; Grotendorst, J., Ed.; John von Neumann Institute for Computing: Jülich, Germany, 2000.
- (25) Vanhaelewyn, G.; Jansen, B.; Pauwels, E.; Sagstuen, E.; Waroquier, M.; Callens, F. *J. Phys. Chem. A* **2004**, *108*, 3308.
- (26) De Cooman, H.; Pauwels, E.; Vrielinck, H.; Sagstuen, E.; Callens, F.; Waroquier, M. *J. Phys. Chem. B* **2008**, *112*, 7298.
- (27) Reference deleted in revision.
- (28) Pogożelski, W. K.; Tullius, T. D. *Chem. Rev.* **1998**, *98*, 1089. Weiland, B.; Hüttermann, J. *Int. J. Radiat. Biol.* **1998**, *74*, 341. Debije, M. G.; Bernhard, W. A. *Radiat. Res.* **2001**, *155*, 687. Zheng, Y.; Cloutier, P.; Hunting, D. J.; Sanche, L.; Wagner, J. R. *J. Am. Chem. Soc.* **2005**, *127*, 16592. Dedon, P. C. *Chem. Res. Toxicol.* **2008**, *21*, 206.
- (29) Becker, D.; Bryant-Friedrich, A.; Trzasko, C.; Sevilla, M. D. *Radiat. Res.* **2003**, *160*, 174. Shukla, L. I.; Pazdro, R.; Becker, D.; Sevilla, M. D. *Radiat. Res.* **2005**, *163*, 591.
- (30) Becker, D.; Adhikary, A.; Sevilla, M. D. In *Charge Migration in DNA Physics, Chemistry and Biology Perspectives*; Chakraborty, T., Ed.; Springer-Verlag: Berlin, Heidelberg, 2007; pp 139–175.
- (31) Hole, E. O.; Sagstuen, E. *Radiat. Res.* **1987**, *109*, 190.
- (32) Rakvin, B.; Herak, J. N. *Radiat. Res.* **1981**, *88*, 240.
- (33) Pauwels, E.; Declerck, R.; Van Speybroeck, V.; Waroquier, M. *Radiat. Res.* **2008**, *169*, 8.
- (34) Bernhard, W. A.; Barnes, J.; Mercer, K. R.; Mroczka, N. *Radiat. Res.* **1994**, *140*, 199. Nelson, W. H.; Sagstuen, E.; Hole, E. O.; Close, D. M. *Radiat. Res.* **1998**, *149*, 75. Close, D. M.; Eriksson, L. A.; Hole, E. O.; Sagstuen, E.; Nelson, W. H. *J. Phys. Chem. B* **2000**, *104*, 9343.

7.6 Paper VI

Schonland ambiguity in the electron nuclear double resonance analysis of hyperfine interactions: principles and practice

H. Vrielinck, H. De Cooman, M. A. Tarpan, E. Sagstuen, M. Waroquier
and F. Callens

Journal of Magnetic Resonance, 2008, 195, 196-205

Copyright 2008 by Elsevier.



Contents lists available at ScienceDirect

Journal of Magnetic Resonance

journal homepage: www.elsevier.com/locate/jmr

Schonland ambiguity in the electron nuclear double resonance analysis of hyperfine interactions: Principles and practice

H. Vrielinck^{a,1}, H. De Cooman^{a,c,2}, M.A. Tarpan^{a,2}, E. Sagstuen^b, M. Waroquier^c, F. Callens^{a,*}

^a Ghent University, Department of Solid State Sciences, Krijgslaan 281-S1, B-9000 Gent, Belgium

^b University of Oslo, Department of Physics, P.O. Box 1048 Blindern, N-0316 Oslo, Norway

^c Ghent University, Center for Molecular Modeling, Proeftuinstraat 85, B-9000 Gent, Belgium

ARTICLE INFO

Article history:

Received 18 June 2008

Revised 12 August 2008

Available online 23 September 2008

Keywords:

ENDOR

Hyperfine couplings

Fitting results

Ambiguity

DFT calculations

ABSTRACT

For the analysis of the angular dependence of electron paramagnetic resonance (EPR) spectra of low-symmetry centres with $S = 1/2$ in three independent planes, it is well-established—but often overlooked—that an ambiguity may arise in the best-fit \vec{g} tensor result. We investigate here whether a corresponding ambiguity also arises when determining the hyperfine coupling (HFC) A tensor for nuclei with $I = 1/2$ from angular dependent electron nuclear double resonance (ENDOR) measurements. It is shown via a perturbation treatment that for each set of M_S ENDOR branches two best-fit A tensors can be derived, but in general only one unique solution simultaneously fits both. The ambiguity thus only arises when experimental data of only one M_S multiplet are used in analysis or in certain limiting cases. It is important to realise that the ambiguity occurs in the ENDOR frequencies and therefore the other best-fit result for an ENDOR determined A tensor depends on various details of the ENDOR experiment: the M_S state of the fitted transitions, the microwave frequency (or static magnetic field) in the ENDOR measurements and the rotation planes in which data have been collected. The results are of particular importance in the identification of radicals based on comparison of theoretical predictions of HFCs with published literature data. A procedure for obtaining the other best-fit result for an ENDOR determined A tensor is outlined.

© 2008 Elsevier Inc. All rights reserved.

1. Introduction

Determining the principal values and directions of the \vec{g} tensor from the angular dependence of spectra is one of the central problems of single crystal electron paramagnetic resonance (EPR) spectroscopy. Already in 1959, Schonland [1] pointed out an ambiguity arising when determining the \vec{g} tensor in the spin Hamiltonian

$$\hat{H}_S = \mu_B \vec{B} \cdot \vec{g} \cdot \hat{S} \quad (1)$$

for low-symmetry paramagnetic centres with effective spin $S = 1/2$ in crystals with orthorhombic and monoclinic symmetry (although the problem is not restricted to these classes of crystal symmetry). For such crystals, \vec{g} , which we assume to be symmetric [2] and represented in an orthonormal reference frame fixed to the crystal, is commonly determined by analysing the angular dependence of the EPR spectrum in the three crystallographic planes $\{ab\}$, $\{bc\}$ and $\{ca\}$. For monoclinic crystals with $\langle b \rangle$ as twofold rotation axis or $\{ac\}$ as mirror plane, $\langle a \rangle$ and $\langle c \rangle$, and hence also $\{ab\}$ and $\{bc\}$ are not perpendicular to one another. It is sometimes more convenient

to perform experiments in the $\{a^*b\}$ and/or $\{bc^*\}$ ($\langle a^* \rangle$ perpendicular to $\langle b \rangle$ and $\langle c \rangle$, $\langle c^* \rangle$ perpendicular to $\langle a \rangle$ and $\langle b \rangle$) planes, instead of in $\{ab\}$ and $\{bc\}$, respectively. Schonland demonstrated that from data analysis in three planes of this kind two distinct best-fit solutions can be found, differing both in principal values and eigenvectors. In this paper we will refer to these two solutions as Schonland conjugate tensors. Only one of them corresponds to the \vec{g} tensor of the paramagnetic defect under study, the other is a fitting result without physical meaning. Outside of these three planes, the EPR positions calculated for the two solutions may differ considerably and a straightforward solution to the problem is to complete the experiments by measurements in a fourth, skewed plane. Recording the powder EPR spectrum can also lift the ambiguity, because the principal g values—but in general not the directions—can be directly determined from it. In addition, Morton and Preston [2] described a procedure to avoid this ambiguity in single crystal EPR by choice of the rotation planes using a two-circle goniometer.

Later papers on \vec{g} tensor analysis and EPR textbooks (see e.g. [3,4]) have extended the work of Schonland and further documented possible ambiguities in fitting results. Nonetheless, in experimental EPR literature, this problem is often not recognised. Yet, it may have serious implications when principal values and directions of the wrong \vec{g} tensor would be interpreted theoretically to infer the molecular structure of the paramagnetic defect.

* Corresponding author. Tel.: +32 9 264 43 52; fax: +32 9 264 49 96.

E-mail address: Freddy.Callens@UGent.be (F. Callens).

¹ Postdoctoral Fellow of the Flemish Research Foundation (FWO-Vlaanderen).

² Research Assistant of the Flemish Research Foundation (FWO-Vlaanderen).

In a similar way as for \vec{g} , one may want to determine the hyperfine coupling (HFC) A tensor—which we also assume to be symmetrical—for a nucleus with $I = 1/2$ in the spin Hamiltonian ($S = 1/2$)

$$\hat{H}_S = \mu_B \vec{B} \cdot \vec{g} \cdot \hat{S} + \hat{S} \cdot \vec{A} \cdot \hat{I} - g_N \mu_N \vec{B} \cdot \hat{I} \quad (2)$$

from the angular dependence of electron nuclear double resonance (ENDOR) spectra. Hence, one may wonder if for a corresponding set of experimental data an analogous Schonland-type ambiguity in the best-fit solution exists. This problem has, to the best of our knowledge, neither been treated yet from a theoretical nor from a practical viewpoint in the literature, although it has been recognised that in the analysis of EPR spectra, treating the HF interaction as a perturbation to first order, the ambiguity does arise [3–5]. Our interest in this matter, and particularly in the ENDOR analysis, arises from our study of the structure of radiation-induced radicals in single crystals of mono- and disaccharides [6–9] and other bio-organic molecules [10–13]. In such crystals, each radical formed is characterised by a set of proton (^1H) HFC tensors, whose principal values and directions are determined from angular dependent ENDOR experiments, and which are assigned to this particular radical based on ENDOR-induced EPR measurements. From a set of semi-empirical rules and equations [14] information on the chemical identity of the radical can be inferred from the size of the principal HFC values, the tensor anisotropy and principal directions. This is, however, often still insufficient for a complete identification of the radical structure. In recent years, “first principles” calculations of A tensors based on density functional theory (DFT) have become increasingly fast and reliable. In our research of these systems, the comparison between calculated and experimental principal HFC values and eigenvectors for proposed radical structures has become a crucial step in the radical model assignment.

Both semi-empirical theoretical interpretation and identification based on comparison with computational results rely strongly on an accurate determination of experimental tensors. From this viewpoint it is important to know whether or not a Schonland-type ambiguity exists, because only the physically relevant tensor provides information on the radical model and can be reproduced in calculations, not its Schonland conjugate. In this paper, we explore this question.

Throughout this paper, we choose $(\vec{e}_a, \vec{e}_b, \vec{e}_c)$ as the reference frame for representation of tensors for orthorhombic crystals and $(\vec{e}_a, \vec{e}_b, \vec{e}_c)$ for monoclinic crystals. Where this choice makes a difference, the results in a $(\vec{e}_a, \vec{e}_b, \vec{e}_c)$ reference frame are also mentioned. The simulations shown in Section 3 are obtained by diagonalisation of the spin Hamiltonians (1) and (2) using the EasySpin routines [15] in Matlab. These simulations demonstrate that for HFC tensors of practical interest in the study of radiation defects in bio-organic molecules like saccharides, the use of first order perturbation theory in the formulae derived for calculating Schonland conjugate tensors is sufficiently accurate.

2. Principle of Schonland ambiguity for the HFC tensor: perturbation theory approach

Schonland [1] demonstrated that in any rotation plane the angular dependence of the EPR resonance field $B_0 = h\nu_{\text{MW}}/g\mu_B$ ($\vec{B} = B_0\vec{l}$), on the rotation angle θ follows

$$g^2 = \vec{l} \cdot \vec{g} \cdot \vec{g} \cdot \vec{l} = \alpha + \beta \cos 2\theta + \gamma \sin 2\theta \quad (3)$$

α , β and γ (being expressed also by the elements of the squared \vec{g} tensor) can directly be calculated from the maximum and minimum g value encountered in this plane, and the angle θ at which the maximum g value occurs [1,3]. Ignoring for the moment the possible

presence of symmetry-related centres (site splitting), whose \vec{g} tensors are related to those of the “original” centre by the symmetry operations of the crystal's point group [4], the occurrence of two best-fit solutions springs from an ambiguity in the positive rotation sense in the planes, thus in the sign of θ or, alternatively, in the sign of γ . Indeed from Eq. (3) it follows that $g^2(\alpha, \beta, \gamma, -\theta) = g^2(\alpha, \beta, -\gamma, \theta)$. Rotation senses may, however, not be clear from EPR experiments alone. When analysing data in three rotation planes, in two of them the sign of γ may be chosen without important consequences, but this fixes the choice in the third plane. When the measurements are performed on three different crystals, it is however not a priori clear which sign has to be chosen. A further complication occurs if, due to site splitting in at least two of the planes, two branches occur in the angular dependence. Then it cannot be decided which branches should be fit together (see further in Section 3.1 and Fig. 1). The two best-fit solutions thus follow from the two sign choices for γ in the third rotation plane.

From these considerations, it is clear that an ambiguity may arise for the A tensor if the ENDOR resonance frequencies in an arbitrary plane show an angular dependence similar to Eq. (3). Under the assumption that the HF splitting is small with respect to the resonance field (high-field approximation), the eigenvalues of the spin Hamiltonian (2) are calculated as (see e.g. [16–18])

$$\begin{aligned} E(M_S, M_I) &= \mu_B g B_0 M_S + K(M_S) M_I \\ K^2(M_S) &= \vec{l} \cdot \vec{K}(M_S) \cdot \left[\vec{K}(M_S) \right]^T \cdot \vec{l} \\ \vec{K}(M_S) &= \frac{\vec{g} \cdot \vec{A}}{g} M_S - g_N \mu_N B_0 \mathbf{1}_{3 \times 3} \end{aligned} \quad (4)$$

and two ENDOR transitions occur at $|K(\pm 1/2)|$. Formally, $\vec{K} \cdot \vec{K}^T$ takes over the role of $\vec{g} \cdot \vec{g}$ in the left hand side of Eq. (3), but in general the angular dependence is more complicated, as also g exhibits angular dependence. However, in the data analysis for radicals in organic solids, the (often not analysed) \vec{g} tensor is nearly isotropic and all ENDOR measurements are performed at approximately the same resonance field B_0 , so that

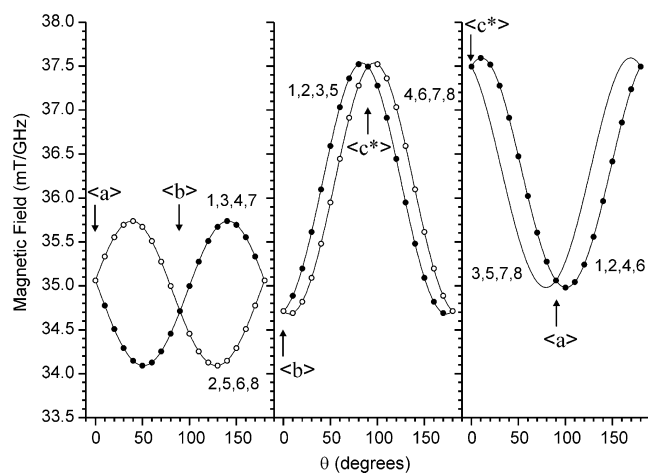


Fig. 1. Angular dependence of EPR field positions normalised to 1 GHz microwave frequency (in units mT/GHz) in three perpendicular rotation planes $\{ab\}$, $\{bc\}$ and $\{ca\}$. Symbols: Calculated for a non-symmetric paramagnetic centre with $S = 1/2$ in a crystal with monoclinic symmetry, exhibiting the \vec{g} tensor 1 in Table 1 for one of the symmetry-related centres (filled circles) and tensor 6 for the other (open circles). Note that in the $\{ca\}$ plane the resonance fields for the two symmetry-related centres coincide. Full lines: Calculated for \vec{g} tensors 1–8 in Table 1, labels refer to the tensor number in Table 1. The simulations illustrate that changing the sign of the M_{ij} element corresponds to changing the rotation sense in the ij plane ($i, j = 1, 2, 3$, see text).

$$\vec{K}(M_S) = \left[\vec{K}(M_S) \right]^T = M_S \vec{A} - g_N \mu_N B_0 \vec{1}_{3 \times 3} \quad (5)$$

is a very good approximation. The angular dependence of the resonance frequencies within each M_S multiplet, $|K(\pm 1/2)|$, then follows (3)

$$K^2(M_S) = \vec{l} \cdot \vec{K}(M_S) \cdot \vec{K}(M_S) \cdot \vec{l} = \alpha + \beta \cos 2\theta + \gamma \sin 2\theta \quad (6)$$

Hence, as for the \vec{g} tensor, for each $\vec{K}(M_S)$ tensor, two best-fit solutions can be derived from angular dependences in three planes. Via Eq. (5) an ambiguity in $\vec{K}(M_S)$ immediately leads to an ambiguity in \vec{A} as well. However, in order to fit the resonance frequencies in both M_S multiplets, the \vec{A} tensors calculated from the best-fit $K(1/2)$ and $K(-1/2)$ solutions should coincide, and we will illustrate in Section 3 that in general this is only the case for one of the solutions. Hence, in principle a Schonland ambiguity does not occur when determining hyperfine interactions from the angular dependence of ENDOR spectra. In practice, however, very often the nuclear resonances in only one of the multiplets can be used for analysis, and the problem of finding two best-fit \vec{A} solutions to the data reappears.

In addition, there are limiting cases where the Schonland conjugate \vec{A} tensors calculated for the two M_S multiplets are nearly identical. When the HF interaction is small compared to twice the nuclear Zeeman energy at all orientations (requiring a small isotropic value and a sufficiently small anisotropy), by neglecting terms quadratic in the HFC tensor Eq. (4) yields that the ENDOR frequencies are found at

$$|K(M_S)| \approx |AM_S - g_N \mu_N B_0| \quad (7)$$

$$\vec{A} = \vec{l} \cdot \vec{A} \cdot \vec{l}$$

and \vec{A} takes over the role of $\vec{K} \cdot \vec{K}$ in Eq. (6). This limiting case often occurs in practice, e.g. for γ -protons, especially when experiments are carried out at microwave frequencies higher than X-band (10 GHz).

In the opposite case of large HFCs, neglect of the term quadratic in the nuclear Zeeman energy in (4) leads to

$$|K(M_S)| = \left| \sqrt{\vec{l} \cdot \vec{A} \cdot \vec{A} \cdot \vec{l}} M_S - g_N \mu_N B_0 \frac{\vec{l} \cdot \vec{A} \cdot \vec{l}}{\sqrt{\vec{l} \cdot \vec{A} \cdot \vec{A} \cdot \vec{l}}} \right| \quad (8)$$

If the anisotropy in \vec{A} is small, it may be verified that for all magnetic field orientations $\vec{l} \cdot \vec{A} \cdot \vec{l} \approx \sqrt{\vec{l} \cdot \vec{A} \cdot \vec{A} \cdot \vec{l}}$, and a Schonland ambiguity arises in $\vec{A} \cdot \vec{A}$. Such HF tensors are typically observed for β -protons and the requirements for neglecting the high-order terms in the nuclear Zeeman frequency are best fulfilled at relatively low microwave frequencies. An ambiguity in $\vec{A} \cdot \vec{A}$ is also encountered when analysing the angular dependence of the HF splitting in the EPR spectrum for large \vec{A} , when the nuclear Zeeman interaction is completely neglected [4,5].

It is worth noting that in these two limiting cases Schonland conjugation becomes independent of B_0 or the microwave frequency (see also Section 3.1.3). In view of certain analogies in the calculation procedures for the Schonland conjugate of a \vec{g} tensor (see Section 3.1.1), one might be tempted to believe that the Schonland conjugate of an \vec{A} tensor can in general be found in this way. This is, however, contradicted by Eqs. (5) and (6). In Section 3.1.2 we illustrate the consequences of making use of the formulae valid in limiting cases for a system where HF and nuclear Zeeman interactions have the same order of magnitude.

The assumptions under which Eq. (5) is derived appear to restrict its scope, although in practice for a lot of systems it may safely be applied. It has been stated that for moderate \vec{g} anisotropy (total anisotropy of the order of 10% of the average g value), as encountered for many free radicals and simple transition metal

complexes, neglecting it introduces errors in obtained \vec{A} tensors in the order of experimental accuracy [4]. The simulations shown in the next section, based on full diagonalisation of the spin Hamiltonian (2), justify *a posteriori* that the order of perturbation used here is appropriate for HFCs up to ~ 100 MHz at moderate (~ 10 GHz, X-band) and higher microwave frequencies. This is in part a result of the fact that the higher order corrections to the ENDOR frequencies for Schonland conjugate tensors are very similar.

3. Practice: finding Schonland conjugate forms and selecting the right solution

In this section, we illustrate the consequences of Schonland ambiguity for the \vec{A} tensor in the analysis of angular dependent ENDOR spectra for various choices of the three rotation planes. Throughout this section experimental alternatives to performing measurements in a fourth independent plane are offered to select the correct form for the \vec{A} tensor out of the two Schonland conjugate possibilities. The first subsection also comprises a recapitulation of the (simpler, but more essential) problem for the \vec{g} tensor for readers less familiar with the problem discussed by Schonland [1].

Another important purpose of this section is to discuss how the other best-fit tensor to the ENDOR data can be found for literature cases where one suspects the wrong Schonland conjugate \vec{A} tensor was chosen. It is clear that the ENDOR spectroscopist, having the experimental data and simulation and fitting tools at hand, can find the other tensor by fitting, changing the rotation sense in one of the planes in which spectra have been recorded. We present here an analytical and fast way of calculating the Schonland conjugate tensor, based on the first order perturbation expressions in Eq. (4). It is important to bear in mind that for an ENDOR experiment, the origin of the ambiguity is in the ENDOR frequencies and hence is directly described by the \vec{K} tensor (Eqs. (5) and (6)) and only indirectly by the \vec{A} tensor. On the other hand, it is the \vec{A} tensor that bears information on the radical structure and that we are ultimately interested in, not \vec{K} .

As will be shown, the calculations imply a sign-indetermination in the principal values of \vec{K} , which introduces further ambiguity in the analysis. As this type of ambiguity also appears when determining other electron magnetic resonance properties (e.g. \vec{g} and/or \vec{A} from EPR spectra), we choose to follow a practical approach, which works quite well for the examples given. Moreover, it has recently been shown that pulsed ENDOR at high field [19] and/or for special pulse sequences [20,21] allows determining absolute signs of HFCs. Relative signs of different couplings, on the other hand, may be obtained from electron nuclear nuclear triple resonance experiments [4].

We will restrict ourselves to three cases often encountered in practice. The first is that of data points collected in three orthogonal planes, more specifically the $\{ab\}$, $\{bc\}$ and $\{ca\}$ planes for orthorhombic and $\{ab\}$, $\{bc\}$ and $\{c'a\}$ planes for monoclinic crystals. In the second subsection, extension to two cases relevant for monoclinic crystals are discussed: analysis of data in the $\{ab\}$, $\{bc\}$ and $\{c'a\}$ planes, and in the $\{a'b\}$, $\{bc\}$ and $\{c'a\}$ planes. For all these cases, due to the occurrence of site splitting, the ambiguity cannot be lifted by explicit knowledge of the rotation sense in the planes. Finally, in Section 3.3, we show that when lifting the degeneracy of the transitions, the Schonland ambiguity in principle is also lifted.

Throughout this section, we denote the tensor in which a Schonland-type ambiguity may arise ($\vec{g} \cdot \vec{g}$, $\vec{K}(M_S) \cdot \vec{K}(M_S)$), and in limiting cases \vec{A} or $\vec{A} \cdot \vec{A}$) as \vec{M} and its elements as M_{ij} ($i, j = 1, 2, 3$, with 1 corresponding to $\langle a \rangle$, 2 to $\langle b \rangle$ and 3 to $\langle c \rangle$). The elements of a Schonland conjugate tensor will be called \vec{M}_{ij} and those of a tensor related to \vec{M} by crystallographic point-group symmetry operations \vec{M}_{ij} .

3.1. Analysis of data in three orthogonal planes: $\{ab\}$, $\{bc^*\}$, $\{c^*a\}$

As explained by Schonland [1] and in Section 2, the occurrence of two best-fit solutions is the result of an ambiguity in the sign of the γ parameters of Eqs. (3) or (6), related to the sense of rotation in the three planes. Labelling the α , β and γ parameters with 3 for rotation in the $\{ab\}$ plane, with 1 for $\{bc^*\}$ and with 2 for $\{c^*a\}$, one finds (see Ref. [1])

$$\begin{aligned} M_{11} &= \alpha_3 + \beta_3 & M_{22} &= \alpha_3 - \beta_3 & M_{12} &= \gamma_3 \\ M_{22} &= \alpha_1 + \beta_1 & M_{33} &= \alpha_1 - \beta_1 & M_{23} &= \gamma_1 \\ M_{33} &= \alpha_2 + \beta_2 & M_{11} &= \alpha_2 - \beta_2 & M_{13} &= \gamma_2 \end{aligned} \quad (9)$$

For this particular choice of planes, i.e. the principal planes of the reference frame in which the \vec{g} and/or A tensors are represented, the ambiguity thus lies in the sign of the off-diagonal elements of the M tensor.

3.1.1. Illustration for the g tensor

We briefly illustrate the problem for the \vec{g} tensor. In Table 1, the principal g values and directions for the eight possible sign combinations of the off-diagonal elements of $M = \vec{g} \cdot \vec{g}$ are given. \vec{g} is calculated from M as its positive symmetrical square root, i.e. the tensor with the same principal directions and whose principal values are the positive square roots of those of M . It is well known that the sign of the principal g values cannot be determined in regular EPR experiments making use of linearly polarised microwaves, so in principle both positive and negative square roots should be considered. However, negative g values are not so common and prac-

Table 1

Principal values and directions of the positive symmetrical square roots of the $\vec{g} \cdot \vec{g}$ tensors obtained by considering the eight possible sign combinations of the off-diagonal elements for $\vec{g} \cdot \vec{g}$ calculated from the tensor in row 1

		Principal value	Direction cosines with respect to		
			a	b	c^*
1	Original M	1.9000	0.1632	0.0594	0.9848
		2.0000	0.7589	-0.6454	-0.0868
		2.1000	0.6304	0.7615	-0.1504
2	$\tilde{M}_{12} = -M_{12}$	1.8957	0.2338	0.1740	0.9566
		2.0086	0.7399	0.6064	-0.2912
		2.0957	-0.6307	0.7759	0.0130
3	$\tilde{M}_{13} = -M_{13}$	1.8957	-0.2338	0.1740	0.9566
		2.0086	-0.7399	0.6064	-0.2912
		2.0957	-0.6307	-0.7759	-0.0130
4	$\tilde{M}_{23} = -M_{23}$	1.8957	0.2338	-0.1740	0.9566
		2.0086	-0.7399	0.6064	0.2912
		2.0957	-0.6307	-0.7759	0.0130
5	$\tilde{M}_{12} = -M_{12}$ $\tilde{M}_{13} = -M_{13}$	1.9000	-0.1632	0.0594	0.9848
		2.0000	-0.7589	-0.6454	-0.0868
		2.1000	0.6304	-0.7615	0.1504
6	$\tilde{M}_{12} = -M_{12}$ $\tilde{M}_{23} = -M_{23}$	1.9000	0.1632	-0.0594	0.9848
		2.0000	-0.7589	-0.6454	0.0868
		2.1000	0.6304	-0.7615	-0.1504
7	$\tilde{M}_{13} = -M_{13}$ $\tilde{M}_{23} = -M_{23}$	1.9000	-0.1632	-0.0594	0.9848
		2.0000	0.7589	-0.6454	0.0868
		2.1000	0.6304	0.7615	0.1504
8	$\tilde{M}_{12} = -M_{12}$ $\tilde{M}_{13} = -M_{13}$ $\tilde{M}_{23} = -M_{23}$	1.8957	-0.2338	-0.1740	0.9566
		2.0086	0.7399	0.6064	0.2912
		2.0957	-0.6307	0.7759	-0.0130

Tensors 1, 5, 6 and 7, form a set with identical principal values, obtained by changing the sign of an even number of off-diagonal elements. The second set, containing 2, 3, 4 and 8, is obtained by changing the sign of an odd number of off-diagonal elements. The tensors within each set are transformed into one another by a symmetry operation of the orthorhombic group: sign changes in the elements M_{ij} and M_{jk} are equivalent to a twofold rotation around the (j) axis or a mirror operation through the (ik) plane ($i, j, k = a, b, c^*$).

tically excluded in the context of radicals in organic crystals, where only small deviations from $g = 2$ are expected. Hence, in this example it makes sense to restrict the choice of signs to positive. In Table 1 one can verify that the eight tensors split up in two sets (1, 5, 6, 7 and 2, 3, 4, 8). Within a set the tensors are transformed into one another by changing the signs of an even number of off-diagonal elements. These transformations are equivalent to the symmetry operations of the orthorhombic group (unity operator and twofold rotations around the x , y and z axes). As a consequence, all four tensors within a set have the same principal values. Changing the sign of an odd number of off-diagonal elements in M transforms a \vec{g} tensor of one set into one of the other. No symmetry operation can be found which transforms two tensors belonging to different sets into one another, which is immediately clear, because they have different principal values. The fact that changing an odd number of off-diagonal elements in sign leads to a tensor with different principal values can be readily understood considering that the secular equation for finding the principal values of $M = \vec{g} \cdot \vec{g}$ contains only one term (part of the constant term) sensitive to the signs of the off-diagonal elements, more specifically $M_{12}M_{13}M_{23}$. This further implies that possible ambiguity with respect to the principal values disappears, if at least one of these off-diagonal elements is zero (which happens e.g. if the radical has higher symmetry).

In Fig. 1 the calculated angular dependence for these eight tensors (solid lines) is compared to that expected to be measured for a non-symmetric paramagnetic centre (i.e. with triclinic or C_1 symmetry) in a monoclinic crystal with the first tensor in Table 1 as \vec{g} , for the first (filled circles) and the sixth tensor for the symmetry related centre (open circles). Fig. 1 clearly illustrates:

- (i) The degeneracy of the resonance fields in the $\{c^*a\}$ plane.
- (ii) Changing the sign of the off-diagonal element M_{ij} is equivalent to changing the rotation sense in the $\{ij\}$ plane.
- (iii) Two symmetry operations of the orthorhombic group do not belong to the monoclinic group. The resonance fields calculated for \vec{g} tensors 3, 5, 7 and 8 do not match the angular dependence in the $\{c^*a\}$ plane. In the following we continue with the example of a non-symmetric centre in a monoclinic crystal and will therefore only consider sign changes in the M_{12} or M_{23} elements.
- (iv) The two Schonland conjugate solutions (two sets of two tensors, (1, 6) and (2, 4), related within a set by monoclinic symmetry operations) fit the “experimental” points equally well and it is thus not possible to decide from these data which \vec{g} tensor is the correct form and which only fits in these three planes.

Fig. 1 also illustrates that in this example, where site splitting occurs, the ambiguity is essential: even if the rotation sense in the three planes is known, it cannot be decided from experiment whether the angular dependence of the filled circles in the $\{ab\}$ plane should be combined with that of the filled circles in the $\{bc^*\}$ plane, leading to tensor 1, or with that of the open circles, leading to the Schonland conjugate tensor 4.

3.1.2. Schonland conjugate of a HFC tensor

We now move on to the ambiguity for the A tensor and focus on the analysis of ^1H couplings by ENDOR spectroscopy. We assume that an ambiguity in the fitting result may arise because the transitions within only one of the M_S multiplets were fitted. Most often, these are the transitions occurring at the higher frequencies. For tensors with positive principal values, and hence a positive trace ($\text{Tr}(A) = 3A_{\text{iso}}$), as for β -protons, these are the $M_S = -1/2$ transitions, for α -protons with negative principal values and A_{iso} , they are those in the $M_S = 1/2$ multiplet. As $g_N(^1\text{H}) > 0$, in either case

$$\vec{K}_{\text{high}} = -\text{sign}(A_{\text{iso}}) \frac{\vec{A}}{2} - g_N \mu_N B_0 \vec{1}_{3 \times 3} \quad (10)$$

Like for \vec{g} , Schonland conjugate forms of \vec{K}_{high} , designated \vec{K}_{high} , can now be found by changing either the 12 or the 23 element of $\vec{M} = \vec{K}_{\text{high}} \cdot \vec{K}_{\text{high}}$ and taking its symmetrical square root. However, an important complication arises immediately, because the square root operation can only be performed when all three principal values of $\vec{K} \cdot \vec{K}$ are positive, which is most often the case, but not in general. Negative principal values of $\vec{K} \cdot \vec{K}$, however, indicate that a Schonland conjugate tensor \vec{A} cannot be found in such cases, as it would have complex principal values. In addition, for each principal \vec{K} value both the positive and the negative square root should in principle be considered. The problem of determining the signs of the principal values already occurs for \vec{K} in a first order analysis of ENDOR data within only one of the M_S multiplets, but inspection of the simulations for all possible sign combinations usually allows the selection of one solution as most plausible. This gives rise to one \vec{A} tensor solution, completely determined except for a possible overall sign reversal. When for some orientations the ENDOR frequencies of the other multiplet are also observed, the ambiguity in the relative signs of the \vec{A} tensor usually vanishes completely.

Returning to the problem of finding the Schonland conjugate form of \vec{K}_{high} , except when at least one of the principal HFC values has a sign opposite to that of A_{iso} and its magnitude is larger than or comparable to $2g_N \mu_N B_0$, all principal values of \vec{K}_{high} are negative and it is safe to assume that those of \vec{K}_{high} are all negative as well.

From the thus obtained tensor the Schonland conjugate tensor \vec{A} can be calculated by reversing Eq. (10)

$$\vec{A} = -2 \left(\vec{K}_{\text{high}} + g_N \mu_N B_0 \vec{1}_{3 \times 3} \right) \text{sign}(A_{\text{iso}}) \quad (11)$$

In the second row of Table 2 we show the principal values and directions of the resulting tensor Schonland conjugate to that given in the first row, for $g_N \mu_N B_0 = 14.9$ MHz ($B_0 = 350$ mT or $g = 2$ at 9.80 GHz, X-band), by changing the sign of M_{12} , i.e. considering ambiguity in the sign of γ_3 . As an illustration, the procedure for

obtaining the original tensor in row 1 of Table 2 from the Schonland conjugate form in row 2 is schematically represented in the Appendix. The original tensor is chosen to have considerable anisotropy and such principal values that for low to moderate microwave frequencies (e.g. X- or Q-band: 34 GHz) the HF and nuclear Zeeman interaction terms have the same order of magnitude. Moreover, the shape of tensor 1 is typical of an α -proton (provided that the signs of all principal values are negative). It is noticeable that the Schonland conjugate tensor 2 may well be interpreted as arising from a β -hydroxyl proton [12,13,22]. This illustrates that Schonland ambiguity can indeed have serious consequences for the radical model selection.

In the third row of Table 2 the Schonland conjugate tensor calculated from the low frequency ENDOR transitions is shown. It is obtained by considering a sign ambiguity in the 12 element of $\vec{K}_{\text{low}} \cdot \vec{K}_{\text{low}}$, where \vec{K}_{low} is calculated by reversing the sign of the first term on the right hand side of Eq. (10). The problem of determining

the signs of the principal \vec{K} values is somewhat more difficult here, as \vec{K}_{low} has positive as well as negative principal values. In principle, all sign combinations should be tested. We have chosen here to present only the result of which the determinant is closest to that of the original tensor, because this property directly appears in the formulae for the second order corrections to the ENDOR resonance frequencies (see e.g. [4]). We recognise, though, that next to the Schonland ambiguity, sign ambiguities may also be very pertinent, especially if $\vec{K}_{\text{low/high}}$ has principal values close to zero. Finally, rows 4 and 5 show the Schonland conjugate forms in the limiting cases with $\vec{M} = \vec{A}$ and $\vec{M} = \vec{A} \cdot \vec{A}$ (see Section 2). In Fig. 2 the calculated ENDOR angular dependences for all these tensors (lines) are compared to those expected to be measured (symbols) for the two symmetry-related centres of a non-symmetric centre in a monoclinic crystal, one of which has a HF interaction characterised by tensor 1 in Table 2.

From Table 2 we conclude that the various conjugate tensors differ strongly both in principal values and directions, not only from the original tensor but also considerably among each other. This presents a serious problem if one wants to validate structural models based on comparison with results from “first principles”

Table 2
Starting with an ENDOR determined HFC tensor \vec{A} in row 1, Schonland conjugate tensors are obtained by considering the ambiguity in the sign of the off-diagonal element M_{12} where the \vec{M} tensors are constructed according to the different possibilities outlined in Sections 2 and 3.1.2 (Eqs. (5), (7) and (8))

		Principal A values (MHz)	Direction cosines with respect to			
			(a)	(b)	(c')	
1	Original \vec{A} tensor	22.50	−0.6861	−0.5967	0.4162	
		41.25	−0.6287	0.7742	0.0734	
		60.00	−0.3660	−0.2113	−0.9063	
	\vec{M}	Principal \vec{A} values (MHz)	Direction cosines with respect to			$\Delta\theta$ (°)
			(a)	(b)	(c')	
2	$\vec{K}_{\text{high}} \cdot \vec{K}_{\text{high}}$	29.58	−0.8887	0.3478	0.2988	58.22
		33.16	0.2014	0.8815	−0.4271	58.37
		61.62	−0.4119	−0.3194	−0.8534	7.39
3	$\vec{K}_{\text{low}} \cdot \vec{K}_{\text{low}}$	27.44	−0.6621	−0.6397	0.3905	3.19
		43.48	−0.6587	0.7452	0.1039	2.96
		59.86	−0.3574	−0.1884	−0.9147	1.48
4	\vec{A}	28.27	−0.8516	0.4665	0.2391	66.08
		32.73	0.3061	0.8128	−0.4956	66.39
		62.75	−0.4256	−0.3488	−0.8350	9.52
5	$\vec{A} \cdot \vec{A}$	30.66	−0.9147	0.1669	0.3680	47.06
		33.67	0.0344	0.9396	−0.3406	47.10
		61.11	−0.4027	−0.2989	−0.8652	5.93

The calculation scheme for obtaining tensor 1 from 2, along with intermediate results, is found in Appendix A. All results are obtained assuming that the resonance frequency data are analysed in the $\{ab\}$, $\{bc\}$ and $\{c'a\}$ rotation planes. Calculations are performed for $g_N \mu_N B_0 = 14.902$ MHz, i.e. $B_0 = 350$ mT, or $g = 2$ at $\nu_{\text{MW}} = 9.8$ GHz. The last column gives the deviation in principal directions with the original tensor in the first row.

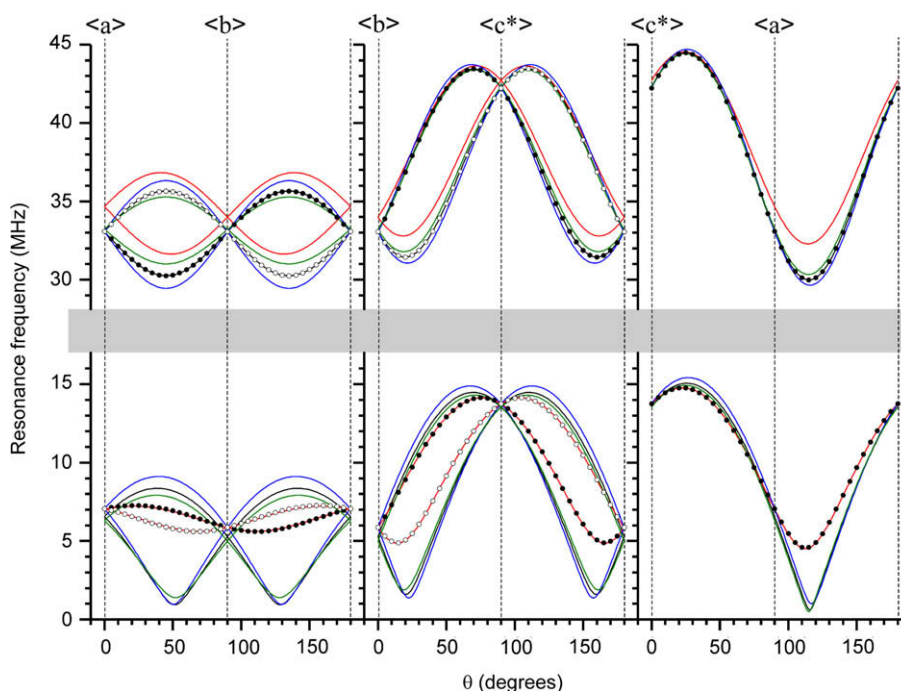


Fig. 2. Angular dependence of ENDOR frequency positions in $\{ab\}$, $\{bc^*\}$ and $\{c^*a\}$ planes, calculated at a microwave frequency of 9.8 GHz ($B_0 = 350$ mT for $g = 2$), for a non-symmetric centre with $S = 1/2$ and isotropic \vec{g} , interacting with a ^1H nucleus in a crystal with monoclinic symmetry. The principal values and directions of the HFC tensors used in the simulations are given in Table 2. Symbols: For a nucleus whose interaction is parameterized by the tensor in the first row of Table 2 for one of the sites (filled circles) and by its monoclinic symmetry-related tensor for the other (open circles). Full lines: For the two symmetry-related sites of an interaction characterised by the tensor in the second (black), third (red), fourth (blue), and fifth (green) tensor in Table 2.

DFT calculations. Not only should one realise that another best-fit tensor may exist, but one should also carefully consider how to calculate it, based on the details of the performed experiments. Fig. 2 clearly demonstrates that, in this general case with nuclear Zeeman and strongly anisotropic HF interactions of the same order of magnitude, an ambiguity can only arise if one considers only one of the M_S multiplets in the fitting. Furthermore, the conjugate tensors calculated with tensors 4 and 5, this is in the small and large HFC limits, respectively, do not render satisfactory agreement with the data points calculated for the original tensor. These observations are in agreement with our theoretical analysis in Section 2 and demonstrate that a Schonland ambiguity for HFC tensors in principle does not exist. Still, in cases of measurements of the transitions within only one of the M_S states in the three planes here considered, it is impossible to decide between two best-fit solutions (1 and 2 or 1 and 3 in Table 2). Thus, if for an \vec{A} tensor given in literature one wants to calculate a Schonland conjugate alternative, in addition to the principal values and directions of the tensor itself, one also needs to know at least if the high or low frequency branches have been considered for analysis. In the following subsections, it will become clear that other details of the experiment are also important for calculating Schonland conjugate tensors.

Analysis procedures to directly obtain the ij components of \vec{A} by fitting the angular dependence of the difference of the squares of the ENDOR frequencies in the two M_S multiplets ($|K^2(-1/2) - K^2(1/2)| = |g_N \mu_N B_0 \vec{l} \cdot \vec{A} \cdot \vec{l}|$, see [4]) may give the impression that an ambiguity with $\vec{M} = \vec{A}$ may still exist when both ENDOR transitions are considered in the analysis. Fig. 2 (blue lines) shows that in general this ambiguity is lifted by simulation of the actual transition frequencies.

3.1.3. Frequency dependence

Eqs. (10) and (11) demonstrate that, apart from the multiplet fitted, the Schonland conjugate \vec{A} tensor also depends on B_0 , and

thus on the microwave frequency at which experiments were performed. To illustrate this, Fig. 3 shows a comparison between calculated ENDOR frequencies for tensors 1 (open and filled circles) and 2 (fully drawn lines) in Table 2 at 34 GHz, focussing on the high frequency branches ($M_S = -1/2$). The two patterns do not perfectly match. This indicates that for sufficiently large and anisotropic HF interactions, complementing the measurements in the

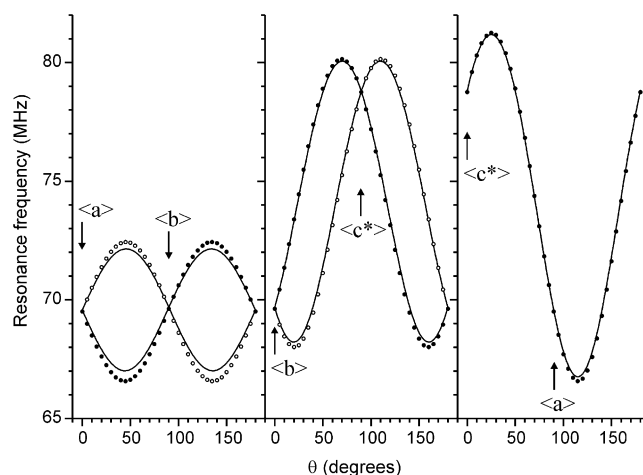


Fig. 3. Angular dependence in $\{ab\}$, $\{bc^*\}$ and $\{c^*a\}$ planes of the high frequency ENDOR branches ($M_S = -1/2$) for a non-symmetric centre with $S = 1/2$ interacting with a ^1H nucleus in a monoclinic crystal, calculated at a microwave frequency of 34 GHz (1214.6 mT for $g = 2$). Symbols: For one of the symmetry-related sites, the interaction is parameterized by the tensor 1 in Table 2 (filled circles) and for the other by its monoclinic symmetry-related tensor (open circles). Full lines: Simulations for the two symmetry-related centres, the interaction of one of which is parameterized by tensor 2 in Table 2. The discrepancy with the angular dependence represented by symbols demonstrates the importance of the microwave frequency in the calculation of the Schonland conjugate form of an \vec{A} tensor.

three planes with experiments at another microwave frequency may be considered as an alternative to measuring in a fourth plane for selecting the right best-fit solution, provided that the crystal can be accurately aligned. In general, it appears to be a less discriminating method.

Table 3 illustrates that in the limiting case of relatively small HFCs, i.e. at high microwave frequency, a real Schonland ambiguity arises. The Schonland conjugate \vec{A} tensors of tensor 1 in Table 2 are calculated from the low and high frequency multiplets at several microwave frequencies. At very high frequency the Schonland conjugate tensors for the high and low frequency branches practically coincide and are nearly equal to tensor 4 in Table 2. At low frequency, we see that in spite of the strong anisotropy, the tensors are also quite similar and, as expected, close to tensor 5 in Table 2. At intermediate frequencies the differences, both in principal values and directions ($\Delta\theta$) are quite considerable. Although not all individual parameters show monotonous relations on the microwave frequency, overall the deviation between the two different Schonland conjugate forms seems to go through a maximum where the HF and nuclear Zeeman interactions are closest in magnitude. These findings are indeed expected from Eqs. (10) and (11) and their analogues for \vec{K}_{low} .

3.2. Experimental data in non-orthogonal planes for monoclinic crystals

In experiments on monoclinic crystals, it may be more convenient to record angular dependences in the crystallographic $\{ab\}$, $\{bc\}$ and $\{ca\}$ planes, or to rotate the crystals around their $\langle a \rangle$ ($\{bc^*\}$ plane), $\langle b \rangle$ ($\{c^*a\}$ plane) and $\langle c \rangle$ axes ($\{a^*b\}$ plane). Because rotation in a fourth off-axis (tilted) plane allows deciding between Schonland conjugate tensors, changing the rotation planes should also have an influence on the relation between the best-fit tensors.

We assume that the angle between the positive $\langle c \rangle$ and $\langle a \rangle$ axes is $\beta = 90^\circ + \delta$. Hence, in the $\vec{e}_a, \vec{e}_b, \vec{e}_c$ frame, the unity vectors along the positive $\langle c \rangle$ and $\langle a^* \rangle$ axes have the Cartesian coordinates

$$\begin{aligned} \vec{e}_c &= (-\sin \delta, 0, \cos \delta) \\ \vec{e}_{a^*} &= (\cos \delta, 0, \sin \delta) \end{aligned} \quad (12)$$

The magnetic field orientations for positive rotations over an angle θ in the $\{bc\}$ and $\{a^*b\}$ planes are then given by

$$\begin{aligned} \vec{l}_{bc} &= (-\sin \theta \sin \delta, \cos \theta, \sin \theta \cos \delta) \\ \vec{l}_{a^*b} &= (\cos \theta \cos \delta, \sin \theta, \cos \theta \sin \delta) \end{aligned} \quad (13)$$

For rotation in the three crystallographic planes $\{ab\}$, $\{bc\}$, $\{ca\}$, Eq. (6) leads to the first and third expression in Eq. (9), but the second line should be replaced by

$$\begin{aligned} M_{22} &= \alpha_1 + \beta_1 \\ M_{33} \cos^2 \delta + M_{11} \sin^2 \delta - 2M_{13} \sin \delta \cos \delta &= \alpha_1 - \beta_1 \\ M_{23} \cos \delta - M_{12} \sin \delta &= \gamma_1 \end{aligned} \quad (14)$$

This result was also obtained by Schonland [1] using $\varepsilon = -\delta$. If we assume ambiguity in the sign of $\gamma_3 = M_{12} = -\tilde{M}_{12}$, all other matrix elements of the two best-fit tensors to the data points are identical, except for

$$\tilde{M}_{23} = M_{23} - 2M_{12} \tan \delta \quad (15)$$

For rotations around the crystallographic axes in the $\{a^*b\}$, $\{bc^*\}$ and $\{c^*a\}$ planes, the second and third line of Eq. (9) should be combined with

$$\begin{aligned} M_{11} \cos^2 \delta + M_{33} \sin^2 \delta + 2M_{13} \sin \delta \cos \delta &= \alpha_3 + \beta_3 \\ M_{22} &= \alpha_3 - \beta_3 \\ M_{12} \cos \delta + M_{23} \sin \delta &= \gamma_3 \end{aligned} \quad (16)$$

If we again assume ambiguity in the sign of γ_3 , all matrix elements for the two best-fit matrices \tilde{M} are identical, except for

$$\tilde{M}_{12} = -M_{12} - 2M_{23} \tan \delta \quad (17)$$

Knowing the ambiguity in \vec{M} , calculating the Schonland conjugate forms for \vec{g} or \vec{A} goes along the line set in Section 3.1.

In Fig. 4 we compare the angular dependence in the $\{a^*b\}$, $\{bc^*\}$ and $\{c^*a\}$ planes of the ENDOR transitions calculated with \vec{A} tensor 1 in Table 2 and its monoclinic symmetric equivalent (filled and open circles) with that for the Schonland conjugated tensors calculated with Eq. (17) (full lines) and with tensor 2 from Table 2 (dashed lines), which is the Schonland conjugated form for rotation in the three orthogonal planes. δ is taken 13° , making the angle between $\langle c \rangle$ and $\langle a \rangle$ 103° . As expected, the full lines perfectly match the dots but the dashed lines do not fit at all in the $\{a^*b\}$ plane. So, in addition to the M_5 multiplet and the microwave frequency, one should also carefully consider the planes in which the experiments

Table 3
Schonland conjugate tensors of the HFC tensor 1 in Table 2, calculated for the high (left) and low (right) frequency ENDOR transitions at various microwave frequencies ($g = 2$), considering the ambiguity in the sign of the off-diagonal M_{12} , arising when resonance frequency data are analysed in the $\{ab\}$, $\{bc^*\}$ and $\{c^*a\}$ rotation planes

ν_{MW} (GHz)	$g_N \mu_N B_0$ (MHz)	\vec{A} (MHz)	$\langle a \rangle$	$\langle b \rangle$	$\langle c^* \rangle$	\vec{A} (MHz)	$\langle a \rangle$	$\langle b \rangle$	$\langle c^* \rangle$	$\Delta\theta$ ($^\circ$)
1	1.52	30.48	-0.9121	0.2046	0.3553	30.86	-0.9160	0.1191	0.3830	5.16
		33.57	0.0693	0.9310	-0.3583	33.81	-0.0097	0.9480	-0.3181	5.17
		61.18	-0.4041	-0.3022	-0.8633	61.03	-0.4010	-0.2951	-0.8673	0.50
3	4.56	30.19	-0.9057	0.2591	0.3354	31.33	-0.9078	-0.0192	0.4190	16.71
		33.42	0.1197	0.9155	-0.3840	34.25	-0.1363	0.9582	-0.2515	16.76
		61.31	-0.4066	-0.3077	-0.8603	60.84	-0.3967	-0.2854	-0.8725	1.56
9.8	14.9	29.58	-0.8887	0.3478	0.2988	27.44	-0.6621	-0.6397	0.3905	61.15
		33.16	0.2014	0.8815	-0.4271	43.48	-0.6587	0.7452	0.1039	61.32
		61.62	-0.4119	-0.3194	-0.8534	59.86	-0.3574	-0.1884	-0.9147	8.86
34	51.7	28.87	-0.8681	0.4204	0.2641	27.18	0.8253	-0.5281	-0.2001	7.59
		32.92	0.2667	0.8435	-0.4662	32.34	0.3514	0.7576	-0.5501	8.43
		62.11	-0.4187	-0.3342	-0.8444	65.56	0.4421	0.3836	0.8108	3.67
94	142.9	28.53	-0.8584	0.4483	0.2493	27.96	-0.8435	0.4867	0.2272	2.68
		32.81	0.2908	0.8257	-0.4833	32.62	0.3223	0.7970	-0.5107	2.90
		62.44	-0.4225	-0.3424	-0.8392	63.23	-0.4297	-0.3576	-0.8292	1.12
270	410.5	28.37	-0.8541	0.4599	0.2429	28.17	-0.8489	0.4733	0.2352	0.93
		32.76	0.3006	0.8176	-0.4910	32.70	0.3116	0.8077	-0.5005	1.01
		62.63	-0.4244	-0.3464	-0.8366	62.89	-0.4268	-0.3516	-0.8332	0.38

The last column gives the deviation in principal directions between the two tensors in the row. The tensors at 9.8 GHz are identical to tensors 2 and 3 in Table 2.

have been carried out when calculating the Schonland conjugate \vec{A} tensor. Furthermore, it may be easily verified that when $(\vec{e}_a, \vec{e}_b, \vec{e}_c)$ is chosen as reference frame for representation of the \vec{g} and/or \vec{A} tensors, expressions identical to (15) and (17) are found, except for a sign change in the second term on the right hand side.

3.3. Lifting the degeneracy by rotating in tilted planes

As a final point, it will be illustrated that the degeneracy between the two best-fit solutions is lifted, along with that of the resonance fields or frequencies for symmetry-related centres, when rotating in tilted planes. So far, the role of symmetry-related centres in deriving the equations has not been explicitly considered, but the simulations demonstrated that the Schonland conjugate of a symmetry-related tensor is the symmetry-related of the Schonland conjugate. This is obvious in Figs. 1, 2 and 4 and can, for the special case of rotation in three orthogonal planes, be verified in Table 1. For the case of monoclinic crystals considered in Section 3.2, one may verify that for the symmetry-related centre, which has $\bar{M}_{12} = -M_{12}$, $\bar{M}_{13} = M_{13}$ and $\bar{M}_{23} = -M_{23}$, Eqs. (14) and (16) still lead to (15) and (17). On the other hand, rotating outside the $\{c^*a\}$ plane for the same monoclinic crystal, e.g. from $(0, \sin \varepsilon, \cos \varepsilon)$ to $(1, 0, 0)$ leads to the expressions

$$\begin{aligned} M_{33} \cos^2 \varepsilon + M_{22} \sin^2 \varepsilon + 2M_{23} \sin \varepsilon \cos \varepsilon &= \alpha_2 + \beta_2 \\ M_{11} &= \alpha_2 - \beta_2 \\ M_{13} \cos \varepsilon + M_{12} \sin \varepsilon &= \gamma_2 \end{aligned} \quad (18)$$

to be combined with, e.g. the first and second line of Eq. 9. Again considering an ambiguity in the sign of γ_3 , the two best-fit solutions for one site differ in the elements

$$\begin{aligned} \tilde{M}_{12} &= -M_{12} \\ \tilde{M}_{13} &= M_{13} + 2M_{12} \tan \varepsilon \end{aligned} \quad (19)$$

The symmetry-related tensor \vec{M} and its Schonland conjugate $\vec{\bar{M}}$ have to be related by the same equations. However, this leads to

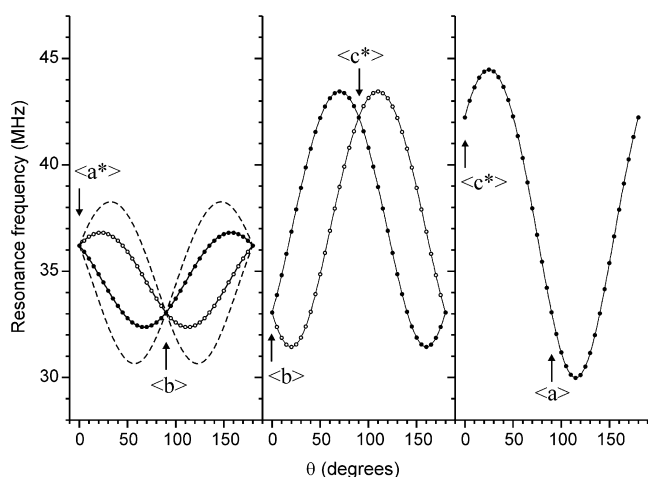


Fig. 4. Angular dependence in $\{a^*b\}$, $\{bc^*\}$ and $\{c^*a\}$ planes of the high frequency ENDOR branches for a non-symmetric centre with $S = 1/2$ interacting with a ^1H nucleus in a monoclinic crystal, calculated at a microwave frequency of 9.8 GHz (350 mT for $g = 2$). Symbols: For one of the symmetry-related sites, the interaction is parameterized by the tensor 1 in Table 2 (filled circles) and for the other by its monoclinic symmetry-related tensor (open circles). Lines: Simulations for the two symmetry-related centres, the interaction for one of which is parameterized by the Schonland conjugate tensor calculated using Eq. (17) (full lines). For comparison, the simulation with the Schonland conjugate tensor in case of rotation in three orthogonal planes (tensor 2 in Table 2) is also shown (dashed lines).

the conclusion that the Schonland conjugate tensors for the two symmetry-related centres are not related by symmetry, because

$$\begin{aligned} \vec{\bar{M}}_{13} &= \vec{M}_{13} + 2\vec{M}_{12} \tan \varepsilon = M_{13} - 2M_{12} \tan \varepsilon \\ \neq \vec{\bar{M}}_{13} &= \vec{M}_{13} = M_{13} + 2M_{12} \tan \varepsilon \end{aligned} \quad (20)$$

It should further be noted from the first line in Eq. (18), that the angular dependences of the two symmetry-related centres no longer coincide, as α and β should differ, since $\bar{M}_{23} = -M_{23}$. This lifting of the degeneracy is clearly observable in Fig. 5. Here, we compare simulated ENDOR angular dependences of the two symmetry-related sites for protons with a HFC tensor 1 in Table 2 and its Schonland conjugate according to Eq. (19). A small tilting angle of $\varepsilon = 2^\circ$ already leads to a significant difference in the tilted $\{c^*a\}$ plane: the symbols and lines coincide for only one of the symmetry-related centres. One can verify that for monoclinic crystals the ambiguity generally is also lifted when one of the rotation planes is not orthogonal to $\{c^*a\}$. For orthorhombic crystals, a similar lifting of the degeneracy is found for angular dependences in planes slightly tilted away from $\{ab\}$, $\{bc\}$ or $\{ca\}$ in the case of four symmetry-related centres.

In spite of this apparent advantage of tilted planes, measurements in crystal symmetry planes and directions should still be preferred, because crystals can be very accurately aligned to such orientations, just due to actual degeneracy of transitions. Inaccuracies in orientation and adjustment of the rotation planes in the fitting will inevitably lead to higher fitting errors and possibly also to additional (local) minima in the total error. Moreover, for systems where a large number of very similar paramagnetic centres are present with partially overlapping EPR and ENDOR spectra, accurate orientation to the $\langle a \rangle$, $\langle b \rangle$ and $\langle c^* \rangle$ axes where angular dependences of the interactions in various planes meet, is absolutely necessary, and reducing the number of lines by coincidence for symmetry-related centres may considerably facilitate the analysis.

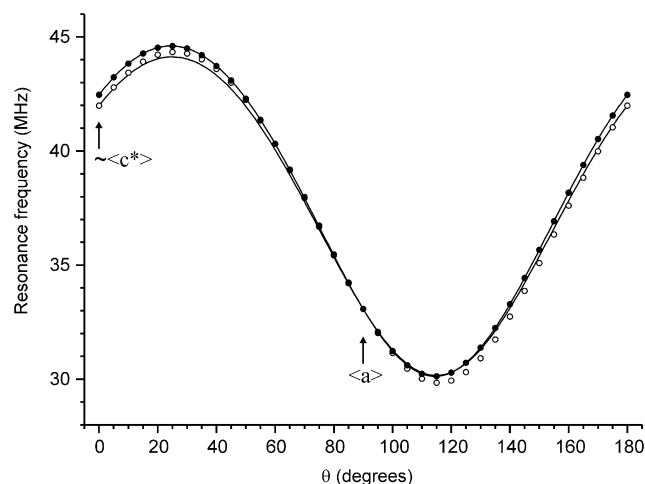


Fig. 5. Angular dependence in a slightly misaligned $\{c^*a\}$ plane (poles $\theta = 92^\circ$ and $\phi = 90^\circ$) of ENDOR frequencies calculated for a non-symmetric centre with $S = 1/2$ interacting with a ^1H nucleus. Symbols: With tensor 1 in Table 2 as \vec{A} for one of the symmetry-related centres (filled circles) and its monoclinic symmetry-related ($\vec{\bar{A}}$) for the other (open circles). Lines: With the Schonland conjugate of tensor 1 in Table 2 for one of the symmetry-related centres ($\vec{\bar{A}}$) and its monoclinic symmetry-related (\vec{A}). The discrepancy between the angular dependences for the second site (open circles and full lines) demonstrates that for this tilted plane, the symmetry-related of the Schonland conjugate tensor is not the Schonland conjugate of the symmetry-related tensor.

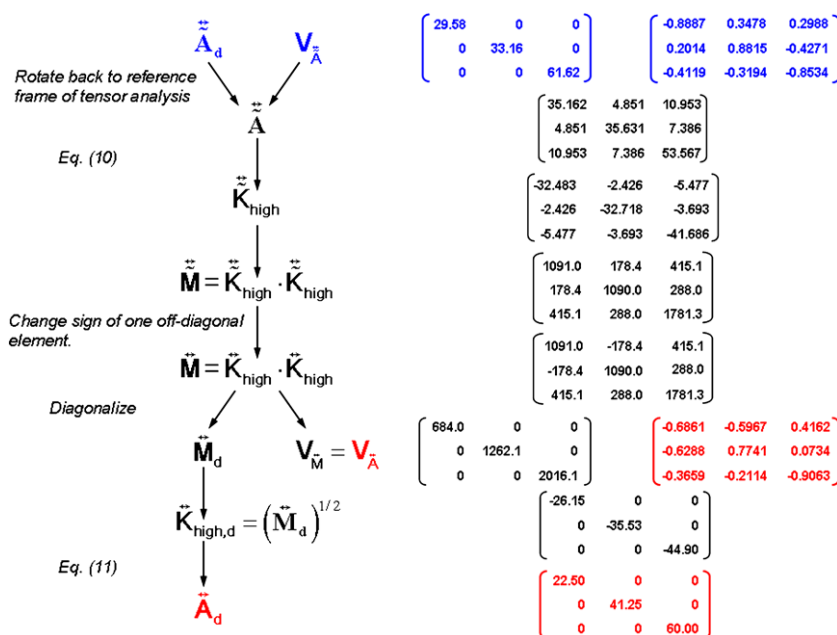


Fig. A. Starting from tensor 2 in Table 1, the Schonland conjugate tensor (tensor 1 in Table 2) is calculated under the assumption that high frequency ENDOR branches (K_{high} , Eqs. (10), (11)) are used in the analysis, and for experimental data in $\{ab\}$, $\{bc\}$ and $\{c'a\}$ planes. $g_{N\mu_N}B_0 = 14.902$ MHz ($B_0 = 350$ mT, $g = 2$ at 9.8 GHz). For the low frequency ENDOR branches (K_{low}), the first term on the right hand side of Eq. (10) and the complete right hand side of Eq. (11) should be changed in sign, as explained in the text. For experimental data in the $\{ab\}$, $\{bc\}$ and $\{ca\}$ planes, Schonland conjugation of M should be performed using Eq. (15), and for the $\{a'b\}$, $\{bc'\}$ and $\{c'a\}$ planes using Eq. (17).

4. Conclusions

In this paper, the possibility of obtaining two distinct, not symmetry-related, best-fit \vec{A} tensor solutions from angular dependent ENDOR measurements is explored for $I = 1/2$ nuclei interacting with an electronic spin $S = 1/2$ with (quasi) isotropic \vec{g} tensor. This problem is particularly important in theoretical interpretations and/or when radical identification based on “first principles” reproduction of \vec{A} tensors is envisaged. This is illustrated in an example where alternative Schonland conjugate forms of an \vec{A} tensor would lead to identification of the interacting nucleus as either a β -hydroxyl or an α -proton. We have confined the discussion to non-symmetric paramagnetic centres in orthorhombic and monoclinic crystals, for which Schonland reported a possible ambiguity for the \vec{g} tensor when restricting the measurements to three symmetry planes (see Section 3). If in the ENDOR measurements the nuclear transitions within the two M_S multiplets both may be observed, for each of them two best-fit \vec{A} tensors can be found, but in general only one tensor fits both the high and low frequency branches. Thus, in principle the Schonland ambiguity for \vec{A} tensors from ENDOR experiments does not exist. However, in practice tensors very often are obtained by fitting transitions within only one of the M_S multiplets, the other not being measured or difficult to analyse because of overlap with other lines, and an ambiguity in the fitting result may exist. We have shown how to calculate the other best-fit tensor, which we call Schonland conjugate, for a given best-fit \vec{A} tensor determined from ENDOR experiments. The result depends on various details of the experiment:

- (1) whether the high or low frequency branches were fitted;
- (2) the magnetic field/microwave frequency;
- (3) the rotation planes in which the data were gathered and also the choice of reference frame.

The results in this paper should encourage ENDOR spectroscopists to measure and analyse ENDOR data in both M_S multiplets, or, when this is not possible or conclusive (see limiting cases), to complement their measurements by experiments in a fourth plane or at another microwave frequency (less discriminating). The paper should enable computational researchers to recognize experimental circumstances which lead to the Schonland ambiguity and provide the means for calculating the other best-fitting tensors where these have not been considered in literature, without aid of simulation and or fitting tools.

Acknowledgment

The authors thank the Flemish Research Foundation (FWO-Vlaanderen) for financial support.

Appendix A

Fig. A.

References

- [1] D.S. Schonland, On the determination of principal g -values in electron spin resonance, Proc. Phys. Soc. Lond. 73 (1959) 788–792.
- [2] J.R. Morton, K.F. Preston, EPR spectroscopy of single crystals using a two-circle goniometer, J. Magn. Reson. 52 (1983) 457–474.
- [3] W.G. Waller, M.T. Rogers, Generalization of methods for determining g tensors, J. Magn. Reson. 9 (1972) 92–107.
- [4] N.M. Atherton, Principles of Electron Spin Resonance, Ellis Horwood–Prentice Hall, 1993.
- [5] A. Lund, T. Vänngård, Note on the determination of principal fine and hyperfine coupling constants in ESR, J. Chem. Phys. 42 (1965) 2979–2980.
- [6] H. De Cooman, E. Pauwels, H. Vrielinck, E. Sagstuen, F. Callens, M. Waroquier, Identification and conformational study of stable radiation-induced defects in sucrose single crystals using density functional theory calculations of electron magnetic resonance parameters, J. Phys. Chem. B 112 (2008) 7298–7307.
- [7] H. De Cooman, E. Pauwels, H. Vrielinck, A. Dimitrova, N. Yordanov, E. Sagstuen, M. Waroquier, F. Callens, Radiation-induced defects in sucrose single crystals, revisited: a combined electron magnetic resonance and density functional theory study, Spectrochim. Acta A 69 (2008) 1372–1383.
- [8] M. Tarpan, E. Sagstuen, E. Pauwels, H. Vrielinck, M. Waroquier, F. Callens, Combined electron magnetic resonance and density functional theory study of

- 10 K X-irradiated β -D-fructose single crystals, *J. Phys. Chem. A* 112 (2008) 3898–3905.
- [9] E. Pauwels, R. Declerck, V. Van Speybroeck, M. Waroquier, Evidence for a Grotthuss-like mechanism in the formation of the rhamnose alkoxy radical based on periodic DFT calculations, *Radiat. Res.* 169 (2008) 8–18.
- [10] K.T. Øhman, A. Sanderud, E.O. Hole, E. Sagstuen, Single crystals of L-O-serine phosphate X-irradiated at low temperatures: EPR, ENDOR, EIE and DFT studies, *J. Phys. Chem. A* 110 (2006) 9585–9596.
- [11] N. Jayatilaka, W.H. Nelson, Structure of radicals from X-irradiated guanine derivatives: an experimental and computational study of sodium guanosine dihydrate single crystals, *J. Phys. Chem. B* 111 (2007) 800–810.
- [12] H. De Cooman, G. Vanhaelewyn, E. Pauwels, E. Sagstuen, M. Waroquier, F. Callens, Radiation-induced radicals in glucose-1-phosphate (I). Electron paramagnetic resonance and electron nuclear double resonance analysis of in situ X-irradiated single crystals at 77 K, *J. Phys. Chem. B*, accepted for publication.
- [13] E. Pauwels, H. De Cooman, G. Vanhaelewyn, E. Sagstuen, F. Callens, M. Waroquier, Radiation-induced radicals in glucose-1-phosphate (II). DFT analysis of structures and possible formation mechanisms, *J. Phys. Chem. B*, accepted for publication.
- [14] W. Gordy, *Theory and Applications of Electron Spin Resonance Techniques of Chemistry* (volume XV), John Wiley and Sons, Inc., 1980.
- [15] S. Stoll, A. Schweiger, EasySpin, a comprehensive software package for spectral simulation and analysis in EPR, *J. Magn. Reson.* 178 (2006) 42–55.
- [16] J.A. Weil, J.H. Anderson, Direct field effects in electron paramagnetic resonance spectra, *J. Chem. Phys.* 35 (1961) 1410–1417.
- [17] M. Iwasaki, Second-order perturbation treatment of the general spin hamiltonian in an arbitrary coordinate system, *J. Magn. Reson.* 16 (1974) 417–423.
- [18] J.A. Weil, Comments on second-order spin-Hamiltonian energies, *J. Magn. Reson.* 18 (1975) 113–116.
- [19] B. Epel, P. Manikandan, P.M.H. Kroneck, D. Goldfarb, High-field ENDOR and the sign of the hyperfine coupling, *Appl. Magn. Reson.* 21 (2001) 287–297.
- [20] T.C. Yang, B.M. Hoffman, A Davies/Hahn multi-sequence for studies of spin relaxation in pulsed ENDOR, *J. Magn. Reson.* 181 (2006) 280–286.
- [21] J.J.L. Morton, N.S. Lees, B.M. Hoffman, S. Stoll, Nuclear relaxation effects in davies ENDOR variants, *J. Magn. Reson.* 191 (2008) 315–321.
- [22] S.E. Locher, H.C. Box, ESR-ENDOR studies of X-irradiated glucose-1-phosphate dipotassium salt, *J. Chem. Phys.* 72 (1980) 828–832.

Chapter 8

Conclusions

Radiation-induced radicals in crystals of sucrose and of the dipotassium salt of glucose 1-phosphate (K₂G1P) were studied. These are relevant mainly in the context of radiation dosimetry and the radiation chemistry of DNA.

Substantial progress was made in unravelling the complex scheme of radiation-induced processes in sucrose:

- the HFC tensors of the three dominant stable radicals (T1-T3) in sucrose were unambiguously determined – thus bringing clarity to conflicting results in the literature –, and their chemical structures were identified. The stable EPR spectrum of solid sucrose (which is used in dosimetric studies) is now to a large extent understood in terms of radical structures. No conclusive explanation was found, however, for the presence of two very similar – but distinguishable – radical species (T2 and T3).
- it has been established that these stable radical species are formed immediately (i.e. within less than 5 minutes) upon room-temperature (RT) irradiation, together with at least six semistable species. One of the latter (U1) initially dominates the EPR spectrum. The semistable species decay in a matter of hours.
- after *in-situ* X-ray irradiation at 10 K, at least nine different radical species are present. Of the four dominant species (R1, R2, R3 and R6), all except R3 were identified with certainty. Upon annealing to RT, the stable T1-T3 species and most likely also the semistable U1 species are formed.

Further EMR measurements and DFT calculations are necessary in order to obtain a (more) complete radiation-chemistry scheme of sucrose. In particular, an extended DFT study should be performed to identify the R3 radical present at 10 K, and EMR measurements after *in-situ* irradiation need to be carried out

at different temperatures between 10 K and RT, together with corresponding DFT calculations, in order to identify the precursors of the dominant stable radicals (T1, T2 and T3) and determine their precise formation mechanisms. In K2G1P, at least seven carbon-centred radical species are present after *in-situ* X-ray irradiation at 77 K. Four species, including the dominant one, were identified. The chemical structure of the dominant radical is identical to that of T2/T3 in sucrose and requires scission of the glucose-phosphate junction, a process that, in DNA, would lead to strand breaks. Knowledge of the formation mechanism of this species would be particularly interesting in this context. Upon annealing, the phosphate radical, which is observed after irradiation at RT and also requires scission of the glucose-phosphate linkage, is formed, but it could not be established which of the carbon-centred radicals is its precursor. EMR experiments after *in-situ* irradiation at 10 K, careful annealing experiments and molecular modelling of possible reaction routes should be employed to resolve these matters.

This study contributes to the more general goal of obtaining insight in the principles governing the radiation chemistry of solid-state carbohydrates and their derivatives. A crucial observation in this respect is that the dominant stable radicals in sucrose and the dominant radical after *in-situ* radiation at 77 K in K2G1P share two common features: the presence of a carbonyl group and a broken oxygen-carbon linkage (in the case of sucrose: the glycosidic bond; in the case of K2G1P: the sugar-phosphate bond). This suggests carbonyl-group formation and oxygen-carbon scission are common processes and indicates that the presence of a phosphate group is not essential for these processes to occur. These results should be extended with analogous research on similar compounds (e.g. other disaccharides), however, before more definite conclusions can be drawn. Knowledge of the formation mechanisms of these radicals (see above) could provide crucial information in this context.

Another important result from a more general point of view is that the radical formation in K2G1P is kinetically – and not thermodynamically – controlled, in correspondence with the results of some very recent studies in the literature on DNA model systems. Further research is required to establish whether this observation applies to other solid-state carbohydrates as well.

This doctoral thesis also provides ample proof of the value of DFT calculations in the study of solid-state organic radicals. They allow discriminating between the various plausible models that emerge from the experimental data, and were crucial for the (unambiguous) identification of most radical species in this work, including the dominant stable radicals in sucrose and the dominant radical after *in-situ* irradiation at 77 K in K2G1P. The accuracy with which the

experimental HFC tensors are reproduced often is remarkable.

DFT calculations were also successfully employed to obtain information that is experimentally not accessible:

- a detailed explanation for observed HFC tensors in terms of the electronic structure of the radical. This was especially the case for the T1 radical in sucrose.
- the influence of the crystalline environment on HFC and g tensors.
- (possible) migration paths for a proton after deprotonation from a cation.
- the conformational freedom of a radical, i.e. the presence and characteristics of different local minima on the potential-energy surface.
- the relative energies of radical species.

Accurate and reliable experimental data to compare the DFT calculations with are of course a prerequisite. Although this may seem straightforward, this study has clearly demonstrated that there are many pitfalls one should be aware of, including sign ambiguities and Schonland ambiguities. It is *the combination* of detailed EMR measurements and advanced DFT calculations that provides a successful and reliable strategy for studying solid-state organic radicals.

Appendix A

Atomic coordinates of the sucrose lattice

Table A.1: Coordinates of the 45 atoms of a sucrose molecule in sucrose single crystals, as reported in Ref. [111]. The coordinates of the other 45 atoms in the unit cell are obtained by a monoclinic $\langle x,y,z \rangle$ to $\langle -x,y+1/2,-z \rangle$ symmetry operation on these coordinates. Carbon atoms are numbered as CX ($X=1-6,1'-6'$) according to the IUPAC convention, hydrogen atoms and oxygen atoms bound to CX are labelled HX and OX respectively, hydroxy hydrogen atoms at CX are labelled HOX. The glycosidic oxygen atom and the glucose and fructose ring oxygen atoms are denoted O1, O5 and O5' respectively.

Atom	Coordinates (10^{-10} m)		
	a*	b	c
C1	3.173	3.116	3.031
C2	3.311	4.133	4.172
C3	3.024	5.543	3.683
C4	3.961	5.841	2.517
C5	3.804	4.797	1.415
C6	4.844	4.969	0.316
C1'	1.092	1.141	3.968
C2'	1.319	1.677	2.559
C3'	0.077	1.660	1.649
C4'	0.686	1.450	0.267
C5'	1.867	0.534	0.568
C6'	3.062	0.713	-0.343
O1	1.816	3.015	2.621
O2	2.432	3.791	5.241
O3	3.263	6.509	4.702

Continued on next page

Continued from previous page

Atom	Coordinates (10^{-10} m)		
	a*	b	c
O4	3.694	7.087	1.914
O5	3.994	3.471	1.940
O6	6.156	4.746	0.803
O1'	0.321	2.050	4.746
O3'	-0.779	2.766	1.766
O4'	-0.225	0.847	-0.639
O5'	2.246	0.822	1.932
O6'	3.456	2.072	-0.483
H1	3.545	2.133	3.364
H2	4.359	4.086	4.518
H3	1.982	5.613	3.343
H4	4.995	5.816	2.898
H5	2.794	4.886	0.981
H6a	4.797	5.983	-0.061
H6b	4.629	4.289	-0.508
H1'a	0.552	0.195	3.920
H1'b	2.064	0.950	4.436
H3'	-0.523	0.770	1.897
H4'	1.042	2.413	-0.120
H5'	1.552	-0.521	0.521
H6'a	3.888	0.104	0.032
H6'b	2.806	0.347	-1.334
HO2	2.882	3.241	5.906
HO3	2.456	6.668	5.196
HO4	3.608	7.759	2.525
HO6	6.369	3.816	0.757
HO1'	0.897	2.826	4.869
HO3'	-0.328	3.560	1.442
HO4'	-0.178	1.339	-1.481
HO6'	3.681	2.420	0.396

Appendix B

Atomic coordinates of the K2G1P lattice

Table B.1: Coordinates of 35 atoms in K2G1P single crystals, as reported in Ref. [165]. The coordinates of the other 35 atoms in the unit cell are obtained by a monoclinic $\langle x, y, z \rangle$ to $\langle -x, y+1/2, -z \rangle$ symmetry operation on these coordinates. Carbon atoms are numbered as CX (X=1-6) according to the IUPAC convention, hydrogen atoms and oxygen atoms bound to CX are labelled HX and OX respectively, hydroxy hydrogen atoms at CX are labelled HOX. The ring oxygen is labelled as O5 and 'W' in the label indicates the atom is part of a crystal water molecule.

Atom	Coordinates (10^{-10} m)		
	a*	b	c
K1	9.273	4.115	-0.146
K2	4.134	0.034	5.912
P	1.995	4.595	-0.844
C1	2.572	2.352	0.492
C2	2.181	1.757	1.844
C3	3.073	2.310	2.948
C4	4.528	2.051	2.606
C5	4.873	2.526	1.193
C6	6.244	2.031	0.787
O1	2.349	3.743	0.507
O2	0.826	2.018	2.187
O3	2.758	1.690	4.194
O4	5.372	2.715	3.536
O5	3.933	2.039	0.216
O6	6.711	2.634	-0.415
O7	0.855	5.491	-0.397

Continued on next page

Continued from previous page

Atom	Coordinates (10^{-10} m)		
	a*	b	c
O8	3.246	5.391	-1.176
O9	1.600	3.624	-1.938
WO1	9.346	1.862	1.703
WO2	8.355	3.918	-2.906
H1	2.049	2.004	-0.212
H2	2.333	0.731	1.807
H3	2.931	3.250	3.046
H4	4.666	1.065	2.687
H5	4.813	3.638	1.186
H6a	6.852	2.266	1.400
H6b	6.097	1.047	0.746
HO2	0.284	1.634	1.566
HO3	2.470	2.356	4.806
HO4	5.882	2.176	3.892
HO6	6.931	2.148	-0.949
WH1a	9.038	1.670	2.335
WH1b	9.901	2.374	1.833
WH2a	8.440	3.096	-3.130
WH2b	9.146	4.098	-3.196

Bibliography

- [1] L. G. Christophorou. *Atomic and molecular radiation physics*. Wiley-Interscience, 1971.
- [2] D. Becker, A. Adhikary, and M. D. Sevilla. *The role of charge and spin migration in DNA radiation damage*, Ch. 7, pages 139-175, in *Charge migration in DNA: perspectives from physics, chemistry, and biology*, T. Chakraborty (ed.). Springer, 2007.
- [3] W. A. Bernhard and M. D. Close. *DNA damage dictates the biological consequences of ionizing irradiation: the chemical pathways*, Ch. 15, pages 431-470, in *Charged particle and photon interactions with matter: chemical, physicochemical and biological consequences with applications*, A. Mozumder and Y. Hatano (eds.). Marcel Dekker, New York, 2004.
- [4] W. A. Bernhard. Solid-state radiation chemistry of DNA: the bases. *Adv. Radiat. Biol.*, 9:199–280, 1981.
- [5] E. Sagstuen and E. O. Hole. *Radiation produced radicals*, Ch. 9, pages 325-382, in *Electron paramagnetic resonance: a practitioner's toolkit*, A. Mozumder and Y. Hatano (eds.). J. Wiley & Sons, Inc., Hoboken, NJ, 2009.
- [6] C. von Sonntag. *The chemical basis of radiation biology*. Taylor and Francis, London, 1987.
- [7] C. von Sonntag and H.-P. Schuchmann. *Carbohydrates*, Ch. 18, pages 481-511, in *Radiation chemistry: present status and future trends*, C. D. Jonah and B. S. M. Rao (eds.), Elsevier science B.V., 2001.
- [8] K. P. Madden and W. A. Bernhard. A 1,2 hydrogen shift and other thermally induced free-radical reactions in X-irradiated methyl alpha-D-glucopyranoside single-crystals – an ESR-ENDOR study. *J. Chem. Phys.*, 84:1712–1717, 1980.

- [9] C. von Sonntag. *Free-radical-induced DNA damage and its repair: a chemical perspective*. Springer, 2006.
- [10] D. M. Close. *From the primary radiation induced radicals in DNA constituents to strand breaks: low temperature EPR/ENDOR studies*, Ch. 18, pages 493-530, in *Radiation induced molecular phenomena in nucleic acids: a comprehensive theoretical and experimental analysis*, M. K. Shukla and J. Leszczynski (eds.). Kluwer Academic Publishers Group, 2008.
- [11] L. Sanche. *Low energy electron damage to DNA*, Ch. 19, pages 531-576, in *Radiation induced molecular phenomena in nucleic acids: a comprehensive theoretical and experimental analysis*, M. K. Shukla and J. Leszczynski (eds.). Kluwer Academic Publishers Group, 2008.
- [12] A. Kumar and M. D. Sevilla. *Radiation effects on DNA: theoretical investigations of electron, hole and excitation pathways to DNA damage*, Ch. 20, pages 577-618, in *Radiation induced molecular phenomena in nucleic acids: a comprehensive theoretical and experimental analysis*, M. K. Shukla and J. Leszczynski (eds.). Kluwer Academic Publishers Group, 2008.
- [13] A. Kumar and M. D. Sevilla. The role of $\pi\sigma^*$ excited states in electron-induced DNA strand break formation: a time-dependent density functional theory study. *J. Am. Chem. Soc., Comm.*, 130:2130–2131, 2008.
- [14] P. Swiderek. Fundamental processes in radiation damage of DNA. *Angew. Chem., Int. Ed.*, 45:4056–4059, 2006.
- [15] A. Adhikary, D. Becker, S. Collins, J. Koppen, and M. D. Sevilla. C5'- and C3'-sugar radicals produced via photo-excitation of one-electron oxidized adenine in 2'-deoxyadenosine and its derivatives. *Nucl. Acids Res.*, 34:1501–1511, 2006.
- [16] A. Kumar and M. D. Sevilla. Photoexcitation of dinucleoside radical cations: a time-dependent density functional study. *J. Phys. Chem. B*, 110:24181–24188, 2006.
- [17] D. K. Khanduri, S. Collins, A. Kumar, A. Adhikary, and M. D. Sevilla. Formation of sugar radicals in RNA model systems and oligomers via excitation of guanine cation radical. *J. Phys. Chem. B*, 112:2168–2178, 2008.
- [18] W. K. Pogozelski and T. D. Tullius. Oxidative strand scission of nucleic acids: routes initiated by hydrogen abstraction from the sugar moiety. *Chem. Rev.*, 98:1089–1107, 1998.

- [19] E. O. Hole and E. Sagstuen. Free-radical formation in crystals of 2'-deoxyguanosine 5'-monophosphate irradiated at 15-K – an electron-spin-resonance study. *Radiat. Res.*, 109:190–205, 1987.
- [20] E. O. Hole, W. H. Nelson, E. Sagstuen, and D. M. Close. Free-radical formation in single-crystals of 2'-deoxyguanosine 5'-monophosphate tetrahydrate disodium salt – an EPR ENDOR study. *Radiat. Res.*, 129:119–138, 1992.
- [21] D. M. Close. Where are the sugar radicals in irradiated DNA? *Radiat. Res.*, 147:663–673, 1997.
- [22] M. G. Debije and W. A. Bernhard. Electron paramagnetic resonance evidence for a C3' sugar radical in crystalline d(CTCTCGAGAG) X-irradiated at 4 K. *Radiat. Res.*, 155:687–692, 2001.
- [23] B. Weiland and J. Hüttermann. Free radicals from X-irradiated 'dry' and hydrated lyophilized DNA as studied by electron spin resonance spectroscopy: analysis of spectral components between 77K and room temperature. *Int. J. Radiat. Biol.*, 74:341–358, 1998.
- [24] W. Gerlach and O. Stern. Das magnetische Moment des Silberatoms. *Z. Phys.*, 9:353–355, 1922.
- [25] A. Abragam and B. Bleaney. *Electron paramagnetic resonance of transitions ions*. Clarendon Press, Oxford, 1970.
- [26] N. M. Atherton. *Principles of electron spin resonance*. Ellis Horwood PTR Prentice Hall, 1993.
- [27] J.-M. Spaeth, J. R. Niklas, and R. H. Bartram. *Structural analysis of point defects in solids: an introduction to multiple magnetic resonance spectroscopy*. Springer-Verlag, 1992.
- [28] D. S. Schonland. On the determination of principal g-values in electron spin resonance. *Proc. Phys. Soc. Lond.*, 73:788–792, 1959.
- [29] J. R. Pilbrow. *Transition ion electron paramagnetic resonance*. Oxford Science Publications, Clarendon Press, Oxford, 1990.
- [30] J. A. Weil, J. R. Bolton, and J. E. Wertz. *Electron paramagnetic resonance – elementary theory and practical applications*. John Wiley & Sons, Inc., New York, 1994.
- [31] Bruker Analytische Messtechnik GMBH. *ER Series User's Manual*. Karlsruhe, 1983.

- [32] <http://www.fys.uio.no/biofysikk/eee/esr.htm>.
- [33] W. H. Nelson. Estimation of errors in eigenvalues and eigenvectors from magnetic resonance results by use of linear data-fitting techniques. *J. Magn. Reson.*, 38:71–78, 1980.
- [34] W. H. Nelson and C. R. Nave. ESR and ENDOR studies of radicals produced in hydroxyproline single crystals by x irradiation at low temperature. *J. Chem. Phys.*, 74:2710–2716, 1981.
- [35] S. Stoll and A. Schweiger. EasySpin, a comprehensive software package for spectral simulation and analysis in EPR. *J. Magn. Reson.*, 178:42–55, 2006.
- [36] R. G. Parr and W. Yang. *Density functional theory of atoms and molecules*. Oxford University Press, New York, 1989.
- [37] W. Koch and M. C. Holthausen. *A chemist's guide to density functional theory*. Wiley-VCH, 2000.
- [38] M. Kaupp, M. Bühl, and G. M. Vladimirov. *Calculation of NMR and EPR parameters: theory and applications*. Wiley-VCH, 2004.
- [39] A. Lund and M. Shiotani. *EPR of free radicals in solids: trends in methods and applications*. Springer, 2003.
- [40] R. Declerck. *Development and implementation of theoretical methods for the calculation of EPR parameters in periodic simulations*. PhD thesis, Center for Molecular Modeling, Ghent University, 2008.
- [41] N. W. Ashcroft and N. D. Mermin. *Solid state physics*. Brooks/Cole, Philadelphia, 1976.
- [42] P. Hohenberg and W. Kohn. Inhomogeneous electron gas. *Phys. Rev.*, 136:B864, 1964.
- [43] W. Kohn and L. J. Sham. Self-consistent equations including exchange and correlation effects. *Phys. Rev.*, 140:A1133, 1965.
- [44] J. M. Frisch *et al.*, Gaussian 03, Revision D.01. Gaussian, Inc., Wallingford, CT, 2004.
- [45] F. Neese. Prediction of electron paramagnetic resonance g values using coupled perturbed Hartree-Fock and Kohn-Sham theory. *J. Chem. Phys.*, 115:11080–11096, 2001.
- [46] <http://www.cpmid.org>.

- [47] R. Declerck, V. Van Speybroeck, and M. Waroquier. First-principles calculation of the EPR g tensor in extended periodic systems. *Phys. Rev. B*, 73:115113–1–8, 2006.
- [48] <http://cp2k.berlios.de>.
- [49] V. Weber, M. Iannuzzi, S. Giani, Hutter J., R. Declerck, and M. Waroquier. Magnetic linear response properties calculations with the Gaussian and augmented-plane-wave method. *J. Chem. Phys.*, *submitted*.
- [50] R. Declerck, E. Pauwels, V. Van Speybroeck, and M. Waroquier. First-principles calculations of hyperfine parameters with the Gaussian and augmented-plane-wave method: application to radicals embedded in a crystalline environment. *Phys. Rev. B*, 74:245103–1–8, 2006.
- [51] H. Hellmann. *Einführung in die Quantenchemie*. Leipzig: Franz Deuticke, 1937.
- [52] R. P. Feynman. Forces in molecules. *Phys. Rev.*, 56:340, 1939.
- [53] P. A. M. Dirac. The quantum theory of the electron. *Proc. Roy. Soc.*, A117:610–624, 1928.
- [54] P. A. M. Dirac. The quantum theory of the electron, Part ii. *Proc. Roy. Soc.*, A118:351–361, 1928.
- [55] G. Breit. The effect of retardation on the interaction of two electrons. *Phys. Rev.*, 34:553–573, 1929.
- [56] L. L. Foldy and S. A. Wouthuysen. On the Dirac theory of spin-1/2 particles and its non-relativistic limit. *Phys. Rev.*, 78:29–36, 1950.
- [57] P. A. M. Dirac. Note on exchange phenomena in the Thomas atom. *Proc. Cambridge Philos. Soc.*, 26:376, 1930.
- [58] S. H. Vosko, L. Wilk, and M. Nusair. Accurate spin-dependent electron liquid correlation energies for local spin-density calculations: a critical analysis. *Can. J. Phys.*, 58:1200–1211, 1980.
- [59] A. D. Becke. Density-functional exchange-energy approximation with correct asymptotic-behavior. *Phys. Rev. A*, 38:3098–3100, 1988.
- [60] J. P. Perdew. Density-functional approximation for the correlation-energy of the inhomogeneous electron-gas. *Phys. Rev. B*, 33:8822–8824, 1986.

- [61] C. Lee, W. Yang, and R. G. Parr. Development of the Colle-Salvetti correlation-energy formula into a functional of the electron-density. *Phys. Rev. B*, 37:785–789, 1988.
- [62] A. D. Becke. A new mixing of Hartree-Fock and local density-functional theories. *J. Chem. Phys.*, 98:1372–1377, 1993.
- [63] P. J. Stephens, F. J. Devlin, C. F. Chabalowski, and M. J. Frisch. Ab-initio calculation of vibrational absorption and circular-dichroism spectra using density-functional force-fields. *J. Phys. Chem.*, 98:11623–11627, 1994.
- [64] G. Lippert, J. Hutter, and M. Parrinello. *Mol. Phys.*, 92:477–488, 1997.
- [65] G. Lippert, J. Hutter, and M. Parrinello. *Theor. Chem. Acc.*, 103:124–140, 1999.
- [66] M. Krack and M. Parrinello. *Phys. Chem. Chem. Phys.*, 2:2105–2112, 2000.
- [67] R. Declerck, E. Pauwels, V. Van Speybroeck, and M. Waroquier. Molecular environment and temperature dependence of hyperfine interactions in sugar crystal radicals from first principles. *J. Phys. Chem. B*, 112:1508–1514, 2008.
- [68] E. Pauwels, T. Verstraelen, H. De Cooman, V. Van Speybroeck, and M. Waroquier. Temperature study of a glycine radical in the solid state adopting a DFT periodic approach: vibrational analysis and comparison with EPR experiments. *J. Phys. Chem. B*, 112:7618–7630, 2008.
- [69] C. J. Pickard and F. Mauri. First-principles theory of the EPR g tensor in solids: defects in quartz. *Phys. Rev. Lett.*, 88:086403/1–4, 2002.
- [70] P. E. Blöchl. Projector augmented-wave method. *Phys. Rev. B*, 50:17953–17979, 1994.
- [71] H. C. Box. *Radiation effects: ESR and ENDOR analysis*. Academic Press, New York, 1977.
- [72] S. I. Weissman. Hyperfine splittings in polyaromatic free radicals. *J. Chem. Phys.*, 22:1378–1379, 1954.
- [73] E. Fermi. *Z. Physik.*, 60:320, 1930.
- [74] C. P. Slichter. *Principles of magnetic resonance*. Springer, 1978.
- [75] W. Gordy. *Theory and applications of electron spin resonance*. Wiley, New York, 1980.

- [76] H. M. McConnell, C. Heller, T. Cole, and R. W. Fessenden. Radiation damage in organic crystals I. $\text{CH}(\text{COOH})_2$ in malonic acid. *J. Am. Chem. Soc.*, 82:766–775, 1960.
- [77] S. I. Weissman, J. Townsend, D. E. Paul, and G. E. Pake. Hyperfine splittings in the paramagnetic resonances of free radicals. *J. Chem. Phys.*, 21:2227, 1953.
- [78] B. Venkataraman and G. K. Fraenkel. Proton hyperfine interactions in paramagnetic resonance of semiquinones. *J. Am. Chem. Soc.*, 77:2707–2713, 1955.
- [79] H. M. McConnell. Indirect proton hyperfine interactions in the paramagnetic resonance spectra of aromatic free radicals. *J. Chem. Phys.*, 24:764–766, 1956.
- [80] H. M. McConnell and D. B. Chesnut. Theory of isotropic hyperfine interactions in π -electron radicals. *J. Chem. Phys.*, 28:107–117, 1958.
- [81] R. W. Fessenden and R. H. Schuler. Electron spin resonance studies of transient alkyl radicals. *J. Chem. Phys.*, 39:2147–2195, 1963.
- [82] J. E. Wertz and J. R. Bolton. *Electron spin resonance: elementary theory and practical applications*. McGraw-Hill, New York, 1972.
- [83] A. J. Dobbs, B. C. Gilbert, and R. O. C. Norman. Electron spin resonance evidence for non-planarity in some oxygen-conjugated carbon radicals. *J. Chem. Soc. D*, 23:1353, 1969.
- [84] A. J. Dobbs, B. C. Gilbert, and R. O. C. Norman. Electron-spin resonance studies .32. information from hyperfine splittings for aliphatic radicals about shape and conformation. *J. Chem. Soc., Perkin Trans. 2*, (6):786, 1972.
- [85] A. Hosseini, A. Lund, and E. Sagstuen. EPR and ENDOR studies of single crystals of 2-oxazolidinone X-irradiated at 295 K. *Phys. Chem. Chem. Phys.*, 4:6086–6091, 2002.
- [86] P. A. Erling and W. H. Nelson. Dependence of α -proton hyperfine couplings on free radical geometry. *J. Phys. Chem. A*, 108:7591–7595, 2004.
- [87] W. A. Bernhard. The use of alpha hyperfine coupling tensors as a measure of unpaired spin density and free radical geometry. *J. Chem. Phys.*, 81:5928–5936, 1984.

- [88] A. J. Dobbs, B. C. Gilbert, and R. O. C. Norman. Electron spin resonance studies .27. geometry of oxygen-substituted alkyl radicals. *J. Chem. Soc. A*, (1):124, 1971.
- [89] H. M. McConnell and J. Strathdee. Theory of anisotropic hyperfine interactions in π -electron radicals. *Mol. Phys.*, 32:129–138, 1959.
- [90] W. Derbyshire. The coupling between an unpaired electron spin and a proton two bonds away. *Mol. Phys.*, 5:225–231, 1962.
- [91] C. Heller and H. M. McConnell. Radiation damage in organic crystals .2. Electron spin resonance of (CO₂H)CH₂CH(CO₂H) in beta-succinic acid. *J. Chem. Phys.*, 32:1535–1539, 1960.
- [92] J. R. Morton. Electron spin resonance spectra of oriented radicals. *Chem. Rev.*, 64:453–471, 1964.
- [93] W. A. Bernhard, D. M. Close, K. R. Mercer, and J. C. Corelli. ESR of X-irradiated single-crystals of 3'-cytidylic acid – hydrogen abstraction from C5' of sugar moiety. *Radiat. Res.*, 66:19–32, 1976.
- [94] H. C. Box, E. E. Budzinski, and H. G. Freund. The gamut of alkoxy radicals. *J. Chem. Phys.*, 81:4898–4902, 1984.
- [95] A.-O. Colson and M. D. Sevilla. Structure and relative stability of deoxyribose radicals in a model DNA backbone: ab initio molecular orbital calculations. *J. Phys. Chem.*, 99:3867–3874, 1995.
- [96] D. Suryanarayana and M. D. Sevilla. INDO study of the anion radicals of acetic acid and acetamide. Nonplanarity and barriers to methyl group rotation. *J. Phys. Chem.*, 84:3045–3049, 1980.
- [97] D. H. Whiffen. The greater-than CH₂ hyperfine coupling in cyclohexadienyl. *Mol. Phys.*, 6:223–224, 1963.
- [98] C.-L. Ko and H. C. Box. Exchangeable proton couplings in free-radicals – radiation products of hydroxyproline HCL. *J. Chem. Phys.*, 68:5357–5362, 1978.
- [99] K. P. Madden and W. A. Bernhard. ESR-ENDOR study of X-irradiated single-crystals of alpha-methyl-D-glucopyranoside. *J. Chem. Phys.*, 70:2431–2437, 1979.
- [100] H. Muto, K. Nunome, and M. Iwasaki. ENDOR studies of superhyperfine couplings of hydrogen-bonded protons .2. Protonated radical-anion in irradiated succinic acid single-crystals. *J. Chem. Phys.*, 61:1075–1077, 1974.

- [101] H. Muto, K. Nunome, and M. Iwasaki. ENDOR studies of superhyperfine couplings of hydrogen-bonded protons .3. Protonated radical-anions in irradiated L-valine hydrochloride monohydrate. *J. Chem. Phys.*, 61:5311–5314, 1974.
- [102] E. E. Budzinski, H. G. Freund, G. Potienko, and H. C. Box. The use of dipolar hyperfine couplings in studies of radiation effects. *J. Chem. Phys.*, 77:3910–3914, 1982.
- [103] E. E. Budzinski and H. C. Box. Alkoxy radicals: delta proton hyperfine couplings. *J. Chem. Phys.*, 82:3487–3490, 1985.
- [104] H. C. Box, E. E. Budzinski, and G. Potienko. Alkoxy radicals: γ proton hyperfine couplings. *J. Chem. Phys.*, 73:2052–2056, 1980.
- [105] A. J. Stone. Gauge invariance of g tensor. *Proc. R. Soc. A*, 271:424, 1963.
- [106] J. Y. Lee and H. C. Box. ESR and ENDOR studies of DL-serine irradiated at 4.2 °K. *J. Chem. Phys.*, 59:2509–2512, 1973.
- [107] H. C. Box and E. E. Budzinski. Primary radiation damage in thymidine. *J. Chem. Phys.*, 62:197–199, 1975.
- [108] S. E. Locher and H. C. Box. ESR-ENDOR studies of X-irradiated glucose-1-phosphate dipotassium salt. *J. Chem. Phys.*, 72:828–832, 1980.
- [109] P. O. Samskog and A. Lund. The alkoxy radical RCHO formed in irradiated single-crystals of rhamnose. *Chem. Phys. Lett.*, 75:525–527, 1980.
- [110] W. A. Bernhard, D. M. Close, J. Hüttermann, and H. Zehner. Alkoxy radical, RCH₂O, as a free-radical product in x-irradiated single crystals of nucleosides and nucleotides. *J. Chem. Phys.*, 67:1211–1219, 1977.
- [111] G. M. Brown and H. A. Levy. Further refinement of structure of sucrose based on neutron-diffraction data. *Acta Crystallogr., Sect. B: Struct. Sci*, 29:790–797, 1973.
- [112] T. Nakajima. Possibility of retrospective dosimetry for persons accidentally exposed to ionizing radiation using electron spin resonance of sugar and mother-of-pearl. *Br. J. Radiol.*, 62:148–153, 1989.
- [113] T. Nakajima and T. Ohtsuki. Dosimetry for radiation emergencies: radiation-induced free radicals in sugar of various countries and the effect of pulverizing on the ESR signal. *Appl. Radiat. Isot.*, 41:359–365, 1990.

- [114] T. Nakajima. ESR of sugar as personnel monitor for radiation emergencies. *Appl. Radiat. Isot.*, 46:819–825, 1995.
- [115] F. A. M. Silveira and O. Baffa. Lyoluminescence and ESR measurements on alanine and sucrose dosimeters. *Appl. Radiat. Isot.*, 46:827–830, 1995.
- [116] N. D. Yordanov and E. Georgieva. EPR and UV spectral study of gamma-irradiated white and burned sugar, fructose and glucose. *Spectrochim. Acta, Part A*, 60:1307–1314, 2004.
- [117] T. Nakajima. Sugar as an emergency dosimeter. *Health Phys.*, 55:951–955, 1988.
- [118] P. Fattibene, T. L. Duckworth, and M. F. Desrosiers. Critical evaluation of the sugar-EPR dosimetry system. *Appl. Radiat. Isot.*, 47:1375–1379, 1996.
- [119] M. Desrosiers and S. Wadley. Time dependence of the radiation-induced EPR signal in sucrose. *Radiat. Prot. Dosim.*, 118:479–481, 2006.
- [120] N. D. Yordanov. Quantitative EPR spectrometry – state of the art. *Appl. Magn. Reson.*, 6:241–257, 1994.
- [121] N. D. Yordanov, V. Gancheva, and E. Georgieva. EPR and UV spectroscopic study of table sugar as a high-dose dosimeter. *Radiat. Phys. Chem.*, 65:269–276, 2002.
- [122] C. J. Flores, E. B. Cabrera, T. Calderón, E. P. Muñoz, E. Adem, J. A. Hernández, J. L. Boldú, P. M. Ovalle, and H. S. Murrieta. ESR and optical absorption studies of gamma- and electron-irradiated sugar crystals. *Appl. Radiat. Isot.*, 52:1229–1234, 2000.
- [123] N. D. Yordanov and Y. Karakirova. Sugar/UV spectrophotometric system for high-energy dosimetry (0.055-160 kGy). *Radiat. Meas.*, 42:121–122, 2007.
- [124] N. D. Yordanov and Y. Karakirova. EPR of gamma irradiated solid sucrose and UV spectra of its solution. An attempt for calibration of solid state/EPR dosimetry. *Radiat. Meas.*, 42:347–351, 2007.
- [125] Y. Karakirova, A. Lund, and N. D. Yordanov. EPR and UV investigation of sucrose irradiated with nitrogen ions and gamma-rays. *Radiat. Meas.*, 43:1337–1342, 2008.
- [126] K. Nakagawa and T. Nishio. Electron paramagnetic resonance investigation of sucrose irradiated with heavy ions. *Radiat. Res.*, 153:835–839, 2000.

- [127] K. Nakagawa and Y. Sato. ESR investigation of sucrose radicals produced by particle irradiation. *Spectrochim. Acta, Part A*, 60:1315–1318, 2004.
- [128] K. Nakagawa and Y. Sato. Analyses of the EPR responses of sucrose and L- α -alanine radicals induced by C, Ne, and Ar ion irradiations. *Spectrochim. Acta, Part A*, 63:851–854, 2006.
- [129] K. Nakagawa, N. Ikota, and K. Anzai. Sucrose radical-production cross-section regarding heavy-ion irradiation. *Spectrochim. Acta, Part A*, 69:1384–1387, 2008.
- [130] E. E. Budzinski, W. R. Potter, G. Potienko, and H. C. Box. Characteristics of trapped electrons and electron traps in single crystals. *J. Chem. Phys.*, 70:5040–5044, 1979.
- [131] H. C. Box, E. E. Budzinski, and H. G. Freund. Electrons trapped in single-crystals of sucrose – induced spin-densities. *J. Chem. Phys.*, 93:55–57, 1990.
- [132] E. Sagstuen, A. Lund, O. Awadelkarim, M. Lindgren, and J. Westerling. Free radicals in X-irradiated single crystals of sucrose: a reexamination. *J. Phys. Chem.*, 90:5584–5588, 1986.
- [133] G. Vanhaelewyn, J. Sadlo, F. Callens, W. Mondelaers, D. De Frenne, and P. Matthys. A decomposition study of the EPR spectrum of irradiated sucrose. *Appl. Radiat. Isot.*, 52:1221–1227, 2000.
- [134] E. R. Georgieva, L. Pardi, G. Jeschke, D. Gatteschi, L. Sorace, and N. D. Yordanov. High-field/high-frequency EPR study on stable free radicals formed in sucrose by gamma-irradiation. *Free Radical Res.*, 40:553–563, 2006.
- [135] H. C. Box and E. E. Budzinski. A variation of the alkoxy radical. *J. Chem. Phys.*, 79:4142–4145, 1983.
- [136] P. O. Samskog, A. Lund, G. Nilsson, and M. C. R. Symons. Primary reactions of localized-electrons in rhamnose crystals studied by pulse-radiolysis and ESR spectroscopy. *J. Chem. Phys.*, 73:4862–4866, 1980.
- [137] P. O. Samskog, L. D. Kispert, and A. Lund. Geometric model of trapped electrons in X-ray-irradiated single-crystals of rhamnose. *J. Chem. Phys.*, 79:635–638, 1983.

- [138] H. C. Box, E. E. Budzinski, and H. G. Freund. Studies of electrons trapped in X-irradiated rhamnose crystals. *Radiat. Res.*, 121:262–266, 1990.
- [139] E. Sagstuen, M. Lindgren, and A. Lund. Electron trapping and reactions in rhamnose by ESR and ENDOR. *Radiat. Res.*, 128:235–242, 1991.
- [140] K. P. Madden and W. A. Bernhard. ESR-ENDOR study of alpha-deuterium-glucopyranose single-crystals X-irradiated at 12-K and 77-K. *J. Phys. Chem.*, 83:2643–2649, 1979.
- [141] K. P. Madden and W. A. Bernhard. Thermally induced free-radical reactions in alpha-D-glucopyranose single-crystals – An electron-spin resonance-electron nuclear double-resonance study. *J. Phys. Chem.*, 86:4033–4036, 1982.
- [142] K. P. Madden and W. A. Bernhard. Free-radical reactions in alpha-methyl-D-glucoside – ESR-ENDOR study. *Radiat. Res.*, 74:486, 1978.
- [143] K. P. Madden and W. A. Bernhard. ESR-ENDOR study of X-irradiated alpha-methyl-D-glucopyranoside single-crystals at 12-K – Influence of hydrogen-bonding on primary alcohol group radiation-chemistry. *J. Chem. Phys.*, 72:31–33, 1980.
- [144] B. Bungum, E. O. Hole, E. Sagstuen, and M. Lindgren. Electron-paramagnetic-resonance of X-irradiated sodium and potassium-salts of glucose-1-phosphate – identification of PO₃²⁻ radicals at room-temperature. *Radiat. Res.*, 193:194–202, 1994.
- [145] B. Bungum. Radiation induced radicals in glucose-1-phosphate studied using ESR and ENDOR techniques (in Norwegian). Master's thesis, Department of Physics, University of Oslo, Norway, 1992.
- [146] G. Vanhaelewyn, E. Pauwels, F. Callens, M. Waroquier, E. Sagstuen, and P. Matthys. Q-band EPR and ENDOR of low temperature X-irradiated beta-D-fructose single crystals. *J. Phys. Chem. A*, 110:2147–2156, 2006.
- [147] M. Tarpan, E. Sagstuen, E. Pauwels, H. Vrielinck, M. Waroquier, and F. Callens. Combined electron magnetic resonance and density functional theory study of 10 K X-irradiated beta-D-fructose single crystals. *J. Phys. Chem. A*, 112:3898–3905, 2008.
- [148] P-O. Samskog, L. D. Kispert, and A. Lund. An electron-spin-resonance study of 77 K alkoxy and hydroxyalkyl radicals in X-ray-irradiated trehalose single-crystals. *J. Chem. Phys.*, 77:2330–2335, 1982.

- [149] P-O. Samskog, L. D. Kispert, and A. Lund. Geometric model of trapped electrons in trehalose single crystals x ray irradiated at 3 K. An EPR study. *J. Chem. Phys.*, 78:5790–5794, 1983.
- [150] P. Moens, P. Devolder, R. Hoogewijs, F. Callens, and R. Verbeeck. Maximum-likelihood common-factor analysis as a powerful tool in decomposing multicomponent EPR powder spectra. *J. Magn. Reson.*, 101:1–15, 1993.
- [151] H. C. Box, E. E. Budzinski, and H. G. Freund. Electron trapping in irradiated single crystals of organic compounds. *J. Chem. Phys.*, 69:1309–1311, 1978.
- [152] H. C. Box, E. E. Budzinski, H. G. Freund, and W. R. Potter. Trapped electrons in irradiated single crystals of polyhydroxy compounds. *J. Chem. Phys.*, 70:1320–1325, 1979.
- [153] H. C. Box and H. G. Freund. Electron spin resonance and electron nuclear double resonance spectroscopy: application to the study of trapped electrons. *Appl. Spectrosc.*, 34:293–295, 1980.
- [154] H. C. Box, E. E. Budzinski, and H. G. Freund. Studies of electrons trapped in X-irradiated rhamnose crystals. *Radiat. Res.*, 121:262–266, 1990.
- [155] H. C. Box, H. G. Freund, and E. E. Budzinski. An unusual electron trapping site in the crystal-structure of dulcitol. *Radiat. Res.*, 122:137–141, 1990.
- [156] P-O. Samskog, A. Lund, and G. Nilsson. Localized-electrons in 1,8-octanediol crystals studied by electron-spin-resonance spectroscopy and pulse-radiolysis. *Chem. Phys. Lett.*, 79:447–451, 1981.
- [157] E. E. Budzinski, W. R. Potter, and H. C. Box. Radiation effects in X-irradiated hydroxy compounds. *J. Chem. Phys.*, 72:972–975, 1980.
- [158] G. Lippert, J. Hutter, P. Ballone, and M. Parrinello. Response function basis sets: application to density functional calculations. *J. Phys. Chem.*, 100:6231–6235, 1996.
- [159] S. Goedecker, M. Teter, and J. Hutter. Separable dual-space Gaussian pseudopotentials. *Phys. Rev. B*, 54:1703–1710, 1996.
- [160] C. Hartwigsen, S. Goedecker, and J. Hutter. Relativistic separable dual-space Gaussian pseudopotentials from H to Rn. *Phys. Rev. B*, 58:3641–3662, 1998.

- [161] G. Vanhaelewyn, B. Jansen, E. Pauwels, E. Sagstuen, M. Waroquier, and F. Callens. Experimental and theoretical electron magnetic resonance study on radiation-induced radicals in α -L-sorbose single crystals. *J. Phys. Chem. A*, 108:3308–3314, 2004.
- [162] E. Pauwels, R. Declerck, V. Van Speybroeck, and M. Waroquier. Evidence for a Grotthuss-like mechanism in the formation of the rhamnose alkoxy radical based on periodic DFT calculations. *Radiat. Res.*, 169:8–18, 2008.
- [163] C. A. Beevers and G. H. Maconochie. The crystal structure of dipotassium glucose-1-phosphate dihydrate. *Acta Crystallogr.*, 18:232–236, 1965.
- [164] N. Narendra and M. A. Viswamitra. Structure of the dipotassium glucose 1-phosphate dihydrate $C_6H_{11}O_9P_2 \cdot 2K \cdot 2H_2O$. *Curr. Sci.*, 53:1018–1020, 1984.
- [165] Y. Sugawara and H. Iwasaki. Structure of disodium uridine diphosphoglucose dihydrate, $C_{15}H_{22}N_2O_{17}P_2 \cdot 2Na \cdot 2H_2O$, and refinement of dipotassium glucose 1-phosphate dihydrate, $C_6H_{11}O_9P_2 \cdot 2K \cdot 2H_2O$ (monoclinic form). *Acta Crystallogr., Sect. C: Cryst. Struct. Commun.*, 40:389–393, 1984.
- [166] D. J. Nelson, M. C. R. Symons, and J. L. Wyatt. Electron-paramagnetic-resonance studies of irradiated D-glucose-6-phosphate ions – relevance to DNA. *J. Chem. Soc. Faraday Trans.*, 89:1955–1958, 1993.
- [167] A. Sanderud and E. Sagstuen. EPR study of X-irradiated hydroxyalkyl phosphate esters – phosphate radical formation in polycrystalline glucose phosphate, ribose phosphate and glycerol phosphate salts at 77 and 295 K. *J. Chem. Soc. Faraday Trans.*, 92:995–999, 1996.